FOSSIL ENERGY

DOE/BC/14653-3
(DE95000111)

INNOVATIVE TECHNIQUES FOR THE DESCRIPTION OF RESERVOIR HETEROGENEITY USING TRACERS

Final Report for the Period
October 1992 to December 1993

By
Gary A. Pope
Kamy Sepehrnoori
Mojdeh Delshad
Luiz Ferreira
Akhil Gupta
Vichai Maroongroge

November 1994

Performed Under Contract No. DE-AC22-90BC14653

University of Texas
Austin, Texas

Bartlesville Project Office
U. S. DEPARTMENT OF ENERGY
Bartlesville, Oklahoma

DISCLAIMER

This report was prepared as an account of work sponsored by an agency of the United States Government. Neither the United States Government nor any agency thereof, nor any of their employees, makes any warranty, expressed or implied, or assumes any legal liability or responsibility for the accuracy, completeness, or usefulness of any information, apparatus, product, or process disclosed, or represents that its use would not infringe privately owned rights. Reference herein to any specific commercial product, process, or service by trade name, trademark, manufacturer, or otherwise does not necessarily constitute or imply its endorsement, recommendation, or favoring by the United States Government or any agency thereof. The views and opinions of authors expressed herein do not necessarily state or reflect those of the United States Government or any agency thereof.

This report has been reproduced directly from the best available copy.

Available to DOE and DOE contractors from the Office of Scientific and Technical Information, P.O. Box 62, Oak Ridge, TN 37831; prices available from (615) 576-8401.

Available to the public from the National Technical Information Service, U.S. Department of Commerce, 5285 Port Royal Rd., Springfield VA 22161

DOE/BC/14653-3
Distribution Category UC-122

INNOVATIVE TECHNIQUES FOR THE DESCRIPTION OF RESERVOIR HETEROGENEITY USING TRACERS

Final Report for the Period
October 1992 to December 1993

by
Gary A. Pope
Texaco Centennial Chair in Petroleum Engineering

Kamy Sepehrnoori
Frank W. Jessen Professor in Petroleum Engineering

Research Associate
Mojdeh Delshad

Graduate Students
Luiz E.A Ferreira, Akhil Datta Gupta, and Vichai Maroongroge

Work Performed Under Contract No. DE-AC22-90BC14653

Prepared for
U.S. Department of Energy
Assistant Secretary for Fossil Energy

Chandra M. Nautiyal, Project Manager
Bartlesville Project Office
P.O. Box 1398
Bartlesville, OK 74005

Prepared by
The University of Texas
Center for Petroleum and Geosystems Engineering
Department of Petroleum Engineering
Austin, TX 78712

TABLE OF CONTENTS

LIST OF FIGURES

SECTION 1

LIST OF TABLES

ABSTRACT

This is the final report of a three year research project on the use of tracers for reservoir characterization. The objective of this research was to develop advanced, innovative techniques for the description of reservoir characteristics using both single-well backflow and interwell tracer tests. Both chemical and miscible compositional reservoir simulators developed at The University of Texas were used as tools in this research and have been improved significantly. The application of the innovative tracer technology to the Elk Hills Naval Petroleum Reserve was also evaluated. The final accomplishments of this project substantially exceeded those promised in the original research proposal to DOE. The following is a summary of the most significant accomplishments:

(1) We implemented and validated tracer modeling features in our compositional simulator (UTCOMP). We have demonstrated the feasibility and usefulness of using tracers under complex flow conditions involving multiple phases with mass transfer and other compositional changes such as actually occur in multiple contact miscible floods with carbon dioxide and other solvents used in enhanced oil recovery.

(2) We developed and applied a new single well tracer test for estimating reservoir heterogeneity. Our chemical flooding compositional simulator (UTCHEM) was used to do this research.

(3) We developed and applied a new single well tracer test for estimating reservoir wettability in-situ. This research shows how reliable estimates of relative permeability and other characteristics of the reservoir related to wettability can be determined from short single well tracer tests. This test is currently scheduled for field testing as part of another project.

(4) We developed a new, simple and efficient method to analyze two well tracer tests based upon type curve matching and illustrated its use with actual field tracer data.

(5) We developed a new method for deriving an integrated reservoir description based upon combinatorial optimization schemes. This method allows tracer data to be included with other reservoir characterization data simultaneously to optimize the reservoir description. This approach is a versatile and powerful solution of the difficult inverse problem.

(6) We developed a new interwell tracer test for reservoir heterogeneity called vertical tracer profiling (VTP) and demonstrated its advantages over conventional interwell tracer testing. This method was evaluated using the combinatorial optimization schemes and tested against our own experimental laboratory data on heterogeneous sandstone slaps that have been characterized using a minipermeameter, tracers, pressure data and production data from both waterfloods and polymerfloods.

(7) We developed a simple and easy analytical method to estimate swept pore volume from interwell tracer data and showed both the theoretical basis for this method and its practical utility. We also have shown how this idea can be applied to estimating saturations from partitioning tracer data without the need to solve the complex flow simulation problem.

(8) We made numerous enhancements to our compositional reservoir simulator such as including the full permeability tensor, adding faster solvers, improving its speed and robustness and making it easier to use (better I/O) for tracer simulation problems. Numerous other enhancements were made during the same three years as part of associated industrially sponsored research projects with the Center for Petroleum and Geosystems Engineering at the University of Texas, for example, the addition of horizontal well modeling.

(9) We applied the enhanced version of UTCOMP to the analysis of interwell tracer data using perfluorocarbons at Elks Hill Naval Petroleum Reserve. This is the first time that this new

Brookhaven tracer technology has been evaluated quantitatively with a tracer model and the first time that residual oil saturations have been estimated using these tracers. These were both very large and geologically complex reservoirs undergoing gas injection.

All of these accomplishments taken together have significantly improved the state of reservoir tracer technology and have demonstrated that it is a far more powerful and useful tool for quantitative reservoir characterization than previously realized or practiced by the industry. Applications of this technology should result in better reservoir management, higher oil recovery, lower costs and lower risks, all of which are vital to the future of the domestic oil industry. The greatest challenge now is the effective transfer of this technology to the working reservoir engineer.

EXECUTIVE SUMMARY

The tracer features in UTCOMP include the capabilities of modeling physical dispersion, partitioning, radioactive decay, adsorption, capacitance, and chemical reactions. UTCOMP development has continued and several significant improvements have been made in the code. These improvements have the combined effect of making the code more versatile and efficient, which serves not only our needs better but that of a large number of external users. These users consist of not only the industrial sponsors of our enhanced oil recovery research at The University of Texas at Austin, but also a large and increasing number of academic users who use our code in a variety of oil recovery research. These users now include the following organizations:

ADREF	Ames Laboratory
Amoco Production Co.	ARAMCO
Arco Oil & Gas Co.	BP Exploration, Inc.
Brookhaven National Laboratory	Conoco, Inc.
Cray Research	Delft University of Technology
Duke University	Elf Aquitaine
Exxon Production Research Company	Idaho National Laboratories
Institute for Energy Technology	INTERA, Inc.
INTEVEP, S.A.	Japan National Oil Corp.
Japan Petroleum Exploration Co., Ltd.	Louisiana State University
Louisiana Tech University	Mobil Exploration and Producing Services
New Mexico Recovery Research Center	Norsk Hydro
Oryx Energy Co.	Oxy USA, Inc.
Pacific Northwest Laboratories	Rice University
Rogaland Research Institute	Sandia National Laboratories
Santa Fe Energy Resources	Scientific Computing Associates, Inc.
Shell Development Co.	Stanford University
Statoil	Technical University of Clausthal, Germany
Technical University of Denmark	Texaco, Inc.
Union Pacific Resources	University of Alaska
University of Houston	University of Michigan
University of Mining and Metallurgy — Poland	University of Oklahoma
University of Reading — England	University of Tulsa
UNOCAL	

A significant effort is required to provide the code and its documentation to these users as well as some support on its use. However, we do benefit from feedback from these users and occasionally even new features to the code.

The innovative techniques for the description of reservoir characteristics using both single-well backflow and interwell tracer tests that have already been reported are a new single-well tracer test for estimating in-situ wettability (Ferreira et al., 1992) and a new single-well tracer test for estimating heterogeneity (Ferreira, 1992) and a new simple and efficient method to analyze two-well tracer tests based on type curve matching (Datta Gupta, 1992; Datta Gupta *et al.*, 1992) and a method for deriving integrated reservoir description based on combinatorial optimization schemes (Datta Gupta, 1992; Pope and Sepehrnoori, 1993; Sen *et al.*, 1992). This final report is the continuation of the innovative techniques for the description of reservoir characteristics and is divided into four sections. The first section discusses the use of a new interwell tracer test for reservoir heterogeneity (vertical tracer profiling) with combinatorial optimization schemes for deriving integrated reservoir description (Pope and Sepehrnoori, 1993; Maroongroge, 1994). The second section is a simple and easy technique of estimating swept volume and residual oil saturation from interwell tracer data (Maroongroge, 1994). The application of this technique to the new interwell tracer test (vertical tracer profiling) is also discussed. In the third section, we discuss an application of the newly developed tracer features in UTCOMP to simulate two interwell gas tracer tests at Elk Hills Naval Petroleum Reserve. The new perfluorocarbon gas tracer technologies used in this interwell test have been developed at Brookhaven National Lab. Results of this simulation study will help in designing a better gas injection scheme to improve oil recovery at Elk Hills Naval Petroleum Reserve. The fourth section gives the results of a new automated history matching procedure for the novel single well tracer test previously developed and reported as part of this project (Pope and Sepehrnoori, 1993). This procedure is a fast and robust method to simultaneously estimate both the residual saturations and relative permeability parameters from the single well wettability tracer test data.

SECTION I
STOCHASTIC RESERVOIR MODELING WITH VERTICAL TRACER PROFILING

SUMMARY

A tracer test where tracers were injected or samples were collected at different locations along the depth of a reservoir was investigated. This is called vertical tracer profiling (VTP) in this report. Stochastic permeability fields generated using information from this tracer test together with a combinatorial optimization called simulated annealing based on the Metropolis algorithm were compared with fields generated using other information. The known field used in this comparison was measured on a sample of Antolini sandstone. The effectiveness of each generated field was evaluated and compared with experimental waterflood and polymerflood data. In the case where the actual vertical variogram was known, results showed that adding tracer data from either a conventional tracer test or VTP could improve the quality of the generated stochastic fields. The horizontal variograms from generated fields were always higher than the data. The closest in terms of shape and values to the data was obtained using VTP. In the case where the actual vertical variogram was unknown, use of VTP could generate a field with a similar vertical variogram to the data. All the generated fields were shown to be effective in matching waterflood and polymerflood data. The computational time required and the complexities of solving this inverse problem are discussed.

INTRODUCTION

An interwell tracer test is done by injecting tracer at one well and producing it at a second well nearby. Tracer production data can be related qualitatively to the flow behavior in a reservoir. Faults, flow barriers, and fluid communication among layers within or between reservoirs can be detected. Numerous papers have been published on using tracer data to characterize a reservoir. In this report, the tracer production data measured at one location will be called an integrated tracer breakthrough curve. Detailed information about layers, flow barriers, and channels in the reservoir may be hidden under this integrated curve.

We propose another kind of tracer test where tracer samples are injected or collected at different locations along the depth of the reservoir. The difference between this kind of tracer test and the conventional tracer test is that tracers are injected or collected at more than one location. In groundwater and hydrology, simulation and field applications of this technique, including both a single-well and two-well tracer test, have been used to evaluate the mean, the apparent permeability ratio among layers, dispersivity, and the position of a no-flow boundary (Pickens *et al.*, 1978, 1981; Huyakorn *et al.*, 1986). By injecting radioactive tracers in an injector together with a logging tool in observation wells located between an injector and a producer, the preferential flow path , injection profile, and width of each zone can be detected. This has been done successfully in the oil field by Shell (Gesink *et al., 1983*), Exxon (Stiles *et al.*, 1983), and Conoco (Albright, 1984). This information is then used to develop a reservoir model for further enhanced oil recovery programs. A combination of injecting different tracers at different depths and making measurements at different depths, either from logs or from samples, can provide much more information than a single integrated measurement. In this report, this kind of tracer test will be called VTP. Because of the difficulty of this problem, this technique has been used by others in only a qualitative manner based on the assumption of no crossflow between layers. There are no publications on general methods for using information to obtain the permeability distribution of a reservoir. For the case of no crossflow, one can see that a ratio of average permeabilities between layers can be calculated directly from the ratio of breakthrough times of tracers. A problem arises in the case of high crossflow, where fluid in the high-permeability layer moves slower and fluid in the low-permeability layer moves faster than in the case of no crossflow. Thus, a permeability ratio cannot be related directly to the ratio of travel times or the first moment of tracer data from

each layer. We will investigate if it is still possible to use this information to characterize a reservoir.

The main objective of this research is to investigate the advantages of using more information from VTP compared to less information from the conventional tracer test. What information can be gained by making more measurements? We will show how the inverse problem can be solved to obtain the permeability distribution of a given reservoir using different measurements. However, these results should be considered only preliminary since much more needs to be done along this line of research.

PROBLEM STATEMENT

Given a frequency histogram or frequency distribution of permeability for a reservoir, is it possible to find an arrangement or structure of these permeabilities? What kind of information will be needed to solve this problem? Using a geostatistical technique, a permeability field can be generated by specifying the variance of the permeability and correlation lengths. Multiple realizations can be generated by varying the seed number of a random number generator. By making multiple simulation runs with different realizations and averaging the results, an error band can be obtained. This creates some difficulties in selecting the correct reservoir model. These permeability fields may not lead to the correct flow characteristics of the reservoir. There is a need to develop a good reservoir model that is less ambiguous and satisfies both the statistical properties and flow behavior of the reservoir. Tracers are useful for this purpose, especially if VTP is used, but what is the best way to use and analyze these data?

APPROACH

Permeability fields generated using different sources of information such as horizontal variogram, vertical variogram, integrated tracer breakthrough curve, and VTP will be compared. The effectiveness of each permeability field will be evaluated using experimental waterflood and polymerflood data. A combinatorial optimization called simulated annealing based on the Metropolis algorithm will be used to generate these permeability fields, minimizing different objective functions. The complexities and difficulties in applying this optimization algorithm will be discussed. The objective function is calculated by summing the squares of the differences between known values and calculated values at each iteration. These values are

(a) horizontal and vertical variograms,
(b) vertical variogram,
(c) vertical variogram together with integrated tracer breakthrough curve,
(d) vertical variogram together with VTP, and
(e) only tracer data from VTP.

First, a known permeability field is needed in order to evaluate the success of a generated field. This known permeability field can come from a laboratory measurement or be generated using a geostatistical technique. The one selected for this report comes from face D of a heterogeneous Antolini sandstone core (Experiment AN-4). The reason is that in this experiment the heterogeneous Antolini sandstone can be represented using a small number of gridblocks (NX $\times$ NY $\times$ NZ = 38 $\times$ 1 $\times$ 14). Experimental data on waterflooding and polymerflooding are also available for fluid-flow behavior comparison. This experiment was performed by Wang (1994). The dimensions of the core and measured core properties are shown in Table 1. Figure 1 shows the distribution of known permeabilities measured using a minipermeameter for each square centimeter. The data showed that both faces of the core have similar permeability distributions. Figures 2 and 3 show the histogram of permeability and the known vertical and horizontal variograms.

The experiment was conducted in the following steps. First, the core was saturated with 100% brine and then a primary tracer test was conducted. Figure 4 shows the primary tracer test

data. The tracer slug size was 5.62 pore volumes. The next step was the first oilflood, which continued until no more water was produced. Then a waterflood was carried out. The endpoint mobility ratio for the waterflood was 1.2. A summary of waterflood data is given in Table 2. All the values were obtained from experiment except for the two exponents of the permeability curves, which were obtained by a history match of the oil recovery using the measured permeability field. Figure 5 shows the estimated relative permeability curves. The experimental and simulated oil recoveries are compared in Fig. 6. This should be considered a preliminary result, since other parameters such as pressure drop should be considered in estimating the permeability curves.

After the waterflood was completed, a second oilflood then followed. Polymerflooding was initiated by injecting a solution of 0.2 wt % (2,000 ppm) active polymer Naflo 3837. The polymer was injected continuously until no more oil was produced. A summary of polymerflood data is given in Table 3. Figure 7 shows relative permeability curves used in the simulation of the polymerflood. The experimental and simulated oil recoveries are compared in Fig. 8. Polymer viscosity vs. polymer concentration data were fitted using a three-parameter model. Measured polymer viscosity at zero shear rate and shear rate at which polymer viscosity became half of polymer viscosity at zero shear were obtained from experiment. Other parameters such as polymer inaccessible pore volume, polymer adsorption, and polymer shear rate coefficient were obtained from correlations (Ganapathy *et al.*, 1991; Wreath, 1989). The increase in oil recovery for polymerflooding is attributed to a decrease in the residual oil saturation. The final oil saturation was 4 saturation percent lower after polymerflooding than after waterflooding starting at the same initial oil saturation. See Wang (1994) for a discussion of this aspect. The ultimate oil recovery was reached in 0.5 pore volumes compared to 1.5 pore volumes for waterflooding.

Simulation of waterflooding and polymerflooding of a homogeneous field are shown in Figs. 9 to 11. The scatter in water-oil ratio data at the end of the waterflood results from the small amount of oil produced compared to water. The amount of oil produced at the end of the waterflood was in the range of 0.1 cc, which was about the accuracy of the measurement. Simulation of polymerflooding for the homogeneous field shows that this polymerflood is not a good displacement process to evaluate the effectiveness of generated permeability fields, because the low mobility ratio decreases the sensitivity of the oil recovery to permeability variations, just as it is designed to do. We include these results to complete the analysis of Experiment AN-4 and to emphasize that the effect of heterogeneity on oil recovery is process-dependent and that polymerflooding can greatly improve oil recovery. For all runs, the same starting permeability field, shown in Fig. 12, was used.

The objective of optimization is to improve the existing solutions using all the information available. Simulated annealing is an approximation algorithm used to solve difficult combinatorial problems where no exact solution can be found. A problem is said to be satisfactorily solved when the solutions can be obtained within a reasonable amount of time. More information about this algorithm can be found elsewhere (Aarts, 1989; Garey, 1979; Kirkpatrick, 1983; Johnson, 1989, 1991; Van Larrhoven, 1987). Our initial effort in this project was completed by Datta Gupta (1992), who applied simulated annealing and genetic algorithms to generate stochastic permeability fields using the vertical variogram and the integrated tracer curve. The use of the genetic algorithm (Goldberg, 1989; Sen *et al.*, 1992), which generates multiple starting configurations and combines the best portion of each configuration to generate a new set of better configurations is a good approach if parallel computing is used.

Simulated annealing is a randomized search algorithm or a search with a probability. It is used in a combinatorial optimization where the variables are discrete and no derivative of the objective function is available. A direct-search algorithm that moves only in the direction of lower objective function (for minimization) will converge to a local minimum depending on the starting point. Allowing an algorithm to make mistakes can improve the final solution. This is done by adding probability to a direct search. The probability can be exponential or linear, and it contains a parameter T (which was temperature in the original applications). As the number of iterations increases, this parameter T is reduced, because once the global minimum is reached, we do not want to jump out of the global minimum. The rate at which this parameter T is reduced is called a cooling schedule. The quality of the solution and the amount of computational time depend on the

cooling schedule and the initial starting temperature, which is problem-dependent and has to be determined by trial and error or numerical experiment. Several authors recommend using an initial starting temperature that results in at least 98% successful moves. Johnson (1989, 1991) performed a numerical experiment with a cooling schedule that showed that for a graph-coloring problem, a successful move of at least 45% was needed, but to be conservative, he recommended a starting temperature with 70% successful moves. The suggested cooling rate was between 0.90 and 0.98 of the previous temperature. Like any other algorithm that uses probability, repeated runs are needed to ensure that the solution is close to or near optimum.

The iteration is started by randomizing or rearranging permeabilities of a known permeability field. The initial field used in this case is shown in Fig. 12. The quality of the solution does not depend on the initial starting field when the starting parameter T is high. At each iteration, the starting field is perturbed by randomly selecting two gridblocks and interchanging the values. Other forms of perturbing the field have been investigated, such as randomly drawing permeability values from a given distribution, or fixing and not fixing the maximum and minimum permeability values. A random number between zero and one is also generated at each iteration. Once the field is perturbed, a new objective function is calculated based on this perturbed field. The difference between the objective function at the new iteration and the last iteration is calculated. If it has decreased, the perturbation is accepted as a new field. If it has not, calculate the probability based on the parameter T and the change in objective function from the previous iteration. If the probability is higher than the random number, the new perturbed field is accepted. The procedure is repeated for a new lower temperature until the desired tolerance is reached. The perturbed field is considered frozen when less than 2% successful moves are obtained consecutively five times.

Run (a) Minimize the Difference Using Known Horizontal and Vertical Variograms

This run was made as a base case for comparison with other runs. There are two reasons for making this run. First, simulated annealing is an approximate algorithm. If the size of a problem is small, it will give an exact solution as with any direct search or greedy algorithm. As the size of problem grows, it will find a good solution close to but not necessarily the same as the known permeability field. To appreciate how well this algorithm works, one must look at the total possible configurations or arrangements of permeabilities. Given n gridblocks to be arranged, there are n! configurations possible. This algorithm will take many fewer iterations than n! to give a reasonable solution. The number of iterations will be discussed below when evaluating the results. Because reservoir horizontal variograms are usually unknown, any permeability fields that give the same flow characteristics as the field obtained from minimizing horizontal and vertical variograms will be considered good solutions. Figure 13 shows an excellent match of both vertical and horizontal variograms for Experiment AN-4. Figure 14 shows the permeability distribution of the generated field. Figure 15 shows the h-scatter plot of this field compared to the known data for each gridblock. If exact solutions were generated, all the points would fall on a 45° line. This case shows that given the histograms of permeability and the vertical and horizontal variograms, simulated annealing will give only approximate solutions. Figure 16 shows a comparison between the measured and simulated tracer responses for this field after matching the horizontal and vertical variograms. The simulated tracer curve is almost the same as when the experimental permeability field was used, which indicates that using both vertical and horizontal variograms is sufficient for this purpose.

Run (b) Minimize the Difference Using Known Vertical Variogram

This run shows that in general using only a vertical variogram will not be enough to obtain a good permeability field. Figure 17 shows the permeability field at the end of a simulated annealing run. Figure 18 shows the vertical and horizontal variograms for this generated field. Even though the vertical variogram matches the data, the permeability distribution does not show the continuity in the horizontal direction that the actual sandstone shows. Multiple runs have been made, and each run gave a different result, but still did not show continuity in the horizontal

direction. These results show that the permeability field obtained from minimizing the known vertical variogram is not unique. Thus, other sources of data that contain information about continuity in the horizontal direction are needed to improve the generated permeability field. One advantage of minimizing only the vertical variogram is the small amount of computational time that it takes to reach the solutions. For each CPU second on the CRAY-YMP, about 5,000 iterations can be made. The total run can be accomplished in just over 100 CPU seconds. This CPU time can be reduced if the code is made more efficient and the optimum cooling schedule is used, but the optimum cooling schedule is problem-dependent. Since it was not within the scope of this report to find the optimum starting temperature and the optimum cooling schedule, a more conservative cooling schedule was used. The starting temperature was chosen so that the number of successful moves would be 98%. The slow cooling rate of 0.95 times the previous temperature and 2,000 iterations for each temperature step was used. At high temperature, the maximum number of iterations was limited to 1,000.

Run (c) Minimize the Difference Using Known Vertical Variogram Together with an Integrated Tracer Breakthrough Curve

This run represents one of the best runs using a vertical variogram together with an integrated tracer breakthrough curve. The field obtained using this method shows more continuity in the horizontal direction than using only the vertical variogram. The generated permeability field is shown in Fig. 19. Figure 20 shows the vertical and horizontal variograms of this field. Figure 21 shows the integrated tracer breakthrough curve compared to the data. Although both the vertical variogram and the integrated tracer breakthrough curve show good agreement with the data, the horizontal variogram is higher than the data. In this run and the next two runs, the cooling rate was reduced to 0.9 and the maximum number of iterations at high temperature was reduced to 500 to save computational time.

Run (d) Minimize the Known Vertical Variogram Together with VTP

The known tracer responses at different locations in this run were obtained from simulation since no data for VTP was available. First, a simulation run was carried out to obtain the known VTP data. In this simulation, one tracer was injected across the face of the core and the measurement was assumed to be taken from each layer. The objective function was the sum of the squares of the differences of vertical variograms plus 13 tracer responses. Figure 22 shows the calculated permeability field from this run. The calculated permeability field also shows more continuity in the horizontal direction than by matching only the vertical variogram. Figure 23 shows the vertical and horizontal variograms of this generated field. This horizontal variogram is the closest to the data of any of the runs made in this study. The smoothness of this horizontal variogram is clearly seen from Fig. 23.

There were some difficulties in simultaneously matching so many curves. The match was not so good as when matching only the vertical variogram together with an integrated curve. To see how well the match compared to Run (c), all of the 13 tracer responses were summed to give an integrated curve. Figure 24 shows the integrated curve from this run compared to the data. We also simulated VTP using the field from Run (c) to see how well the tracer responses from each layer would match those of simulated data. The match for each layer was not good.

For Runs (a) to (d), we made an assumption that the vertical variogram was known. Our experience is that the quality of the solutions depends a lot on the vertical variogram. In actual reservoir applications, information about the vertical variogram is obtained from logs and core data at well locations, and these may not be very accurate or may not be available at all wells. This motivated us to investigate how VTP could provide information about the vertical and horizontal variograms.

Run (e) Minimize the Known Tracer Data from VTP

In this run, the simulated tracer test was done by injecting each layer with one tracer. A total of 13 different tracers were simulated. The tracer responses were calculated at a single location (surface location). Therefore, the total of 13 tracer-breakthrough curves were generated.

These tracer responses were calculated by summing all streamlines originating from each gridblock at the injector.

This run was made to investigate if VTP can be used in the case where the vertical variogram is not available or not reliable. The objective function is to minimize sum of the squares of the differences of all the known and calculated 13 tracer breakthrough curves at each iteration. Figures 25 to 35 show the 13 calculated tracer responses compared to the synthetic data. Figure 36 shows the calculated permeability field. As one can see, the major features of low permeability streaks at the top followed by series of high- and low-permeability streaks are present. Although the generated permeability field only shows qualitative resemblance to the known field, it shows much improvement from the starting random field. Figures 37 and 38 show the vertical and horizontal variograms from this field. The vertical variogram shows some resemblance with the known vertical variogram. The major difference is at a lag distance of 12 cm, where the highest contrast of permeability values occur. As in other runs, the horizontal variogram shows higher values than the known horizontal variogram. This run took approximately 10 CPU hours on our IBM RISC-6000/530 workstation.

EVALUATING THE EFFECTIVENESS OF PERMEABILITY FIELDS FROM SIMULATED ANNEALING

In order to compare how good each permeability field is, the same physical data given in Tables 2 and 3 were used in all runs. For comparison purposes only, a homogeneous field result is also shown.

Comparison with AN-4 Waterflood Data

Figures 39 through 42 show the oil recovery and water oil ratio as functions of pore volume for the homogeneous case, the known permeability field, Run (a), and Run (b). Oil recovery and water oil ratio from Runs (c) and (d) are shown in Figs. 43 to 46. Figures 47 and 48 show results from Run (e). All the water-oil ratios computed using different fields agree with the experimental data except Run (b). Gravity also does not affect the recovery because the pressure head is small.

Comparison with AN-4 Polymerflood Data

Figure 49 shows the oil recovery for polymerflooding for all the fields. The displacement is piston-like and thus heterogeneity has little or no effect on oil recovery. Thus, this is not a good comparison when evaluating the effectiveness of different fields. But it does show that one can virtually eliminate moderate degrees of heterogeneity by using polymer.

DISCUSSION

Minimizing the tracer response requires a lot of computational time. Each tracer response is equivalent to one simulation run. At each perturbation, a new pressure field is required. Although we have used an efficient solver together with an efficient semianalytical technique (Datta Gupta, 1992) to solve for tracer concentrations, the total CPU time is still very large, since so many simulations are required. Without the use of the semianalytical technique, it is not possible to complete a run. As shown by Johnson (1989, 1991) in his graph-coloring problem, many iterations can be saved by using a good starting configuration. Starting the iteration by minimizing the vertical variogram first and then optimizing the tracer response together with the vertical variogram at a low temperature may not give a solution as good as starting the field at a high temperature. The reason is that the field obtained from minimizing the vertical variogram may not contain information about the known field (as shown in Fig. 17) and thus it may not be a correct path leading to the solution. To take full advantage of this method, one has to start the iteration using a field closer to the known field. Another problem is the difficulty in choosing a good starting temperature. If the starting temperature is too high, randomization will occur. If the temperature is chosen too low, the field will be frozen. Experimenting with different starting

temperatures is then required if one desires to start the iteration at a low temperature.

For each CPU second on the CRAY-YMP, four iterations or simulations were performed. The total number of iterations required is generally in the order of 60,000 (this number of iterations is a very small fraction of the total number of possible solutions). The number of iterations required can vary depending on the starting temperature, the cooling schedule used, and the stopping criteria. For this size of problem (number of blocks NX × NY × NZ= 494), it will require 10,000 seconds or more on the CRAY-YMP. Many runs have also been made using our IBM-RISC 6000. If running in batch mode, it takes approximately one day to complete a run on this RISC 6000.

More than 20 permeability fields have been investigated by minimizing the vertical variogram together with an integrated tracer breakthrough curve and also with VTP. The results always show an improvement over using just the vertical variogram, but still not close to the known field. The main features, such as high- and low-permeability streaks, can be seen.

Because the information about crossflow and the vertical variogram is contained in the tracer data from VTP, we speculate that a better field should be generated using this information. There are two reasons why, using more information, Run (d) did not give much improvement over using less information, Run (c). The first one is that we cannot fully match all 13 tracer responses as well as we matched one integrated curve. Since there are more functions to be matched, more computational time is required. The computational time required to match one curve is already very great. Therefore, it is not practical to reduce the cooling schedule further. (Another method that is more efficient and practical is being investigated to utilize additional tracer data.) The second reason is the assumption of a known vertical variogram in Run (c), which is contained in the VTP. In any case, the flow behavior of the fields generated using either an integrated breakthrough curve or VTP agree with the single-phase flow of tracer data and also waterflooding data.

Tracer data from VTP are shown to be an important tool to generate a field that gives the same flow behavior for both single-phase and two-phase displacements as does the known field without making any assumption about the known vertical variogram. Although we have not shown any results using only an integrated curve for comparison, experience with other permeability fields show more randomness after matching only the integrated curve.

We have presented the results of permeability fields obtained from using different sources of information together with the fluid-flow behavior in these fields. Oil recovery and water-oil ratio show excellent agreement with the experimental data for waterflooding. For polymerflooding, the displacement is favorable and thus heterogeneity has little effect on the oil recovery. If a good displacement process is used, the effect of heterogeneity can be minimized.

Depending on what kind of enhanced oil recovery process is used after tracer injection, the generated field should be evaluated using the same process and as close to the field conditions as possible. For a miscible displacement where the density of the displacing fluid is different from the displaced fluid, such as a CO_2 miscible flood, heterogeneity may have more effect on the oil recovery of the calculated field than the immiscible waterflood displacement shown in this report.

In the case where the vertical variogram is available, it is possible to generate a field that has the main qualitative features of the known field. The horizontal variograms from different runs are always higher than data. Of all the horizontal variograms, Run (d) shows the greatest smoothness and is closest to the data. Although the horizontal variogram cannot be determined directly, the generated fields give the same result in a single-phase, matched-density displacement and in an immiscible displacement. Using only tracer data from the proposed VTP, the vertical variogram can be qualitatively inferred. This generated field also satisfied tracer data and waterflooding data.

Simulated annealing is a good optimization algorithm but requires a large number of iterations. The quality of the solutions depends on the number of iterations. Therefore, we next investigated an alternative procedure that takes much less computational time and yet produced superior results.

The problem can be handled by limiting the solution space to a more likely possible solution by making an assumption that the horizontal variogram of the reservoir can be expressed

in a functional form with different parameters. Simulated annealing is used to generate a field according to the variogram function and a multiple nonlinear parameter estimation is used to history match the tracer data. Since simulation is performed only at the end of each simulated annealing run, a lot of computational time can be saved. Any variogram model can be used (nugget effect, hole effect, sill, or without sill). The following example models are given together with model equations.

1. Linear (2 parameters, c_o and b_l)

$$\gamma_1(h) = c_0 + b_l h \quad ; c_0 \geq 0$$

2. Spherical (3 parameters, c_o, c_s, and a_s)

$$\gamma_2(h) = c_0 + c_s \left\{ 1.5 \frac{h}{a_s} - 0.5 \left(\frac{h}{a_s} \right)^3 \right\} \quad ; c_0, c_s \geq 0,\ h \leq a_s$$

$$\gamma_2(h) = c_0 + c_s \quad ; c_0,\ c_s \geq 0,\ h > a_s$$

3. Exponential (3 parameters, c_o, c_e, and a_e)

$$\gamma_3(h) = c_0 + c_e \left\{ 1.0 - \exp\left(\frac{h}{a_e} \right) \right\} \quad ; c_0, c_e, h \geq 0$$

4. Rational quadratic (3 parameters, c_o, c_r, and a_r)

$$\gamma_4(h) = c_0 + \frac{c_r h^2}{\left\{ 1 + \frac{h^2}{a_r} \right\}} \quad ; c_0, c_r, a_r, h \geq 0$$

5. Wave (3 parameters, c_o, c_w, and a_w)

$$\gamma_5(h) = c_0 + c_w \left\{ 1 - \frac{a_w}{h} \sin \frac{h}{a_w} \right\} \quad ; c_0, c_w, a_w, h \geq 0$$

6. Power (3 parameters, c_o, b_p, and l_d)

$$\gamma_6(h) = c_0 + b_p h^{l_d} \quad ; c_0, b_p, h \geq 0, l_d \leq 2$$

7. Nested

$$\gamma_7(h) = \sum_{i=1}^{n} \gamma_i(h) \quad ; h \geq 0$$

Figures 50 to 53 show different variogram models. The following is the proposed procedure:

1. Obtain an upper bound of horizontal variogram by making one simulated annealing run minimizing the known vertical semivariogram.

$$e(\mathbf{m}) = \sum_{\text{all i}} \{\gamma_{vc}(h_i) - \gamma_{va}(h_i)\}^2$$

In the above expression, $\gamma_{vc}(h)$ and $\gamma_{va}(h)$ are the computed and experimental vertical variograms, respectively.

2. Choose a horizontal variogram model and make an initial guess of the parameters.
3. Make one simulated annealing run minimizing the following objective function.

$$e(\mathbf{m}) = \sum_{\text{all i}} \lambda_{1i}\{\gamma_{vc}(h_i) - \gamma_{va}(h_i)\}^2 + \sum_{\text{all j}} \lambda_{2j}\{\gamma_{hc}(h_j) - \gamma_{ha}(h_j)\}^2$$

$$\lambda_{1i} = 1/\{\gamma_{va}(h_i) + \gamma_{vc}(h_i)\}^2$$

$$\lambda_{2j} = 1/\{\gamma_{ha}(h_j) + \gamma_{hc}(h_j)\}^2$$

$\gamma_{hc}(h)$ and $\gamma_{ha}(h)$ are the computed and experimental horizontal variograms, respectively. λ_{1i} and λ_{2j} are the weights for the two parts of the objective function.

4. Call UTCHEM to get a tracer response corresponding to the permeability field from simulated annealing.
5. Estimate a new set of parameters (horizontal variogram) by history matching tracer data using the following objective function.

$$e(\mathbf{m}) = \sum_{\text{all i}} \left\{ C_{i,c}(\vec{\alpha},t) - C_{i,a}(\vec{\alpha},t) \right\}^2$$

$C_c(t)$ and $C_a(t)$ correspond to the computed and actual tracer histories.

Assuming tracer production data can be written as a nonlinear function of parameters to be estimated, then for each tracer data point i

$$C_i = F(\vec{\alpha}, t_i) \qquad i = 1, n \,.$$

Using a Taylor's series and expanding C up to the first order term around the initial estimate $\vec{\alpha}_0$:

$$C_{i,a} = F(\vec{\alpha}_0, t_i) + (\alpha_1 - \alpha_0)\left[\frac{\partial F(\vec{\alpha},t_i)}{\partial \alpha_1}\right]_{\vec{\alpha}_0} + \ldots + (\alpha_{np} - \alpha_0)\left[\frac{\partial F(\vec{\alpha},t_i)}{\partial \alpha_{np}}\right]_{\vec{\alpha}_0}$$

$$C_{i,a} - F(\vec{\alpha}_0, t_i) = (\alpha_1 - \alpha_0)\left[\frac{\partial F(\vec{\alpha},t_i)}{\partial \alpha_1}\right]_{\vec{\alpha}_0} + \ldots + (\alpha_{np} - \alpha_0)\left[\frac{\partial F(\vec{\alpha},t_i)}{\partial \alpha_{np}}\right]_{\vec{\alpha}_0} .$$

The above equation can be written as

$$\omega_i = \beta_1 \upsilon_{i,1} + \beta_2 \upsilon_{i,2} + \ldots + \beta_{np} \upsilon_{i,np}$$

where

$$\omega_i = C_{i,a} - F(\vec{\alpha}_0, t_i)$$

$$\beta_j = \alpha_j - \alpha_j^0 \quad ; j = 1,2,\ldots n_p$$

$$\upsilon_{i,j} = \left[\frac{\partial F(\vec{\alpha}, t_i)}{\partial \alpha_j}\right]_{\vec{\alpha}_0} \quad ; i = 1, n \quad j = 1, n_p$$

This system of equations becomes n (data point) equations in n_p (number of parameters) unknowns. This is a multiple linear regression with parameters β_j. At each iteration, a new set of parameters (β_j) is estimated and the objective function is calculated as

$$e(\mathbf{m}) = \sum_{i}^{\text{n data point}} (\omega_i - \hat{\omega}_i)^2$$

where

$$\hat{\omega}_i = \beta_1 \upsilon_{i,1} + \beta_2 \upsilon_{i,2} + \ldots + \beta_{n_p} \upsilon_{i,n_p}$$

$$\omega_i = C_{i,a} - F (\vec{\alpha}_0, t_i)$$

The derivative of this function with respect to the parameters is computed numerically.

6. Generate a horizontal variogram according to the model and the new parameters.
7. Repeat steps 3-7 until convergence is reached.

To illustrated these procedures, a permeability field is generated using the MDM method (Yang, 1990). The generated field is shown in Fig. 54. This permeability field is used as the synthetic data (actual permeability field). Figure 55 compares the produced tracer concentration from the simulation of the tracer flow in the actual permeability field to the produced tracer concentration from the above procedure using a spherical horizontal variogram model. The produced tracer concentration from a random permeability field is also plotted on the same figure. The simulated produced tracer concentration matches the synthetic data well. Figure 56 shows the permeability field generated using the proposed procedure and Figure 57 shows a scatter plot of the permeabilities for each gridblock. This plot shows good results since most of the points are close to the 45° line. The derived horizontal variogram is shown in Fig. 58. Simulation of a waterflood with endpoint mobility ratio of 15 is shown in Figs. 59 and 60.

Another run was made to see the sensitivity of selecting a different variogram model. Figure 61 compares the produced tracer concentrations from synthetic data and from the above procedure using an exponential horizontal variogram model. Figure 62 shows the generated permeability field. The scatter plot is shown in Fig. 63, and Fig. 64 shows the derived horizontal semivariogram. The generated permeability fields from using two different models satisfy the vertical variogram and also the tracer data. The derived permeability fields and horizontal variograms are close to the synthetic data. Oil recovery and water-oil ratio from the waterflood also show good agreement with the synthetic data. The results indicate that the generated permeability field is not sensitive to the variogram model selection. The advantages of this new procedure are less computational time (2,000 CPU seconds on Cray YMP compared to 15,000 CPU seconds) and better results. It should now be feasible to use a 3D model, do multiple realizations, and include multiphase flow.

Table 1. Core Properties (Experiment AN-4, Face D)

Dimension (L × H × W, cm)	39 × 14 × 5
Bulk Volume (cm^3)	2,439
Pore Volume (cm^3)	331
Porosity	0.14
$\sigma_{\ln k}$	0.82
V_{DP}	0.56
Maximum Permeability (md)	974.7
Minimum Permeability (md)	24.9
Arithmetic Average (md)	338.9
Standard Deviation (md)	205.4

Table 2. Waterflooding Data

Temperature (°C)	20
Injection Rate (cc/min)	0.2
Interstitial Velocity (ft/day)	1.02
Oil Type	Texas Ranger Crude
μ_w	1.07
μ_o	9.5
S_{oi}	0.81
S_{or}	0.48
k^o_{rw}	0.14
k^o_{ro}	0.89
e_w	1.0
e_o	1.2

Table 3. Polymerflooding Data

Temperature (°C)	20
Polymer	Naflo 3837
Interstitial Velocity (ft/day)	0.07
Polymer Injection	Continuously
Polymer Screen Factor	12.5
Polymer Concentration	0.2 wt%
Polymer Plateau Viscosity	15.5
S_{oi}	0.84
S_{or}	0.44
k^o_{rw}	0.08
k^o_{ro}	0.94
e_w	3.0
e_o	2.0

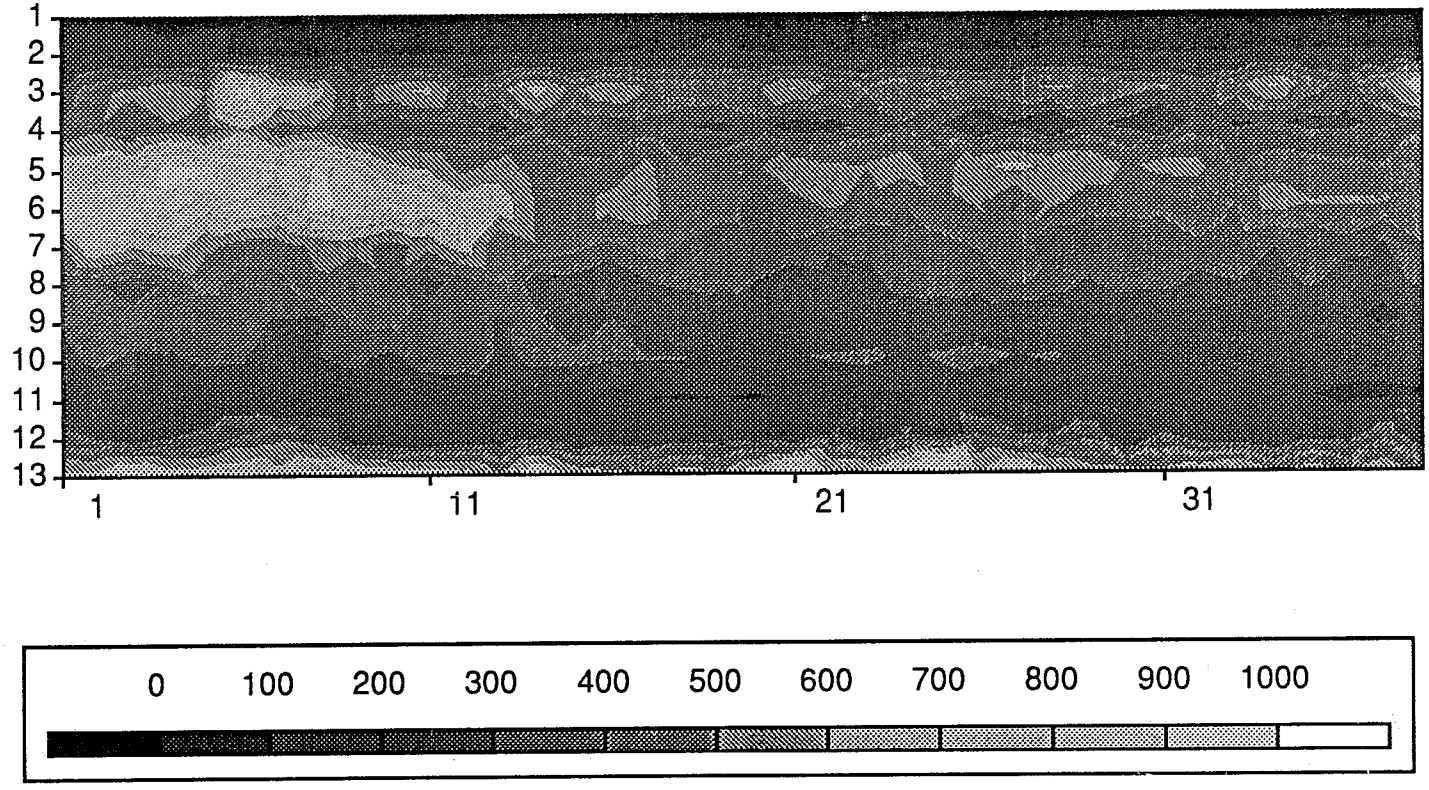

Fig. 1. Permeability distribution measured from face D of Antolini sandstone core (Experiment AN-4)

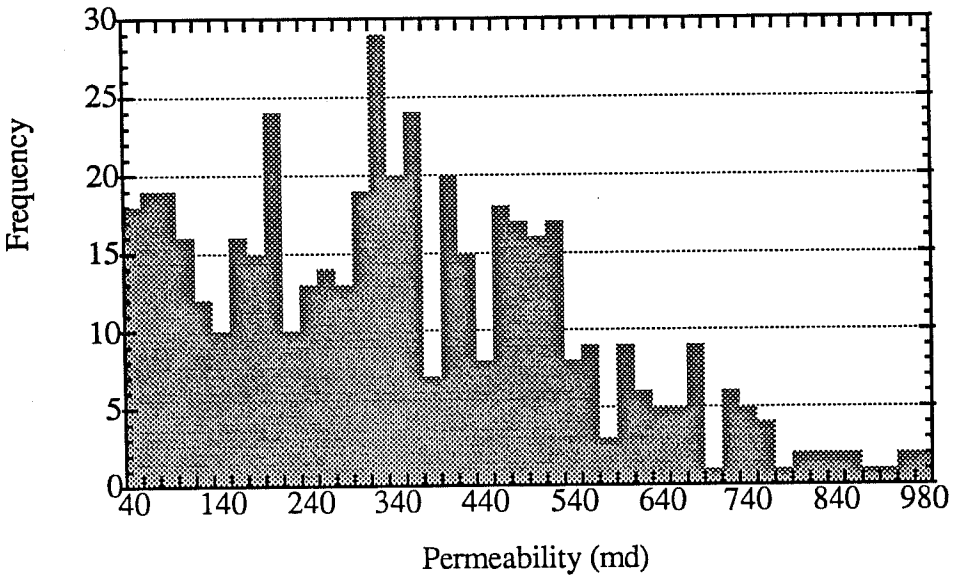

Fig. 2. Frequency histogram for permeability data from face D of heterogeneous Antolini sandstone core (Experiment AN-4)

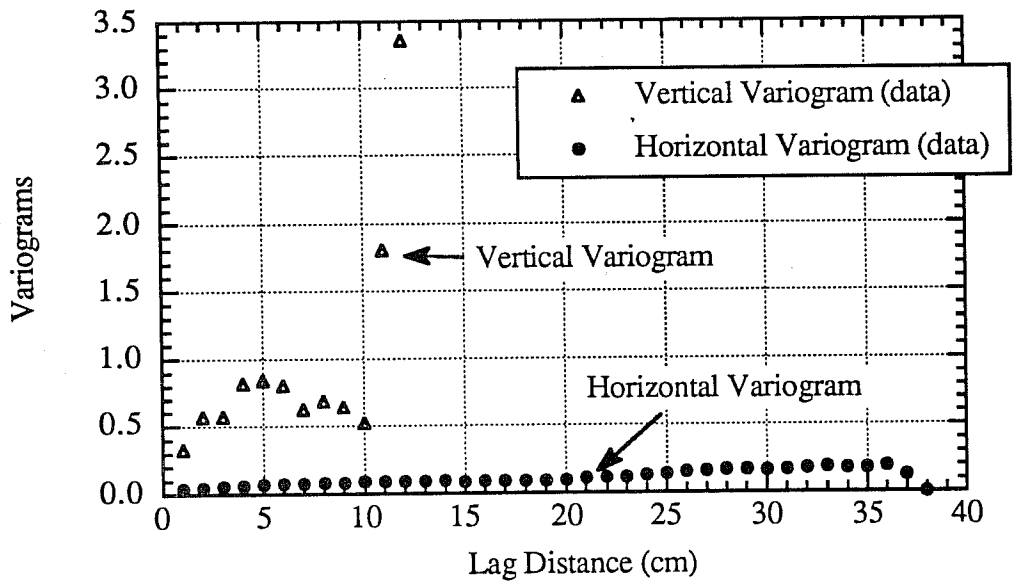

Fig. 3. Measured variograms from face D of heterogeneous Antolini core (Experiment AN-4)

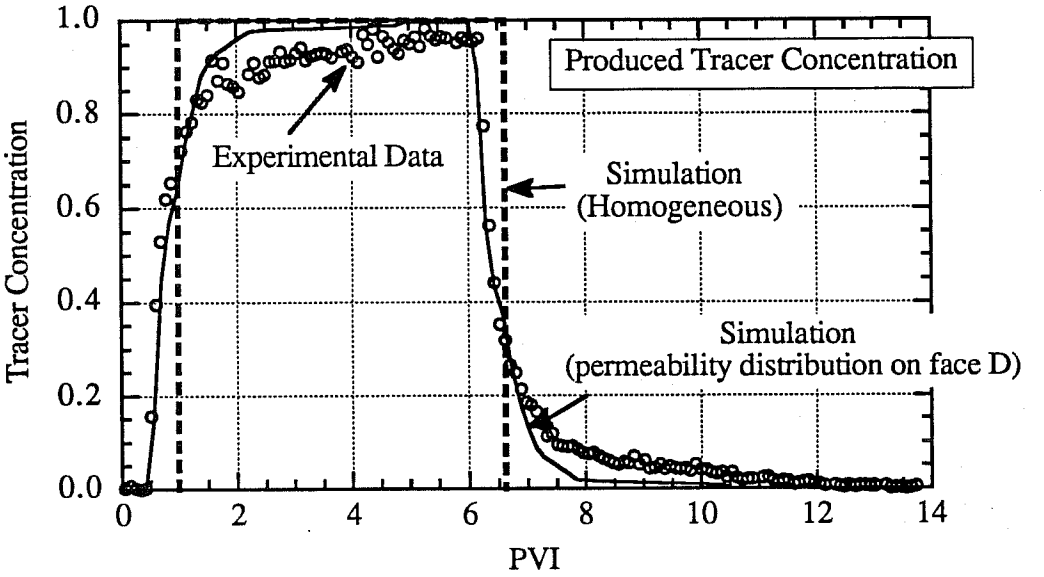

Fig. 4. Comparison of primary tracer injection data of Experiment AN-4 and simulations

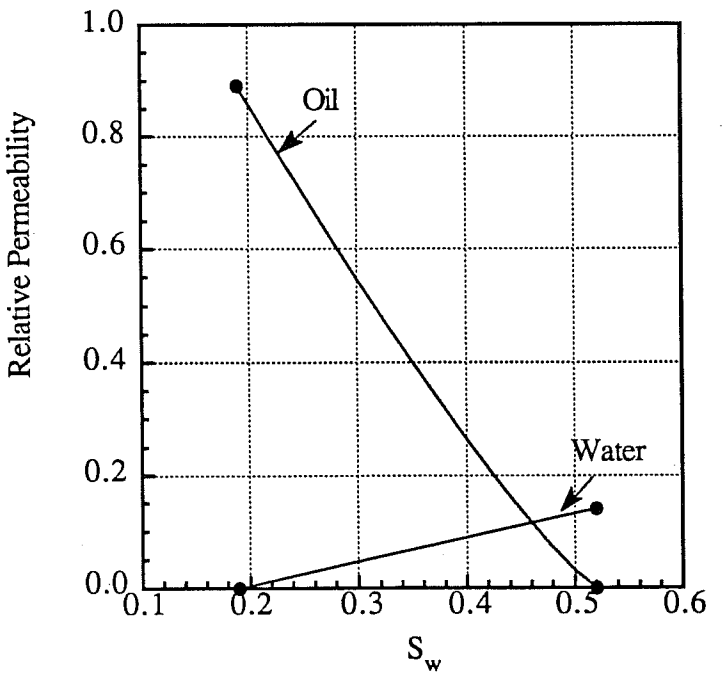

Fig. 5. Relative permeability curves used in history matching AN-4 waterflood data ($e_w = 1$, $e_o = 1.2$)

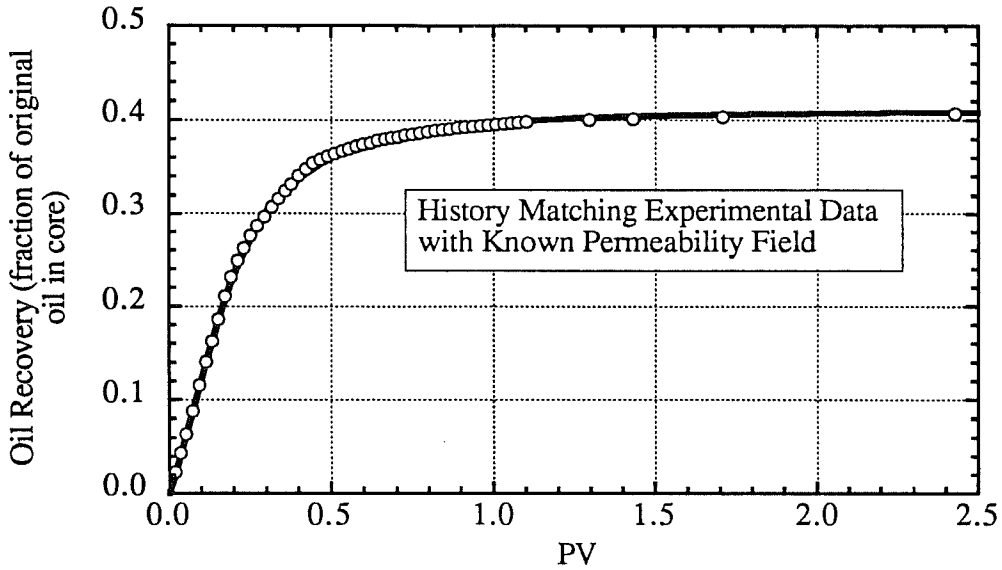

Fig. 6. Comparison between waterflood data (AN-4) and simulation using $e_w = 1$, $e_o = 1.2$

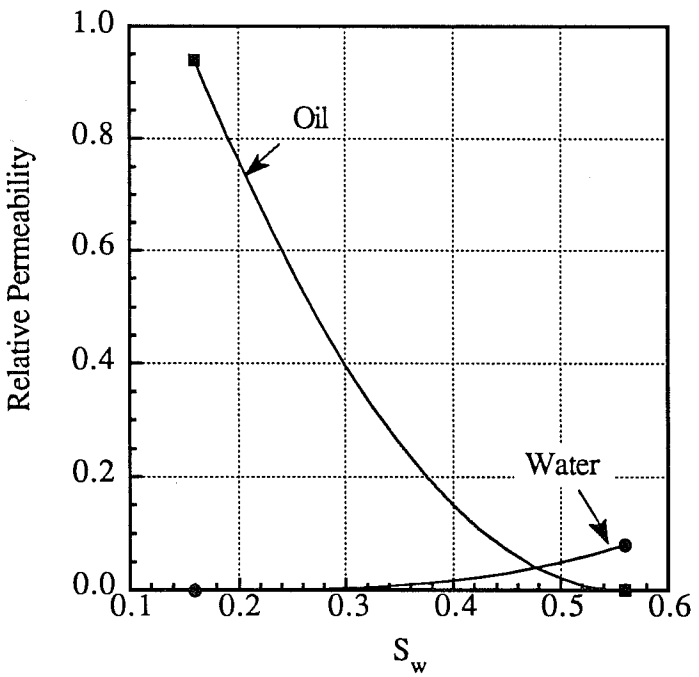

Fig. 7. Relative permeability curves used in history matching AN-4 polymerflood data ($e_w = 3.0$, $e_o = 2.0$)

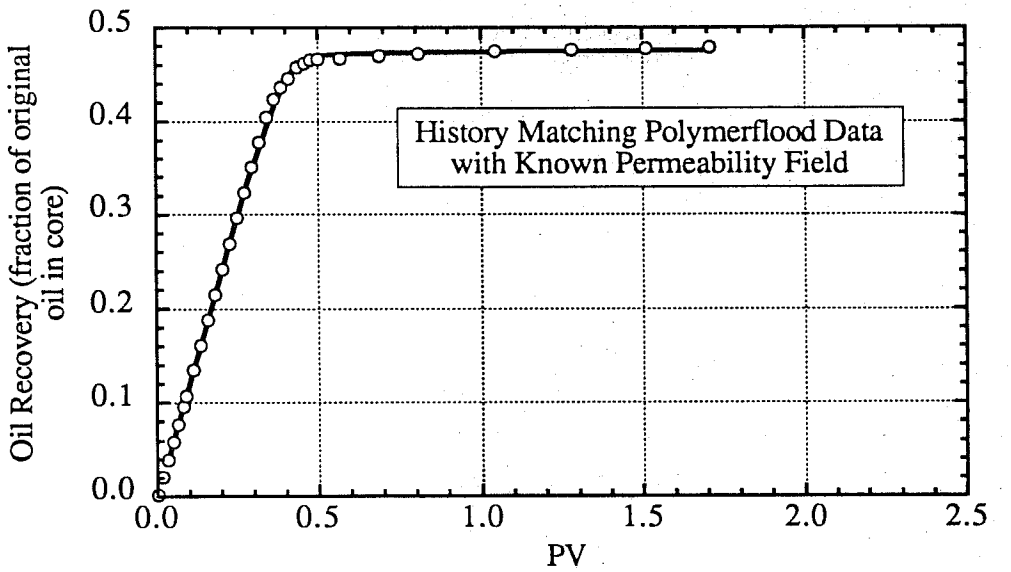

Fig. 8. Comparison between polymerflood data (AN-4) and simulation ($e_w = 3.0$, $e_o = 2.0$)

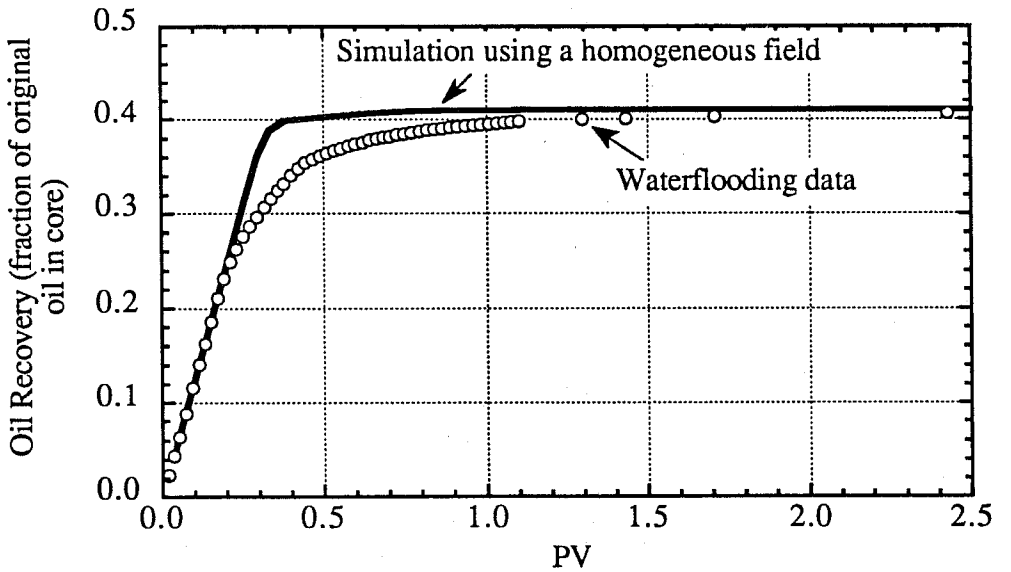

Fig. 9. Comparison between waterflood data (AN-4) and simulation using a homogeneous field

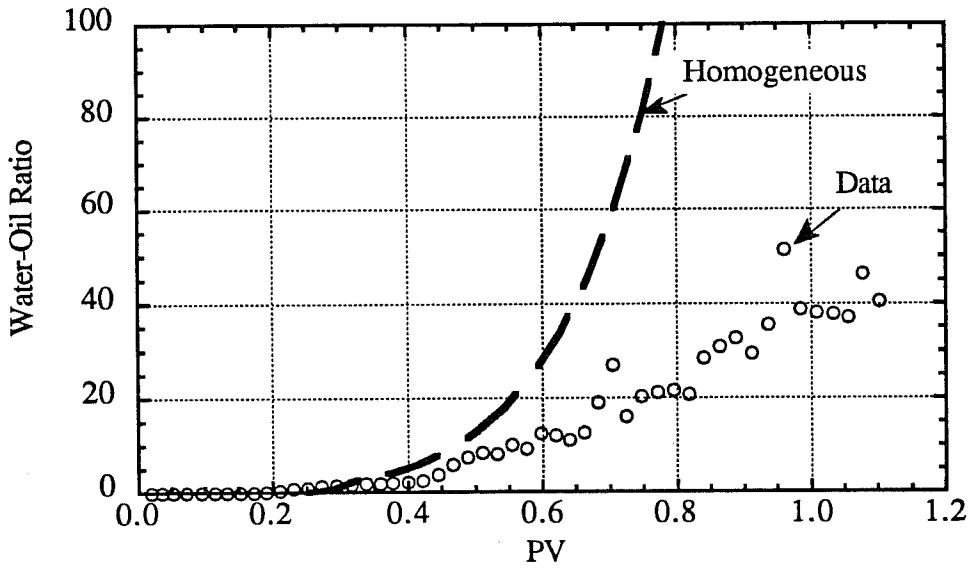

Fig. 10. Effect of heterogeneity on water-oil ratio between a homogeneous field and data

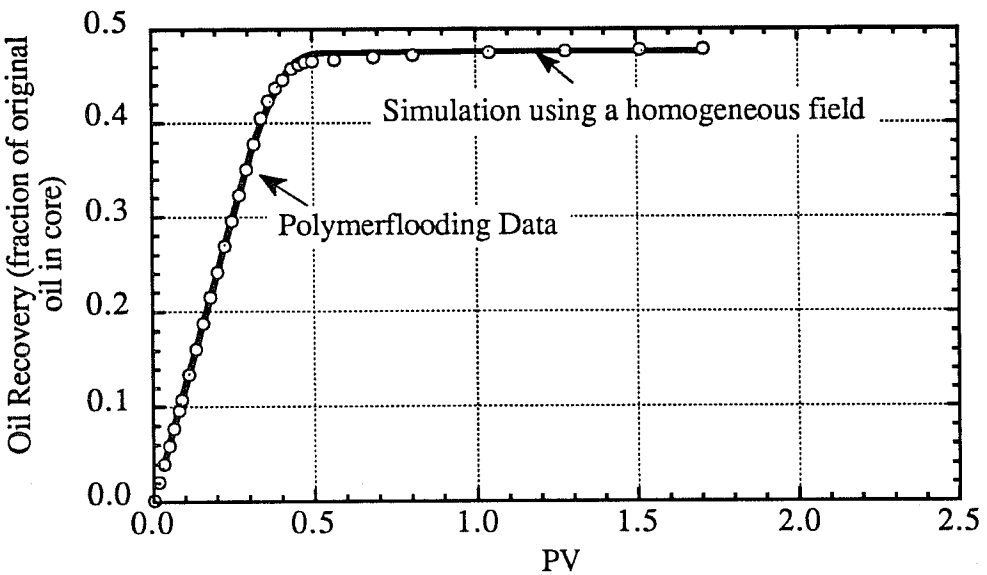

Fig. 11. Comparison between polymerflood data (AN-4) and simulation results using a homogeneous field

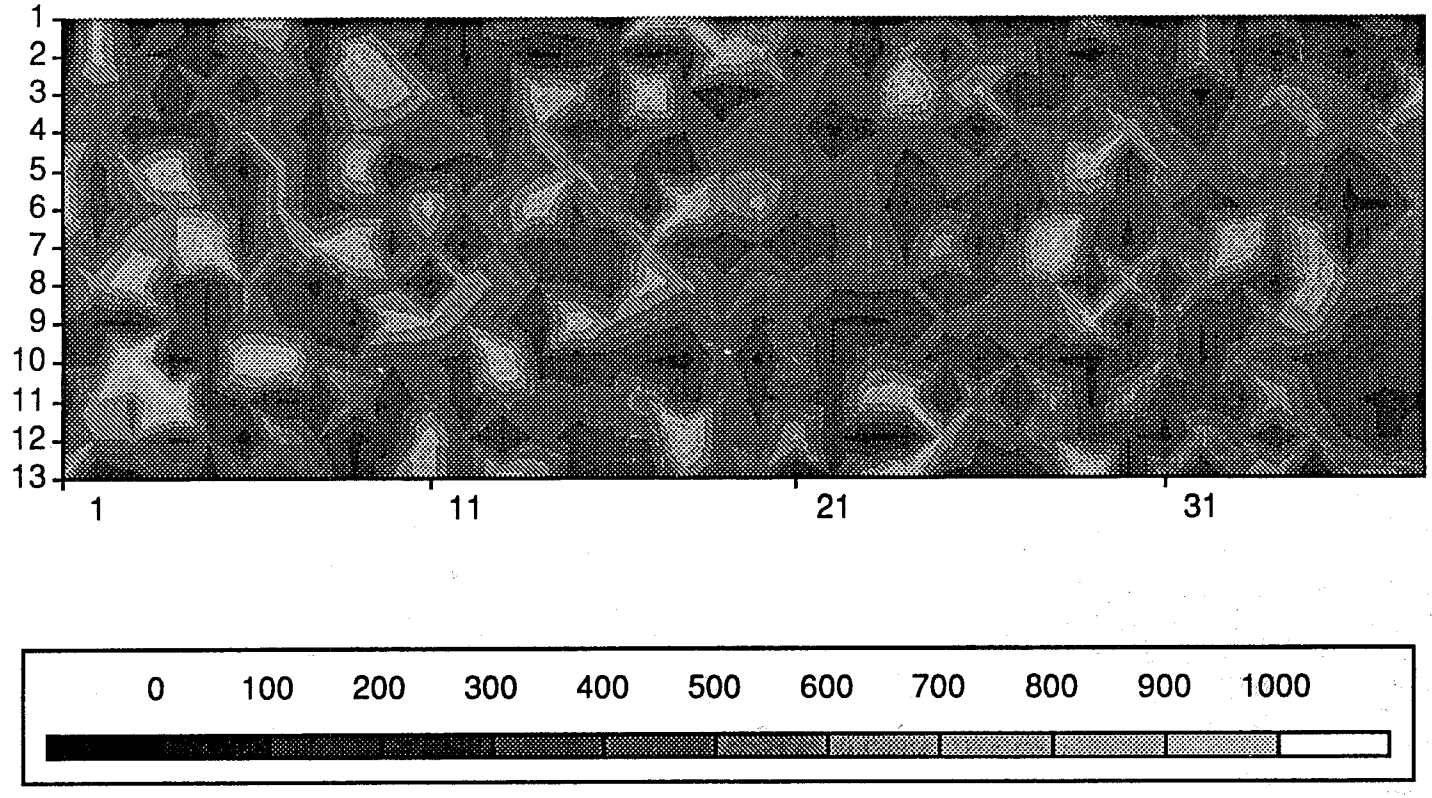

Fig. 12 Starting random permeability field

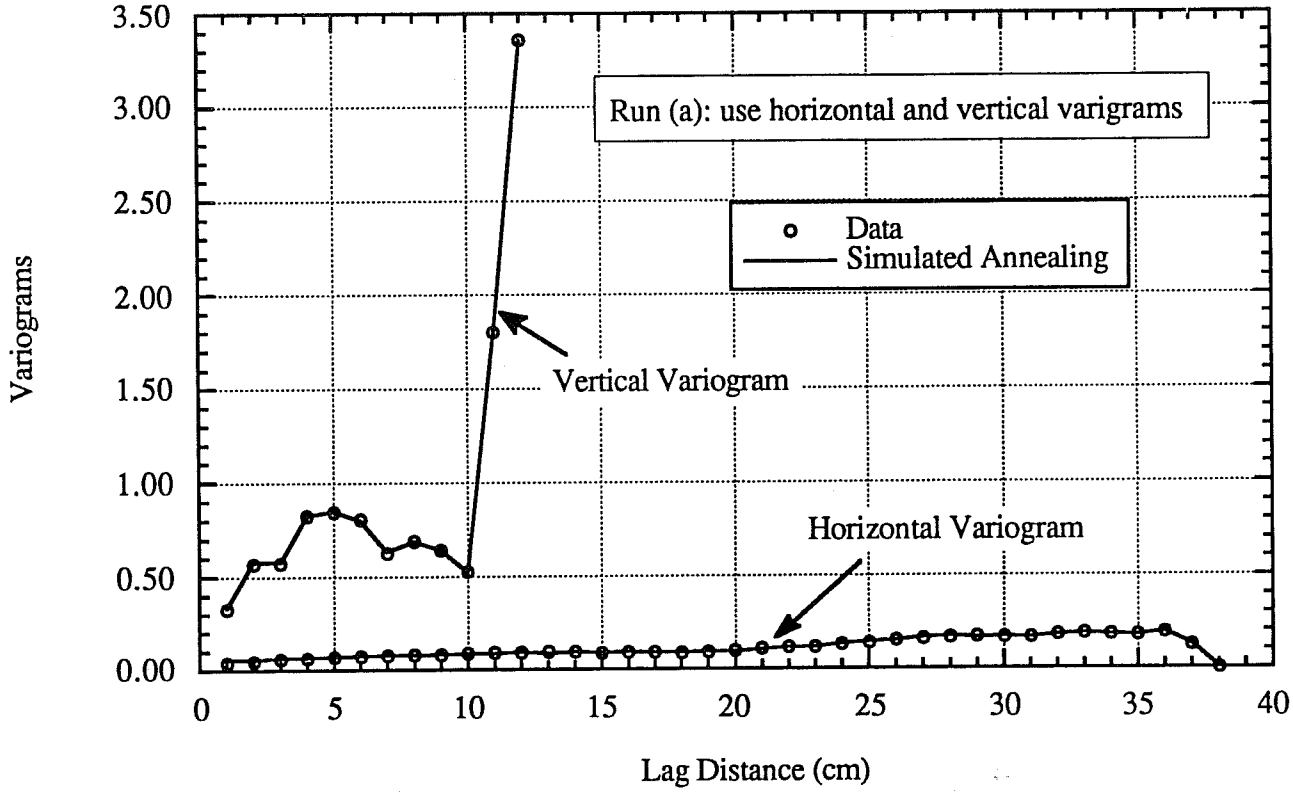

Fig. 13. Comparison between variograms of data and simulated annealing

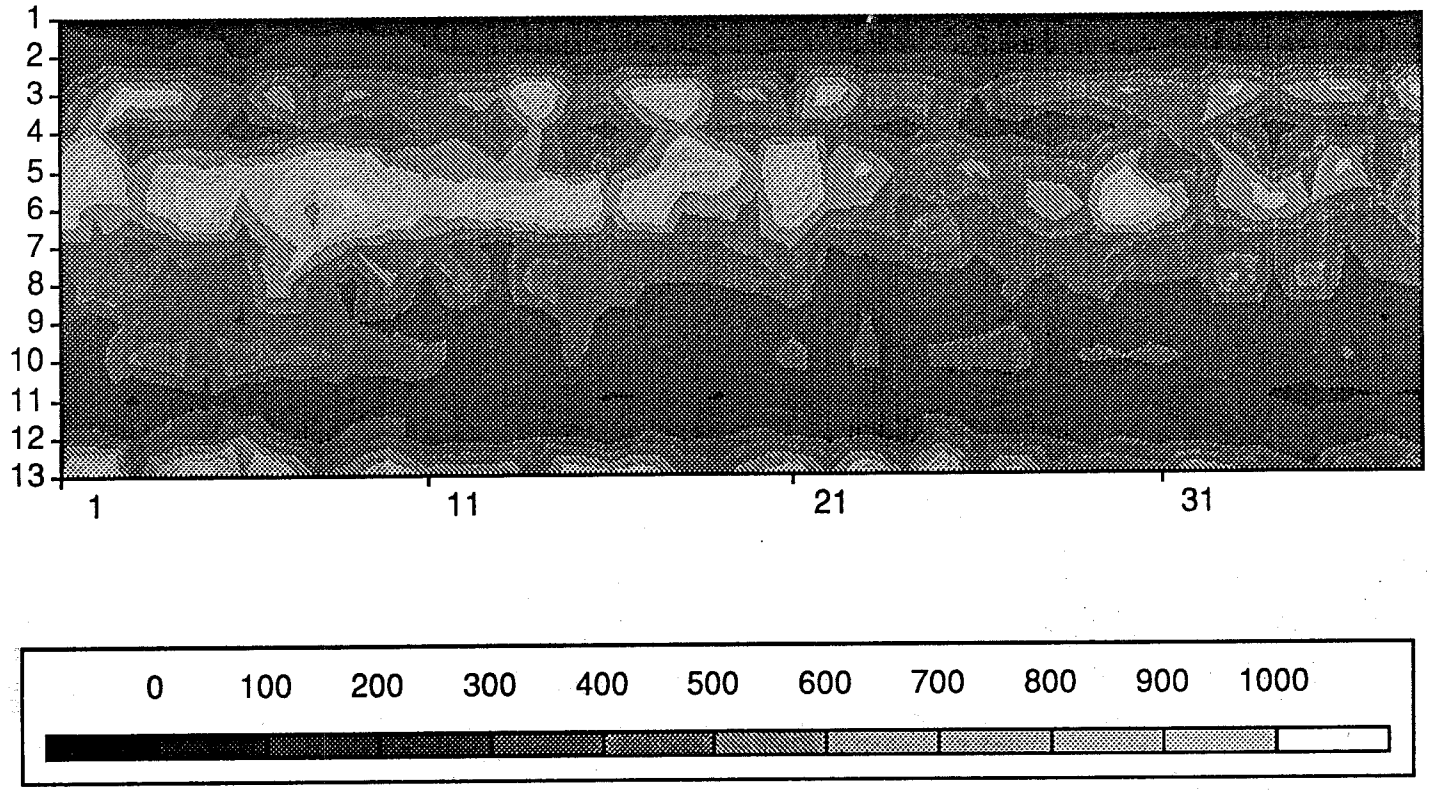

Fig. 14. Permeability field generated from Run (a) using horizontal and vertical variograms

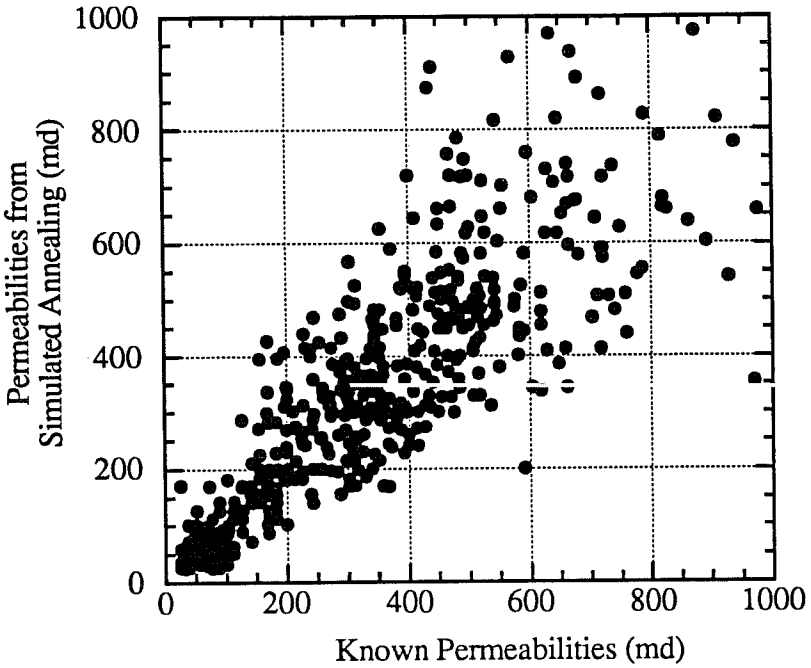

Fig. 15. Comparison at each gridblock between known permeabilities and permeabilities generated from Run (a) using horizontal and vertical variograms

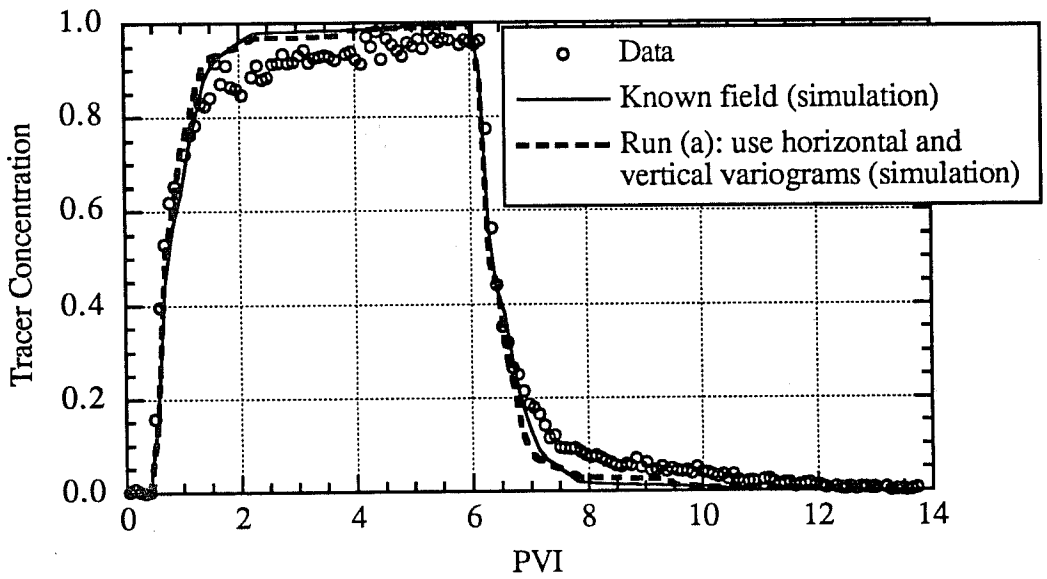

Fig. 16. Comparison of primary tracer injection data of Experiment AN-4 and simulations

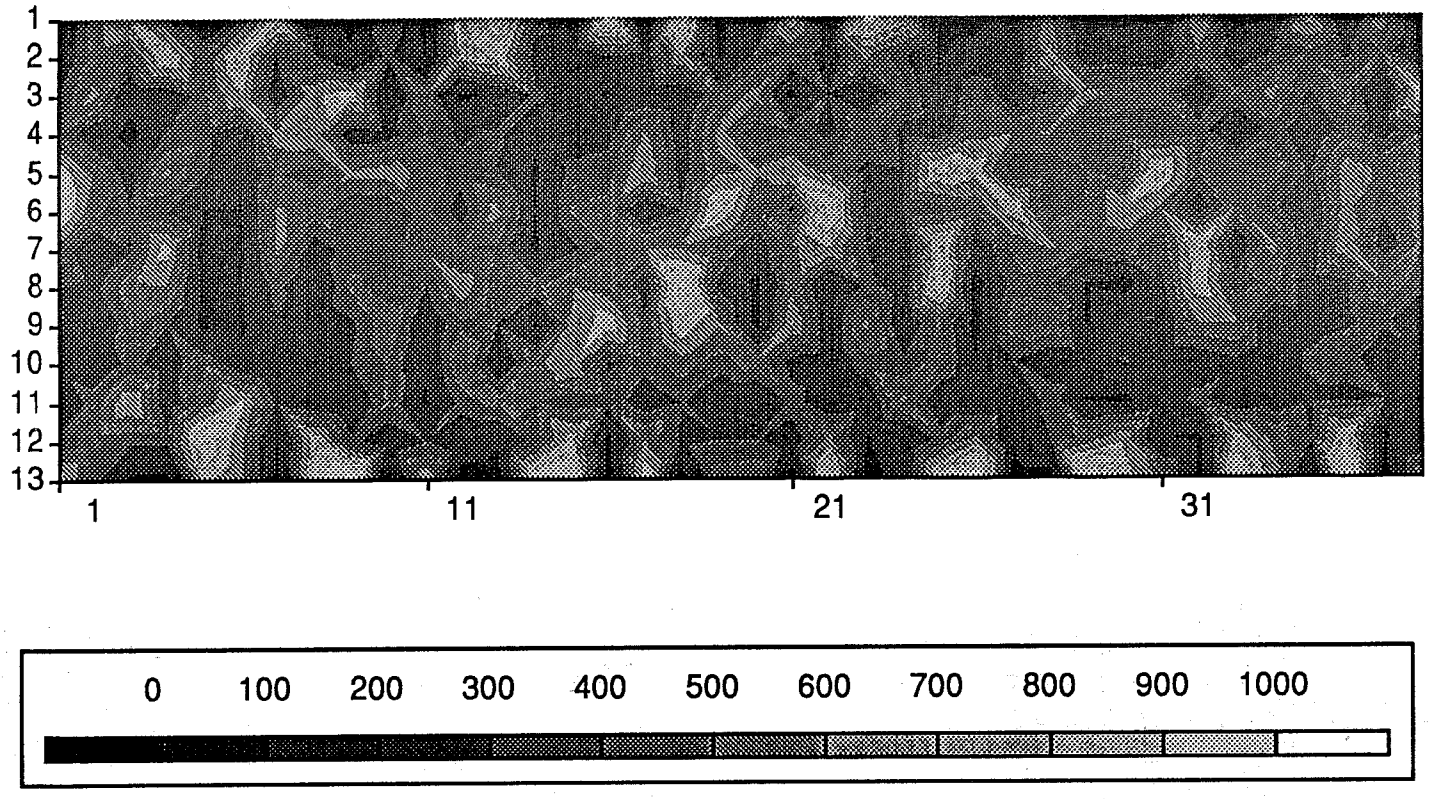

Fig. 17. Permeability field generated from Run (b) using only vertical variogram

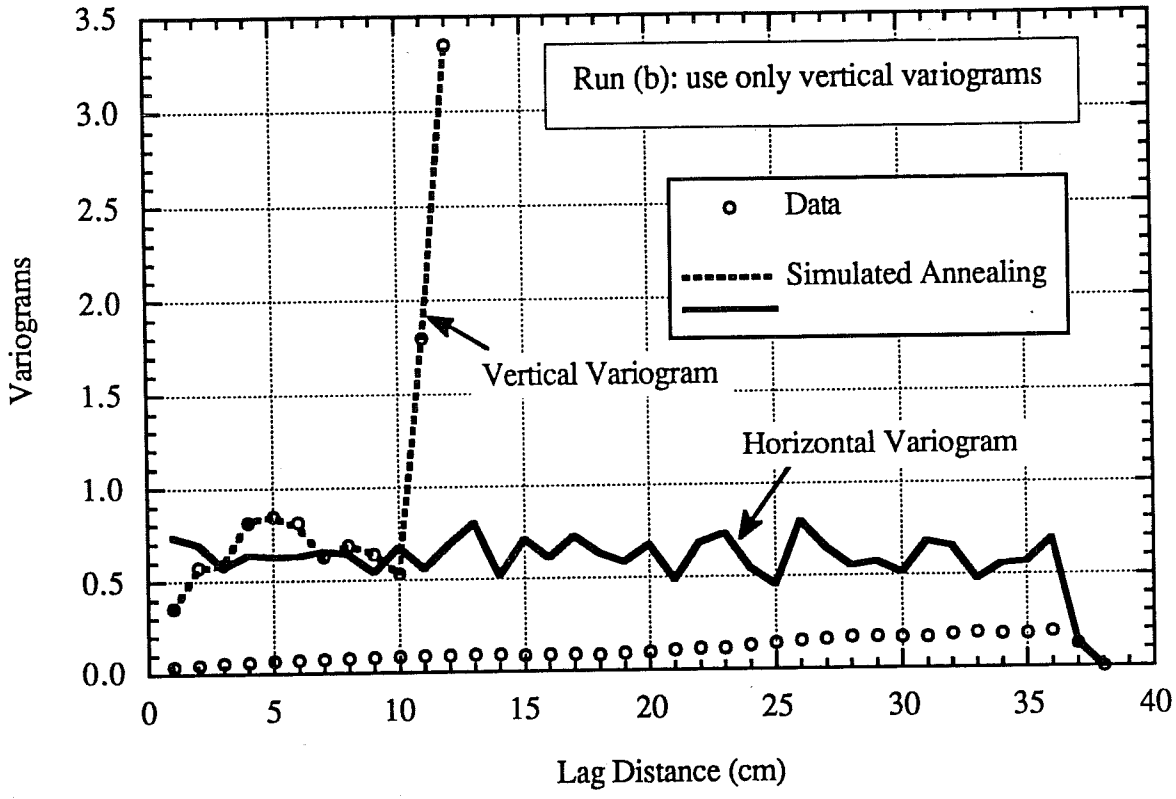

Fig. 18. Comparison between variograms of data and simulated annealing

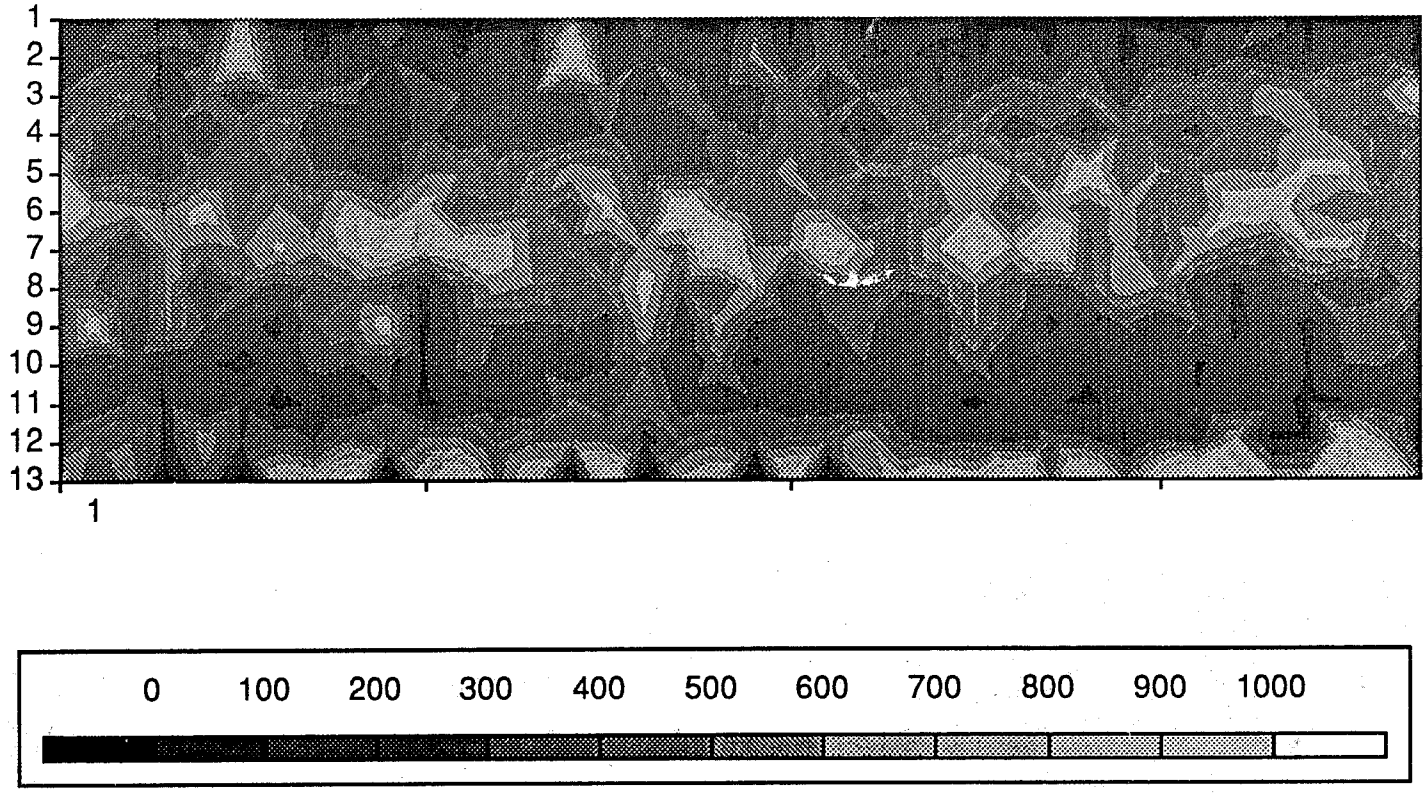

Fig. 19. Permeability field generated from Run (c) using vertical variogram together with an integrated breakthrough curve

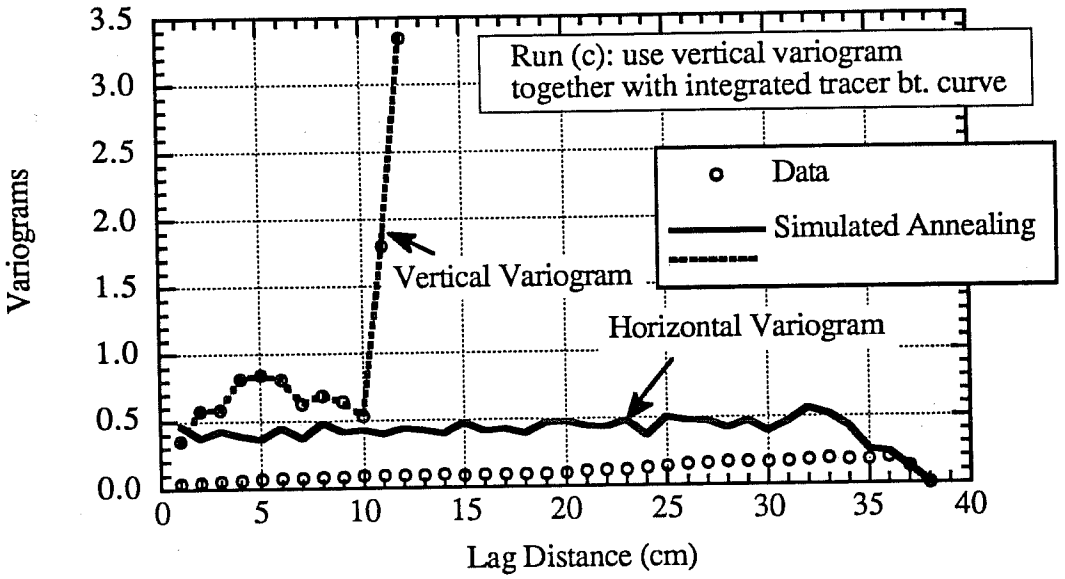

Fig. 20. Comparison between variograms of data and simulated annealing

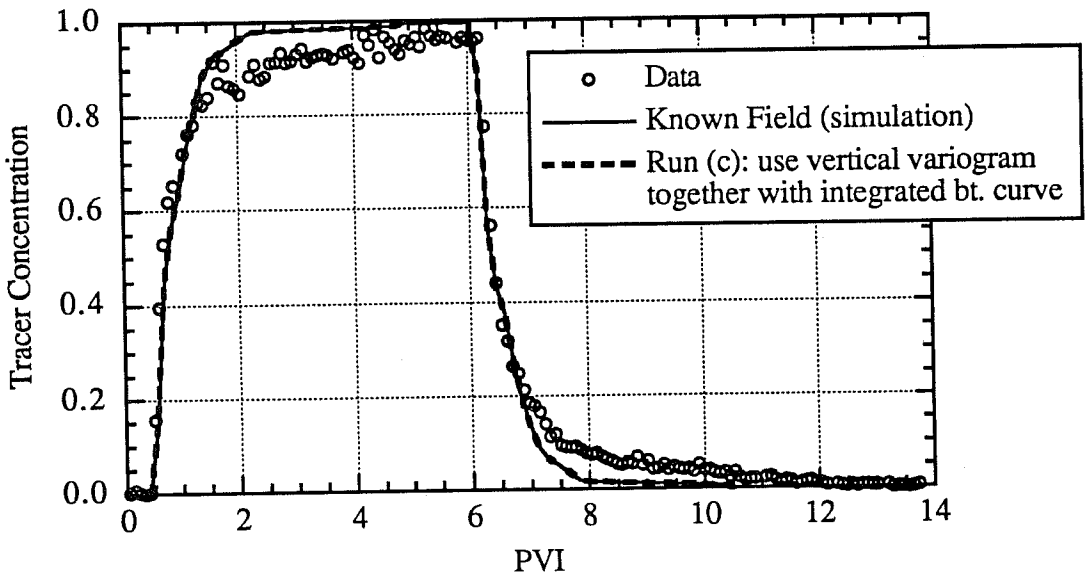

Fig. 21. Comparison of primary tracer injection data of Experiment AN-4 and simulations

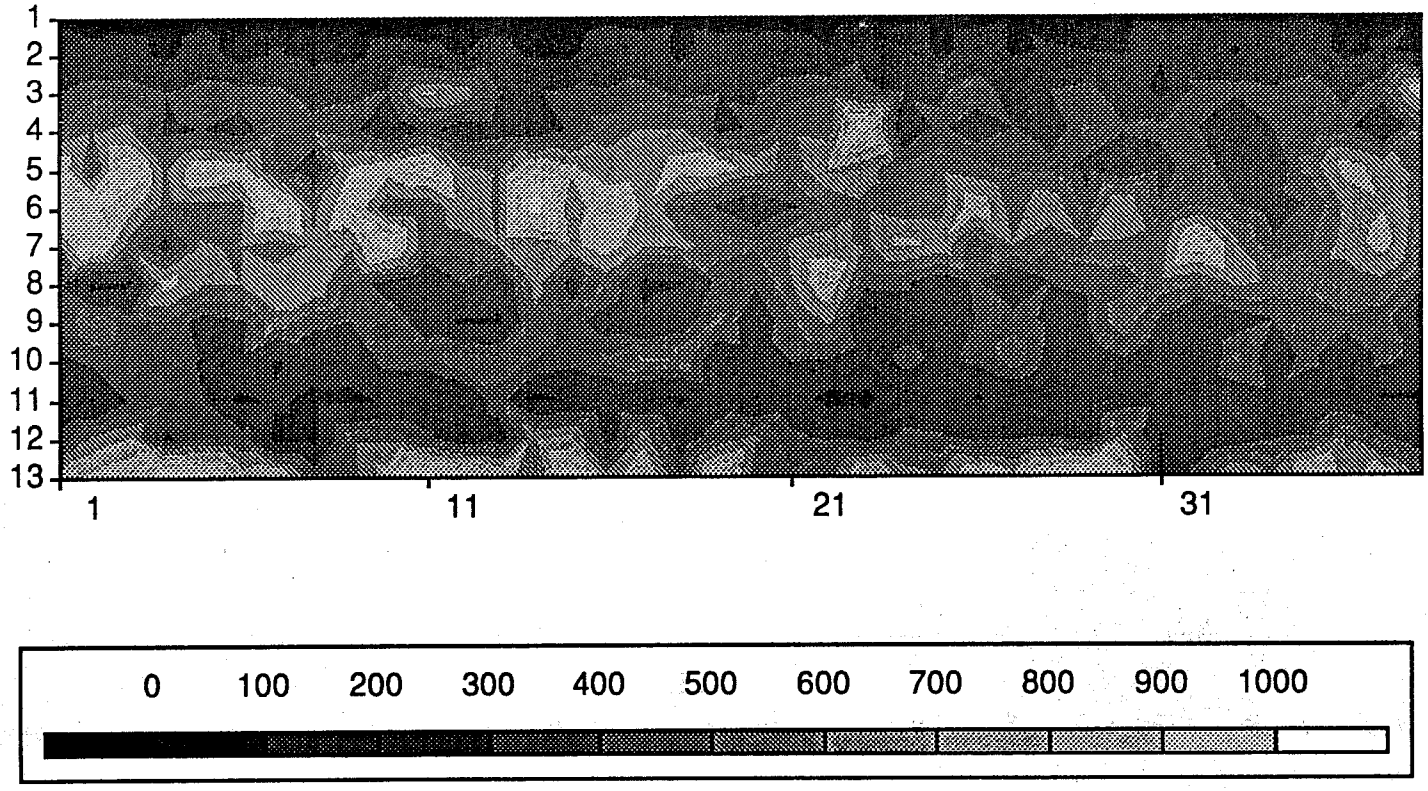

Fig. 22. Permeability field generated from Run (d) using vertical variogram together with VTP

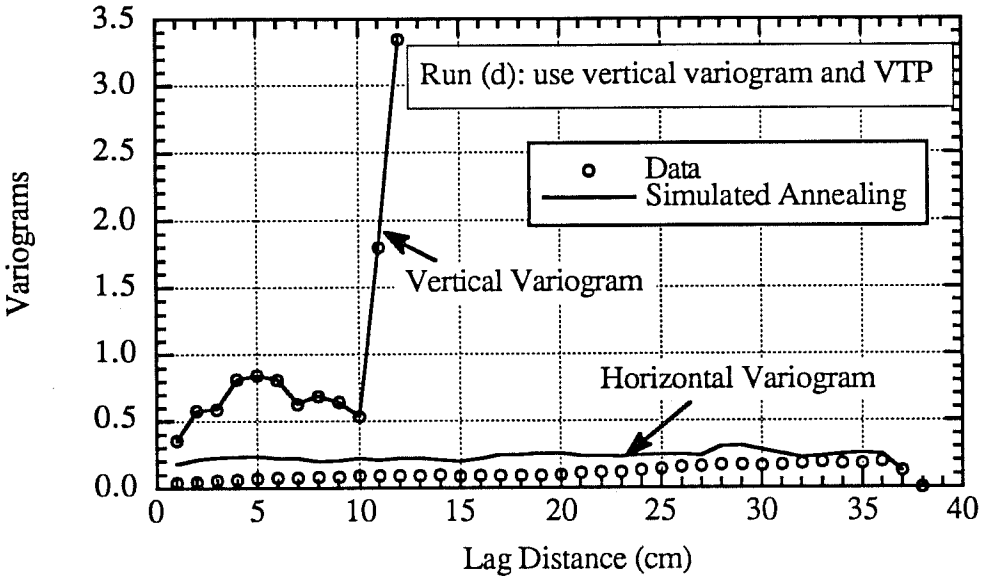

Fig. 23. Comparison between variograms of data and simulated annealing

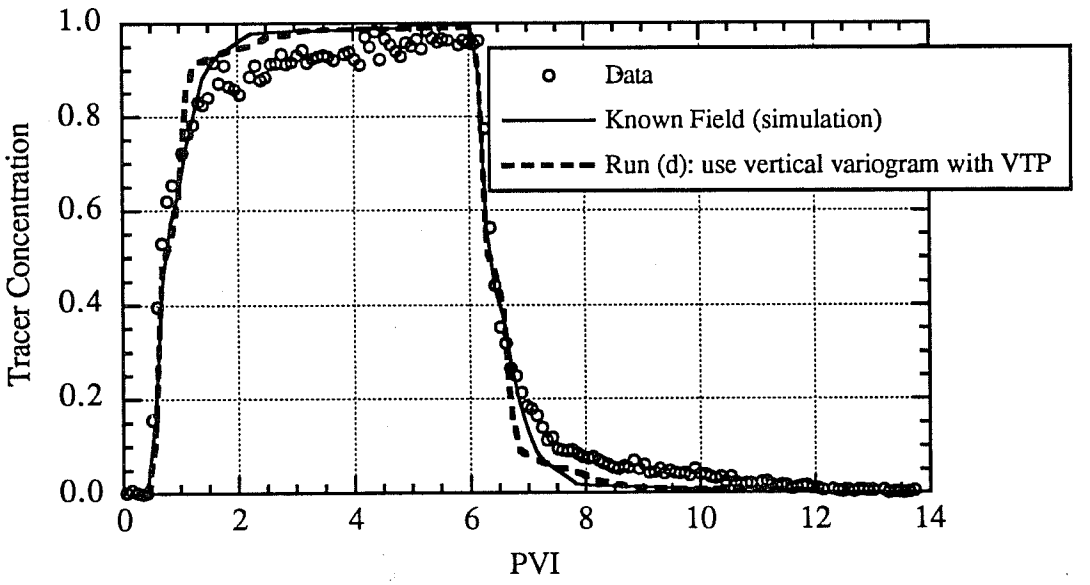

Fig. 24. Comparison of primary tracer injection data of Experiment AN-4 and simulations

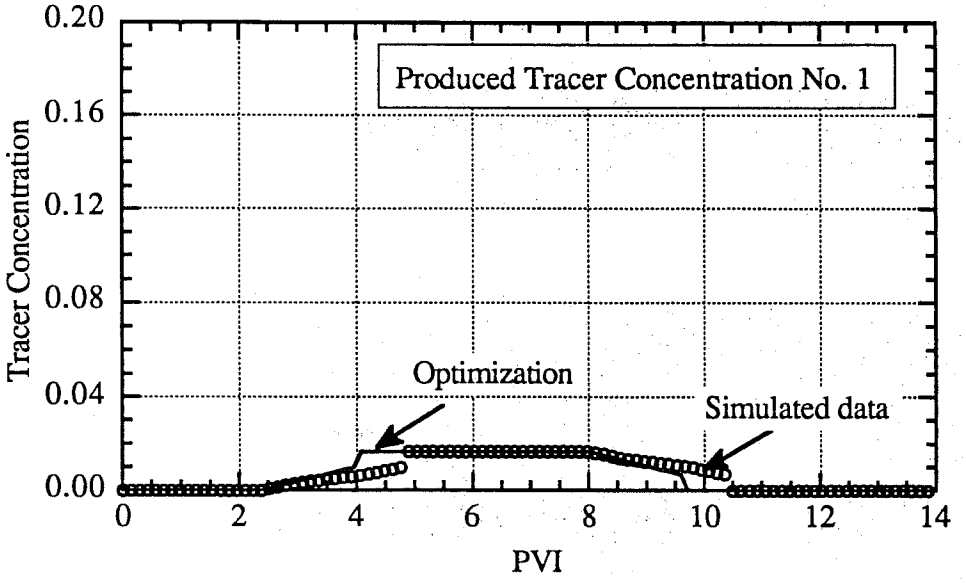

Fig. 25. Comparison between data and simulated annealing

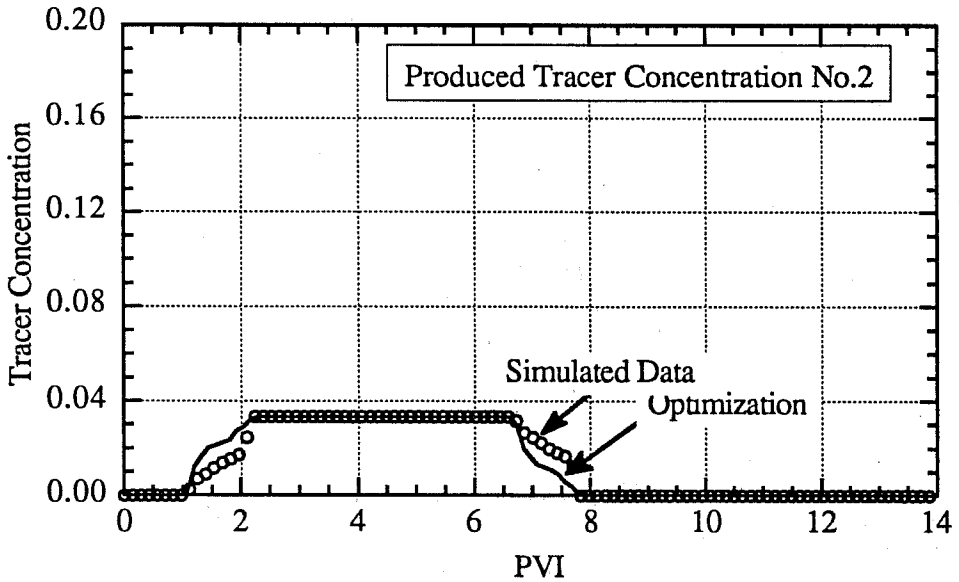

Fig. 26. Comparison between data and simulated annealing

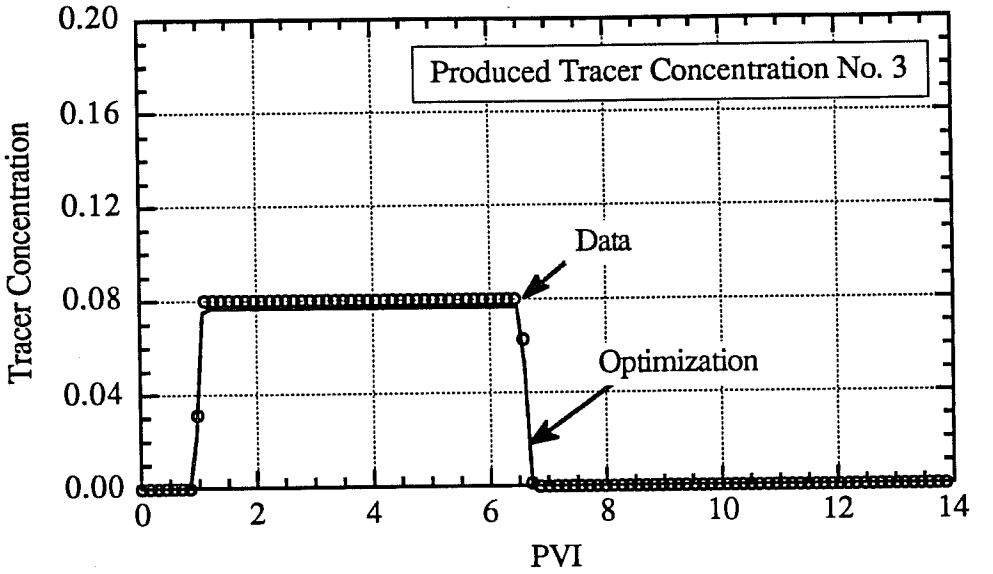

Fig. 27. Comparison between data and simulated annealing

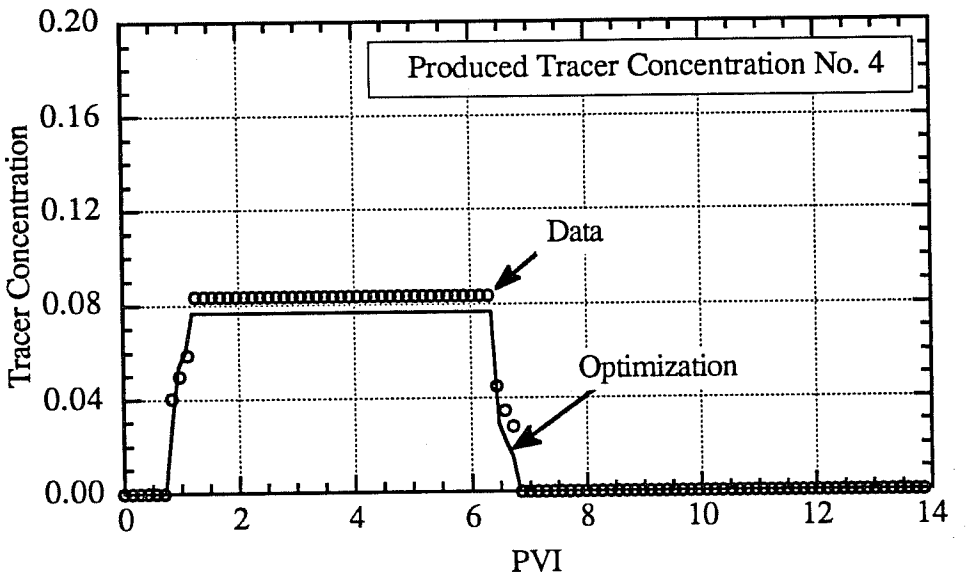

Fig. 28. Comparison between data and simulated annealing

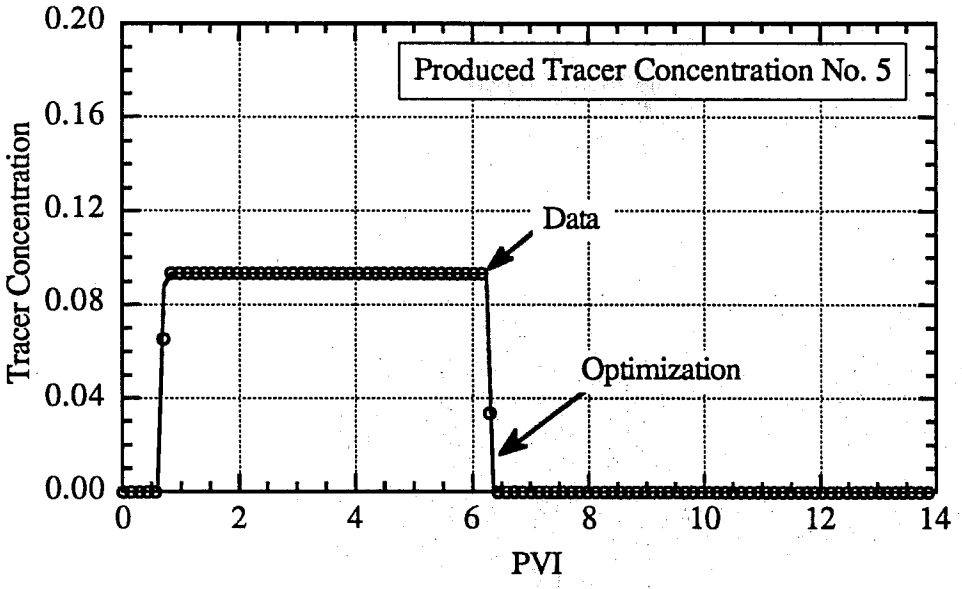

Fig. 29. Comparison between data and simulated annealing

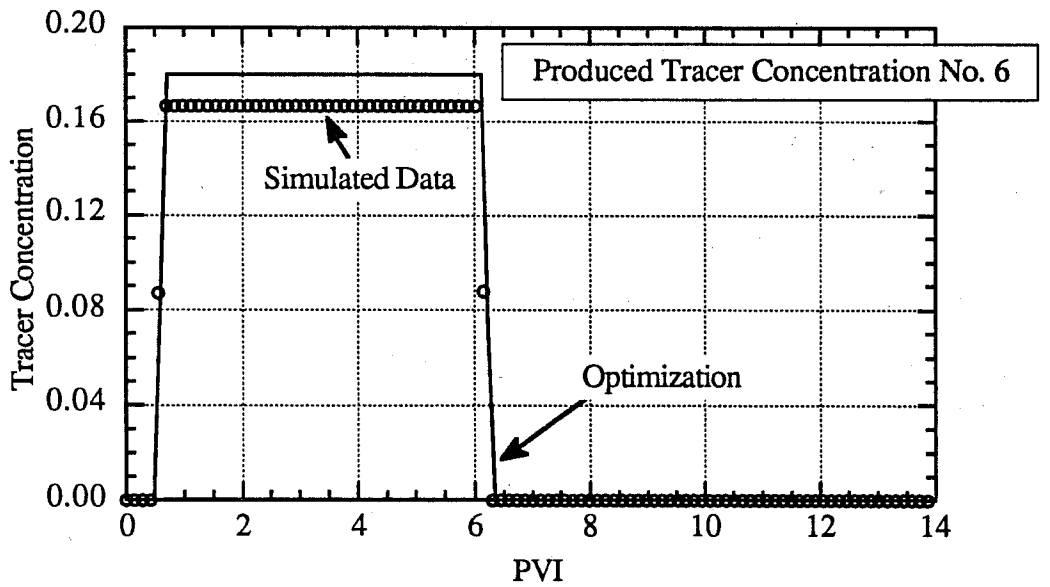

Fig. 30. Comparison between data and simulated annealing

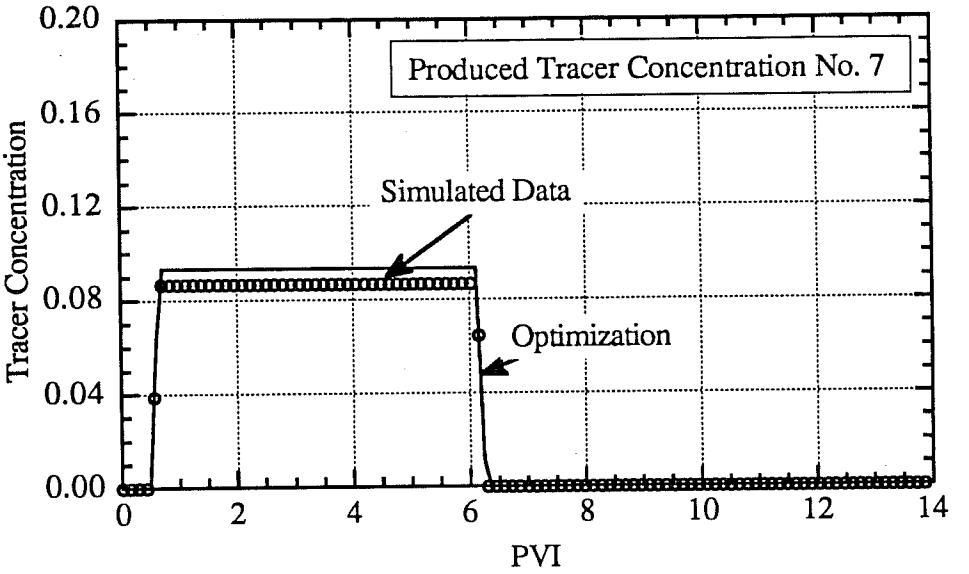

Fig. 31. Comparison between data and simulated annealing

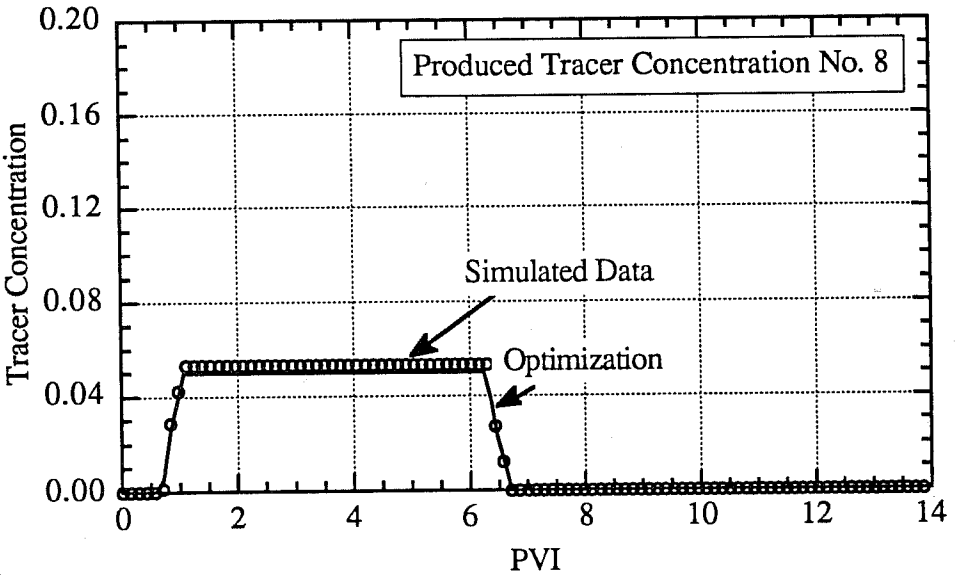

Fig. 32. Comparison between data and simulated annealing

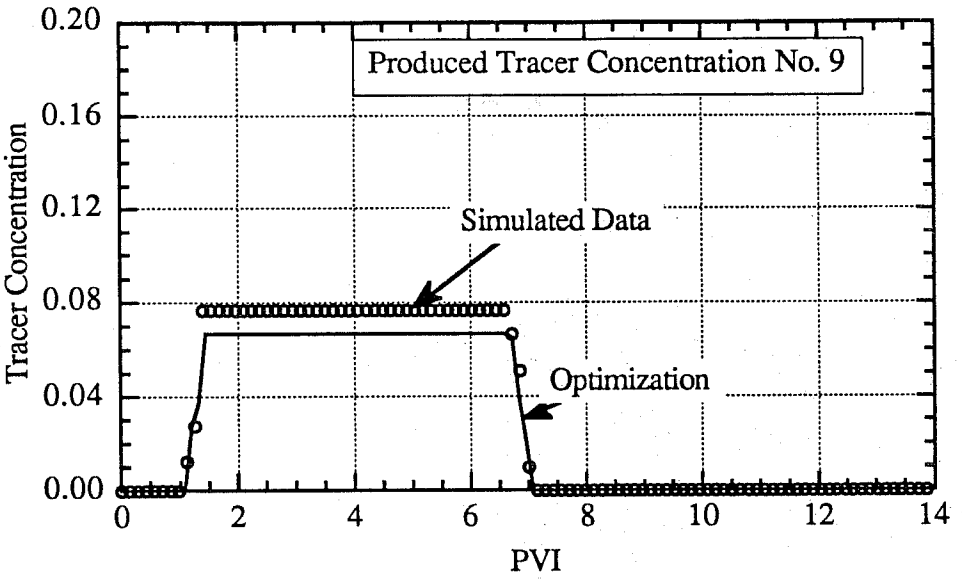

Fig. 33. Comparison between data and simulated annealing

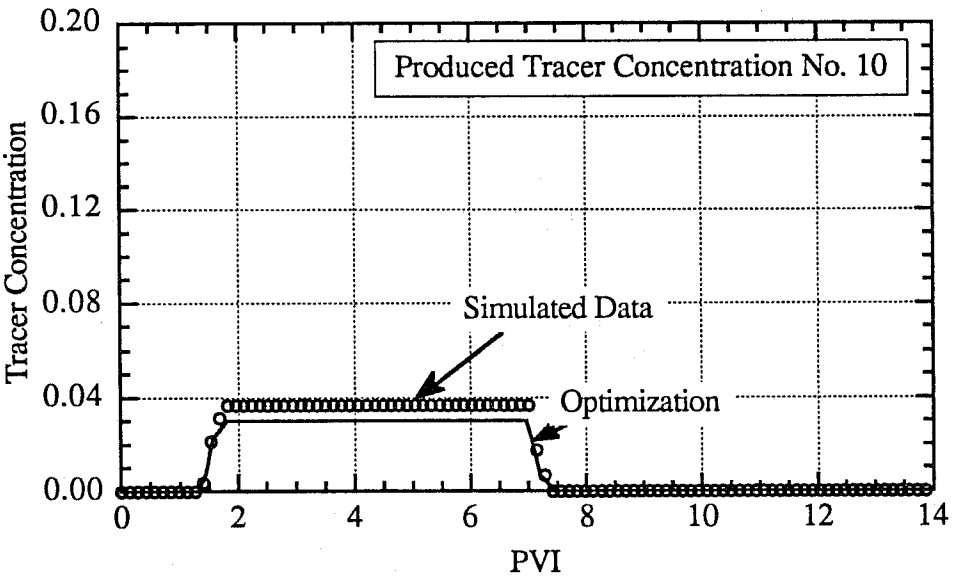

Fig. 34. Comparison between data and simulated annealing

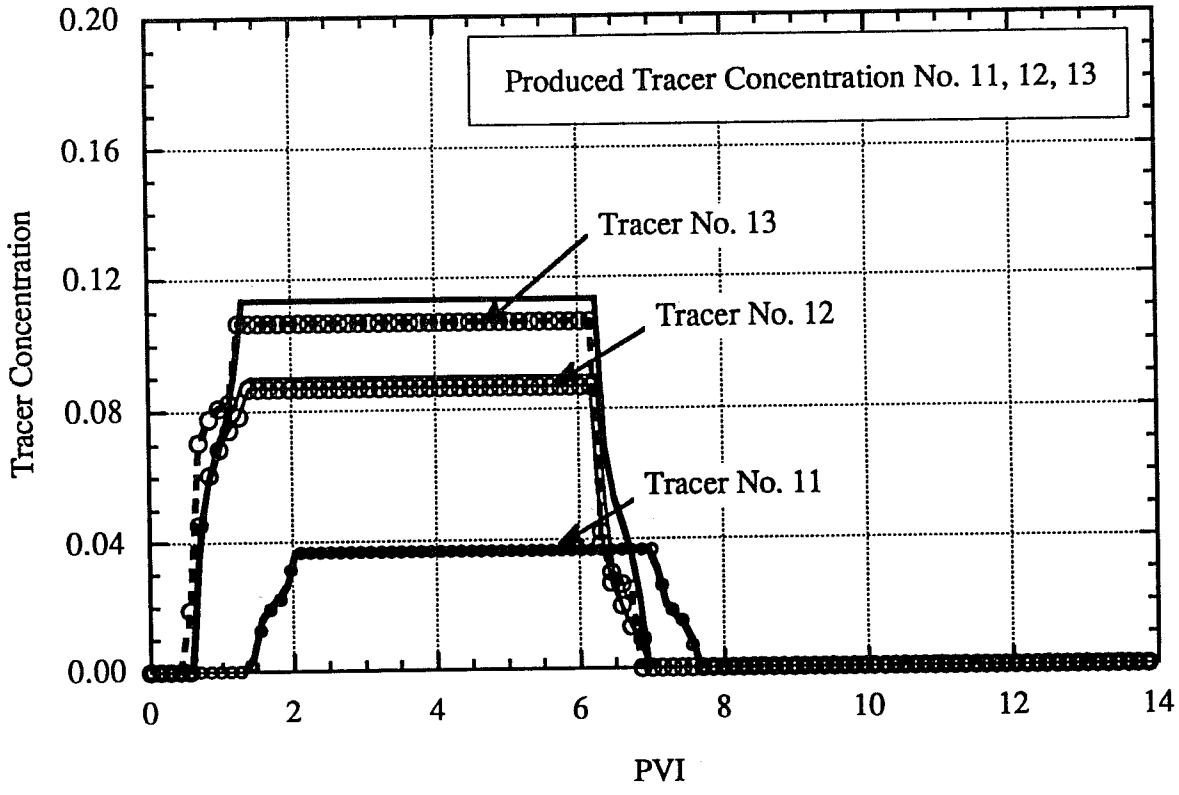

Fig. 35. Comparison between data and simulated annealing

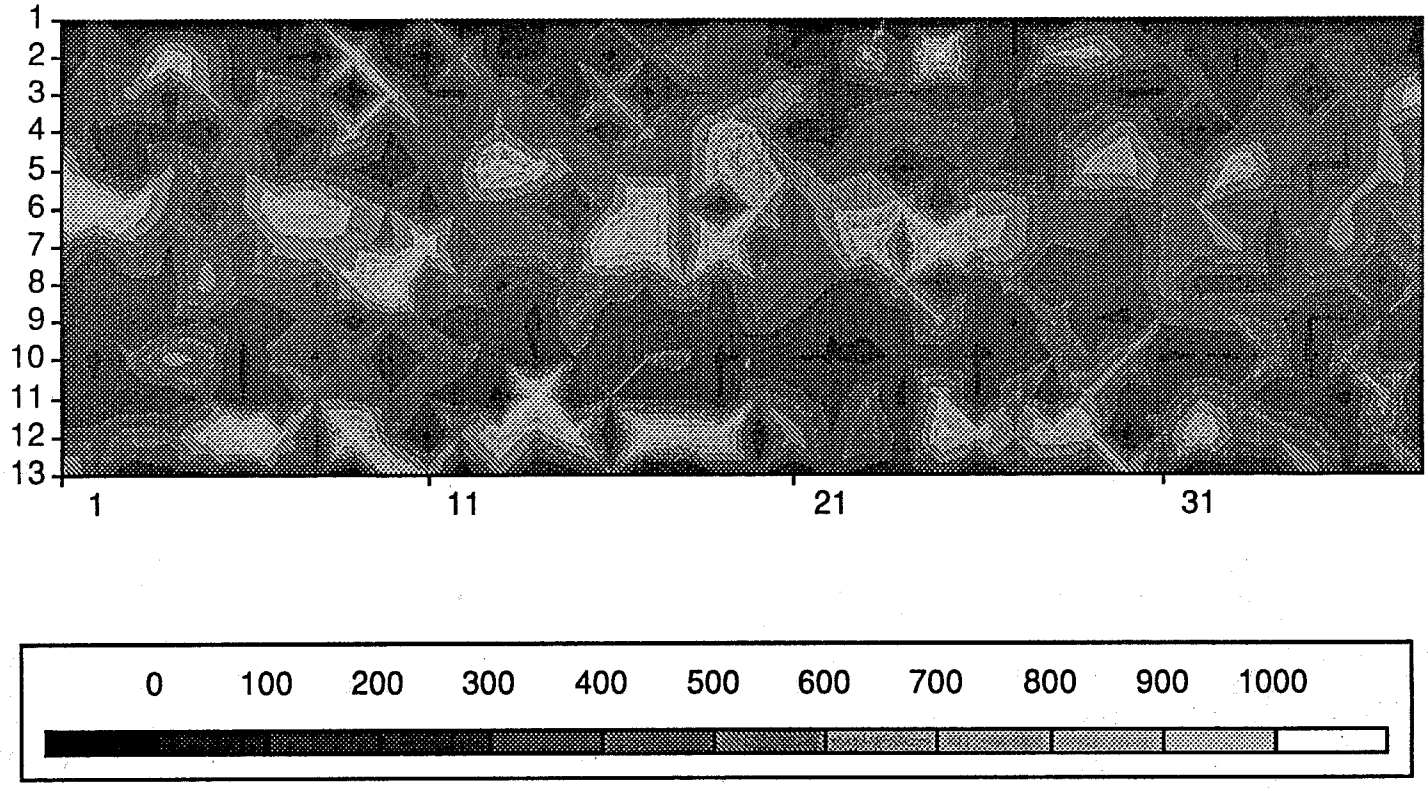

Fig. 36. Permeability field generated from Run (e) using only tracer data from VTP

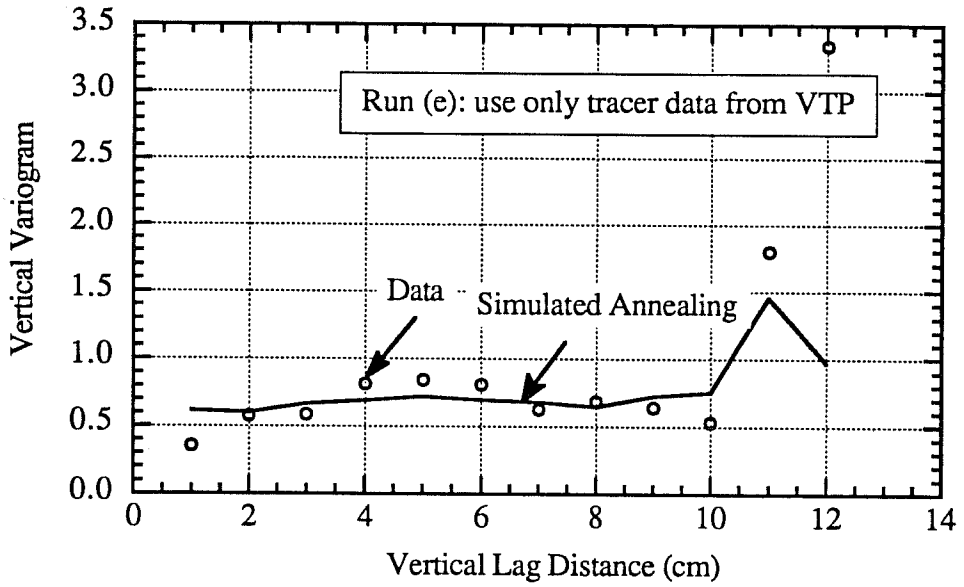

Fig. 37. Comparison between vertical variogram of data and simulated annealing

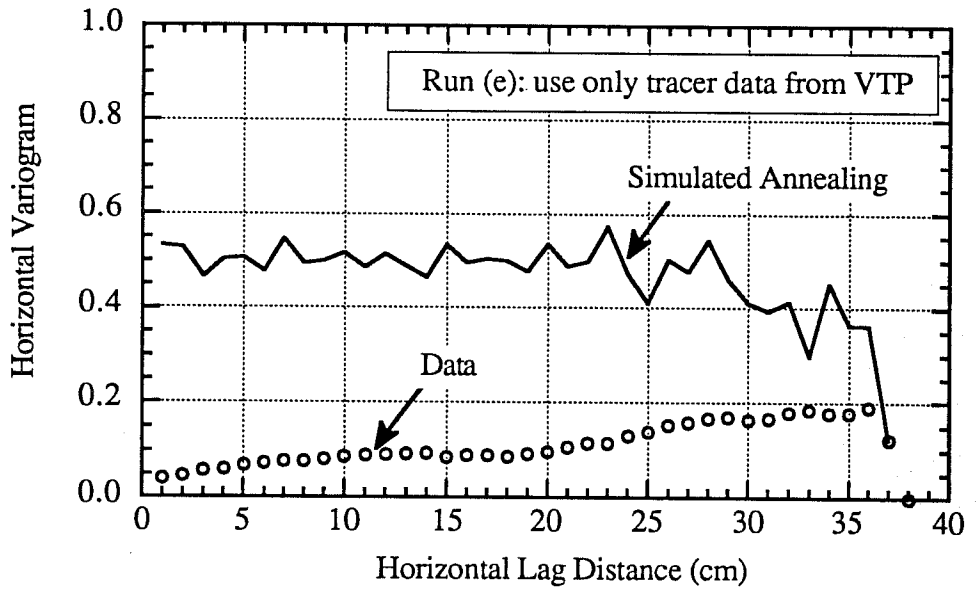

Fig. 38. Comparison between vertical variogram of data and simulated annealing

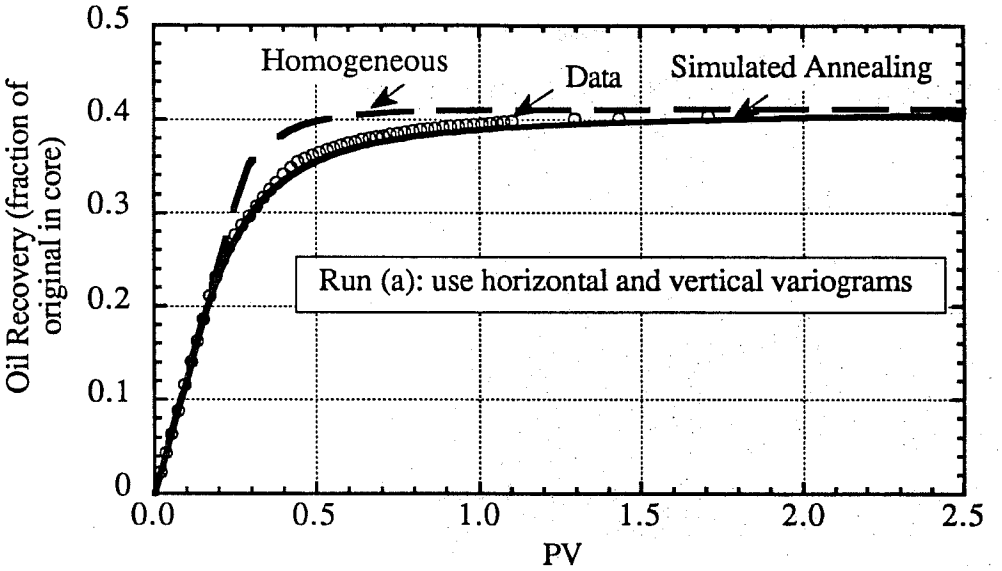

Fig. 39. Comparison between waterflood data and simulated annealing

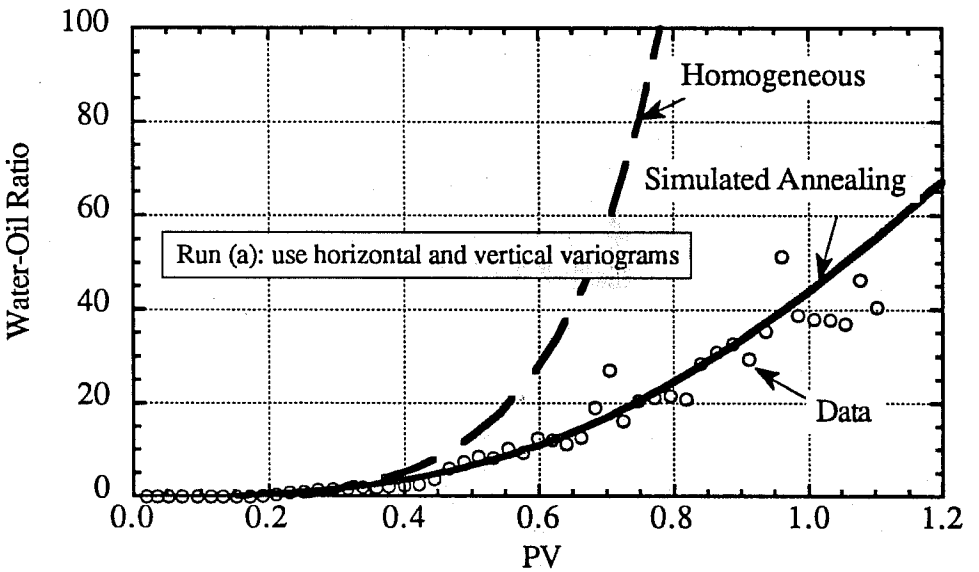

Fig. 40. Comparison between water-oil ratio of data and simulated annealing

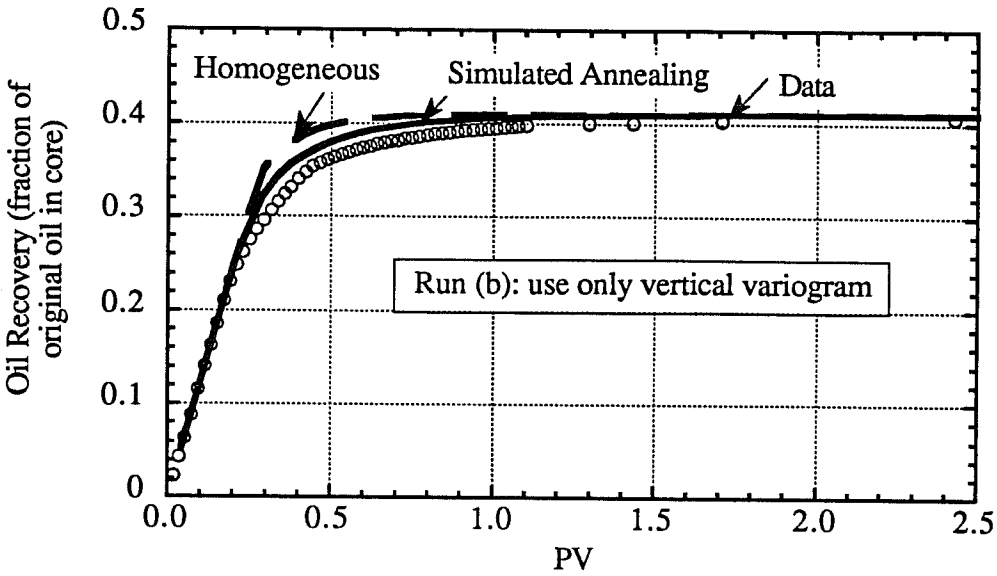

Fig. 41. Comparison between waterflood data and simulated annealing

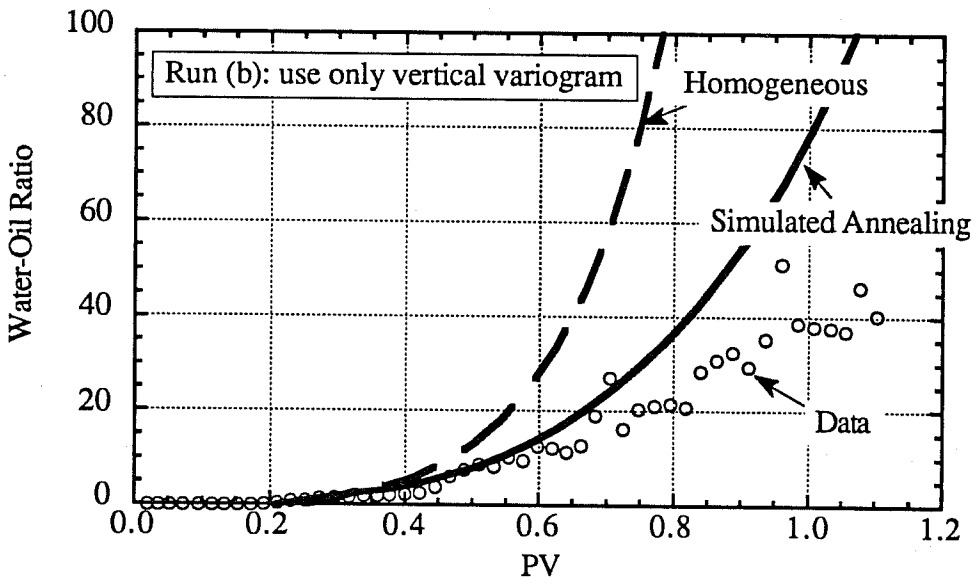

Fig. 42. Comparison between water-oil ratio of data and simulated annealing

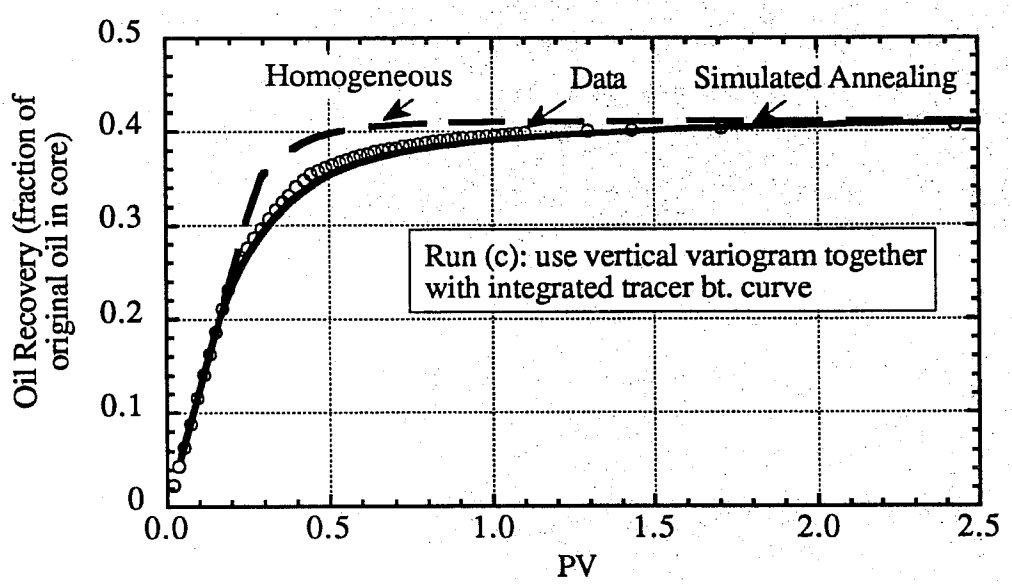

Fig. 43. Comparison between waterflood data and simulated annealing

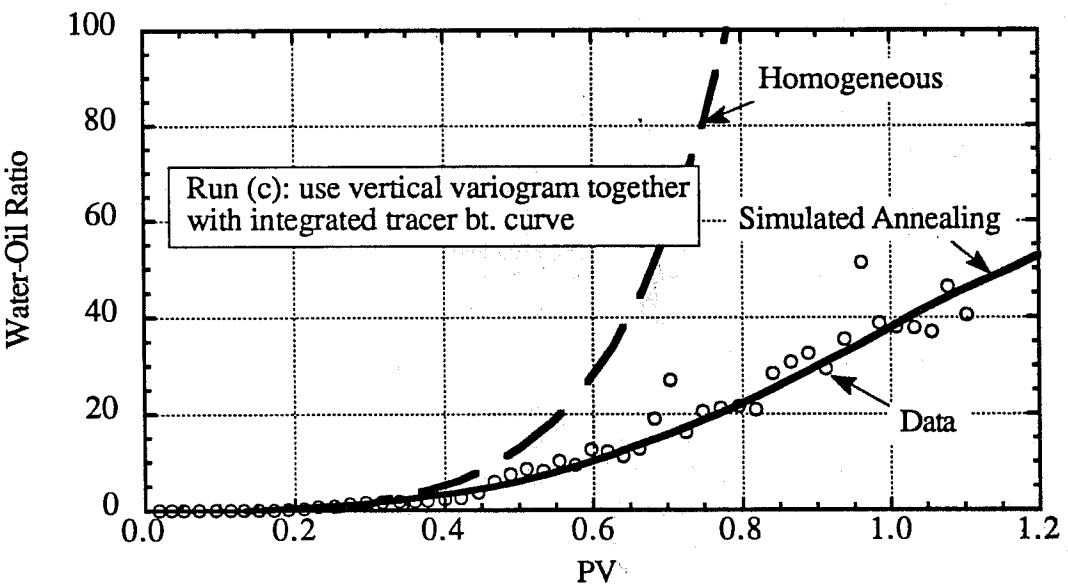

Fig. 44. Comparison between water-oil ratio of data and simulated annealing

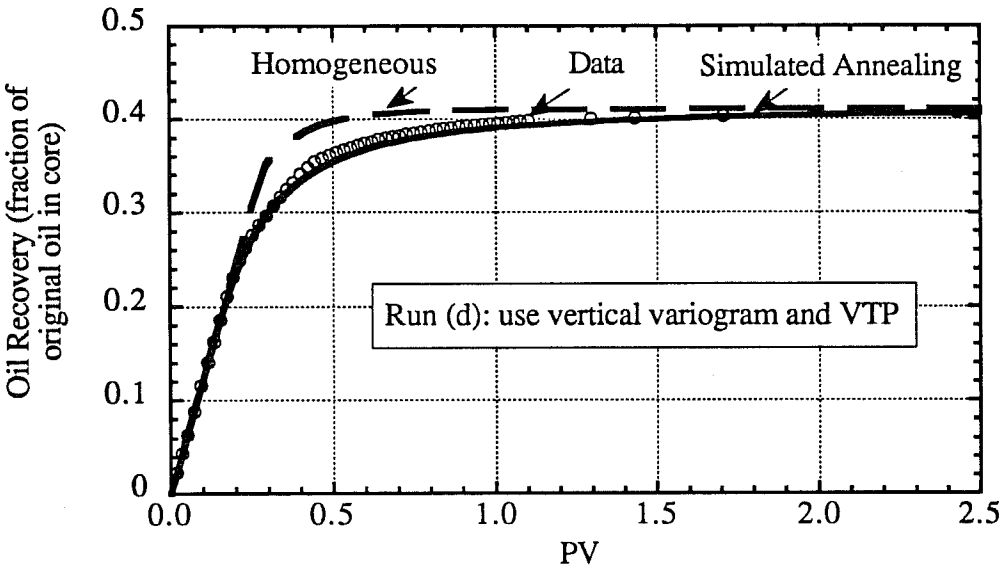

Fig. 45. Comparison between waterflood data and simulated annealing

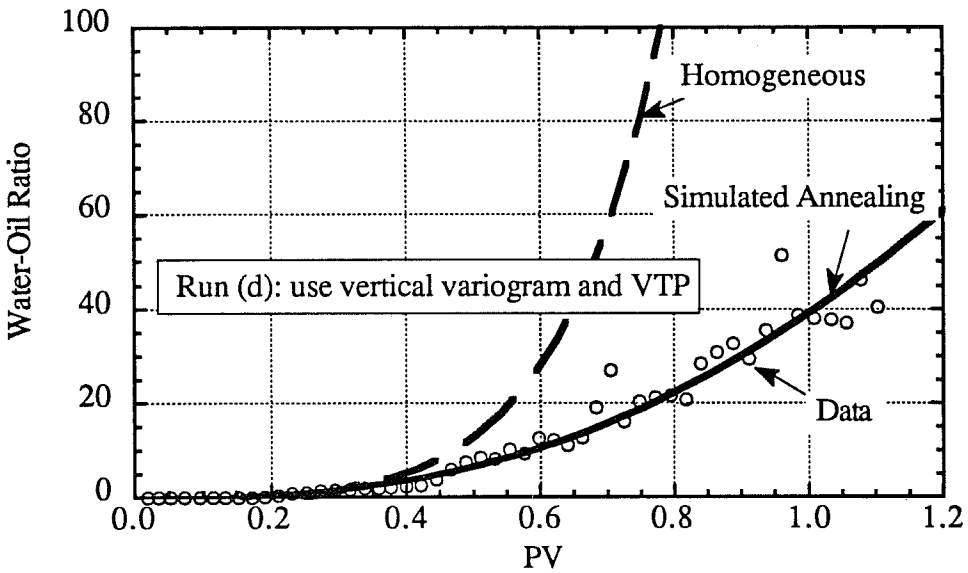

Fig. 46. Comparison between water-oil ratio of data and simulated annealing

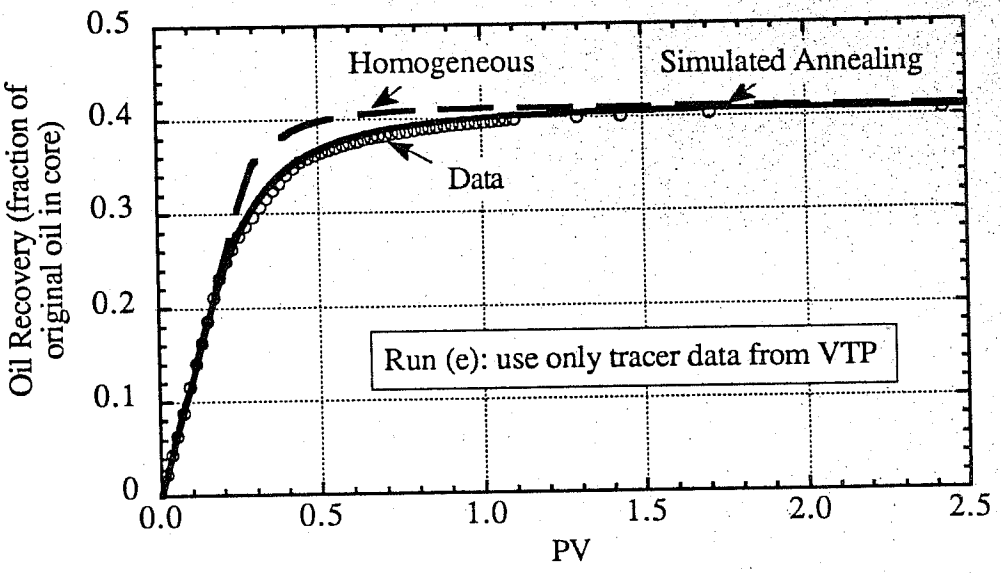

Fig. 47. Comparison between waterflood data and simulated annealing

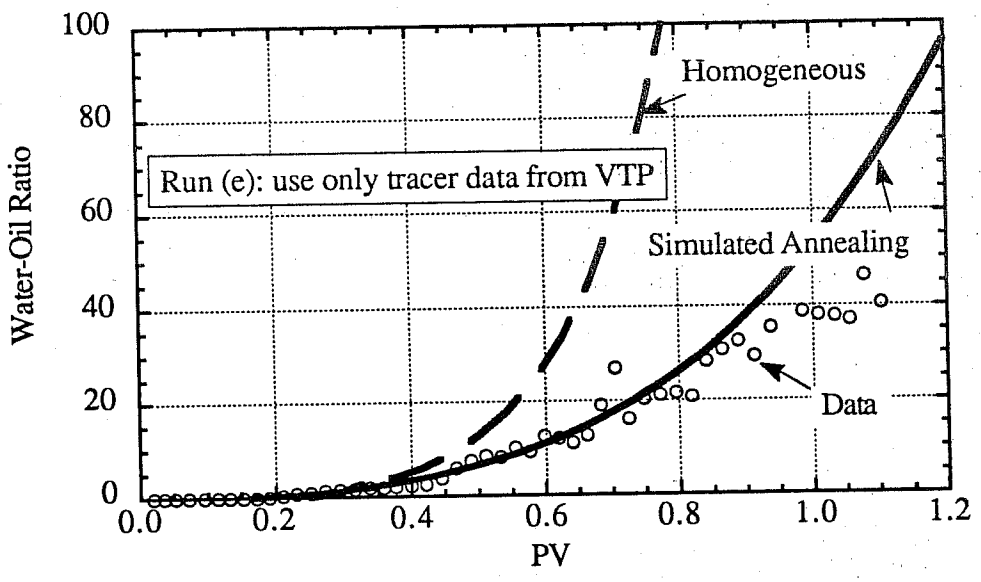

Fig. 48. Comparison between water-oil ratio of data and simulated annealing

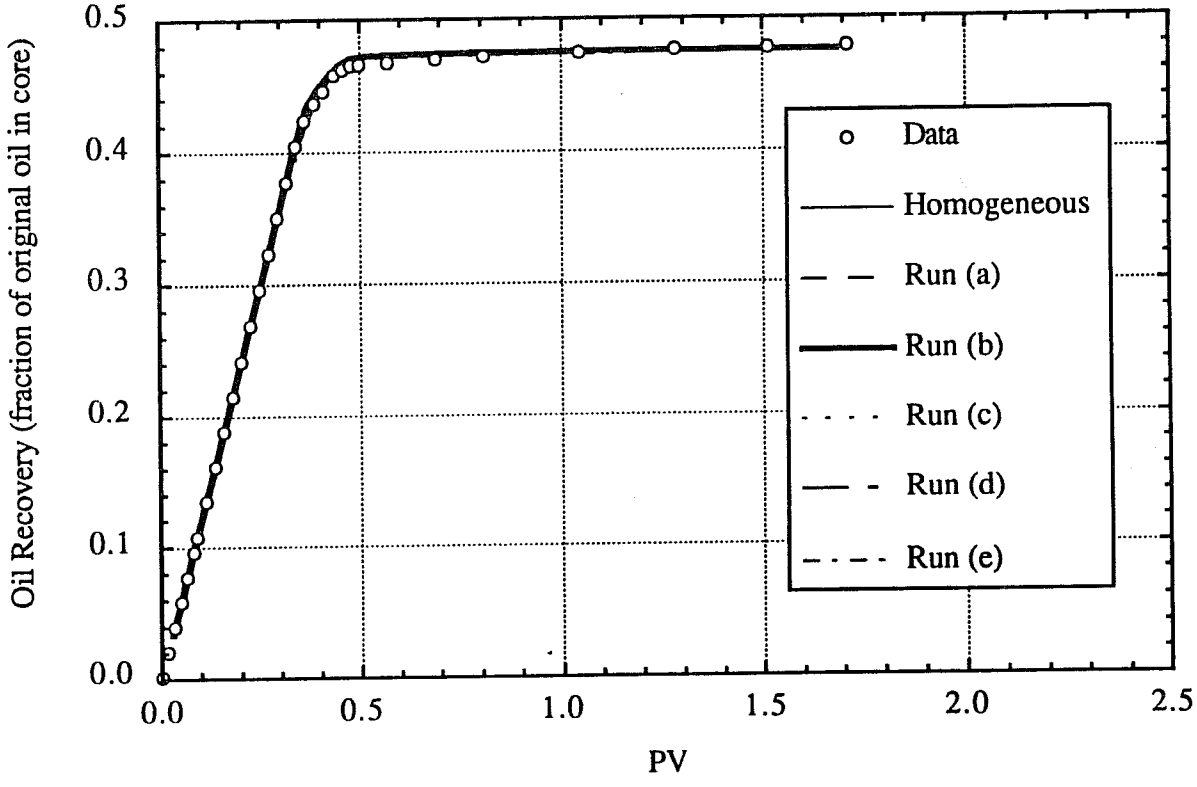

Fig. 49. Comparison between oil recovery from polymerflooding data and simulated annealing

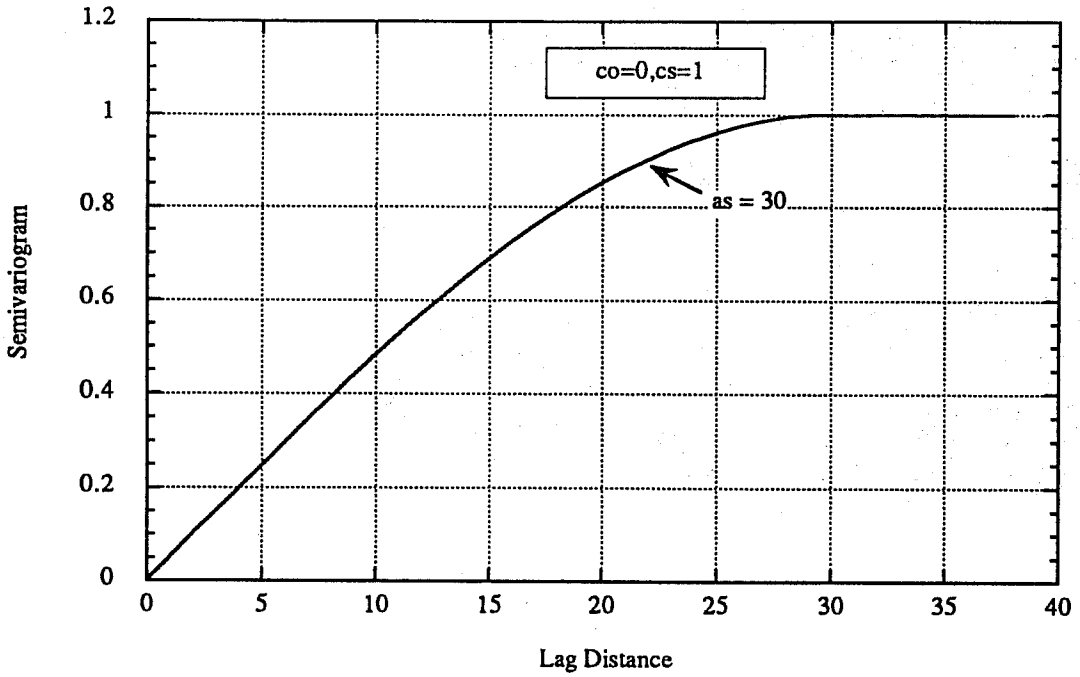

Fig. 50. Spherical model as a function of 3 parameters (c0,cs,as)

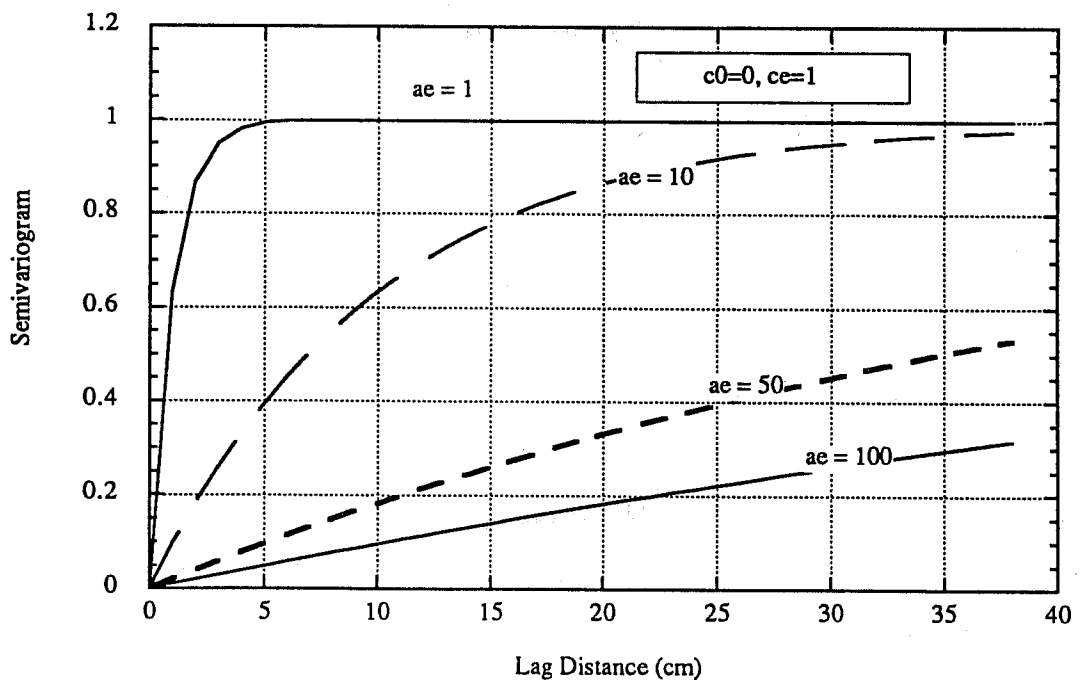

Fig. 51. Exponential model as a function of 3 parameters (c0,ce,ae)

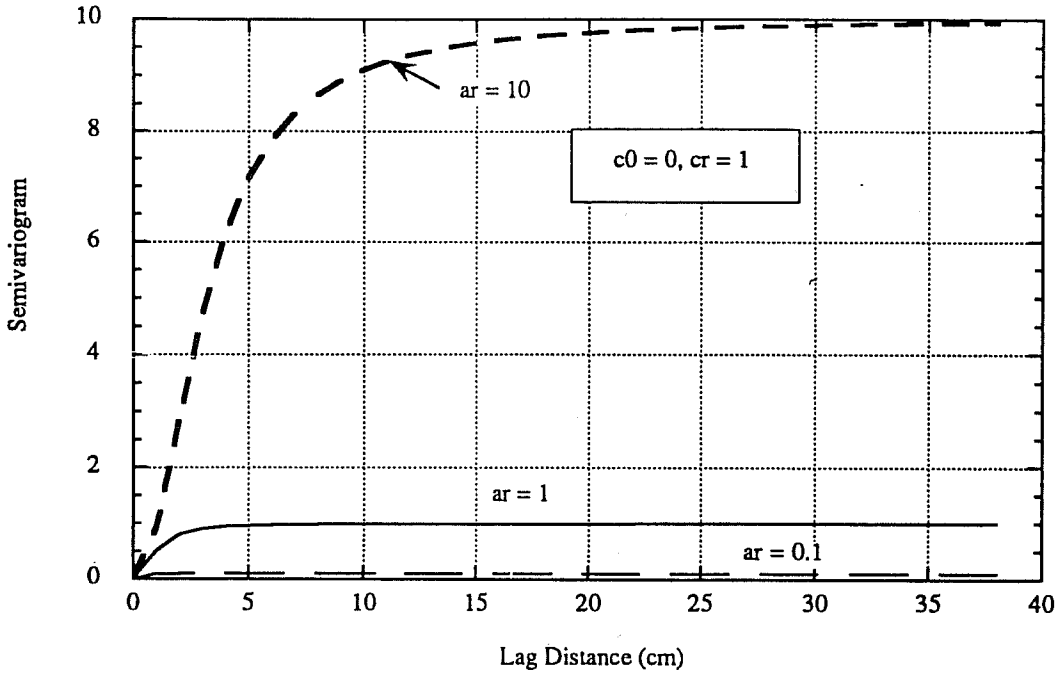

Fig. 52. Rational quadratic model as a function of 3 parameters (c0,cr,ar)

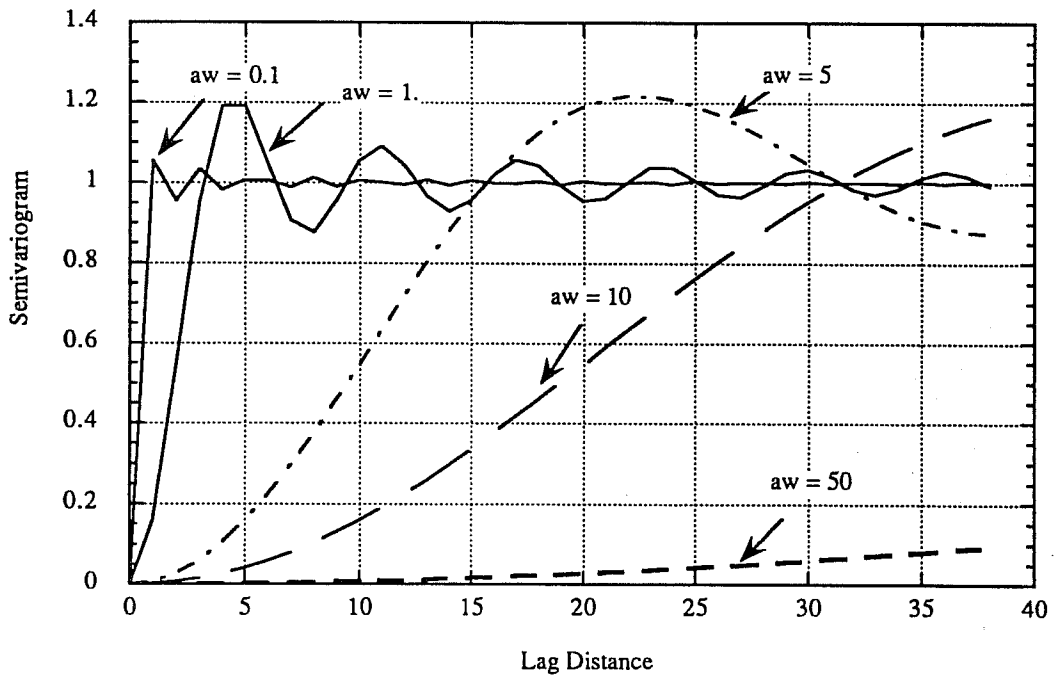

Fig. 53. Wave model as a function of 3 parameters (c0,cw,aw)

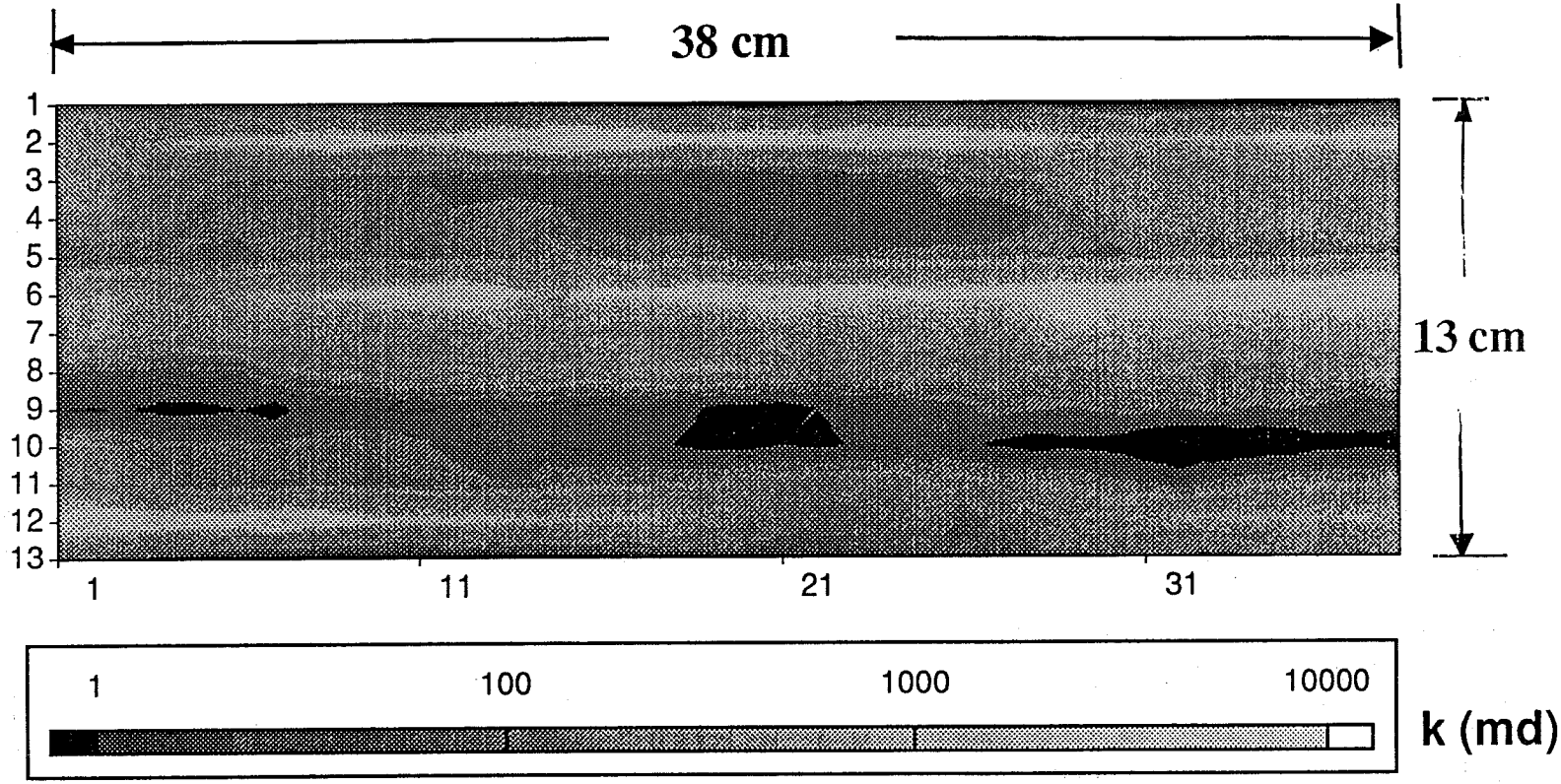

Fig. 54. Synthetic Data Generated Using MDM with $V_{DP} = 0.78$ and $\lambda_{DX} = 2$

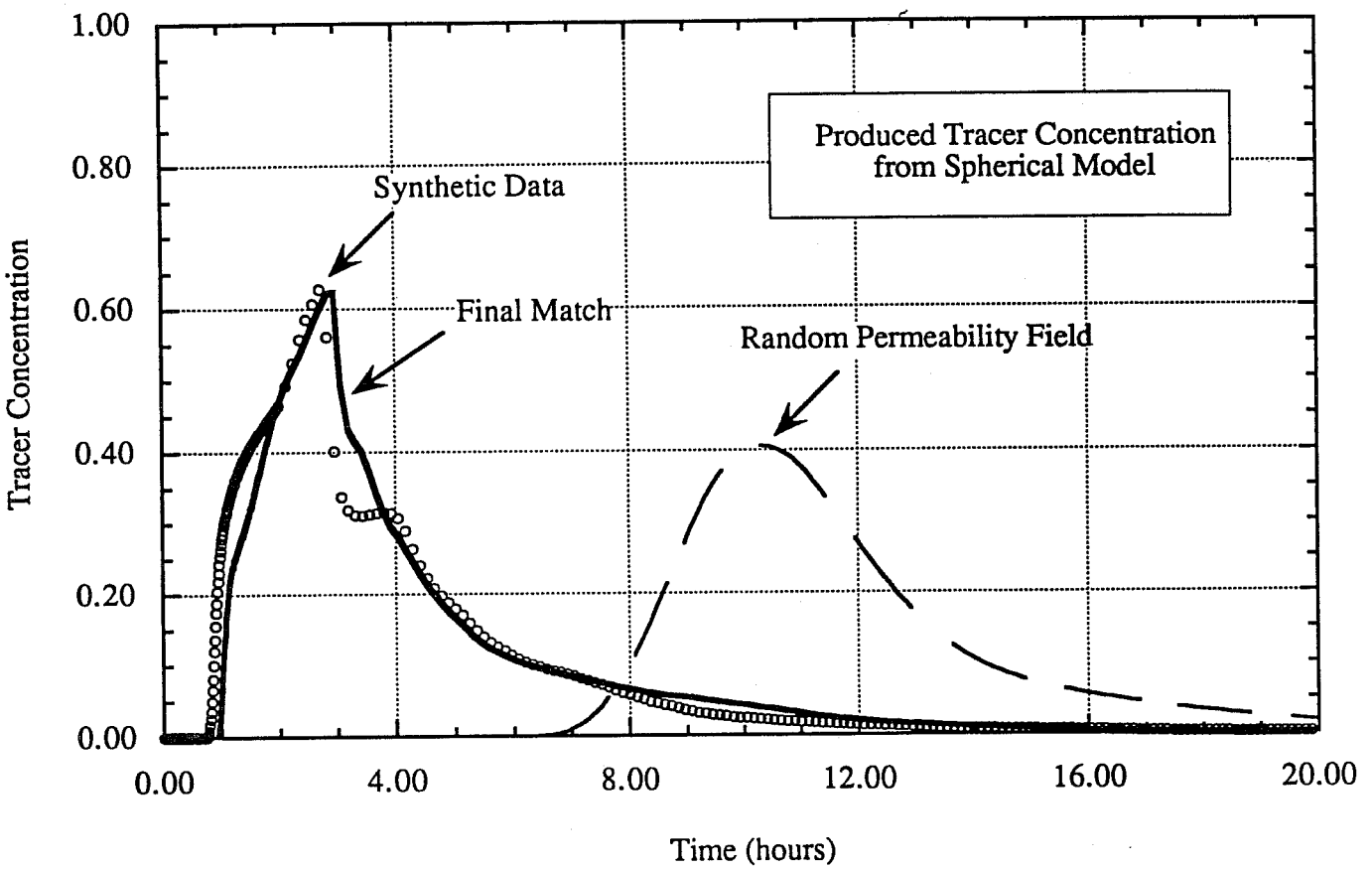

Fig. 55. Produced tracer concentrations from history matching using spherical model

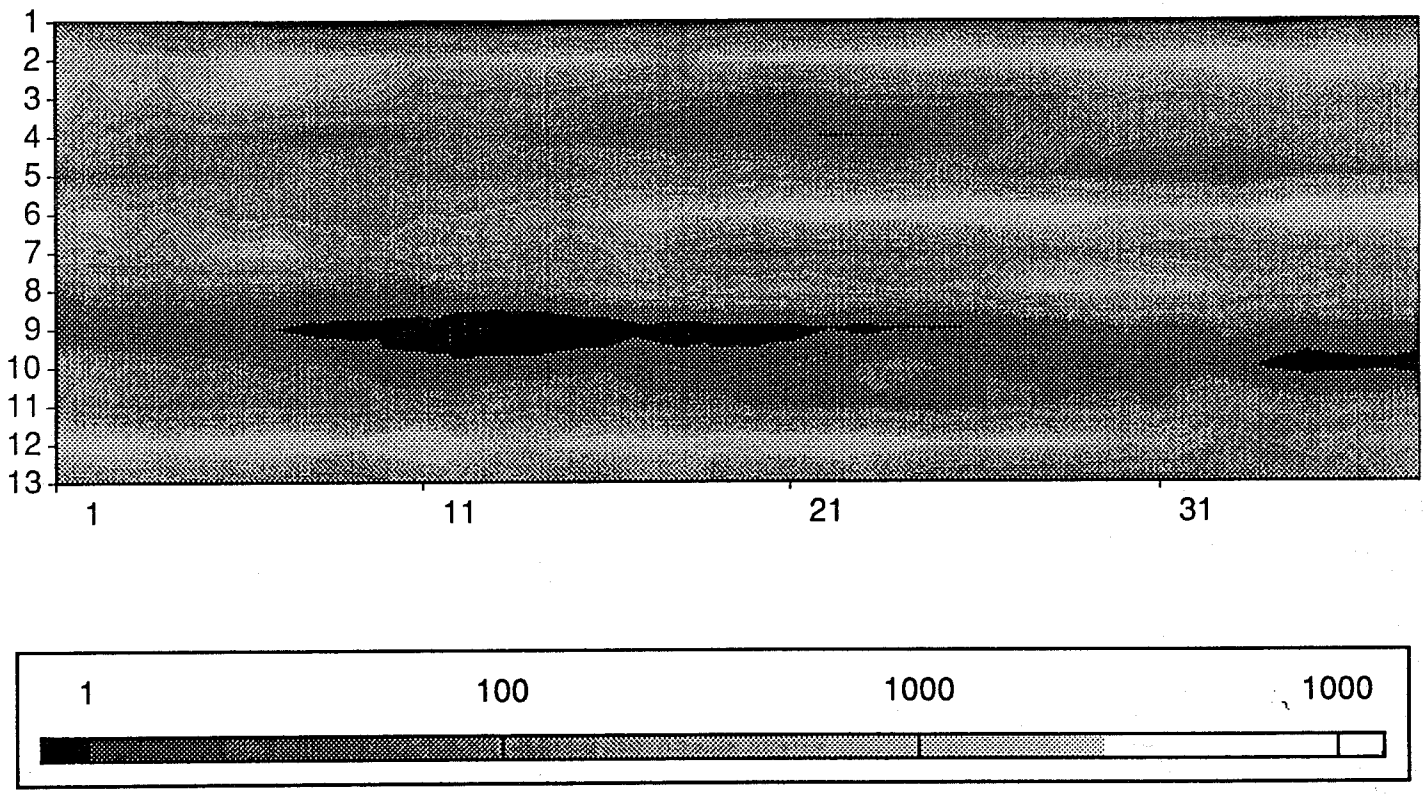

Fig. 56. Permeability distribution obtained from matching tracer data and using spherical model (Run No.utgstr3-7)

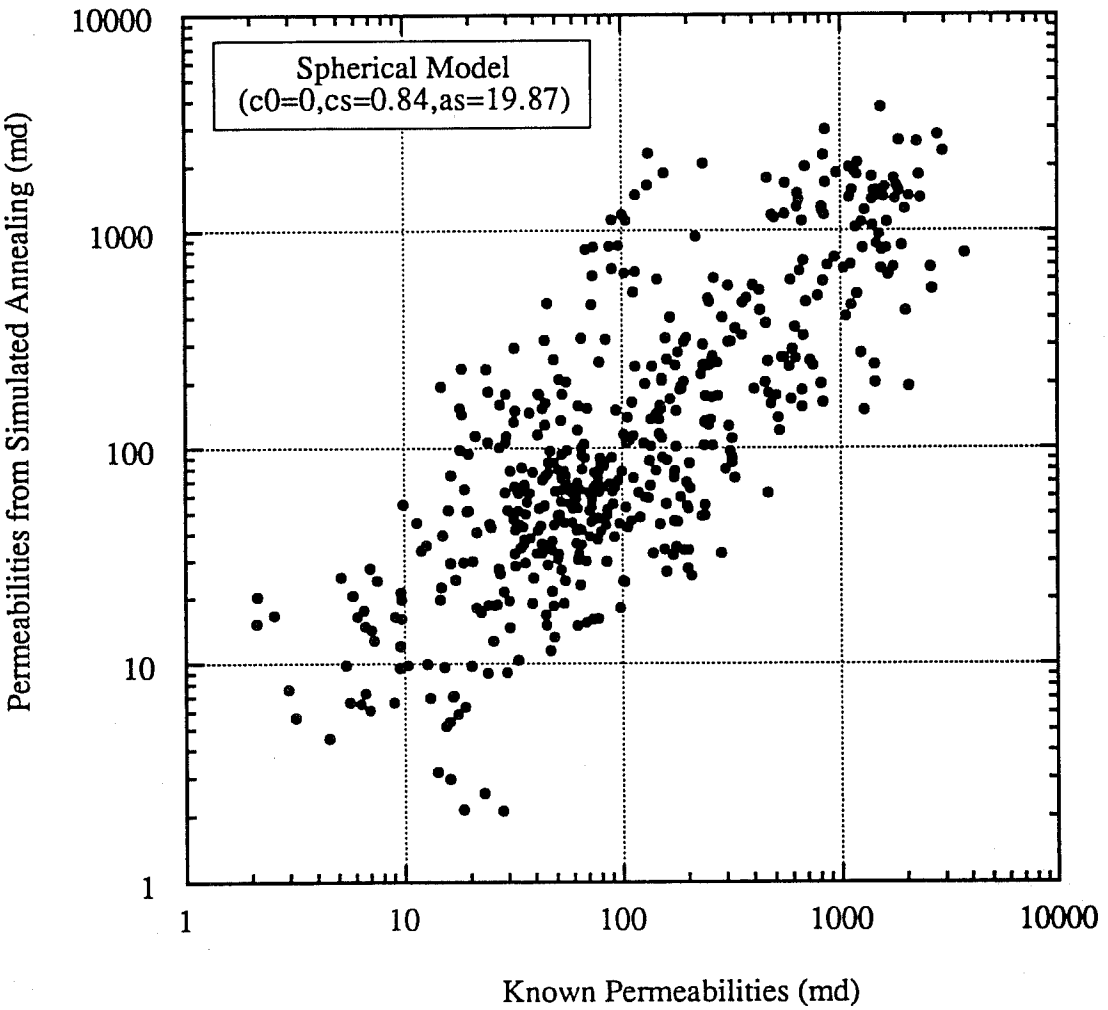

Fig. 57. Comparison at each gridblock between known permeabilities and permeabilities generated from matching tracer data

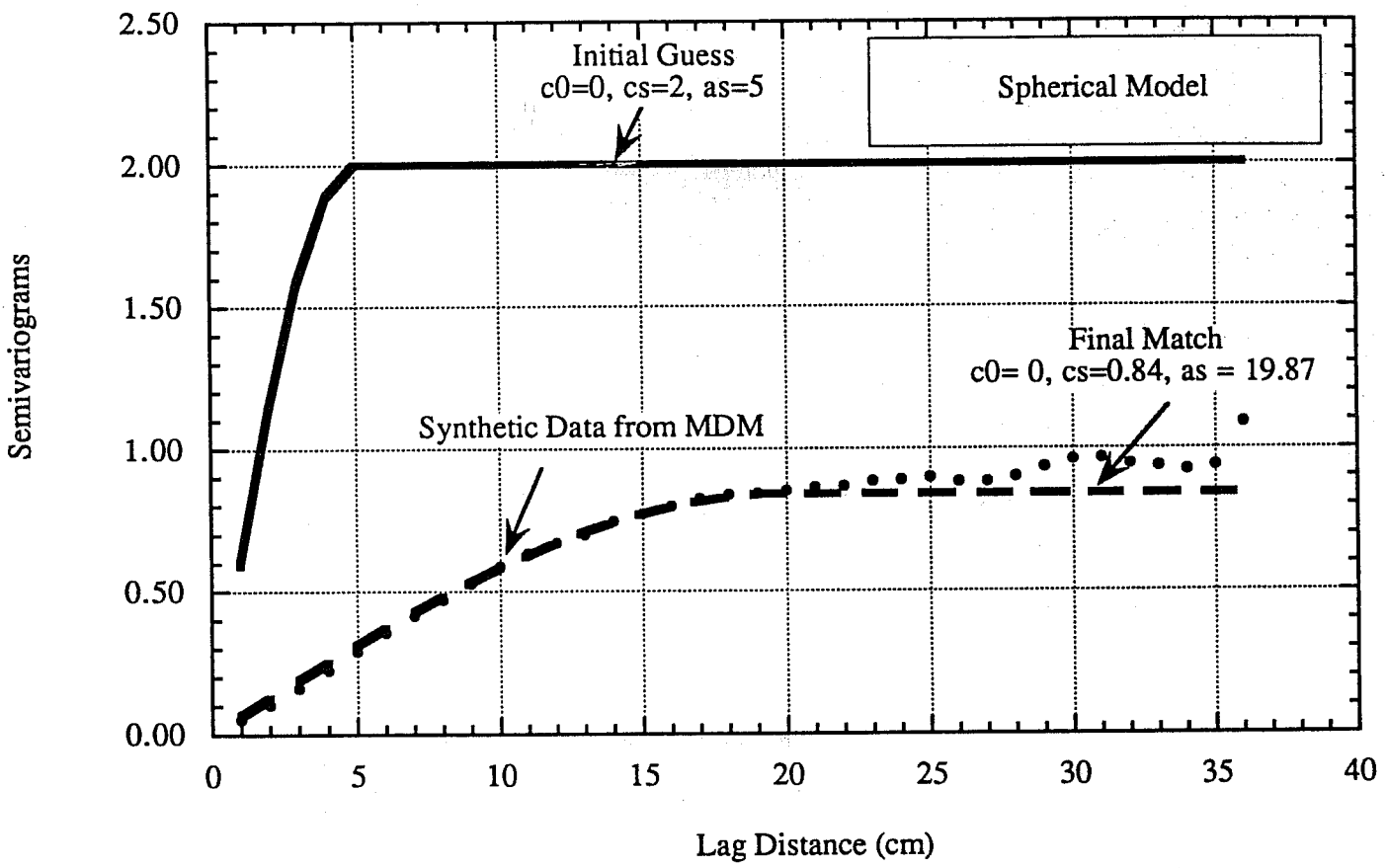

Fig. 58. Horizontal semivariogram obtained using spherical variogram model (Run No.UTGSTR3-7)

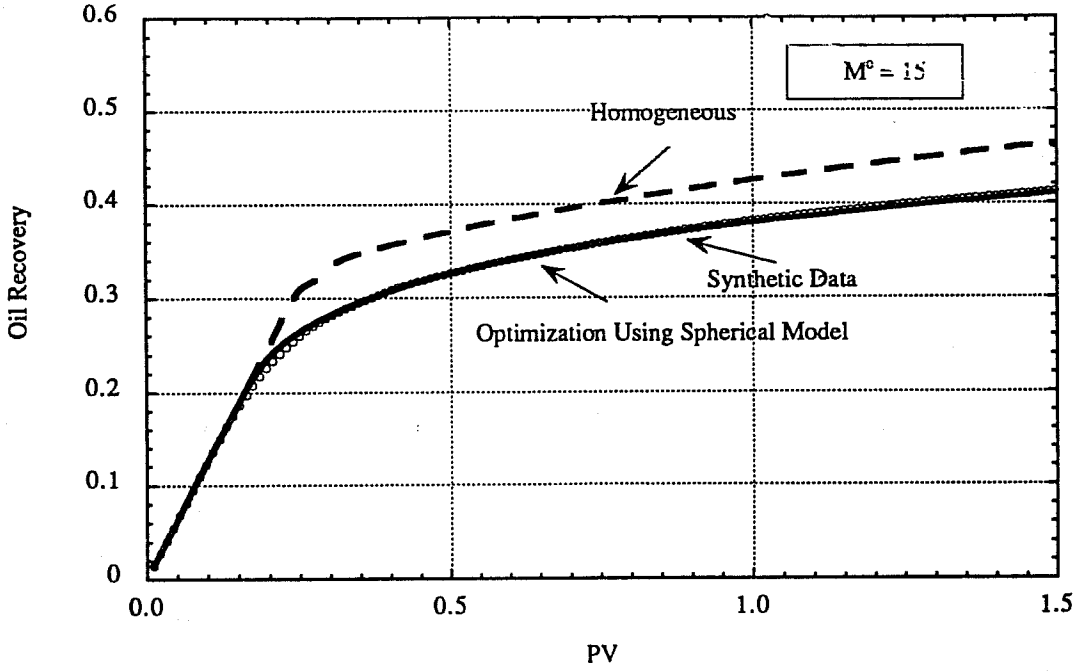

Fig. 59. Effect of heterogeneity on oil recovery

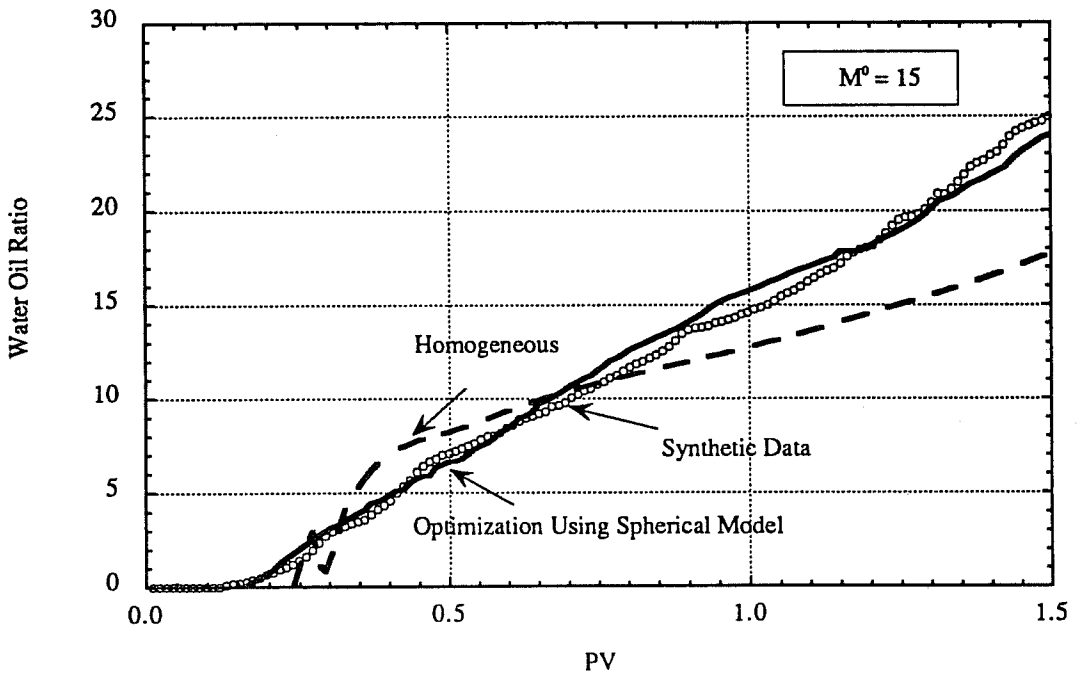

Fig. 60. Effect of heterogeneity on water-oil ratio

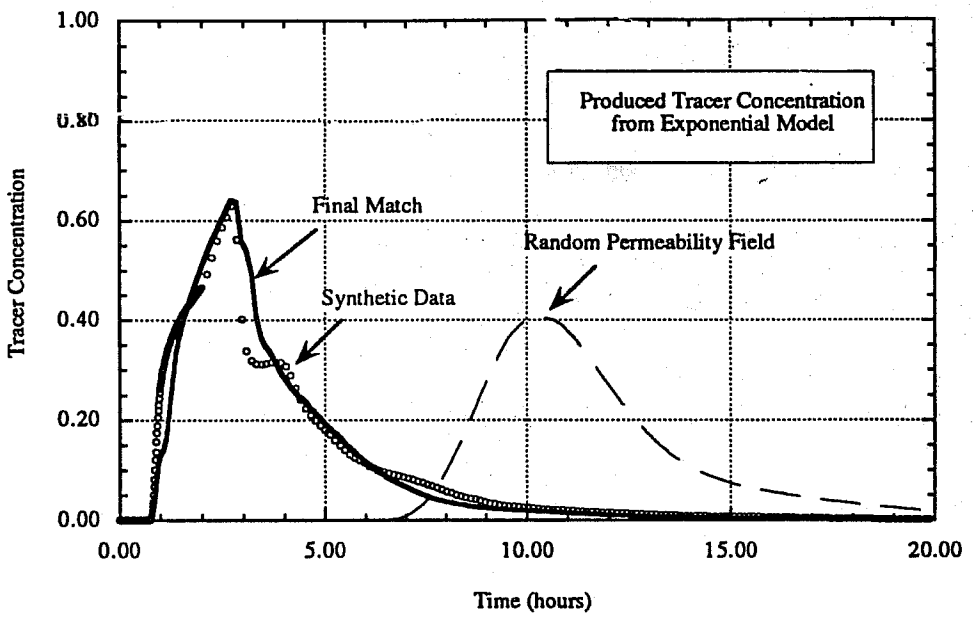

Fig. 61. Produced tracer concentrations from history matching using exponential model

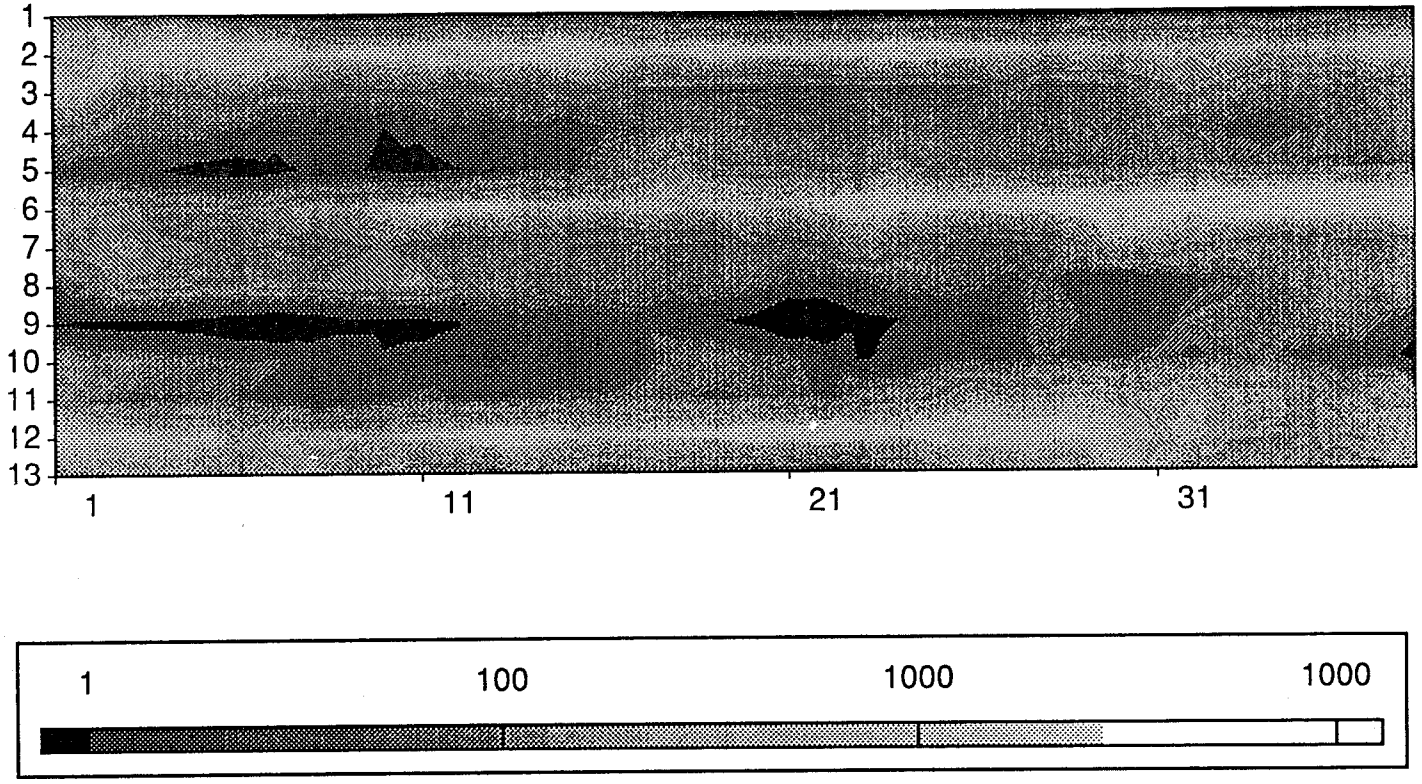

Fig. 62. Permeability distribution obtained from matching tracer data and using exponential model (Run No.utgstr1&2)

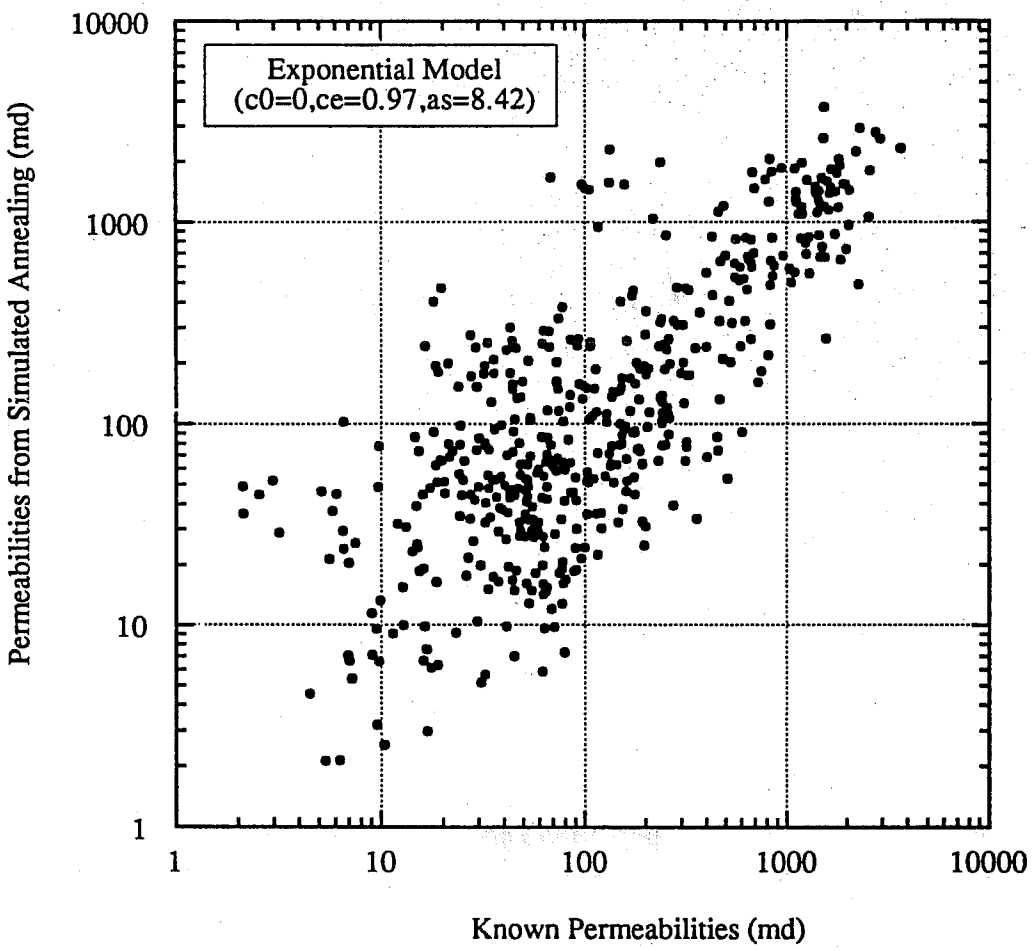

Fig. 63. Comparison at each gridblock between known permeabilities and permeabilities generated from matching tracer data

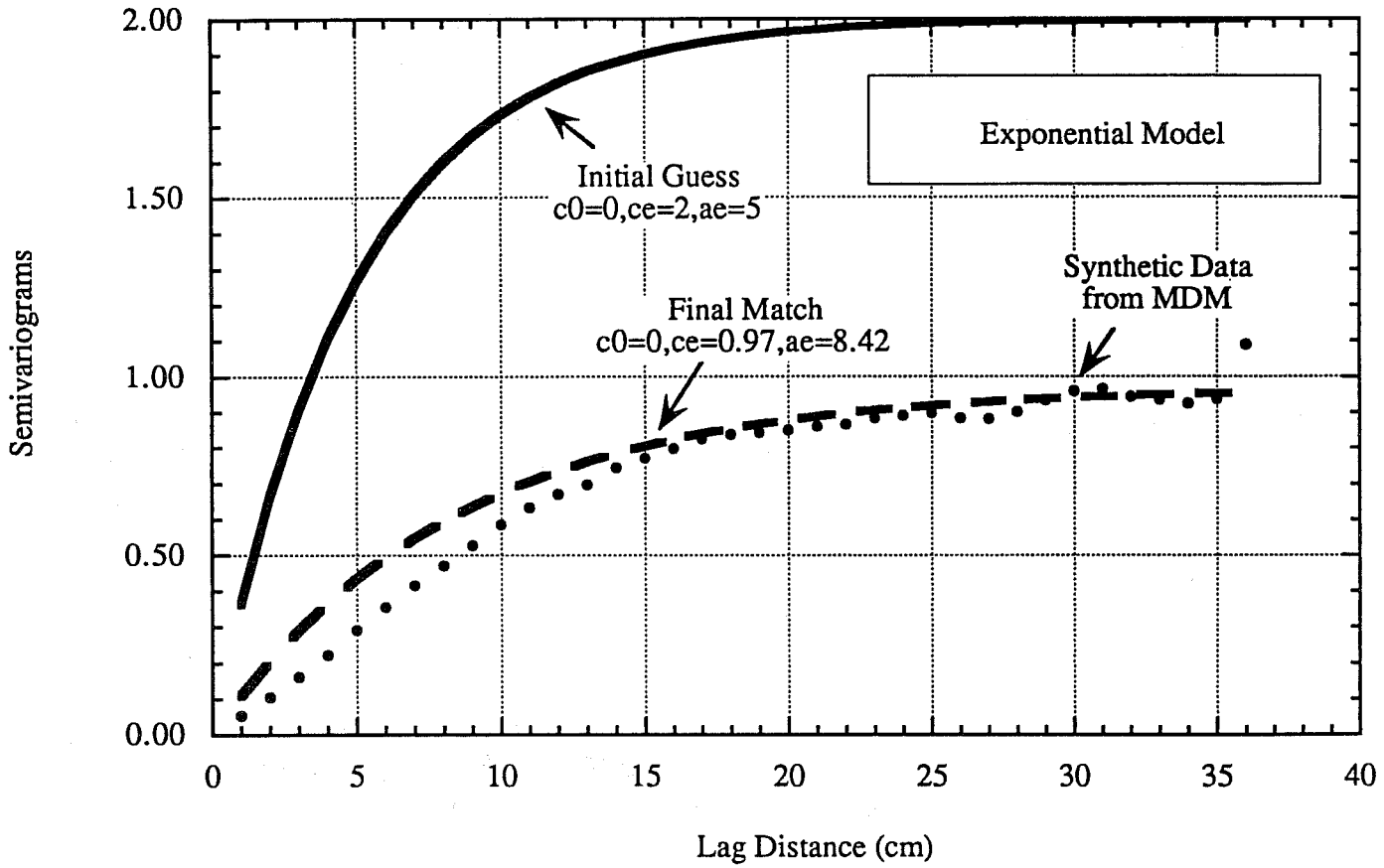

Fig. 64. Horizontal semivariograms obtained using exponential model (Run No.UTGSTR1&2)

SECTION II
SWEPT VOLUME, RESIDUAL OIL SATURATION, AND FLOW PATTERN USING THE FIRST-MOMENT METHOD

SUMMARY

This report investigates the accuracy of swept volume calculated from the first-moment method using tracer production data from an interwell tracer test. Because of heterogeneity, a tracer response has a long tail and much information is contained during this period. It is more likely in an actual field application that this tail will not be accounted for because the test is stopped too early or the produced tracer concentration falls below the detectable limit. Results of swept volume calculated from the first-moment method of tracer production data are compared with ones from reservoir tracer concentration contours from simulations. It is shown that the lower the cutoff concentration, the smaller is the difference between the swept volumes from the first moment and the reservoir tracer concentration contours. A tracer with a lower detectable limit will give a better result than a tracer with a higher detectable limit. Furthermore, the reservoir swept volume can be different depending on the type of flooding process. There are an optimum injected slug size and concentration that yield an optimum swept volume for different flooding processes.

The first-moment method is extended for partitioning tracers to determine the residual oil saturation in-situ between wells. The theory is presented and then verified using 3D simulation data. It is found that this method can give an accurate residual oil saturation for a very heterogeneous reservoir and a nonuniform (local) distribution of residual phase. There is no assumption required about the shape of the partitioning and nonpartitioning tracers. This method is being applied to a field application using data from a field gas tracer test of the Shallow Oil Zone (SOZ) reservoir located at the Elk Hills Naval Petroleum Reserve in California (NPRC). Results are reported in Section III.

The application of the first-moment method to determine the residual phase saturation is further extended to obtain a saturation map of a residual phase. This is done using simulated data from a new tracer test called Vertical Tracer Profiling (VTP). Results show that VTP can provide insight into the flow pattern of a reservoir where a conventional tracer test cannot. In the limiting case of a noncommunicating layered reservoir, the swept volume and residual phase saturation of each layer can be obtained with VTP. Furthermore, if crossflow is small, a saturation map of the residual phase can be estimated. The difference between the calculated residual phase volume from VTP and simulated data increases with the degree of crossflow. For a reservoir with large crossflow, exact location of the residual phase may not be so critical as for a reservoir with small crossflow because of greater sweep efficiency. Bypassing or undetection of the residual phase by injected tracers is not likely for a reservoir with large crossflow. The use of selective injection combined with VTP is shown to provide the most information about crossflow and reduce the chance of bypassing the residual phase by injected tracers.

INTRODUCTION

Many authors have related the first and second moments of a tracer response to the degree of physical dispersion for different boundary conditions (Levenspeil and Smith, 1957; Van der Laan, 1958; Aris, 1958). Some of these results are tabulated in Himmelblau and Bischoff (1968). Beier and Sheely (1988) used the first-moment method to estimate the reservoir swept volumes between wells at the MCA unit in New Mexico. Tester *et al.* (1982) used cutoff fractional recovery of tracer to define a truncated integral mean volume. He defined the 90% truncated integral mean volume as

$$\langle V \rangle_{90} = \frac{Q \int_0^{t_{90}} c\, t\, dt}{\int_0^{t_{90}} c\, dt}, \qquad (1)$$

where t_{90} is the time at which 90% of the injected tracer has been recovered. Robinson (1985) used the internal residence-time distribution to evaluate the fluid flow and temperature pattern of a geothermal reservoir. He also showed that in a tracer experiment, the tail of a residence-time distribution curve can be extrapolated using different functions and the calculated pore volume is not sensitive to these functions. The accuracy of the swept pore volume as a function of effective or cutoff concentration from the first-moment method compared to actual reservoir swept pore volume has not been reported in the literature.

This report investigates the swept volume calculated using the first-moment method with the tracer production data from an interwell tracer test as a function of cutoff concentrations. Because of heterogeneity, a tracer response has a long tail and much information is contained during this period. It is more likely in an actual field application that this tail is not accounted for because the test is stopped too early or the produced tracer concentration falls below the detectable limit. The detectable limit depends on the kind of tracers and also the analytical method used to analyze the tracer samples. Therefore, the swept volume varies with the minimum detectable concentrations or cutoff concentrations.

The following is the problem statement. Can the first-moment method be used in an actual field application to obtain an accurate estimate of the reservoir swept volume? If so, what are the underlying assumptions of this method and how accurate or reliable is the result compared to actual reservoir swept volumes ?

This report is divided into three sections. The first section involves 2- and 3D simulations of tracer flow using different well patterns. The swept volumes from the first moment of simulated tracer production data are then compared with reservoir tracer concentration contours from simulations. The next section is an extension of the first-moment method applied to partitioning tracers for the purpose of residual phase saturation determination. The last section combines the first-moment method with tracer production data from VTP to determine the flow pattern inside the reservoir and investigate the possibility of obtaining a saturation map of the residual phase.

SIMULATION STUDY OF SWEPT VOLUMES

The assumptions in this study are constant injection and production rates and that tracers are not adsorbed on the rock surface. The following procedure is used in this study. First, stochastic permeability fields are generated using geostatistical techniques. Second, these field are used as input in a finite-difference numerical reservoir simulator to simulate an interwell tracer test using nonadsorbed tracers. The tracer production data from the simulator are used in the first-moment calculation. A subroutine is implemented in the simulator to count the number of gridblocks that encounter tracer concentrations greater than some specified cutoff value. These numbers are contours of reservoir tracer concentrations. Because of numerical dispersion, these contours will be higher than the actual swept volume. By averaging the contours of different tracers, numerical dispersion is then minimized. These two results are compared as functions of cutoff concentrations.

The first moment with respect to volume is defined as

$$\bar{V} = \frac{\int_0^\infty c\, V\, dV}{\int_0^\infty c\, dV} . \qquad (2)$$

For constant injection and production rates,

$$\bar{t} = \frac{\int_0^\infty c\, t\, dt}{\int_0^\infty c\, dt} \qquad (3)$$

and

$$\bar{V} = Q\bar{t} , \qquad (4)$$

where Q = rate between injector and producer.

The amount of tracer produced at any producer can be calculated from

$$m_p = Q_p \int_0^\infty c\, dt , \qquad (5)$$

$$Q = \frac{m_p}{m_i} Q_i \qquad (6)$$

The following patterns are used in this simulation study: a five-spot pattern with balanced injection and an irregular pattern with unbalanced injection. Both homogeneous and heterogeneous and 2D and 3D are used.

Five-Spot Pattern with Balanced Injection

The pattern under study is a square of size 620 ft x 620 ft and is 20 ft thick. Four injectors located at the corners are operating at 1,000 ft^3/day. The producer is located in the middle and producing at constant pressure. Tracer is injected at Injector 1 located at the lower left corner of this pattern. The tracer injection interval is 10 days. All tracer concentrations in this study are normalized by the initial injected concentrations. Figure 1 shows an areal view of the five-spot grid, well location, and different swept volumes.

2D, homogeneous five-spot pattern

This is a test case before making a more complicated investigation. The objective is to show that the procedure of using tracer concentration contours from a finite-difference numerical reservoir simulator as a way of obtaining the swept volume is accurate. The grid size used is 31 x 31 x 1 (NX x NY x NZ). For this simple case, the swept volume is 25% of the total pore volume. Figure 2 shows tracer production data used in the first-moment calculation. The breakthrough time is 300 days and the peak is located at 380 days. Tracer response shows a long tail because of the flow pattern. Table 1 shows the result of the first-moment calculation at different cutoff

concentrations. At a cutoff concentration of 10^{-3}, the first-moment calculation shows 4% lower swept volume than the tracer concentration contours. This is because of the slow moving tracers along the outer streamlines that have not been accounted for in the first-moment calculation. At longer time or smaller cutoff concentration, the two methods approach the same correct answer as shown in Fig. 3. This is a good example to show the effect of cutoff concentration in the first-moment method. For a more realistic field with heterogeneity, one would expect the difference to increase if tracer responses are truncated at high cutoff concentration. This effect will be shown in the next simulation run.

2D, heterogeneous five-spot pattern

To see the effect of heterogeneity on the swept volume calculation, the same input as in the homogeneous case is used except for the permeability field which was generated using the MDM (Yang, 1990) with a seed number of 87,654, V_{DP} of 0.81 (σ_{lnk} = 1.7, CV=2.231), correlation lengths in both the X and Y directions of 300 ft. Figure 4 shows the permeability field from the MDM. Four tracers were simulated and each is injected in a different injector. The names of these four hypothetical tracers correspond to the number of their injector. The use of multiple tracers enables different regions to be investigated. Figures 5 and 6 show the simulated production data. Tracers 2 and 4 break through about the same time at 170 days of injection and peak at 240 days. The next tracer to break through is Tracer 1 at 300 days which is about the same time as in the homogeneous case followed by Tracer 3 at 350 days. The late breakthroughs of the last two tracers and long tails compared to the homogeneous case indicate that the area around Injectors 1 and 3 have low permeabilities. The early breakthroughs of Tracers 2 and 4 indicate the possibility of channeling and a high-permeability area between the producer and Injectors 2 and 4. This analysis agrees with the observation of the permeability field that shows a high-permeability area located at the upper-right corner, or near Injector 4, and also near Injector 2. Tables 2 to 4 show results of the first-moment calculation from the four tracer responses.

Figures 7 and 8 show comparisons between swept volumes from the first-moment calculation and tracer concentration contours as a function of cutoff concentration. At a cutoff concentration of 10^{-3}, the swept volume from the first moment is always lower than that from the contours. Because streamlines that contain injected tracers have not reached the producer, they have not been accounted for in the first-moment calculation. The amount of tracer produced as a function of cutoff concentration is shown in Table 5. As the cutoff concentration is lowered, more weight is put on the tail of the tracer responses and thus the swept volumes approach those from the contours. The difference between the two calculations ranges from 1 to 8% at a cutoff concentration of 10^{-3}. At a cutoff concentration of 10^{-4}, the maximum difference is about 6% between Injector 2 and the producer. However, the first-moment calculation shows about 1 to 2% difference for other injectors. At the small cutoff concentration of 10^{-6}, the two calculations give the same results.

3D, heterogeneous five-spot pattern

We have investigated the swept volumes in 2D simulation, and the results from the first-moment method agree well with the tracer concentration contours. In the actual field, the flow is 3D. The objective of this run is to include the 3D flow effects with realistic heterogeneity. The permeability field was generated using the MDM (Yang, 1990) with a seed number of 87654, V_{DP} of 0.90, correlation length in both the X and Y directions of 300 ft and zero correlation length in the vertical direction. The generated permeability field is shown in Fig. 9. The grid size used was 31 x 31 x 5 (NX x NY x NZ). All other data were unchanged from the previous two cases except for the grid size in the Z direction and the permeability field.

Figures 10 and 11 shows simulated tracer production data. Comparing this run with the 2D case, all four tracers show earlier breakthrough times, lower peak values and longer tails than for the 2D case because of heterogeneities. The first tracer to break through is Tracer 1 followed by Tracers 3, 4, and 2, in that order. Tracer 2 has the longest tail and thus indicates that the

highest heterogeneity is between Injector 2 and the producer. The early breakthrough time of Tracer 1 indicates that the area between Injector 1 and the producer has the highest permeability. Since this breakthrough time and peak location are not very different from those of the other tracers, it is not likely that there would be a channel between this injector and the producer. Tracer 3 shows a double peak, which is a characteristic of high-permeability contrast between layers.

Tables 6 to 9 show the results of the first-moment calculations. Figures 12 to 15 compare swept volumes obtained from the two methods as a function of cutoff concentrations. From the tracer concentration contours, the largest swept volume is between Injector 2 and the producer and the smallest volume is between Injector 3 and the producer. The swept volume between Injector 4 is slightly higher than that between Injector 1 and the producer. At the large cutoff concentration of 10^{-3}, the first-moment method gives much lower volume than the actual volumes. The largest difference is about 24% with Tracer 2, and the smallest is 9% with Tracer 3. As the cutoff concentration is lowered, the differences between the two methods become smaller. At a cutoff concentration of 10^{-5}, the difference ranges from 2 to 10%. At a cutoff concentration of 10^{-6}, Tracer 3 indicates less than 1% difference between the two methods. When all tracers are produced, the two methods will converge to the same answer.

To confirm results from the UTCHEM simulator and the procedures used to eliminate numerical dispersion in calculating tracer concentration contours, a streamline model using a semianalytical technique based on transit-time calculation was used to double-check the swept volumes. Figures 16 to 19 compare tracer production data from the 3D, semianalytical technique developed by Kurihara (1994) and from UTCHEM 5.1. Table 10 shows swept volumes from summing the product of flow rate and transit times using 12,000 streamlines, and also swept volume from tracer concentration contours from UTCHEM 5.1. The total swept volume will sum to 100% when an infinite number of streamlines are used. The good agreement of the tracer production data and swept volumes obtained from the semianalytical technique and UTCHEM 5.1 shows that the swept volume from tracer concentration contours is correct and free of numerical dispersion.

Irregular Pattern with Unbalanced Injection

The objective of this run is to show that the first moment can be applied to any well pattern, well rate, and any degree of heterogeneity as long as the assumptions of nonadsorbed tracer and constant rate are not violated. The shape of the reservoir is a square of length 165 ft on each side. The thickness is 20 ft and porosity is 25%. The grid size is 30 x 30 x 1 (NX x NY x NZ). Two injectors and two producers are used in this simulation. Injector 1 injects water at a constant rate of 280.75 ft^3/D and Injector 2 injects at a constant rate of 168.45 ft^3/D. Both producers are producing at the same constant pressure. Two tracers were used so that more regions can be investigated. The names of the tracers again correspond to the names of their injectors; Tracer 1 is injected at Injector 1 and Tracer 2 is injected at Injector 2.

2D, homogeneous irregular pattern

Figure 20 shows the well locations and streamlines for this homogeneous field. Figures 21 and 22 show simulated tracer production data at the two producers. Using the first-moment method, four different swept volumes or regions can be computed since they are investigated by different tracers. These volumes are labeled V_{s1}, V_{s2}, V_{s3}, and V_{s4} as shown in Fig. 20. Tables 11 to 14 show results from the first-moment calculations. Figures 23 and 24 compare the swept volumes calculated using the first moment to the swept volumes from the tracer concentration contours.

2D, heterogeneous irregular pattern

The permeability field is generated using the Turning Band Method (Yang, 1990). The correlation length is 70 ft along one axis and 233 ft along the perpendicular axis. In order to simulate channeling between the injector and producer, the permeability field is rotated 30 degrees. Figure 25 shows the generated permeability field. The same boundary conditions as in the

homogeneous case are used. Producer 2 produces all of the injected fluid from Injector 1 plus about half of the injected fluid from Injector 2. Tracer 1 from Injector 1 does not reach Producer 1 because of the heterogeneity. Producer 2 produces both Tracer 1 from Injector 1 and Tracer 2 from Injector 2. Figures 26 and 27 show the simulated production data at Producer 1 and Producer 2, respectively.

Tables 15 to 17 show results from first-moment calculations. Figure 28 shows the streamlines for V_{s1}. Figures 29 and 30 compare the swept volumes from the first-moment method and tracer concentration contours. The swept volume between Injector 1 and Producer 2 is the volume swept by Tracer 1 (V_{s1}). The swept volume between Injector 2 and Producer 2 is the volume swept by Tracer 2 (V_{s2}). The rest of the volume swept by Tracer 2 is called V_{s3} and includes the volume between Injector 2 and Producer 1. As simulation results show, the swept volumes from the first-moment method also work for the case of an irregular well pattern.

In this study, a large amount of tracer is injected to ensure that the whole reservoir is completely swept. In an actual field tracer test, the amount of tracer used is another factor in the designing of a tracer test. If the amount of tracer injected is too small, the reservoir volume investigated will also be small. Thus, the actual reservoir volume seen by a particular tracer will depend on the amount of tracer injected. Even if the same amount of tracer is injected, the injected concentration and slug size can be different. For the same amount of tracer injected, if the slug size is too large, the injected concentration will be low or vice versa. For chemical or gas flooding processes, the cost of the injected chemical could be high and there is an effective concentration below which the displacing fluid is ineffective. This effective concentration depends on the flooding process, or is process-dependent. Therefore, the swept volume for different processes could be different depending on the amount of chemical used and the effective or cutoff concentration. For a given amount of chemical used, there is an optimum injected slug size and concentration for different processes that yield the maximum swept volume.

RESIDUAL OIL SATURATION DETERMINATION

Besides calculating the swept volume between wells from the tracer breakthrough curve of a nonpartitioning tracer, the first-moment method can also be used to estimate the average residual oil saturation between two wells. The method is based on the chromatographic separation of two chemical tracers. The velocity of each chemical tracer depends on its partition coefficient. A tracer with a higher partition coefficient will spend more time in the oil phase compared to one with a lower partition coefficient. Hence, the velocity of a higher-partitioning tracer is lower and breakthrough time is longer. If the partition coefficients are known, the chromatographic separation of the two tracers can be used to calculate the residual oil saturation in the region swept by the two tracers. This idea is not new. It was applied in a single-well tracer test by Dean (1971). Cooke (1971) also claimed a patent for both the single-well and interwell tracer test for residual oil saturation. Dean (1980) used the method of moments to estimate the residual oil saturation from a single-well tracer test. Tang and Harker (1990) used a landmark comparison and a recovery-profile crossplot technique to estimate the residual oil saturation from a gas flood at the Golden Spike carbonate reservoir. The landmark comparison used a point on the production data of both the partitioning and nonpartitioning tracers to compare the travel times and relate them to the residual phase saturation. The basis of the chromatographic transformation is that tracer production data for nonpartitioning and partitioning tracers can be collapsed into a single curve. The equivalent concentration on the two tracer responses is then mapped onto the travel times and residual oil saturation can be calculated. Tang and Harker (1991) pointed out that the method works for a heterogeneous reservoir because the streamlines for both the nonpartitioning and partitioning tracers remain the same. The only assumption is that the distribution of residual oil saturation must be uniform. For reservoirs with nonuniform distribution of residual oil saturation, another transformation must be made, and this transformation only works for the special case of a reservoir with ordered layers: low residual oil saturation for a high-permeability layer.

In this study, the residual oil saturation for different partitioning tracers is derived from the first-moment method separately. The first-moment method uses all the information from the whole

tracer response. Therefore, it is not limited by the shape of the tracer responses of the nonpartitioning and partitioning tracers. The use of the first-moment method to determine residual oil saturation for an interwell tracer test has not been published in the literature. The theory will be presented for the following cases: 1D with and without physical dispersion for a uniform distribution of the residual phase and 2D without physical dispersion for a nonuniform distribution of the residual phase. Next, 3D simulation of known residual phase saturation was conducted and compared with results from the first-moment method. Applications to field data are reported in Section III.

Theory

The material balance for a partitioning tracer in 1D flow with no physical dispersion and instantaneous pulse tracer injection can be written as

$$\phi \frac{\partial}{\partial t}[c_{i,w}S_w+c_{i,o}S_o] + \frac{\partial}{\partial x}[c_{i,w}u_w+c_{i,o}u_o] = \frac{m_t\delta(x)\delta(t)}{\phi A[S_w+K_{Ti}S_o]}. \quad (7)$$

The term on the right side is a source term. At constant residual oil saturation, Eq. 7 can be written as

$$\phi S_w \frac{\partial c_{i,w}}{\partial t} + S_{or}\frac{\partial c_{i,o}}{\partial t} + \frac{\partial}{\partial x}[c_{i,w}u_w] = \frac{m_t\delta(x)\delta(t)}{\phi A[S_w+K_{Ti}S_{or}]}. \quad (8)$$

Substituting

$$F_i = S_w+K_{Ti}S_{or}, \quad (9)$$

$$c_{i,o} = K_{Ti}c_{i,w}, \quad (10)$$

and

$$S_w = 1- S_{or} \quad (11)$$

in Eq. 8 gives

$$\phi (1- S_{or}) \frac{\partial c_{i,w}}{\partial t} + S_{or}\frac{\partial (K_{T,i}c_{i,w})}{\partial t} + \frac{\partial}{\partial x}[c_{i,w}u_w] = \frac{m_t\delta(x)\delta(t)}{\phi AF_i}. \quad (12)$$

At constant rates, u_w is a constant and can be taken out of the derivative. Also, the tracer partition coefficient can be assumed to be a constant.

$$\phi (1- S_{or}) \frac{\partial c_{i,w}}{\partial t} + S_{or}K_{T,i}\frac{\partial c_{i,w}}{\partial t} + u_w \frac{\partial c_{i,w}}{\partial x} = \frac{m_t\delta(x)\delta(t)}{\phi AF_i} \quad (13)$$

Upon rearranging, Eq. 13 becomes

$$\frac{\partial c_{i,w}}{\partial t} + \frac{u_w}{\phi F_i}\frac{\partial c_{i,w}}{\partial x} = \frac{m_t\delta(x)\delta(t)}{\phi AF_i}. \quad (14)$$

Equation 14 is based on the following assumptions:

1. 1D flow of water at residual oil saturation,
2. constant injection and production rates, and
3. constant and uniform residual oil saturation and tracer partitioning coefficient.

The initial and boundary conditions are

$$c_{i,w}(t=0, x) = 0 \tag{15}$$

$$c_{i,w}(t, x=0) = 0 . \tag{16}$$

The solution of Eqs.14 to 16 can be obtained using the Laplace transform. The Laplace transform of Eq. 14 is

$$s\bar{c}_{i,w}(s,x) + \frac{u_w}{\phi F_i}\frac{d\bar{c}_{i,w}(s,x)}{dx} = \frac{m_t \delta(x)}{\phi A F_i} . \tag{17}$$

Taking the Laplace transform of Eq. 17 gives

$$s\bar{\bar{c}}_{i,w}(s,p) + \frac{u_w}{\phi F_i}\left(p\bar{\bar{c}}_{i,w}(s,p) - \bar{c}_{i,w}(s,x=0)\right) = \frac{m_t}{\phi A F_i} \tag{18}$$

$$\bar{c}_{i,w}(s,x=0) = 0 \tag{19}$$

$$s\bar{\bar{c}}_{i,w}(s,p) + \frac{u_w}{\phi F_i}\left(p\bar{\bar{c}}_{i,w}(s,p)\right) = \frac{m_t}{\phi A F_i} \tag{20}$$

$$\bar{\bar{c}}_{i,w}(s,p) = \frac{m_t}{\phi A F_i}\left(\frac{1}{s + \frac{u_w p}{\phi F_i}}\right) \tag{21}$$

$$\bar{\bar{c}}_{i,w}(s,p) = \frac{m_t}{A u_w}\left(\frac{1}{p + \frac{F_i \phi s}{u_w}}\right) . \tag{22}$$

Applying the inverse Laplace transform to Eq. 22 gives

$$\bar{c}_{i,w}(s,x) = \frac{m_t}{A u_w}\exp\left(-\frac{F_i \phi x}{u_w}\right) . \tag{23}$$

Applying the inverse Laplace transform to Eq. 23 gives

$$c_{i,w}(t,x) = \frac{m_t}{A u_w}\delta\left(t - \frac{F_i \phi x}{u_w}\right) . \tag{24}$$

At x=L, we have

$$c_{i,w}(t,x=L) = \frac{m_t}{Au_w}\,\delta\left(t-\frac{F_i\phi L}{u_w}\right). \tag{25}$$

The first moment is defined as

$$\bar{t} = \frac{\int_0^\infty c_{i,w} V\, dV}{\int_0^\infty c_{i,w}\, dV}. \tag{26}$$

At constant rates, the first moment with respect to time can be written as

$$\bar{t} = \frac{\int_0^\infty c_{i,w} t\, dt}{\int_0^\infty c_{i,w}\, dt}. \tag{27}$$

Substituting $c_{i,w}$ from Eq. 25 in the definition of the first moment with respect to time gives

$$\bar{t} = \frac{\int_0^\infty \frac{m_t}{Au_w}\,\delta\left(t-\frac{F_i\phi L}{u_w}\right) t\, dt}{\int_0^\infty \frac{m_t}{Au_w}\,\delta\left(t-\frac{F_i\phi L}{u_w}\right) dt} \tag{28}$$

$$= \frac{\int_0^\infty \delta\left(t-\frac{F_i\phi L}{u_w}\right) t\, dt}{\int_0^\infty \delta\left(t-\frac{F_i\phi L}{u_w}\right) dt}. \tag{29}$$

Using the relationships

$$\int_{-\infty}^{\infty} \delta(t-\tau)\, f(t)\, dt = f(\tau) \int_{-\infty}^{\infty} \delta(t-\tau)\, dt \tag{30}$$

and

$$\int_{-\infty}^{\infty} \delta(t-\tau)\, dt = 1, \tag{31}$$

we obtain

$$\bar{t}_i = \frac{F_i \phi L}{u_w}. \tag{32}$$

The first moment of tracer j can also be written as

$$\bar{t}_j = \frac{F_j \phi L}{u_w}. \tag{33}$$

Subtracting Eq. 33 from Eq. 32 and substituting $q = u_w/A$ gives

$$\bar{t}_i - \bar{t}_j = \frac{(F_i - F_j)\, \phi LA}{q} \tag{34}$$

Substituting F_i and F_j in Eq. 34 and solving for S_{or} in the pore volume gives

$$S_{or} = \frac{(\bar{t}_i - \bar{t}_j)\, q}{(K_{Ti} - K_{Tj})\, \phi AL} \tag{35}$$

Multiplying Eq. 35 by pore volume gives S_{or} in actual volume:

$$S_{or} = \frac{(\bar{t}_i - \bar{t}_j)\, q}{(K_{Ti} - K_{Tj})}. \tag{36}$$

S_{or} can also be obtained by taking the ratio of Eqs. 32 and 33. After rearranging, S_{or} is

$$S_{or} = \frac{(1-R_t)}{R_t(K_{Tj}-1) - (K_{Ti}-1)}, \tag{37}$$

where

$$R_t = \frac{\bar{t}_i}{\bar{t}_j}. \tag{38}$$

Equations 35 to 38 are derived from a 1D instantaneous pulse tracer injection with no physical dispersion. The material balance equation describing the 1D flow of a partitioning tracer with physical dispersion is

$$\phi \frac{\partial}{\partial t}[c_{i,w}S_w + c_{i,o}S_o] + \frac{\partial}{\partial x}[c_{i,w}u_w + c_{i,o}u_o] - \phi S_w K_l \frac{\partial^2 c_{i,w}}{\partial x^2} = 0 . \quad (39)$$

At S_{or}, u_0 is zero. Substituting $c_{i,o}$ with $K_{T,i}\, c_{i,w}$ in the above equation, we have

$$\phi \frac{\partial}{\partial t}[c_{i,w}(1-S_{or}) + K_{T,i}c_{i,w}S_{or}] + \frac{\partial}{\partial x}[c_{i,w}u_w] - \phi S_w K_l \frac{\partial^2 c_{i,w}}{\partial x^2} = 0 . \quad (40)$$

At constant S_{or} and rates,

$$\phi[(1-S_{or}) + K_{T,i}S_{or}] \frac{\partial}{\partial t} c_{i,w} + u_w \frac{\partial}{\partial x} c_{i,w} - \phi S_w K_l \frac{\partial^2 c_{i,w}}{\partial x^2} = 0 \quad (41)$$

$$F_i = (1-S_{or}) + K_{T,i}S_{or} \quad (42)$$

$$\phi F_i \frac{\partial c_{i,w}}{\partial t} + u_w \frac{\partial c_{i,w}}{\partial x} - \phi S_w K_l \frac{\partial^2 c_{i,w}}{\partial x^2} = 0 . \quad (43)$$

We change the above equation using the following dimensionless variables:

$$c_D = \frac{c_{i,w} - c_I}{c_J - c_I} \quad (44)$$

$$t_D = \frac{q\, t}{\phi A L} \quad (45)$$

$$x_D = \frac{x}{L} \quad (46)$$

$$N_{Pe} = \frac{u L}{\phi K_l} . \quad (47)$$

Equation 43 is now

$$F_i \frac{\partial c_D}{\partial t_D} + \frac{\partial c_D}{\partial x_D} - \frac{S_w}{N_{Pe}} \frac{\partial^2 c_D}{\partial x_D^2} = 0 \quad (48)$$

and the initial and boundary conditions are

$$c_D (t_D = 0, x_D) = 0 \quad (49)$$

$$c_D (t_D, x_D = 0) = \delta (t_D) . \quad (50)$$

Taking the Laplace transform of Eq. 48 gives

$$s\bar{c}_D - c_D(t_D=0,x_D) + \frac{1}{F_i}\frac{\partial \bar{c}_D}{\partial x_D} - \frac{S_w}{F_i N_{Pe}}\frac{\partial^2 \bar{c}_D}{\partial x_D^2} = 0 \qquad (51)$$

$$s\bar{c}_D + \frac{1}{F_i}\frac{d\bar{c}_D}{dx_D} - \frac{S_w}{F_i N_{Pe}}\frac{d^2\bar{c}_D}{dx_D^2} = 0\,. \qquad (52)$$

The general solution is

$$\bar{c}_D = c_1 \exp(\lambda_1 x) + c_2 \exp(\lambda_2 x)\,, \qquad (53)$$

where λ_1 and λ_2 are the negative and positive roots of the characteristic equation. When $x \rightarrow \infty$, $c_D \rightarrow 0$ and $\bar{c}_D \rightarrow 0$. Thus, c_2 must be 0. When $x = 0$, $c_1 = \bar{c}_D\,(s, x=0)$:

$$\bar{c}_D\,(s,x_D) = \bar{c}_D(s,x_D=0)\exp(\lambda_1 x_D) \qquad (54)$$

so that λ_1 is given by

$$\lambda_1 = \frac{N_{Pe}}{2S_w} - \sqrt{\frac{N_{Pe}^2}{4\,S_w^2} + \frac{F_i N_{Pe} s}{S_w}}\,. \qquad (55)$$

The Laplace transform of the boundary condition (Eq. 50) is

$$\bar{c}_D\,(s,x_D=0\,) = 1 \qquad (56)$$

$$\bar{c}_D\,(s,x_D) = \exp(\lambda_1 x)\,. \qquad (57)$$

Taking the inverse Laplace transform of Eq. 54 gives

$$c_D\,(t_D,x_D) = \frac{1}{2\sqrt{\frac{\pi S_w t_D^3}{F_i N_{Pe}}}}\, x_D \exp\left[\frac{-(x_D - \frac{t_D}{F_i})^2}{4\frac{S_w t_D}{F_i N_{Pe}}}\right]. \qquad (58)$$

At $x_D = 1$, the solution is

$$c_D\,(t_D,x_D=1) = \frac{1}{2\sqrt{\frac{\pi S_w t_D^3}{F_i N_{Pe}}}} \exp\left[\frac{-(1 - \frac{t_D}{F_i})^2}{4\frac{S_w t_D}{F_i N_{Pe}}}\right]. \qquad (59)$$

Figure 31 shows the solution for different partitioning tracers. Van der Laan (1958) and Aris (1958) showed that the first moment can be conveniently related to the solution in Laplace space by

$$\int_0^\infty c_D \, dt_D = \lim_{s \to 0} \bar{c}_D \tag{60}$$

$$\int_0^\infty c_D \, t_D \, dt_D = - \lim_{s \to 0} \frac{d\bar{c}_D}{ds} \, . \tag{61}$$

Therefore,

$$\lim_{s \to 0} \bar{c}_D = 1 \tag{62}$$

$$\frac{d\bar{c}_D}{ds} = \frac{-1}{2\sqrt{\frac{S_w}{F_i N_{Pe}}}} \sqrt{s + \frac{4F_i S_w}{N_{Pe}}} \tag{63}$$

$$\lim_{s \to 0} \frac{d\bar{c}_D}{ds} = - F_i \tag{64}$$

$$\bar{t}_{D,i} = \frac{\int_0^\infty c_D \, t_D \, dt_D}{\int_0^\infty c_D \, dt_D} \tag{65}$$

$$= F_i \tag{66}$$

and

$$\bar{t}_i = \frac{F_i \phi H A}{Q} \, . \tag{67}$$

The first moment with respect to time is the same as for the case without physical dispersion. Therefore, Eqs. 35 through 38 can be used to obtain S_{or}.

The time at which the maximum produced tracer concentration occurs is found by taking the derivative of c_D (Eq. 59) with respect to t_D and equating it to 0. The resulting equation is

$$t_{D \text{ at } c_{D\max}} = \sqrt{\frac{9 F_i^2 S_w^2}{N_{Pe}^2} + F_i^2} - \frac{3 F_i S_w}{N_{Pe}} \tag{68}$$

The maximum produced tracer concentration is found by substituting $t_{D \text{ at } c_{D\max}}$ in Eq. 59. It is generally believed that the produced tracer concentration vs. time is symmetric and the peak always occurs at $t_D = F_i$ (or at 1 PV for a CD equation). As pointed out by Levenspeil and Smith (1957) for a CD equation, this is true only when physical dispersion is small. Equation 68 shows that

$t_{D\ at\ c_{Dmax}}$ is either less than or equal to F_i. Figure 32 shows the produced tracer concentration at different N_{Pe} and the locus of $c_{D\,max}$. Figure 33 shows $t_{D\ at\ c_{Dmax}}$ vs. N_{Pe} compared to the first moment. The $t_{D\ at\ c_{Dmax}}$ is approaching the first moment only at large NPe or small physical dispersion. Therefore, erroneous results can occur if the peak time is substituted in place of the first moment when using Eqs. 35 through 38 to calculate S_{or}.

At small dispersion or $N_{Pe} \rightarrow \infty$, the right side of Eq. 68 reduces to F_i. Substituting F_i for t_D in Eq. 59, the maximum produced tracer concentration is

$$c_{D\,max} = \frac{1}{2\sqrt{\frac{\pi S_w}{N_{Pe}}\ F_i}} \quad . \tag{69}$$

Thus, the maximum produced tracer concentration is inversely proportional to F_i. The maximum produced tracer concentration of another partitioning tracer having partition coefficient = $K_{T,j}$ can be calculated from

$$c_{D\,max,j} = \frac{F_i\ c_{D\,max,i}}{F_j} \quad . \tag{70}$$

Equation 70 is the basis of the landmark comparison or transformation used by Tang and Harker (1990) that the tracer response of a partitioning tracer can be generated from a nonpartitioning tracer. For continuous tracer injection, Marie (1981) solved the CD equation similar to Eq. 48 using the Laplace transform. For an equation of the form

$$a\frac{\partial^2 c_D}{\partial x_D^2} - b\frac{\partial c_D}{\partial x_D} - c\frac{\partial c_D}{\partial t_D} = 0 \tag{71}$$

$$c_D\,(t_D = 0, x_D) = 0 \tag{72}$$

$$c_D\,(t_D > 0, x_D = 0) = 1, \tag{73}$$

the solution is

$$c_D\,(t_D, x_D) = \frac{1}{2}\left[\left(1 - \mathrm{erf}\frac{x_D - b\,t_D}{2\sqrt{at_D}}\right) + \exp\left(\frac{bx}{a}\right)\left(1 - \mathrm{erf}\frac{x_D + b\,t_D}{2\sqrt{at_D}}\right)\right]. \tag{74}$$

Substituting $a = S_W\,(N_{Pe}\,F_i)^{-1}$, $b = F_i^{-1}$, and $c = 1$ gives

$$c_D\,(t_D, x_D) = \frac{1}{2}\left[\left(1 - \mathrm{erf}\frac{x_D - \frac{t_D}{F_i}}{2\sqrt{\frac{S_w t_D}{N_{Pe} F_i}}}\right) + \exp\left(\frac{x_D N_{Pe}}{S_w}\right)\left(1 - \mathrm{erf}\frac{x_D + \frac{t_D}{F_i}}{2\sqrt{\frac{S_w t_D}{N_{Pe} F_i}}}\right)\right] \tag{75}$$

The second term is small and can be neglected to give

$$c_D(t_D, x_D) = \frac{1}{2}\left(1 - \operatorname{erf}\frac{x_D - \frac{t_D}{F_i}}{2\sqrt{\frac{S_w t_D}{N_{Pe} F_i}}}\right). \tag{76}$$

The above solution is valid under the following assumptions:
1. 1D single-phase flow of water at constant residual oil saturation,
2. constant rates and constant tracer partition coefficient, and
3. continuous injection of tracer.

For a step tracer injection of size t_{Ds}, the use of superposition gives the following solution:

$$c_D(t_D, x_D) = -\frac{1}{2}\operatorname{erf}\left(\frac{x_D - \frac{t_D}{F_i}}{2\sqrt{\frac{S_w t_D}{N_{Pe} F_i}}}\right) + \frac{1}{2}\operatorname{erf}\left(\frac{x_D - \frac{(t_D - t_{Ds})}{F_i}}{2\sqrt{\frac{S_w (t_D - t_{Ds})}{N_{Pe} F_i}}}\right). \tag{77}$$

At the outlet end, the solution is

$$c_D(t_D, x_D{=}1) = -\frac{1}{2}\operatorname{erf}\left(\frac{1 - \frac{t_D}{F_i}}{2\sqrt{\frac{S_w t_D}{N_{Pe} F_i}}}\right) + \frac{1}{2}\operatorname{erf}\left(\frac{1 - \frac{(t_D - t_{Ds})}{F_i}}{2\sqrt{\frac{S_w (t_D - t_{Ds})}{N_{Pe} F_i}}}\right) \tag{78}$$

Figure 34 shows these solutions for $K_{T,i}$ values of 0, 1, 2, and 5, respectively. It is interesting to see whether the above equations are valid if the residual oil saturation is not uniformly distributed. The simplest case of all is the layered reservoir case, where the residual oil saturations are different for each layer but the permeabilities and pore volumes are the same for all layers. In this case, the overall tracer concentration is related to the tracer concentration from each layer by

$$c_{DT} = \frac{\sum_{k=1}^{n} c_{Dk}}{n} \tag{79}$$

$$t_{DT} = t_{Dk} \tag{80}$$

$$\frac{\int_0^\infty c_{DT}\, t_{DT}\, dt_{DT}}{\int_0^\infty c_{DT}\, dt_{DT}} = \frac{\sum_{k=1}^{n} \int_0^\infty c_{Dk}\, t_{Dk}\, dt_{Dk}}{n \int_0^\infty c_{Dk}\, dt_{Dk}} \tag{81}$$

$$\bar{t}_{DT} = \frac{\sum_{k=1}^{n} \bar{t}_{Dk}}{n} = \frac{\sum_{k=1}^{n} F_k}{n} \tag{82}$$

$$S_{or,T} = \frac{\sum_{k=1}^{n} S_{or,\,k}}{n} \quad . \tag{83}$$

Equation 83 shows that the residual oil saturation calculated from the first moment of the total tracer concentration is an average from all layers.

In an actual reservoir, the flow is not 1D. It can be shown that the same equations for S_{or} are also valid for 2D flow. The proof using a streamfunction closely follows that of Datta Gupta (1992) for a nonpartitioning tracer. The tracer response for a single streamline without dispersion is

$$c_s(t) = \delta(t - \tau(\Psi)) \quad . \tag{84}$$

The overall tracer response is given by

$$c(t) = \frac{1}{\Psi_{total}} \int_0^{\Psi_{total}} \delta(t - \tau(\Psi))\, d\Psi \quad . \tag{85}$$

The first moment in time is given by

$$\bar{t} = \int_0^t c(t)\, t\, dt \quad . \tag{86}$$

Substituting c(t) in the definition of the first moment, we obtain

$$\bar{t} = \int_0^t \frac{1}{\Psi_{total}} \int_0^{\Psi_{total}} \delta(t - \tau(\Psi))\, d\Psi \; t\, dt \tag{87}$$

$$= \frac{1}{\Psi_{total}} \int_0^{\Psi_{total}} d\Psi \int_0^t \delta(t - \tau(\Psi))\; t\, dt \quad . \tag{88}$$

Using the relationships

$$\int_{-\infty}^{\infty} \delta(t-\tau)\, f(t)\, dt = f(\tau) \int_{-\infty}^{\infty} \delta(t-\tau)\, dt \tag{89}$$

and

$$\int_{-\infty}^{\infty} \delta(t-\tau)\, dt = 1 \, , \tag{90}$$

$$\bar{t} = \frac{1}{\Psi_{total}} \int_0^{\Psi_{total}} d\Psi \; \tau(\Psi) \; . \tag{91}$$

The Ψ and τ coordinates must be changed to x and y coordinates using the transformation

$$\int_D d\Psi \, d\tau = \int_{D^*} \left| \frac{\partial(\Psi,\tau)}{\partial(x,y)} \right| dx \, dy \; , \tag{92}$$

where

$\left| \frac{\partial(\Psi,\tau)}{\partial(x,y)} \right|$ is the Jacobian of transformation

$$\Psi = \Psi(x,y) \tag{93}$$

$$\tau = \tau(x,y) \; . \tag{94}$$

As discussed by Bear (1988), the equations that describe the geometry of streamlines in 3D flow are

$$\Psi = \Psi(x,y,z) = \text{constant} \tag{95}$$

$$\lambda = \lambda(x,y,z) = \text{constant.} \tag{96}$$

These are two families of surfaces whose intersections are streamlines. The relationship between v_x, v_y, v_z and the streamfunctions λ and Ψ are

$$\vec{v} = \text{grad}\,\lambda \times \text{grad}\,\Psi \; , \tag{97}$$

or

$$v_x = \frac{\partial\lambda}{\partial y}\frac{\partial\Psi}{\partial z} - \frac{\partial\lambda}{\partial z}\frac{\partial\Psi}{\partial y} \tag{98}$$

$$v_y = \frac{\partial\lambda}{\partial z}\frac{\partial\Psi}{\partial x} - \frac{\partial\lambda}{\partial x}\frac{\partial\Psi}{\partial z} \tag{99}$$

$$v_z = \frac{\partial\lambda}{\partial x}\frac{\partial\Psi}{\partial y} - \frac{\partial\lambda}{\partial y}\frac{\partial\Psi}{\partial x} \; . \tag{100}$$

For 2D flow in the X-Y plane , $\lambda = z =$ constant. Therefore,

$$v_x = -\frac{\partial \Psi}{\partial y} \tag{101}$$

$$v_y = \frac{\partial \Psi}{\partial x} \tag{102}$$

$$v_z = 0 . \tag{103}$$

From Eq. 25, the transit time of a partitioning tracer i along a streamline is given by

$$\tau = \int \frac{F_i}{v_w} \, ds , \tag{104}$$

where s is the distance traveled and F_i is the retardation factor of tracer i. The total velocity of the aqueous phase can be related to s:

$$v_w = -\lambda \frac{dp}{ds} \tag{105}$$

$$ds = -\frac{\lambda}{v_w} dp . \tag{106}$$

Substituting ds in Eq. 104 gives

$$\tau = -\int \frac{F_i \lambda}{v_w^2} \, dp \tag{107}$$

$$\frac{\partial \tau}{\partial p} = -\frac{F_i \lambda}{v_w^2} \tag{108}$$

$$\frac{\partial p}{\partial x} = -\frac{v_x}{\lambda} \tag{109}$$

$$\frac{\partial \tau}{\partial x} = \frac{\partial \tau}{\partial p} \frac{\partial p}{\partial x} = \frac{F_i \lambda}{v_w^2} \frac{v_x}{\lambda} = \frac{F_i v_x}{v_w^2} \tag{110}$$

$$\frac{\partial \tau}{\partial y} = \frac{\partial \tau}{\partial p} \frac{\partial p}{\partial y} = \frac{F_i \lambda}{v_w^2} \frac{v_y}{\lambda} = \frac{F_i v_y}{v_w^2} . \tag{111}$$

Substituting $\frac{\partial \tau}{\partial x}$, $\frac{\partial \tau}{\partial y}$, $\frac{\partial \Psi}{\partial x}$, and $\frac{\partial \Psi}{\partial y}$ in the Jacobian of transformation results in

$$\left|\frac{\partial(\Psi,\tau)}{\partial(x,y)}\right| = \begin{vmatrix} \frac{\partial\Psi}{\partial x} & \frac{\partial\Psi}{\partial y} \\ \frac{\partial\tau}{\partial x} & \frac{\partial\tau}{\partial y} \end{vmatrix} \tag{112}$$

$$= \begin{vmatrix} v_y & -v_x \\ \frac{F_i v_x}{v_w^2} & \frac{F_i v_y}{v_w^2} \end{vmatrix} \tag{113}$$

$$= \frac{F_i (v_x^2 + v_y^2)}{v_w^2} \tag{114}$$

$$= F_i \tag{115}$$

$$\int_D d\Psi\, d\tau = \int_{D^*} \left|\frac{\partial(\Psi,\tau)}{\partial(x,y)}\right| dx\, dy \tag{116}$$

$$\int_D d\Psi\, d\tau = \int_{D^*} F_i\, dx\, dy \tag{117}$$

$$F_i = F_i(x, y)\,. \tag{118}$$

Define an integral mean value of F_i as

$$\overline{F}_i = \frac{\int_{D^*} F_i\, dx\, dy}{A} \tag{119}$$

$$\int_D d\Psi\, d\tau = \overline{F}_i \int_{D^*} dx\, dy = \overline{F}_i A\,. \tag{120}$$

The dimension of the stream function (Ψ) is L^2/T

$$\Psi_{total} = \frac{Q}{H\phi} \tag{121}$$

$$\bar{t} = \frac{1}{\Psi_{total}} \int_0^{\Psi_{total}} d\Psi\ \tau(\Psi) \tag{122}$$

$$\bar{t} = \frac{\bar{F}_i A \phi H}{Q} . \qquad (123)$$

The first moment with respect to time for a 2D geometry is thus the same as for the 1D case (Eqs. 32 and 33). Therefore, the working equations for S_{or} (Eqs. 35 through 38) do not change. The assumptions are constant rates, no physical dispersions, single-phase flow of water at residual oil saturation, and constant tracer partitioning coefficient. Thus, the above derivation is valid for heterogeneous reservoirs and nonuniform distribution of residual oil. The calculated S_{or} is a volume-averaged value.

Simulation

The application of this method is first demonstrated using simulation data. This is a hypothetical case in which the actual residual oil saturation is known. Since the accuracy of this method depends on the tracer partition coefficient, the calculation of this number is important and will be discussed in the next section.

In this simulated example, the objective is to estimate the volume of contaminants or residual oil saturation in place between wells using partitioning tracers. The in situ contaminant in this example is trichloroethene (TCE), which is nonuniformly distributed in the reservoir at residual saturation. Figure 35 shows the distribution of TCE. The same reservoir used in the 3D heterogeneous swept volume calculation is used in this simulation. The simulation is done by injecting two different partitioning tracers, one with $K_T = 0$ and the other with $K_T = 50$. Different parts of the reservoir can be investigated by using more than two tracers or conducting the test at different times. Figures 36 to 39 show the simulated tracer production data from the four injectors. Figure 38A shows that a nonpartitioning and a partitioning tracer can have a different shape for a nonuniform residual phase distribution. From Figs. 9 and 35, one can see that the residual oil is distributed in the high-permeability area. The effect of heterogeneity on the partitioning tracer is lessened by the residual phase, and there is only one single peak in the tracer response compared to two for the nonpartitioning tracer. If the shapes of the nonpartitioning and partitioning tracer responses are different, the chromatographic transformation used by Tang and Harker (1991) is not valid, because all the tracer responses cannot be collapsed into a single curve. To illustrate this point, another simulation run was made using the same input as this run, except a residual oil saturation of 10% was uniformly distributed for the whole reservoir. Figure 38B shows simulated tracer production data from the heterogeneous permeability field and uniform residual oil saturation. The similar shape of the three tracers with different partitioning coefficients can be clearly seen. Compare Figs. 38A and 38B; the tracer responses of the partitioning tracer having K_T of 50 are quite different. Using the chromatographic transformation of Tang and Harker (1991), the tracer production data for a tracer with K_T of 25 collapses into the same curve as a nonpartitioning tracer (Fig. 38C).

Figures 40 to 43 compare TCE volumes calculated from Eq. 36 and tracer concentration contours of tracer with K_T of 50. The agreement is good. The largest difference is about 8% between Injector 2 and the producer because the tracer responses have very long tails.

Calculation of Tracer Partition Coefficients

The type of tracer can be categorized by its carrier phase. Two types of tracers used for residual oil saturation determination are water tracers and gas tracers. For a tracer that partitions between an aqueous and oleic phase, the partition coefficient is defined as

$$K_{T,i} = \frac{c_{i,o}}{c_{i,w}} . \qquad (124)$$

The unit of the concentrations is volume per volume basis. For a system containing two phases and two components such as water and trichloroethene (TCE, $CHCCl_3$), the equations describing

tracer i in this liquid-liquid equilibrium are

$$\hat{f}_i^{oleic} = \hat{f}_i^{aq} \tag{125}$$

$$x_i^{oleic}\gamma_i^{oleic}f_i^{o} = x_i^{aq}\gamma_i^{aq}f_i^{o} \tag{126}$$

$$x_i^{oleic}\gamma_i^{oleic} = x_i^{aq}\gamma_i^{aq} \tag{127}$$

$$K_i = \frac{x_i^{oleic}}{x_i^{aq}} = \frac{\gamma_i^{aq}}{\gamma_i^{oleic}} \tag{128}$$

$$K_{T,i} = \frac{x_i^{oleic}\zeta^{oleic}}{x_i^{aq}\zeta^{aq}} = \frac{\gamma_i^{aq}\zeta^{oleic}}{\gamma_i^{oleic}\zeta^{aq}}\,. \tag{129}$$

For a tracer injected with the gas phase and partitioned between the vapor and oleic phase, the partition coefficient is defined as

$$K_{T,i} = \frac{c_{i,o}}{c_{i,g}}\,. \tag{130}$$

The equations describing vapor-liquid equilibrium are

$$\hat{f}_i^{l} = \hat{f}_i^{v} \tag{131}$$

$$x_i\gamma_i^{l}f_i^{o} = y_i P\hat{\phi}_i \tag{132}$$

$$\Phi_i = \hat{\phi}_i\frac{P_i^{vap}}{f_i}\,. \tag{133}$$

At low pressure, Φ_i is equal to 1. Therefore, the equations reduce to

$$x_i\gamma_i^{l}P_i^{vap} = y_iP \tag{134}$$

$$K_i = \frac{y_i}{x_i} = \frac{\gamma_i^{l}P_i^{vap}}{P} \tag{135}$$

$$K_{T,i} = \frac{\zeta^{l}}{K_i\zeta^{v}} = \frac{P\zeta^{l}}{\gamma_i^{l}P_i^{vap}\zeta^{v}} = \frac{\zeta^{l}}{K_i\zeta^{v}} \tag{136}$$

Equation 136 is valid under the following assumptions:
1. the vapor phase is an ideal gas and

2. the fugacities of liquid are independent of pressure.
For an ideal solution, the activity coefficient is unity and thus Eqs. 134 and 135 reduce to Raoult's law:

$$x_i P_i^{vap} = y_i P \tag{137}$$

$$K_i = \frac{y_i}{x_i} = \frac{P_i^{vap}}{P} . \tag{138}$$

The activity coefficients can be estimated using various activity coefficient models such as UNIFAC. The UNIFAC model is based on the solution-of-groups model. The interactions among groups are independent of the molecules where groups occur. UNIFAC can predict the activity coefficients of the liquid phases. Details of this model can be found elsewhere (Reid *et al.*, 1988).

As Eqs. 129 and 136 show, if the activity coefficient can be calculated, the tracer partition coefficient can be obtained without assuming an ideal solution. The UNIFAC model is valid only for liquid-liquid or vapor-liquid equilibrium at low pressure. At high pressure, an equation of state or a different approach should be used. Examples of how to determine the partition coefficients of a water and a gas tracer will be illustrated.

Example 1: alcohol (C_4H_9OH) as a water tracer in trichloroethene (TCE, $CHCCL_3$) and water

The problem is to find the partitioning coefficient of C_4H_9OH (tracer) in a liquid-liquid mixture of TCE (oleic phase) and water (aqueous phase) at 20°C and 1 atm. The problem can be solved by using Eq. 129 with the activity coefficients from the UNIFAC model. Sandler (1989) has a computer program in BASIC to calculate the activity coefficients from the UNIFAC model. Two computer runs need to be made for each binary system. The first binary system is alcohol (0.01 mole fraction) and TCE (0.99 mole fraction). The second binary system is alcohol (0.01 mole fraction) and water (0.99 mole fraction). The first step is to write the compound as different chemical groups. The alcohol is composed of 3 CH_3, 1 CH_2, 1 CH, and 1 OH group. Water is 1 H_2O. TCE is composed of 1 CH=C, and 3 Cl(C=C) group.

$$\gamma_i^{aq} = 41.5385$$
$$\gamma_i^{oleic} = 7.9458$$
$$\zeta^{oleic} = 1.462 \text{ g/cc} = 0.011 \text{ mol/cm}^3$$
$$\zeta^{aq} = 0.998 \text{ g/cc} = 0.0554 \text{ mol/cm}^3$$

Thus, the partition coefficient of alcohol (as tracer) in TCE-water is

$$K_{Ti} = \frac{\gamma_i^{aq}\zeta^{oleic}}{\gamma_i^{oleic}\zeta^{aq}} \tag{129}$$

$$= \frac{41.5385 \times 0.011}{7.9458 \times 0.0554}$$

$$= 1.04 \quad \frac{\text{volume of tracer i in oleic phase}}{\text{volume of tracer i in aqueous phase}}$$

Example 2: PMCP as a tracer in air-decane binary system

The next example is another tracer called perfluoromethylcyclopentane (PMCP) in an air-decane system (vapor-liquid equilibrium) at 1 atm and 60°F. At this low pressure, the vapor phase can reasonably be assumed to be an ideal gas and the liquid-phase activity coefficient can be calculated from the computer program. Equation 136 is used in this case. The binary system used in this run is PMCP (0.01 mole fraction) and decane (0.99 mole fraction). PMCP is composed of 4 CF_2, 1 CF, and 1 CF_3 groups. Decane is composed of 2 CH_3 and 8 CH_2 groups. Substituting the values in Eq. 136 gives

$$K_{T,i} = \frac{P\,\zeta^{l}}{\gamma_i^{l}\,P_i^{vap}\,\zeta^{v}} \qquad (136)$$

$$\zeta^{l} = 0.32 \text{ lb mol/ft}^3$$

$$\zeta^{v} = 0.002644 \text{ lb mol/ft}^3$$

$$P_i^{sat} = 0.2784 \text{ bar}$$

$$P = 1 \text{ bar}$$

$$\gamma_i^{l} = 7.4352$$

$$K_{Ti} = \frac{1. \times 0.32}{7.4352 \times 0.2784 \times 0.002644}$$

$$= 58.5 \ \frac{\text{volume of tracer i in oleic phase}}{\text{volume of tracer i in vapor phase}} .$$

The partition coefficients for alcohols from butanol to decanol as water tracers together with their solubilities in water have been tabulated in Table 18.

APPLICATION OF THE FIRST-MOMENT METHOD TO SIMULATED DATA FROM VERTICAL TRACER PROFILING

A more desirable objective is be able to obtain a saturation map of the contaminant in place so that the most effective remediation can be used. In the above example, if the test is conducted at the same time for all injectors, there would be only two tracer breakthrough curves. Thus, the TCE volume calculated will be the TCE volume of the whole reservoir. Since the TCE volume calculated is the volume average over the path traveled by the tracer, more tracer breakthrough curves should give higher resolution to the location of the contaminant. As shown in the example, the horizontal resolution of TCE volume is improved by obtaining more tracer breakthrough curves using more injectors. For the same reasons, obtaining more tracer breakthrough curves in the vertical direction should give more resolution in the vertical direction. A method used to obtain multiple tracer breakthrough curves in the vertical direction is called Vertical Tracer Profiling (VTP). Figure 44 shows a schematic diagram of VTP.

For a noncommunicating layered reservoir, it is easily seen that the swept volumes and the TCE volumes calculated from VTP will be the results of each layer. The problem is with a communicating reservoir with crossflow. There are two kind of information that can be obtained from VTP: the flow pattern inside a reservoir and residual oil saturation.

For single-phase flow, the degree of crossflow can be calculated from an effective length-thickness ratio (R_L). This number is defined as

$$R_L = \frac{L}{H}\sqrt{\frac{k_Z}{k_X}} . \qquad (137)$$

The larger R_L, the more crossflow the reservoir has. In order to investigate the flow pattern inside a reservoir from VTP, simulation runs were made at R_L values of 0, 0.22, 2.2, and 22. R_L was varied by lowering the vertical permeability and keeping other variables constant. Different methods have been used to average the ratio of vertical to horizontal permeabilities. For simplicity, this ratio is calculated from the ratio of vertical to horizontal permeabilities for each gridblock. For example, let the distance between the injector and the producer be 438 ft (L) and the total thickness be 20 ft (H). Therefore, when the vertical permeability is the same as the horizontal permeability, R_L is 22. Figures 45 to 50 show simulated tracer production data from a conventional tracer test and from VTP at different layers for $R_L = 0$. Figure 51 shows that the total swept volume between Injector 1 and the producer from the conventional tracer test approaches the total swept volume from the tracer concentration contours. Figures 52 to 54 compare the swept volumes from the first moment of tracer production data from VTP and the tracer concentration contours of each layer. As expected, the swept volumes from VTP agree with the swept volumes from the tracer concentration contours because there is no crossflow. These results show that the use of VTP can give residual phase saturation for each layer compared to residual phase saturation between wells. At $R_L = 0.22$, Fig. 55 shows simulated tracer production data from a conventional tracer test. The simulated tracer production data from VTP by layer are shown in Figs. 56 to 60. Figures 61 to 64 compare the swept volumes from the first moment of the conventional tracer test and VTP to tracer concentration contours. Results for $R_L = 2.2$ and 22 are shown in Figs. 65 to 83. As R_L increases, the difference between the swept volume from the contours and from the first moment increases because of crossflow among layers. At $R_L = 22$, layer 5 shows about 12% difference. Figure 84 compares TCE volume from the first moment of tracer production data from a conventional tracer test and the tracer concentration contours. The total TCE volume between wells from the first moment of a conventional tracer test agrees with the value from the tracer concentration contours. Figures 85 to 87 compare TCE volumes from the first moment of tracer production data from VTP and from the tracer concentration contours for different layers. The TCE volumes from tracer concentration contours are larger than those from the first moment except for layer 5 because of large crossflow among the layers.

The tracer response measured at layer 5 is a result of tracer injected from all layers. Thus, it is difficult to determine the degree of crossflow. In this simulated example, it is easy to see the degree of crossflow because the swept volumes are plotted vs. the tracer concentration contours. In actual data, the injection profile together with results from VTP can be used to estimate the flow pattern inside the reservoir. VTP can be combined with selective injection as shown in Fig. 88. The test is done by injecting tracer in different layers so that tracer response measured at the producer can be easily traced back to the injection layer. Another advantage of this technique is that the injected fluid can be evenly distributed to all layers. If there is high permeability contrast in the injection well and the crossflow is small, the injected fluid will not be distributed equally to all the layers. The layer with the lowest permeability will accept the least amount of fluid and tracer. The produced tracer concentration may fall below the detection limit or some parts of the reservoir may not be swept. If the contaminant is in that particular layer, it will go undetected. Figures 89 and 90 show the tracer production data from VTP with selective injection from layers 1 and 5 at $R_L = 0.22$. Figure 91 shows the residual phase saturation calculated from the first-moment method using tracer production data from a conventional tracer test (Fig. 44) compared to that from the tracer concentration contours. Figure 92 shows the residual phase saturation from the first-moment method using tracer production data from VTP with selective injection (Fig. 88) compared to that from the tracer concentration contours. The difference between the residual phase saturation from the first-moment method using tracer production data from VTP with selective injection and that from the tracer concentration contours is less than 2%. The results indicate that layer 5 contains a larger volume of TCE than layer 1 which agrees well with the saturation contours in Fig. 35.

CONCLUSIONS

In summary, the application of the first-moment method to tracer production data from the conventional tracer test can provide information about the swept volume and residual oil saturation between wells. The application of the first moment to tracer data from VTP can provide information about the flow pattern and residual oil for each layer of a reservoir with small R_L. When combining selective injection with VTP, less uncertainty and better description of flow inside the reservoir can be obtained.

Although the vertical resolution of the residual oil for a reservoir with large crossflow cannot be obtained using VTP, it may not be so important as for a reservoir with small crossflow, because a reservoir with large crossflow has a better sweep efficiency and less chance for the contaminant to go undetected. For a reservoir with small crossflow, a more exact contaminant location is preferred because of poor sweep efficiency. In this case, the saturation map can be obtained using multiple injection wells and VTP with selective injection.

Table 1. Results of First-Moment Calculation for 2D, Homogeneous Five-Spot Pattern

Normalized Cutoff Concentration	Tracer Recovery (%)	First Moment (Days)	Swept Volume from First-Moment Calculation (%)
10^{-3}	91.24	437.17	20.754
10^{-4}	99.11	471.82	24.331
10^{-5}	99.91	479.00	24.90
10^{-6}	99.99	480.11	24.977

Table 2. Results of First-Moment Calculation for Tracer 1 for 2D Heterogeneous Five-Spot Case

Normalized Cutoff Concentration	Tracer Recovery (%)	First Moment (Days)	Swept Volume from First-Moment Calculation (%)
10^{-3}	97.12	470.45	23.77
10^{-4}	99.54	476.90	24.70
10^{-5}	99.94	478.66	24.89
10^{-6}	99.99	479.04	24.92

Table 3. Results of First-Moment Calculation for Tracer 2 for 2D Heterogeneous Five-Spot Case

Normalized Cutoff Concentration	Tracer Recovery (%)	First Moment (Days)	Swept Volume from First-Moment Calculation (%)
10^{-3}	88.6	268.34	12.37
10^{-4}	95.39	292.02	14.49
10^{-5}	99.84	373.08	19.38
10^{-6}	99.98	378.47	19.69

Table 4. Results of First-Moment Calculation for Tracer 3 for 2D Heterogeneous Five-Spot Case

Normalized Cutoff Concentration	Tracer Recovery (%)	First Moment (Days)	Swept Volume from First-Moment Calculation (%)
10^{-3}	87.69	643.68	29.37
10^{-4}	99.26	698.24	36.06
10^{-5}	99.90	703.96	36.59
10^{-6}	99.99	705.15	36.68

Table 5. Results of First-Moment Calculation for Tracer 4 for 2D Heterogeneous Five-Spot Case

Normalized Cutoff Concentration	Tracer Recovery (%)	First Moment (Days)	Swept Volume from First-Moment Calculation (%)
10^{-3}	88.54	289.19	13.32
10^{-4}	98.98	344.53	17.74
10^{-5}	99.86	354.72	18.43
10^{-6}	99.98	356.97	18.57

Table 6. Results of First-Moment Calculation for Tracer 1 for 3D Heterogeneous Five-Spot Case

Normalized Cutoff Concentration	Tracer Recovery (%)	First Moment (Days)	Swept Volume from First-Moment Calculation (%)
10^{-3}	83.39	204.10	8.86
10^{-4}	96.01	280.90	14.03
10^{-5}	99.26	368.00	19.00
10^{-6}	99.63	382.00	19.84

Table 7. Results of First-Moment Calculation for Tracer 2 for 3D Heterogeneous Five-Spot Case

Normalized Cutoff Concentration	Tracer Recovery (%)	First Moment (Days)	Swept Volume from First-Moment Calculation (%)
10^{-3}	76.61	249.15	9.93
10^{-4}	92.80	367.13	17.73
10^{-5}	99.00	593.10	30.60
10^{-6}	99.90	626.30	32.60

Table 8. Results of First-Moment Calculation for Tracer 3 for 3D Heterogeneous Five-Spot Case

Normalized Cutoff Concentration	Tracer Recovery (%)	First Moment (Days)	Swept Volume from First-Moment Calculation (%)
10^{-3}	85.99	249.39	11.16
10^{-4}	97.69	320.54	16.29
10^{-5}	99.49	347.94	18.01
10^{-6}	99.92	360.05	19.09

Table 9. Results of First-Moment Calculation for Tracer 4 for 3D Heterogeneous Five-Spot Case

Normalized Cutoff Concentration	Tracer Recovery (%)	First Moment (Days)	Swept Volume from First-Moment Calculation (%)
10^{-3}	82.41	226.14	9.70
10^{-4}	96.78	323.04	16.27
10^{-5}	99.22	368.31	19.01
10^{-6}	99.92	404.70	21.00

Table 10. Comparison Between Swept Volumes from a Finite-Difference Simulator and Semianalytic Technique Based on Transit Time

Swept Volume Between Producer and Injector	Using Tracer Concentration Contours from UTCHEM5.1	Using Transit-Time Calculations
1	21.58	21.10
2	36.86	34.60
3	19.50	19.00
4	23.14	22.40

Table 11. Results of First-Moment Calculation for Tracer 1 at Producer 1 for 2D Homogeneous Irregular Pattern

Normalized Cutoff Concentration	Tracer Recovery (%)	First Moment (Days)	Swept Volume from First-Moment Calculation (%)
10^{-3}	37.81	338.03	26.36
10^{-4}	39.17	385.93	31.18
10^{-5}	39.26	391.46	31.70
10^{-6}	39.27	392.17	31.76

Table 12. Results of First-Moment Calculation for Tracer 1 at Producer 2 for 2D Homogeneous Irregular Pattern

Normalized Cutoff Concentration	Tracer Recovery (%)	First Moment (Days)	Swept Volume from First-Moment Calculation (%)
10^{-3}	59.56	270.62	33.25
10^{-4}	60.66	294.68	36.87
10^{-5}	60.73	296.75	37.17
10^{-6}	60.73	297.00	37.20

Table 13. Results of First-Moment Calculation for Tracer 2 at Producer 1 for 2D Homogeneous Irregular Pattern

Normalized Cutoff Concentration	Tracer Recovery (%)	First Moment (Days)	Swept Volume from First-Moment Calculation (%)
10^{-3}	68.71	124.80	10.61
10^{-4}	69.49	132.93	11.43
10^{-5}	69.54	133.79	11.51
10^{-6}	69.55	133.91	11.53

Table 14. Results of First-Moment Calculation for Tracer 2 at Producer 2 for 2D Homogeneous Irregular Pattern

Normalized Cutoff Concentration	Tracer Recovery (%)	First Moment (Days)	Swept Volume from First-Moment Calculation (%)
10^{-3}	28.54	483.98	17.10
10^{-4}	30.31	548.45	20.57
10^{-5}	30.43	556.05	20.94
10^{-6}	30.45	557.07	20.99

Table 15. Results of First-Moment Calculation for Tracer 1 at Producer 2 for 2D Heterogeneous Irregular Pattern

Normalized Cutoff Concentration	Tracer Recovery (%)	First Moment (Days)	Swept Volume from First-Moment Calculation (%)
10^{-3}	98.37	93.63	18.99
10^{-4}	99.66	104.62	21.50
10^{-5}	99.92	109.71	22.61
10^{-6}	99.98	112.48	23.19

Table 16. Results of First-Moment Calculation for Tracer 2 at Producer 1 for 2D Heterogeneous Irregular Pattern

Normalized Cutoff Concentration	Tracer Recovery (%)	First Moment (Days)	Swept Volume from First-Moment Calculation (%)
10^{-3}	49.18	153.50	9.34
10^{-4}	49.45	156.95	9.61
10^{-5}	49.49	157.60	9.65
10^{-6}	49.49	157.69	9.66

Table 17. Results of First-Moment Calculation for Tracer 2 at Producer 2 for 2D Heterogeneous Irregular Pattern

Normalized Cutoff Concentration	Tracer Recovery (%)	First Moment (Days)	Swept Volume from First-Moment Calculation (%)
10^{-3}	41.92	436.03	22.62
10^{-4}	48.76	710.62	42.88
10^{-5}	50.07	870.26	53.92
10^{-6}	50.33	947.76	59.03

Table 18. Partition coefficients for various alcohols in PCE-water system at 20°C (liquid-liquid equilibrium)

Tracer Name	γ_i^{aq}	γ_i^{oleic}	$\frac{\gamma_i^{aq}}{\gamma_i^{oleic}}$	K_{Ti} (vol/vol)	solubility in water at 20°C (wt %)
2-Methyl, 2-Butanol ($C_5H_{12}O$)	144	8.46	17.0	2.98	12.15
2,3-Dimethyl, 2-Butanol ($C_6H_{14}O$)	399.7	7.46	53.6	9.4	-
1-Hexanol ($C_6H_{14}O$)	426.3	7.45	57.2	10.01	0.62
1-Heptanol ($C_7H_{16}O$)	1194.8	6.64	179.9	31.5	0.17
1-Octanol ($C_8H_{18}O$)	3362.4	5.95	565.1	98.9	0.042
1-Nonanol ($C_9H_{20}O$)	9505.0	5.35	1776.6	310.9	0.014
1-Decanol ($C_{10}H_{22}O$)	26947.6	4.82	5590.8	978.4	0.0036

$$\text{Ratio of molar densities} = \frac{\zeta_i^{oleic}}{\zeta_i^{aq}} = 0.175 \ \frac{\text{mole/cc of oil}}{\text{mole/cc of water}}$$

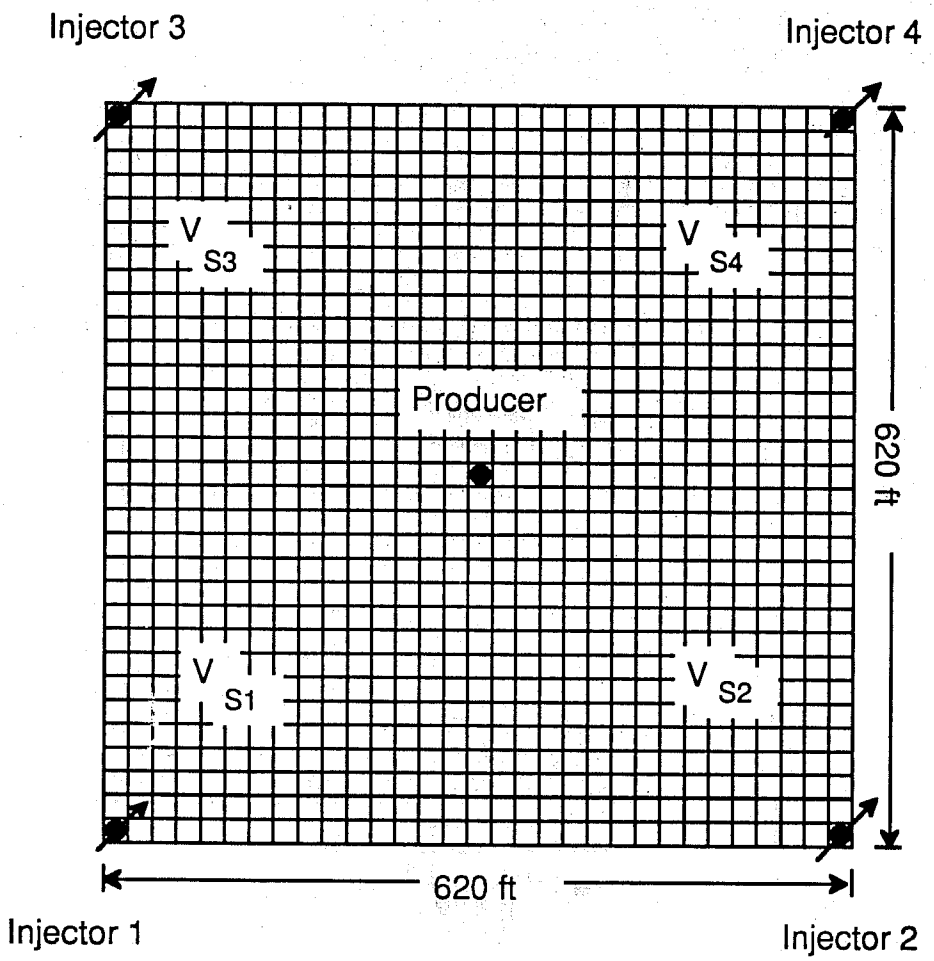

Fig. 1. Areal view of the five-spot grid, well location, and swept volume

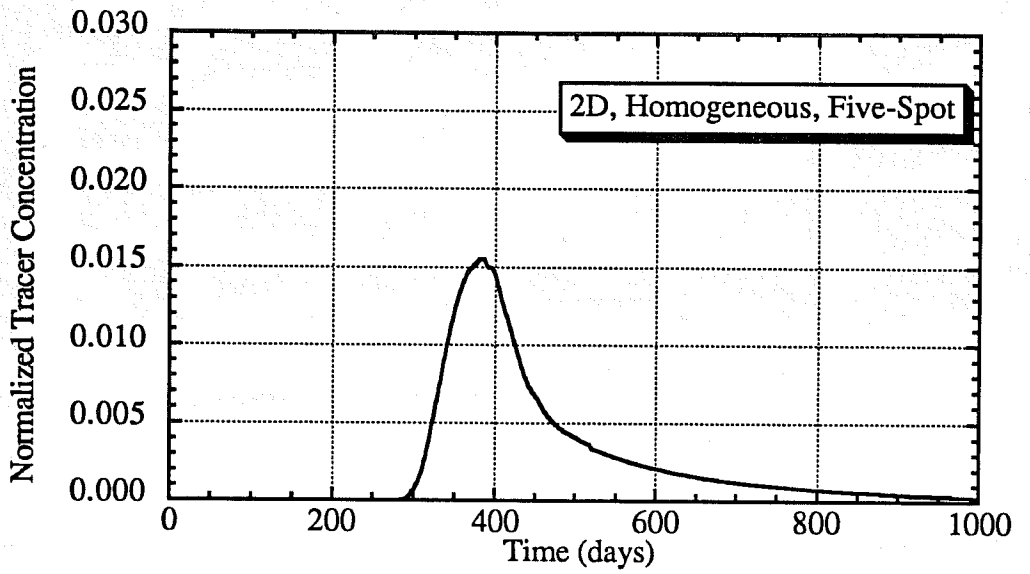

Fig. 2. Simulated tracer production data from a 2D, homogeneous, five-spot pattern (Run No. SWVR12)

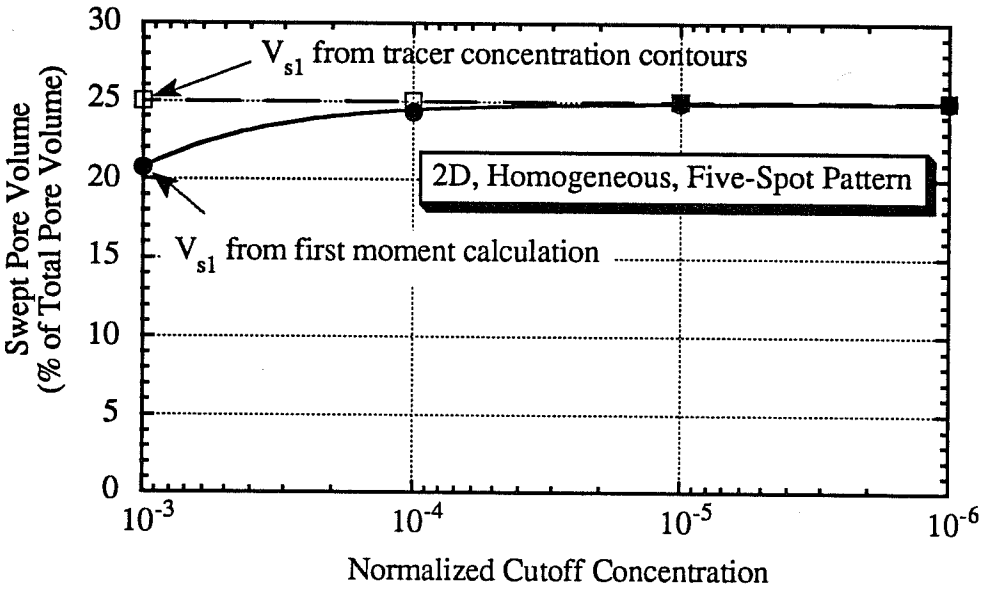

Fig. 3. Comparison between swept volumes calculated from the first moment method and tracer concentration contours from simulation (Run No. SWVR12)

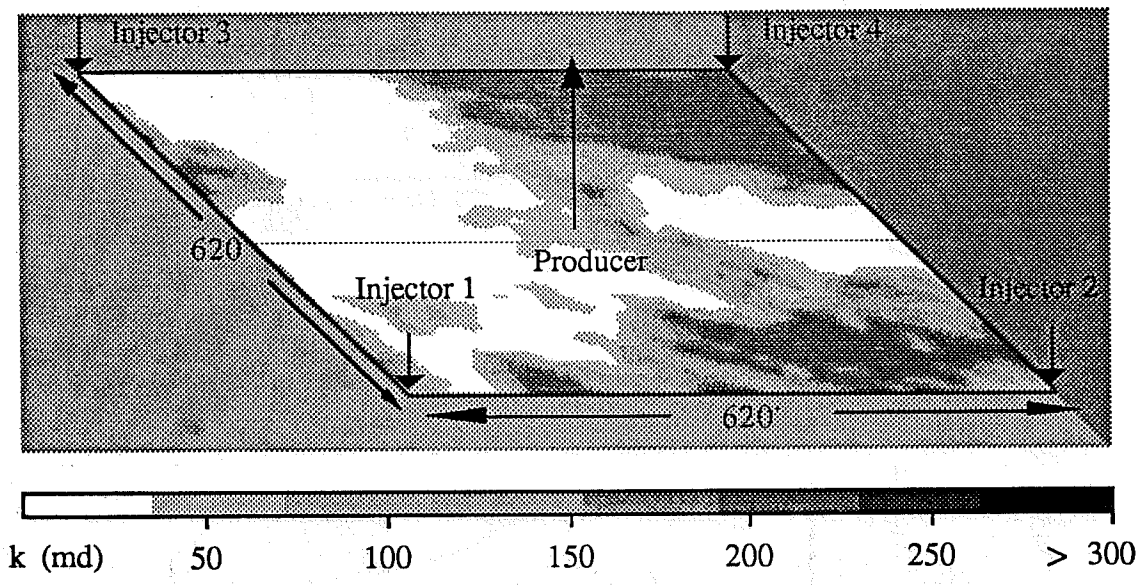

Fig. 4. Permeability field used in the simulation of 2D, heterogeneous, five-spot pattern (Run No. SWVR13-16)

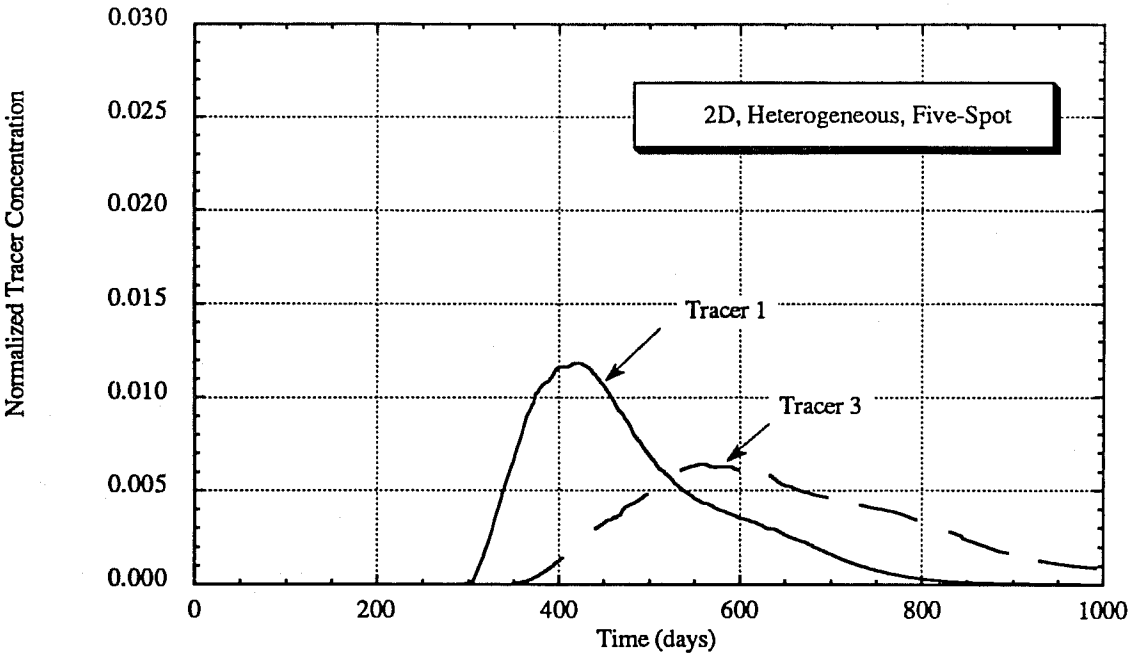

Fig. 5. Simulated tracer production data from a heterogeneous five-spot pattern (Run No. SWVR13-16)

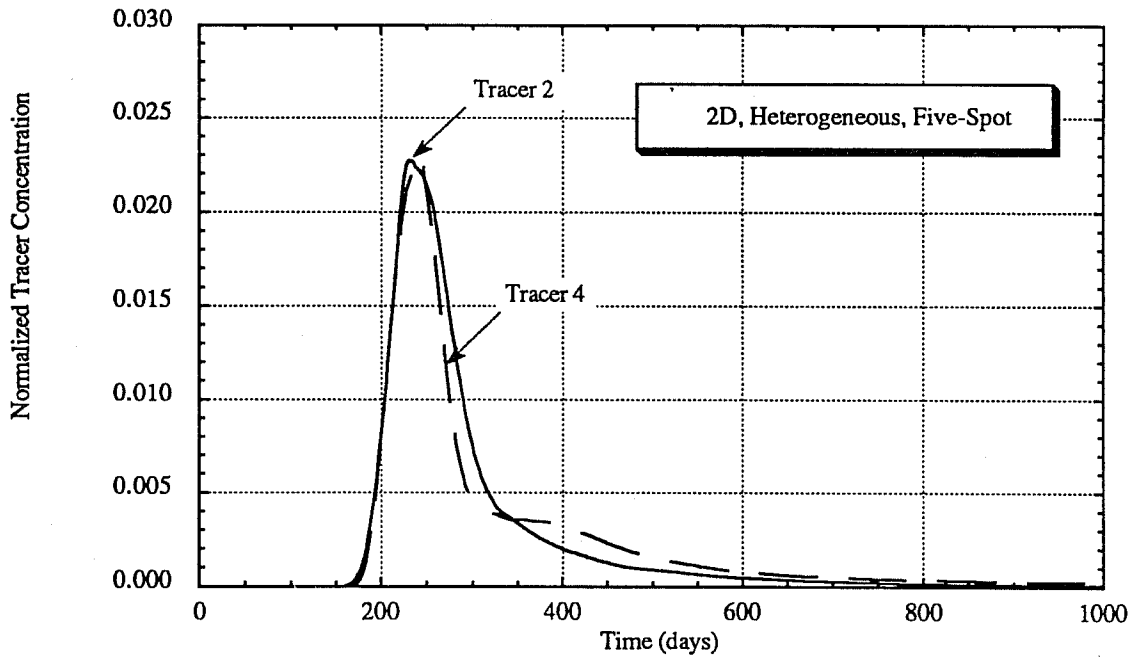

Fig. 6. Simulated tracer production data from a heterogeneous five-spot pattern (Run No. SWVR13-16)

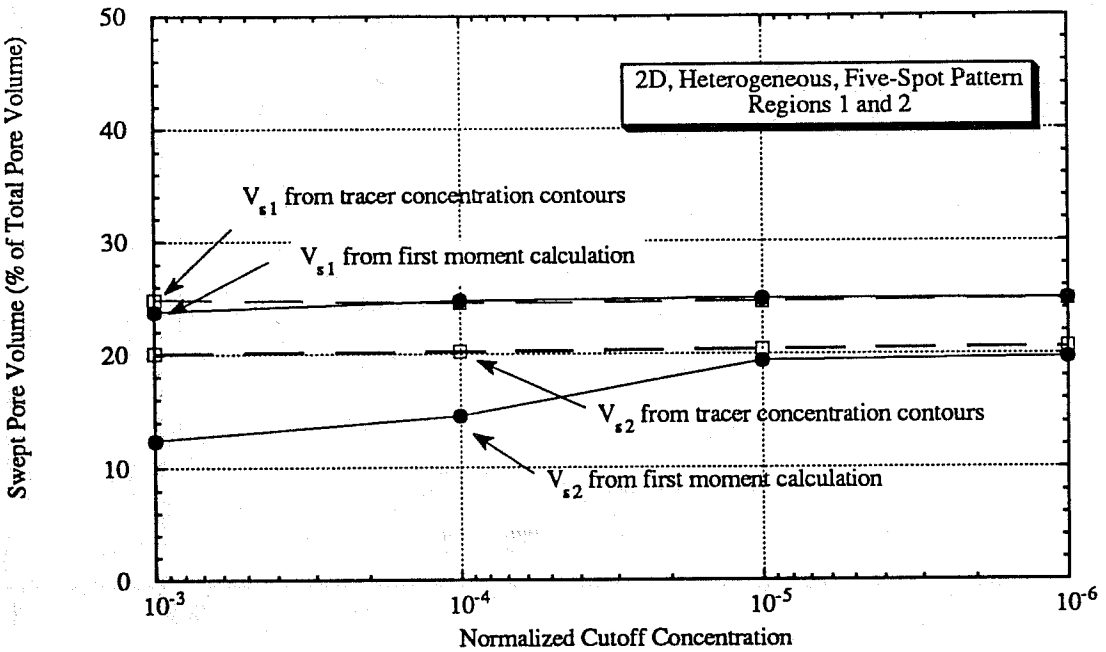

Fig. 7. Comparison between swept volumes calculated from the first moment method and tracer concentration contours from simulation (Runs No. SWVR13-16)

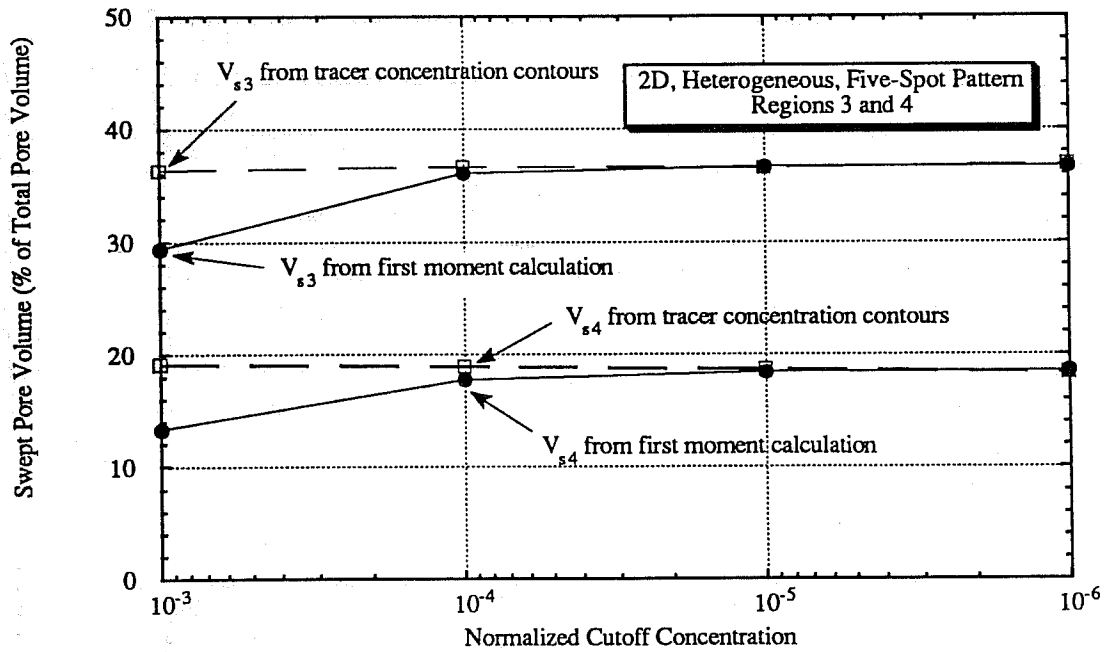

Fig. 8. Comparison between swept volumes calculated from the first moment method and tracer concentration contours from simulation (Runs No. SWVR13-16)

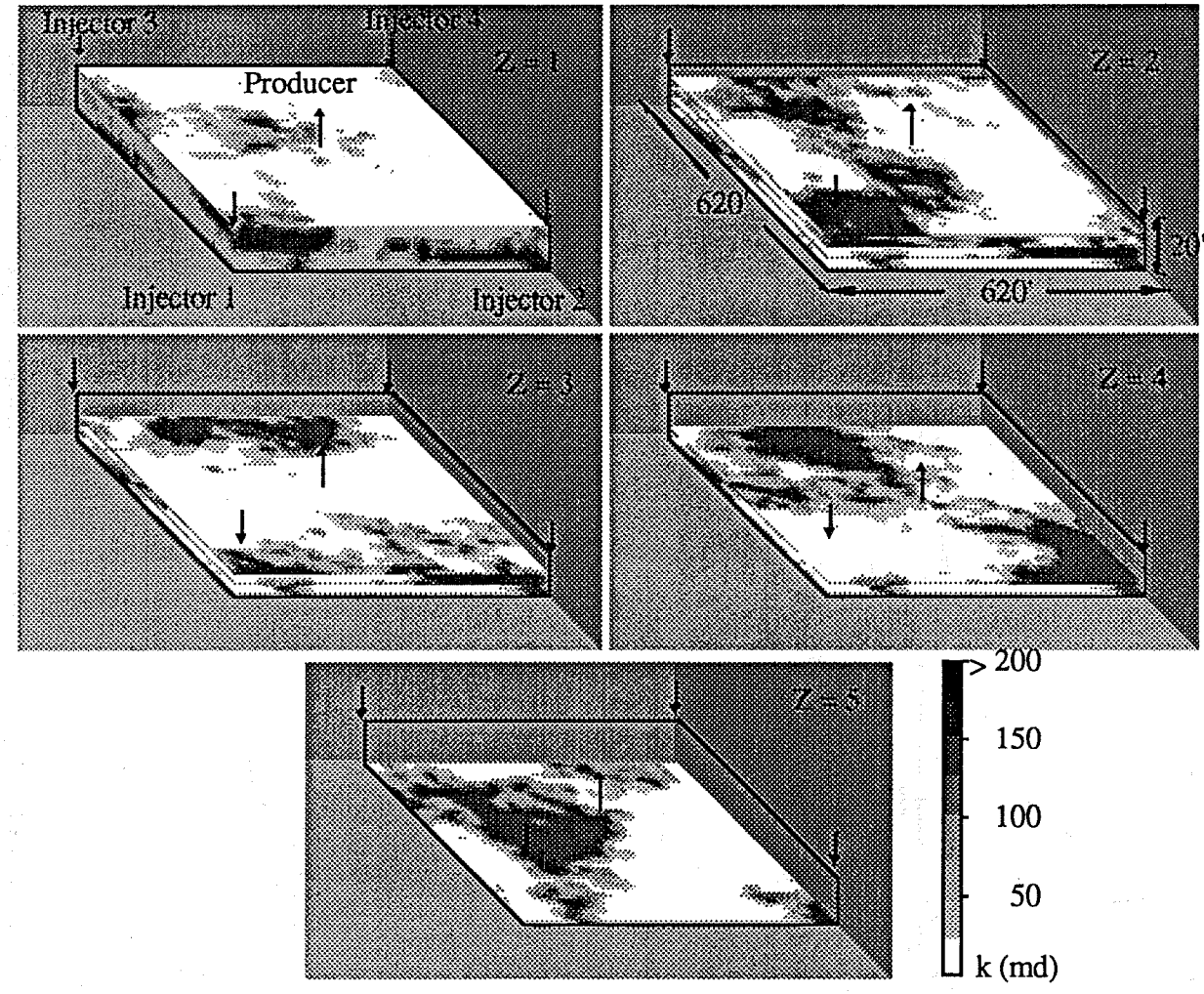

Fig. 9. Permeability field used in the simulation of 3D, heterogeneous, five-spot pattern

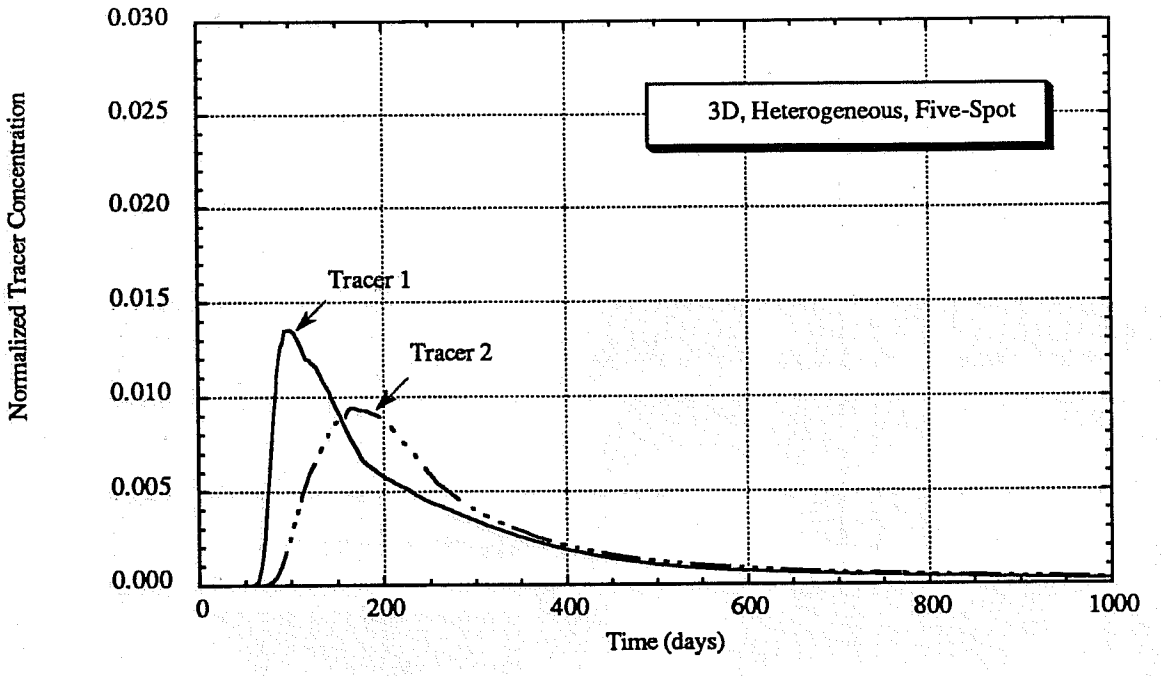

Fig. 10. Simulated tracer production data from a 3D, heterogeneous, five-spot pattern (Runs No. SWVR17 to 19)

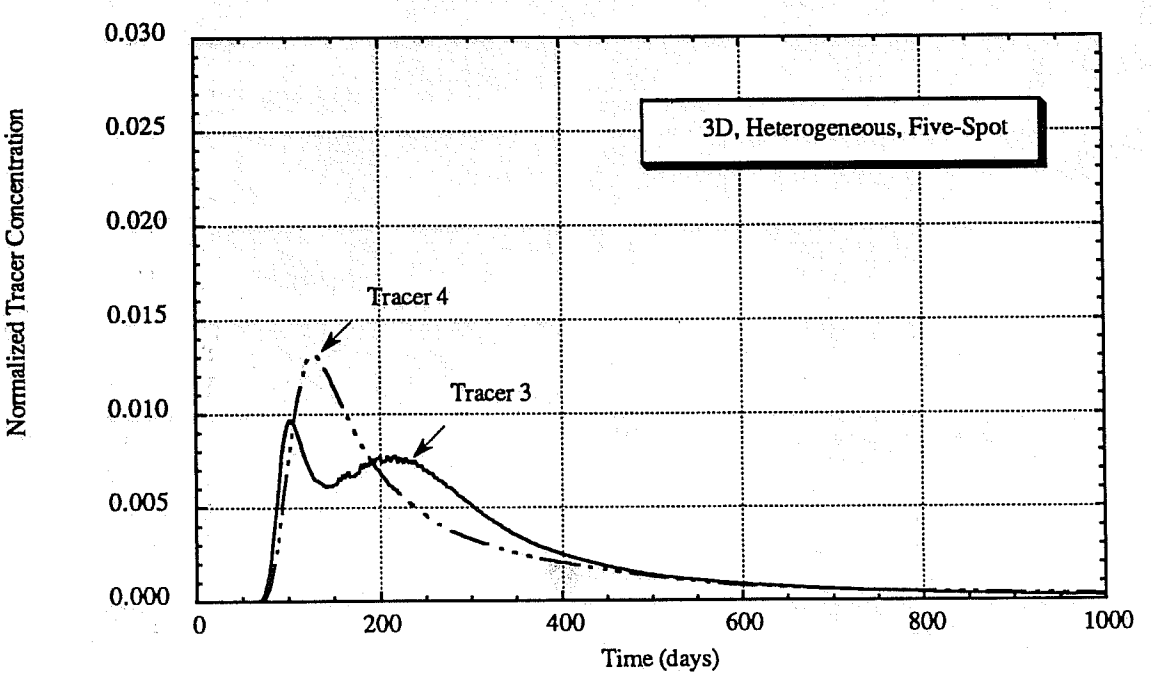

Fig. 11. Simulated tracer production data from a 3D, heterogeneous, five-spot pattern (Runs No. SWVR17 to 19)

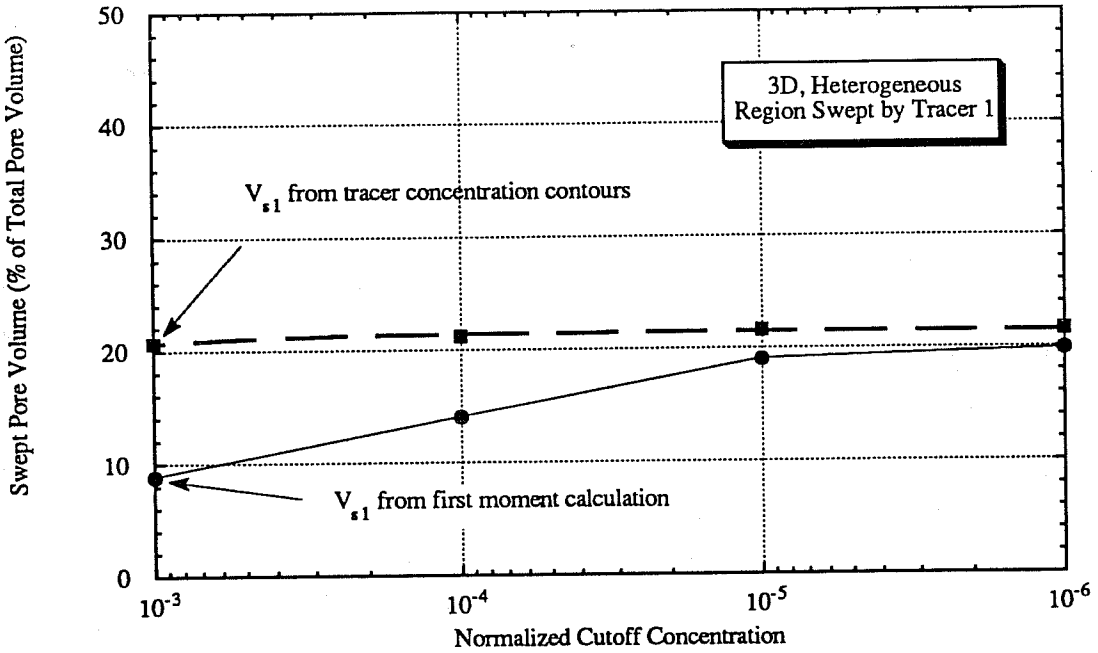

Fig. 12. Comparison between swept volumes calculated from the first moment method and tracer concentration contours from simulation (Run No. SWVR17)

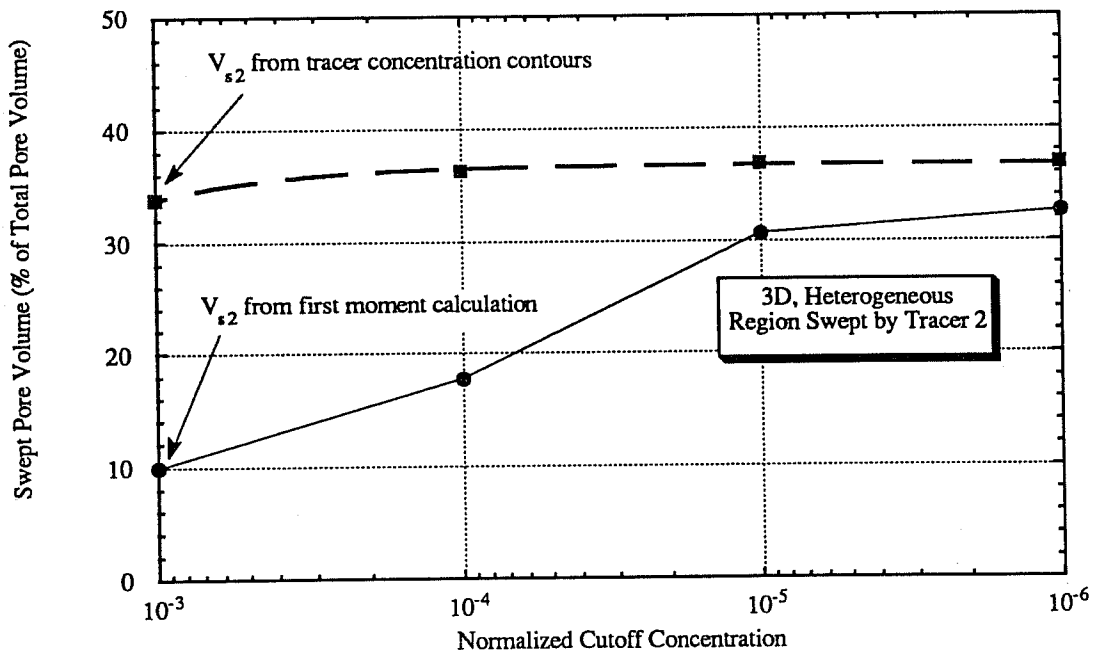

Fig. 13. Comparison between swept volumes calculated from the first moment method and tracer concentration contours from simulation (Run No. SWVR19)

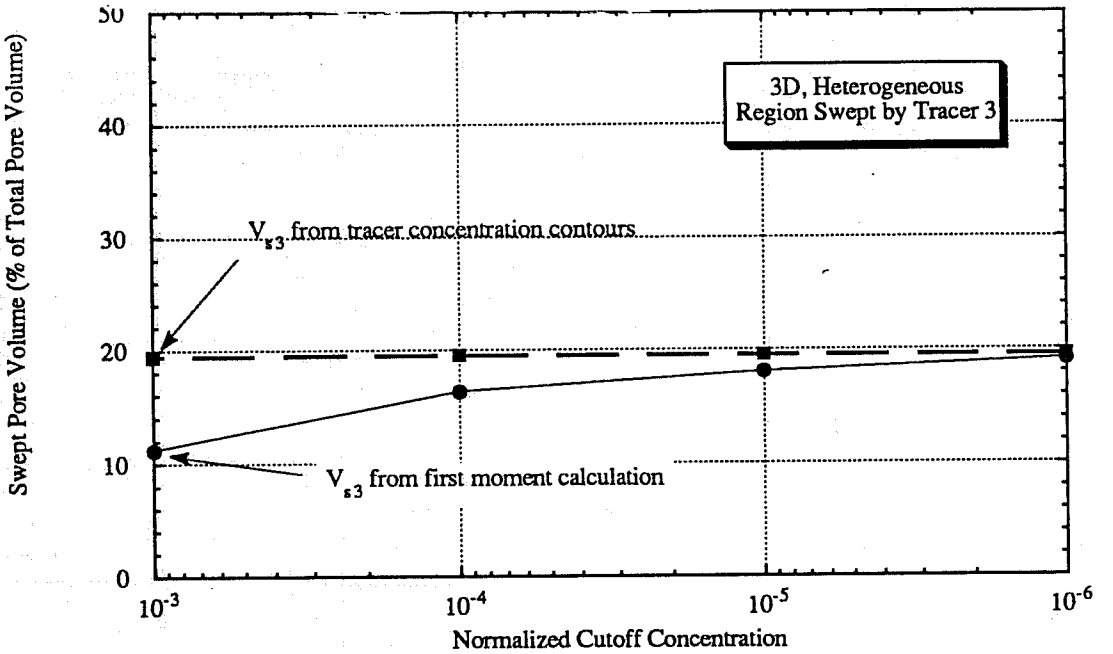

Fig. 14. Comparison between swept volumes calculated from the first moment method and tracer concentration contours from simulation (Run No. SWVR19)

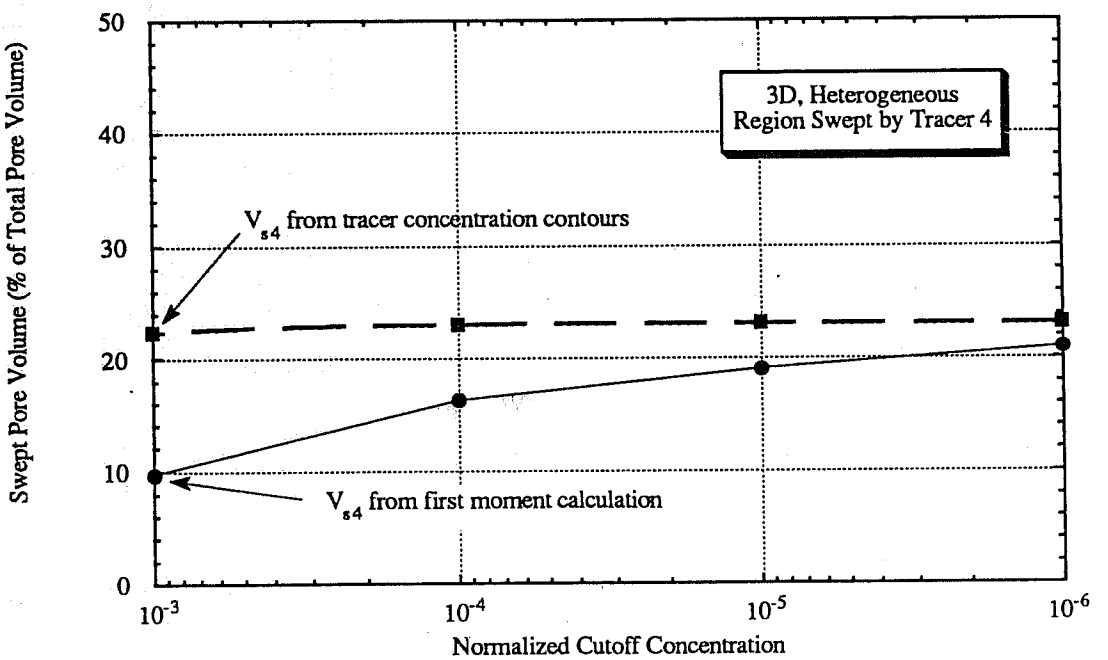

Fig. 15. Comparison between swept volumes calculated from the first moment method and tracer concentration contours from simulation (Run No. SWVR19)

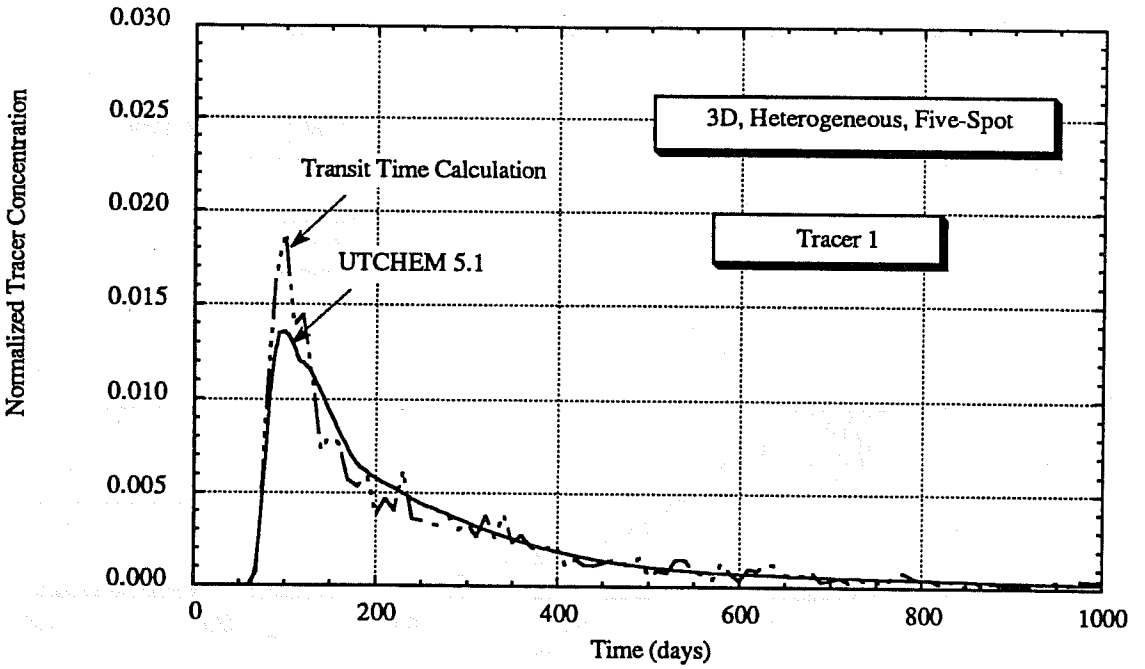

Fig. 16. Comparison between simulated tracer production data from UTCHEM 5.1 with TVD and transit time calculation

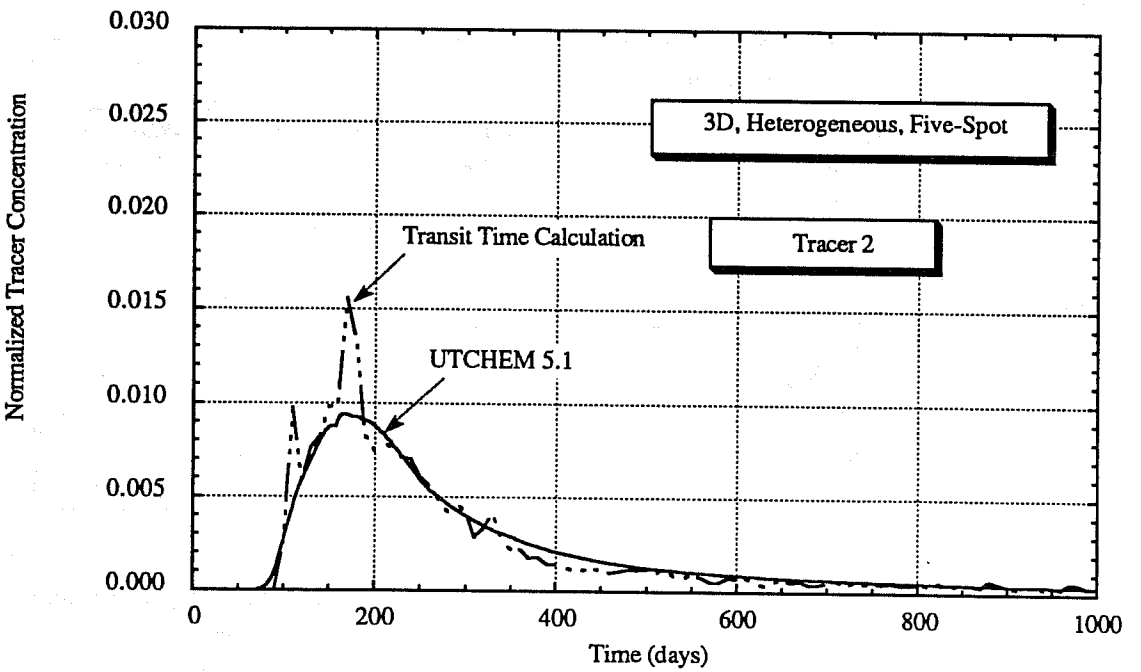

Fig. 17. Comparison between simulated tracer production data from UTCHEM 5.1 with TVD and transit time calculation

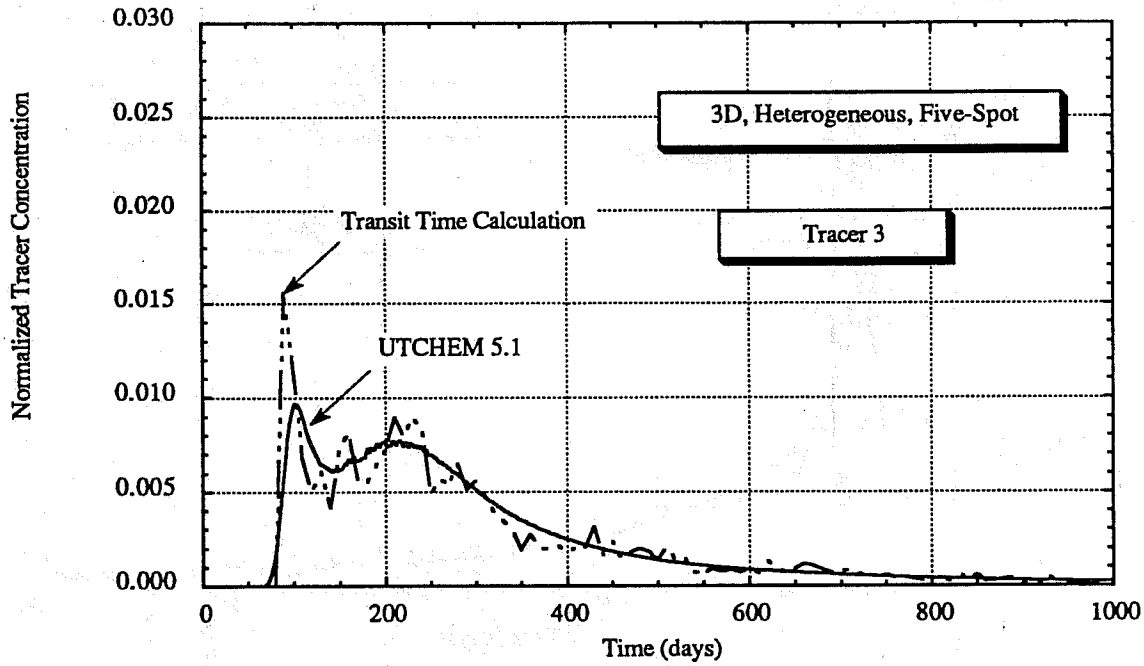

Fig. 18. Comparison between simulated tracer production data from UTCHEM 5.1 with TVD and transit time calculation

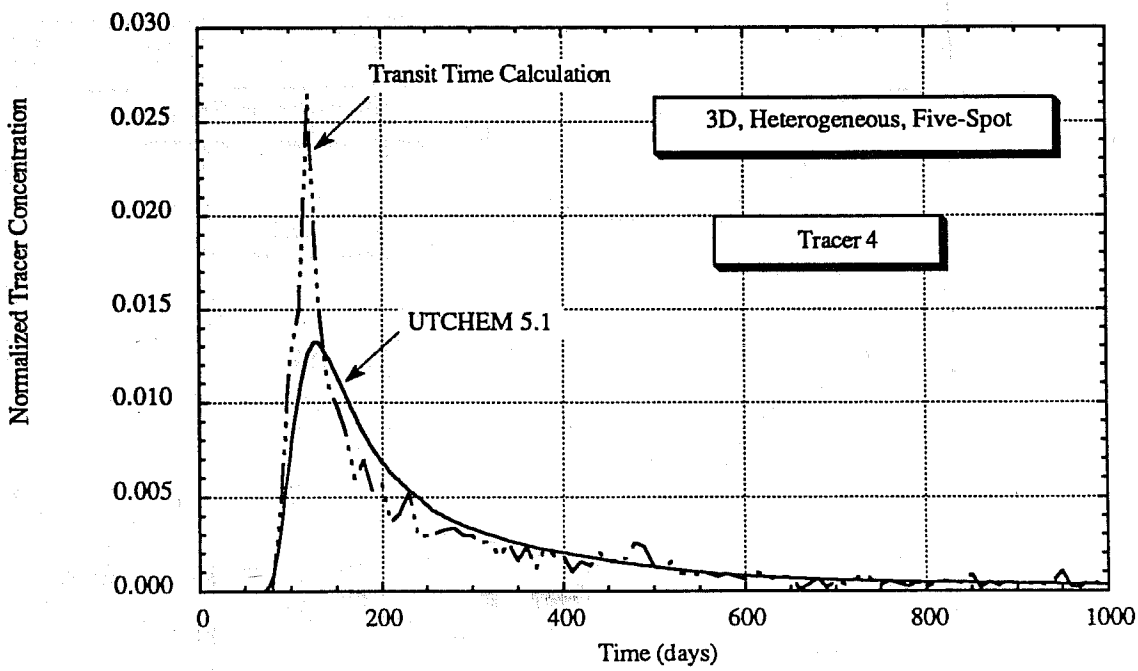

Fig. 19. Comparison between simulated tracer production data from UTCHEM 5.1 with TVD and transit time calculation

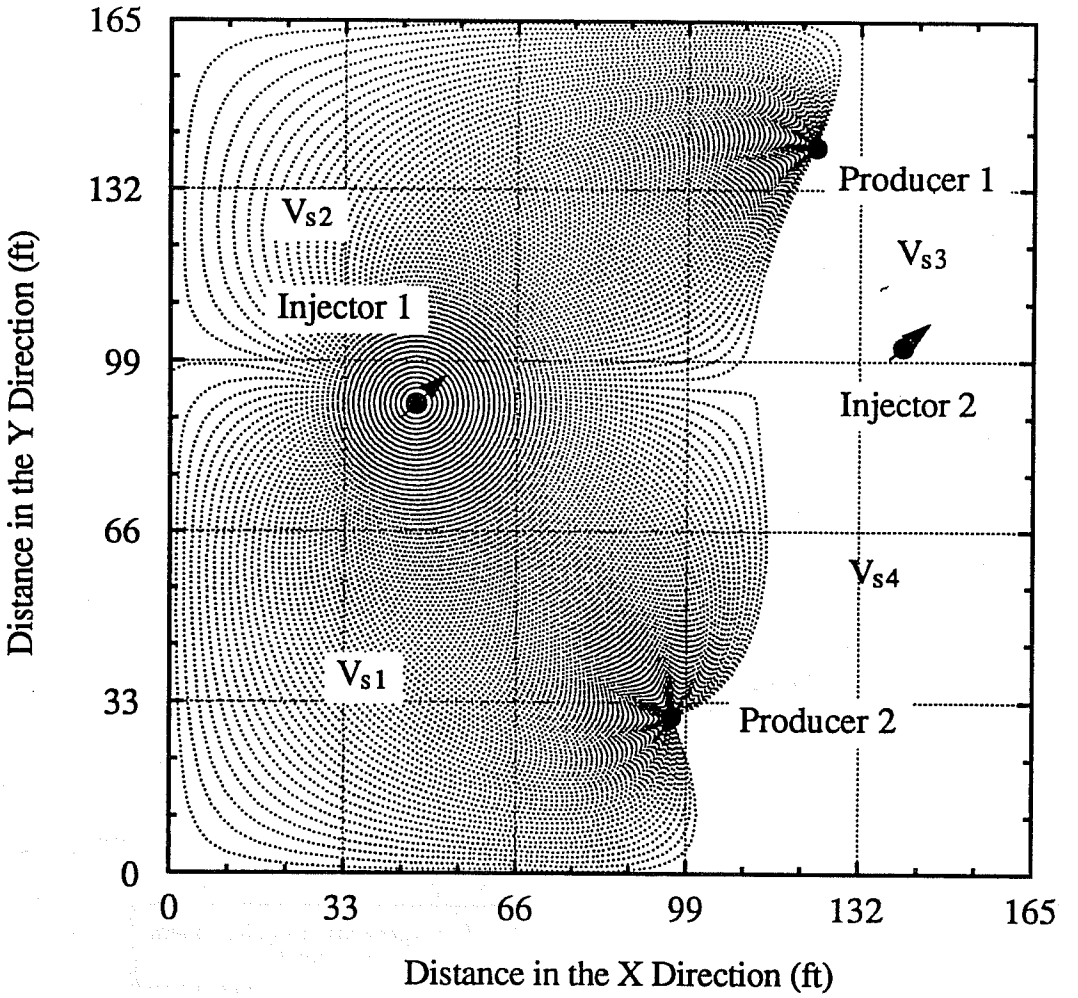

Fig. 20. Areal view showing streamlines from Injector 1 and different swept volumes

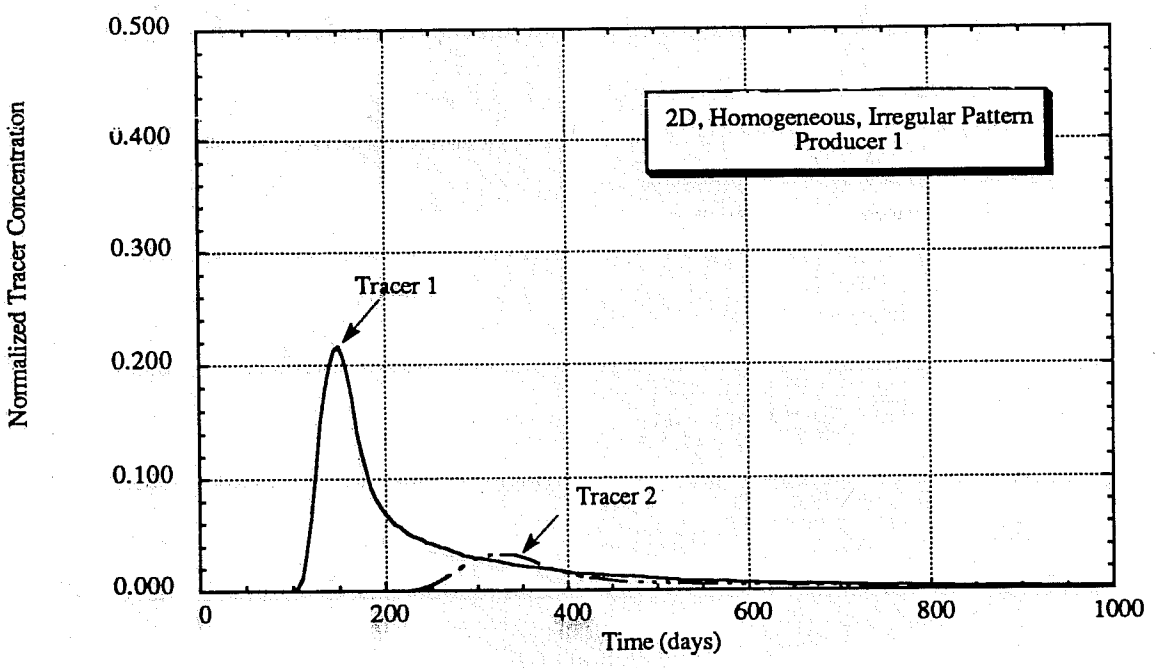

Fig. 21. Simulated tracer production data from Producer 1 for a homogeneous irregular pattern (Run No. SWVR9)

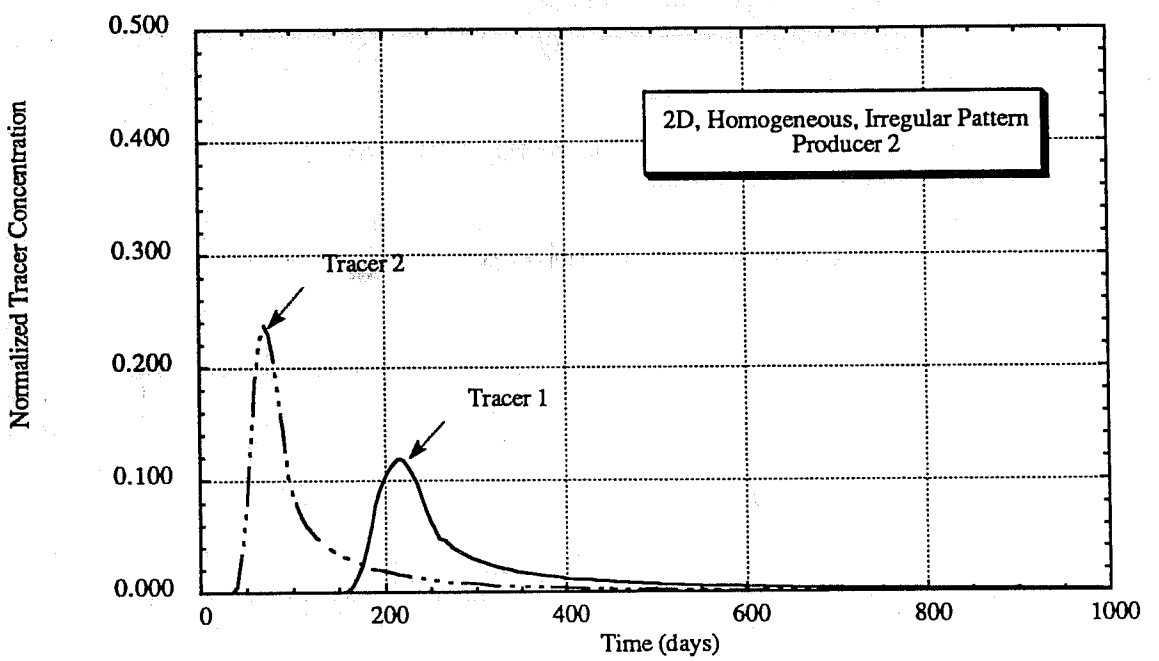

Fig. 22. Simulated tracer production data from Producer 2 for a homogeneous irregular pattern (Run No. SWVR9)

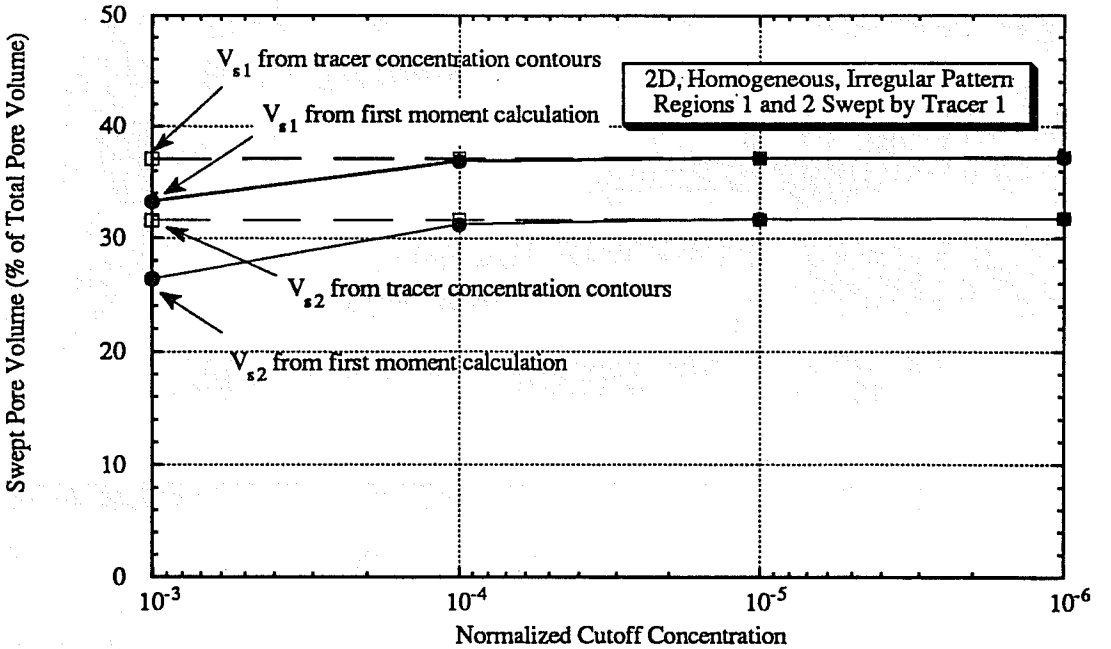

Fig. 23. Comparison between swept volumes calculated from the first moment method and tracer concentration contours from simulation (Runs No. SWVR1 and 9)

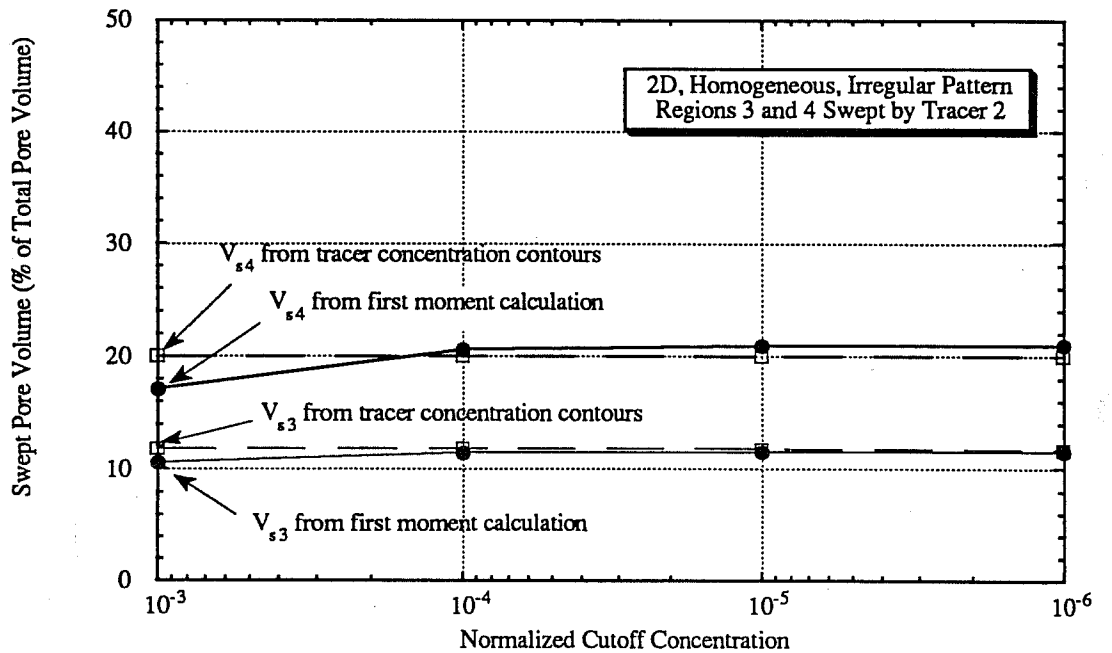

Fig. 24. Comparison between swept volumes calculated from the first moment method and tracer concentration contours from simulation (Runs No. SWVR1 and 9)

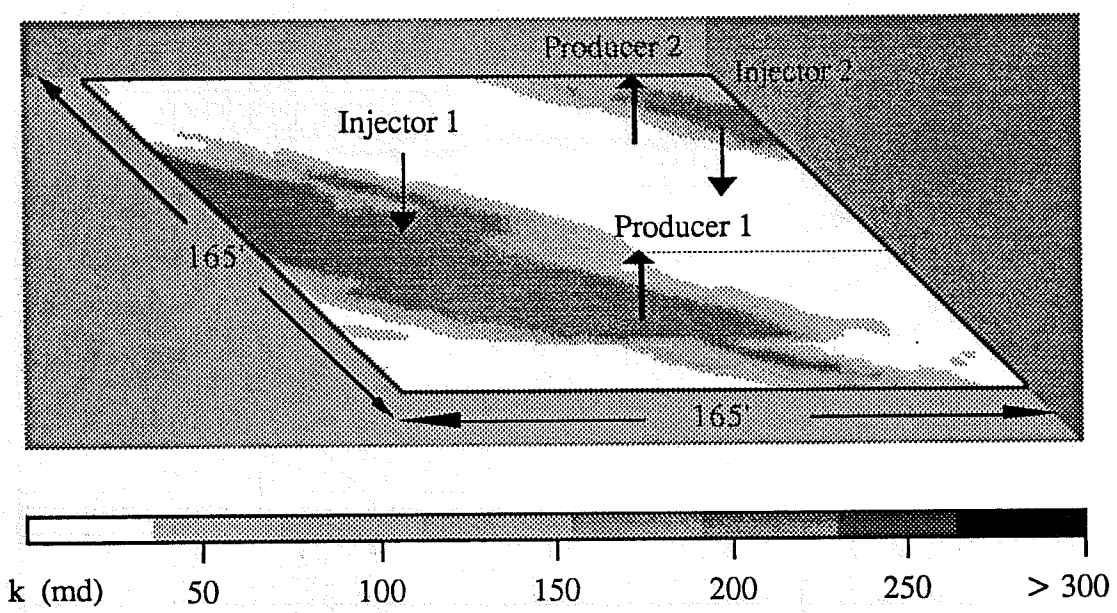

Fig. 25. Permeability field used in the simulation of 2D, heterogeneous, irregular pattern (Run No. SWVR4 and SWVR6)

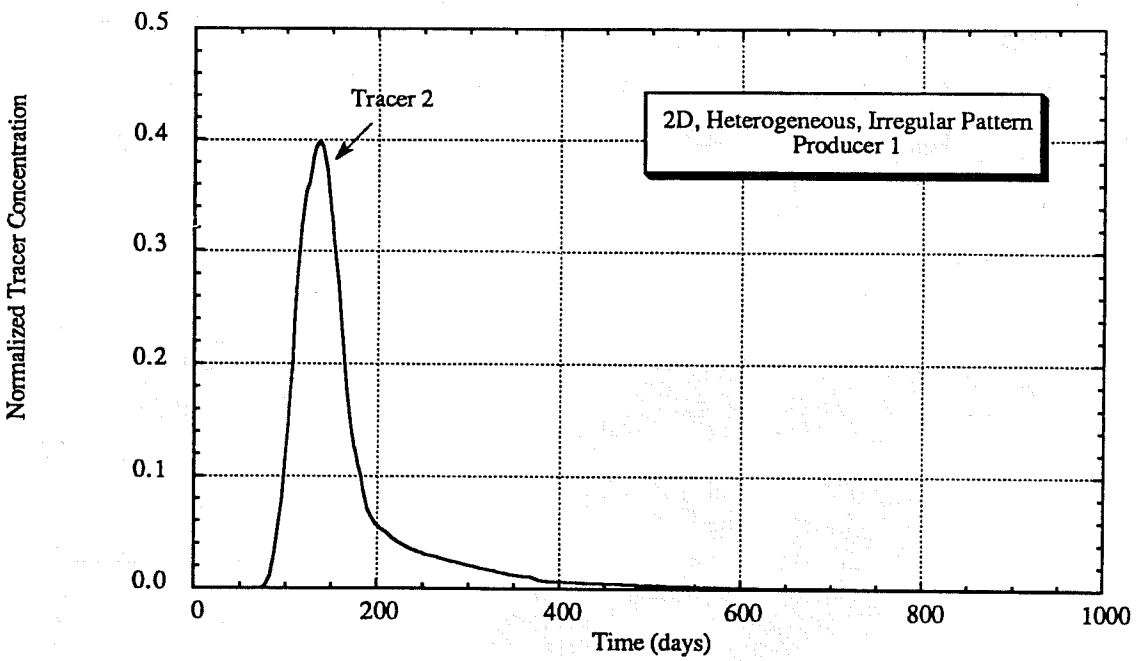

Fig. 26. Simulated tracer production data from Producer 1 for a heterogeneous irregular pattern (Run No. SWVR6)

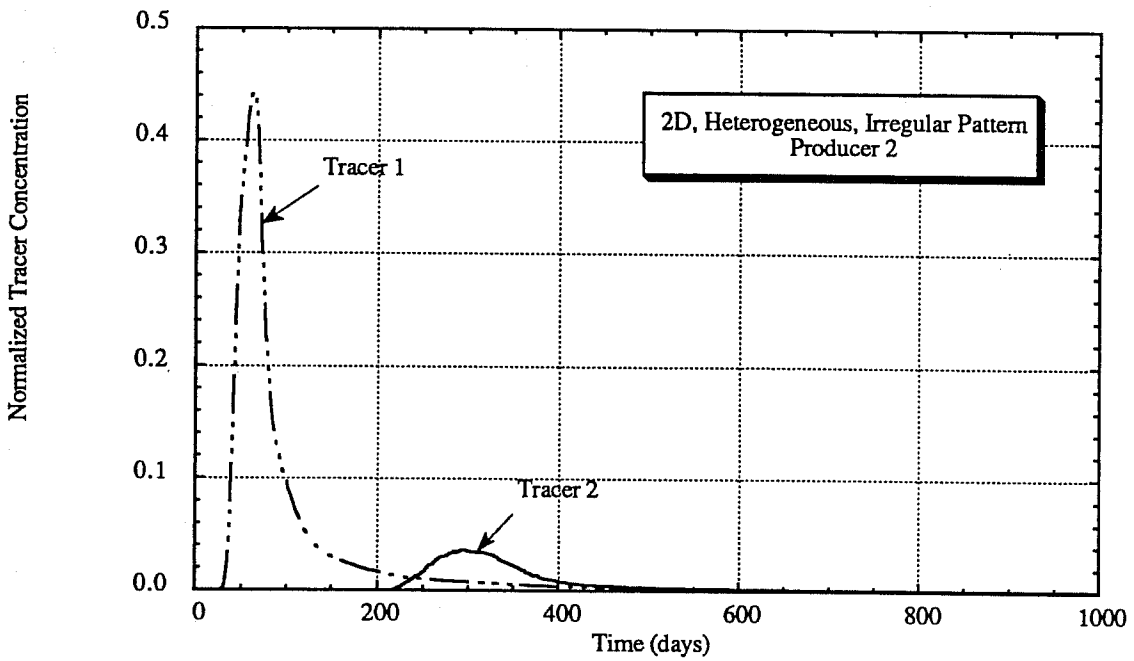

Fig. 27. Simulated tracer production data from Producer 2 for a heterogeneous irregular pattern (Run No. SWVR4)

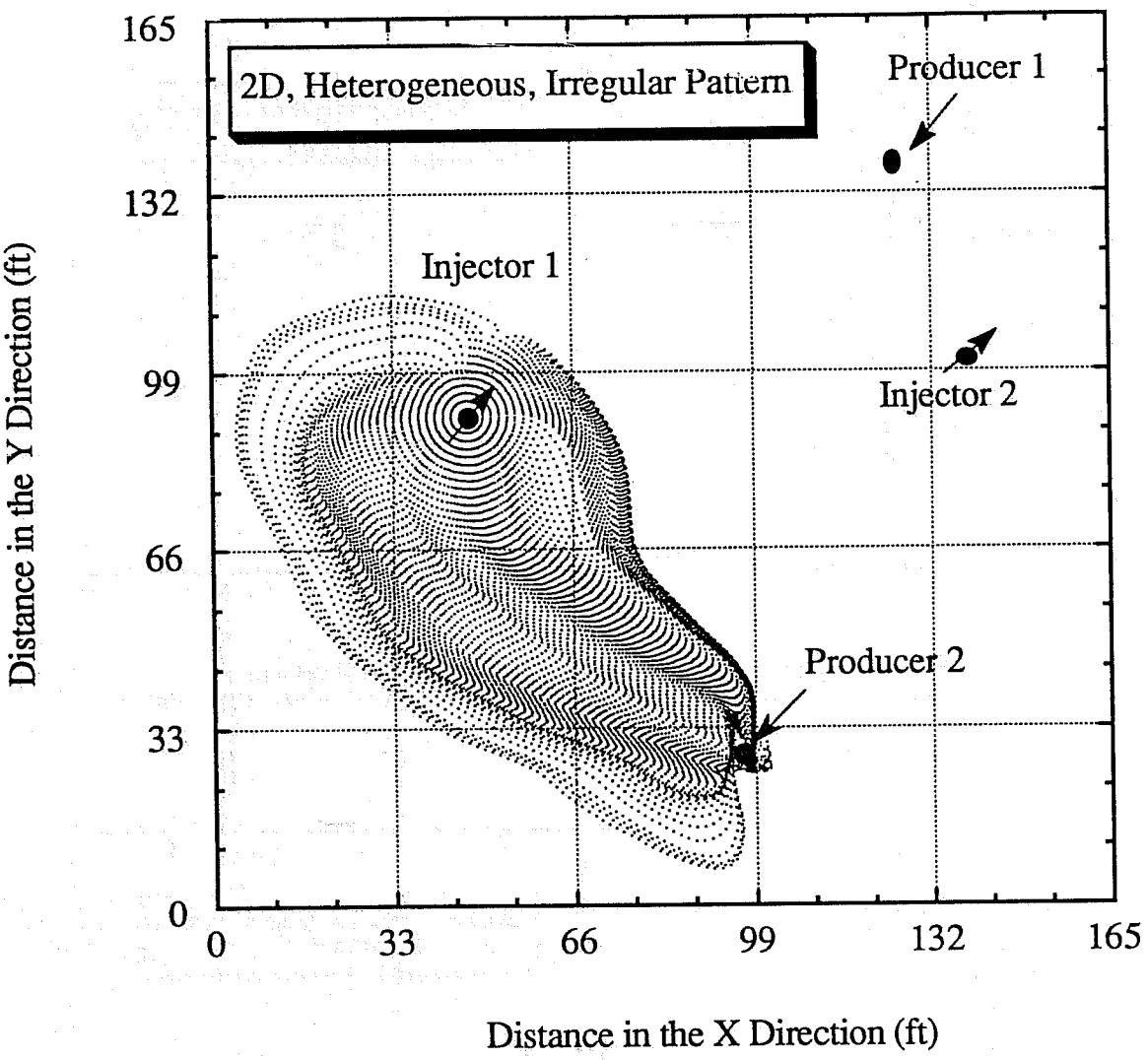

Fig. 28. Streamlines showing volume swept by Tracer 1 (V_{s1})

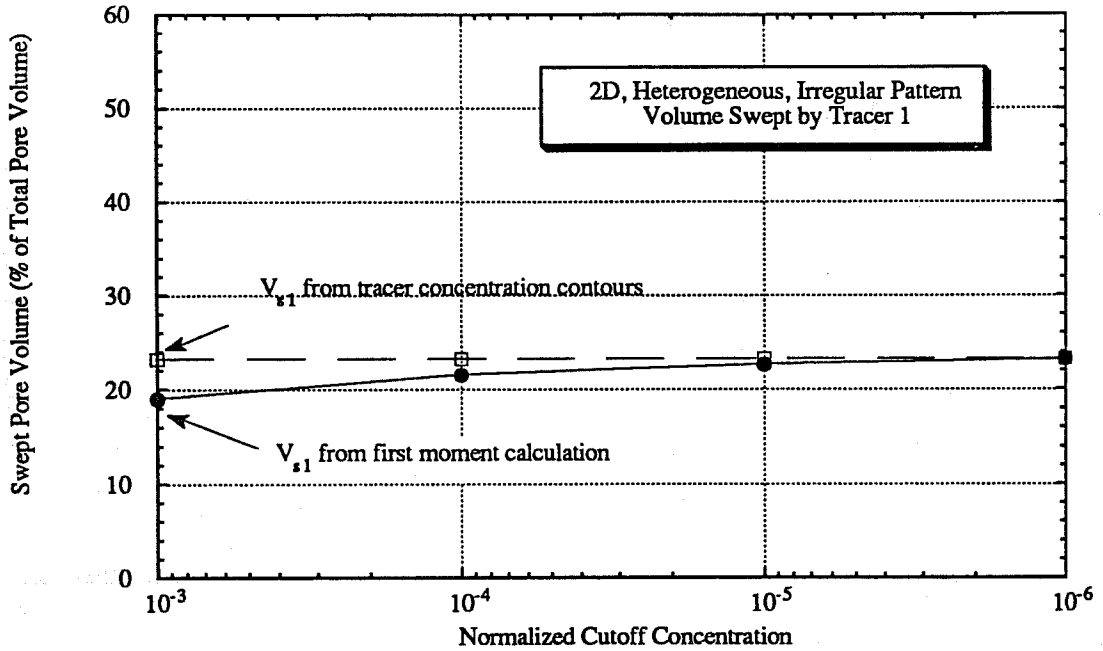

Fig. 29. Comparison between swept volumes calculated from the first moment method and tracer concentration contours from simulation (Runs No. SWVR4 and 6)

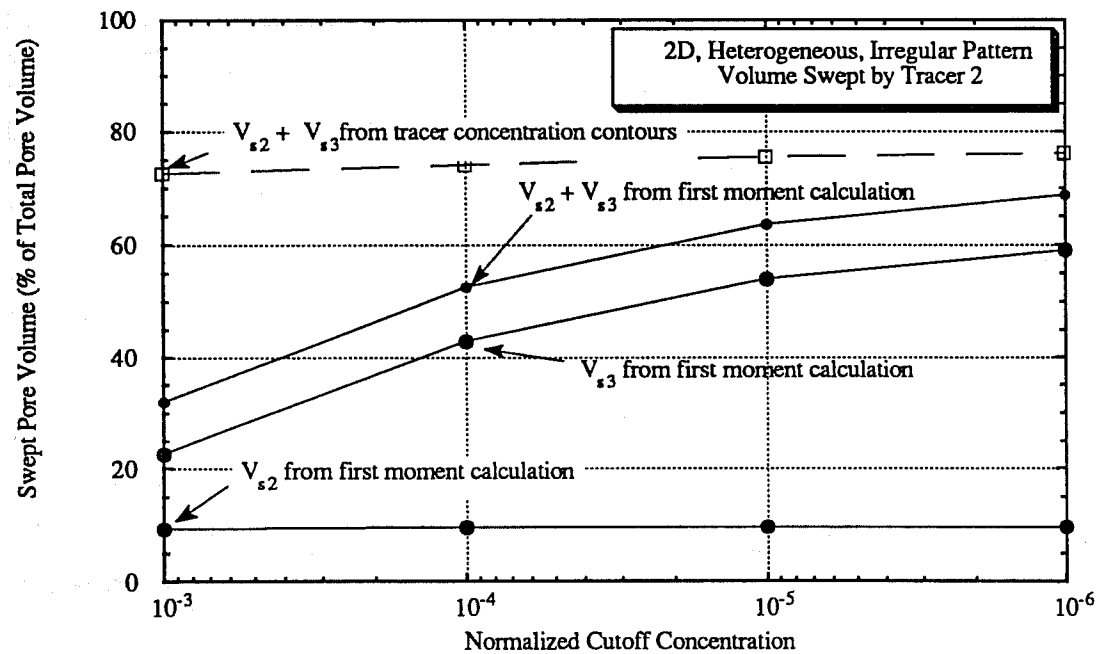

Fig. 30. Comparison between swept volumes calculated from the first moment method and tracer concentration contours from simulation (Runs No. SWVR4 and 6)

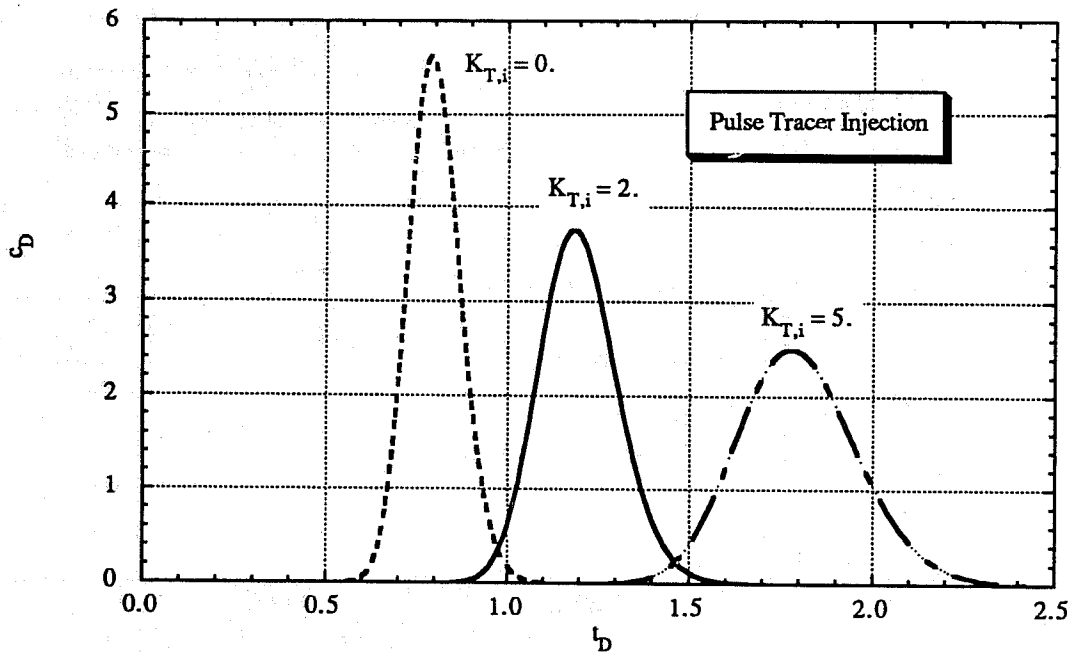

Fig. 31. Solution of the CD equation for partitioning tracers (N_{Pe} = 200, pulse tracer injection, S_{or} =0.2)

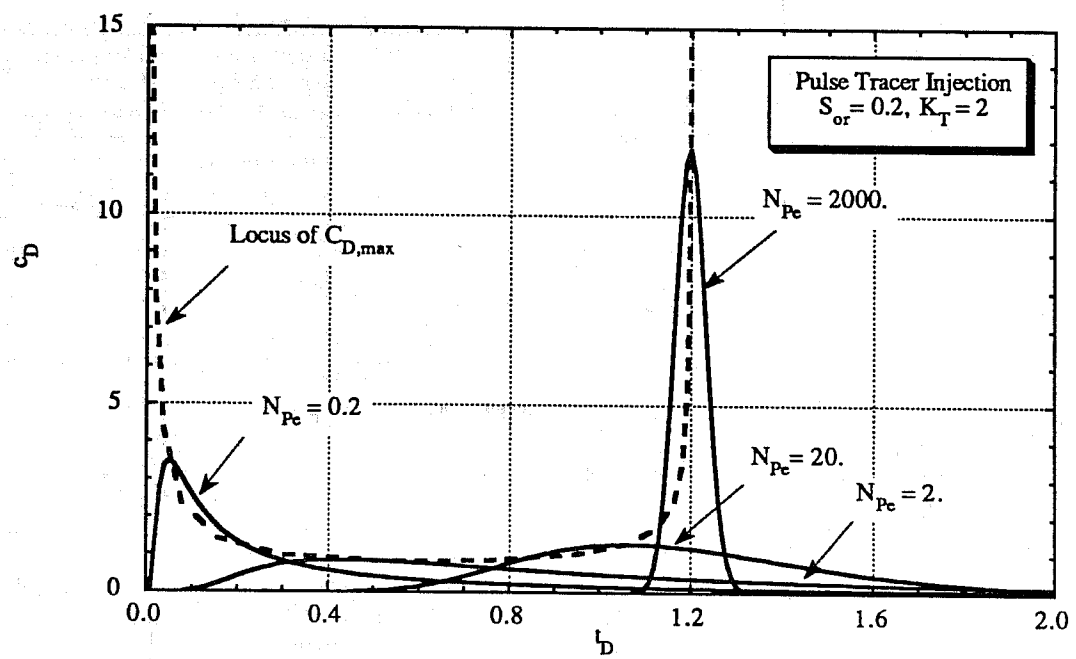

Fig. 32. Effect of physical dispersion on the produced tracer concentrations of a partitioning tracer with a pulse tracer injection

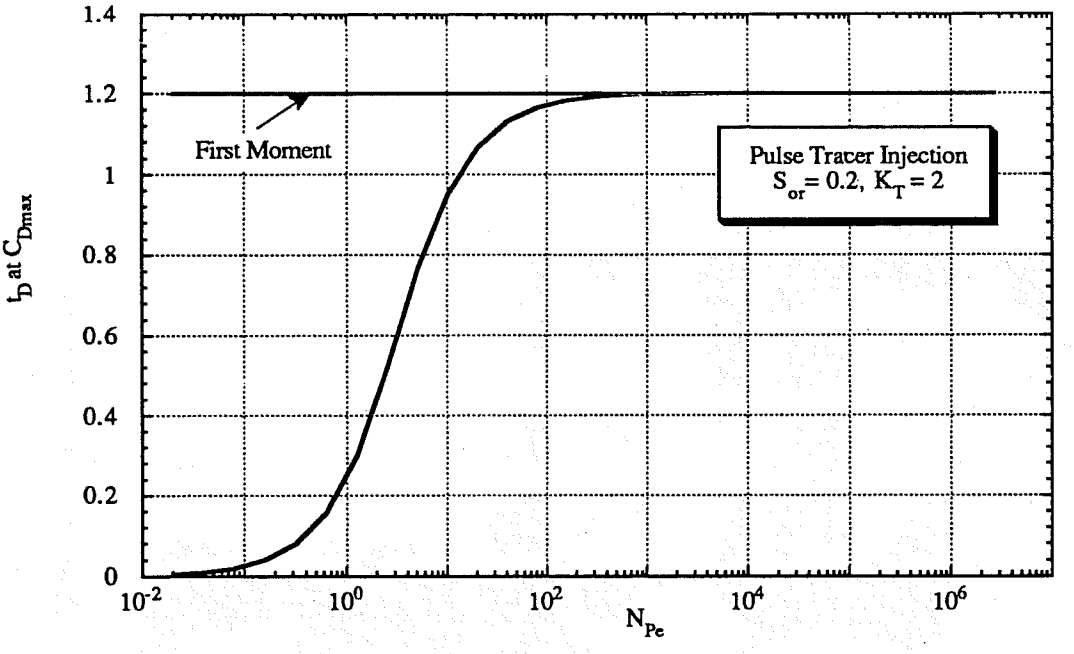

Fig. 33. Comparison of t_d at C_{Dmax} vs. the first moment at different N_{Pe}

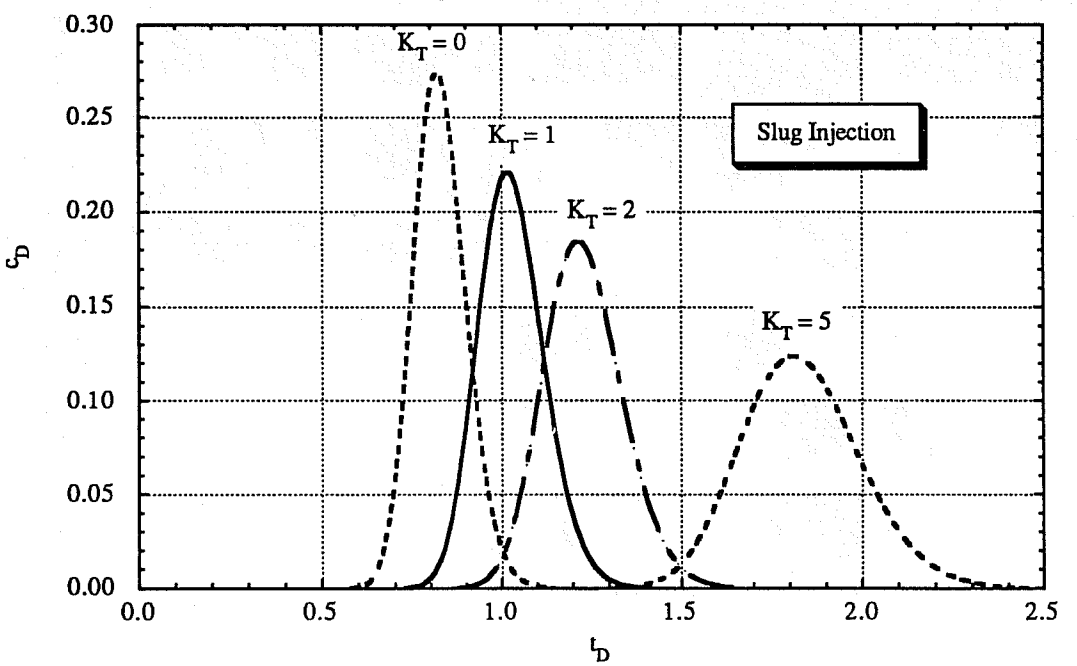

Fig. 34. Solution of CD equation for partitioning tracers (N_{Pe} = 200, t_{Ds} = 0.05)

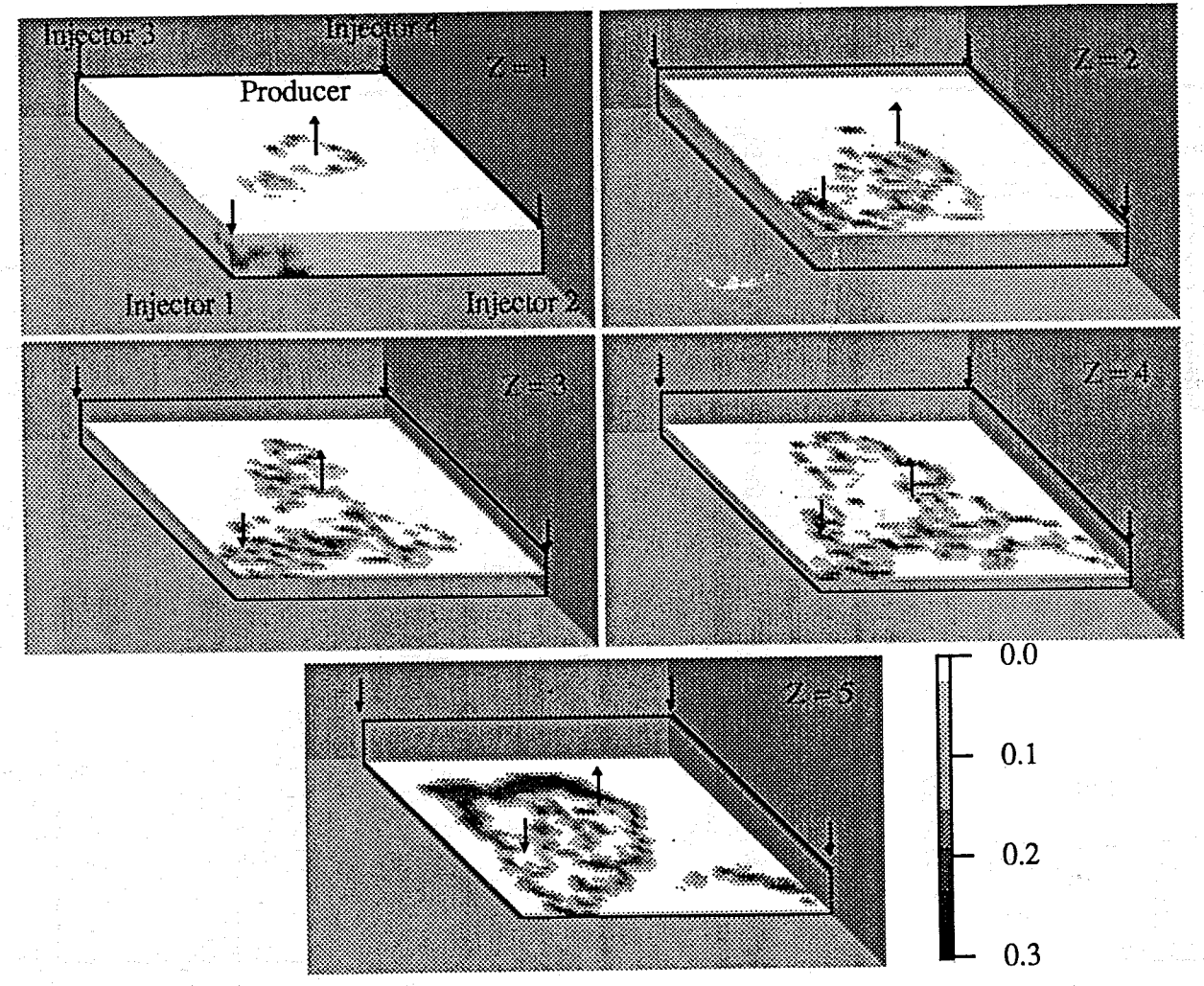

Fig. 35. TCE saturation used in the 3D simulation of residual phase saturation determination

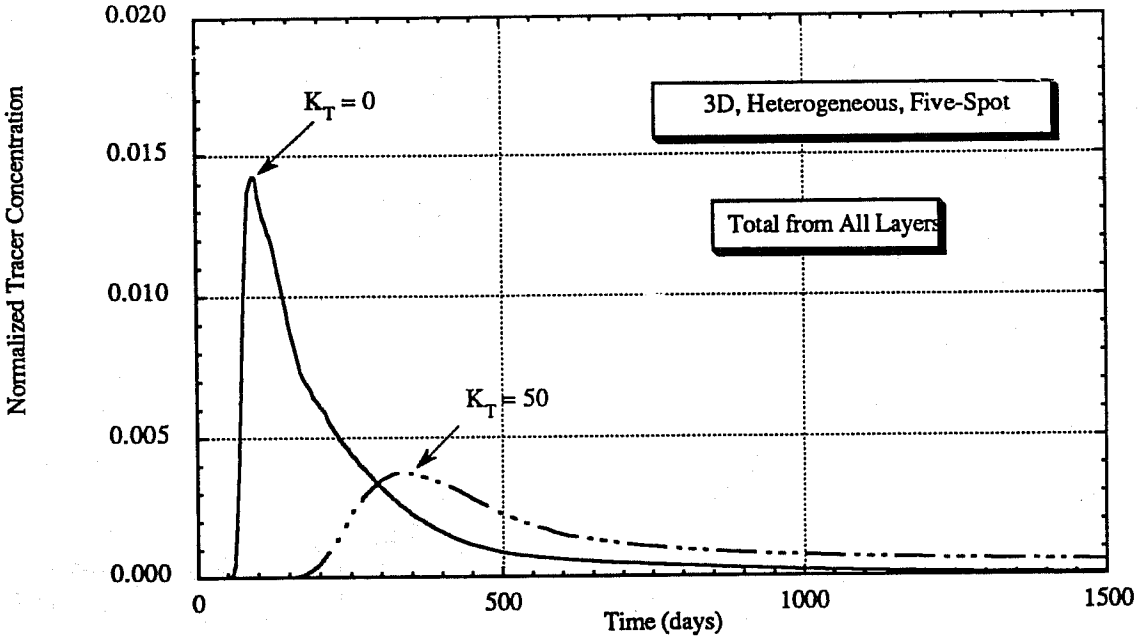

Fig. 36. Simulated tracer production data from Injector 1 (Run No. SWVR31)

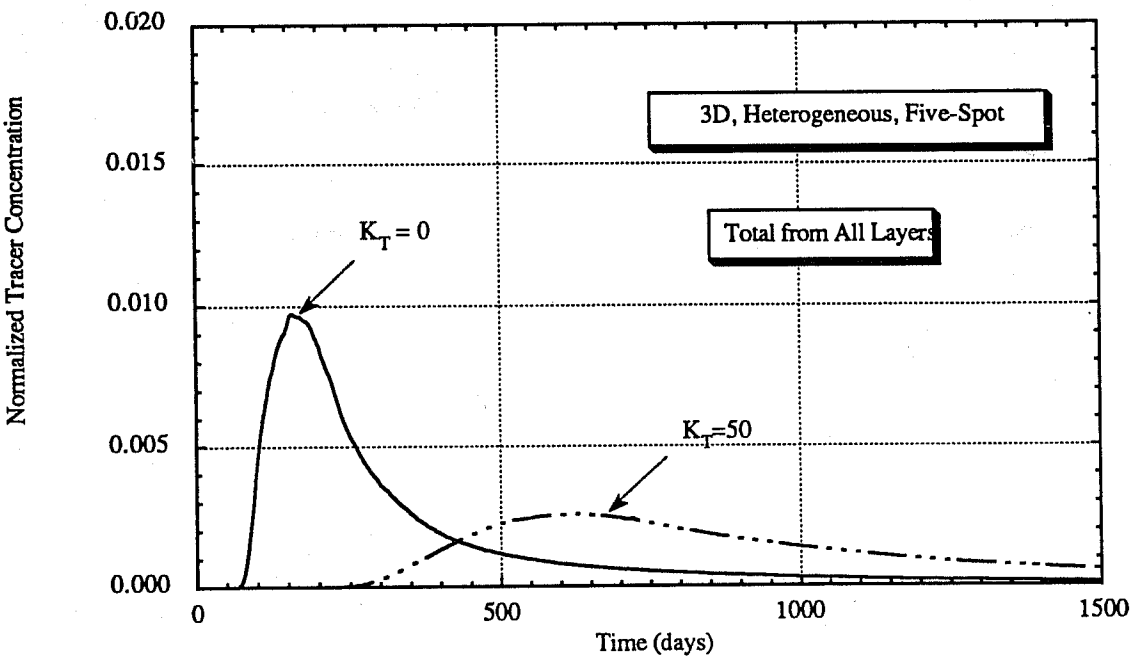

Fig. 37. Simulated tracer production data from Injector 2 (Run No. SWVR32)

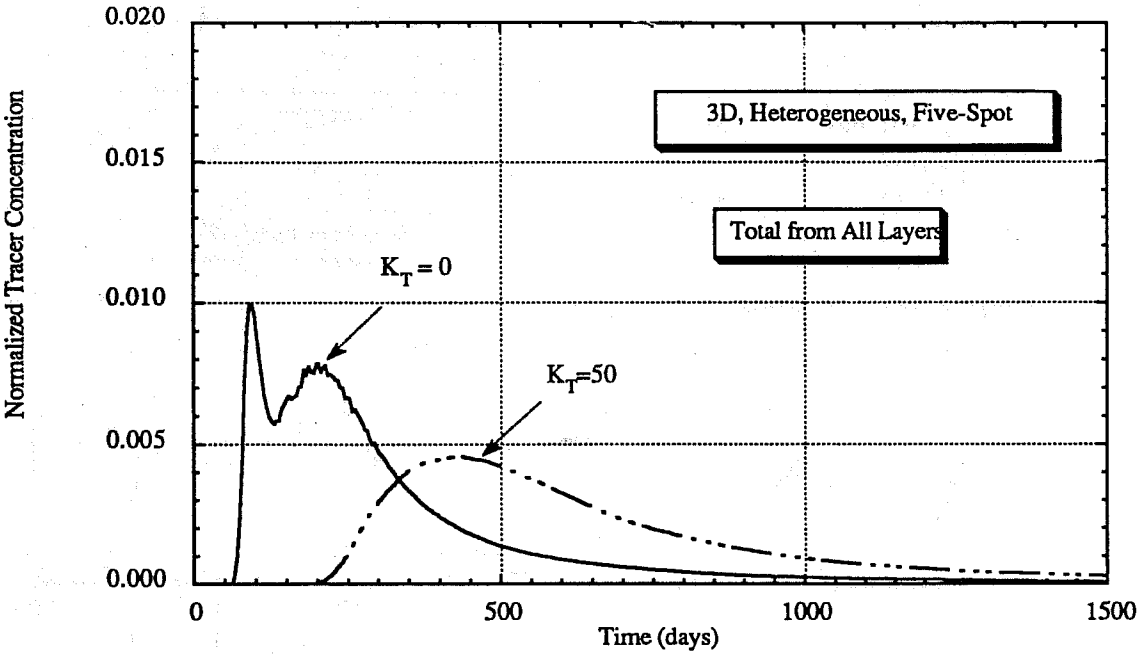

Fig. 38A. Simulated tracer production data from Injector 3 (Run No. SWVR33)

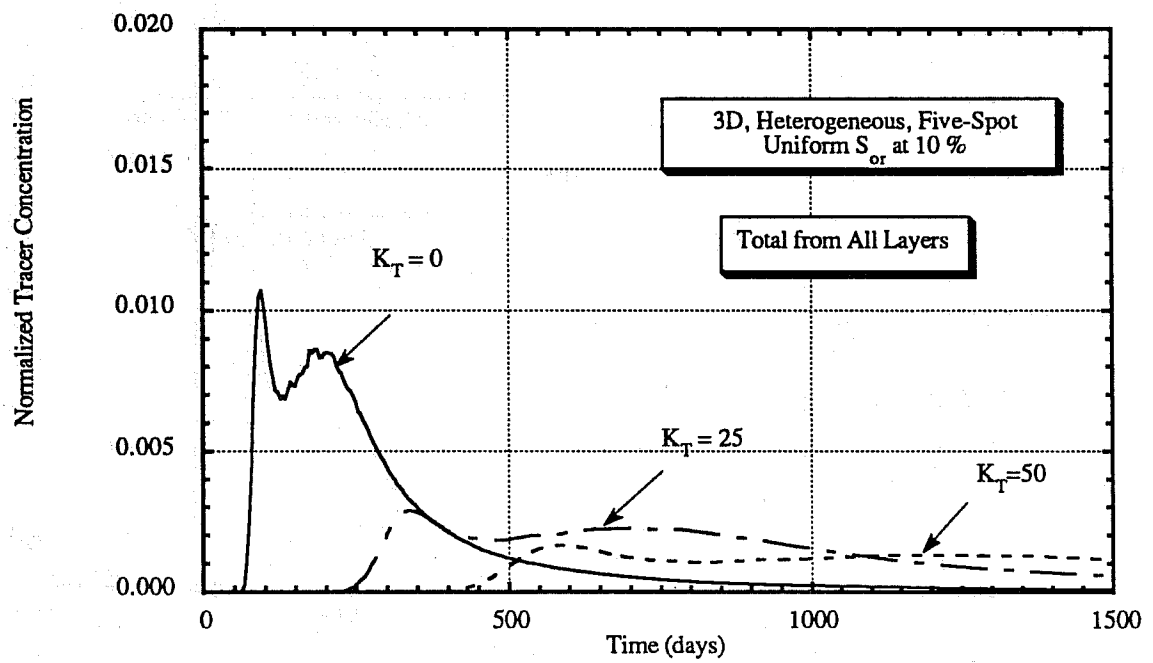

Fig. 38B. Simulated tracer production data from Injector 3 (Run No. SWVR33P2)

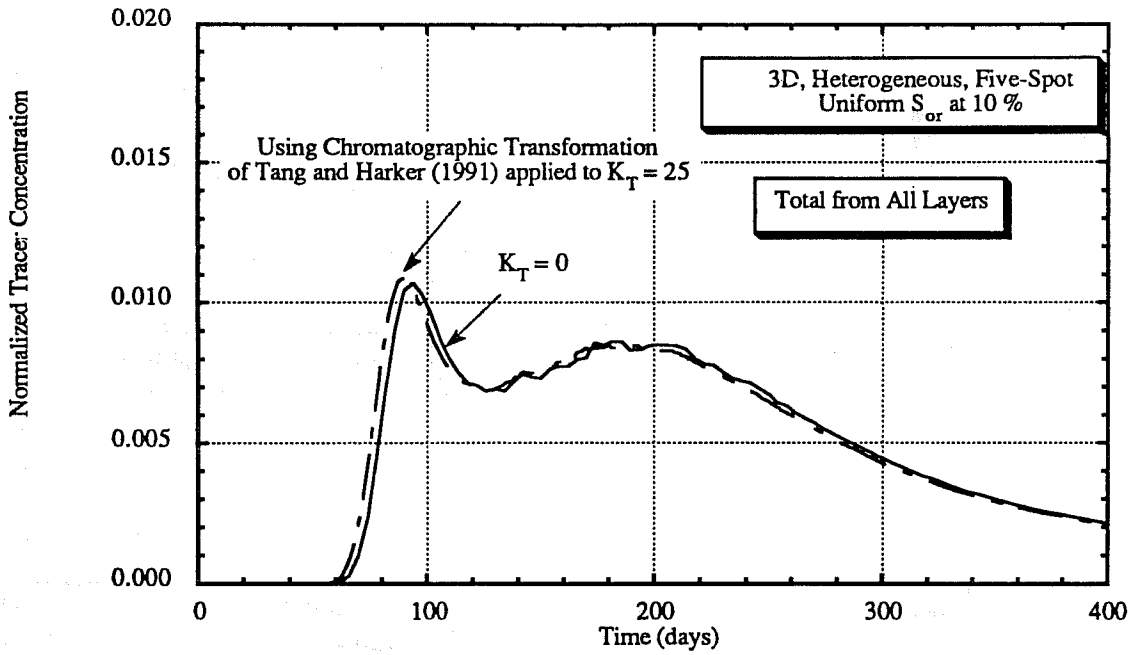

Fig. 38C. Chromatographic transformation showing production data of different partitioning tracers collapsed into a single curve if the reservoir has uniform S_{or}

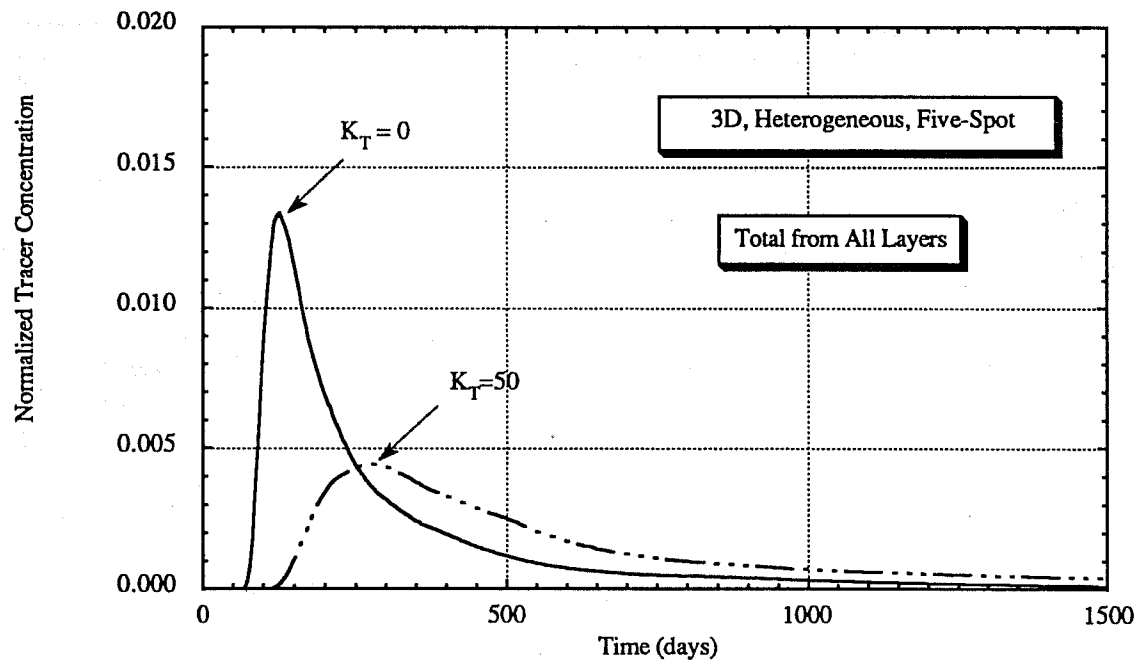

Fig. 39 Simulated tracer production data from Injector 4 (Run No. SWVR34)

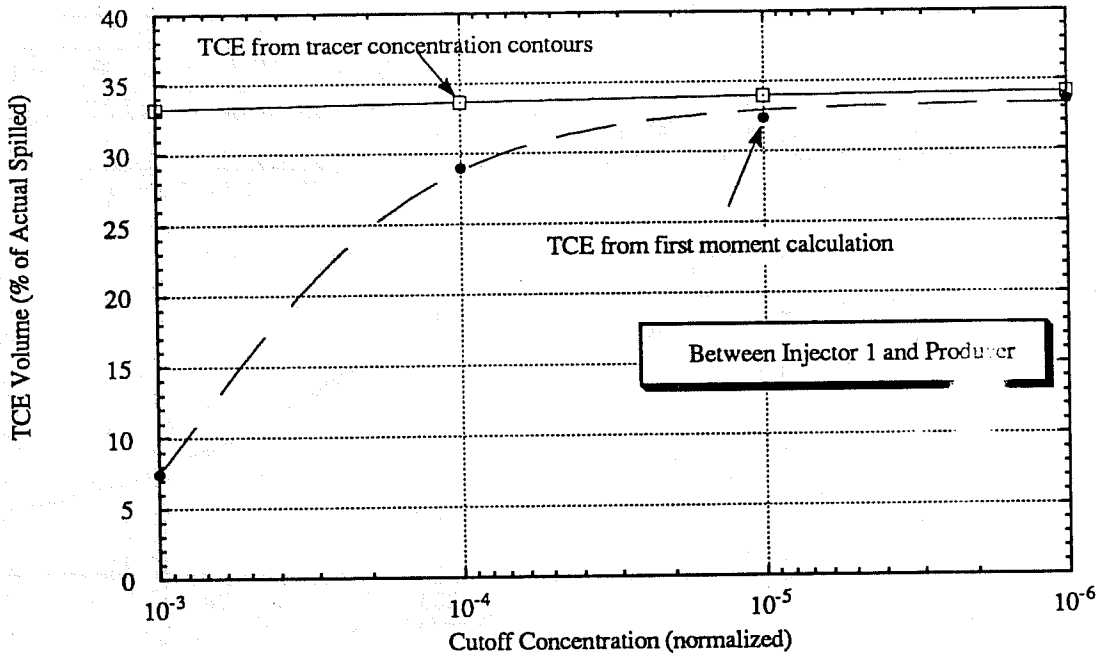

Fig. 40. Comparison between TCE volumes calculated from the first moment method and tracer concentration contours (Run No. SWVR31-34)

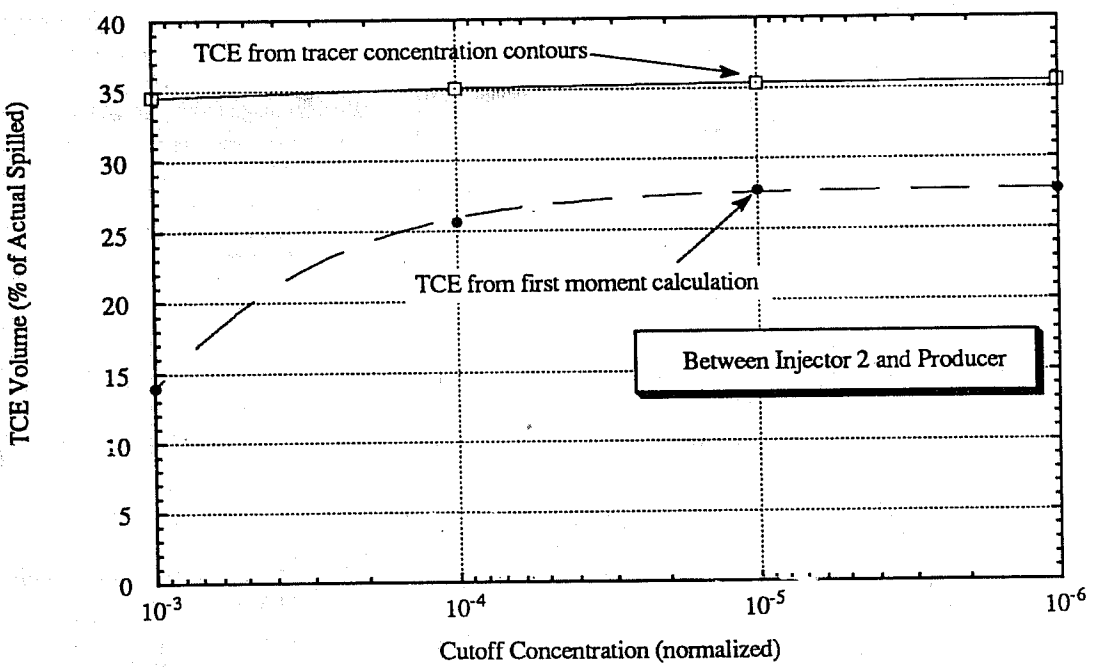

Fig. 41 Comparison between TCE volumes calculated from the first moment method and tracer concentration contours (Run No. SWVR31-34)

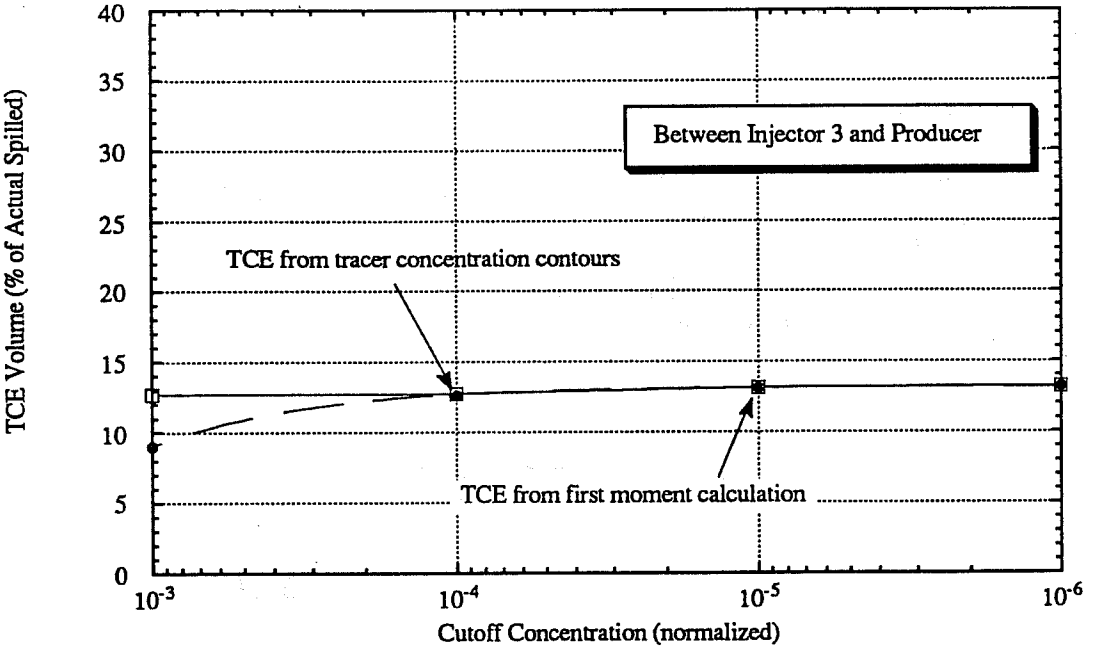

Fig. 42. Comparison between TCE volumes calculated from the first moment method and tracer concentration contours (Run No. SWVR31-34)

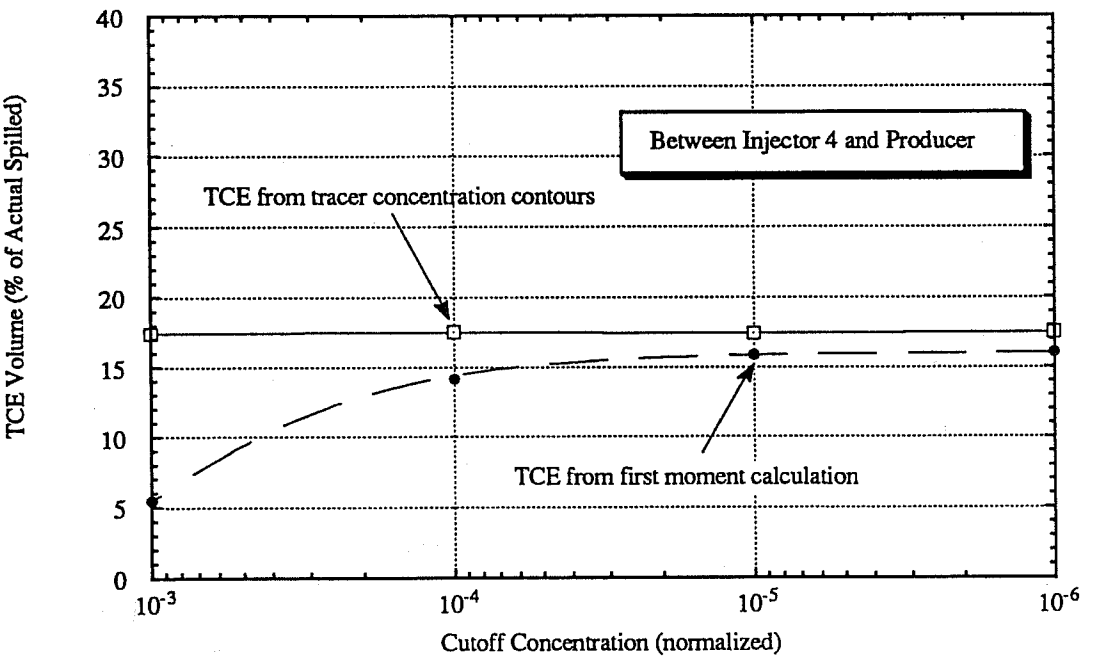

Fig. 43. Comparison between TCE volumes calculated from the first moment method and tracer concentration contours (Run No. SWVR31-34)

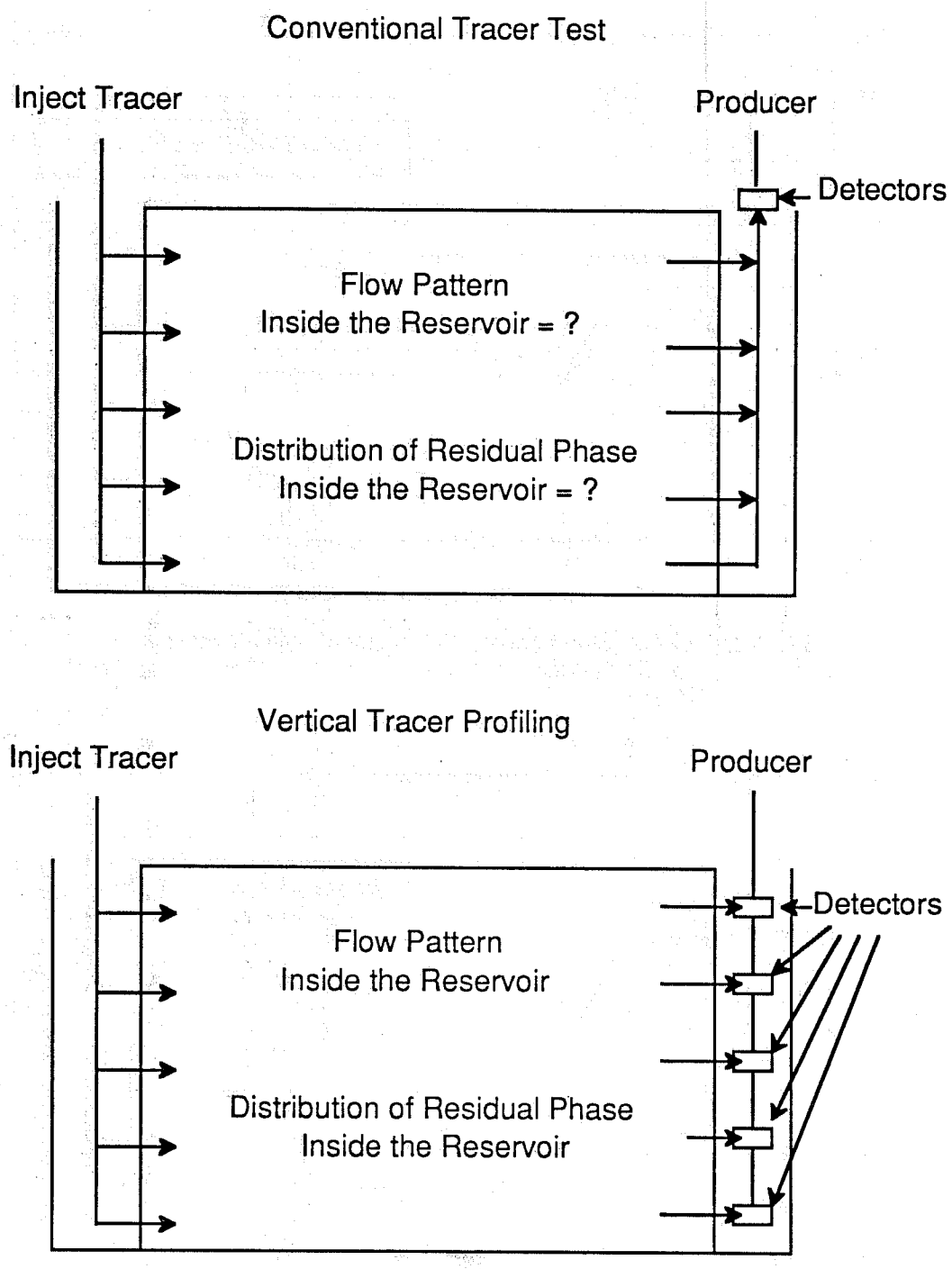

Fig. 44. Schematic diagram comparing Vertical Tracer Profiling to a conventional tracer test

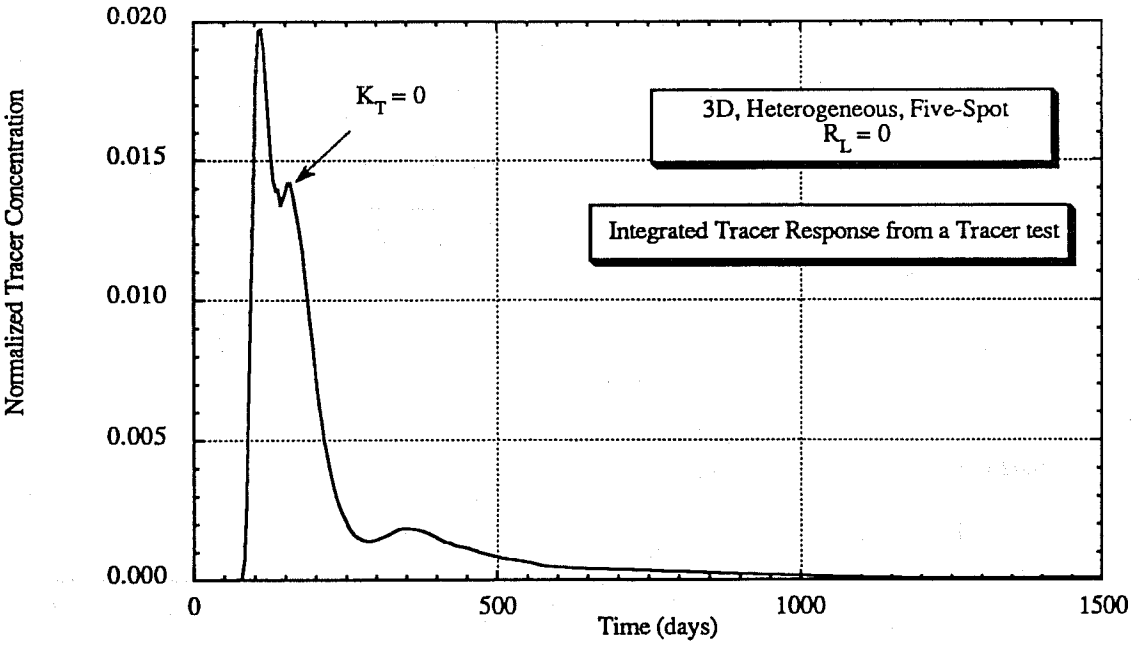

Fig. 45. Simulated tracer production data from Injector 1 (Run No. SWVR35)

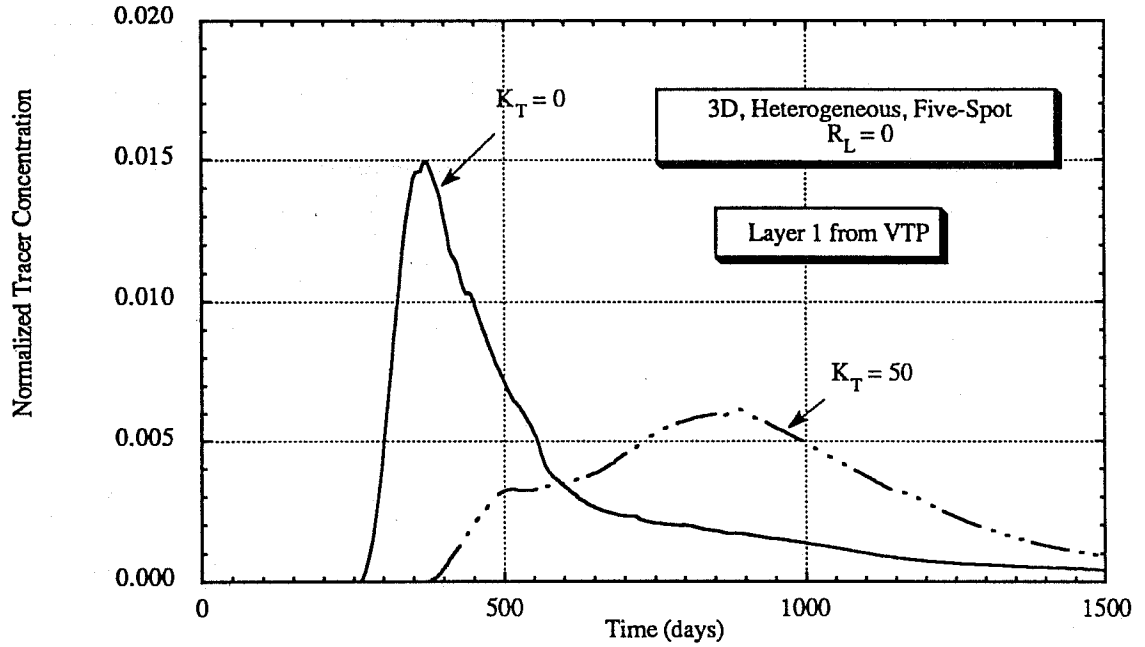

Fig. 46. Simulated tracer production data from Injector 1 (Run No. SWVR35)

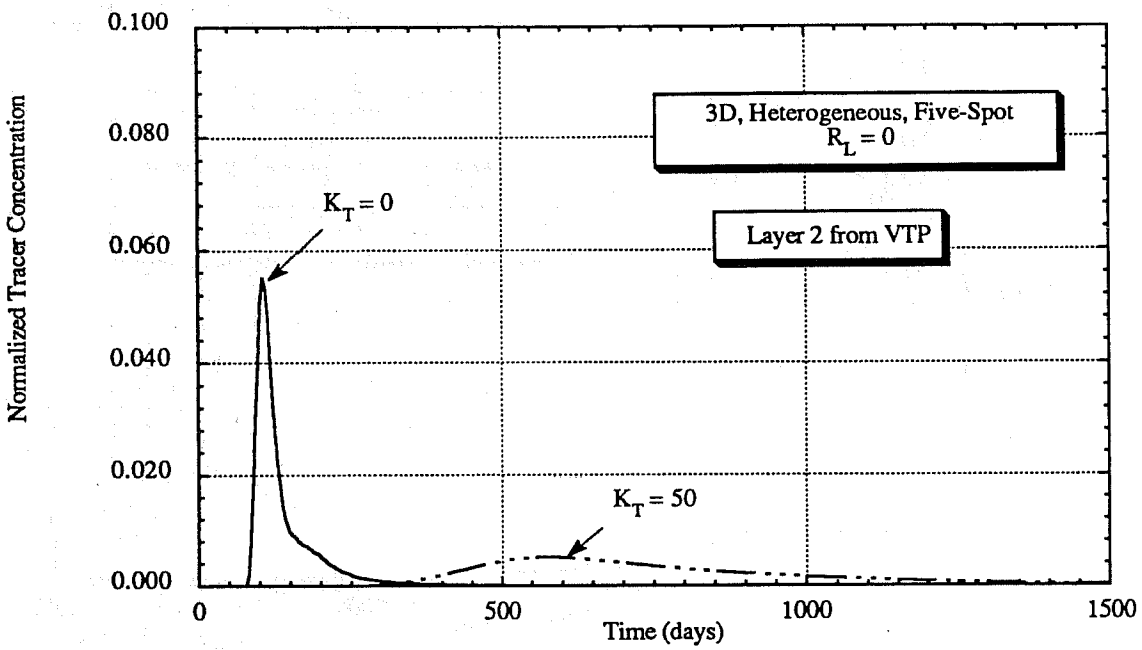

Fig. 47. Simulated tracer production data from Injector 1 (Run No. SWVR35)

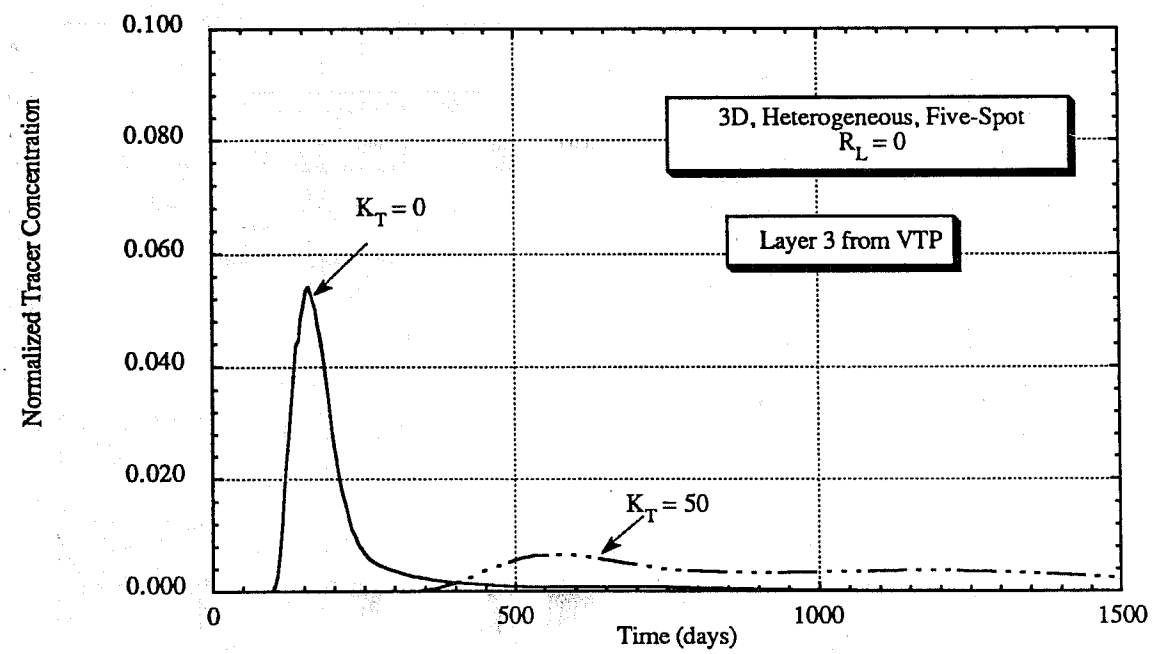

Fig. 48. Simulated tracer production data from Injector 1 (Run No. SWVR35)

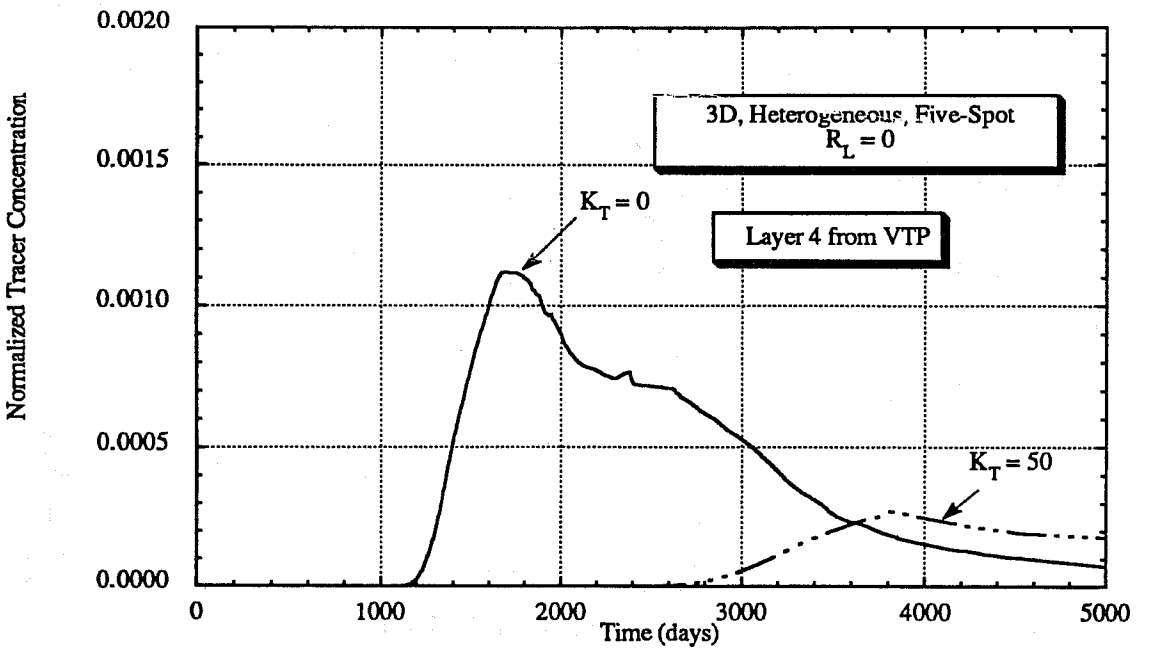

Fig. 49. Simulated tracer production data from Injector 1 (Run No. SWVR35)

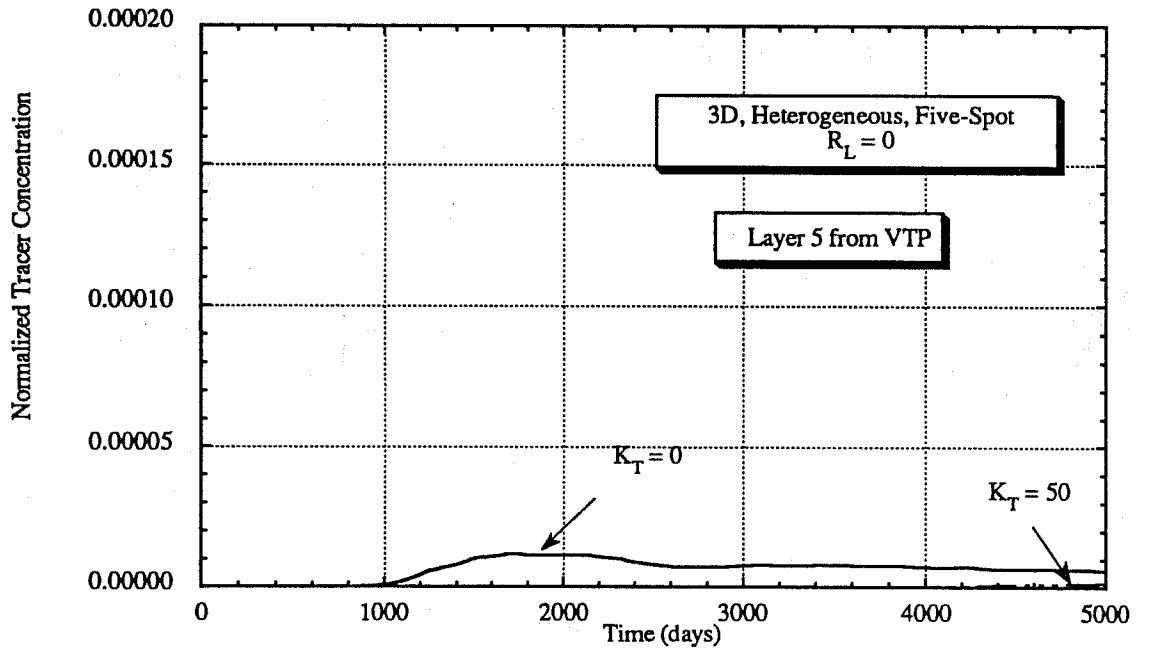

Fig. 50. Simulated tracer production data from Injector 1 (Run No. SWVR35)

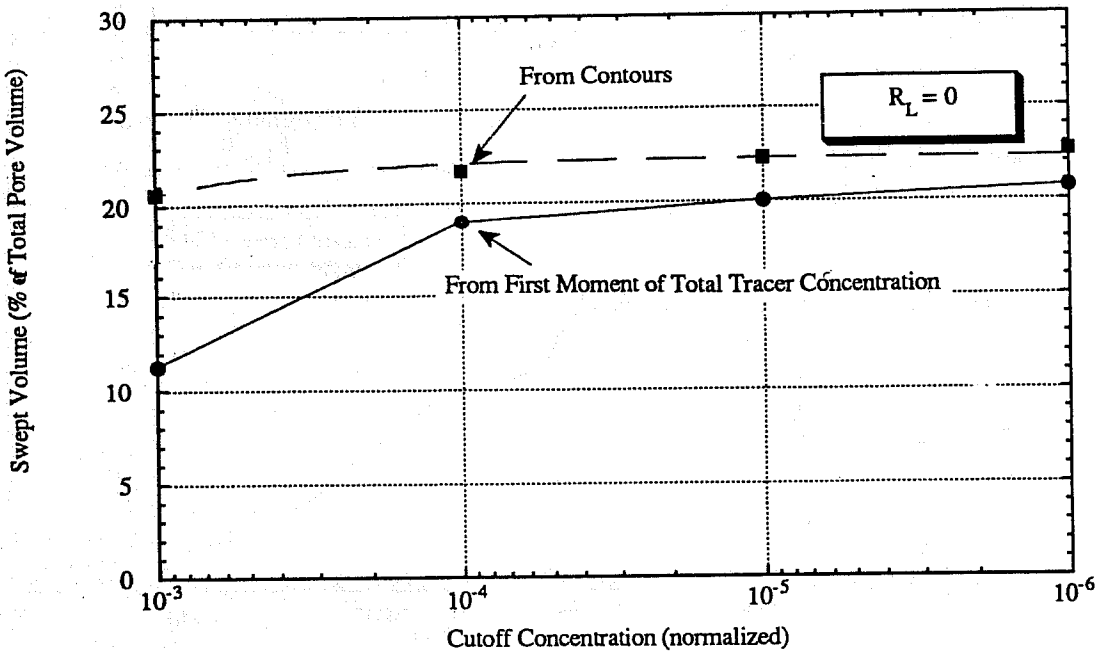

Fig. 51. Comparison between swept volumes from tracer concentration contours and the first moment of tracer production from VTP (Run No. SWVR35)

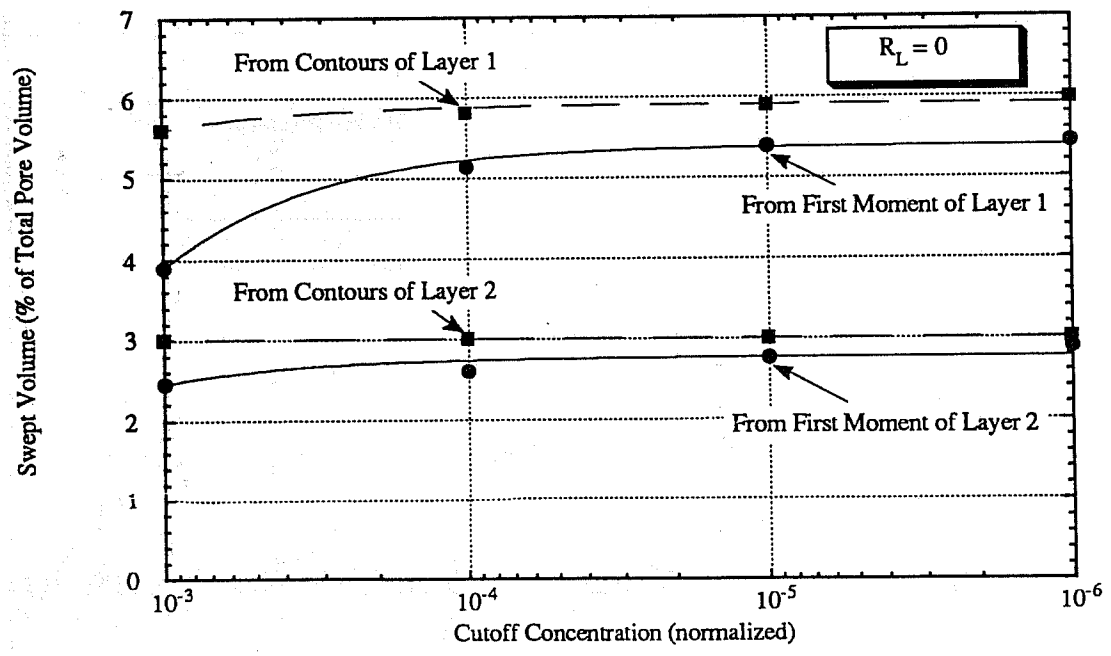

Fig. 52. Comparison between swept volumes from tracer concentration contours and the first moment of tracer production data from VTP (Run No. SWVR35)

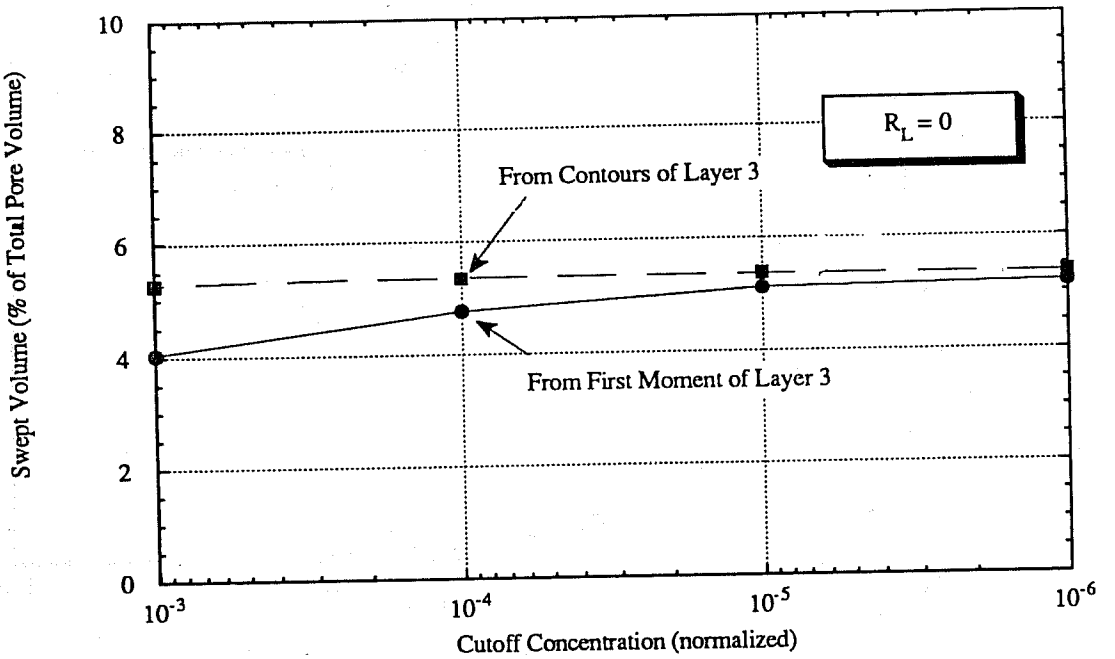

Fig. 53. Comparison between swept volumes from tracer concentration contours and the first moment of tracer production data from VTP (Run No. SWVR35)

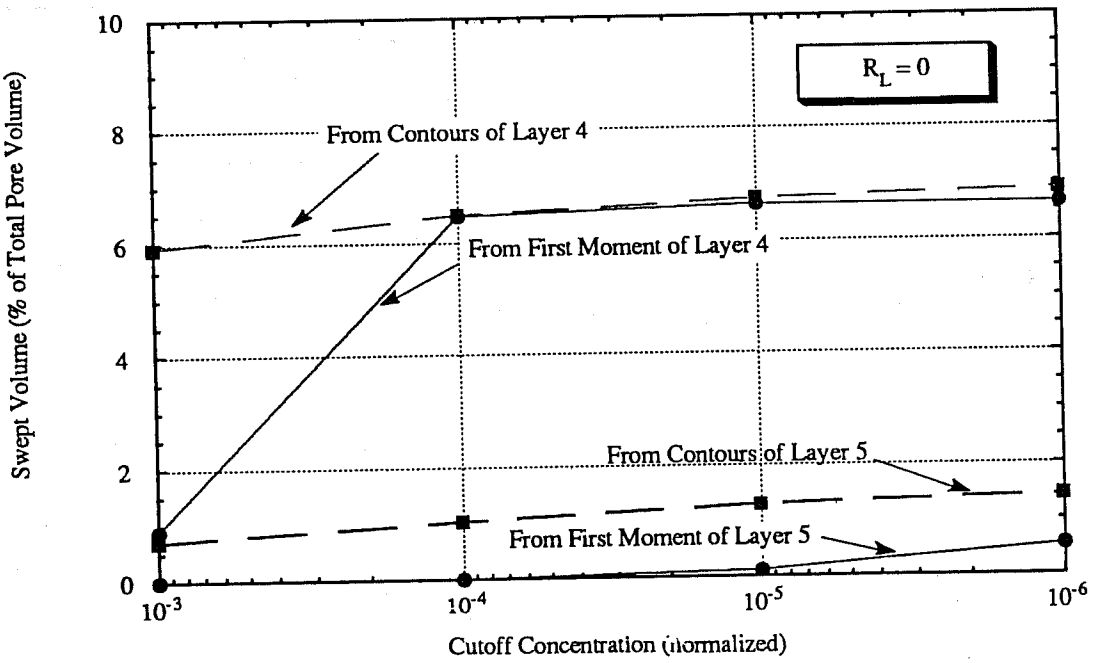

Fig. 54. Caparison between swept volumes from tracer concentration contours and The first moment of tracer production data from VTP (Run No. SWVR35)

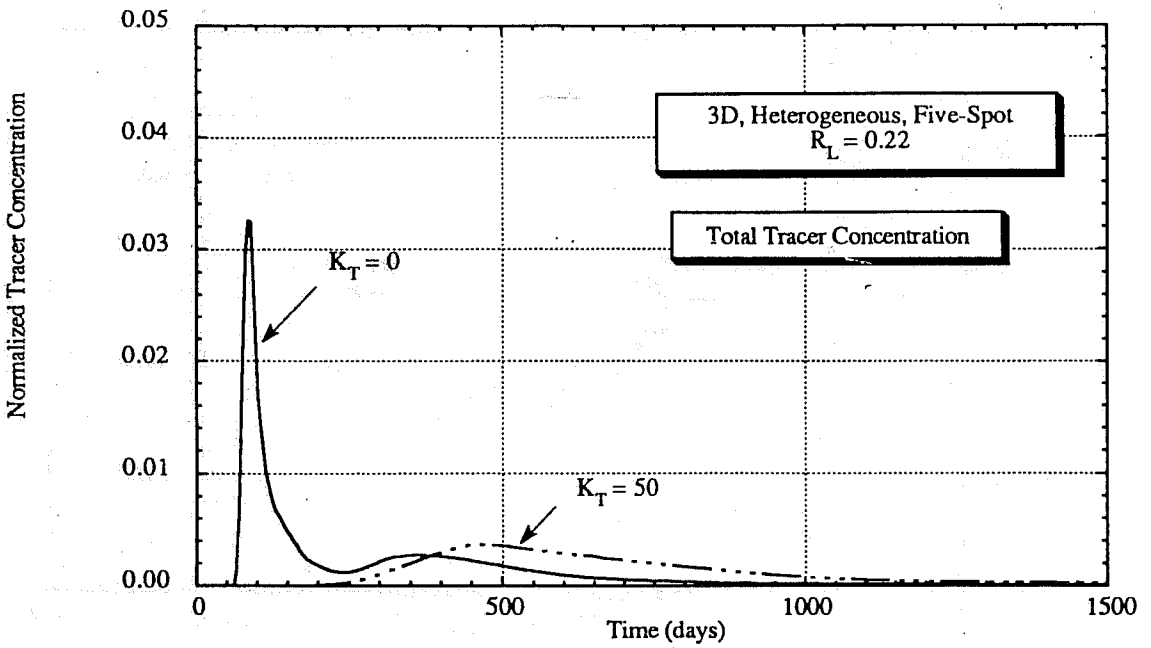

Fig. 55. Simulated tracer production data from a conventional tracer test (Run No. SWVR41)

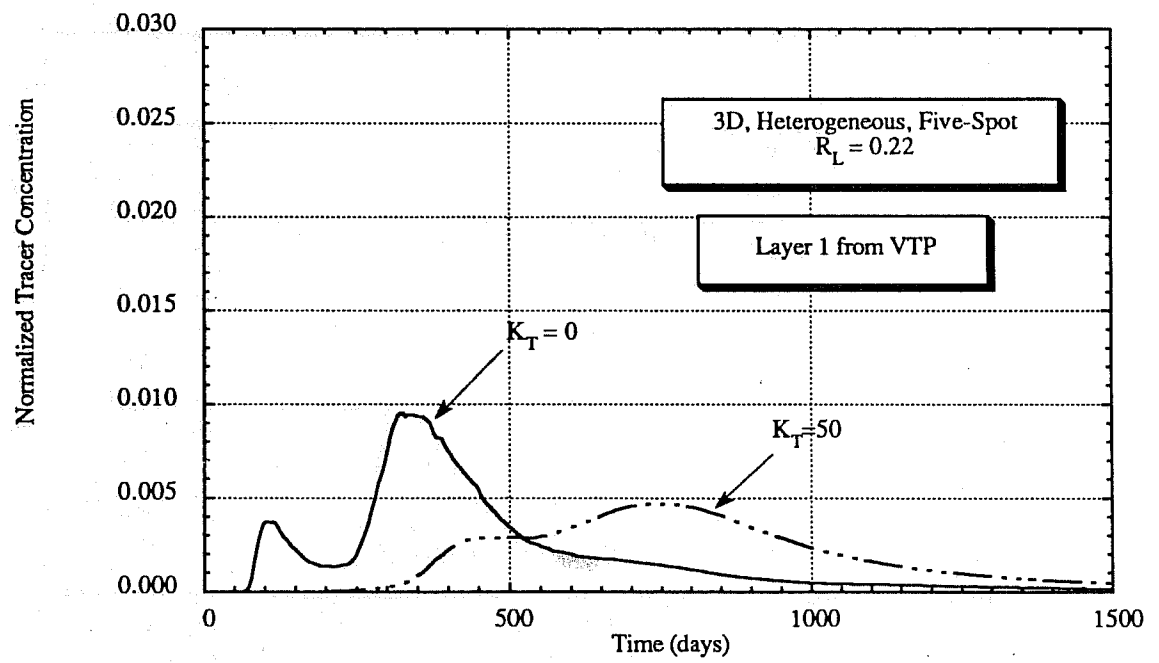

Fig. 56. Simulated tracer production data from VTP (Run No. SWVR41)

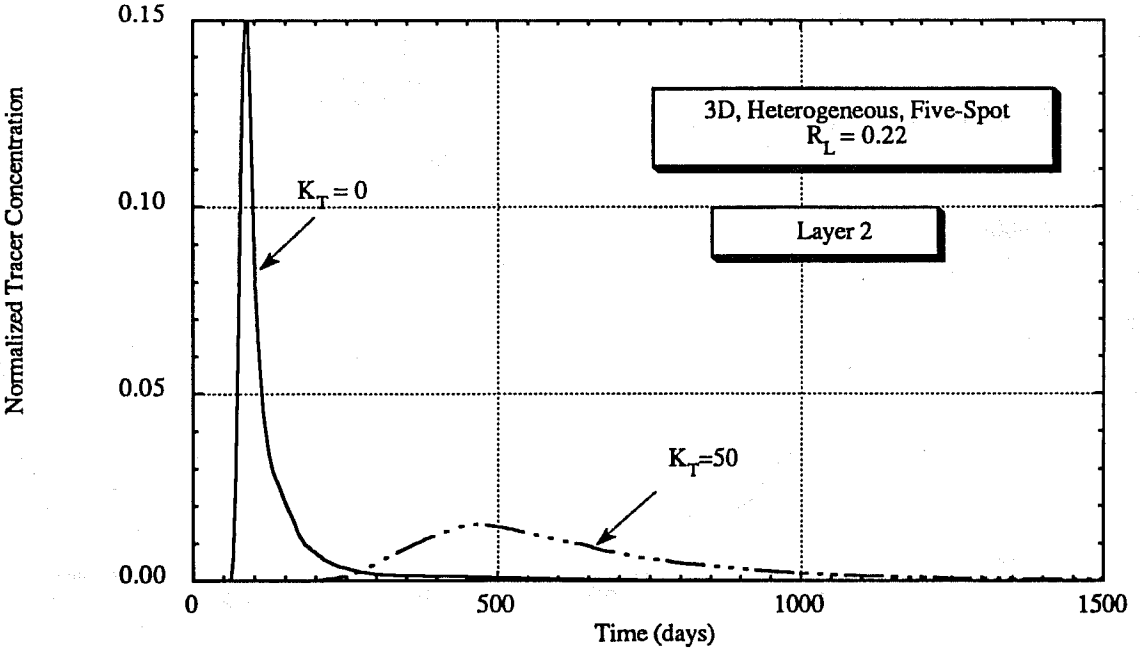

Fig. 57. Simulated tracer production data from VTP (Run No. SWVR41)

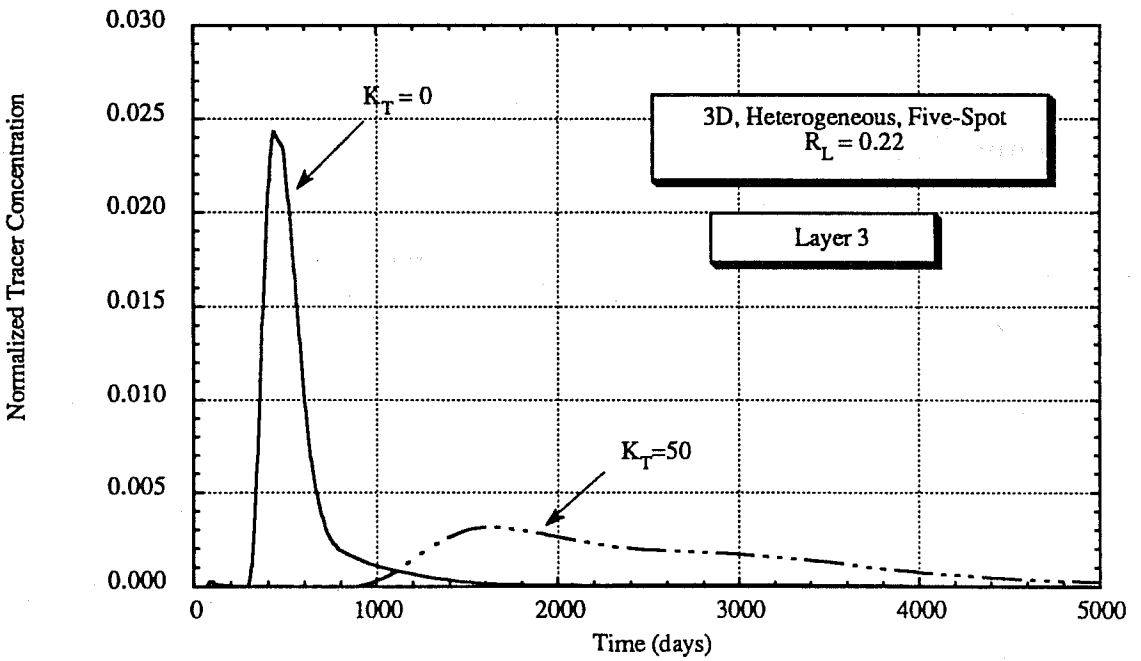

Fig. 58. Simulated tracer production data from VTP (Run No. SWVR41)

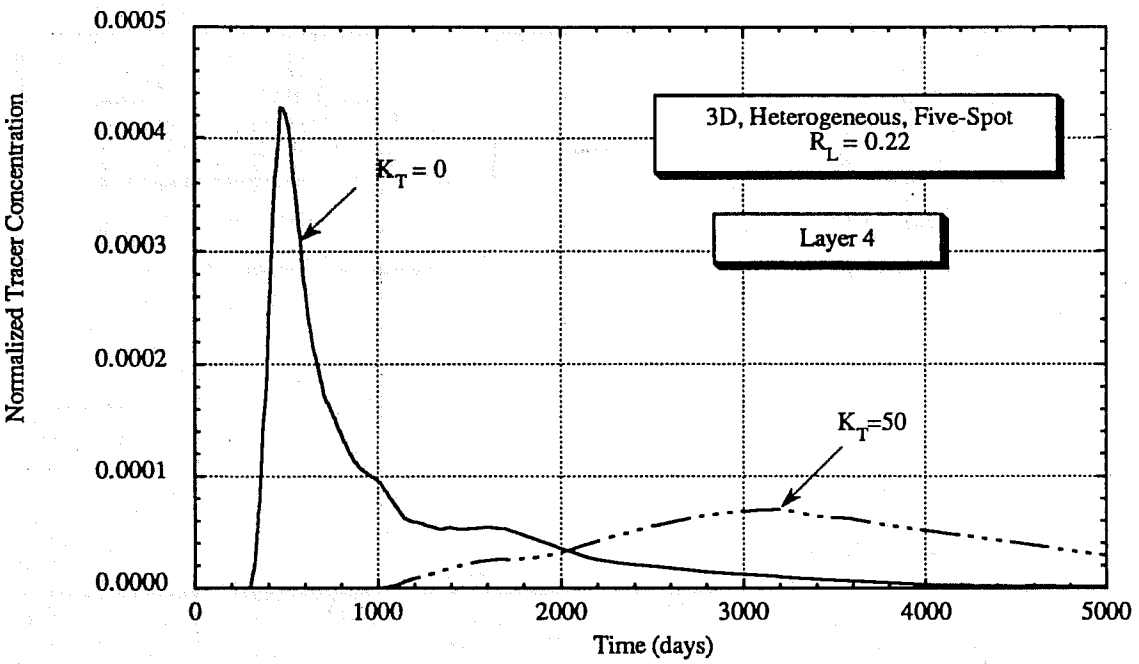

Fig. 59. Simulated tracer production data from VTP (Run No. SWVR41)

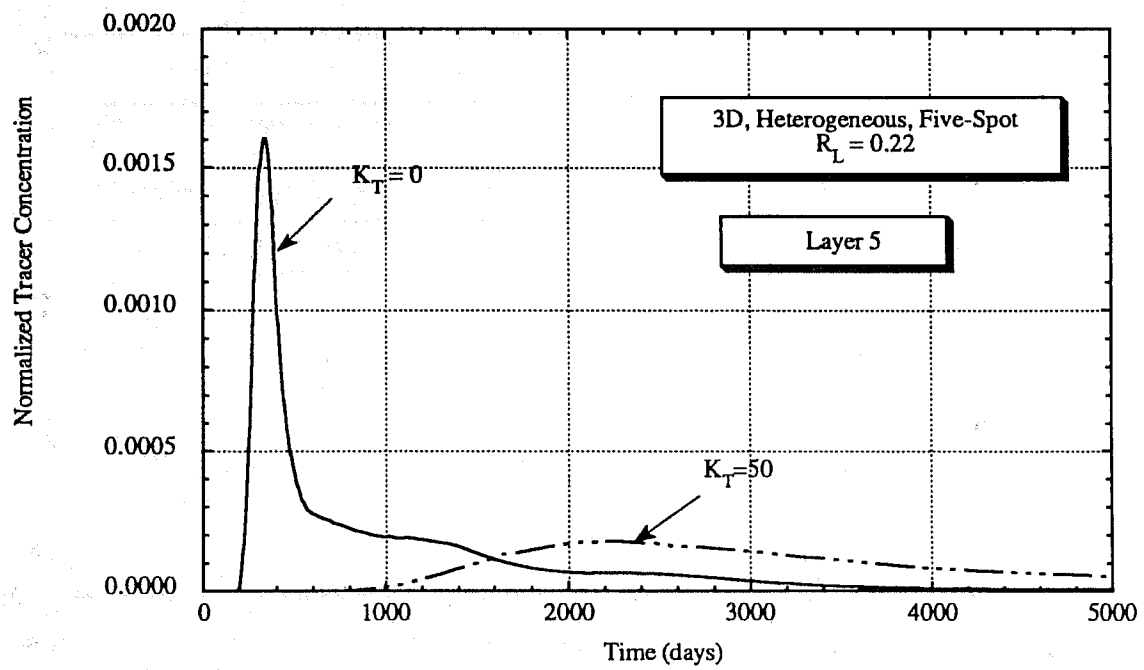

Fig. 60. Simulated tracer production data from VTP (Run No. SWVR41)

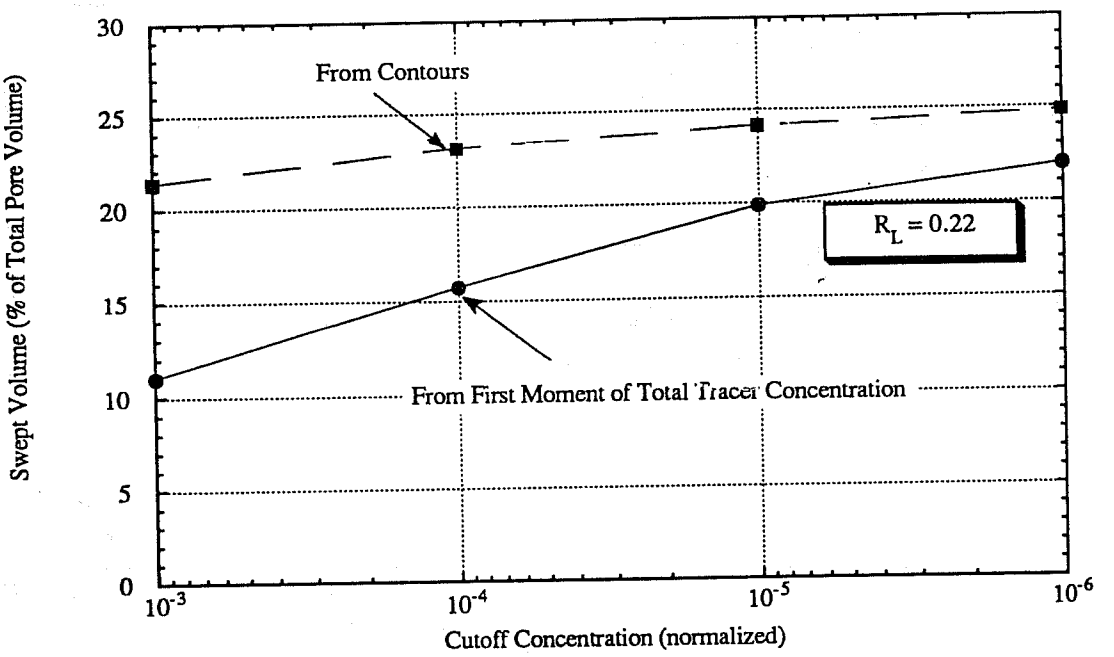

Fig. 61. Comparison between swept volumes from tracer concentration contours and from the first moment of tracer production data (Run No. SWVR41)

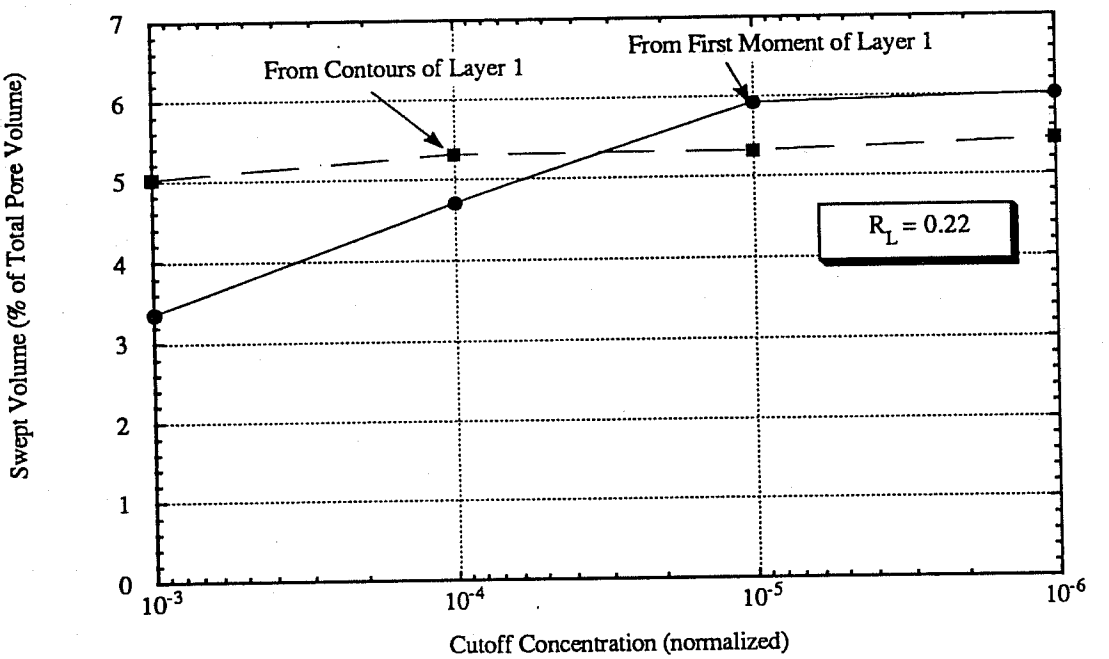

Fig. 62. Comparison between swept volumes from tracer concentration contours and from the first moment of tracer production data from VTP (Run No. SWVR41)

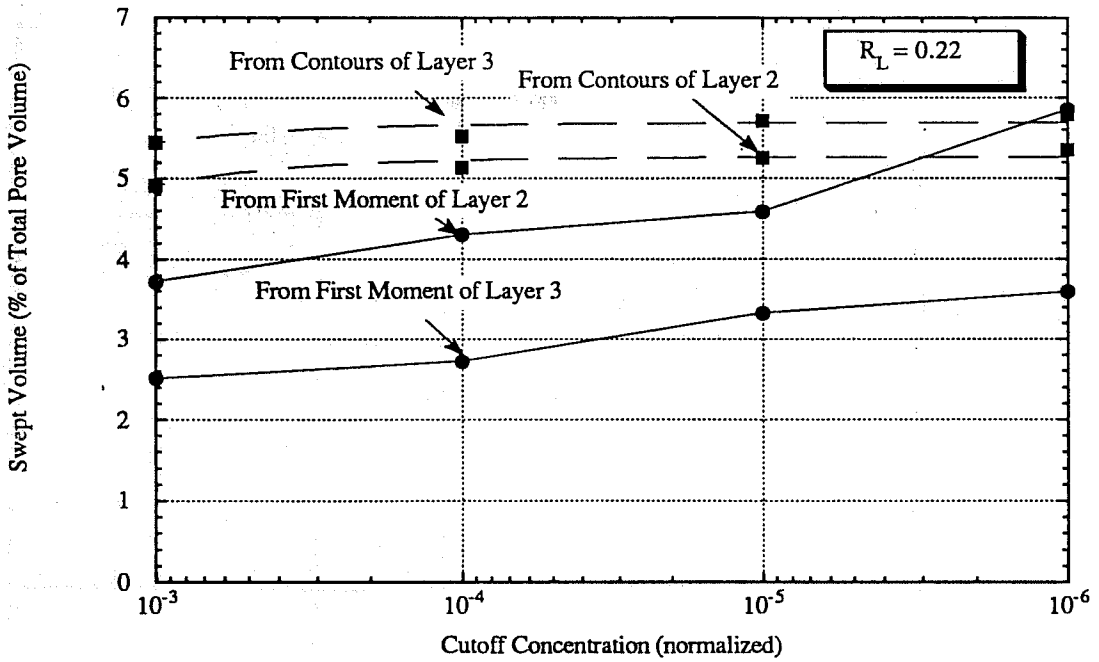

Fig. 63. Comparison between swept volumes from tracer concentration contours and from the first moment of tracer production data from VTP (Run No. SWVR41)

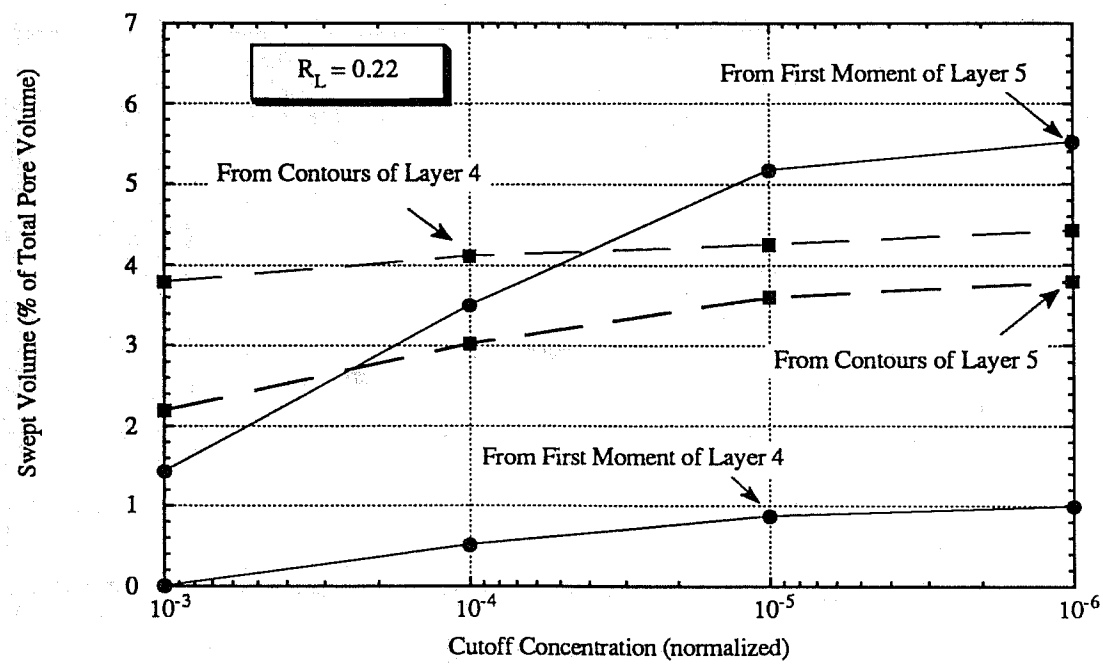

Fig. 64. Comparison between swept volumes from tracer concentration contours and from the first moment of tracer production data from VTP (Run No. SWVR41)

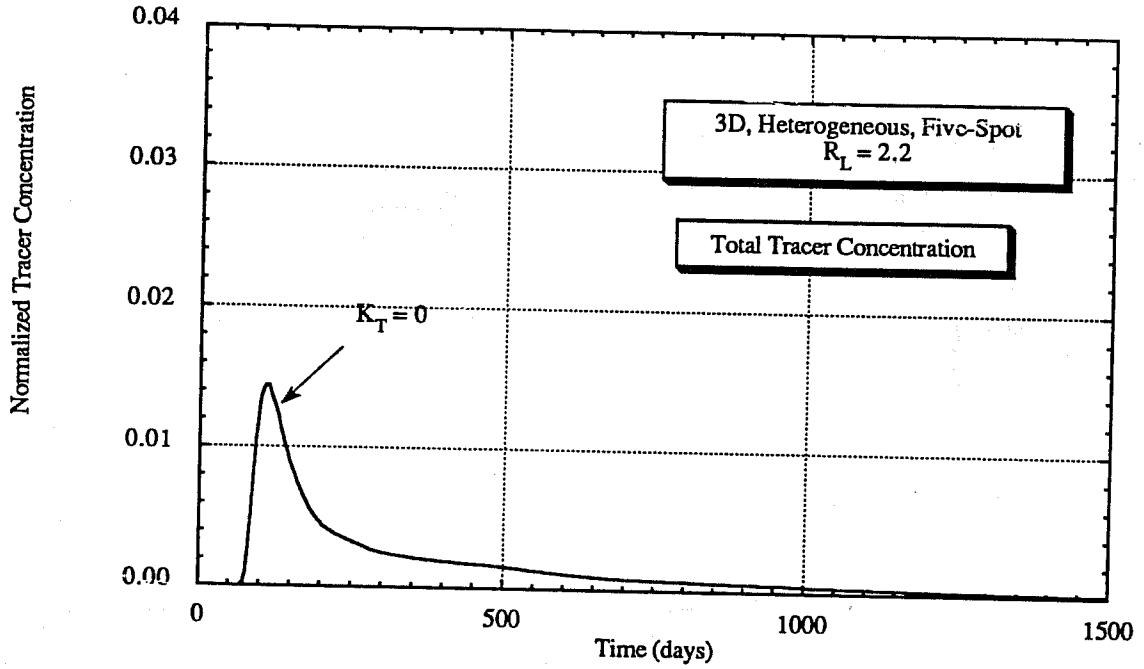

Fig. 65. Simulated tracer production data from a conventional tracer test (Run No. SWVR42)

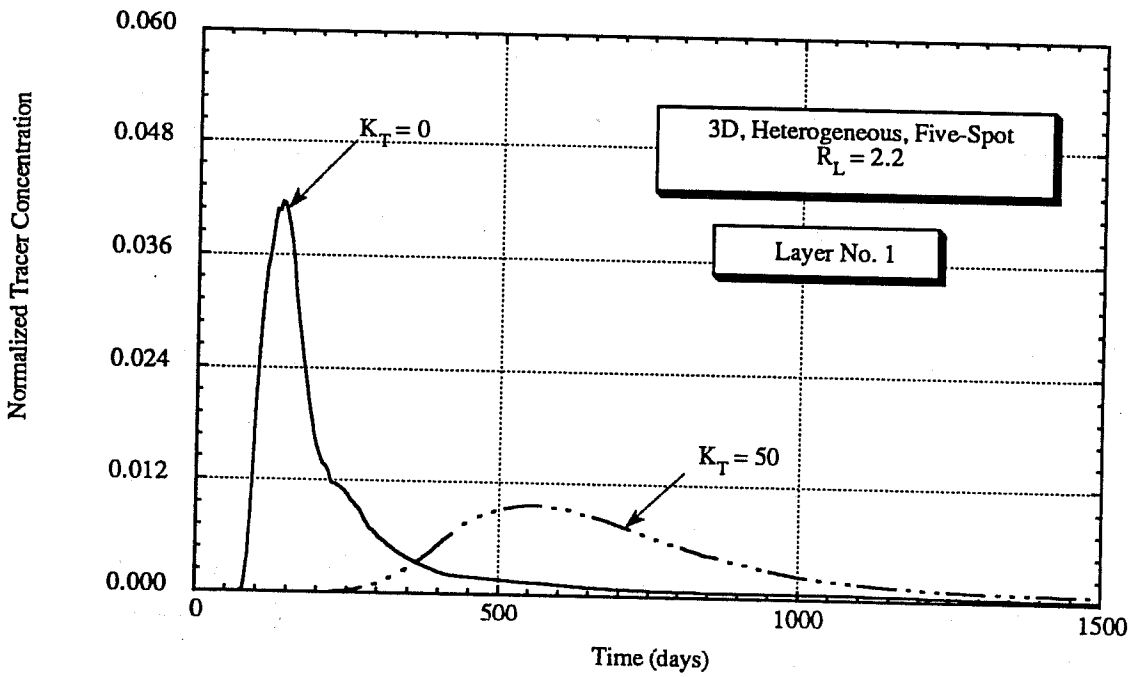

Fig. 66. Simulated tracer production data from VTP (Run No. SWVR42)

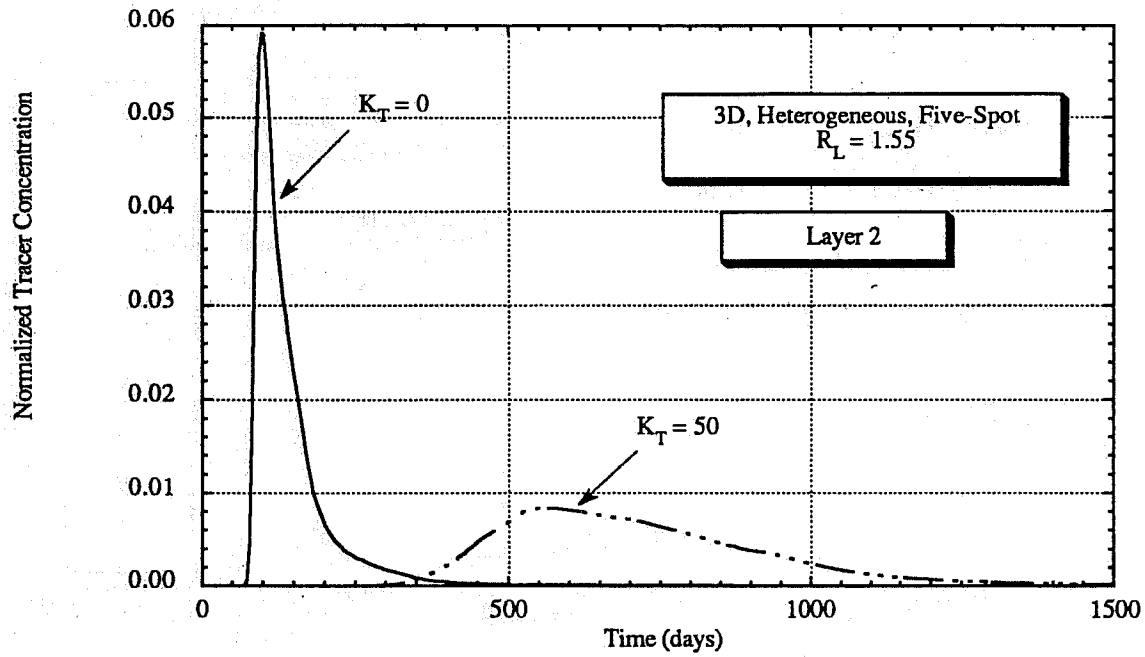

Fig. 67. Simulated tracer production data from VTP (Run No. SWVR42)

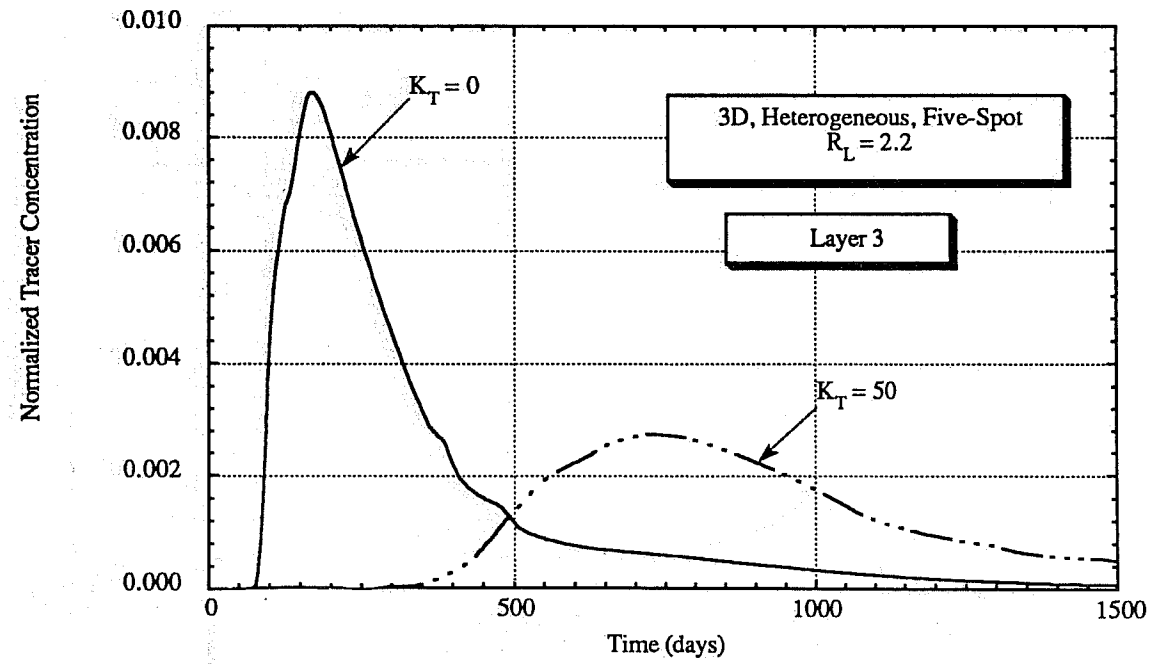

Fig. 68. Simulated tracer production data from VTP (Run No. SWVR42)

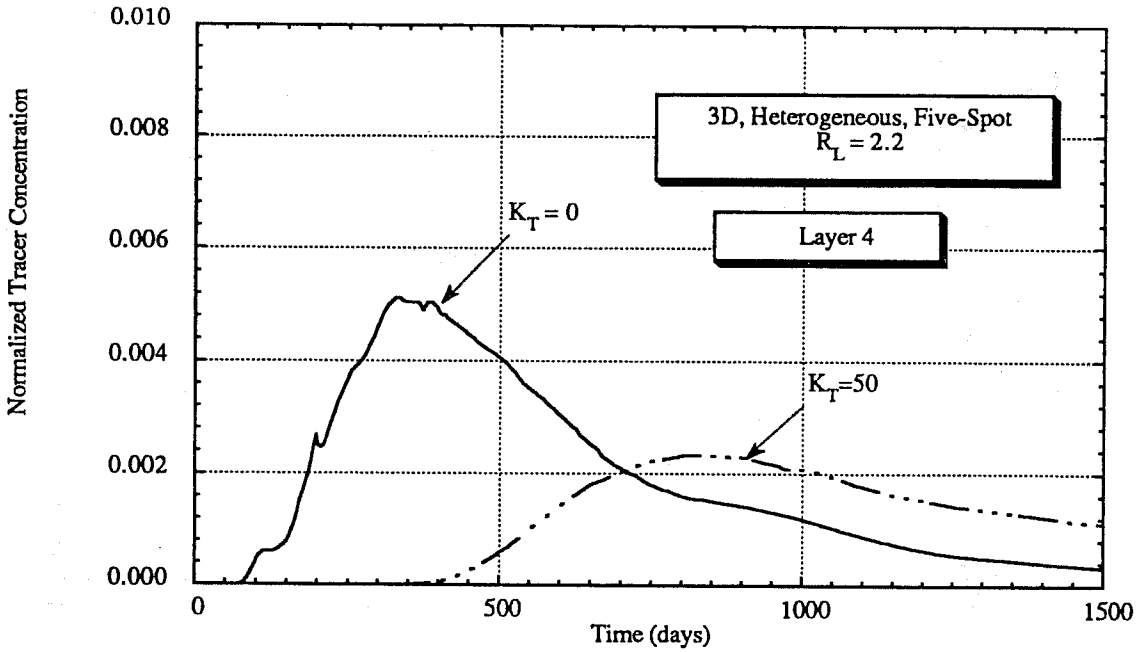

Fig. 69. Simulated tracer production data from VTP (Run No. SWVR42)

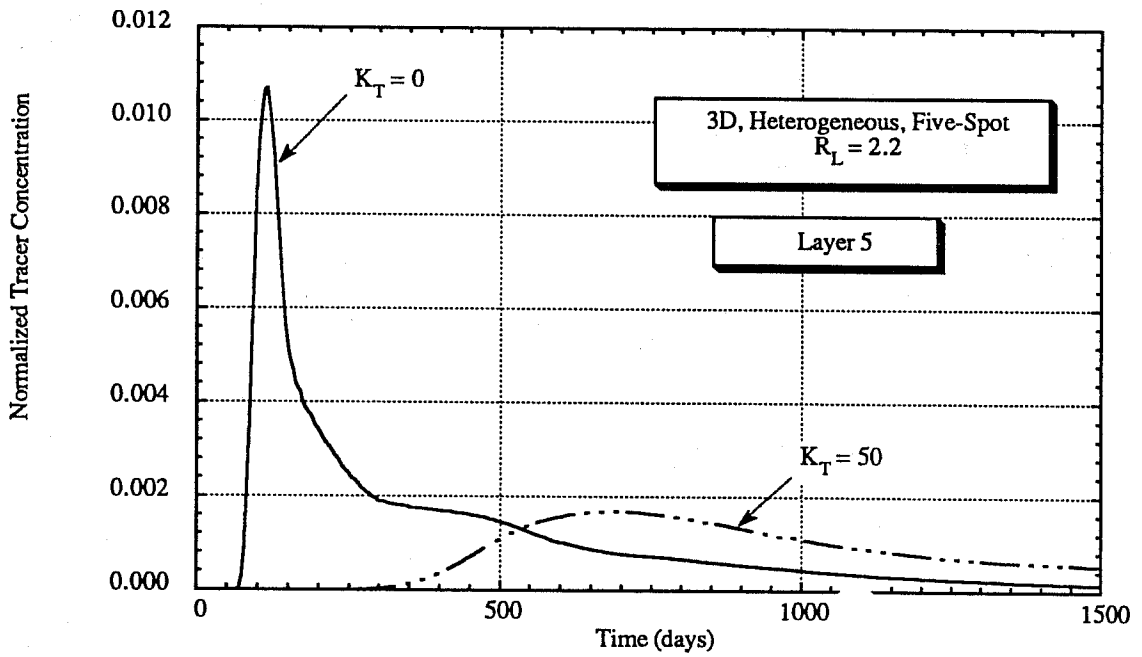

Fig. 70. Simulated tracer production data from VTP (Run No. SWVR42)

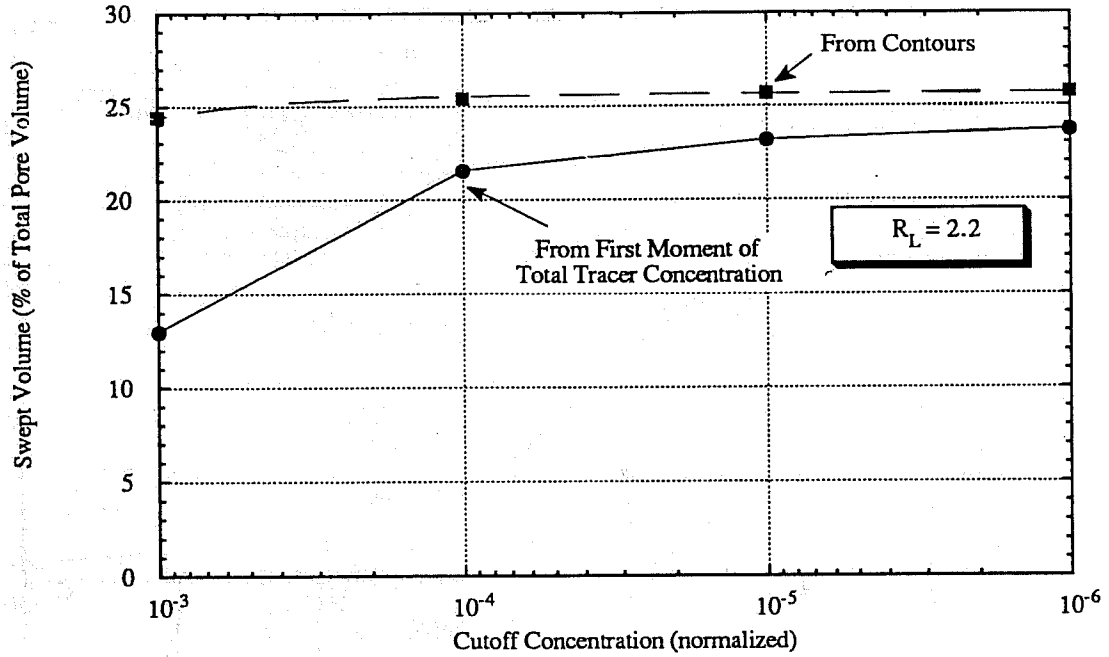

Fig. 71. Comparison between swept volumes from tracer concentration contours and the first moment of tracer production data (Run No. SWVR42)

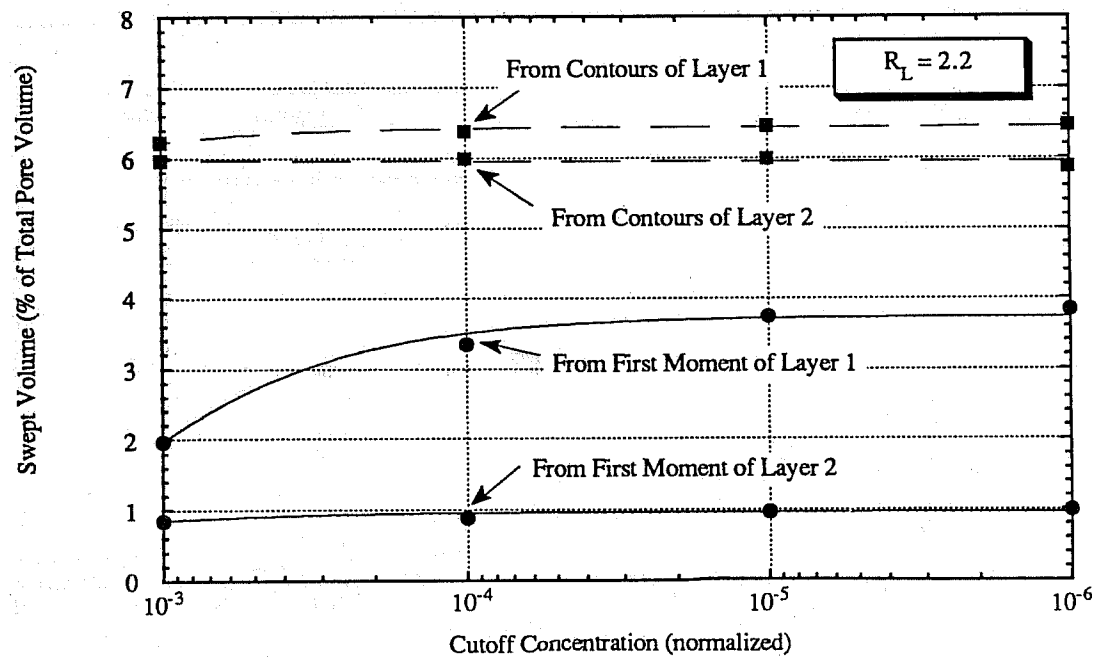

Fig. 72. Comparison between swept volumes from tracer concentration contours and the first moment of tracer production data from VTP (Run No. SWVR42)

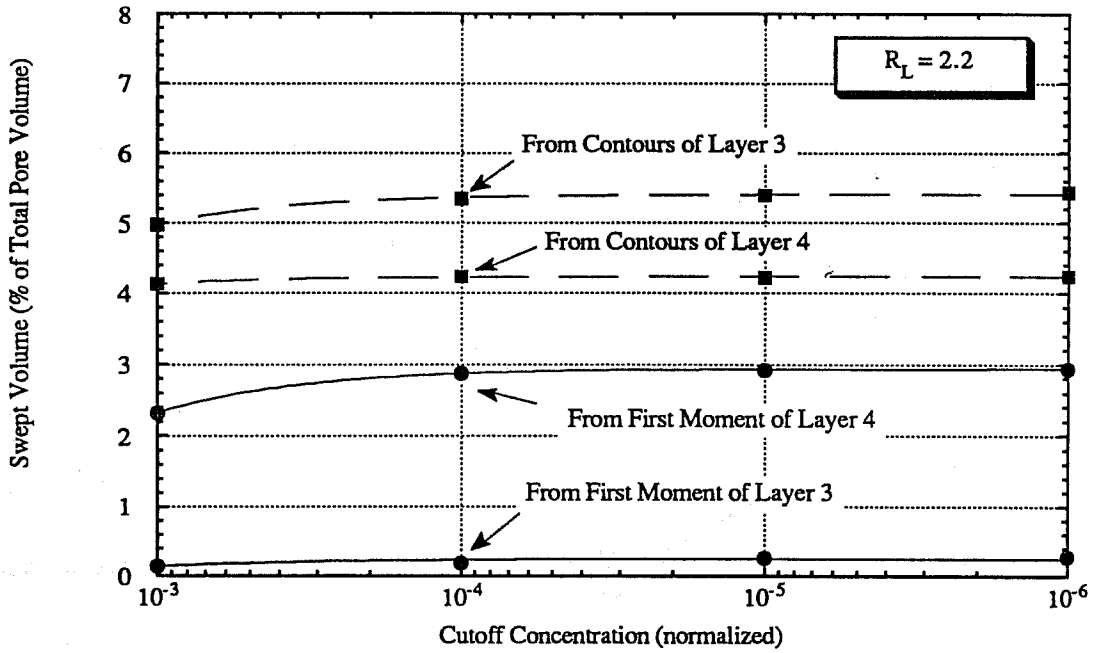

Fig. 73. Comparison between swept volumes from tracer concentration contours and the first moment of tracer production data from VTP (Run No. SWVR42)

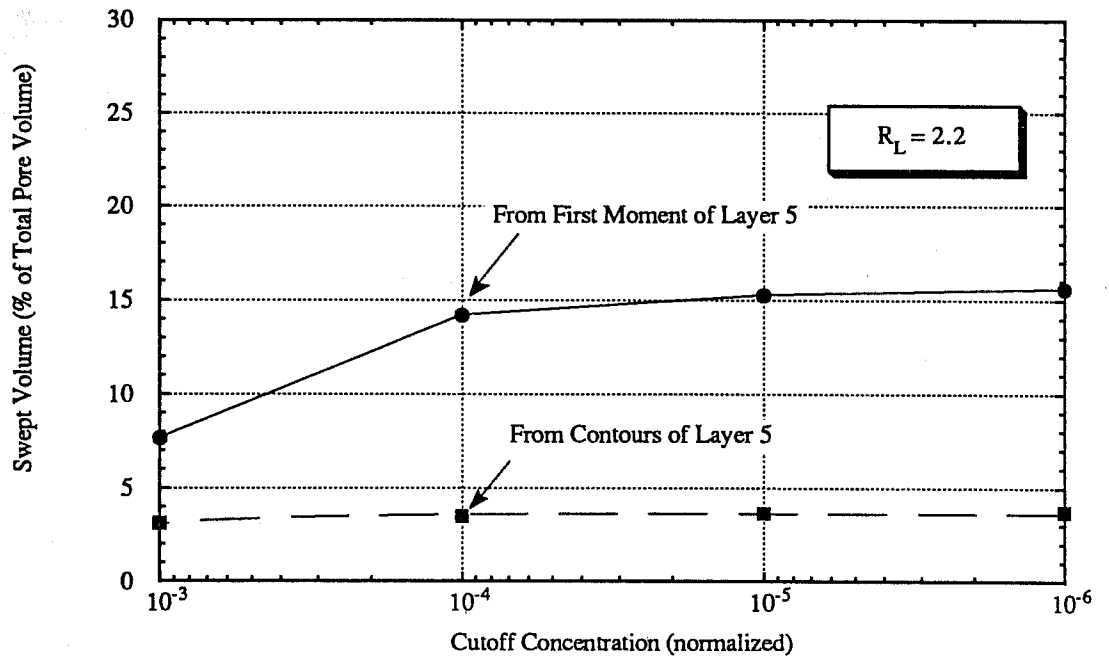

Fig. 74. Comparison between swept volumes from tracer concentration contours and the first moment of tracer production data from VTP (Run No. SWVR42)

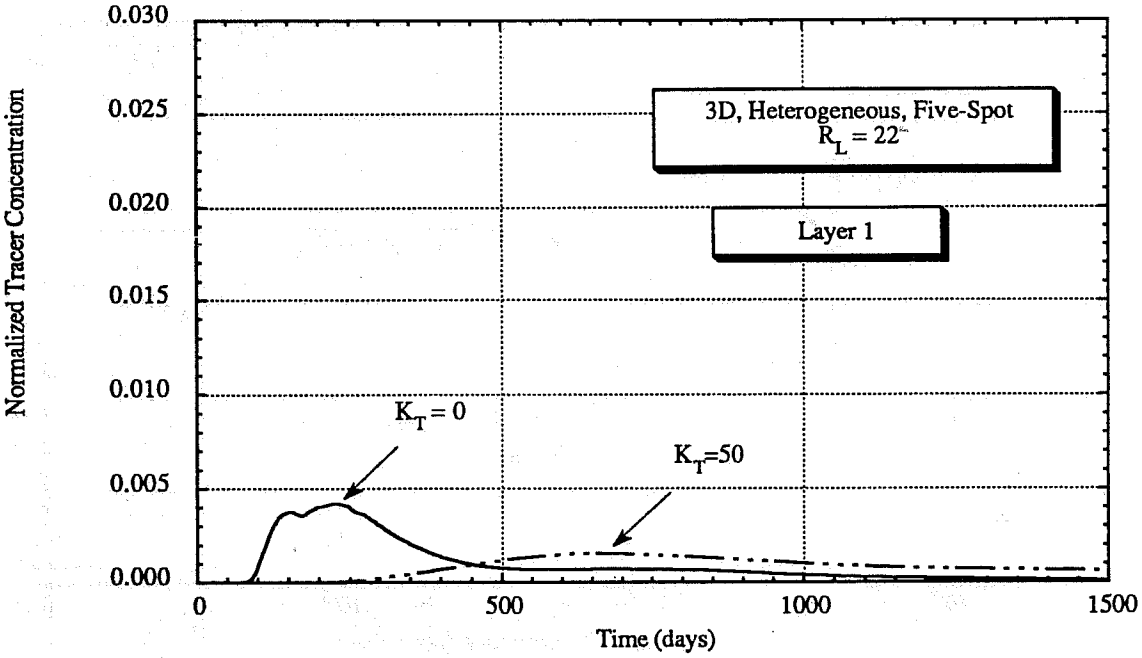

Fig. 75. Simulated tracer production data from VTP (Run No. SWVR31)

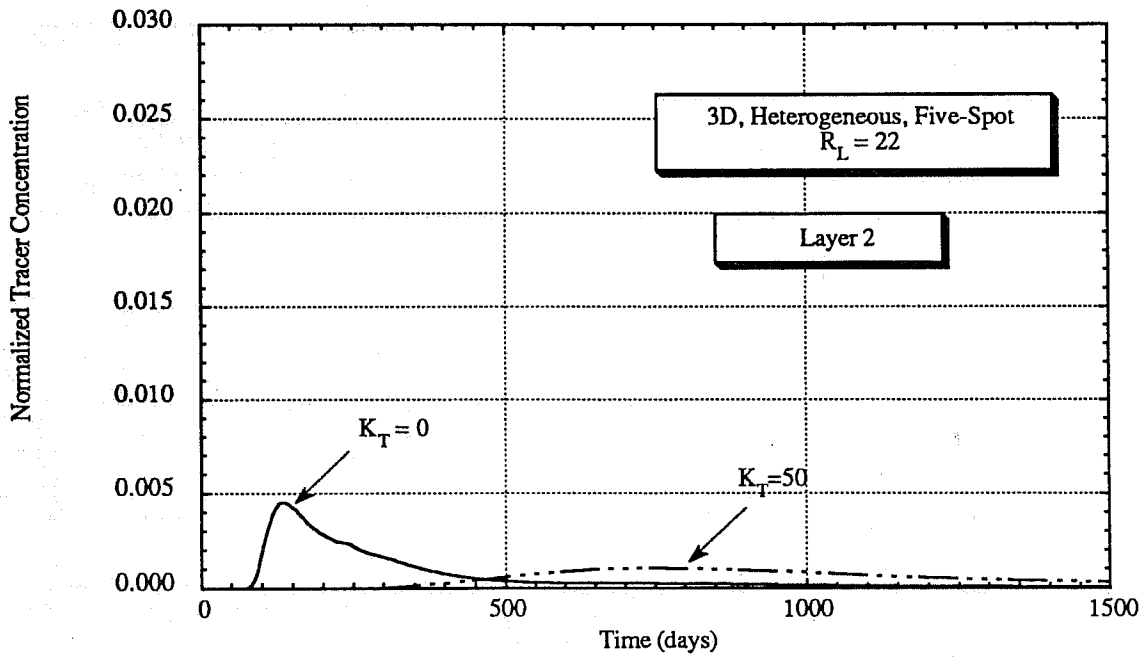

Fig. 76. Simulated tracer production data from VTP (Run No. SWVR31)

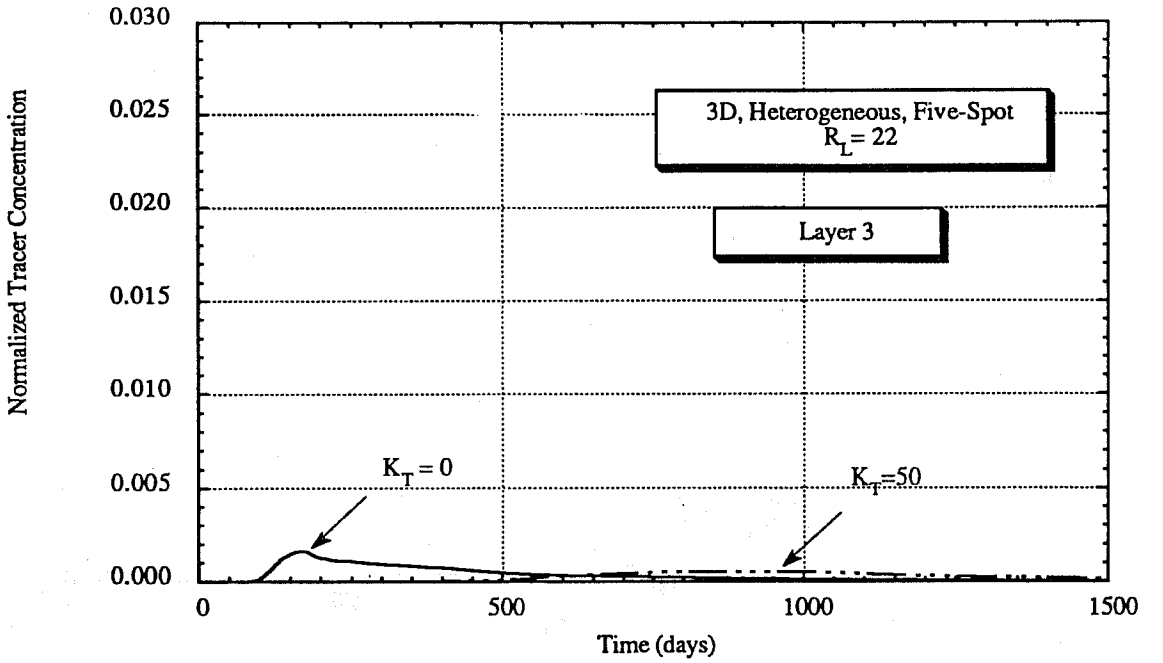

Fig. 77. Simulated tracer production data from VTP (Run No. SWVR31)

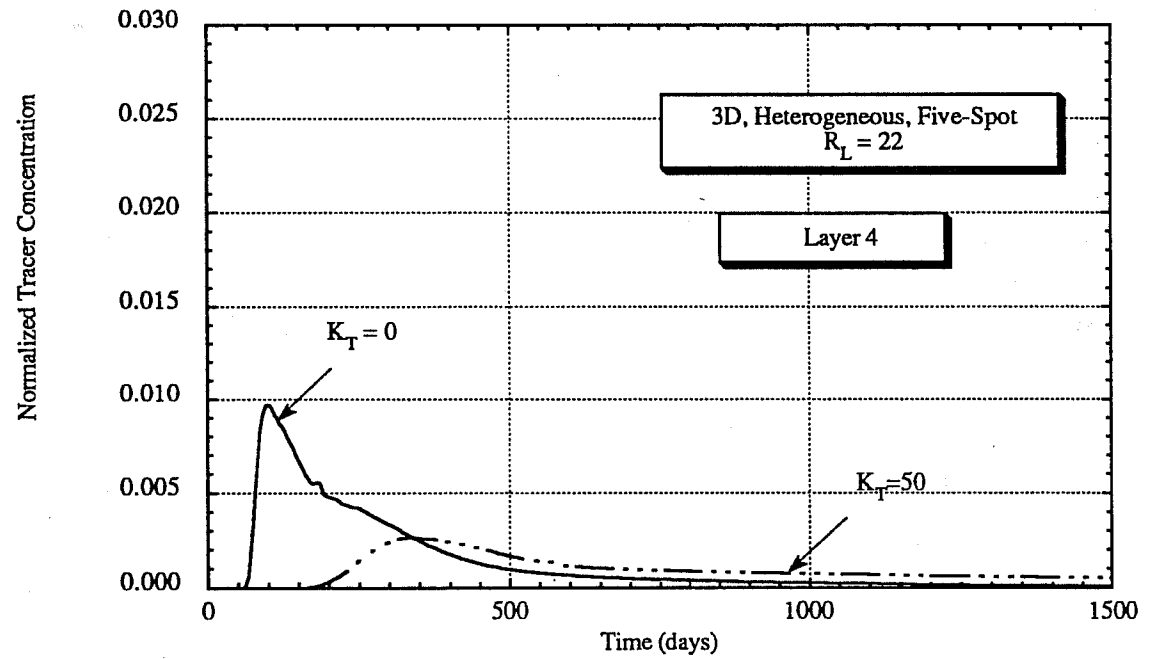

Fig. 78. Simulated tracer production data from VTP (Run No. SWVR31)

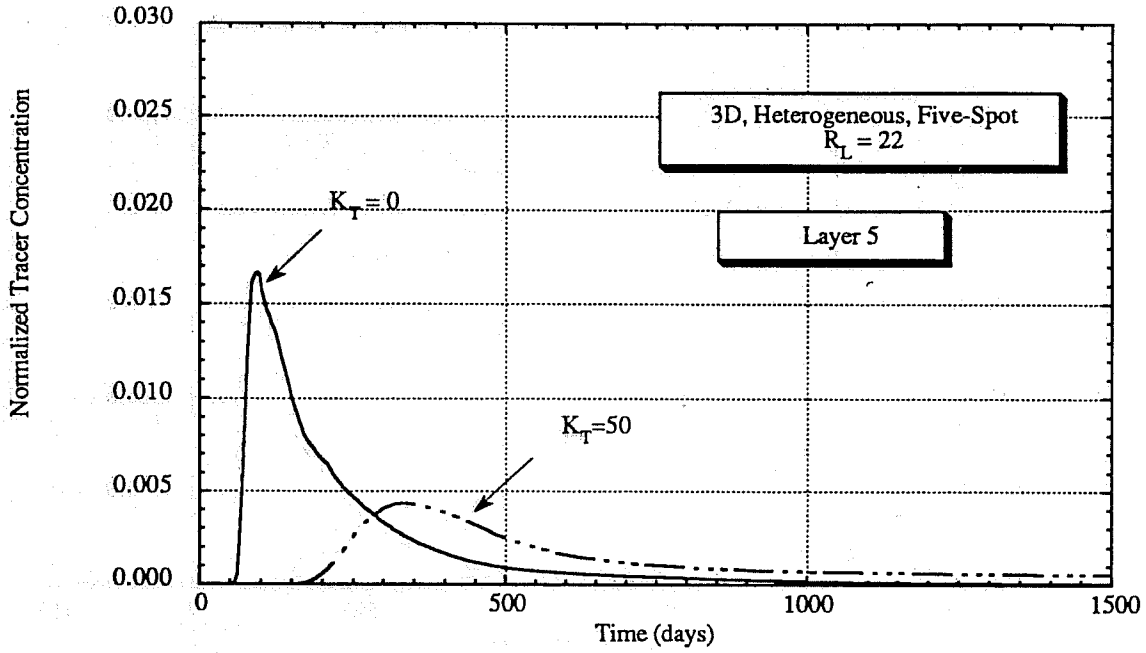

Fig. 79. Simulated tracer production data from VTP (Run No. SWVR31)

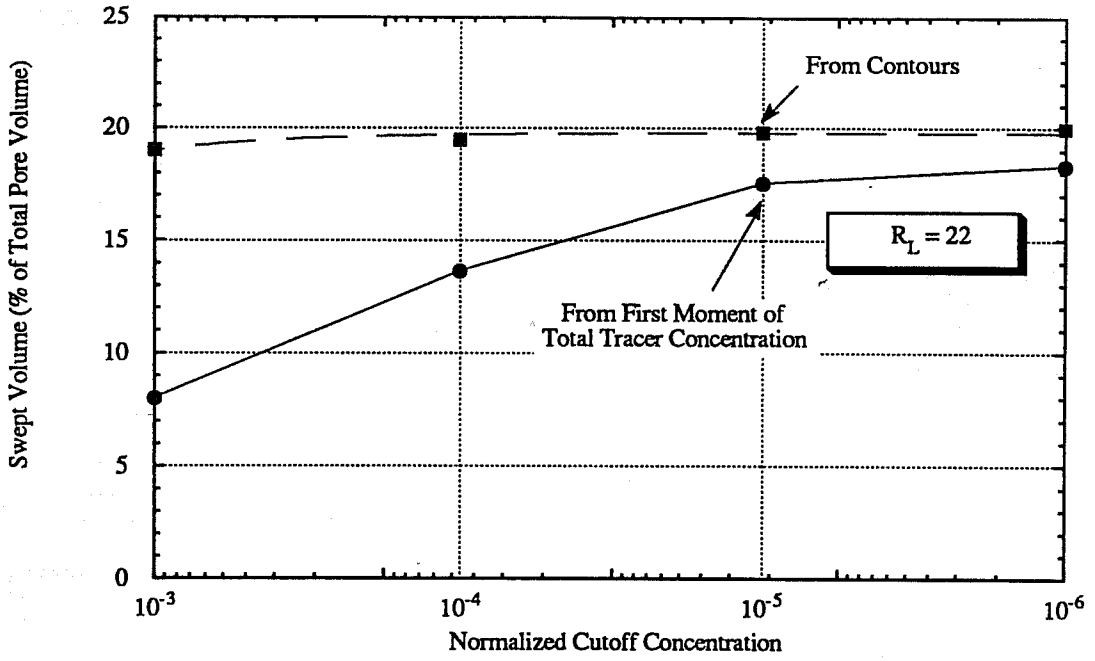

Fig. 80. Comparison between swept volumes from tracer concentration contours and the first moment of tracer production data (Run No. SWVR31)

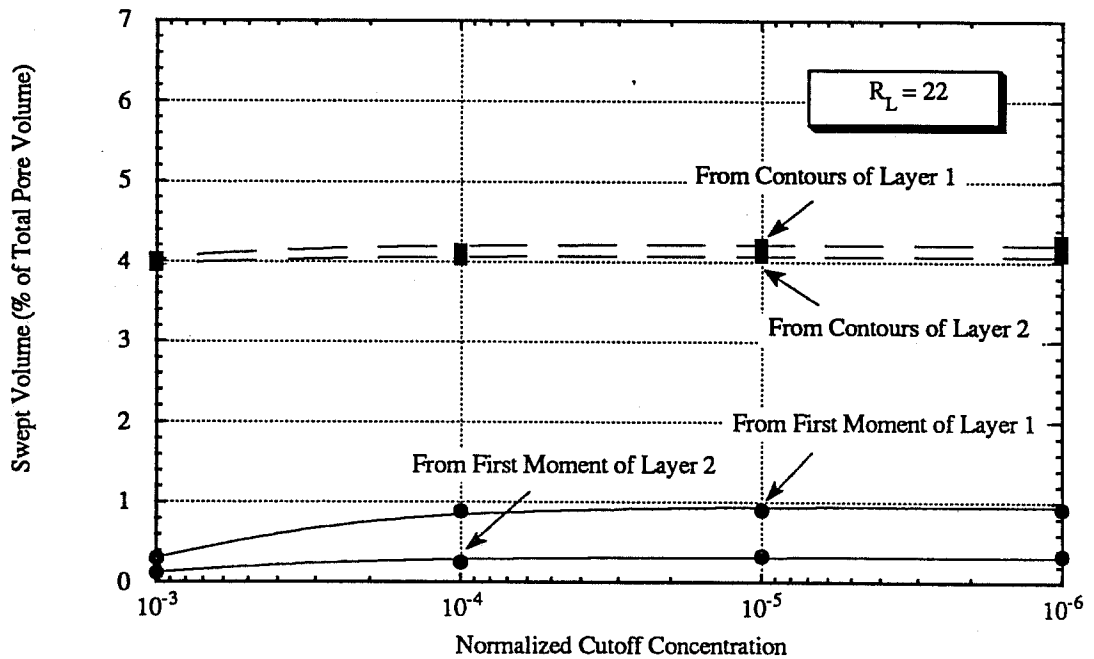

Fig. 81. Comparison between swept volumes from tracer concentration contours and the first moment of tracer production data from VTP (Run No. SWVR31)

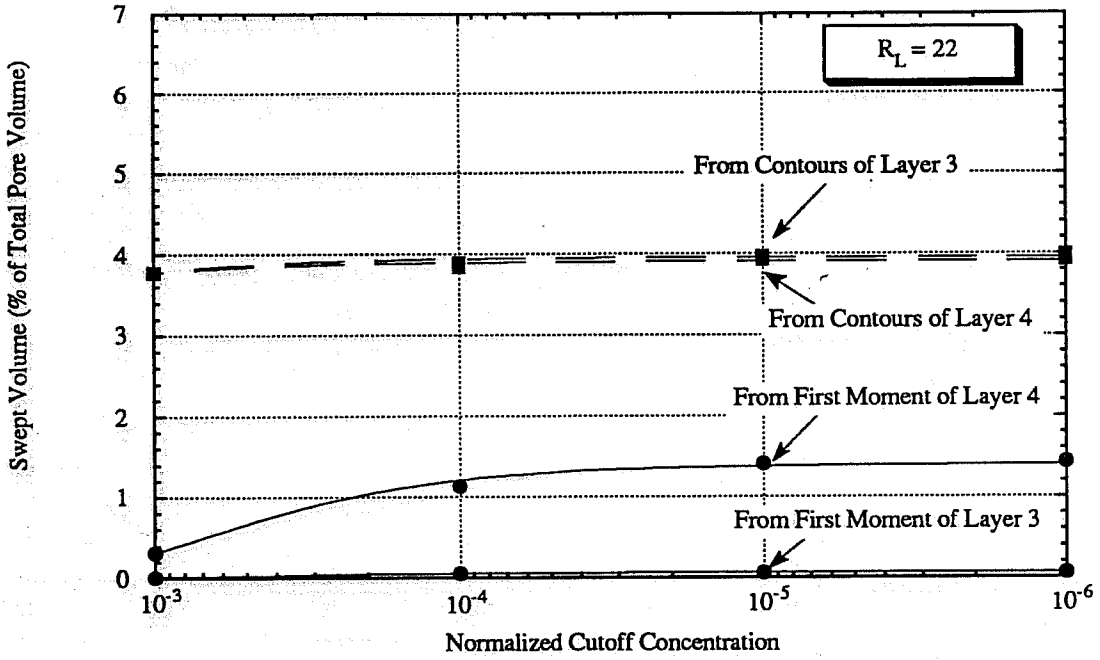

Fig. 82. Comparison between swept volumes from tracer concentration contours and the first moment of tracer production data from VTP (Run No. SWVR31)

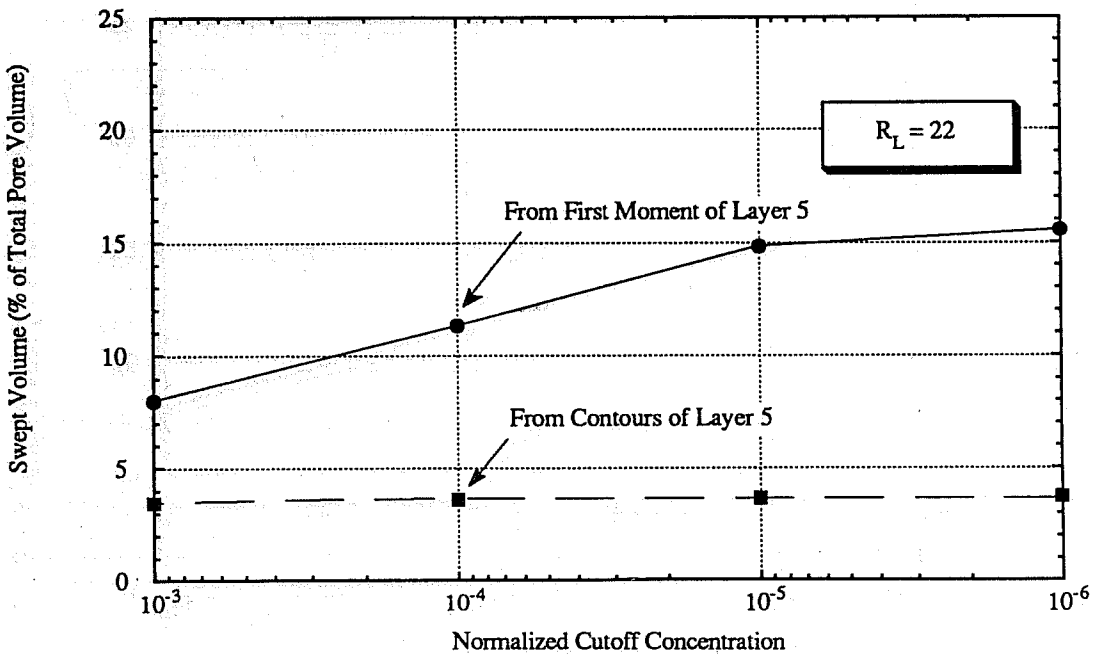

Fig. 83. Comparison between swept volumes from tracer concentration contours and the first moment of tracer production data from VTP (Run No. SWVR31)

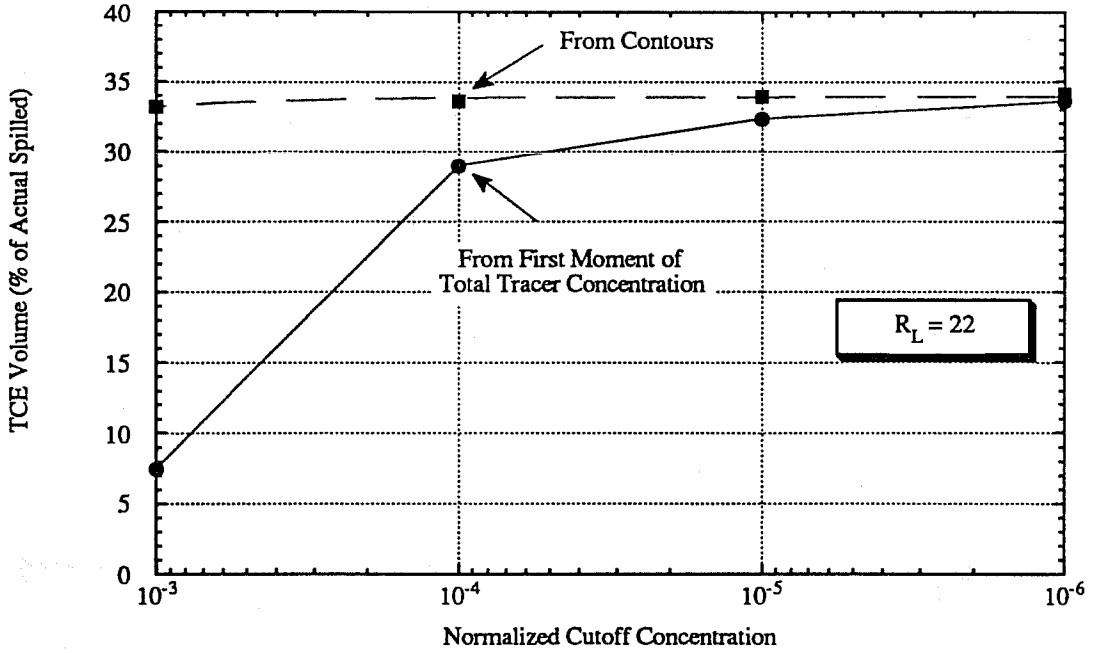

Fig. 84. Comparison between TCE volumes from tracer concentration contours and the first moment of tracer production data (Run No. SWVR31)

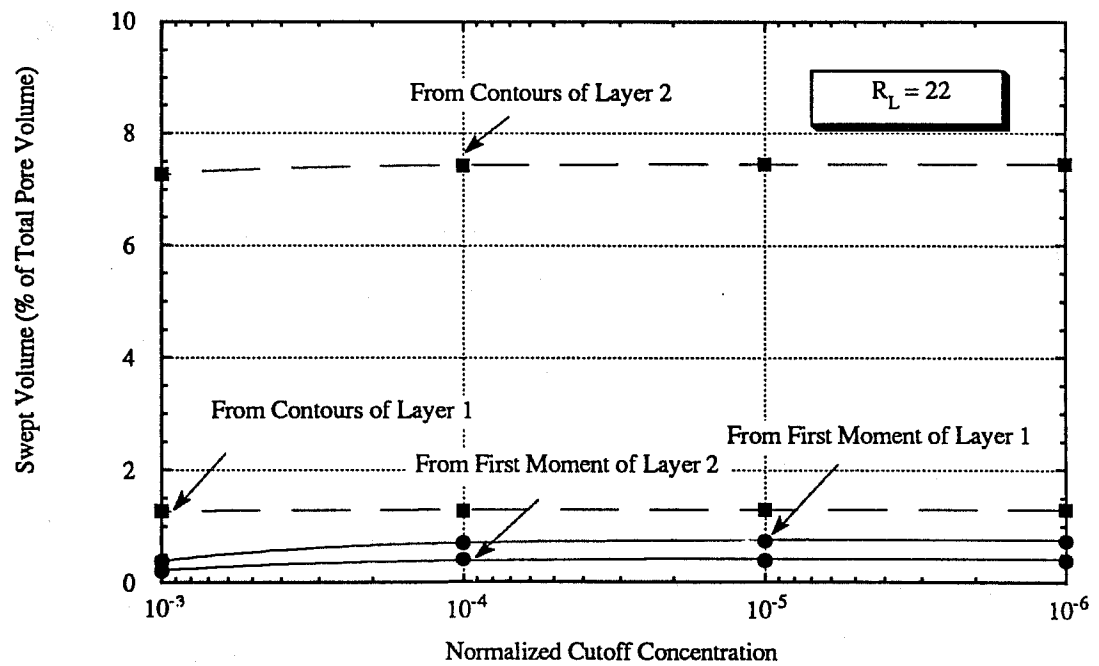

Fig. 85. Comparison between TCE volumes from tracer concentration contours and the first moment of tracer production data from VTP (Run No. SWVR31)

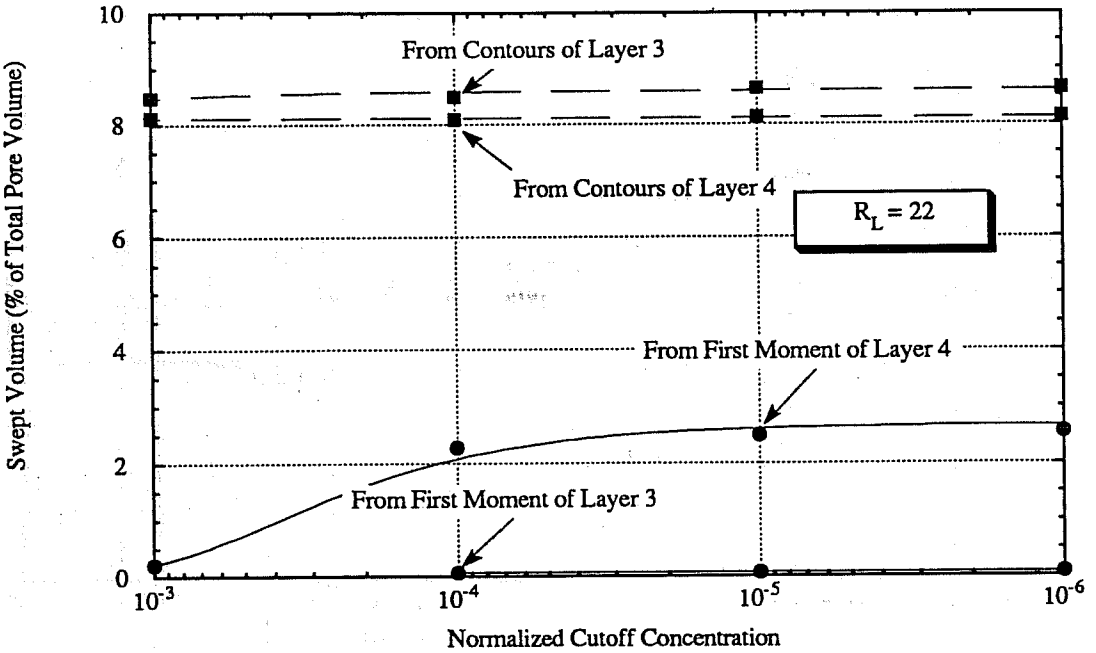

Fig. 86. Comparison between swept volumes from tracer concentration contours and the first moment of tracer production data from VTP (Run No. SWVR31)

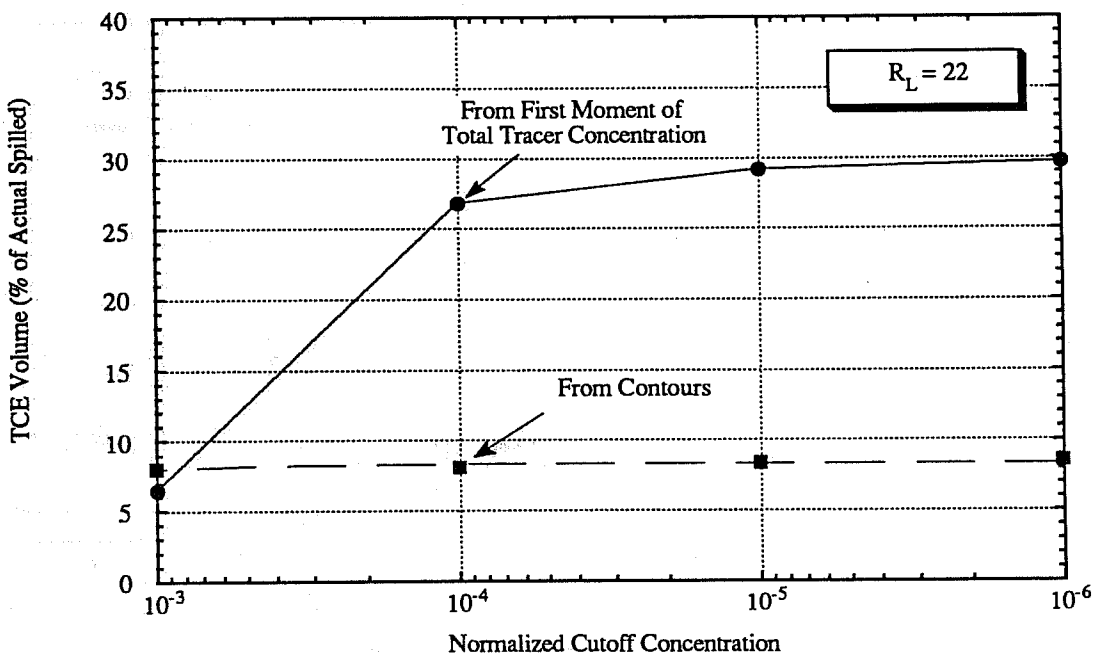

Fig. 87. Comparison between TCE volumes from tracer concentration contours and the first moment of tracer production data from VTP (Run No. SWVR31)

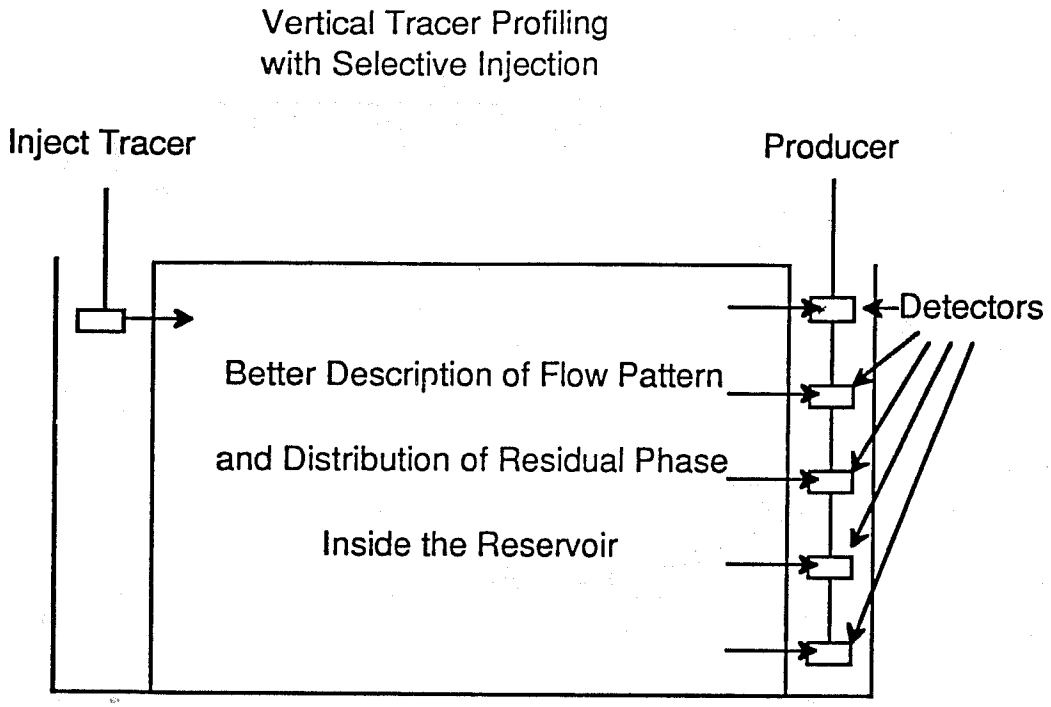

Fig. 88. Schematic diagram of Vertical Tracer Profiling with selective injection

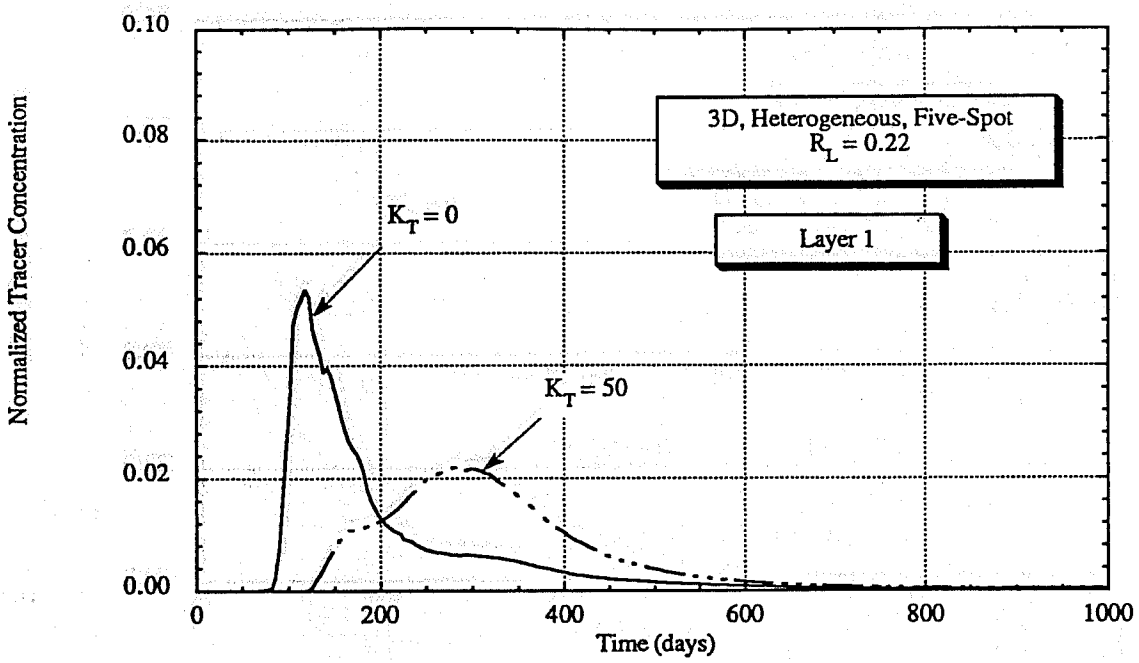

Fig. 89. Simulated tracer production data from VTP with selective injection (Run No. SWVR44)

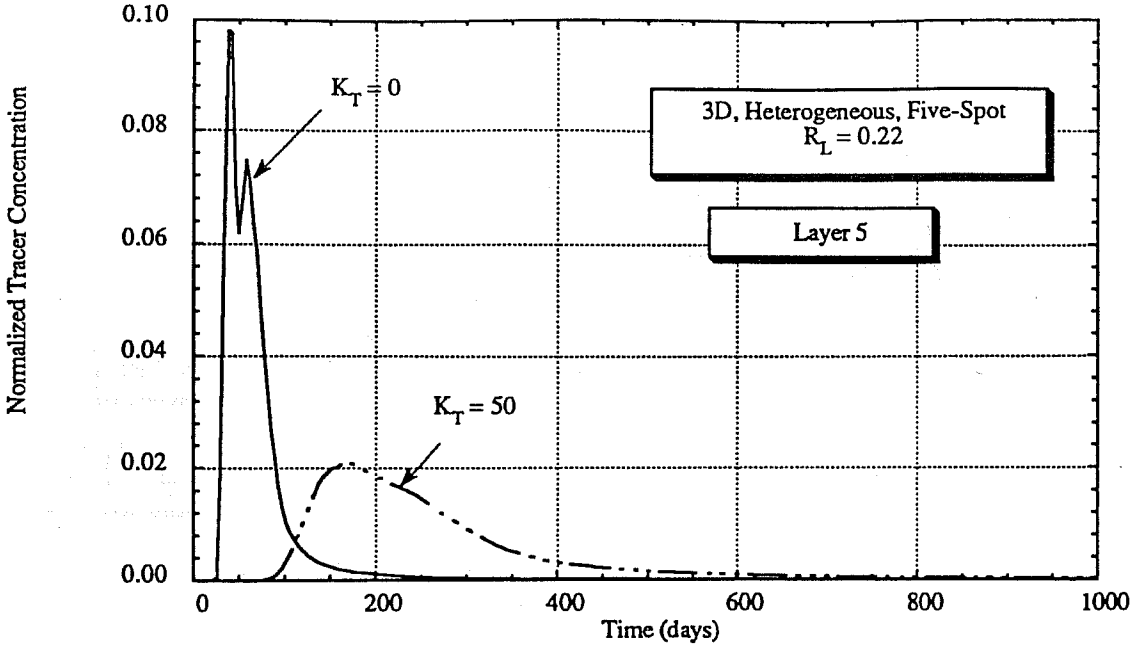

Fig. 90. Simulated tracer production data from VTP with selective injection (Run No. SWVR43)

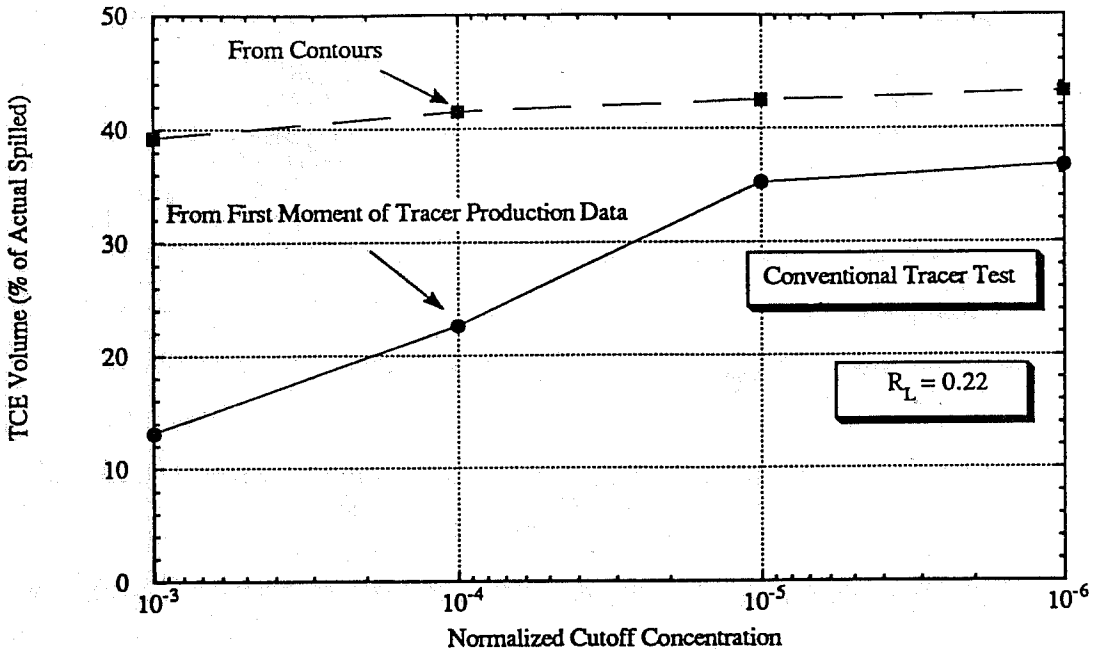

Fig. 91. Comparison between swept volumes from tracer concentration contours and from the first moment of tracer production data from a tracer test (Run No. SWVR41)

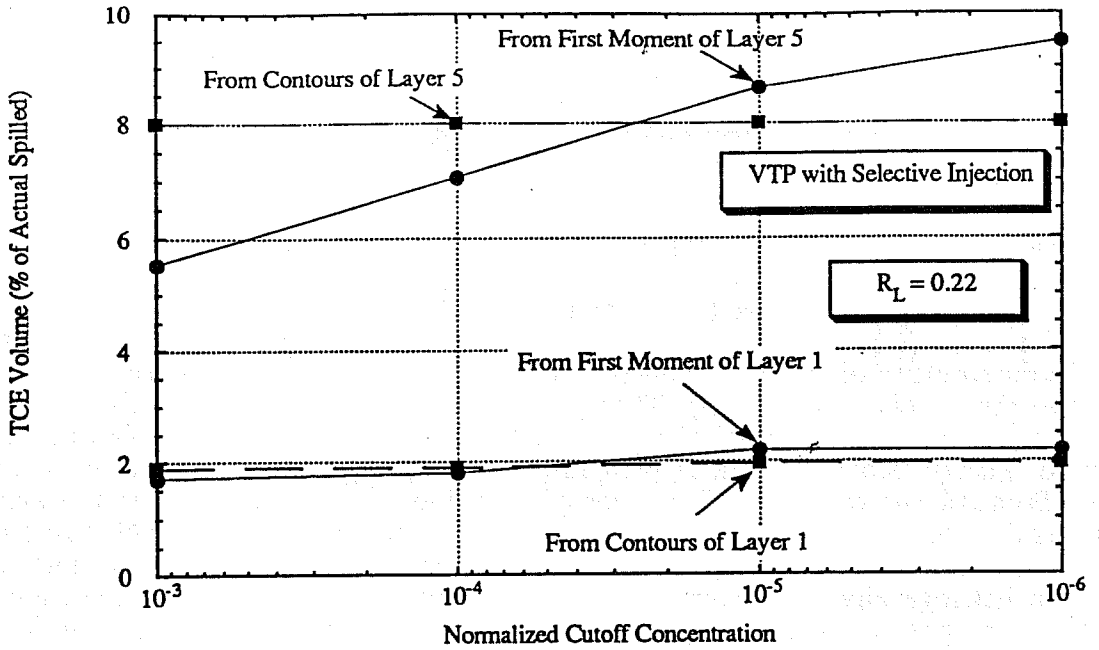

Fig. 92. Comparison between swept volumes from tracer concentration contours and from the first moment of tracer production data from VTP with selective injection (Run No. SWVR44,45)

SECTION III
ANALYSIS, INTERPRETATION, AND SIMULATION OF PERFLUOROCARBON GAS TRACER TESTS AT ELK HILLS

SUMMARY

Two field tracer tests have been conducted by Bechtel Corp. using perfluorocarbon gas tracers. The first test was done using perfluoromethylcyclopentane (PMCP) and two isomers of perfluorodimethylcyclohexane (oc,ot-PDCH), while the second test was done using perfluoromethylcyclohexane (PMCH). The main objectives of these tests are to evaluate the new perfluorocarbon tracers as hydrological gas tracers and to characterize the 26R reservoir. The total amounts of tracers recovered from 14 sampling wells were each less than 2% of the amount injected. Data also showed a lot of fluctuation compared to conventional tracer data. Analysis of these tracer data indicates that the data from the first tracer test are significant while data from the second test are more likely to be noise. Reservoir simulations were conducted to take into account areal sweep, heterogeneity and anisotropy, dispersion, dilution from other injectors, interference of other producers, position of tracer injection wells and observation wells, perforation intervals, change in well conditions, and tracer partitioning. The reservoir description used average reservoir properties based on data in Rial (1990) and the 26R Reservoir Perfluorocarbon Tracer Field Study Recommendation (Watson, 1990). Additional information was provided by Mr. John Yu of Bechtel Petroleum Operations, Inc. and Dr. Gunnar Senum of Brookhaven National Laboratory. Simulation results for both tracer tests also supported the data analysis. Results of these tracer tests indicate that the injected gas migrates up structure and out of the 26R reservoir into the 31S reservoir. Along the southeast boundary of the 26R where the upper 26R sands disappear, there is a transition of the lower 26R sand into NA shales of the 31S reservoir. In this area, fluid communications also exist from the injected gas in the upper 26R through the lower 26R and into the 31S reservoir. The results of this study agree with the study conducted by Rial (1990) that injected gas migrates out of 26R through the NA shales in the northwest-southeast limit of the 26R. The results of this study should help in designing the gas injection operation of the 26R and 31S for maximum oil recovery. Data from the second tracer test are insufficient at this time to draw any conclusions about migration across the main 26R fault. The next tracer test should be conducted using a larger amount of tracer. Results from the next test could help answer some of the questions from the second test. If a more detailed reservoir description is desired, detailed geologic descriptions with multiphase flow effects can be added. However, given limited time and data quality, the description used in this study is sufficient to achieve the desired objectives.

Another interwell, perfluorocarbon gas tracer test was conducted at the Shallow Oil Zone (SOZ) reservoir also located at the Elk Hills Naval Petroleum Reserve in California (NPRC). Data obtained from this tracer test were analyzed for residual oil saturation. The tracer partition coefficients of the PFT's were predicted using different methods (Raoult's law, UNIFAC, and the Peng-Robinson equation of state). Analysis of the tracer data indicates residual oil saturations from 8% to higher than 20% between Injector 34-10G and Well 81-10G.

CHARACTERIZATION OF THE 26R AND THE 31S RESERVOIRS

A good tracer for reservoir characterization is one which has all of the following properties: unique, low detection limit, conservative, stable at reservoir conditions, non-toxic, inert, and inexpensive. It is difficult to find a tracer that will satisfy all of the above criteria. The gas tracers used for a gas reservoir can be divided into radioactive tracers and nonradioactive tracers. Examples of radioactive tracers are tritiated hydrocarbon gases and ^{85}Kr. These tracers are subject to strict regulation. Examples of nonradioactive tracers are inert gases such as helium and sulfur hexafluoride (SF_6). The inert gases are expensive because a large quantity is needed due to high detection limits. Sulfur hexafluoride is probably the most well-known and successfully used gas tracer. Other kinds of tracers being evaluated are perfluorocarbon tracers (PFT's). PFT's have

been used in the past as atmospheric tracers. Brookhaven National Lab has developed PFT technologies and used them successfully as geologic tracers in the North Sea Ekofisk oil field (Senum *et al.*, 1990) and at the Shallow Oil Zone located at the Elk Hills Naval Petroleum Reserve No. 1 (Senum *et al.*, 1992). These PFT's are currently being evaluated at the 26R and 31S reservoirs at Elk Hills Naval Petroleum Reserve No. 1. The main objectives of the 26R tracer test project are to evaluate the PFT technologies and to characterize the 26R reservoir.

There are many difficulties involved in interpreting these tracer data. The 26R and 31S are very complicated reservoirs. Within the 26R alone, the sands could be divided into 18 distinct layers based on continuous shales. The 31S reservoir also contains many different shales and sands. Some producers were shut-in during this tracer test to control gas production updip, which resulted in some loss of tracer data. The discontinuous sampling after tracer breakthrough also decreased the usefulness of the tracer data. Therefore, the interpretation of these tracer results is only very approximate. The objectives of this report are to

1. decide if the given data are artificial or real responses of the reservoirs,
2. evaluate the new perfluorocarbon gas tracers, and
3. be able to answer the following questions concerning the 26R and 31S reservoirs:

a) Is there fluid communication along the northwest-southeast boundary of the 26R and 31S?

b) How is the fluid communicated inside the 26R reservoir?

c) On the southeast boundary of the 26R where the two upper sequences of the 26R disappear, is there fluid communication from the upper sequences to the lower sequences of the 26R and to the 31S NA reservoir?

d) Is the major fault that divides the 26R reservoir into two halves communicating, partially communicating, or noncommunicating?

Overview of the 26R Reservoir

The following information on the geology of the 26R and 31S NA reservoirs is taken from the 26R Reservoir Perfluorocarbon Tracer Field Study Recommendation (Watson, 1990). The 26R reservoir is located at the Elk Hills Naval Petroleum Reserve No.1 in Kern County, California. It is a northwest-southeast trending, elongated, Stevens sandstone reservoir located in Sections 22R, 25R, 26R, 27R, 35R, and 36R. Table 1 summarizes some data for the 26R reservoir. Figure 1 shows the production rates for the 26R reservoir.

The 26R sand is divided into lower and upper sequences. Each sequence can be divided into subdivisions or megaunits based on reservoir-wide thin shale and petrophysical analysis of core data. The upper sequence or upper 26R consists of two megaunits: the A-C megaunit and the C-F megaunit. The lower sequence or lower 26R consists of 3 megaunits. These are the F-K, K-N, and N-O megaunits. Table 2 gives the average properties of these megaunits.

There is a main fault in the 26R reservoir that divides the pool into an eastern sector and a western sector. The gas-oil contact is not uniform across the 26R reservoir. As much as 600 ft of relief is present on the gas-oil contact across this reservoir due to a partial flow barrier and operating conditions. The gas-oil contact is at approximately 5,650 ft subsea for the eastern sector and 5,780 ft subsea for the western sector. Figure 2 shows a structure map of the 26R reservoir and the location of the main fault. This reservoir has an average net sand thickness of 500 ft.

The relation of the 26R sands to their equivalents (NA shales) located to the north and southeast is unknown. The limit of the 26R reservoir is estimated from the location where the 26R sands terminate (along the updip in the northwest-southeast direction and in the southeastern direction). There is reason to believe that the 26R sands communicate with the NA shales of the 31S because both reservoirs appear to have a common gas cap. In the southeastern boundary of the 26R, the upper sequence (A-F) is not present and the lower sequence (F-P) is transitional with the NA shales. Figure 3 shows a cross section of the 26R reservoir in the southwest-northeast direction.

Overview of the 31S Reservoir

Figure 4 shows the production history of the 31S reservoir. Figure 5 shows a structure

map of the 31S reservoir in relation to the 26R reservoir. Figure 6 shows a cross section of the 31S in relation to the 26R and Fig. 7 gives more details of this cross section. The 31S NA shales are located at Elk Hills on Naval Petroleum Reserve No.1 in Sections 2G, 3G, 4G, 5G, 6G, 22R, 23R, 24R, 25R, 26R, 27R, 35R, 36R, 30S, 31S, 32S, 33S, 34S, 35S, and 36S in T30S, R23E, and R24E, in Kern County, California. The 31S NA shales consists of shale, siltstone and sandstone beds. Geologically, the shales are equivalent to the 26R sands. The structure of the 31S NA shales is that of a 7.5-mile-long anticline with an overall WNW-ESE trend. The crest of the structure lies in the northwest quarter of Section 31S, where the top of the N shale reaches 3,470 ft subsea and the top of the A shale is at 3,570 ft subsea. The N shale of the 31S is less than 100 ft thick over the crest and a fairly consistent 100 to 250 ft thick along the anticlinal axis. The thickness increases to 300 to 400 ft on the flanks of the structure, partially because of increasing dips. Along the southwest flank of the structure where the shale has a 26R sand equivalent, the unit exceeds 1,300 ft in thickness. The A shale of the 31S is consistently about 200 ft thick along the anticline axis and like the N shale, thickens on the flanks to more than 400 to 500 ft. The A shale thickens to more than 1,000 ft on the southwest flank. Table 3 shows some properties of the cores taken from the 31S NA shales.

Perfluorocarbon Gas Tracers

The perfluorocarbon tracers (PFT's) are a family of perfluorinated alkyl cycloalkanes. Table 4 lists different PFT's and their formulas. The detection limit of PFT's is 10^{-15} liter of PFT per liter of reservoir gas (Senum *et al.*, 1992). The lower detection limit of PFT's compared to the detection limit of SF_6 makes PFT's very promising gas tracers. The different partition coefficients of the different PFT's can be used in principle to determine the amount of a residual hydrocarbon phase provided the partition coefficients can be accurately estimated as a function of composition, temperature, and pressure. Bernard (1988) reported mutual binary solubility data of perfluoromethylcyclohexane and hydrocarbons. Dugstad (1992) measured the partition coefficients of PMCP and PMCH in slim-tube experiments at high pressure and temperature using methane/decane and nitrogen/decane fluids. Estimations of the partition coefficients of PFT's using simple activity coefficient models such as the Wilson and the Whitson equations were also investigated by Dugstad (1992), but the results were not successful. For this study, Institutt for Energiteknikk (Hundere, 1991) measured the partition coefficients of the PFT's using 44.137 g of 26R oil, 0.6 mol of methane, 0.02 mol of ethane, and 0.02 mol of propane. The laboratory data were matched by fine tuning of binary interaction parameters in the Peng-Robinson equation of state. The binary interaction parameters of the PFT's were in the range of 0.18 to 0.22 at the conditions of the 26R reservoir (200°F, 2,400 psia). The simulated partition coefficients were found to be very sensitive to the binary interaction parameters. This implies that accurate data under specific reservoir conditions are needed for each application. The physical properties and partition coefficients of four PFT's used at the 26R tracer project are given in Table 5.

The Peng-Robinson equation of state (Peng and Robinson, 1976) is a two-parameter equation with pressure given by a cubic function of molar volume:

$$P = \frac{RT}{v - b} - \frac{a(T)}{v(v + b) + b(v - b)} \tag{1}$$

The constants a(T) and b for a pure component are computed from

$$a(T) = \Omega_a \frac{\alpha (RT_c)^2}{P_c} \tag{2}$$

$$b = \Omega_b \frac{RT_c}{P_c} \tag{3}$$

with

$$\Omega_a = 0.45724 \quad (4)$$

$$\Omega_b = 0.0778 \quad (5)$$

$$\alpha = [\,1 + m(1 - \sqrt{\frac{T}{T_c}})\,]^2 \quad (6)$$

where

$$m = 0.37464 + 1.54226\,\omega - 0.26992\,\omega^2 \quad (7)$$

When applied to multicomponent mixtures, the mixing rules are given by

$$a = \sum_{i=1}^{n_c} \sum_{k=1}^{n_c} x_i\, x_k\, a_{ik} \quad (8)$$

$$a_{ik} = (1 - \delta_{ik})\sqrt{a_i\, a_k} \quad (9)$$

and

$$b = \sum_{i=1}^{n_c} x_i\, b_i \quad (10)$$

where, for each component, a_i is computed from Eq. (2) and b_i from Eq. (3).

The amount of PMCP injected was 30 g, which is 0.1 mol since its molecular weight is 300 g/mol. PMCP at 60°F and 1 atm is a liquid. After being diluted with methanol and injected with gas into the reservoir at 2,400 psia and 200°F, it vaporized into the gas phase. The gas tracer was transported inside the reservoir by injected gas to the producers. The gas samples were collected at the well and samples were analyzed for tracer concentration at standard conditions of 60°F and 1 atm. The volume of 0.1 mol of PMCP at standard conditions can be calculated using the ideal gas law as follows:

$$V = \frac{nRT}{P}$$

$$= \frac{0.1\ [\text{mol}] \times 82.06\ [\text{cm}^3\text{atm mol}^{-1}\ \text{K}^{-1}] \times (273.15 + 15.56)\ \text{K}}{1\ [\text{atm}]}$$

$$= 2370.63\ \text{cm}^3 \text{ or } 2.37 \text{ standard L}$$

The injected tracer concentration used in the 26R tracer test is calculated as follows

$$C_{0,\,\text{PMCP}} = \frac{V_{\text{PMCP as gas at standard conditions}}}{V_{\text{Injected gas at standard conditions}}}$$

$$= \frac{V_{\text{PMCP as gas at standard conditions}}}{Q_{\text{Injected gas}}\,\Delta t}$$

$$= \frac{2.37 \text{ [standard L]}}{10{,}000 \text{ [Mscf/D]} \times 1000 \text{ [scf/Mscf]} \times 28.317 \text{ [standard L/scf]} \times 18 \text{ [D]}}$$

$= 4.65 \times 10^{-10}$ L/L or 465 pL/L .

For the two isomers of PDCH, 30 g each were injected together with PMCP in the first stage. The calculated injected concentrations are 349 pL/L.

The injected PMCH concentrations in the second-stage tracer test are calculated in the same manner. A total of 800 g of PMCH were injected in four injectors. Each injector received 200 g of PMCH. These tracers were injected over a period of approximately 17 days. Table 6 shows the flow rates and the injected PMCH concentrations at the four injectors.

Objectives of the 26R Gas Tracer Test Project

Pressure maintenance in the 26R reservoir is done by injecting gas in the crest of the 26R structure and also in the NA shales of the 31S reservoir. These two reservoirs do not appear to be independent of each other, but the geological and engineering data are not sufficient to be sure of this. Hence, the general objectives of this tracer test project were to determine the migration of injected gas, either updip into the 31S NA or downdip inside the 26R reservoir. Another main objective is to determine the fluid communication among layers inside the 26R. Tables 7 and 8 show the injection rate for each megaunit in the western and eastern sectors during June 1990 (the most recent data available to us). The gas injection rates during the tracer tests from November 1991 are shown in Table 9 (Yu, 1993). The combined gas injection rate for 26R and NA is approximately 170-180 MMscf/D.

The 26R tracer test project is divided into many stages (Watson, 1990 and Yu, 1993), as follows.

Stage 1

Stage 1 began on November 17, 1991 and ended on December 4, 1991. Thirty grams of each PFT (PMCP, oc-PDCH, and ot-PDCH) were diluted with 146 gal of methanol and injected with gas into 366U-26R. Approximately 7 gal of methanol were used per day. The objective of this first stage was to find out where the injected gas migrates to, either updip, downdip, or inside the 26R reservoir. Samples from the 14 producers listed in Table 10 were collected and analyzed for PFT concentrations.

Stage 2

The second stage started on April 3, 1992 and ended on April 19, 1992. Two hundred grams of PMCH diluted with 150 gal of methanol were used in each injector in the western sector. The first objective was to determine if the gas injected into the western sector migrated to the eastern sector or if the fault was a barrier to flow. The second objective was to determine if the gas injected into the 26R reservoir migrated updip into the NA reservoir.

Stage 3

The objective was to determine if the injected gas in the eastern sector migrated downdip into the other layers of the 26R reservoir. The procedure will be to inject different PFT's for different layers in Injector 388U-26R. This test has not yet been conducted.

Stage 4

Results of the earlier stages can help in the planning of this final test.

Results of Stages 1 and 2

Figures 8 to 21 show PFT concentrations from the 14 sampling wells in the 26R and 31S NA areas. The concentrations are plotted separately for the two stages. For the first-stage tracer test, the PFT concentrations are plotted vs. elapsed time since November 17, 1991. Results of the

second stage are plotted vs. elapsed time since April 3, 1992, the starting date of the second stage. Figures 22 and 23 show gas production rates during the tests. For most of the wells located in 26R, the gas production rates do not change significantly. For wells located in 31S, the fluctuations in the gas production rates are caused by changes in operating conditions to control excessive gas production.

Data Analysis and Interpretation of the First-Stage Tracer Test

The first question that needs to be answered is whether the data are merely noise or actual responses from the test. This is done by estimating the produced tracer concentrations at the sampling wells and comparing these to the detectable limit of the PFT's. If the calculations show that the produced tracer concentrations are well below the detectable limit (less than 10^{-14} pL/L), the data should be considered noise. Otherwise, the data should be considered as valid. The calculation is done by diluting the amount of tracer injected by the volume of the gas in the reservoir. Assuming a 200 ft thick gas cap, an average porosity of 25%, an average gas saturation of 60%, and a distance between Injector 366U-26R and Well 378A-26R of 1,450 ft, the volume of reservoir gas at 60°F and 1 atm is

$$V = \frac{\pi r^2 H \phi S_g}{B_g}$$

$$= 2.55 \times 10^{10} \text{ scf or } 7.22 \times 10^{11} \text{ standard L}$$

The produced tracer concentration at Well 378A-26R is obtained by diluting the volume of gas tracer with the volume of the reservoir gas at 60°F and 1 atm:

$$C_{\text{at 378A-26R}} = \frac{2.37 \text{ standard L of PMCP}}{7.22 \times 10^{11} \text{ standard L of reservoir gas}}$$

$$= 3.2 \times 10^{-12} \frac{\text{standard L of PMCP}}{\text{standard L of reservoir gas}}$$

$$= 3.2 \frac{\text{pL of PMCP}}{\text{standard L of reservoir gas}}.$$

This produced tracer concentration does not include the dilution by injected gas. As one can see this number is only two orders of magnitude greater than the detectable limit of 0.01 pL/L. Considering that this well is the closest to the injector and a large amount of gas is injected to maintain the reservoir pressure, more tracer should be injected for a better result. This could be one reason why there is so much noise in the data. A look at the produced tracer concentration at Well 378A-26R shows that the peak concentration is 3.5 pL/L at 250 days, which is consistent with our estimation. Although this calculation involves many assumptions, the results should be correct within an order of magnitude. The fact that this estimation is so close to the data also should not lead us to believe that our assumptions are accurate. This is only a rough estimate.

Assuming that the injected tracer travels in the same layer, the produced tracer concentrations at different sampling wells should be inversely proportional to the distance squared.

$$C_{\text{at 332XU-36R}} = \frac{d^2_{\text{366U-26R to 378A-26R}} \times C_{\text{at 378A-26R}}}{d^2_{\text{366U-26R to 332XU-36R}}}$$

$$= \frac{1450^2 \times 3.5}{3875^2}$$

$$= 0.49 \text{ pL/L}$$

This result is also consistent with the data. The peak tracer concentration at Well 332XU-36R located on the same straight line as Well 378A-26R and at a distance of 3,875 ft from Injector 366U-26R shows 0.45 pL/L compared to 0.49 pL/L from the calculation.

A careful look at the produced tracer concentrations vs. elapsed time plots from some of the sampling wells such as Wells 326-26R, 332XU-36R, 362-26R, and 378A-26R indicates an approximate bell-shaped distribution. This is another reason to believe that the data are not noise.

Table 11 shows the distance from the tracer injection well to the sampling wells and the average velocity for the first test.

The next step is to calculate the amount of tracer produced at each sampling well. The amount of tracer produced can be obtained by integrating the area under the curve of the produced tracer concentrations vs. elapsed time plot and multiplying by the gas production rate of the sampling wells:

$$m_{\text{tracer prod}} = Q_{\text{prod}} \int_0^{\infty} c \, dt$$

The gas production rates are assumed to be constant and are shown in Table 9. Table 13 shows the amount of tracer produced at the sampling wells.

The distribution of injected gas into different sectors with reference to the major fault is an important issue. Does the majority of the injected gas migrate to 31S or stay inside the 26R? Is the major fault a complete barrier to flow? If not, what is the percentage of flow across this fault? The distribution of injected gas into different sectors can be determined only if complete recovery of tracers is obtained. The amount of tracer recovered depends on the following factors: number of sampling wells used, the duration of time the sampling wells are opened, and the completion intervals. Figure 24 shows the location of the sampling wells and amount of PMCP produced from the first stage as a percentage of total PMCP produced. The wells that produced most tracers are located in the western sector. These are Wells 326A-26R, 336U-26R, and 347A-26R. Well 322A-36R shows about 19.5% (from total produced) of PMCP, but there is a possibility that this is noise in the data because most of the area is under a single data point (18 pL/L at 400 days).

All of the wells in 31S experienced a large increase in gas-oil ratio. Table 12 shows the gas-oil ratio for the sampling wells. There are fluctuations in the gas-oil ratio but the values in Table 12 are representative of the actual values. Hence, not all of the sampling wells in the 31S area were opened during the test as indicated in the produced tracer concentrations vs. elapsed time plots. Wells 362-26R and 384-26R were shut in after 300 days. Well 383-26R was opened 350 days after the test. Well 386A-26R was also shut in after 280 days. If these wells had been open the entire test period, more tracer could have been produced.

Since we cannot discuss the unproduced tracers, we will make some observations about the produced tracers. Table 14 shows the average amount of PMCP produced per well in different sectors. The western and eastern sectors produced about the same amount of tracers, while in the 31S area, less was produced because the wells were shut in and had lower completion intervals (C and D shales and 31S sands). Only one well was sampled in the southeastern area (NA shales of the 31S) . It is unknown from this first stage tracer test if the major fault that divides 26R is a barrier to flow, because Injector 366U-26R intersects the fault and PMCP could be injected in both sectors. We will discuss this later when interpreting the second-stage tracer test.

There are many possibilities that could lead to an early breakthrough and also to small amounts of tracers produced. The most likely scenario is that 26R and 31S share the same gas cap

and the injected gas filled this gas cap by moving updip into 31S, where the wells are completed in the NA shales. At the same time, it is moving downdip to the lower 26R, where the producing wells are completed (see Table 10 for the completion intervals).

A simple material balance calculation on the injected gas shows that there exists good communication between the gas injectors and the producers. The total injection rate for 26R is around 170 MMscf/D. Total gas production rate is about 150 MMscf/D and total oil production rate is 18,000 STB/D. Assuming that the solution gas is 1,000 scf/STB, the amount of free gas produced is obtained by subtracting the solution gas from the total amount of gas produced and is about 132 MMscf/D, or about 80% of the injected gas.

The volume of the gas cap can be roughly estimated from the total gas injection rate and the breakthrough time by making reasonable assumptions. These are an average porosity of 25%, a constant tracer partition coefficient of 0.65 for PMCP, a gas formation volume factor of 0.0078 reservoir volume, per surface volume and single-phase flow of gas at residual oil and water saturations of 30% and 15%, respectively.

$$V_{\text{gas cap}} = \frac{t^{bt} Q_{inj} B_g}{\phi\left[1+ (K_T-1)S_{or}-S_{wr}\right]}$$

$$= \frac{200\ [D] \times\ 170 \times 10^6 [scf/D] \times 0.0078\ [ft^3/scf]}{0.25\left[1+ (0.65 - 1)\ 0.3 - 0.15\right]}$$

$$= 1.42 \times 10^9\ ft^3 \text{ or } 51 \text{ square mile-ft}$$

This number is reasonable compared to the thickness of the first three megaunits of 26R. The actual volume of the gas cap should be greater than 51 square mile-ft, since the injected gas does not sweep the whole gas cap at the time of breakthrough.

The idea that 26R and 31S share the same gas cap and that there is good communication between 26R and 31S can be supported by much evidence. This evidence will also show that there is good vertical communication among all geological units within each reservoir. The first evidence comes from pressure data. Pressure measured in the gas cap of 26R is around 2,500 psig and is around 2,400 psig in 31S . The higher pressure in 26R could be the result of a higher gas injection rate in this area. The second evidence comes from tracer data. As the injected tracers move updip into the 31S area and downdip into the 26R area, they also move downward into the lower geological sequences (see Fig. 7 for the order of these geological sequences in the 26R and 31S areas). In the 26R reservoir, tracers injected in the upper 26R were produced in the lower 26R. These tracers were also produced in the 31S area from the equivalent of the 26R sands or NA shales, the B, C, and D shales, and also from the upper and lower 31S sands. The breakthrough times of these tracers at the sampling wells were also consistent with the depths of the well completions and the distance away from the tracer injector. Wells completed shallower broke through earlier than those completed deeper. Well 332XU-36R is located farther from the tracer injector compared to Well 378A-26R and shows a breakthrough time of 350 days compared to 200 days.

For wells located in the 31S area, Well 362-26R is located farther from the tracer injector but is completed at a shallower depth. Well 362-26R is located updip and completed higher in the B and 31S sands compared to the C and D shales where Well 363-26R is completed. The oil, water, and gas production rates for Well 362-26R are 32 STBO/D, 1 STBW/D, and 1,041 Mscf/D. The gas-oil ratio is 32,531 scf/STB. The oil, water and gas production rates for Well 363-26R are 52 STBO/D, 683 STBW/D, and 561 Mscf/D. The gas-oil ratio is 10,788 scf/STB. The breakthrough times of these two wells are at 200 days and Well 362-26R shows a higher peak tracer concentration because of less dilution. Well 382-26R is completed in the N, A, and B shales

while Well 384-26R is completed in lower geological units (B, UL31S). The oil, water, and gas production rates for Well 382-26R are 15 STBO/D, 0 STBW/D, and 593 MSCF/D. The gas-oil ratio is 39,533 scf/STB. The oil, water, and gas production rates for Well 384-26R are 17 STBO/D, 0 STBW/D, and 854 Mscf/D. The gas-oil ratio is 50,235 scf/STB. These two wells produced at about the same gas-oil ratio because they are both completed above the gas-oil contact and Well 384-26R is located closer to the 26R gas injectors than is Well 382-26R. Data indicate a breakthrough time of 200 days for Well 382-26R. Well 384-26R was shut in between 200 to 260 days and data show tracer breakthrough after the well was reopened. The breakthrough time at Well 384-26R could be about the same as for Well 382-26R. The peak tracer concentration at Well 384-26R is also higher at 2.1 pL/L compared to 1 pL/L at Well 382-26R. The peak tracer concentration of (oc+ot) PDCH at 360 days appears to be noise because it is only one point.

Well 383-26R is located between Wells 382-26R and 384-26R but is completed lower. The oil, water, and gas production rates for Well 383-26R are 81 STBO/D, 117 STBW/D, and 1,486 Mscf/D. The gas-oil ratio is 18,348 scf/STB. The well was opened 350 days after tracer injection and the data indicate some tracer breakthrough after the well was opened. The well was shut in 60 days later because of excessive gas production. Well 386A-26R is located close to the tracer injector and completed in the B shale. The oil, water, and gas production rates for Well 386A-26R are 26 STBO/D, 2 STBW/D, and 776 Mscf/D. The gas-oil ratio is 29,846 scf/STB. This well was shut in between 200 to 260 days after tracer injection. Once the well was reopened, the data indicated a peak tracer concentration of 3.4 pL/L. There are no tracer data after 280 days.

Another interesting result is that the concentrations of two other tracers, oc-PDCH and ot-PDCH, are generally lower than PMCP concentrations and they breakthrough at about the same time as PMCP. This result is consistent with the partition coefficients of these tracers, since PMCP has a lower partition coefficient compared to PDCH. A lower-partitioning tracer will spend less time in the oleic phase compared to a higher-partitioning tracer. As a result, the breakthrough time will be earlier and the tracer concentration higher. However, comparison of the breakthrough times is uncertain because of poor quality data at these very low tracer concentrations.

Simulation of the First-Stage Tracer Test

Given a set of fluid flow data or tracer data, it is not difficult for one to develop a reservoir model based only on these data. However, it is difficult to develop a model that is also consistent with the geology. The first step in building a reservoir model is from data analysis. The data include a structural map of the reservoirs, production data, material balance of the injected gas, petrophysical properties, recovery mechanism, and positions of gas-oil contact and perforation intervals. Once the initial reservoir model based on data analysis is developed, a decision has to be made on what parameters, and the range of these parameters, need to be adjusted so that the model gives the same responses as the reservoir. Figure 25 shows a cross section of a conceptual flow model of the 26R and 31S reservoirs based on data interpretation.

Simulation Model

The next step is to decide the area to be simulated and how to grid it. Using production rates from the wells and a steady-state streamline model, each injector was assigned a rate by counting the number of streamlines from the producer back to the injector. Figure 26 shows an areal picture of the streamlines assuming that 26R is in full communication with 31S. The area to be simulated is approximately 1.5 square miles and is divided into a 26 × 43 grid (NX × NY). Figure 27 shows the areal grid used in this simulation study. The locations of the wells are such that no two wells are in neighboring grids.

The 26R sands can be divided into 18 different layers based on the continuous shales. Rial (1990) used 20 vertical gridblocks in the simulation of this reservoir. If the same number were used here, this would bring the total number of gridblocks to 22,360 (26 × 43 × 20). The use of a large number of gridblocks in the vertical direction is necessary to model the effects of gravity, multiphase flow, and detailed reservoir heterogeneity. In the tracer test, the flow is mainly single-phase except for wells completed below the gas-oil contact or in the transition zone. For the reservoir description side, the material balance of the injected gas indicates good communication

from the injectors to the producers. The use of single-phase flow and good fluid communication among the layers enables us to use a smaller number of gridblocks in the vertical (Z) direction because gravity has no effect on the flow behavior and some degree of reservoir heterogeneity could be represented with physical dispersion. Figure 28 shows a cross section of the simulated reservoir. The initial assumption was that an even gas-oil contact exists across both reservoirs. This assumption is contradictory to the belief that an uneven or multiple gas-oil contacts exist across the 26R reservoir. Some adjustments may be needed during simulation.

The number of gridblocks in the vertical direction (NZ) is 4. The total number of gridblocks is 4,232. The number of gridblocks is kept to a minimum so that multiple runs can be made economically. Each gridblock in the vertical direction represents one megaunit of the 26R sands. The first and second gridblocks in the vertical direction represent the upper sequence from layers A to E, while the third and fourth vertical gridblocks represent part of the lower sequence of the 26R sands above the gas-oil contact (layer F and below). Average reservoir properties are taken from Tables 1 and 2. An average porosity of 25% was used in the 26R area and 16% for the 31S area. The vertical permeabilities are one-tenth of the horizontal permeabilities. Anisotropy is also included by doubling the permeabilities in the X direction. The elongated shape of the 26R reservoir suggests preferential flow in the northwest-southeast direction (Y direction) compared to the X direction. Table 15 summarizes the reservoir properties used in the simulations.

Initially the hydrocarbon components were lumped into seven pseudocomponents using an expert system for UTCOMP developed at The University of Texas by Khan (1992). Table 16 shows the fluid description. An average water saturation for 26R is taken from Table 2. The same water saturation for 26R is used in 31S so that a single phase of gas can be simulated. Simulation results will show that some adjustments may be needed to obtain better results for wells perforated in the lower shales and sands for both the 26R and 31S areas.

Since single-phase flow of gas will be simulated, the total number of hydrocarbon components can be reduced from seven to two without affecting the results. This reduction helps reduce unnecessary computation performed in the flash calculations. This is done by using only methane and the heaviest components (C_{24+}). The hydrocarbon compositions of these two components are adjusted to give the same gas and oil saturations as using seven pseudocomponents at the same pressure and temperature. The overall mole fraction of methane and C_{24+} used are 0.82 and 0.18, respectively.

In summary, we have transformed two very complicated reservoirs (26R and part of 31S) into a simple reservoir description by making some assumptions to aid in the interpretation and to reduce computational time. The main assumptions are

1. single phase flow of gas at constant residual oil and water saturations,
2. constant tracer partition coefficients,
3. no adsorption of tracer,
4. heterogeneity can be represented by physical dispersions,
5. good fluid communication exists between the 26R sands and NA shales in the northwest-southeast limit of 26R,
6. the major fault that divides 26R into two equal halves is not a barrier to flow, and
7. there is an even gas-oil contact for both reservoirs.

Simulation results will show that some of these initial assumptions may need to be adjusted to give a better match to the field tracer data. Although the initial reservoir description is simple, it includes many fluid-flow effects such as 3D flow, areal sweep, heterogeneity and anisotropy, physical dispersion, dilution from other injectors, interference of other producers, positions of tracer injection wells and observation wells, perforation intervals, change in well conditions, and tracer partitioning.

Transport Parameters

There are many parameters that could influence tracer breakthrough times and produced peak tracer concentrations, such as heterogeneity, anisotropy, multiphase flow, degree of physical dispersion, effective thickness, fluid saturations, and tracer partition coefficients. As mentioned

earlier, the decision was made to simulate only a single-phase flow of gas at residual oil and water saturations. The simulation results will show the validity of this assumption. Therefore, the parameters that affect the tracer responses most are the effective thickness and degree of physical dispersion. These two parameters are related closely to the degree of heterogeneity. The effect of uncertainty in the tracer partition coefficients is small compared to that of reservoir heterogeneity.

Data on dispersion in the laboratory and in the field have been published by many authors. It has been found that dispersivity increases with the length scale of observation. Neuman (1990) fit two separate regression lines to the data with the length scale of observation less than 100 m and greater than 100 m. The expression for the regression line when the scale of observation is greater than 100 m is $\alpha_{aL} = 0.32\, L_s^{0.83}$. Using the distance of 1450 ft (442 m) between Injector 366U-26R and Well 378A-26R, the calculated apparent longitudinal dispersivity is 50 m, or 165 ft. In this study, apparent dispersivities of 100 and 150 ft were used for both the longitudinal and transverse dispersivities.

The second parameter is the effective thickness of the reservoir. The effective thickness is not the same as the net thickness of the reservoir but is the portion of reservoir that contributes to the flow. The effective thickness is different in different parts of the reservoirs. In the initial model, a constant effective thickness from the top of sands to the gas-oil contact is assumed to be the same for both reservoirs. This parameter will be adjusted and the effect of changing this parameter will be discussed. Since the simulated reservoir is very close to a homogeneous one, the effective thickness should be much smaller than the actual reservoir thickness. As calculated in the data-analysis section, a gas-cap volume of 50 square mile-ft is obtained using the total injection rate of the whole field (170 MMscf/D) and an average tracer breakthrough time of 200 days. The simulated area is around 1.5 square miles and thus an effective thickness of 34 ft is obtained. Keep in mind that not all of the injected gas gets produced or stays inside the simulated area. Thus, this number could be lower. An effective thickness of 60 ft was used in the first simulation.

Simulation Results

Figures 29 to 37 show results of two simulation runs using input data from Table 15 and different dispersivities and effective thicknesses. The first run used an effective thickness of 60 ft and longitudinal and transverse dispersivities of 100 ft. The second run used an effective thickness of 30 ft and longitudinal and transverse dispersivities of 150 ft. The first run, with the larger effective thickness, shows a late breakthrough compared to the data with the exception of Wells 336-26R and 347-26R. The peak tracer concentration at 220 days for Well 336-26R is probably noise because it is much higher than other neighboring points. Results of the first run indicate a smaller effective thickness as expected from the calculation.

An effective thickness of 30 ft and dispersivities of 150 ft were used in the second run. Results indicate a better match for Wells 326-26R, 363-26R, 378A-26R, 383-26R, and 384-26R. Wells 336-26R and 347-26R show an earlier breakthrough than the data. Compared to wells located near the tracer injector (Well 366U-26R), Wells 336-26R and 347-26R are completed lower than Wells 378A-26R and 326-26R . Well 378A-26R was completed from 5,019 to 5,444 ft subsea while the completion intervals for Wells 336-26R and 347A-26R were 5,811 to 5,921 and 5,573 to 6,078 ft subsea, respectively. Well 326-26R was also completed lower than Well 378A-26R at 5,592 to 5,898 ft subsea. All four of these wells are oil producers and are completed in the transition zone or below the gas-oil contact.

The oil, water, and gas production rates for these wells are 281/235/5,191 for Well 326-26R, 225/224/5,765 for Well 336-26R, 280/45/3,605 for Well 347-26R, and 112/39/524 for Well 378A-26R, STBO/D, STBW/D, and Mscf/D, respectively. The gas-oil ratio for Wells 326-26R, 336-26R, 347-26R, and 378A-26R are 18,473, 25,622, 12,875, and 4,679 scf/STB, respectively. Wells 326-26R, 336-26R, and 347-26R are located in the western sector and produce much more free gas than Well 378A-26R even though they are completed lower.

Simulation results indicate much thicker reservoir sands at Wells 336-26R and 347-26R compared to 378A-26R. The reservoir thickness at Well 326-26R is also larger than at Well 378A-26R. This is consistent with other studies finding that there is an uneven gas-oil contact across the

main fault. The average gas-oil contact in the western sector (5,780 ft subsea) is lower than the average gas-oil contact in the eastern sector (5,650 ft subsea). The difference in gas-oil contacts makes the pore volume in the eastern sector smaller than the western sector. The simulated reservoir has a uniform thickness for both sectors, therefore, the breakthrough times and the peak concentration do not match the data well. The tracer concentration data at Well 378A-26R shows distinct peaks compared to simulation results, possibly caused by heterogeneity. Simulation results show no breakthrough at Well 332XU-36R after 550 days.

For the sampling wells located in the 31S area, the use of a smaller effective thickness gives better results than a larger one. This is so for two reasons. First, the 26R sands are thinner near the northwest-southeast limit as shown in Fig. 3. The NA shales of 31S reservoir become thicker away from this limit. The NA shales of 31S also have lower porosity compared to the 26R sands. Second, gravity causes the injected gas to move updip toward 31S. The sampling wells in 26R were completed in the transition zone (below the gas-oil contact) and they are located downdip of the structure. The sampling wells in 31S are located updip, and most of them were completed above the gas-oil contact as supported by the production rates of these wells. It is easier for gas to move updip than downdip and below the gas-oil contact because of gravity. Well 363-26R shows a reasonable match except that the area under the curve is greater. Wells 383-26R and 384-26R also show reasonable matches with the data. The simulated (oc+ot) PDCH concentrations are lower than PMCP, in agreement with the data, because they have higher partition coefficients. Simulation shows a late breakthrough at Well 362-26R compared to the data because this well is farther away than Well 363-26R. Well 362-26R is also completed higher in the B shale, U31S, while Well 363-26R is completed in the C and D shales and closer to the gas-oil contact. In the simulation, the same effective thicknesses for these wells are used. Adding multiphase flow to the C and D shales could give a better match for Well 362-26R.

In summary, the simulation results match reasonably well with the data. The simulated tracer production curves show a gradual increase and decrease in tracer concentrations whereas the tracer data are erratic. The areas under the simulated tracer breakthrough curves are greater than for the data, which indicates less tracer was produced than predicted. Simulation results show smaller PDCH concentrations than PMCP concentration in agreement with the data. The differences are caused mainly by the use of uniform thicknesses for both reservoirs. Better results could be obtained by adjusting the effective thickness according to the thickness above the gas-oil contact at different well locations.

Data Analysis and Interpretation of the Second-Stage Tracer Test

The results of the second-stage tracer test also show a lot of fluctuation. In this test, more tracers were injected compared to the first stage (800 g of PMCH compared to 30 g each of PMCP, oc-PDCH, and ot-PDCH in the first stage). Table 17 shows the amount of PMCH produced at each sampling well and Fig. 38 shows the locations of these sampling wells. The total amount of PMCH produced is smaller than the amount of PMCP produced. The breakthrough times for PMCH are even shorter than those for PMCP and are generally in the range of 100 days. Table 18 shows the average velocity of PMCH for different sampling wells.

If the produced tracer concentrations from the sampling wells are plotted vs. sampling date, it can be seen that some of the data, such as that for Well 382-26R and Well 383-26R show similar shapes of produced PMCP and PMCH concentrations. The wells that show peak concentrations of PMCH higher than those of PMCP are 326-26R, 332XU-26R, 363-26R, and 382-26R. Are all of these responses real or just some of them? The wells that are important in the second stage are wells located in the eastern sector. If the responses of the wells in this area are real, then the major fault is not a barrier to flow. The responses from Wells 378A and 332XU-26R located in the eastern sector might be real since they are more consistent compared to Well 327-25R. The produced tracer concentration at Well 378A-26R can be estimated using the same procedures as in the interpretation of the first stage. The distance between the center of the four injectors to Well 378A-26R is approximately 2,750 ft. The volume of the reservoir gas at standard condition is calculated using

$$V = \frac{\pi r^2 H \phi S_g}{B_g}$$

$$= \frac{\pi \times 2750^2 \times 200 \times 0.25 \times 0.6}{0.0078}$$

$$= 9.138 \times 10^{10} \text{ scf or } 2.588 \times 10^{12} \text{ standard L.}$$

The amount of PMCH in moles is 800 g divided by its molecular weight (350 g/mol), which is 2.286 moles. The volume of PMCH is

$$V = \frac{nRT}{P}$$

$$= \frac{2.286 \text{ [mol]} \times 82.06 \text{ [cm}^3\text{•atm •mol}^{-1} \text{ •K}^{-1}\text{]} \times (273.15 + 15.56) \text{ K}}{1 \text{ [atm]}}$$

$$= 54159 \text{ cm}^3 \text{ or } 54.16 \text{ standard L.}$$

The estimated concentration of PMCH at Well 378A-26R is then

$$C_{\text{at 378A-26R}} = \frac{54.16 \text{ standard L of PMCH}}{2.588 \times 10^{12} \text{standard L of reservoir gas}}$$

$$= 2.1 \times 10^{-11} \frac{\text{standard L of PMCH}}{\text{standard L of reservoir gas}}$$

$$= 21 \frac{\text{pL of PMCH}}{\text{standard L of reservoir gas}}.$$

This calculation gives an estimated tracer concentration about one order of magnitude higher than the calculation of tracer concentration in the first stage. The data show that the highest peak occurs at 100 days with the peak PMCH concentration of only 1.3 pL/L (compared to 21 pL/L from the above calculation). The smaller peak concentration is possible because more tracer could be produced later.

The next question is how to interpret the early breakthrough of 100 days of PMCH. The early breakthrough times of PMCH in the second stage are not consistent with the breakthrough times of PMCP in the first stage. The nearest injector for PMCH is Injector 356-26R, which is located 1,900 ft from Well 378A-26R while the PMCP injector is located 1,450 ft from Well 378A-26R. The lowest completion at Injector 356-26R is 4,829 ft subsea compared to 4,684 ft subsea at Injector 366U-26R. At 378A-26R, the highest completion is at 5,019 ft subsea. In the vertical direction, the distance from the closest PMCH injector to Well 378A-26R is 190 ft and the distance from PMCP injector to Well 378A-26R is 335 ft. The shortest distance between Injector 356-26R and Well 378A-26R is 1,909 ft compared to 1488 ft between Injector 366U-26R and Well 378A-26R. Figure 39 shows a schematic diagram of the shortest distances from the PMCP injector (Injector 366U-26R) and the closest PMCH injector (Injector 356-26R) to Well 378A-26R. Is it possible that a more retarded tracer (PMCH) injected 137 days after PMCP can travel a greater distance in the same direction through the fault and breakthrough at the same time as PMCP? This is possible if PMCH is injected in the same layer as the completion interval of Well

378A-26R and there is poor vertical communication between the PMCP injector and Well 378A-26R. The data indicate that the opposite is true. Simulation results given below support this fact.

Simulation Results

Figures 40 to 48 show the simulation results for the second stage. The same reservoir description as in the first stage was used. At Well 378A-26R, located in the eastern sector of the 26R reservoir, simulations show a late breakthrough of 220 days of PMCH compared to 60 days after PMCH injection. The simulated PMCH concentration increases slowly and reaches 0.1 pL/L at 400 days. A larger simulated peak can be expected after 400 days. The simulated breakthrough time of PMCH is consistent with the simulated breakthrough time of PMCP. As expected from the analysis, PMCH should breakthrough later than PMCP because of the greater distance PMCH has to travel. There is a possibility that the peak at 300 days could be a real breakthrough. Simulations show no tracer breakthrough at Well 332XU-36R. For other wells located in the 26R reservoir, simulation results show much higher concentrations of PMCH compared to the data. This is also consistent with the larger amount of PMCH used in the second stage compared to the first stage. If there is a breakthrough, the concentration should be in the range of 10 to 100 pL/L, as estimated previously.

There are two possibilities if there is no breakthrough of PMCH in the eastern sector. The first possibility is that the main fault is a barrier to flow and the second possibility is that the data are not sufficiently good. The first possibility is true if there is breakthrough of PMCH in other sampling wells but not in the eastern sector of the 26R reservoir. The second possibility is true if there is no breakthrough of PMCH at all. Wells 336-26R and 347-26R do not have enough data after 100 days. Well 326-26R has data up to 370 days, but the data show much lower concentrations than in the simulations. For sampling wells located in the 31S reservoir, Well 363-26R shows a larger PMCH concentration than the data. Other sampling wells may not have good data because of the short sampling period. There are only two wells that have enough data points to be evaluated. These problems with the data prevent us from making a conclusion about the main fault at this time. Sampling should be continued to see if a larger peak PMCH concentration occurs. We speculate that the remaining tracer stayed in the gas cap of 26R and 31S, with the majority of the tracer in the western sector of 26R. The remaining tracer should be recovered later if it is still detectable.

RESIDUAL OIL SATURATION DETERMINATION FOR THE SHALLOW OIL ZONE RESERVOIR (SOZ)

The Shallow Oil Zone (SOZ) reservoir is located at the Elk Hills Naval Petroleum Reserve in California (NPRC). This reservoir has been producing oil since 1920's. The total estimated reserves are 500 million barrels of oil and the production rate is 15,000 barrels of oil per day from 550 production wells. The average reservoir pressure is 18 psig and the reservoir temperature is 140°F. This reservoir is undergoing a gas injection program to increase the reservoir pressure to 25 psig. The objectives of the tracer test project at the SOZ reservoir were to test the new tracer technology (perfluorocarbon tracers, PFT's) developed by Gunnar Senum of Brookhaven National Lab (BNL) (Senum *et al.*, 1992) in a petroleum reservoir and to investigate the flow behavior of the injected gas so that a better plan for an EOR project can be implemented in the future.

The tracer test was carried out by injecting PMCH (perfluoromethylcyclohexane) and PMCP (perfluoromethylcyclopentane) into Well 34-10G undergoing a gas injection rate of 150 Mscf/D. The injected PMCP and PMCH concentrations were 89,330 and 97,000 pL/L, respectively. Two other tracers, oc-PDCH (perfluo cis 1,2-dimethylcyclohexane) and ot-PDCH (perfluo trans 1,4 dimethylcyclohexane) were injected into Well 44-10G undergoing a gas injection rate of 75 Mscf/D. The injected oc-PDCH and ot-PDCH concentrations were 64,700 and 139,000 pL/L, respectively. The injection intervals for these two wells were 75-100 ft above the gas/oil contact. Well 34-10G was completed in sublayers Pa, A, A1, and B of the SS-1 with an average net thickness of 45 ft. Well 44-10G was completed lower in sublayer D with an average net thickness of 15 ft. Gas samples were taken at wells located around the two tracer injection wells

and then sent to BNL for analysis. The gas cap wells were produced at low rates, about 1 Mscf/D. Figure 49 shows a map of the area (Senum *et al.*, 1992).

Data obtained from this tracer test were analyzed for residual oil saturation. The accuracy of the residual oil saturation relies heavily on the accuracy of tracer partition coefficients that have to be measured with the reservoir fluid at reservoir conditions. The composition of the reservoir fluid used in this study was obtained from PVT data of fluid collected from Well 73-11G (Reudelhuber, 1952) and shown in Table 19. The hydrocarbon components were lumped into eight pseudocomponents using an expert system for UTCOMP developed at The University of Texas by Khan (1992). Table 20 gives the fluid description computed using this expert system. Estimation of the tracer partition coefficients is based upon vapor-liquid equilibrium using different assumptions; ideal gas and ideal liquid (Raoult's law), ideal gas and nonideal liquid, and the Peng-Robinson equation of state base on the critical temperature, critical pressure, accentric factor, and binary interaction parameters of the PFT's.

Since the reservoir in this test zone is at a low pressure of 19 psia (Pande, 1991) and moderate temperature of 140°F, the vapor-liquid equilibrium of the PFT's should follow Raoult's law. Raoult's law relates vapor pressure which is a function of temperature to the equilibrium ratio (K value).

$$K_i = \frac{y_i}{x_i} = \frac{P_i^{vap}}{P}$$

The vapor pressures for PMCP and PMCH were estimated using the Antoine and the Wagner equations (Reid *et al.*, 1988). The vapor pressures of PMCP and PMCH from correlations were 1.575 and 0.585 bar, respectively. The vapor pressure for PMCP may not be as accurate as for PMCH because the vapor pressure correlation for PMCP is not available and so the vapor pressure of perfluorocyclohexane is used instead. To ensure that the vapor pressures from correlations were accurate, the Peng-Robinson equation of state was used to double checked these numbers. First, the boiling points or the vapor pressure at 1 atm of both PMCP and PMCH were checked and agreed with boiling point data. Then, the vapor pressures of the PFT's at reservoir temperature of 140°F were predicted using the Peng-Robinson equation of state. The vapor pressures for PMCP and PMCH from the Peng-Robinson equation of state were 1.45 and 0.55 bar, respectively. The vapor pressures from correlations agree with the ones from the Peng-Robinson equation of state. In this study, the vapor pressure of 1.45 bar for PMCP and 0.585 bar for PMCH at 140°F were used.

Raoult's law assumes that there is no interaction between PMCP or PMCH molecules and hydrocarbons in the liquid phase. This may not be the case since the PFT's contain fluorine which is different from hydrocarbon. The interaction can be accounted for by using the activity coefficients. Many different activity coefficients models can be found in the literature. The most widely used is the UNIFAC group contribution method. Using the oil compositions from Well 73-11G, the activity coefficients of PMCP and PMCH in the oleic phase are 6.11 and 9.357, respectively. The equilibrium ratio is calculated using

$$K_i = \frac{y_i}{x_i} = \frac{\gamma_i^l P_i^{vap}}{P}.$$

The equilibrium ratio is converted to the partition coefficient using

$$K_{Ti} = \frac{\zeta^l}{K_i \zeta^v}.$$

The ratio of the molar densities of the oleic to gaseous phase is estimated to be 72.768 using the

Peng-Robinson equation of state.

Figures 50 and 51 show results of equilibrium ratio versus pressure at different temperatures using PFT's binary interaction parameter of 0 and 0.22. Based on experimental data on the partition coefficients of PFT's measured using the 26R reservoir fluid at 2400 psia pressure and 200°F temperature, the binary interaction parameter is in the range of 0.18 to 0.22. (The 26R reservoir is a reservoir located at Elk Hills Naval Petroleum Reserve No.1.) The partition coefficients are very sensitive to the binary interaction parameters. More experimental data are needed to correlate the binary interaction parameters used in the Peng-Robinson equation of state to the tracer partition coefficients at different conditions.

The equilibrium ratios and the tracer partition coefficients from different methods are tabulated in Tables 21 and 22. Comparing different methods, Raoult's law gives the lowest equilibrium K value and the Peng-Robinson equation of state with $\delta_{ij} = 0.22$ gives the highest equilibrium K value. Table 22 indicates a large uncertainty of the tracer partitioning coefficients from different methods. The binary interaction parameters in the Peng-Robinson equation of state are used to correct for the nonideality between molecules. At the conditions of the SOZ reservoir (19 psia, 140°F), the binary interaction parameters should not be as high as the numbers obtained from the conditions of the 26R reservoir (2400 psia, 200°F). The predicted tracer partition coefficient using $\delta_{ij} = 0.22$ is more likely to be too high and the actual tracer partition coefficient should be in between the numbers predicted by the equation of state using $\delta_{ij} = 0$ and 0.22. Comparing all the methods, the UNIFAC model should give the best estimate of the tracer partitioning coefficients at these reservoir conditions (19 psia, 140°F). Therefore, the tracer partition coefficient predicted using the UNIFAC model will be used to calculate the residual oil saturation of the SOZ reservoir.

Figures 54 and 55 show tracer production data from Well 25-10G and 81-10G. Figures 56 and 57 show cumulative recovery of PMCP and PMCH vs. time at Well 25-10G and 81-10G, respectively. With this set of data, the recovery is very small and the test was stopped very prematurely. Extrapolation of the tail of a tracer response to complete recovery may not be very meaningful when recovery is small. The extrapolation technique also requires tracer production data from other surrounding wells so that the total amount of tracer is conserved and these data are not available. Because of the above reasons, applying the first moment calculation to this set of data may not give good results. As shown in the simulation example, the residual oil saturation calculated using the higher cutoff concentration (10^{-3}) will be lower than the actual value (Figs. 40-43 of Section II). Using data from Well 81-10G, the calculated R_t is 0.84 without extrapolation of the tail of tracer response. Using Eqs. 37 and 38 of Section II and K_T from the UNIFAC model, the calculated residual oil saturation from the first moment method is 5%. Extrapolation of the tail of PMCH to the same cumulative PMCP recovery (0.09% injected) using an exponential function gives the first moment with respect to time of 356 days compared to 266 days without extrapolation. The calculated R_t is 0.75 and the corresponding residual oil saturation is 10%. There are no assumptions made regarding the distribution of S_{or} when applying the first moment method.

In an oil reservoir, the distribution of residual oil in the reservoir is more uniform compared to the distribution of spilled contaminants given in the simulation example (Section II). The uniformity of the oil saturation is suggested from the similarity of the shape of tracer production data for PMCP and PMCH at Well 25-10G (Fig. 54). When the distribution of residual phase is uniform, the tracer response of different partitioning tracers can be collapsed into a single curve as illustrated in Fig. 38C of Section II and point by point or a landmark comparison of Tang and Harker (1991) can be applied. The assumption used is that dispersion is a result of heterogeneity or the flow is mainly convective flow. Therefore, the ratio of the first moment or R_t in Eqs. 37 and 38 of Section II is the same as the ratio of the travel time of the equivalent concentrations on the nonpartitioning and partitioning tracer breakthrough curves.

Figure 58 shows the residual oil saturation vs. cumulative tracer recovery using data from Well 81-10G and Eqs. 37 and 38 of Section II. Figure 58 indicates that the residual oil saturation

is not uniform. If the distribution of residual oil is uniform, a single value of S_{or} should be obtained at any cumulative tracer recovery. If we assume a layered and ordered reservoir model (low S_{or} in high permeability layer), by correlating the peak of the tracer production data, there are 3 layers of different residual oil saturations. (The number of peaks is subjective and the corresponding residual oil saturations will be different .) The residual oil saturations are 8%, 13% and greater than 20%. The present of the third layer can be seen from the tracer response of PMCP but not PMCH. The S_{or} for the third layer could not be determined since the test was stopped before the third peak of PMCH broke through. If the test had continued, the calculated S_{or} for the third layer should be greater than 20%. Data from Well 25-10G is not as good as Well 81-10G and it is not used in this calculation. In the Proposed Collaborative Experiment Between Chevron Oil Field Research Corp. (COFRC) and Brookhaven National Laboratory (BNL) dated Jan. 17 of 1991, the residual oil saturation is estimated to be 40-60% in the test zone. This field example shows that although the first moment method is a very powerful method, it requires good quality data for interpretation.

CONCLUSIONS

The main conclusions from this study are the following.

1. The PFT data show a lot of fluctuation or noise.
2. The data from the first-stage tracer test of the 26R reservoir are significant.
3. There is fluid communication along the northwest-southeast boundary of the 26R and 31S reservoirs.
4. In the southeast boundary of the 26R reservoir where the two upper sequences of 26R disappear, fluid communication exists between the upper 26R and 31S NA through the lower 26R.
5. Inside the 26R reservoir, good fluid communication exists between the gas injectors in the upper 26R and the producers in the lower 26R
6. At this time, there is not enough information from the second stage tracer test of the 26R reservoir to determine if the main fault is a barrier to flow. PMCH data from wells located in the eastern sector appear to be noise. With the existing data, simulation results show much larger PMCH concentrations for wells located in the western sector of 26R and in 31S compared to these data.
7. For the tracer tests conducted at the shallow oil zone reservoir (SOZ), analysis of the tracer data indicates residual oil saturations from 8% to higher than 20% between Injector 34-10G and Well 81-10G.

For the 26R reservoir, more tracer data should be collected to see if larger PMCH concentrations breakthrough. A comparison between PMCH and PMCP data should give some indications as to whether the data are real or just noise. If there is a real breakthrough for PMCH in the western sector but not in the eastern sector, the main fault is a barrier to flow. This would give evidence other than the uneven gas-oil contact for both sectors.

For tracer tests conducted in the future, the injected concentration should be in the range of 100,000 pL/L. As indicated by Gunnar (1990), the PFT's are not expensive. Because a large amount of gas is injected and both the 26R and 31S contains the gas cap, it is better to use more tracers for better results and ease of interpretation. If the wells are shut in to control reservoir voidage, nothing can be done, but when the wells are not shut-in, tracer data should be collected.

A simple reservoir description has some limitations in that it cannot give the same solution or detailed information that a complicated reservoir description can. At the same time, it has advantages because it requires less computational time and effort. However, if the assumptions are clearly stated and understood, the simple reservoir description is as good as a complicated one. In this study, there are some discrepancies between the simulation results and the first-stage tracer test. The discrepancies are caused by the assumptions used in the simulation model. Although the flow is mainly single-phase in the upper 26R and NA of 31S, the flow is actually multiphase in the lower 26R and the C and D shales. The use of single-phase flow may still be applicable, but the effective thicknesses above the gas-oil contact at different well locations must be taken into account so that better matches to the breakthrough times are possible. If a complicated model is desired, a

better reservoir description could be used so that heterogeneity can be included. More gridblocks in the vertical direction should be used to capture detailed information about these reservoirs. It would require much more time and effort to include multiphase flow and detailed geologic data in the simulations. However, the data analysis and simulation model used in this study are sufficient to achieve all the objectives of the tests.

Table 1. General Information About the 26R Reservoir (from MER Performance Review)

Original Oil in Place	423.7 MMB
Estimated Recoverable Oil	211.9 MMB
Cumulative Production (8/31/90)	174.5 MMB
Remaining Reserves (9/1/90)	37.4 MMB
Drive	Gravity Drainage with Gas Injection for Pressure Maintenance
Active Producers (9/90)	50
Active Injectors (9/90)	9
Gas-Oil Ratio (8/90)	8521 scf/STB
Water Cut (8/90)	16.6%
Avg. Reservoir Pressure (8/89)	2520 psig

Table 2. Average Properties of 26R Sands

Megaunit	Porosity (%)	Permeability (md)	Water Saturation (%)
A-C	23.23	178	15.5
C-F	25.80	365	14.2
F-K	21.98	218	12.9
K-N	26.48	191	14.7
N-O	26.48	191	14.7

Table 3. Average Properties of Cores from 31S NA Shales

	No. of Samples	Mean Value
Porosity (%)	639	16.93
Permeability (md)	697	1.22
Water Saturation (%)	227	51.68
Oil Saturation (%)	390	12.92

Table 4. Current Available PFT's (adapted from Senum *et al.*, 1990)

No.	Symbol	Name (perfluoro-)	Chemical Formula
1	PDCB	dimethylcyclobutane	C_6F_{12}
2	PMCP	methylcyclopentane	C_6F_{12}
3	PMCH	methylcyclohexane	C_7F_{14}
4	oc-PDCH	ortho[a](cis)[b]-DCH[c]	C_8F_{16}
5	mt-PDCH	meta(trans)-DCH	C_8F_{16}
6	pc-PDCH	para(cis)-DCH	C_8F_{16}
7	PECH	ethylcyclohexane	C_8F_{16}
8	ot-PDCH	ortho(trans)-DCH	C_8F_{16}
9	mc-PDCH	meta(cis)-DCH	C_8F_{16}
10	pt-PDCH	para(trans)-DCH	C_8F_{16}
11	1 PTCH	1-trimethylcyclohexane	C_9F_{18}
12	2 PTCH	2-trimethylcyclohexane	C_9F_{18}

a ortho, meta, and para mean the 1, 2-, 1, 3-, and 1, 4-isomers.
b cis and trans means the alkyl groups (e.g., methyl) are on the same or opposite sides, respectively, of the molecule plane.

Table 5. Tracer Physical Properties and Partition Coefficients

Tracer	T_{fp} (°C)	T_b (°C)	ρ_L at 20°C (g/cc)	P_c (psia)	T_c (°R)	ω	Wt (lb_m/ lb mol)	δ_{ij}	K_T (vol./ vol.)
PMCP	-45	48	1.72	330.75	811.89	0.458	300.	0.22	0.65
PMCH	-39	76	1.80	310.17	870.03	0.482	350.	0.22	0.88
(oc+ot) PDCH	-22	102.6	1.87	274.89	915.57	0.532	400.	0.18	1.12

Table 6. Injected PMCH Concentrations for the Second-Stage Tracer Test

Injectors	Rate (MSCF/D)	C_0 (pL/L)
334-26R	20,000	1,400
344U-26R	17,953	1,561
355-26R	14,000	2,001
356-26R	25,000	1,121

Table 7. Injection Rate for the Western Sector of the 26R Reservoir

Megaunit	Injector 334-26R (Mscf/D)	Injector 344U-26R (Mscf/D)	Injector 355-26R (Mscf/D)	Injector 356-26R (Mscf/D)	Total Western Sector Injection (Mscf/D)
A-B	(A,B,B1) 10907	(A) 10944	(A,B,B1) 4735	(A,B,B1) 6013	32600
D-E	(D,E1) 4037	(C,D) 7008	(D) 2031	(C,D,E1,E2,E3) 18972	32048
F-J				(F,J) 2319	2319
K-M					0
N-P					0
Total Injection Volume by Well	14944	17953	6766	27304	66967

Table 8. Injection Rate for the Eastern Sector of the 26R Reservoir

Megaunit	Injector 366U-26R (Mscf/D)	Injector 377-26R (Mscf/D)	Injector 388U-26R (Mscf/D)	Injector 312A-36R (Mscf/D)	Injector 322-36R (Mscf/D)	Total Eastern Sector Injection (Mscf/D)
A-B	(A,B,B1) 0	(B1) 1514	(B,B1) 888			2402
D-E	(D,E1) 0	(D,E1,E2, E3) 20116	(C,D,E1, E2,E3) 18850	(D) 17282	(D,E1,E2) 19258	75506
F-J				(F) 5451	(F) 0	5451
K-M						0
N-P						0
Total Injection Volume by Well	0	21630	19738	22732	19258	83359

Table 9. Gas Injection Rates During the 26R Tracer Test

Injector Name	Gas Injection Rate (Mscf/D)
366U-26R (PMCP)	10,000
334-26R (PMCH)	20,000
344U-26R (PMCH)	17,953
355-26R (PMCH)	14,000
356-26R (PMCH)	25,000
377-26R	21,630
388U-26R	19,738
312A-36R	22,732
322A-36R	19,258
328-25R	10,000

Table 10. Completion Intervals for Tracer Injectors and Sampling Wells

Well Name	Well Completion	Perforation Interval (ft subsea)
366U-26R (PMCP)	A-E2	4339-4684
334-26R (PMCH)	A-E1	4554-4851
344U-26R (PMCH)	A-D	4415-4535
355-26R (PMCH)	A-D	4219-4486
356-26R (PMCH)	A-J	4249-4829
314A-26R	U26R	5198-5398
322-36R	L26R	-
386A-26R	B	-
327-25R	U31S	-
383-26R		-
326-26R	L26R	5592-5898
336-26R	UL26R	5811-5921
347-26R	UL26R	5573-6078
378A-26R	L26R	5019-5444
362-26R	B,U31S	-
363-26R	C,D	-
382-26R	N,A,B	-
384-26R	B,UL31S	-
332XU-36R	N,A	-

A = A Shale, B = B Shale, C = C Shale, D = D Shale, U = Upper, L = Lower, 31S = 31 Sands

Table 11. Average Velocity Between Injector 366U-26R and Sampling Wells

Well Name	Distance in ft from Tracer Injection Well (366U-26R)	Breakthrough Time (days)	Average Velocity (ft/day)
314A-26R	3625	220	16.5
322-36R	3700	220	16.8
386A-26R	1350	260	5.2
327-25R	2700	400	6.8
383-26R	2450	400	6.1
326-26R	2700	200	13.5
336-26R	2000	200	10.0
347-26R	1450	120	12.1
378A-26R	1450	200	7.3
362-26R	2625	200	13.1
363-26R	1875	200	9.4
382-26R	2850	200	14.3
384-26R	1850	260	7.1
332XU-36R	3875	380	10.2

Table 12. Production Rates and Gas-Oil Ratios of the Sampling Wells

Well Name	Oil (STB/D)	Water (STB/D)	Gas (Mscf/D)	Gas-Oil Ratio (scf/STB)
314A-26R	947	25	496	524
322-36R	76	9	1205	15855
386A-26R	26	2	776	29846
327-25R	22	146	310	14091
383-26R	81	117	1486	18348
326-26R	281	235	5191	18473
336-26R	225	224	5765	25622
347-26R	280	45	3605	12875
378A-26R	112	39	524	4679
362-26R	32	1	1041	32531
363-26R	52	683	561	10788
382-26R	15	0	593	39533
384-26R	17	0	854	50235
332XU-36R	120	2	2485	20708

Table 13. Amount of PMCP and PDCH Produced at Sampling Wells

Well Name	PMCP (std L)	oc-PDCH (std L)	ot-PDCH (std L)
314A-26R	0.0008	0.00166	0.00177
322-36R	0.00907	0.00174	0.00199
386A-26R	0.0004	0.00002	0.00002
327-25R	0.00014	0.00000	0.00001
383-26R	0.00059	0.00008	0.00011
326-26R	0.00686	0,00408	0.00116
336-26R	0.01148	0.00648	0.00599
347-26R	0.00766	0.00704	0.00345
378A-26R	0.00148	0.00056	0.00040
362-26R	0.00325	0.0011	0.00117
363-26R	0.00101	0.0001	0.00021
382-26R	0.00092	0.001	0.00135
384-26R	0.00086	0.00032	0.00011
332XU-36R	0.00125	0.00025	0.00024
Total	0.04577	0.02450	0.01800

Table 14. Average PMCP Produced per Well in Different Sectors

Sector	Average PMCP Produced per Well (std. liter)
Western Sector of the 26R Reservoir	0.0067
Eastern Sector of the 26R Reservoir	0.0053
31S Reservoir	0.0024

Table 15. Reservoir Description of 3D Tracer Flow at Conditions of the 26R Reservoir

Area (square mile)	
NX × NY × NZ	26 × 43 × 4
Porosity (fraction)	0.25 (26R), 0.16 (31S)
Permeability from top to bottom (md)	178, 365, 218, and 191
Constant Water Saturation from top to bottom (fraction)	0.155, 0.142, 0.129, and 0.147
Oil Saturation (fraction)	0.3
Residual Oil Saturation (fraction)	0.4
Reservoir Temperature (°F)	200
Initial Reservoir Pressure (psia)	2400
Longitudinal Dispersivity (ft)	100 and 150
Transverse Dispersivity (ft)	100 and 150
Tracer Injection Interval from first to second stage (days)	18 and 17
Total Number of Tracers Used	3
Number of Injectors	18
Number of Producers	29

Well Name	Gridblock Completed in the Z Direction	Gas Rate (lb mol/D)
366U-26R (PMCP)	1 and 2	15923
334-26R (PMCH)	1 and 2	14103 and 5214
344U-26R (PMCH)	1 and 2	7131 and 4558
355-26R (PMCH)	1 and 2	12687.2 and 5437
356-26R (PMCH)	1, 2, and 3	3855, 12178, and 1489
377-26R	1 and 2	5961 and 1883
388U-26R	1 and 2	9484
312A-26R	2 and 3	1812
322-26R	2	2234 and 13730
328-25R	1 and 2	584 and 12406
314A-26R*	4	1311
322-36R*	4	3186
325-26R*	4	5817
386A-26R*	4	2050
327-25R*	4	819
383-26R*	4	3958
326-26R*	3 and 4	13220
336-26R*	4	15242
347-26R*	4	9532
378A-26R*	3 and 4	1385
362-26R*	2 to 4	2752
363-26R*	4	1483
382-26R*	1 to 4	1568
384-26R*	2 to 4	2258
332XU-36R*	3 and 4	6570
315-26R	4	12207
358A-26R	4	7469
353-26R	2 to 4	1258
361-26R	2 to 4	2945
317-25R	4	1005
326-25R	4	3279

312-36R	4	7935
338-25R	4	1719
371-25R	4	1793
381-35R	4	4690
331-26R	2 to 4	111
341A-26R	2 to 4	674
322-26R	2 to 4	74
315-25R	4	8281

Note: Wells with asterisks are tracer sampling wells.

Table 16. Initial Fluid Descriptions

Initial Hydrocarbon Composition (mole fraction)

CO_2	0.0022	C_{7-13}	0.0985
C_1	0.7228	C_{14-23}	0.0525
C_{2-3}	0.0559	C_{24^+}	0.0227
C_{4-6}	0.0454		

Component Critical Properties

Component	P_{ci} (psia)	T_{ci} (°R)	V_{ci} (cu ft/lb mol)	ω_i	Parachor	W_{ti} (lb_m/lb mol)
CO_2	1069.87	547.56	1.506	0.2250	49.00	44.01
C_1	667.20	343.08	1.586	0.008	71.00	16.04
C_{2-3}	655.26	616.19	2.876	0.1290	133.94	36.78
C_{4-6}	488.65	835.81	4.979	0.2417	230.85	70.15
C_{7-13}	333.91	1057.62	8.668	0.5782	368.15	129.38
C_{14-23}	251.11	1287.40	15.531	0.8660	675.64	241.50
C_{24^+}	240.42	1599.33	28.562	1.2116	989.33	441.28

Table 17. Amount of PMCH Produced at Sampling Wells

Well Name	PMCH (std L)
314A-26R	0.00031
322-36R	0.00046
386A-26R	0.00207
327-25R	0.00015
383-26R	0.00065
326-26R	0.01488
336-26R	0.00462
347-26R	0.00255
378A-26R	0.001
362-26R	0.00066
363-26R	0.00133
382-26R	0.00232
384-26R	0.00087
332XU-36R	0.00161
Total	0.03300

Table 18. Average Velocity Between the Closest PMCH Injector and Sampling Wells

Well Name	Horizontal Distance from Closest Tracer Injection Well (ft)	Breakthrough Time (days)	Average Velocity (ft/day)
314A-26R	1375	120	11.5
322-36R	4125	300	13.75
386A-26R	1900	130	14.6
327-25R	3300	220	15
383-26R	2500	260	9.6
326-26R	1500	90	16.7
336-26R	1375	110	12.5
347-26R	1000	110	9.1
378A-26R	1900	100	19.0
362-26R	2150	100	21.5
363-26R	1375	120	11.5
382-26R	2750	100	27.5
384-26R	2100	120	17.5
332XU-36R	4500	240	18.8

Table 19. Hydrocarbon Analysis of Reservoir Fluid Sample from Well 73-11G of the SOZ Reservoir

Component	Weight %	Mole %	Density @ 60°F (gm/cc)	°API @ 60°F	MW
C1	0.158	2.679			
C2	0.003	0.027			
C3	0.017	0.106			
i-C4					
n-C4	0.012	0.057			
i-C5					
n-C5	0.007	0.033			
C6	0.055	0.207			
Heavier	99.748	96.891	0.9296	20.6	280

Table 20. SOZ Fluid Description from Well No. 73-11G and Expert System in UTCOMP

Component	Mole Fraction	Pc (psia)	Tc (°R)	Vc (cuft/lb-mole)	ω	MW (lb-m/lb-mole)
C1	0.0268	667.2	343.08	1.59	0.0080	16.04
C2-3	0.0013	629.5	648.49	3.12	0.144	41.25
C4-6	0.0030	453.5	885.61	5.56	0.2769	79.24
C7-14	0.4200	320.4	1080.94	9.30	0.6054	137.85
C15-22	0.2389	247.1	1298.16	15.94	0.8816	249.85
C23-31	0.1481	235.0	1474.70	22.88	1.1195	367.46
C32-45	0.1049	238.6	1671.13	31.83	1.3130	519.22
C46+	0.0570	257.1	1981.73	47.76	1.2393	786.26

Methane was added from 2.68 % to 3.3 % to match the bubble point pressure (140 psia) of the lab data at 140°F.

Table 21. Equilibrium Ratio or K value from Different Methods at Conditions of the SOZ Reservoir

Tracer Name	K value from Raoult's Law	K value from Peng-Robinson EOS ($\delta_{ij} = 0$)	K value from Unifac Model	K value from Peng-Robinson EOS ($\delta_{ij} = 0.22$)
PMCP	1.14	1.9	6.97	46.7
PMCH	0.45	0.73	4.29	28.8

Table 22. Tracer Partition Coefficients from Different Methods at Conditions of the SOZ Reservoir

Tracer Name	K_T from Raoult's Law	K_T from Peng-Robinson EOS ($\delta_{ij} = 0$)	K_T from Unifac Model	K_T from Peng-Robinson EOS ($\delta_{ij} = 0.22$)
PMCP	63.8	38.3	10.44	1.56
PMCH	161.7	99.7	16.96	2.53

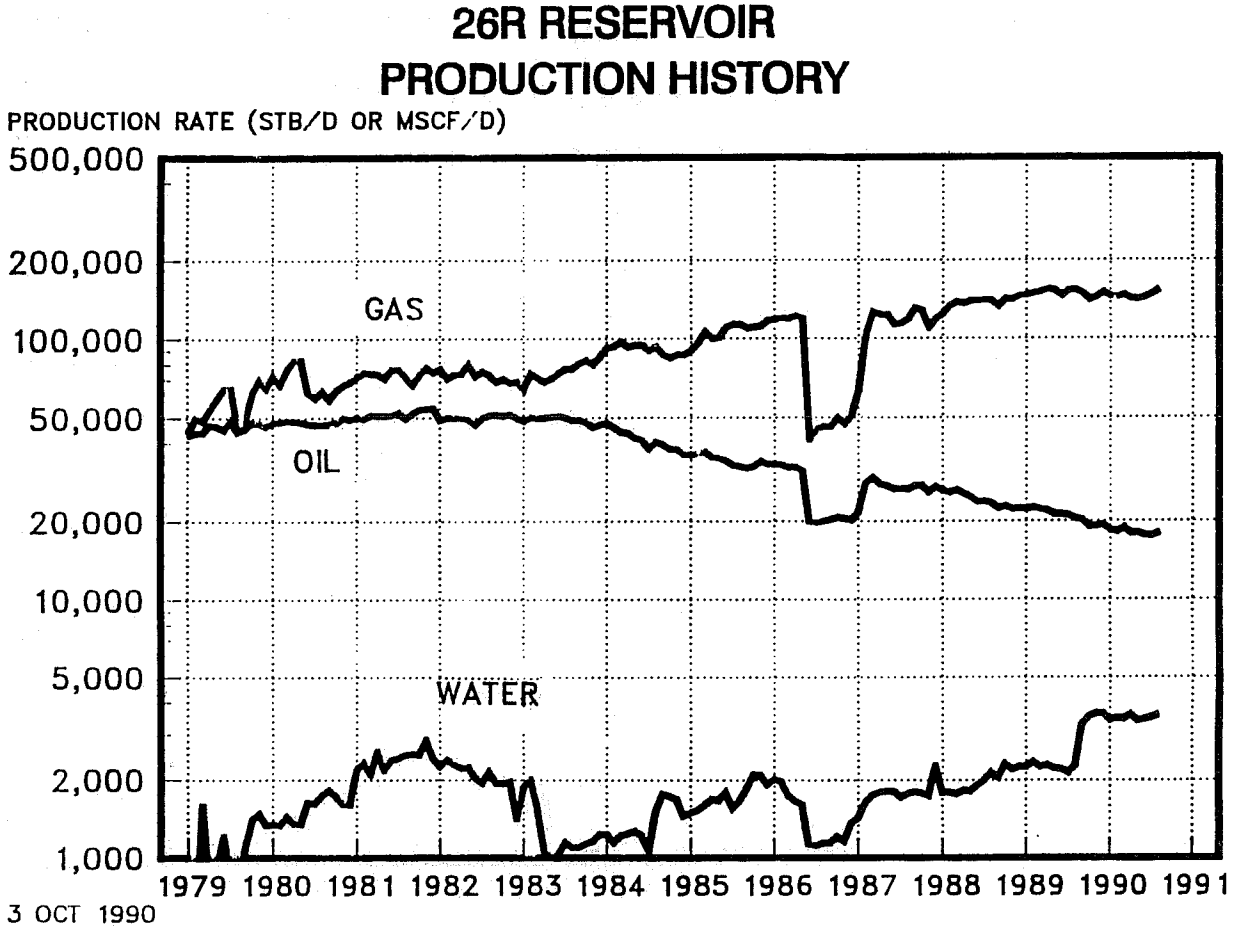

Fig. 1 26R reservoir production history (from MER Performance Review, 1990)

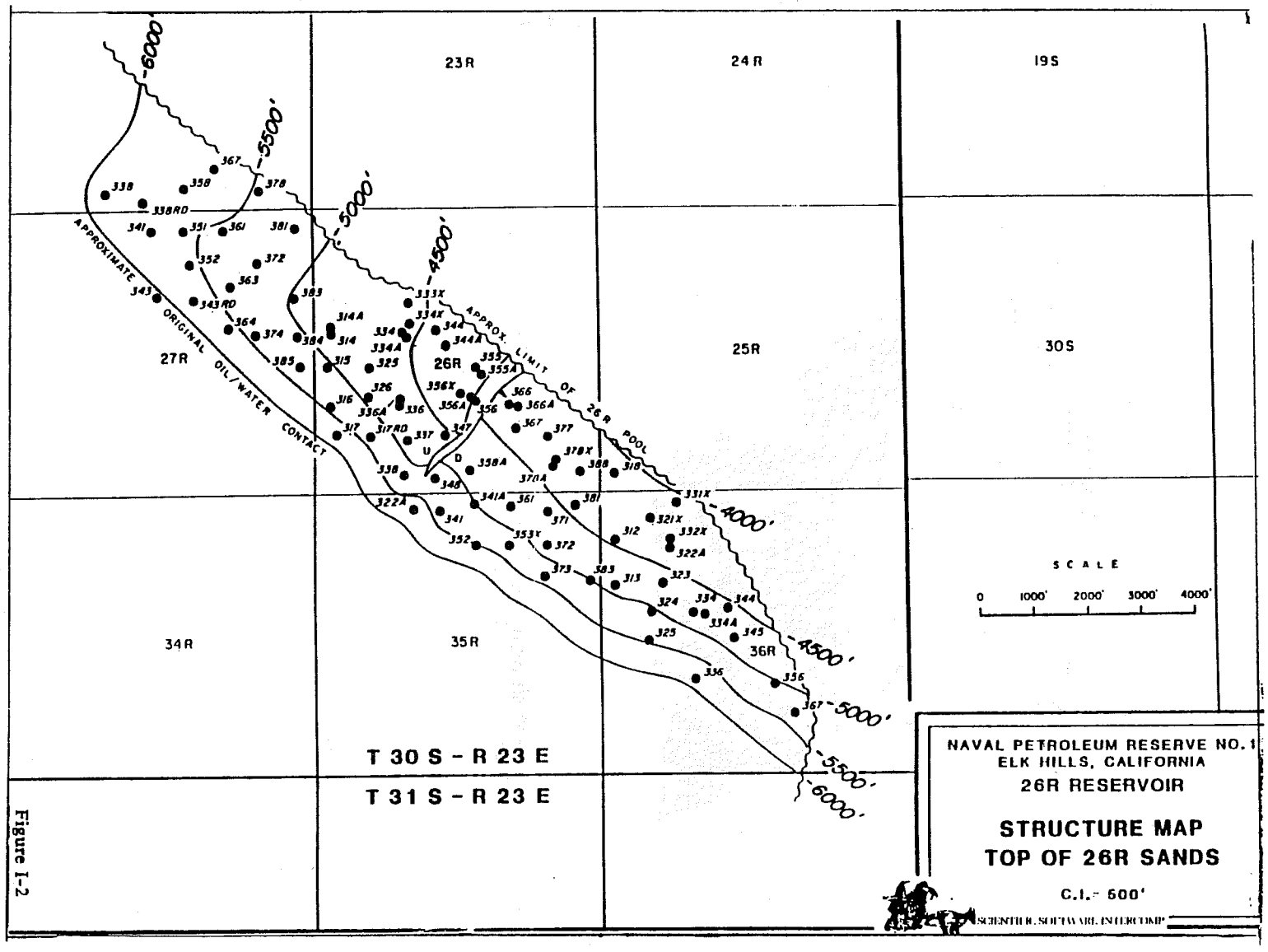

Figure I-2

Fig. 2 Structure map of the 26R reservoir (from Rial, 1990)

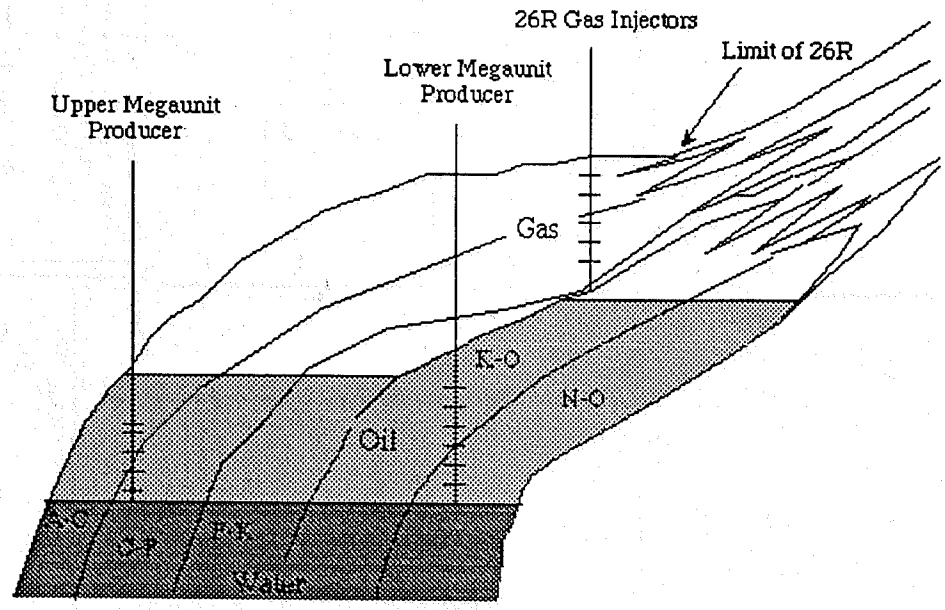

Fig. 3 Cross-section showing locations of producers relative to gas injectors for 26R gas injection project (from MER Performance Review, 1990)

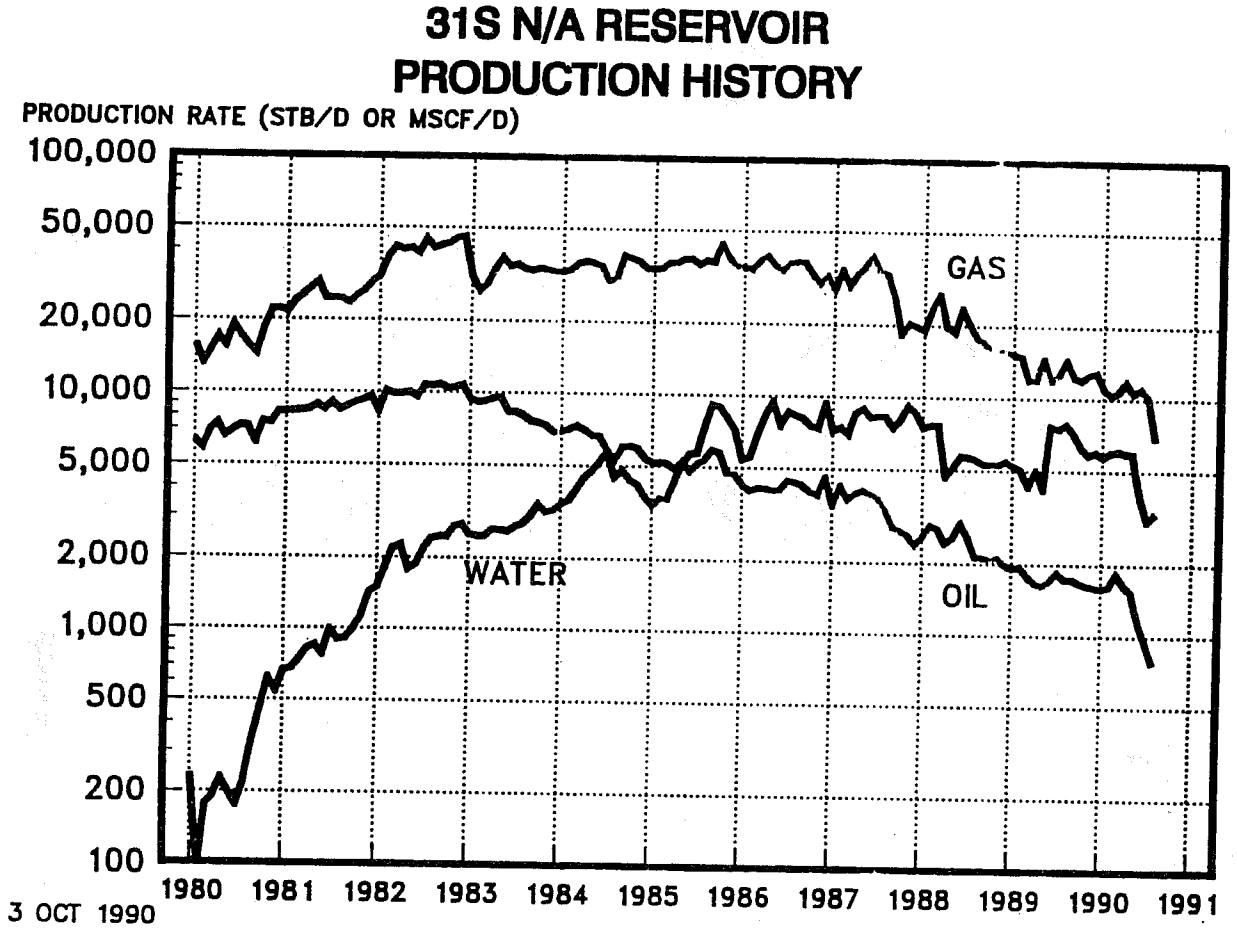

Fig. 4 31S N/A reservoir production history (from MER Performance Review, 1990)

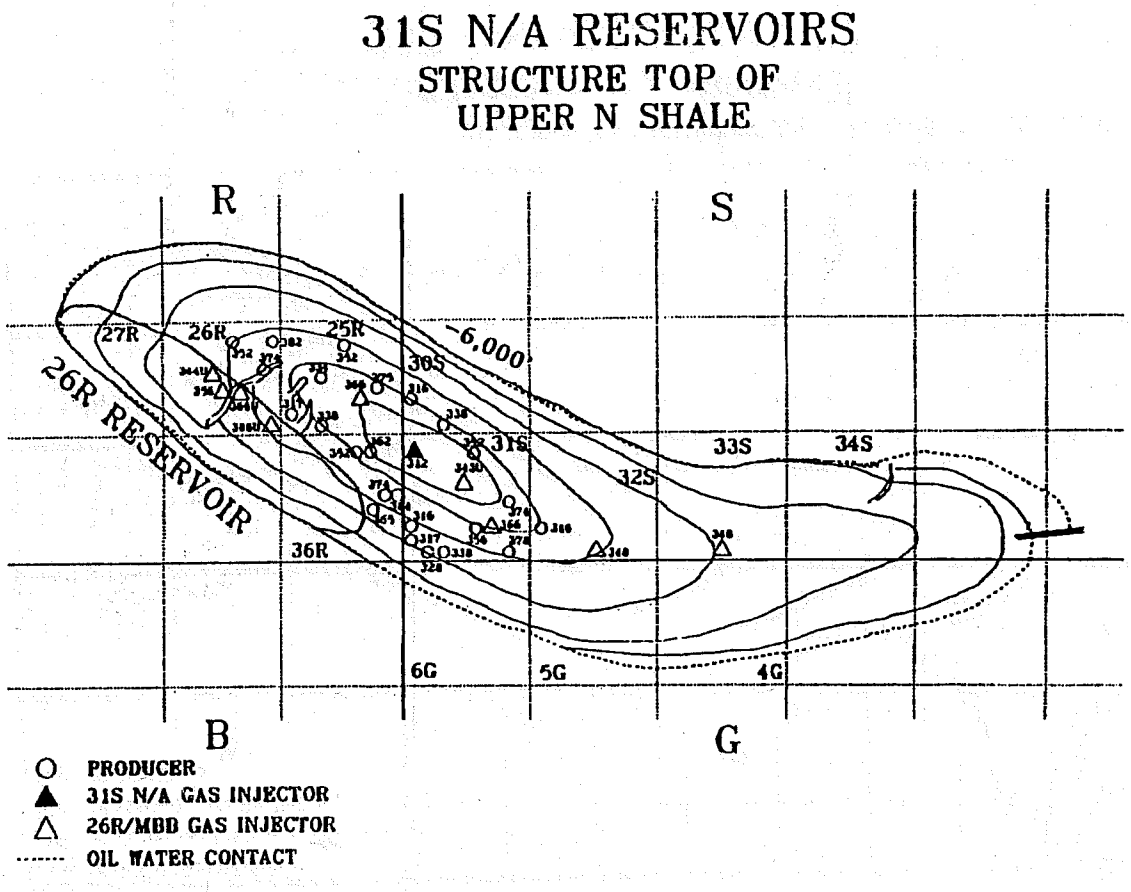

Fig. 5 Structure map of 31S reservoir

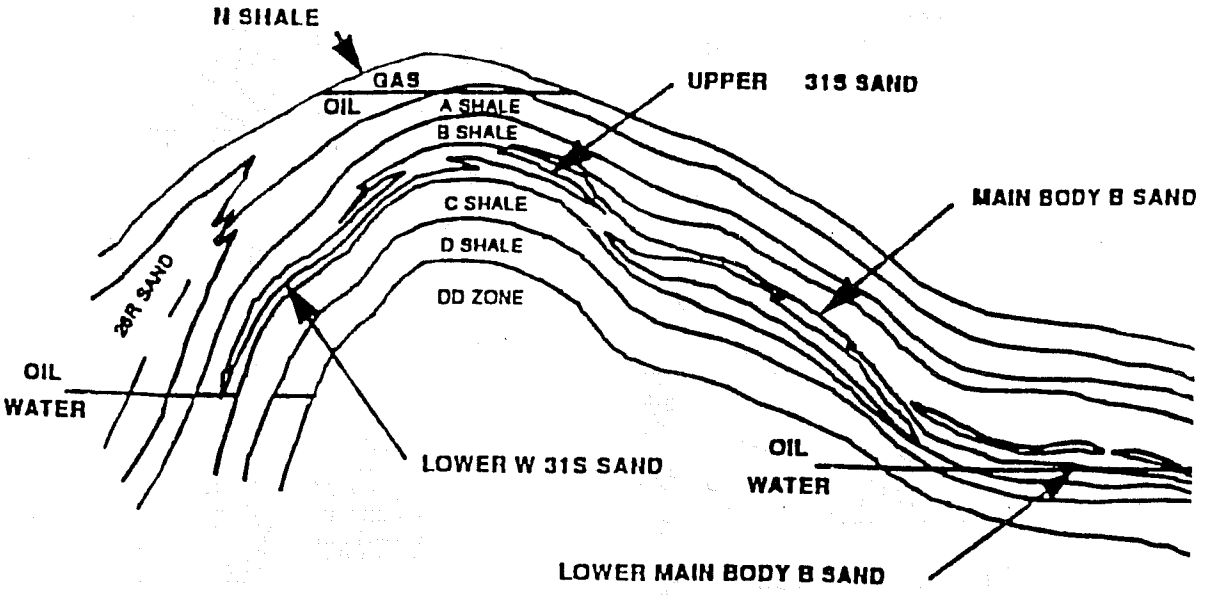

Fig. 6 Cross-section showing relationship between 26R sands and NA shales of 31S reservoir

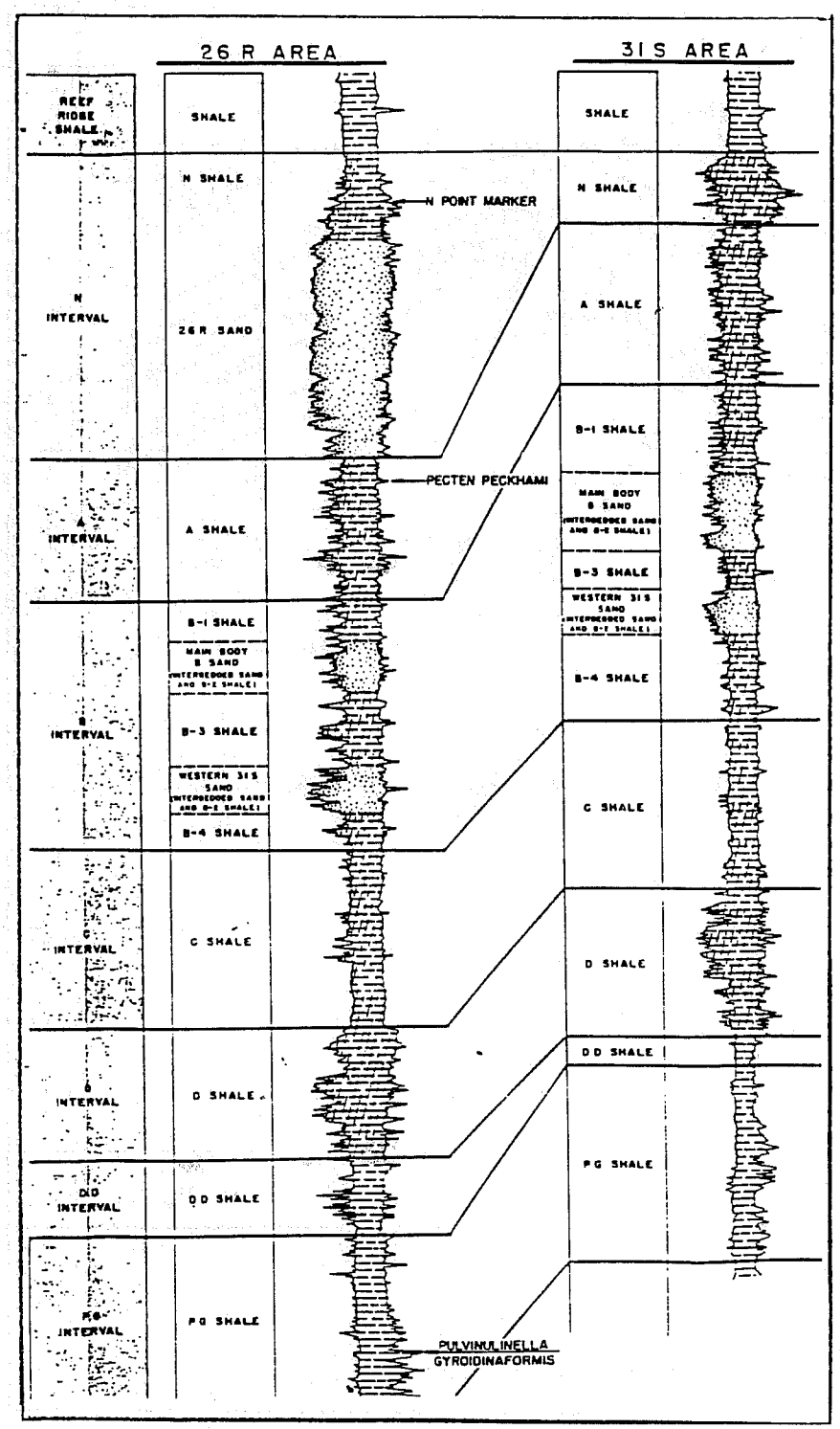

Fig. 7 Composite cross-section showing 26R interval and the relationship between the N/A reservoir interval in the 31S area
(from Watson, 1990)

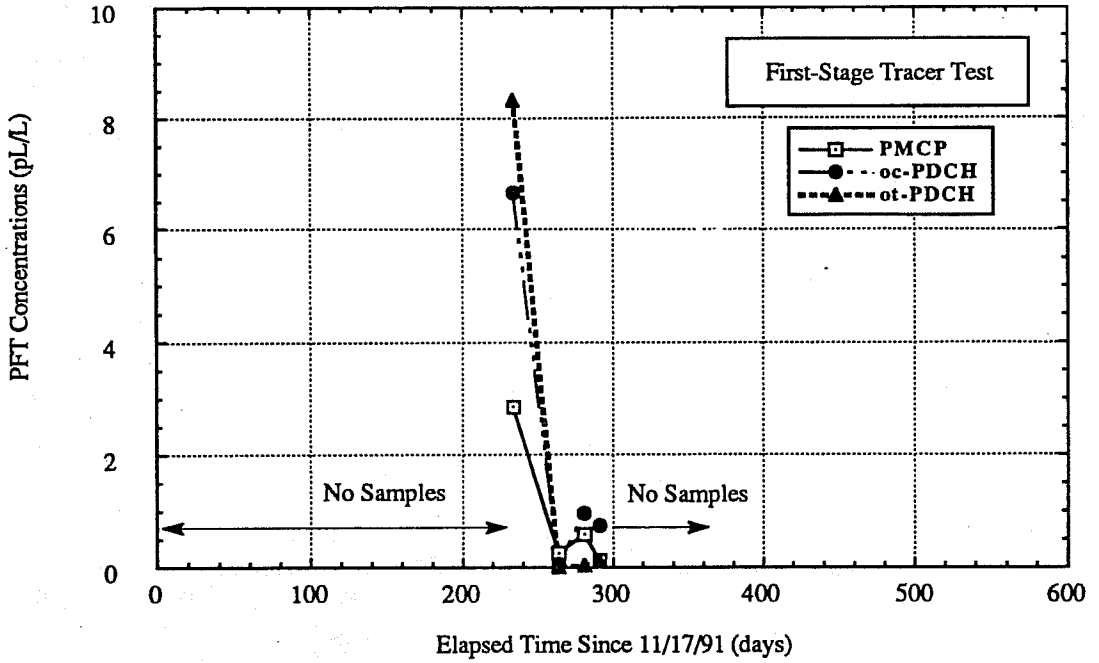

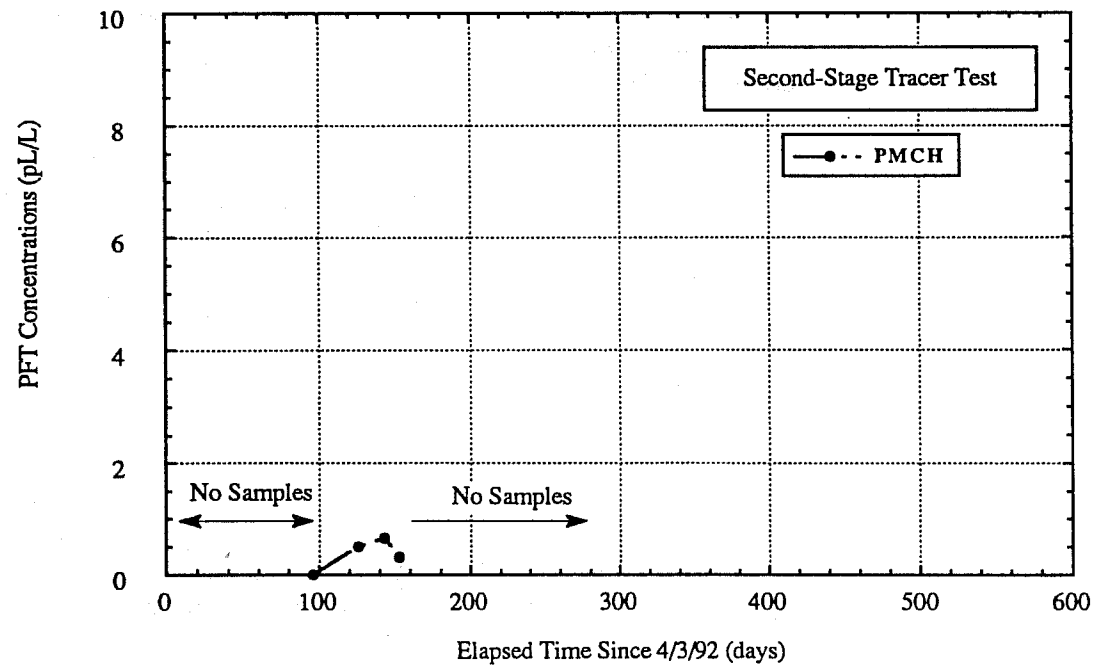

Fig. 8 Produced PFT concentrations from Well No. 314A-26R

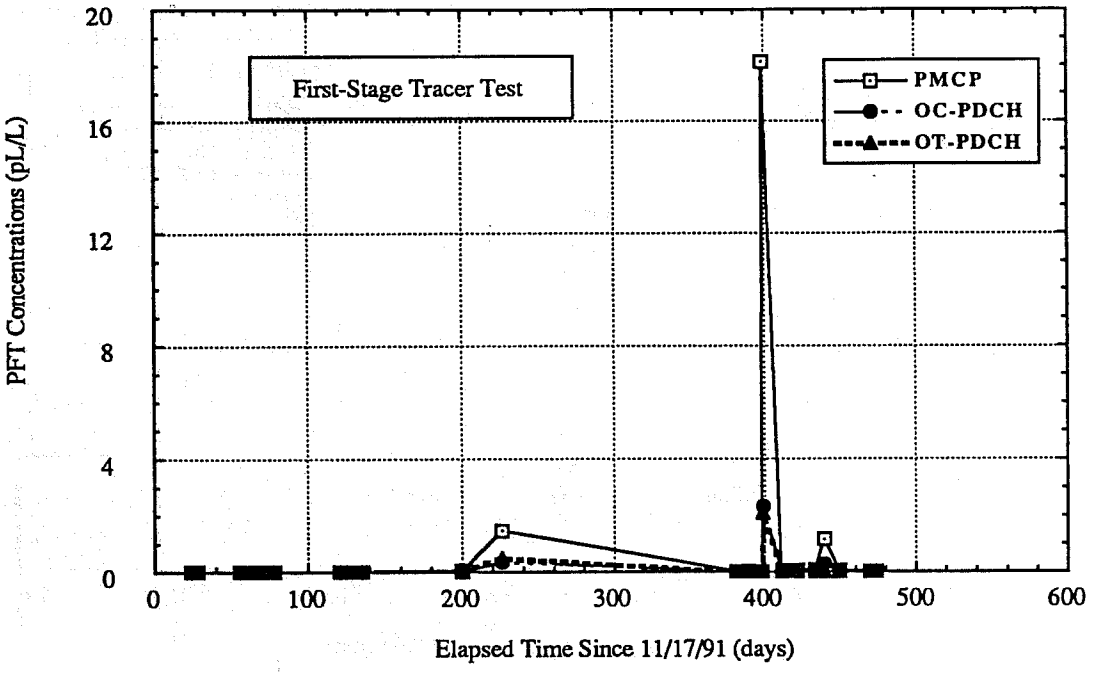

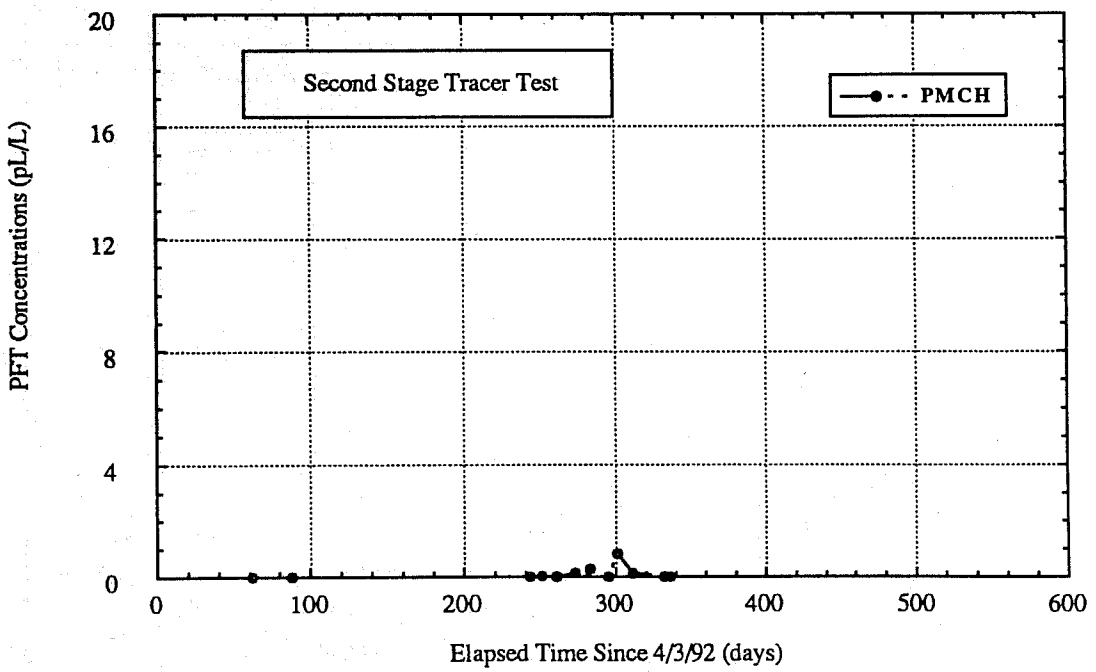

Fig. 9 Produced PFT Concentration from Well No. 322-36R

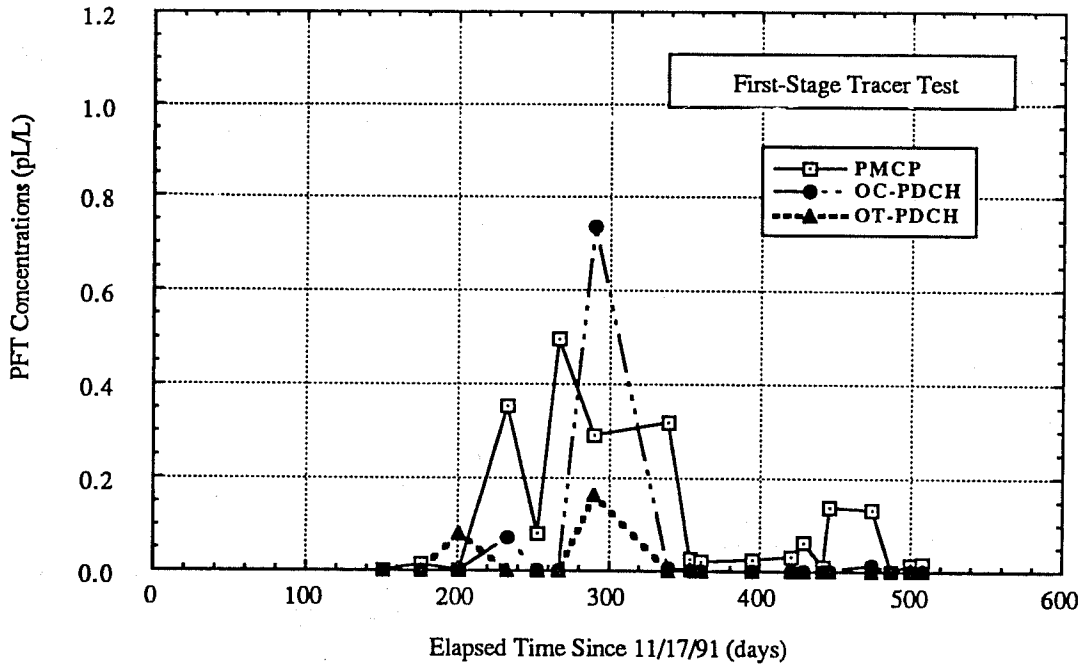

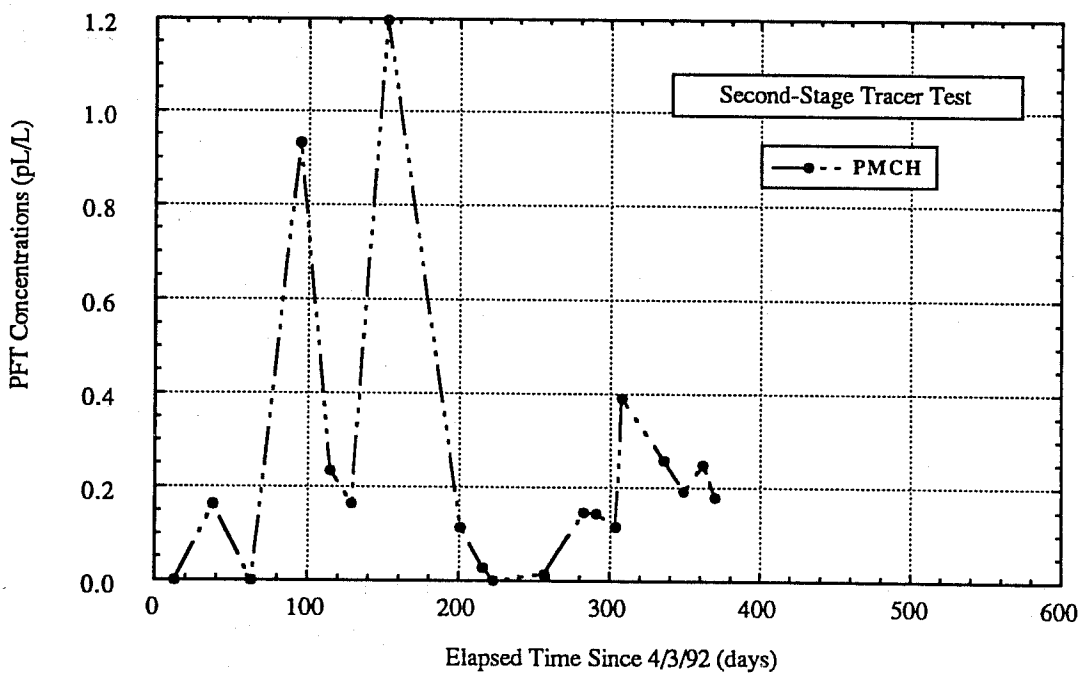

Fig. 10 Produced PFT concentrations from Well No. 326-26R

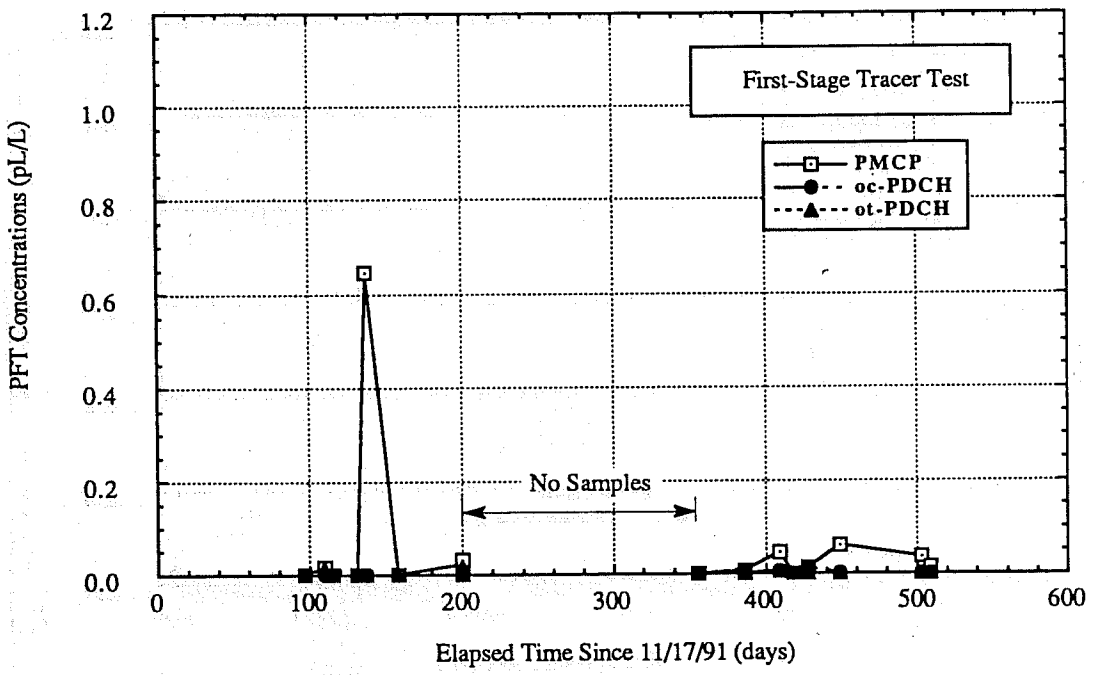

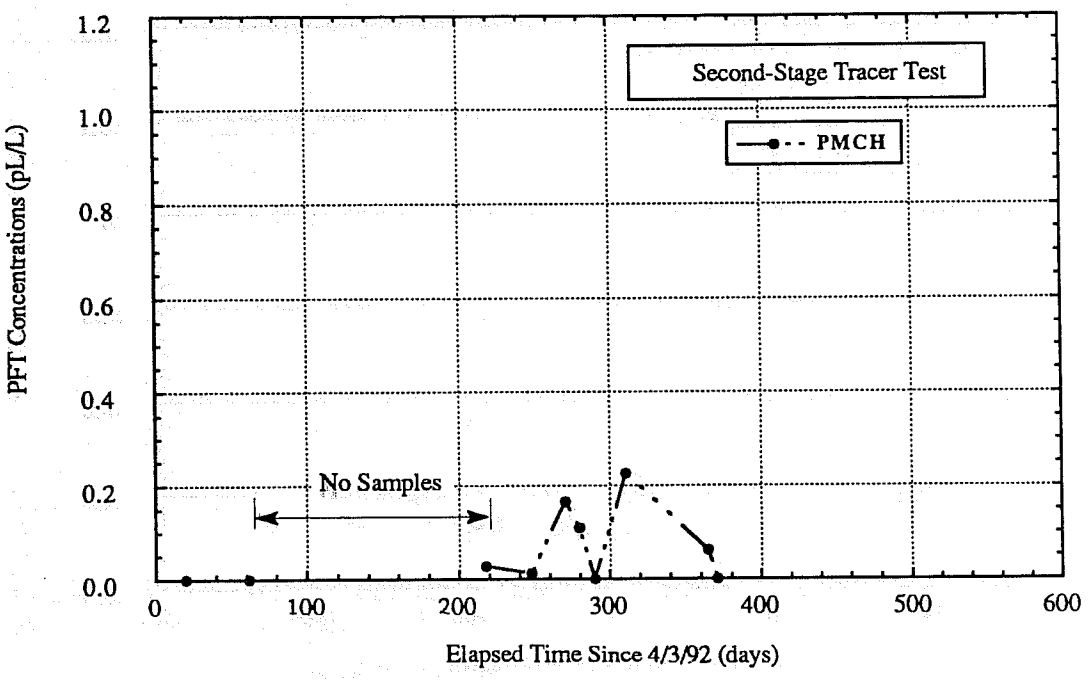

Fig. 11 Produced PFT concentrations from Well No. 327-25R

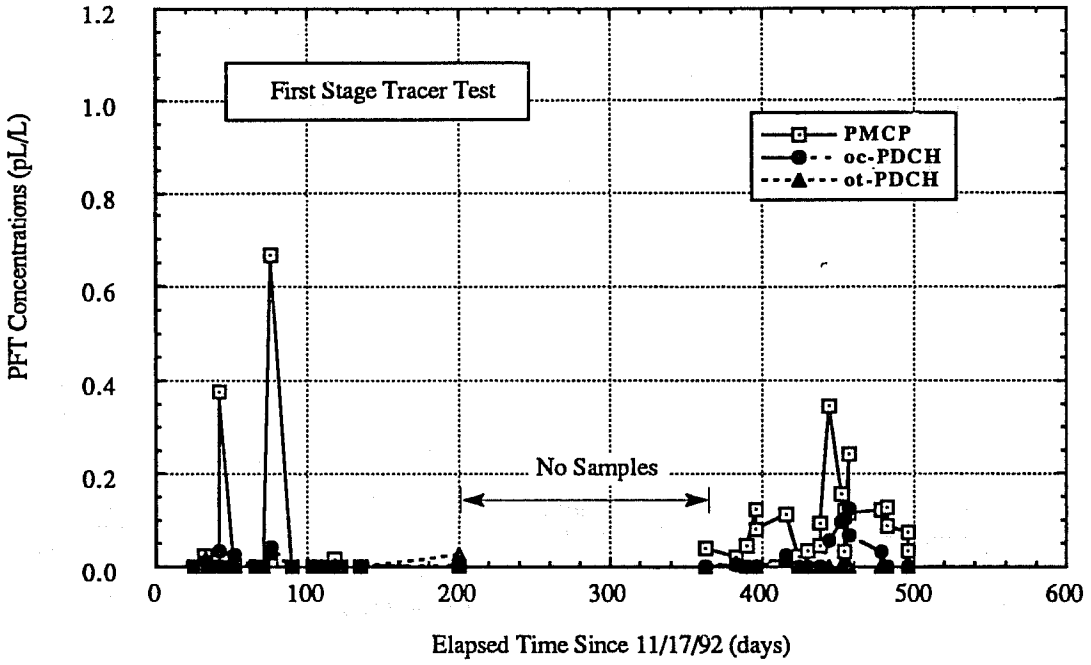

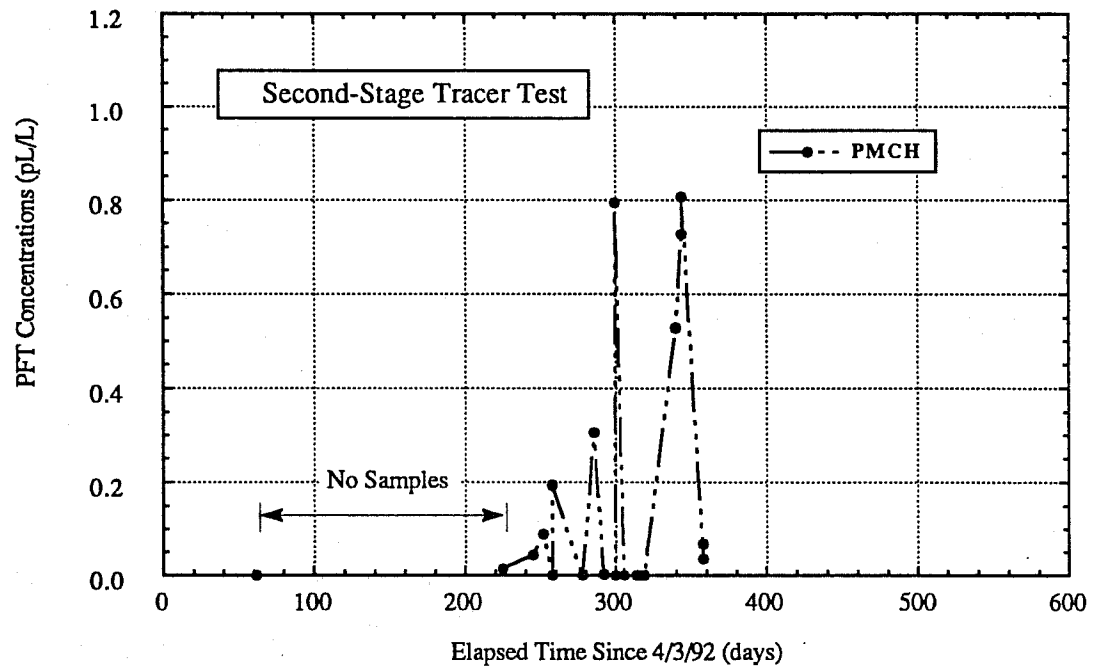

Fig. 12 Produced PFT concentrations from Well No. 332XU-36R

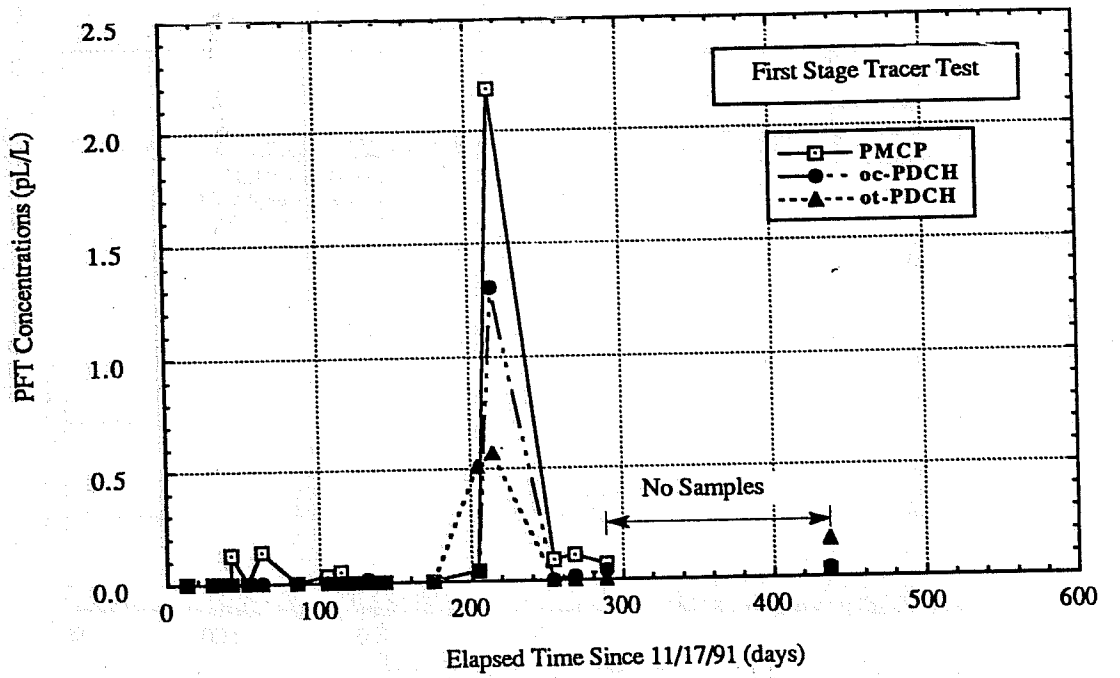

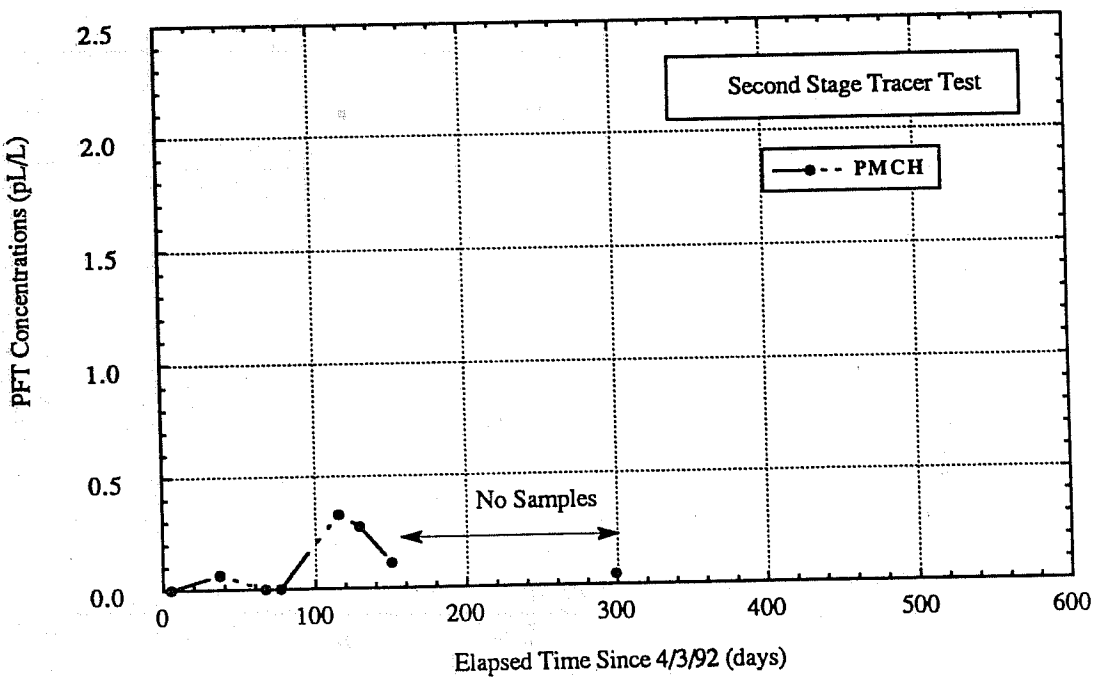

Fig. 13 Produced PFT concentrations from Well No. 336-26R

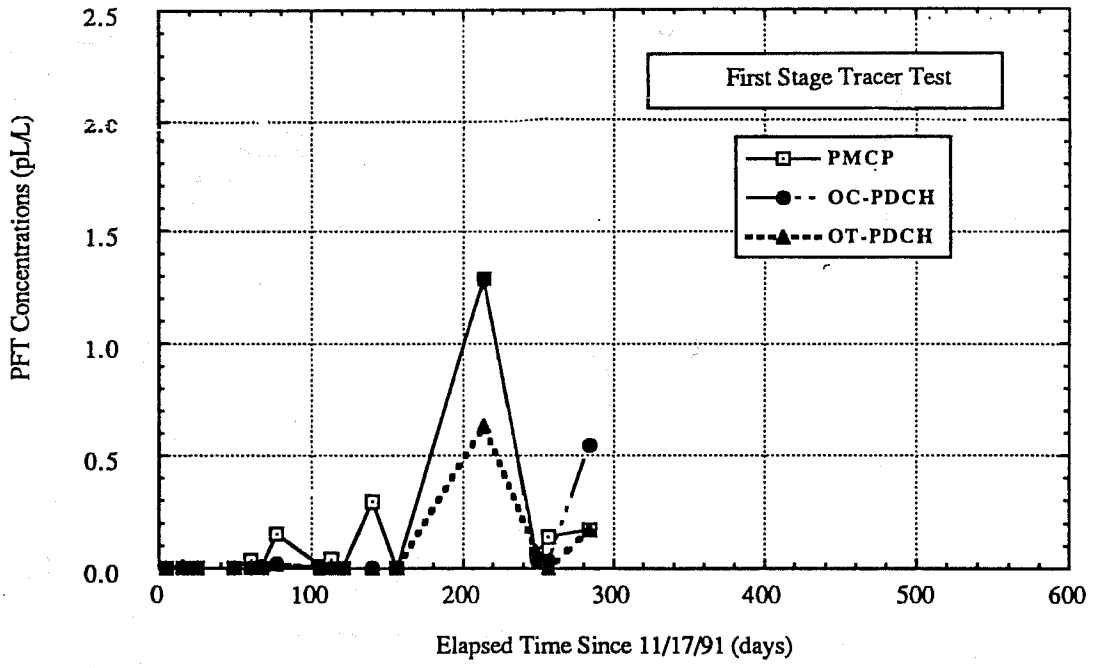

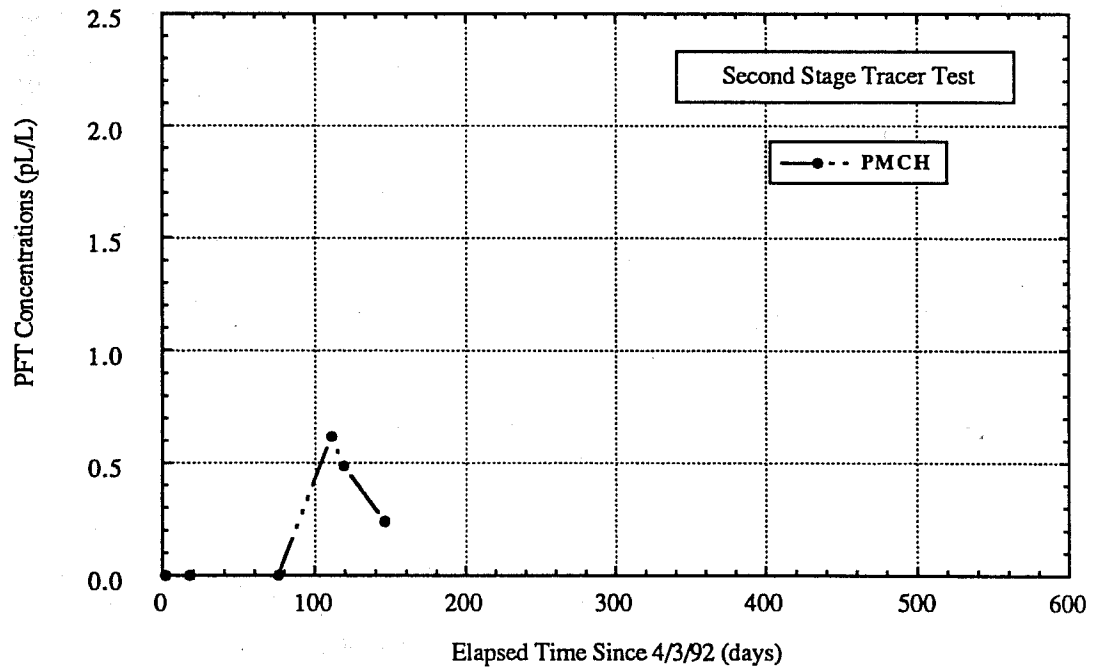

Fig. 14 Produced PFT concentrations from Well No. 347-26R

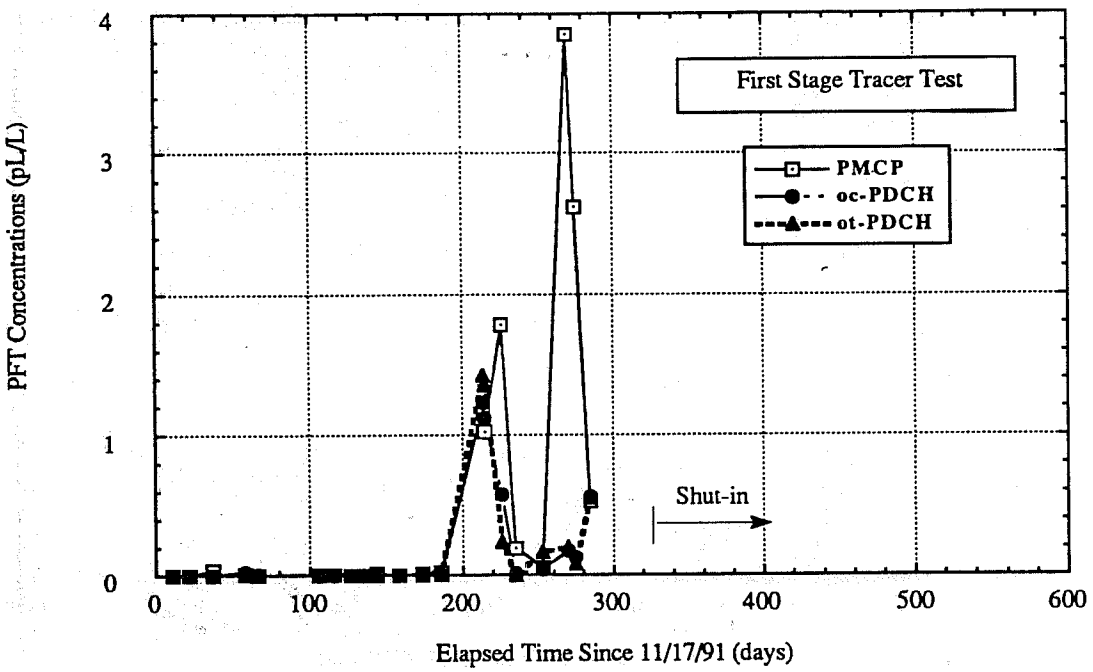

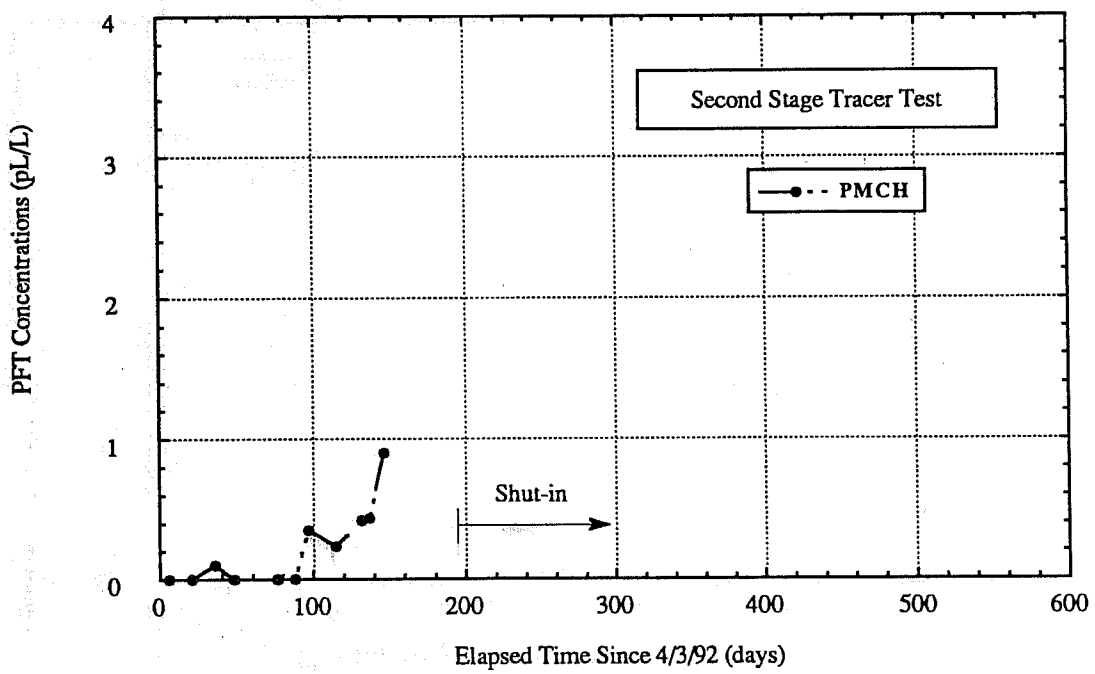

Fig. 15 Produced PFT concentrations from Well No. 362-26R

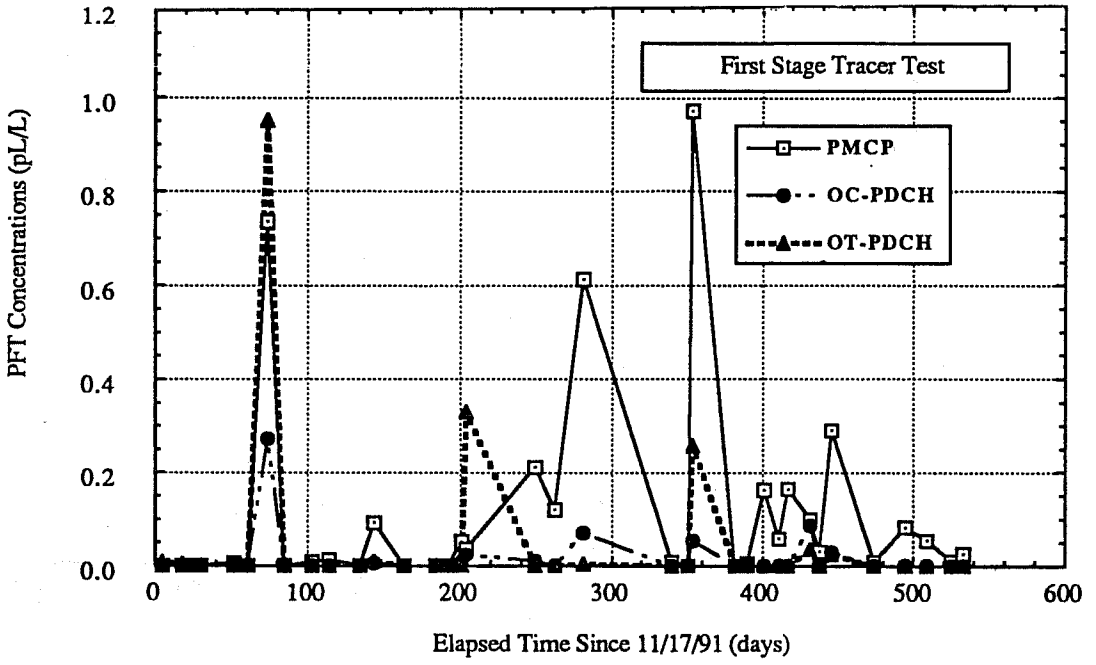

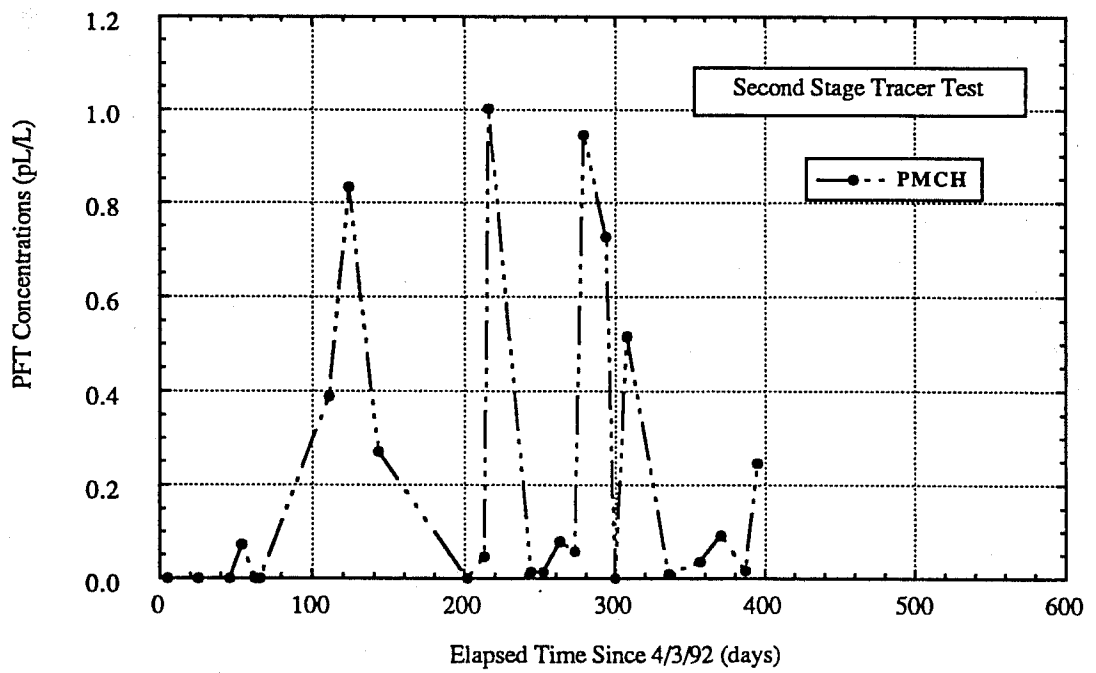

Fig. 16 Produced PFT concentrations from Well No. 363-26R

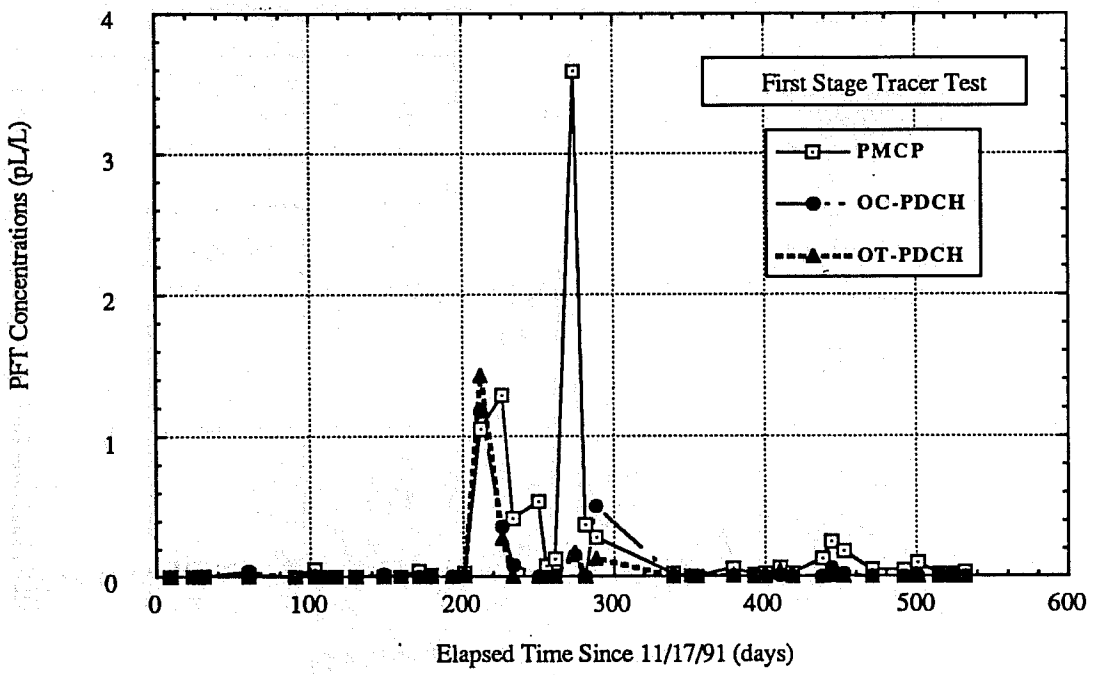

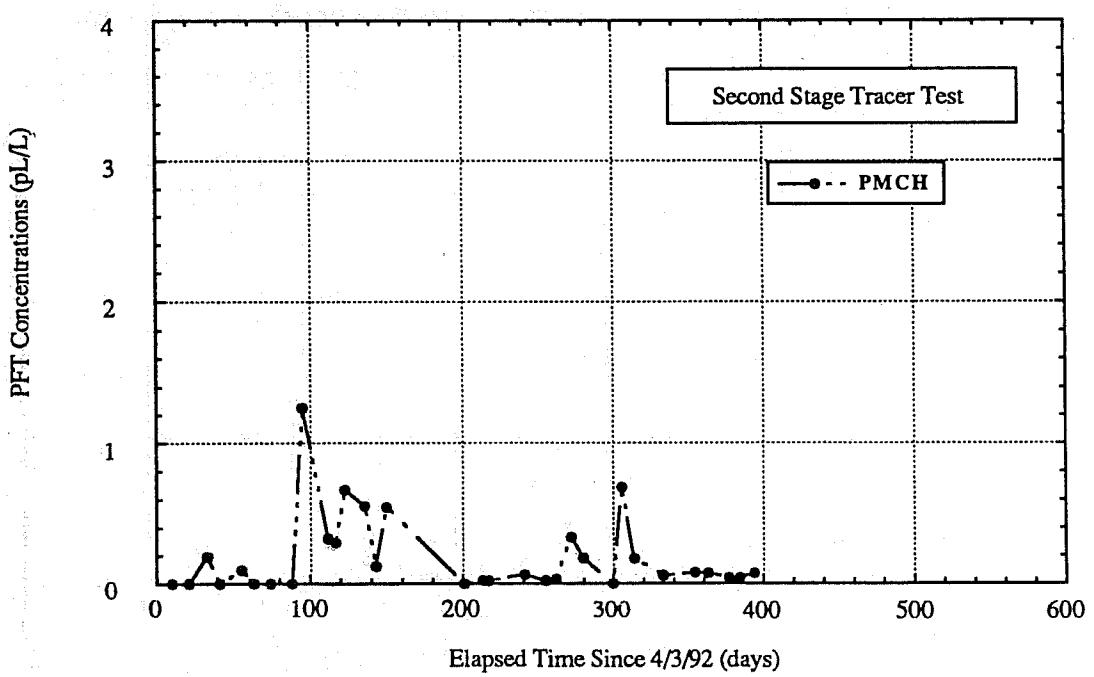

Fig. 17 Produced PFT concentrations from Well No. 378A-26R

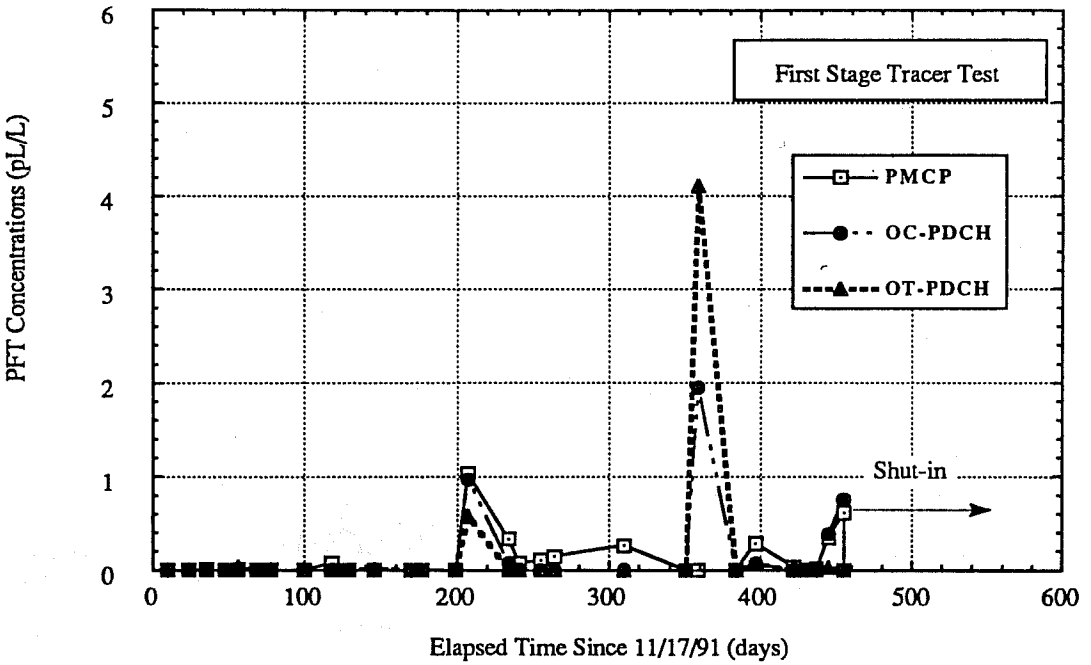

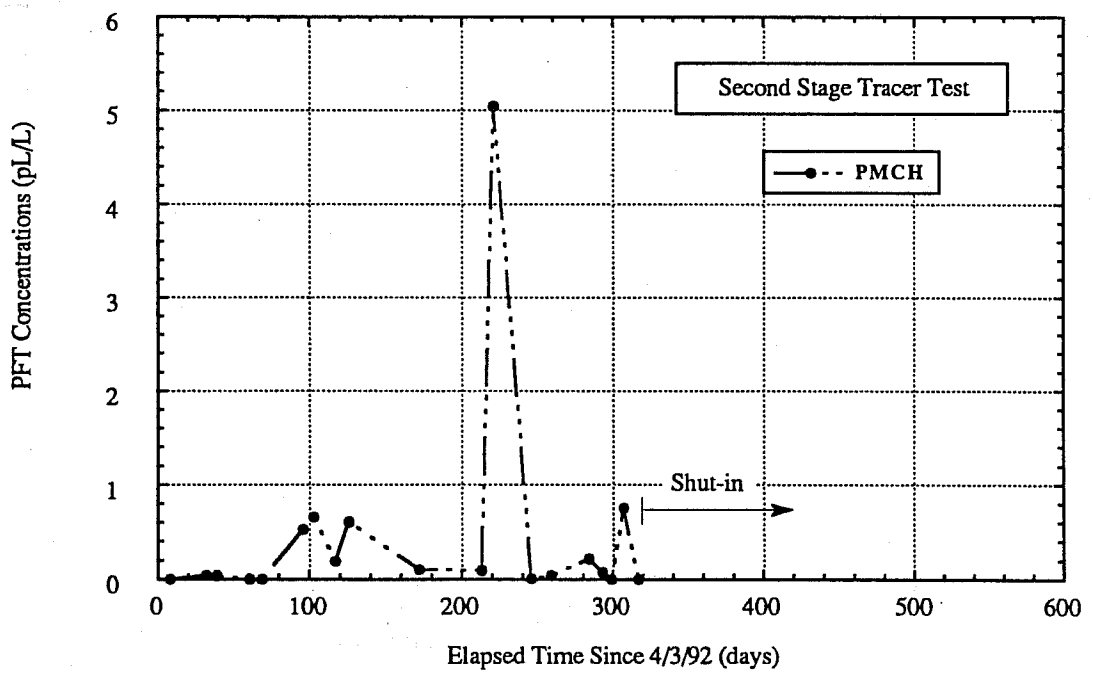

Fig. 18 Produced PFT concentrations from Well No. 382-26R

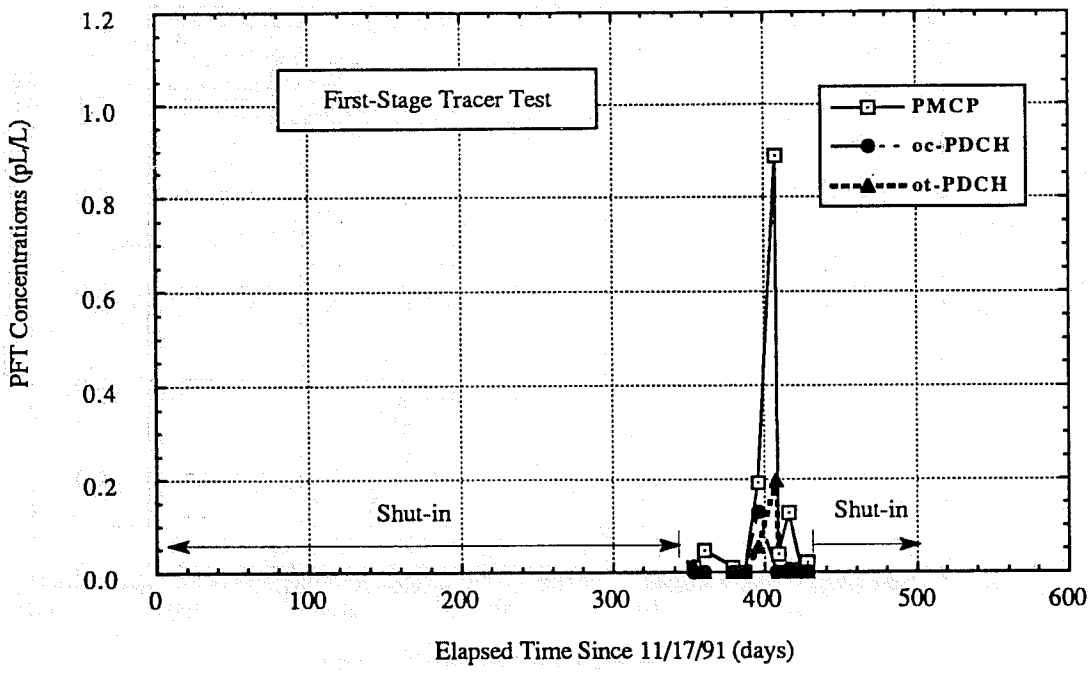

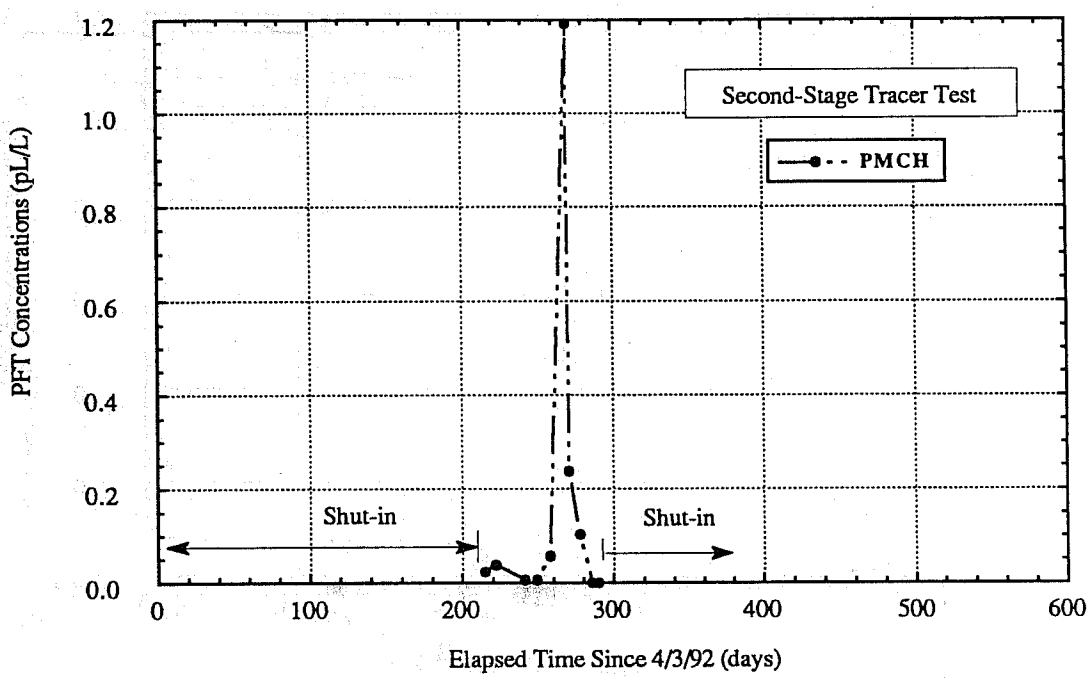

Fig. 19 Produced PFT concentrations from Well No. 383-26R

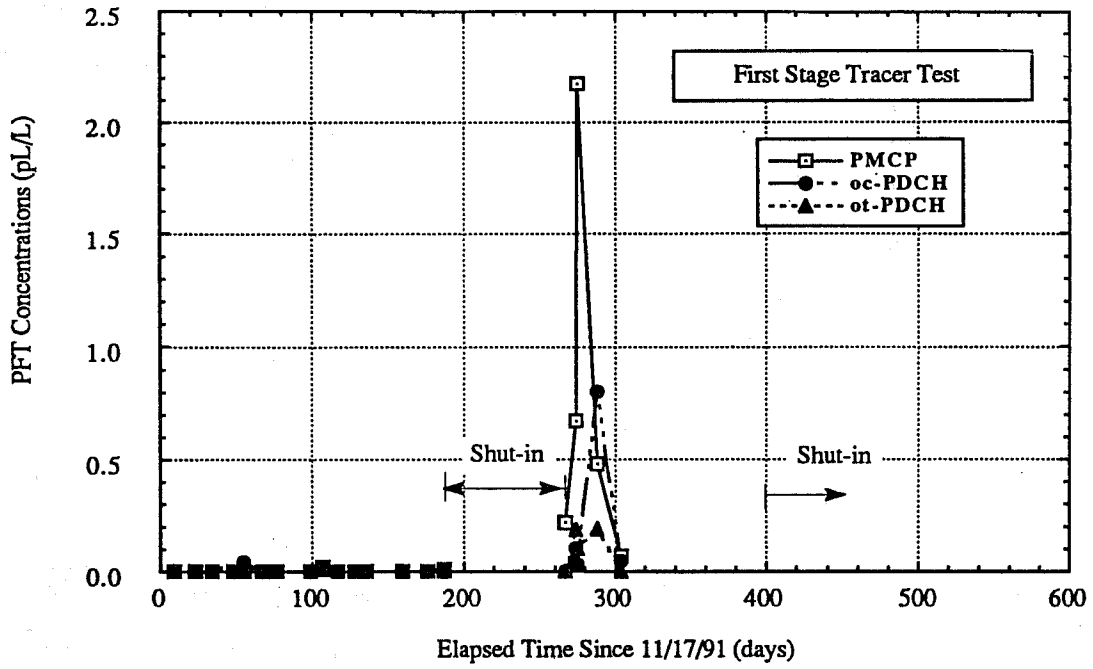

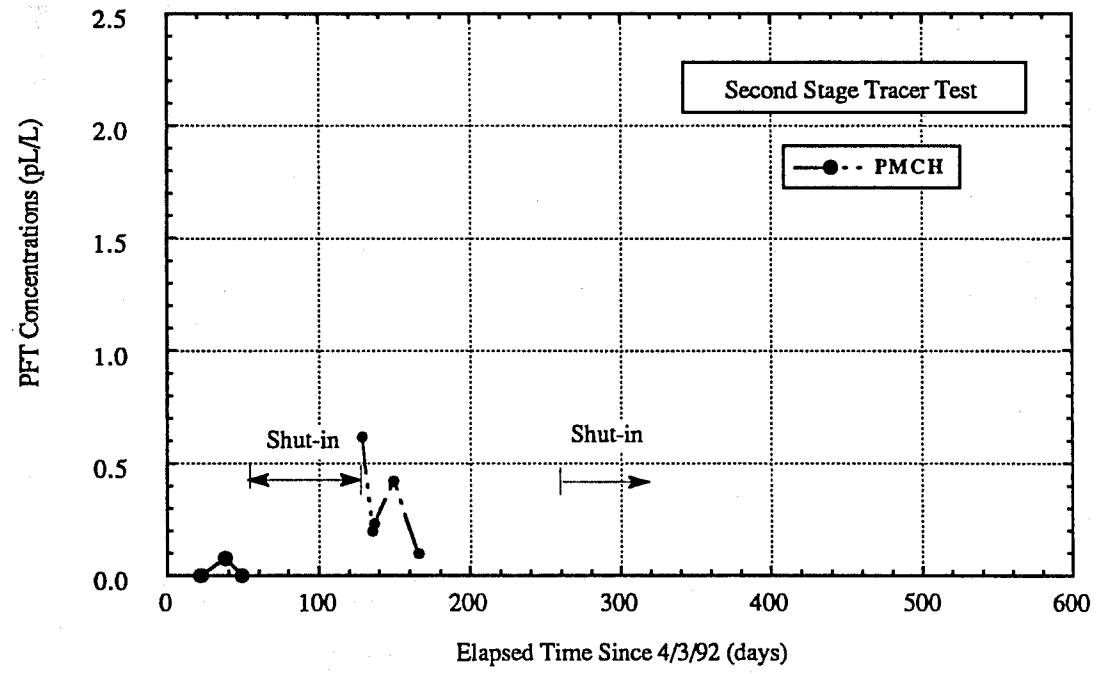

Fig. 20 Produced PFT concentrations from Well No. 384-26R

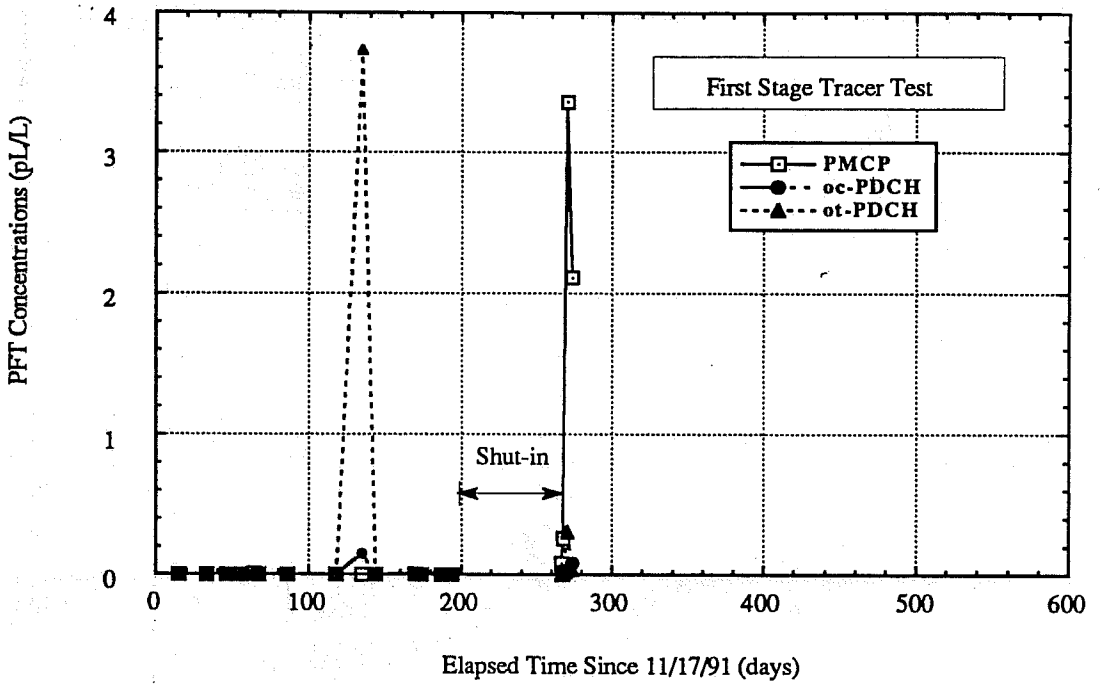

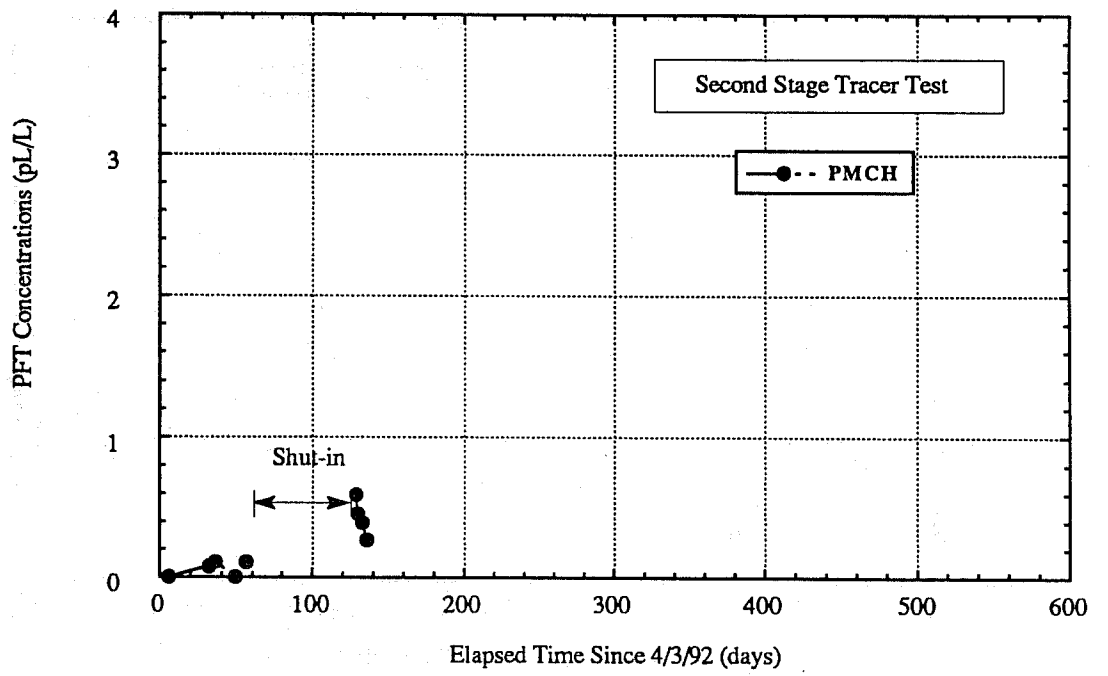

Fig. 21 Produced PFT concentrations from Well No. 386A-26R

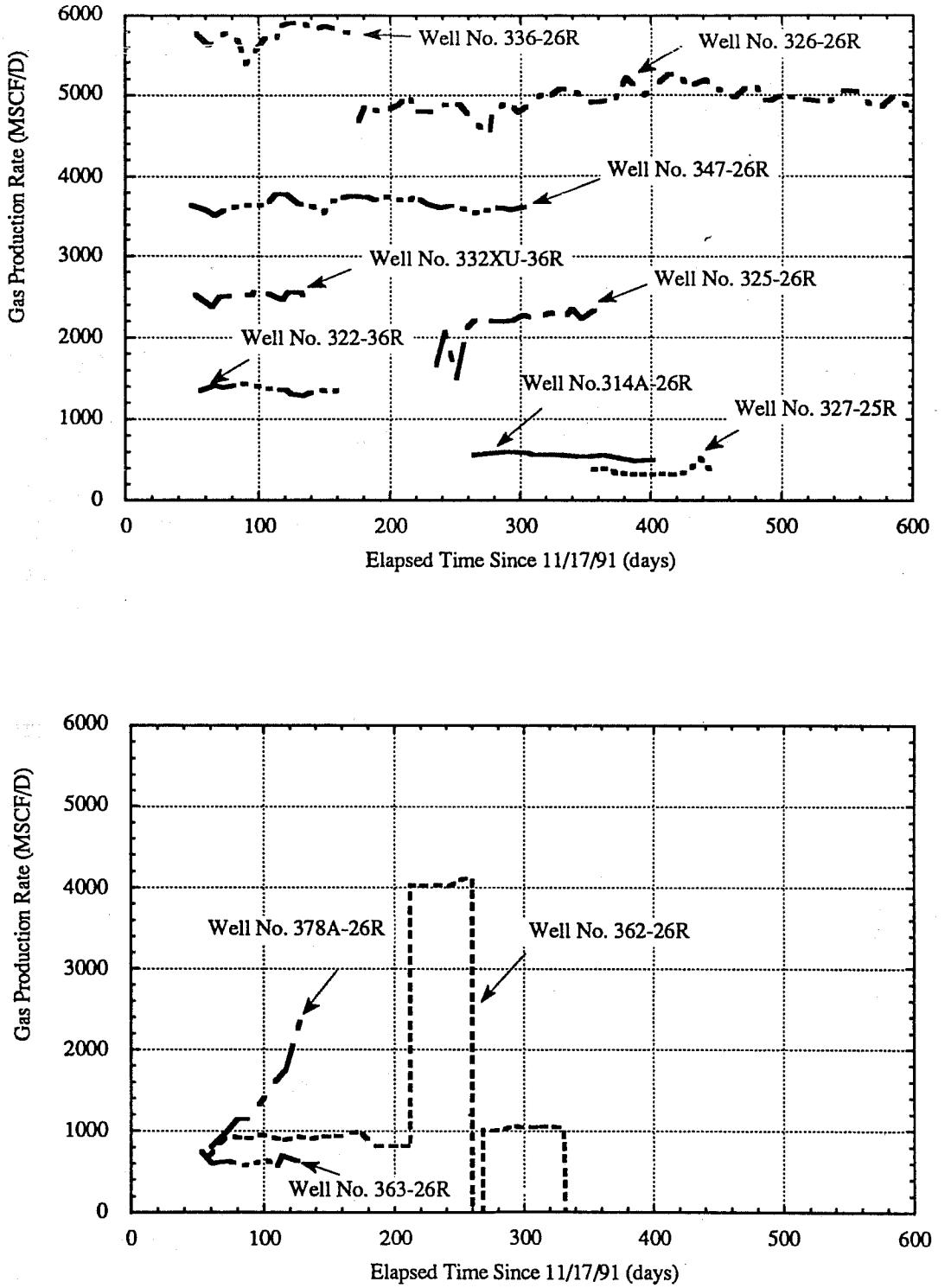

Fig. 22 Gas production histories for sampling wells (from Wells 314-378A)

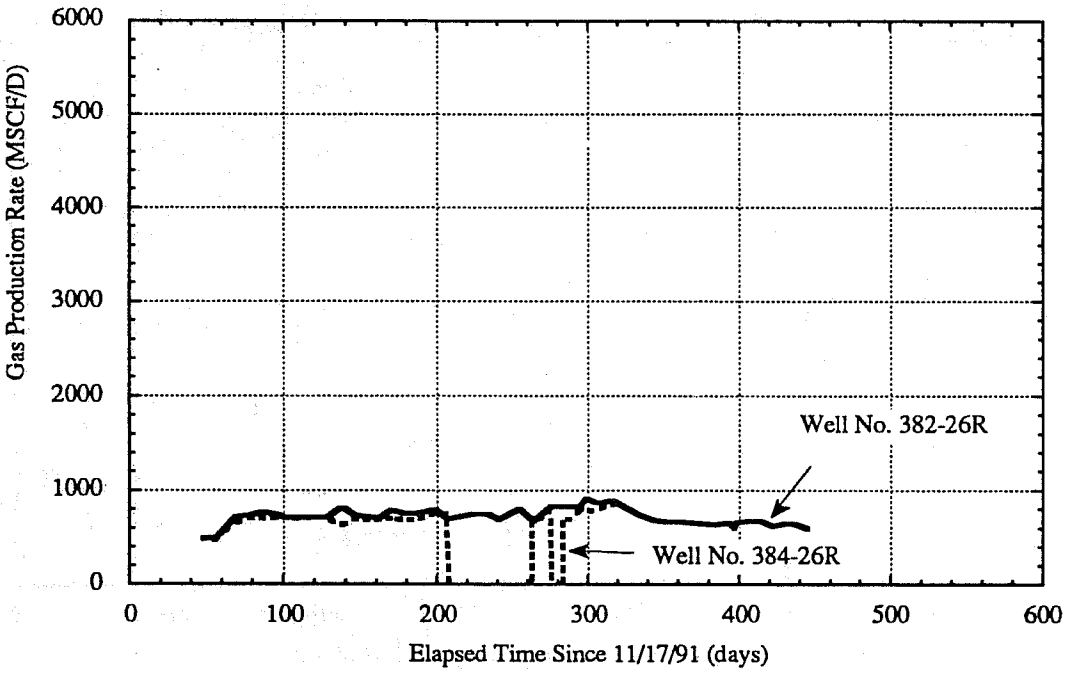

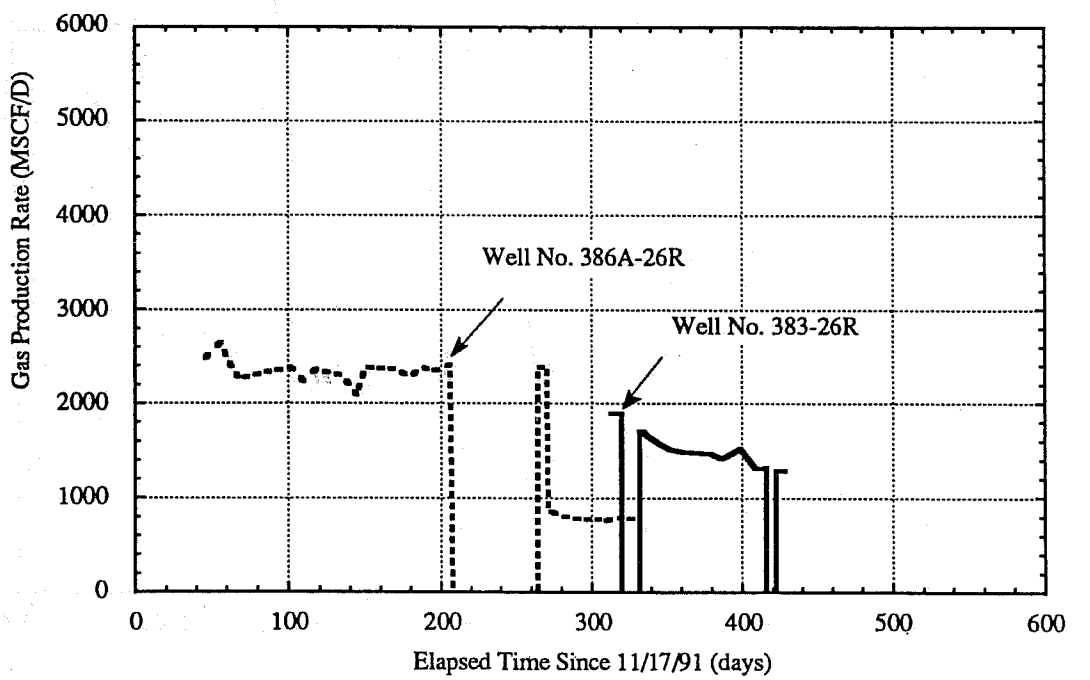

Fig. 23 Gas production histories for sampling wells (from Wells 382-386A)

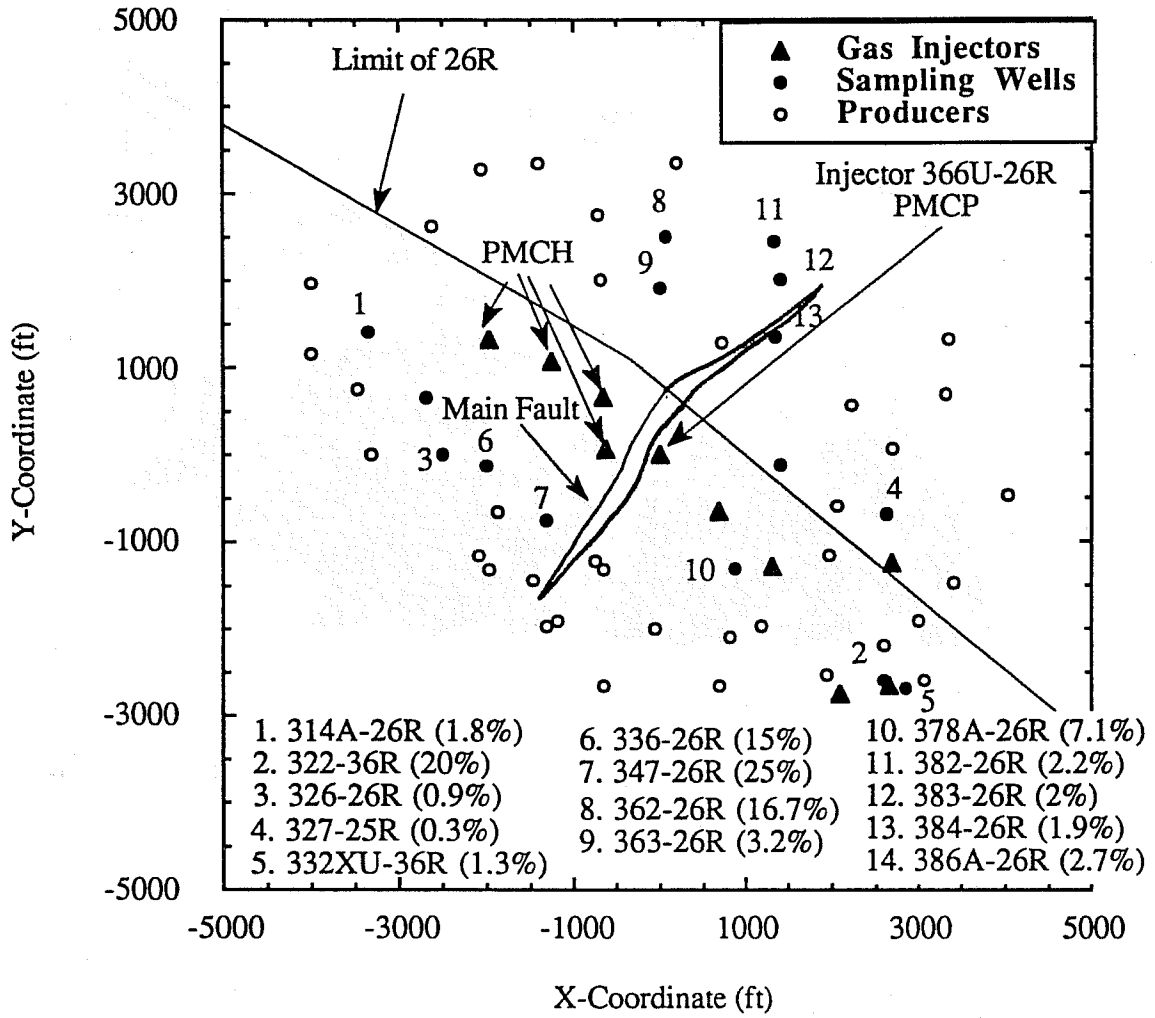

Fig. 24 Map of 26R showing amount of PMCP produced at each sampling well (amount in percent of total PMCP produced)

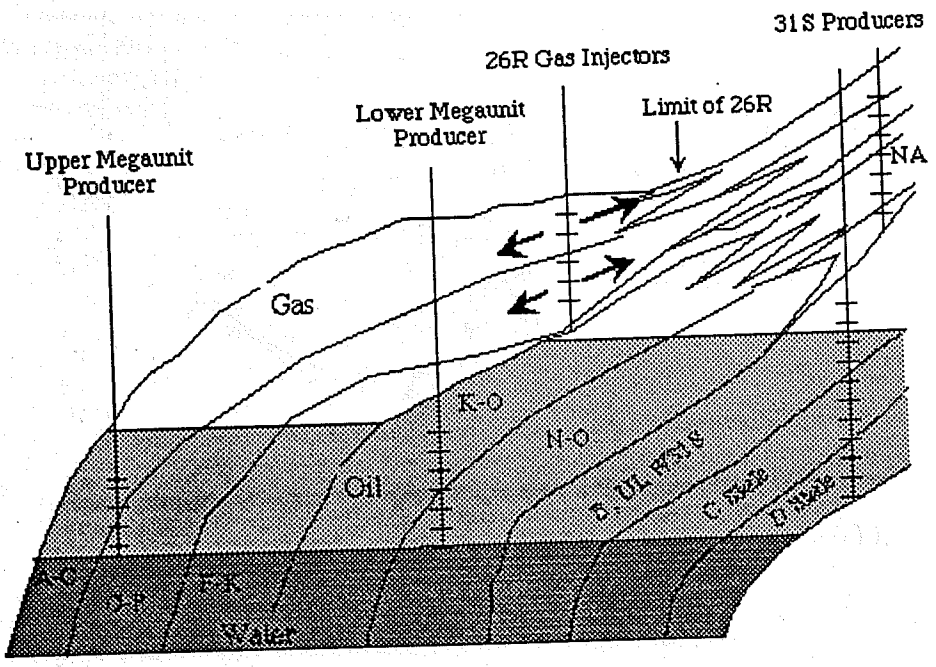

Fig. 25 Schematic conceptual model of 26R and 31S reservoirs

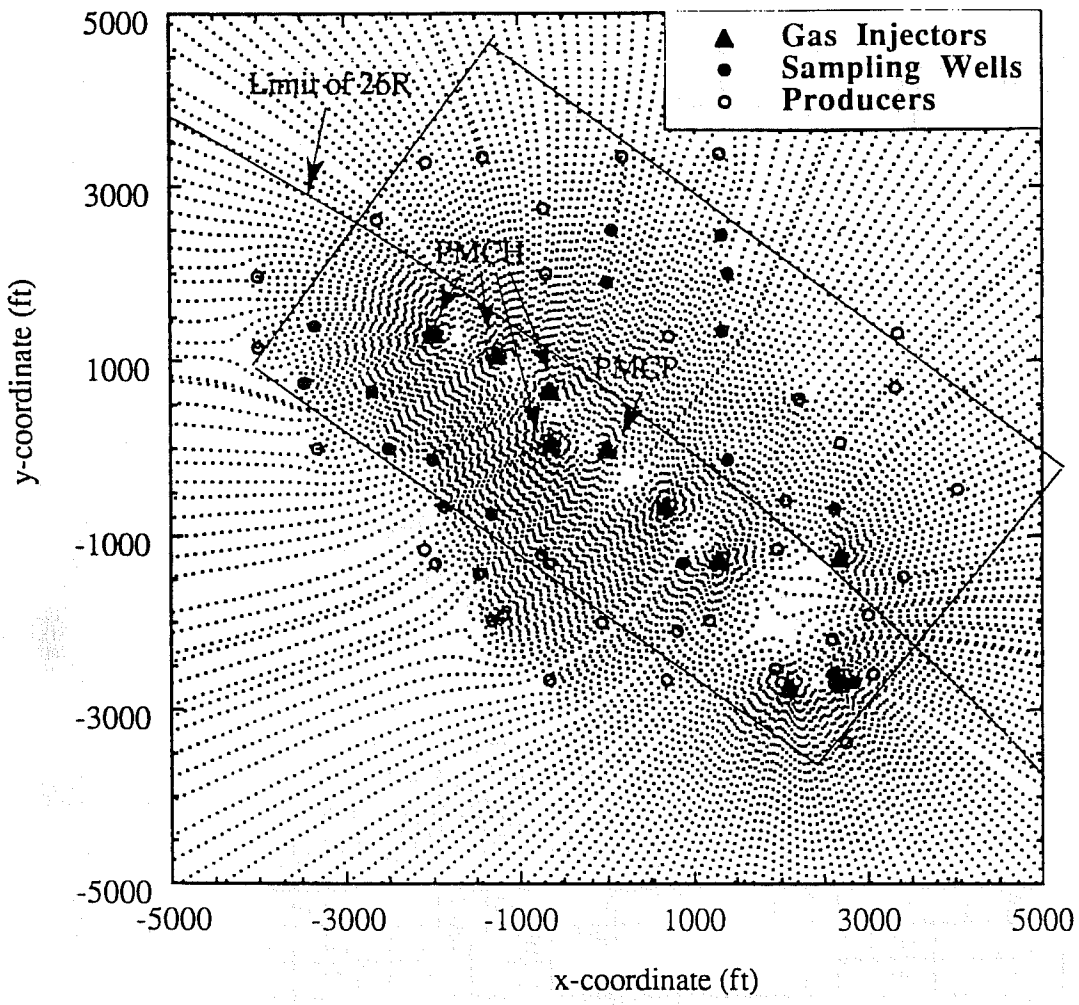

Fig. 26 Map of 26R and 31S showing streamlines and area to be simulated inside the square

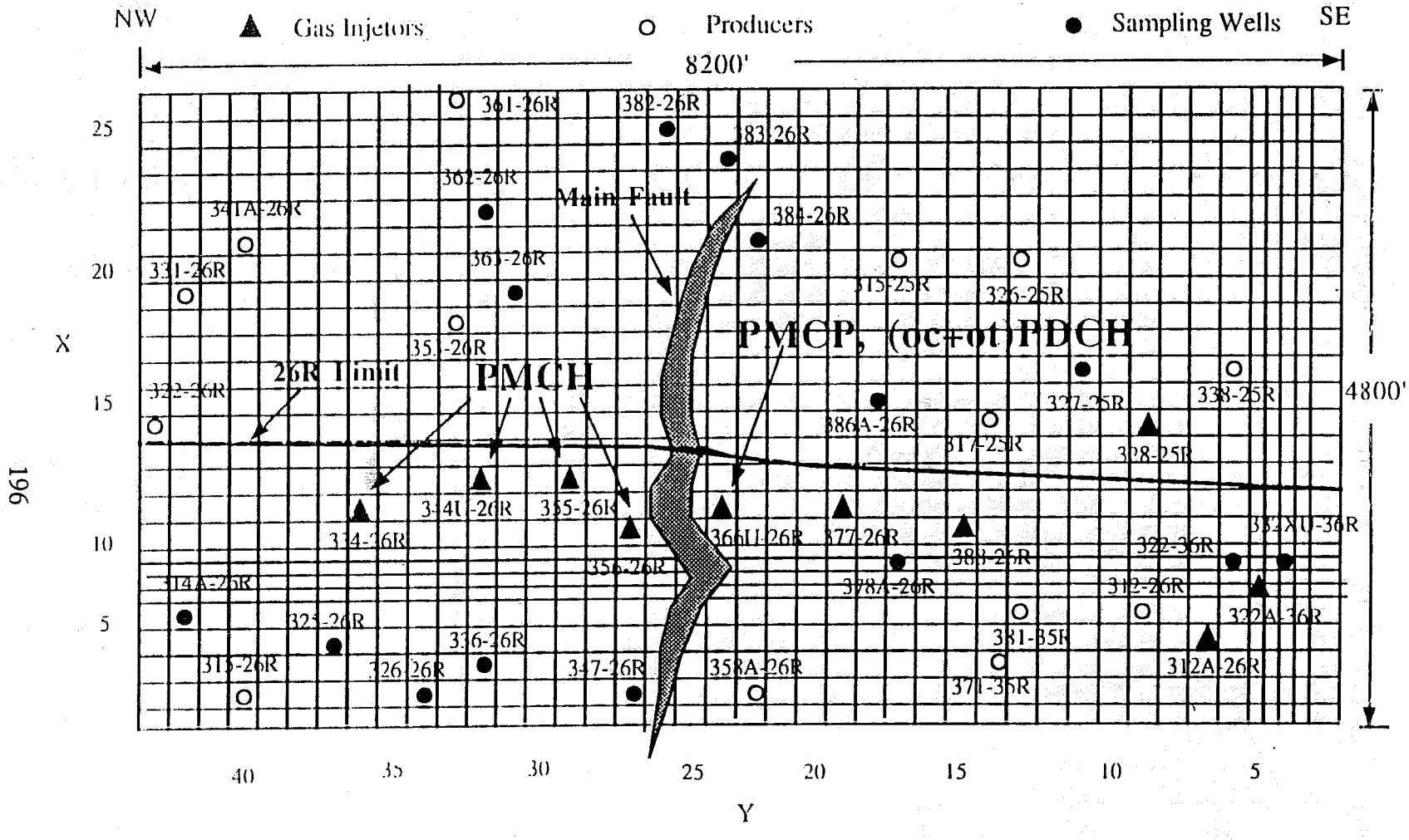

Fig. 27 Simulation grids used in this study

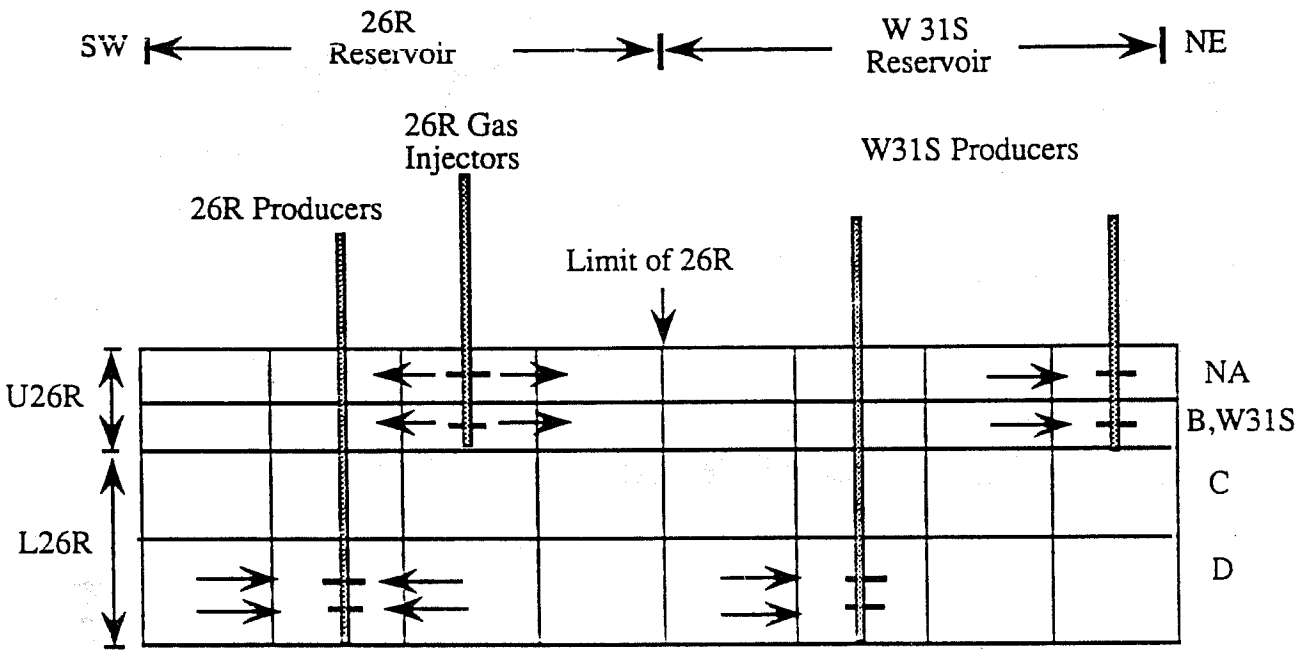

Fig. 28 Cross-section showing simulation model

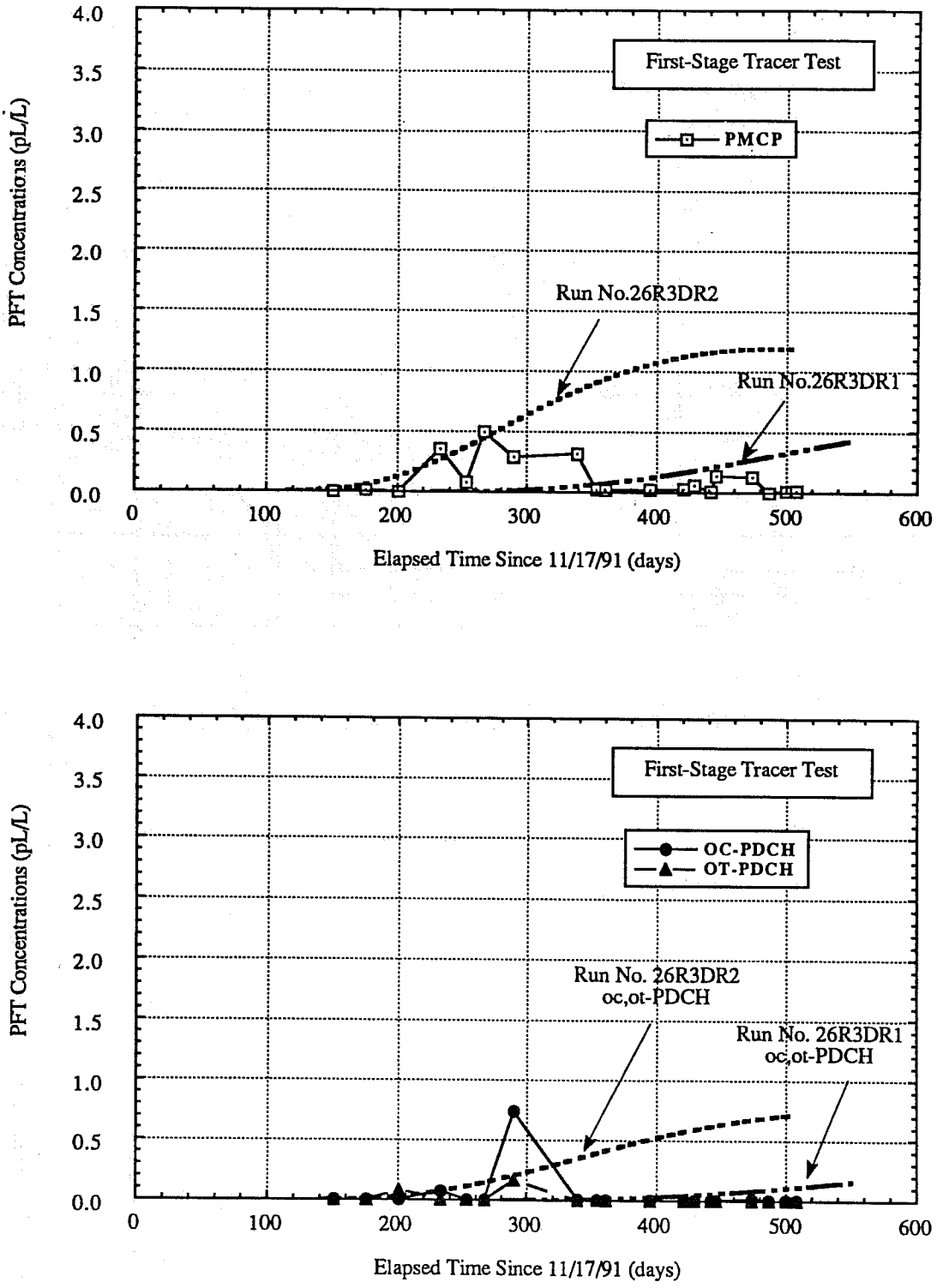

Fig. 29. Comparison of produced PFT concentrations from Well No. 326-26R between data and simulations

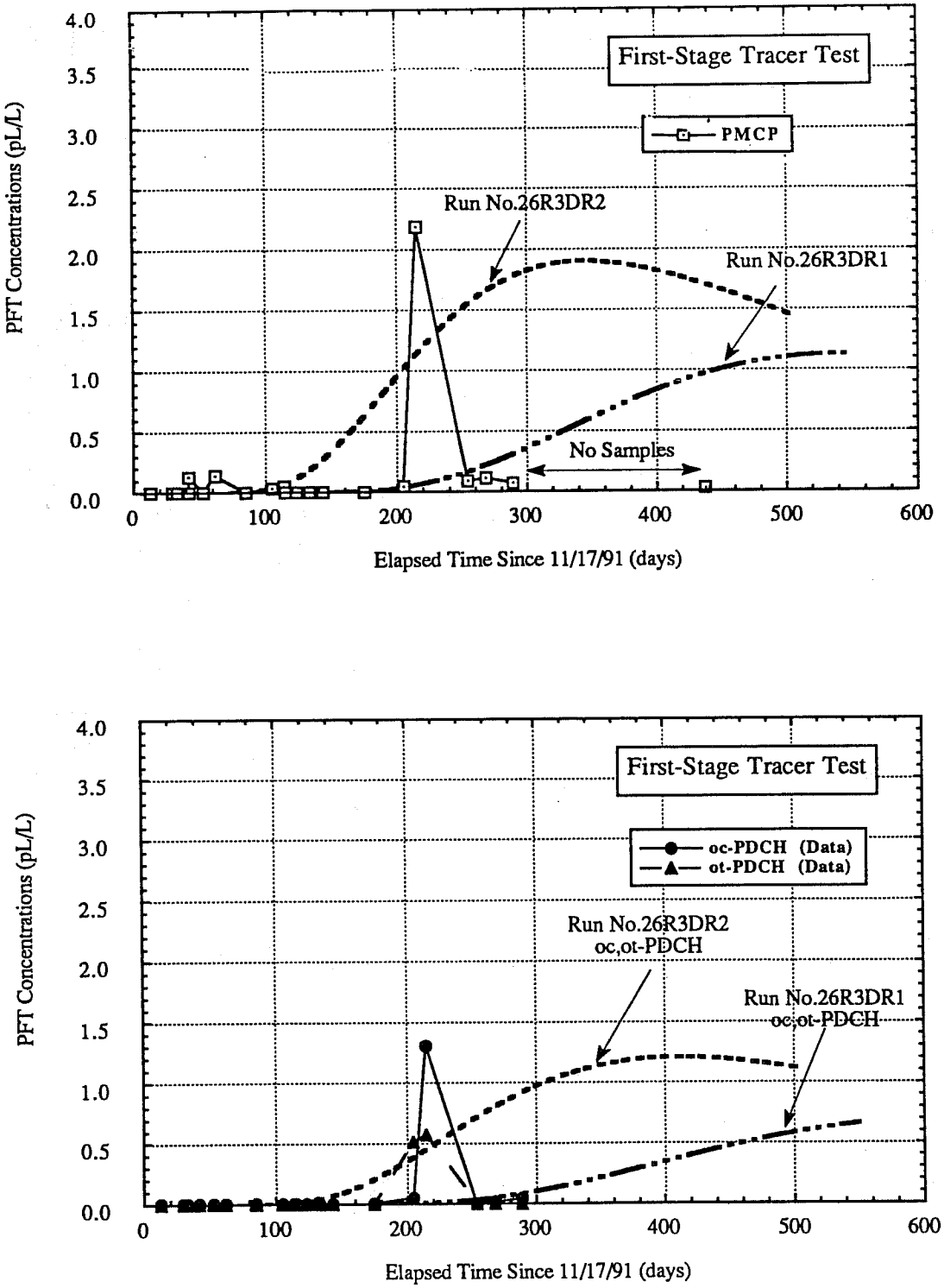

Fig. 30. Comparison of produced PFT concentrations from Well No. 336-26R between data and simulations

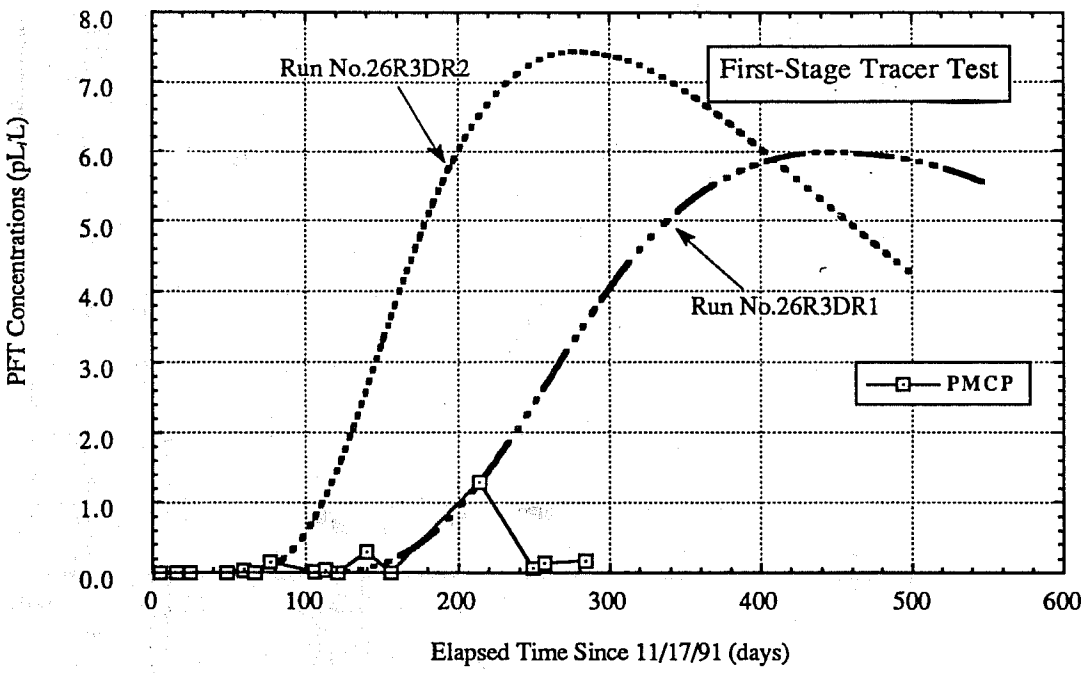

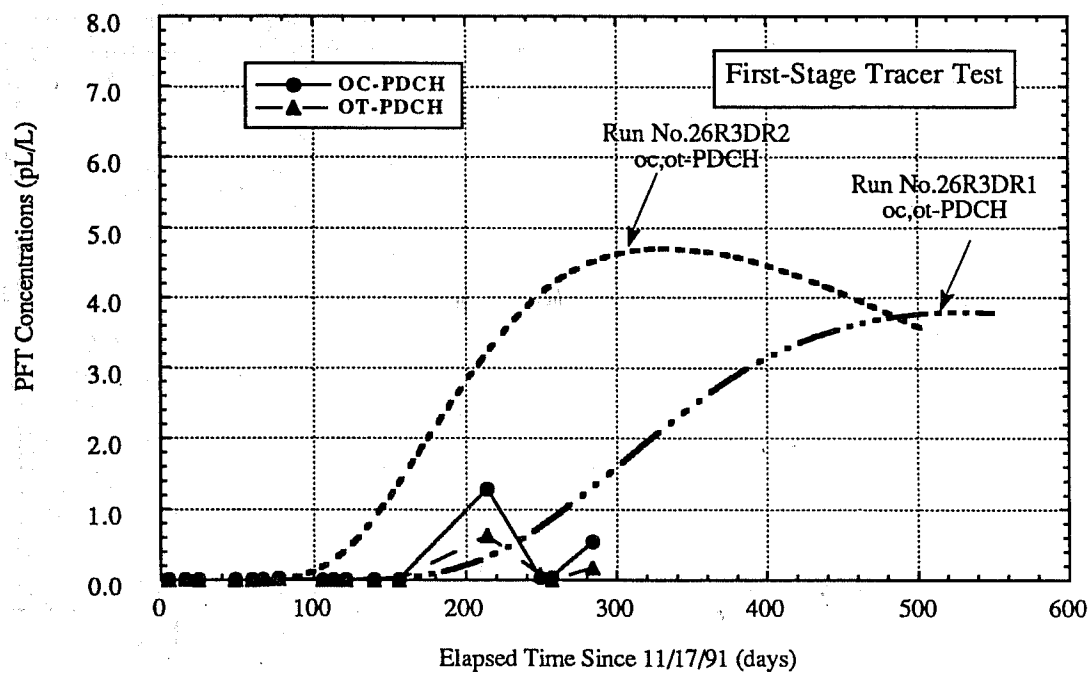

Fig. 31. Comparison of produced PFT concentrations from Well No. 347-26R between data and simulations

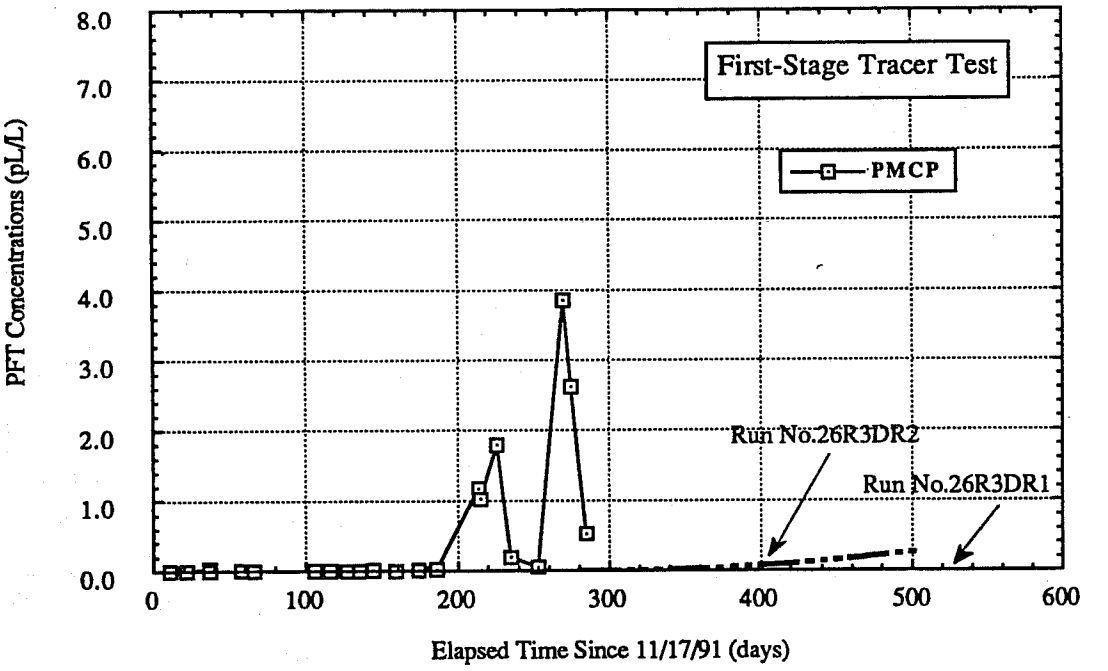

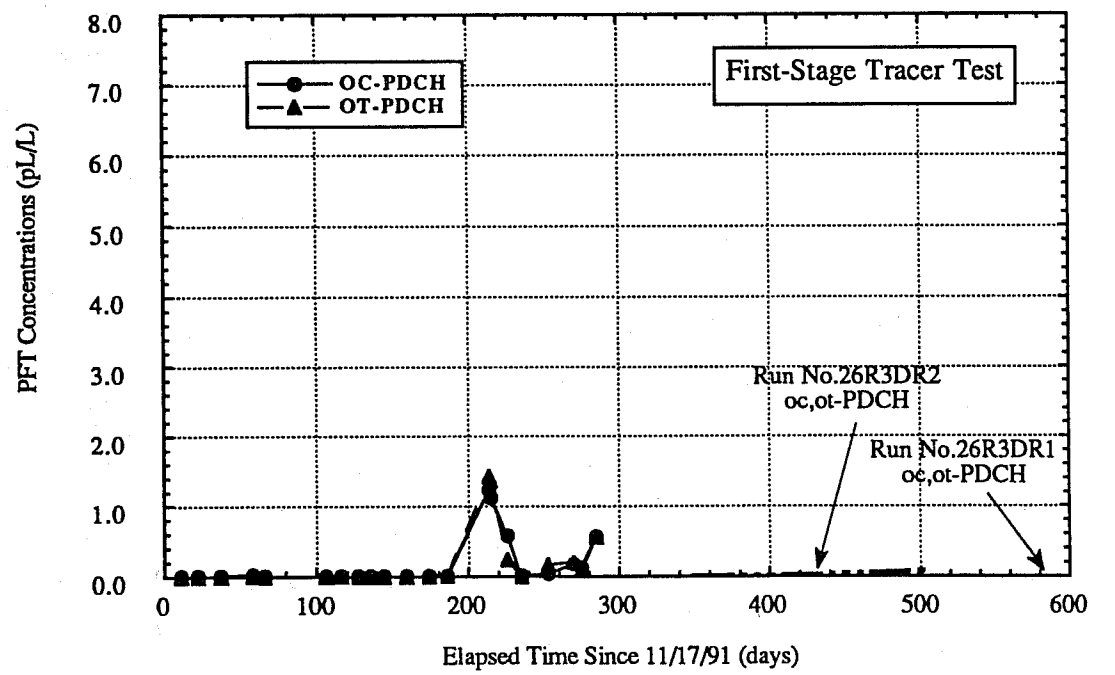

Fig. 32. Comparison of produced PFT concentrations from Well No. 362-26R between data and simulations

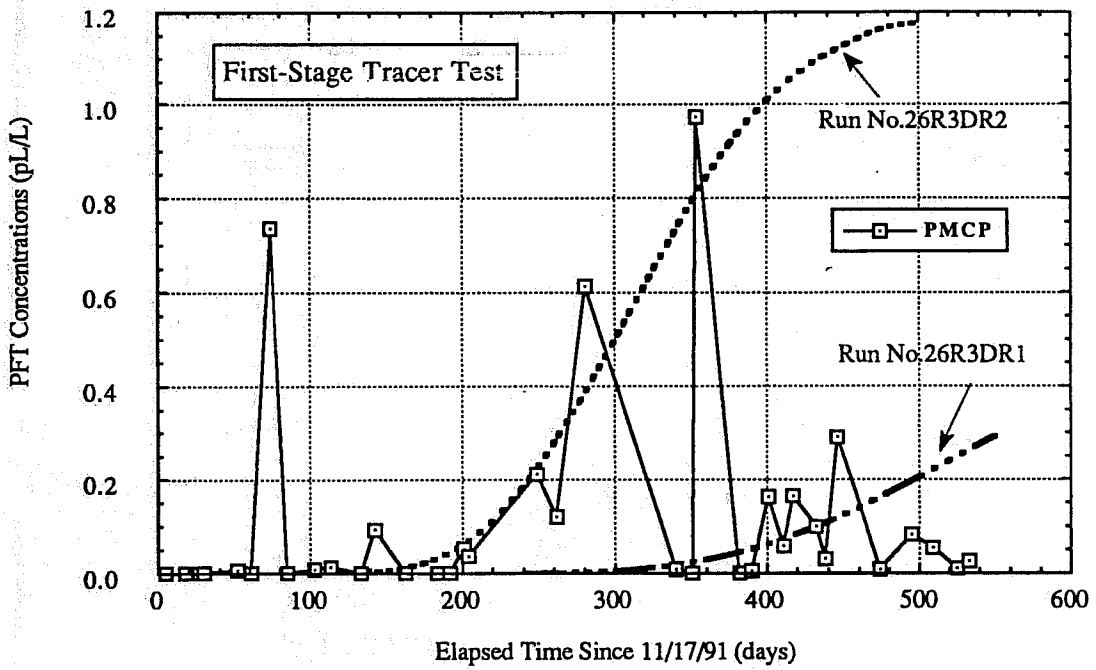

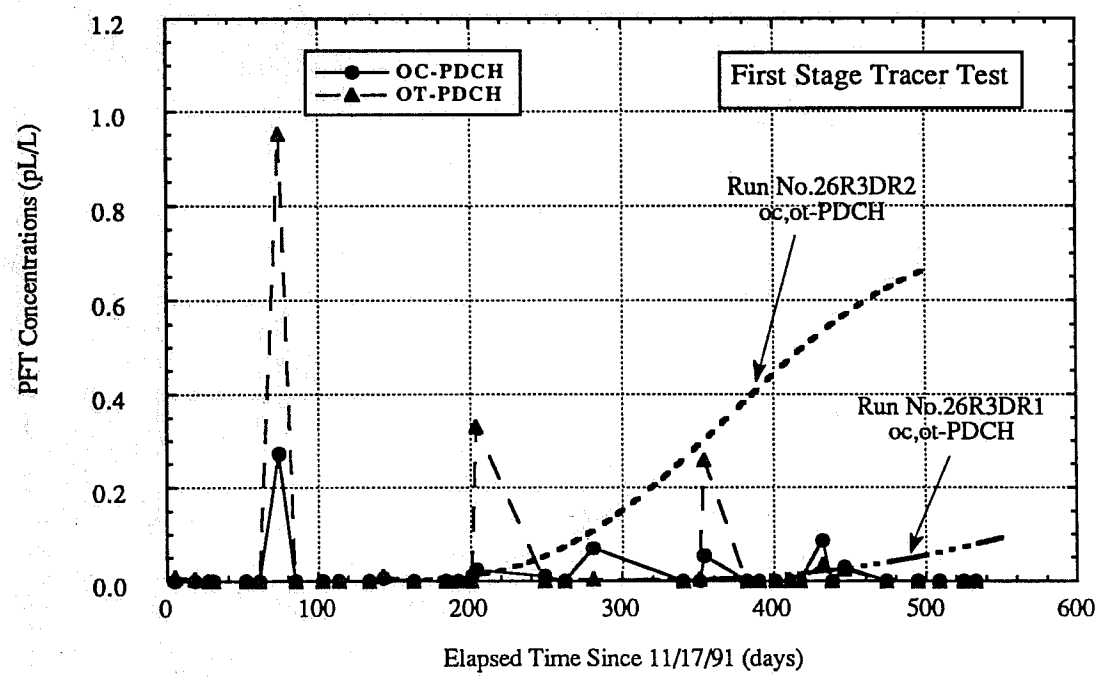

Fig. 33. Comparison of produced PFT concentrations from Well No. 363-26R between data and simulations

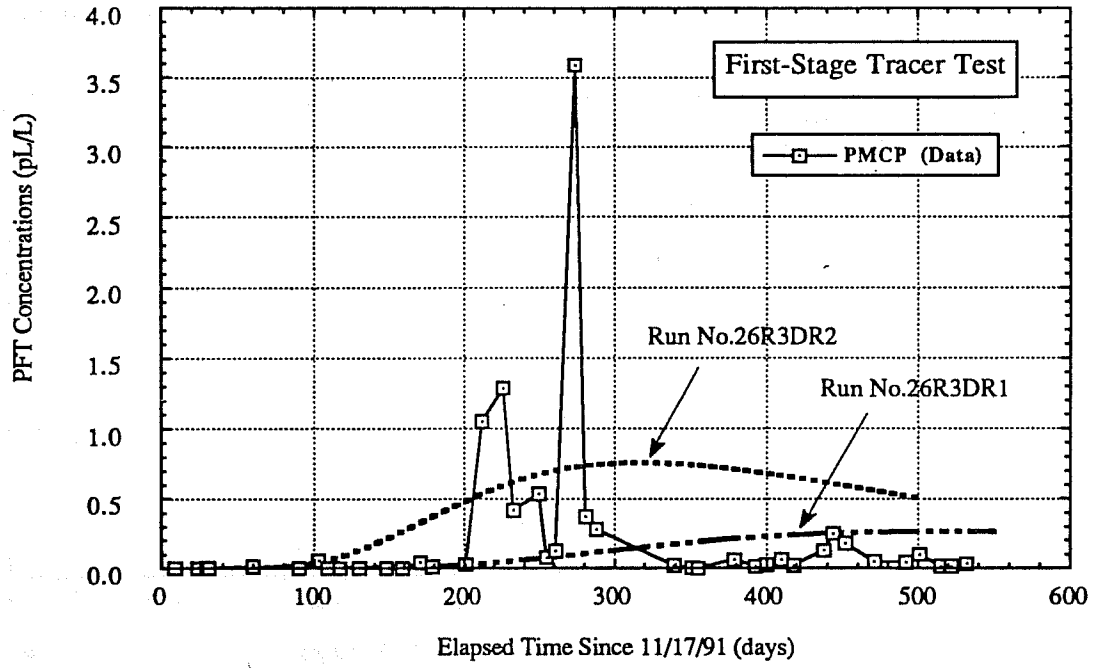

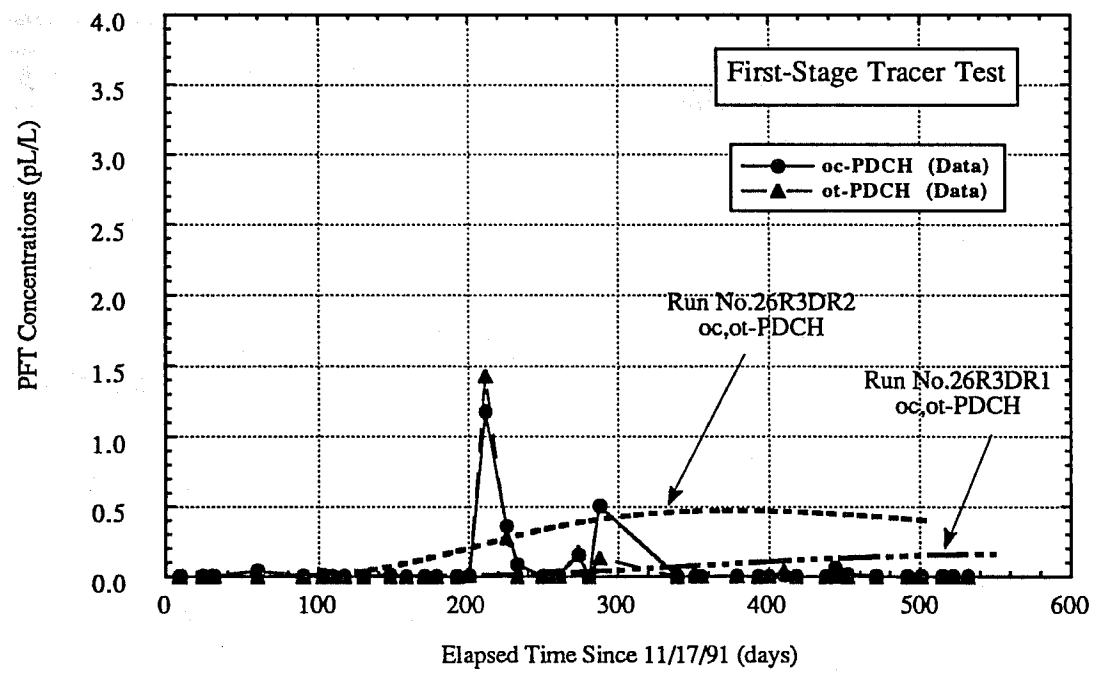

Fig. 34. Comparison of produced PFT concentrations from Well No. 378A-26R between data and simulations

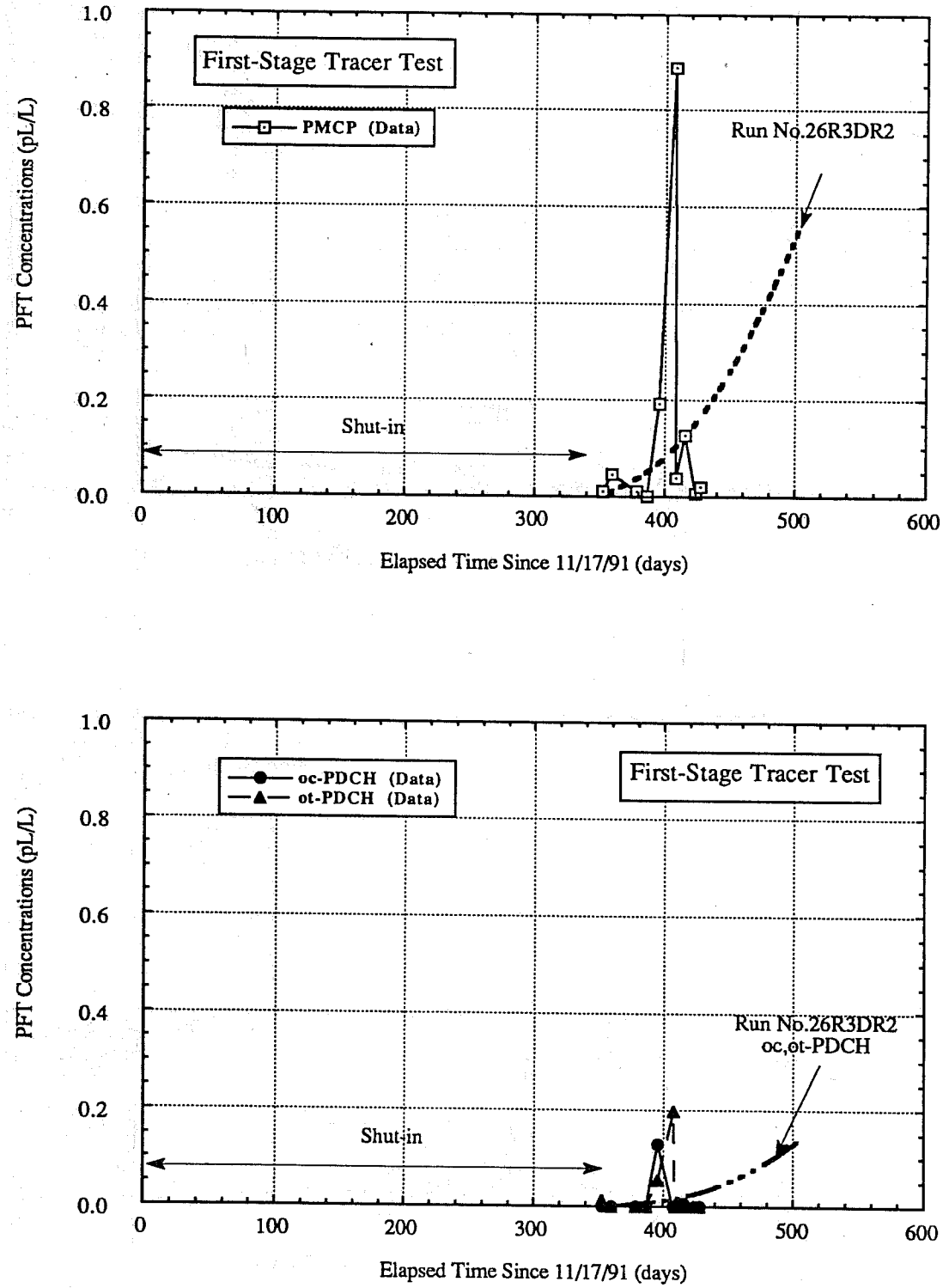

Fig. 35. Comparison of produced PFT concentrations from Well No. 383-26R between data and simulations

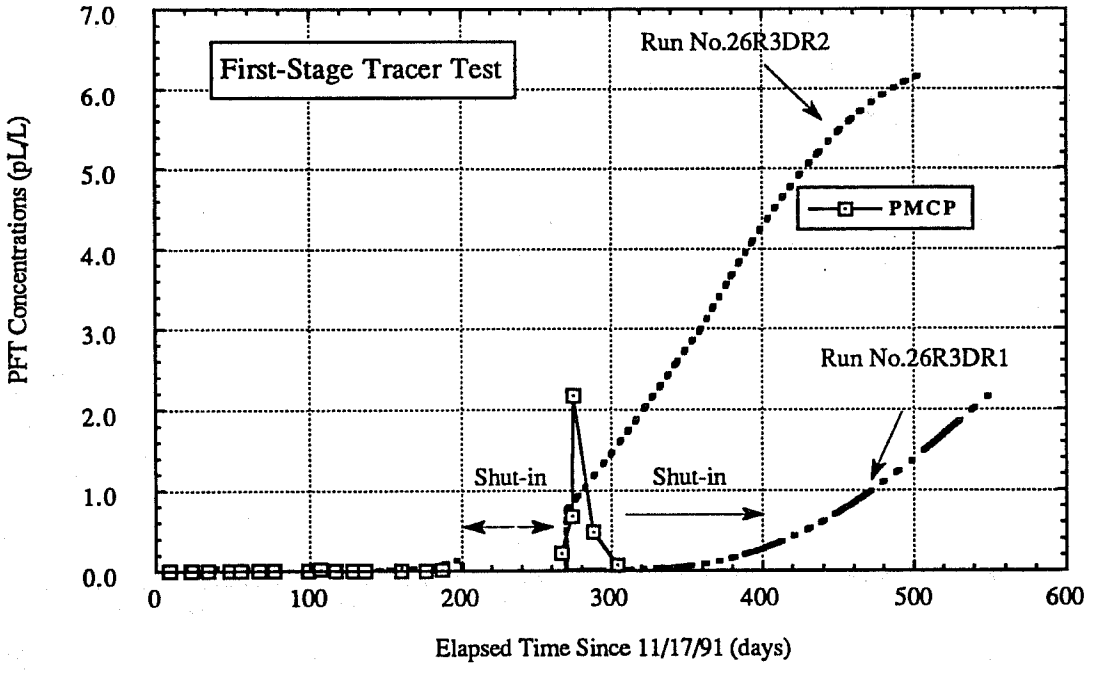

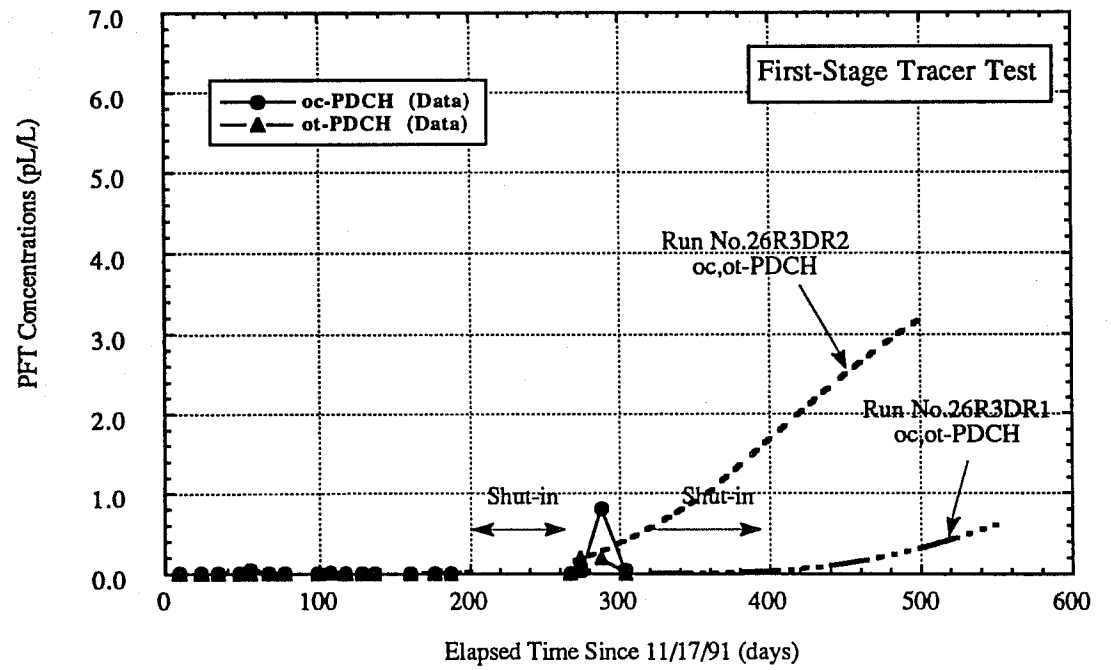

Fig. 36. Comparison of produced PFT concentrations from Well No. 384-26R between data and simulations

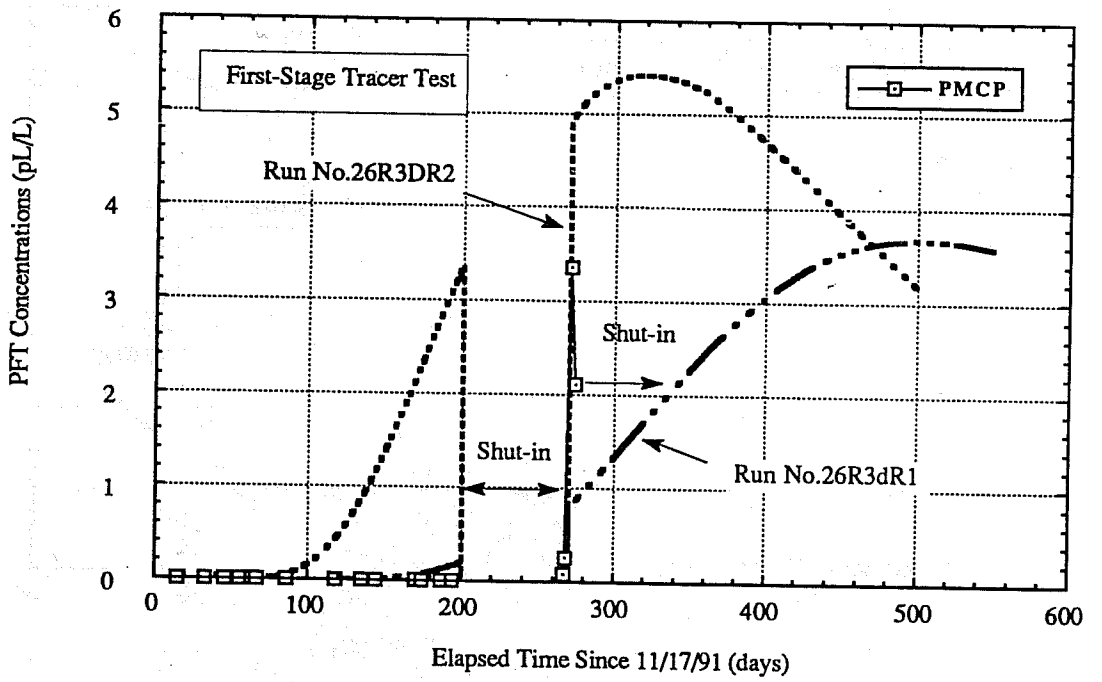

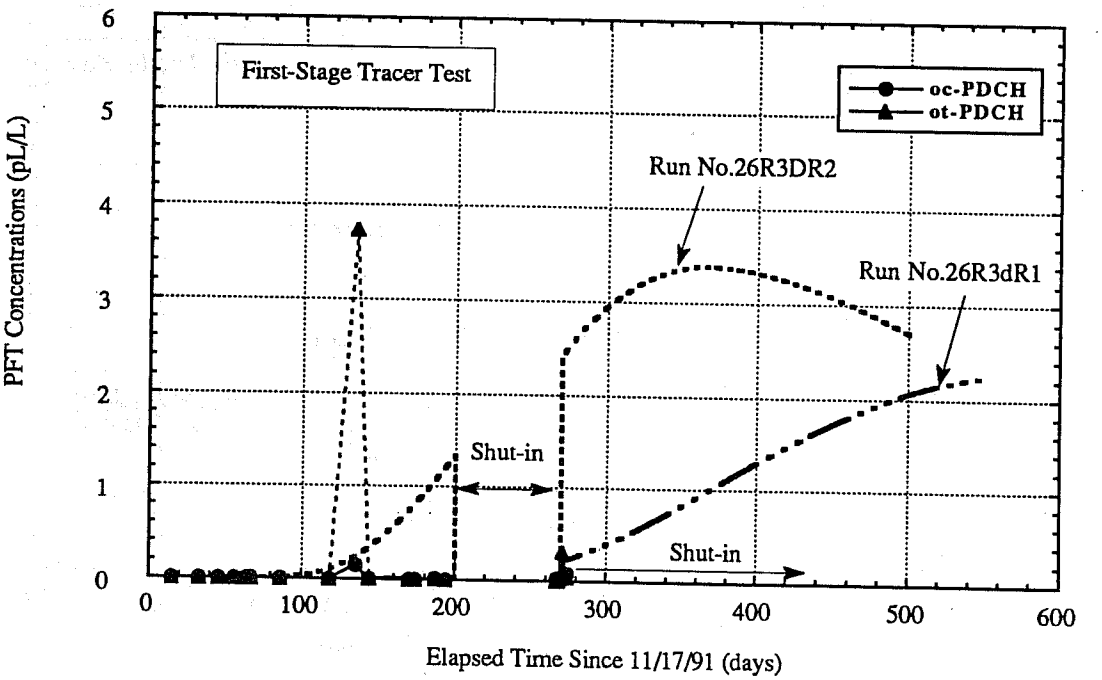

Fig. 37. Comparison of produced PFT concentrations from Well No. 386A-26R between data and simulations

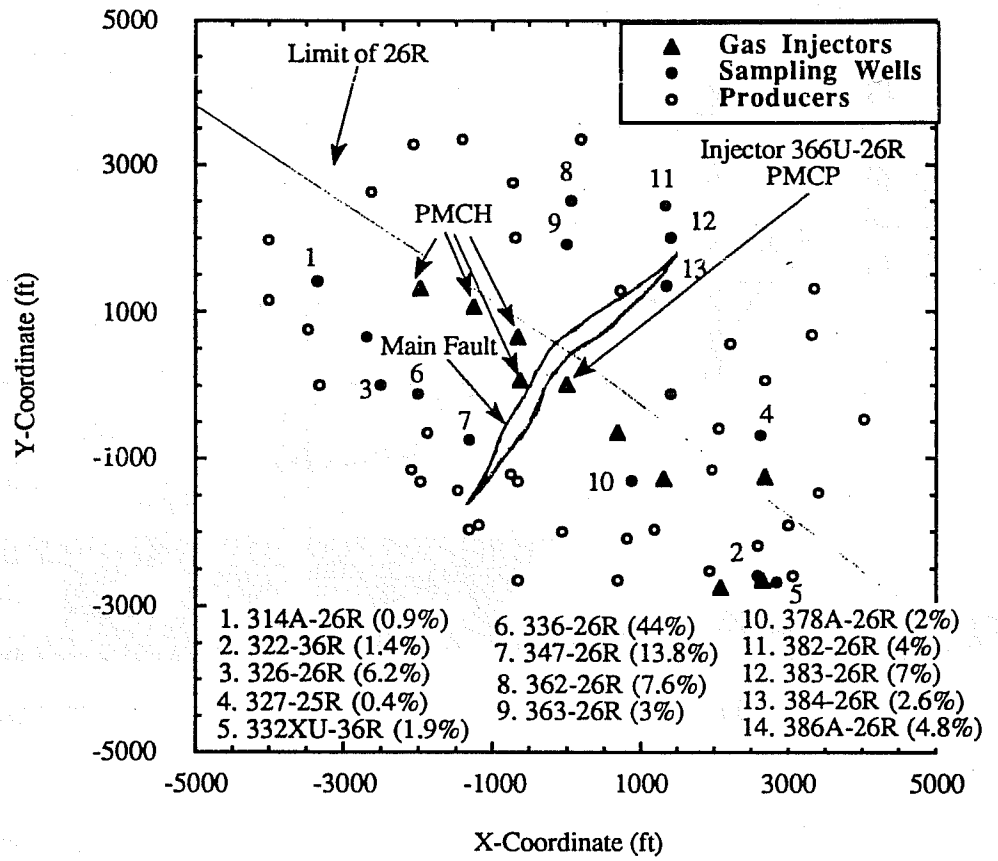

Fig. 38. Map of 26R showing amount of PMCH produced at each sampling well (amount in percent of total PMCH produced)

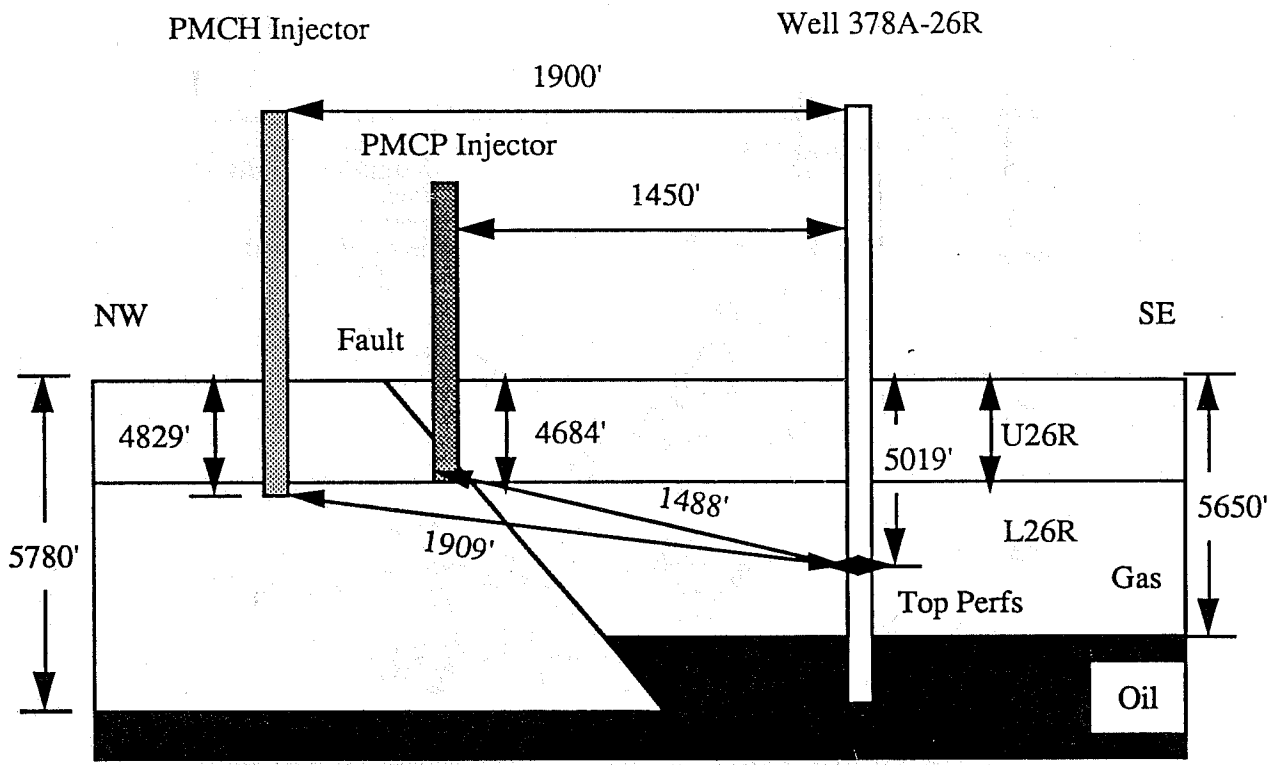

Fig. 39. Schematic diagram showing distances from PMCP injector and the closest PMCH injector to Well 378A-26R

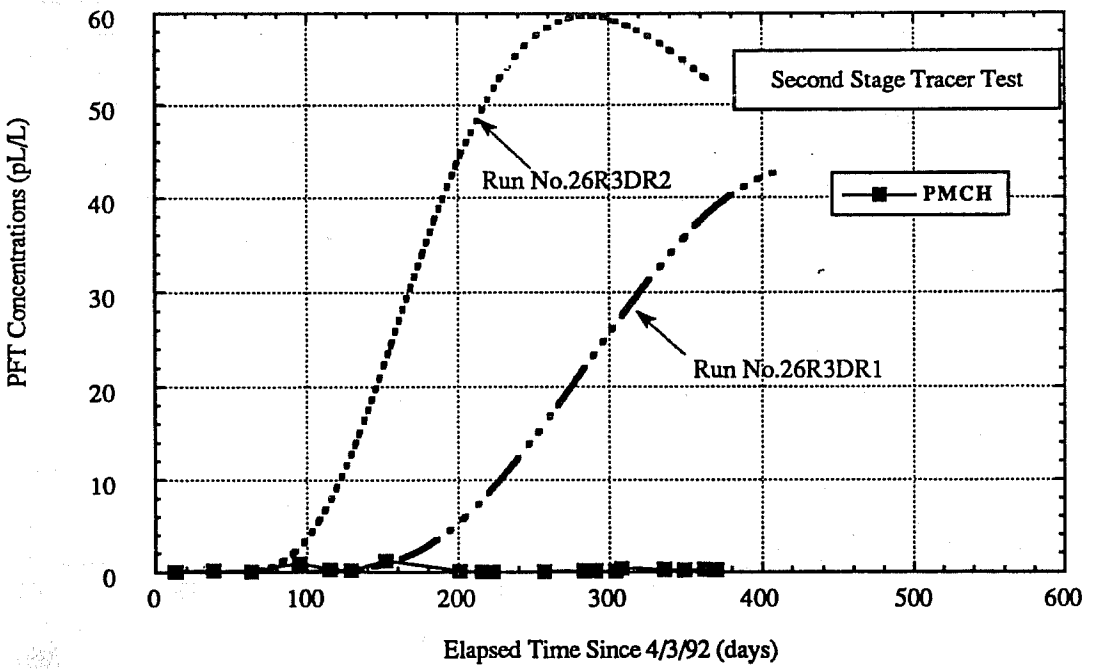

Fig. 40. Comparison of produced PFT concentrations from Well No. 326-26R between data and simulations

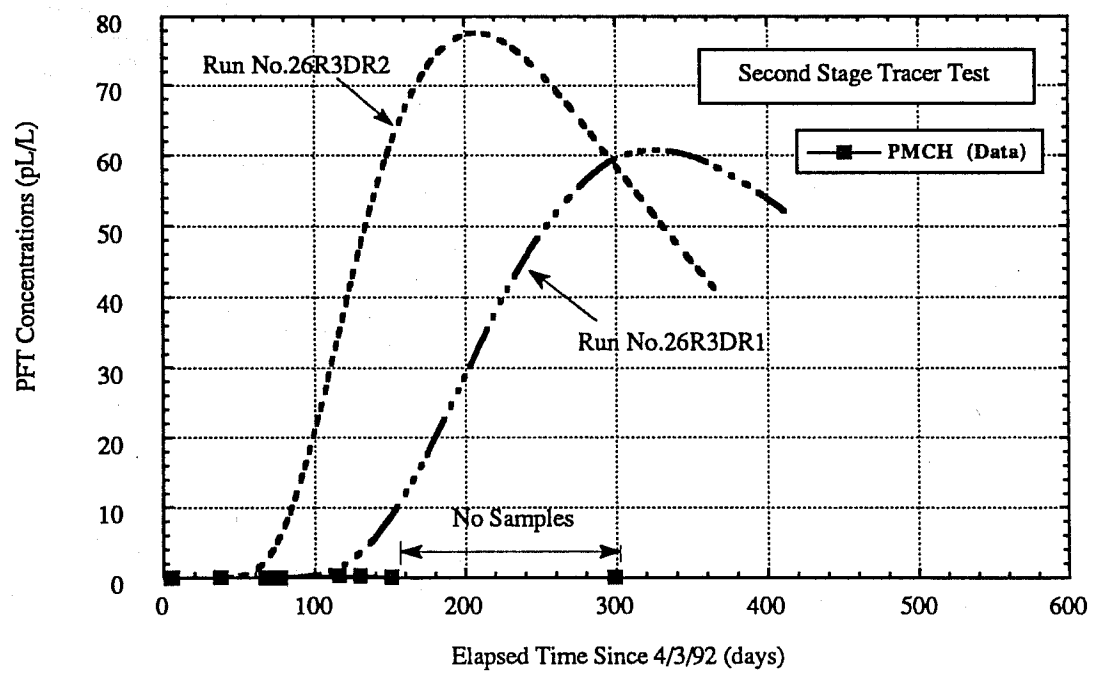

Fig. 41. Comparison of produced PFT concentrations from Well No. 336-26R between data and simulations

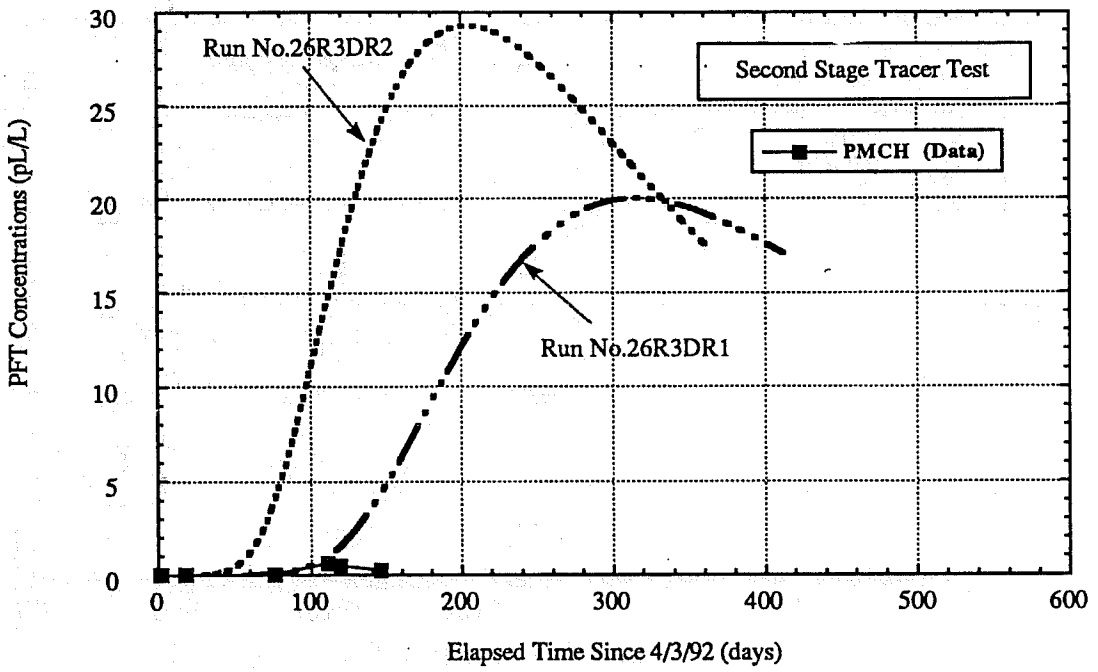

Fig. 42. Comparison of produced PFT concentrations from Well No. 347-26R between data and simulations

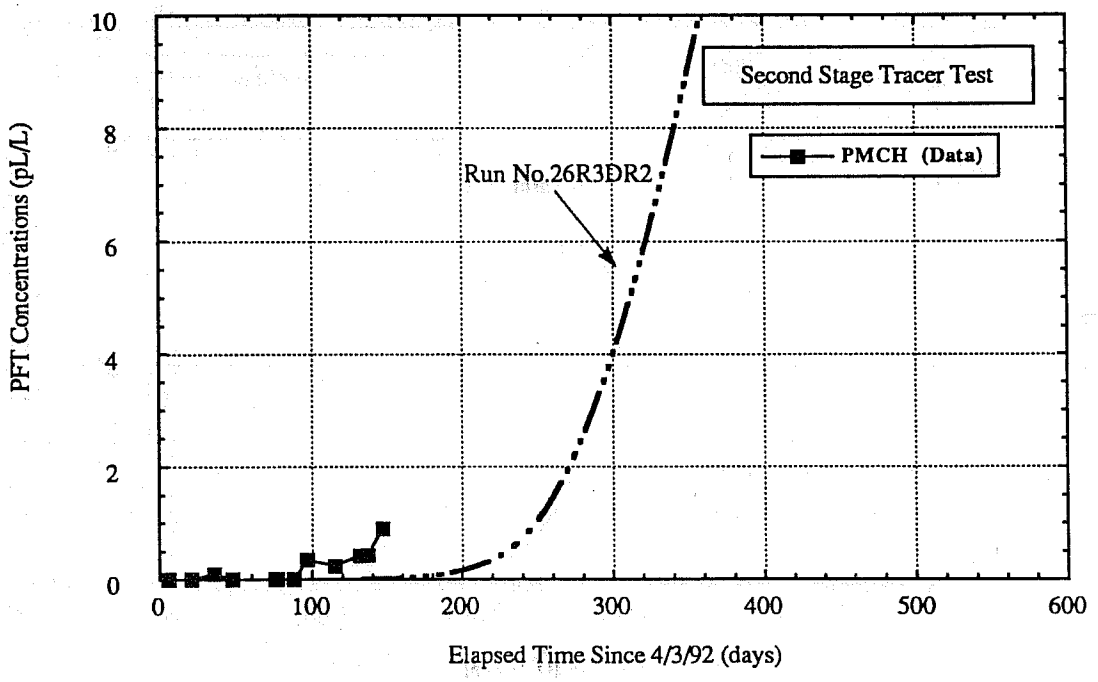

Fig. 43. Comparison of produced PFT concentrations from Well No. 362-26R between data and simulations

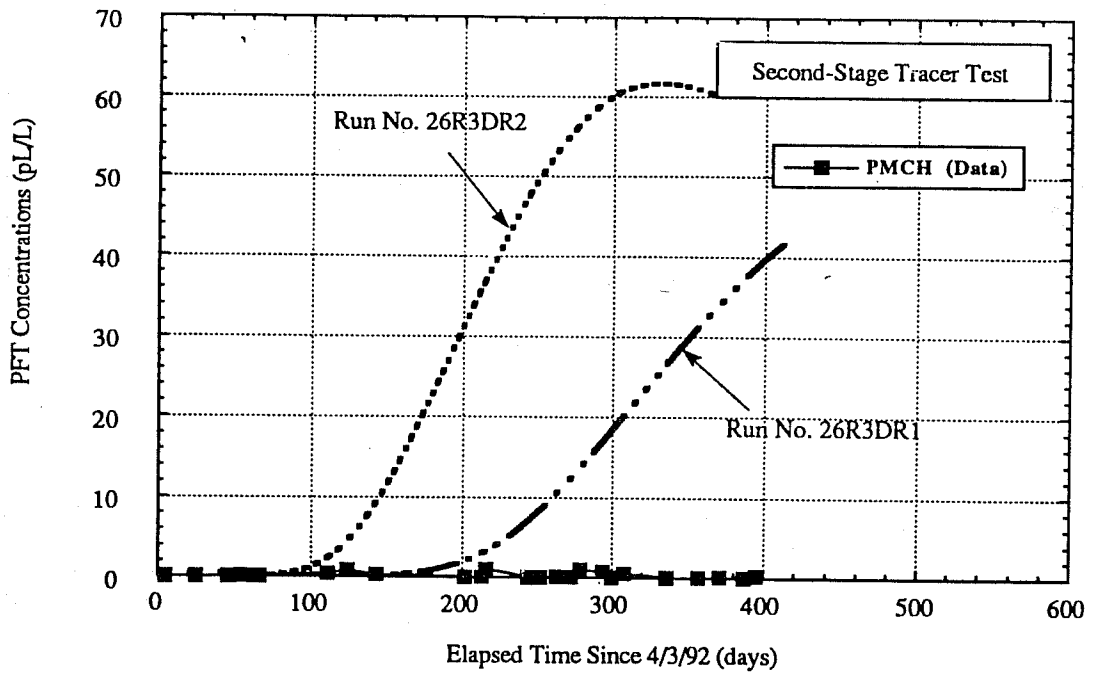

Fig. 44. Comparison of produced PFT concentrations from Well No. 363-26R between data and simulations

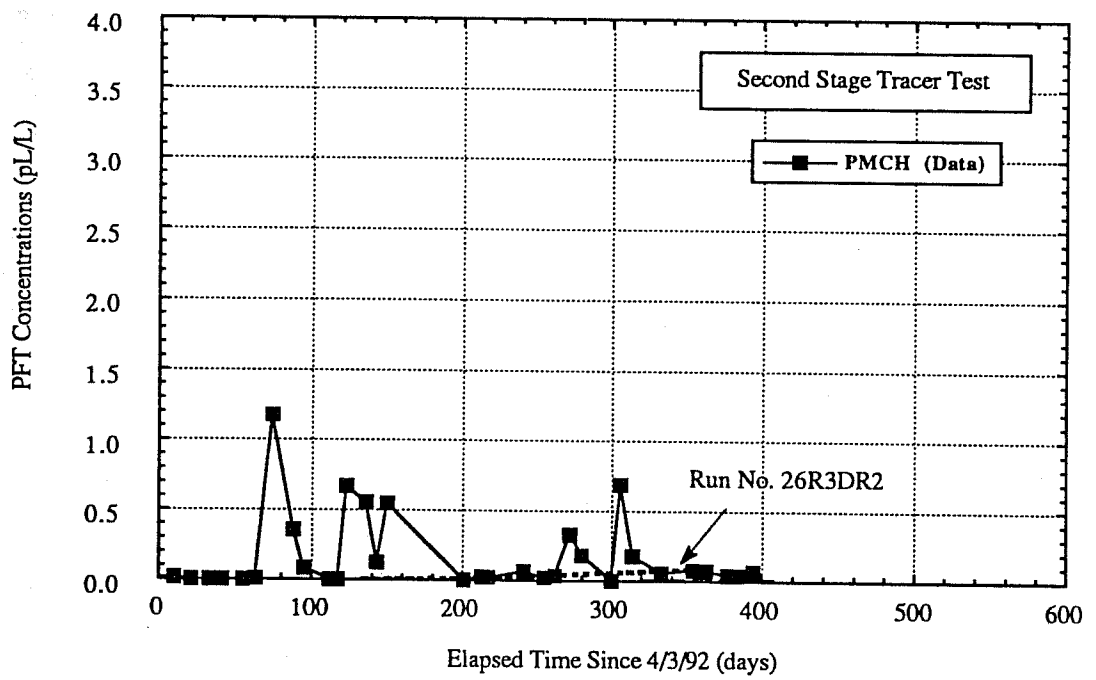

Fig. 45. Comparison of produced PFT concentrations from Well No. 378A-26R between data and simulations

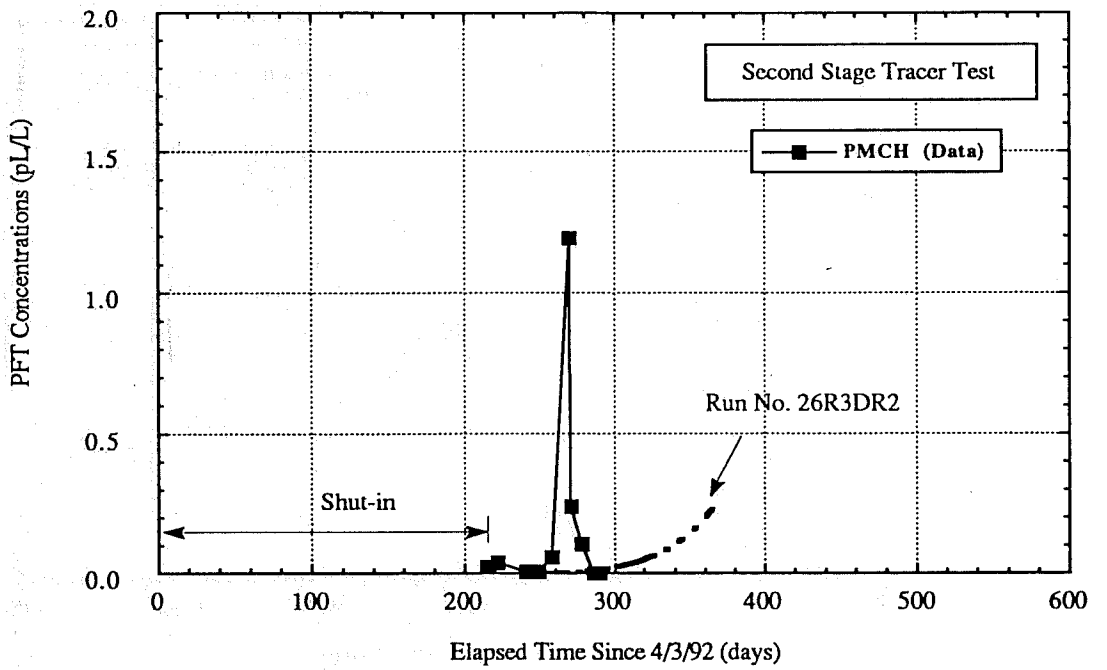

Fig. 46. Comparison of produced PFT concentrations from Well No. 383-26R between data and simulations

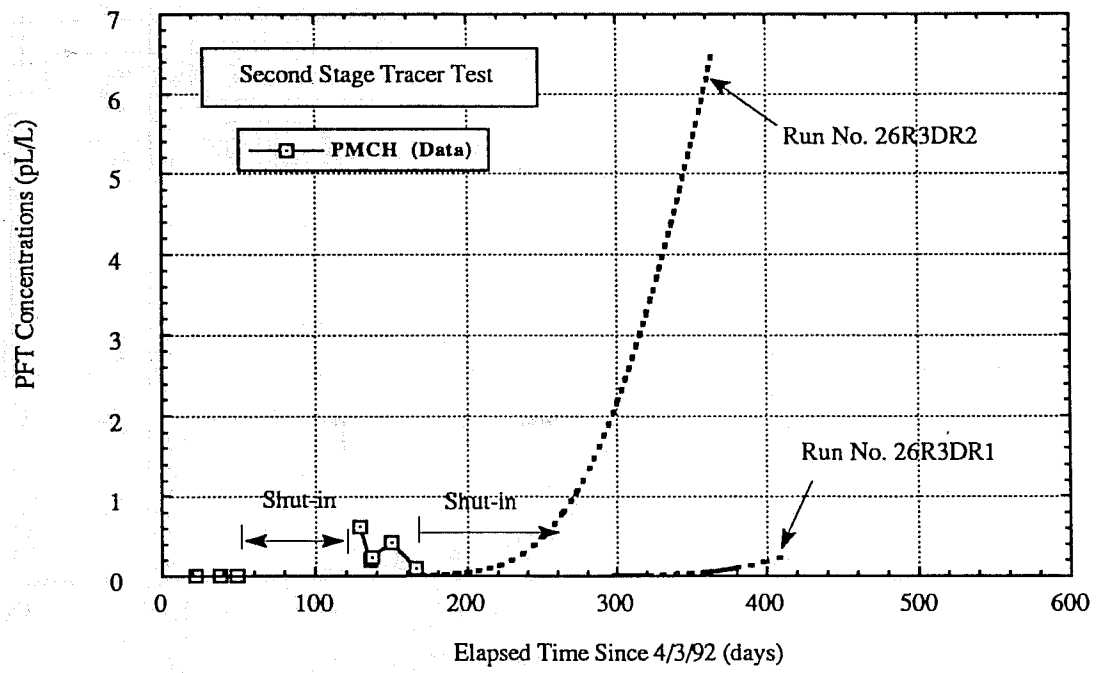

Fig. 47. Comparison of produced PFT concentrations from Well No. 384-26R between data and simulations

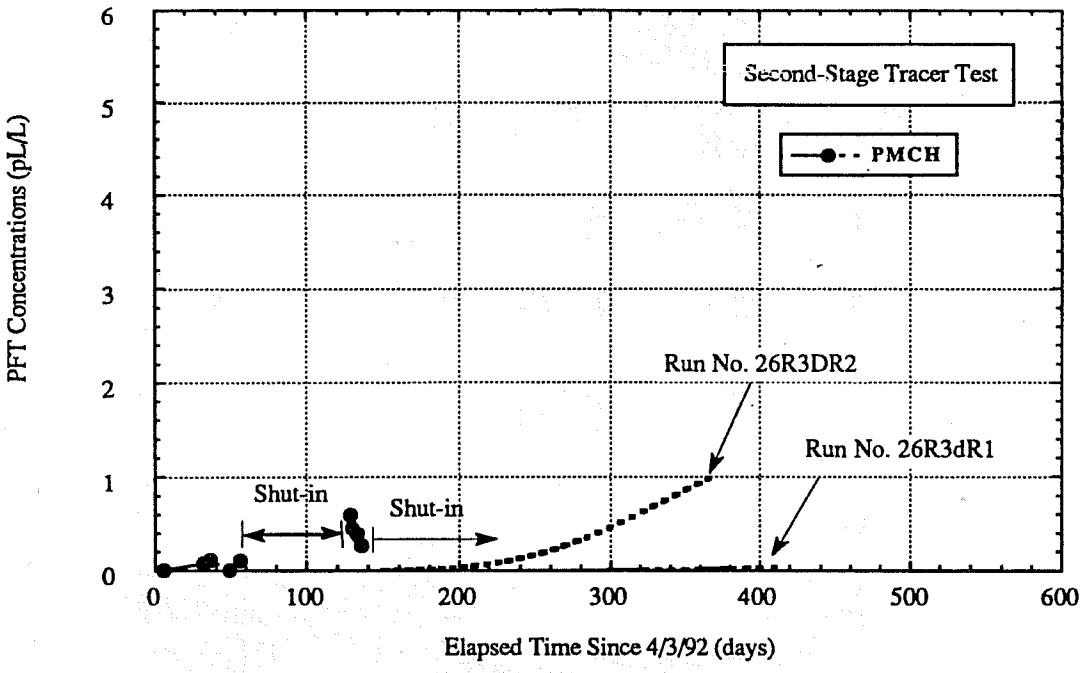

Fig. 48. Comparison of produced PFT concentrations from Well No. 386A-26R between data and simulation

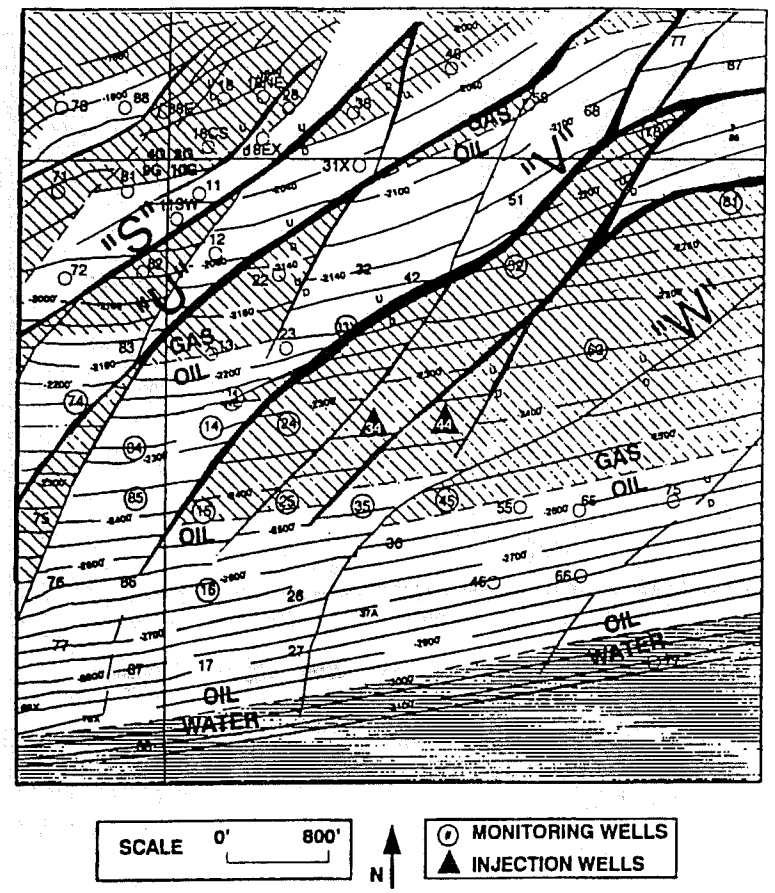

Fig. 49. Areal map of the SOZ reservoir showing tracer injectors and sampling wells

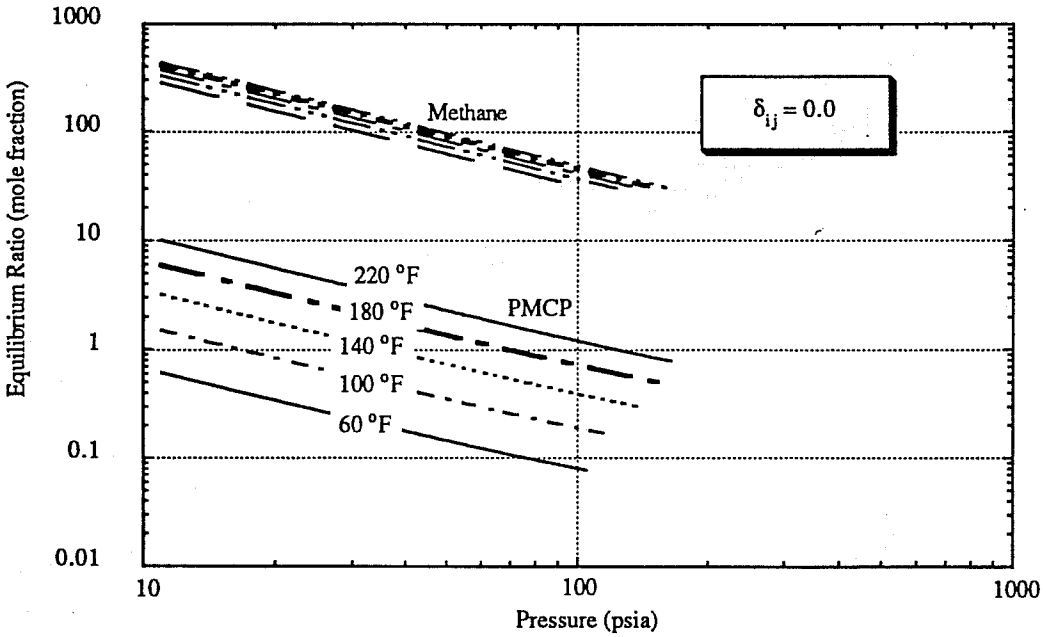

Fig. 50. Equilibrium ratio vs. pressure for PMCP from the Peng-Robinson equation of state using fluid descriptions from Well No. 73-11G

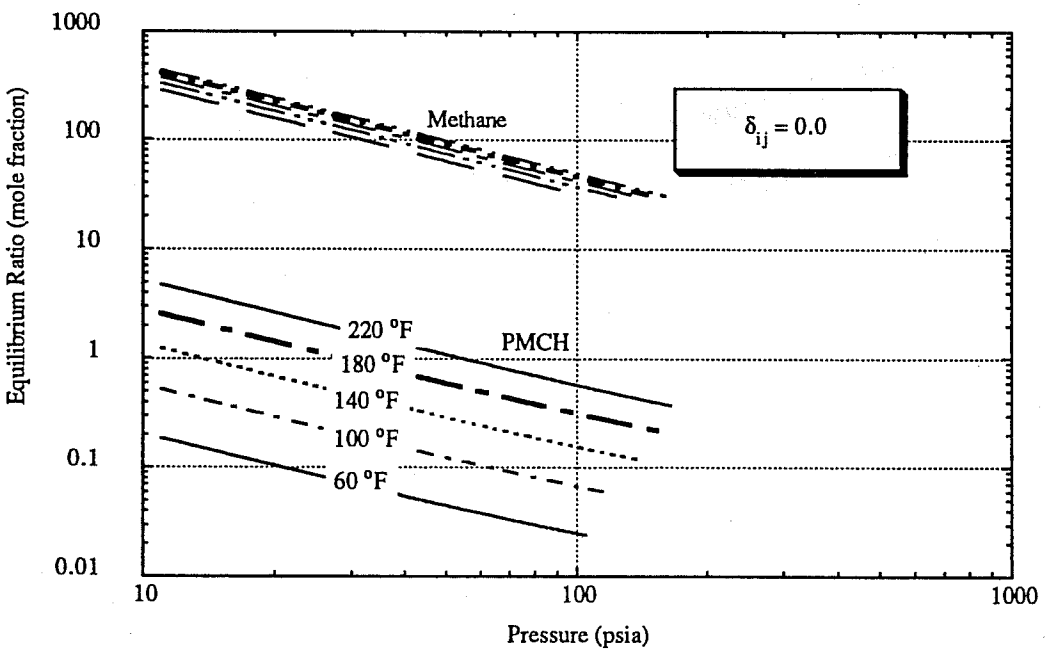

Fig. 51. Equilibrium ratio vs. pressure for PMCH from the Peng-Robinson equation of state using fluid descriptions from Well No. 73-11G

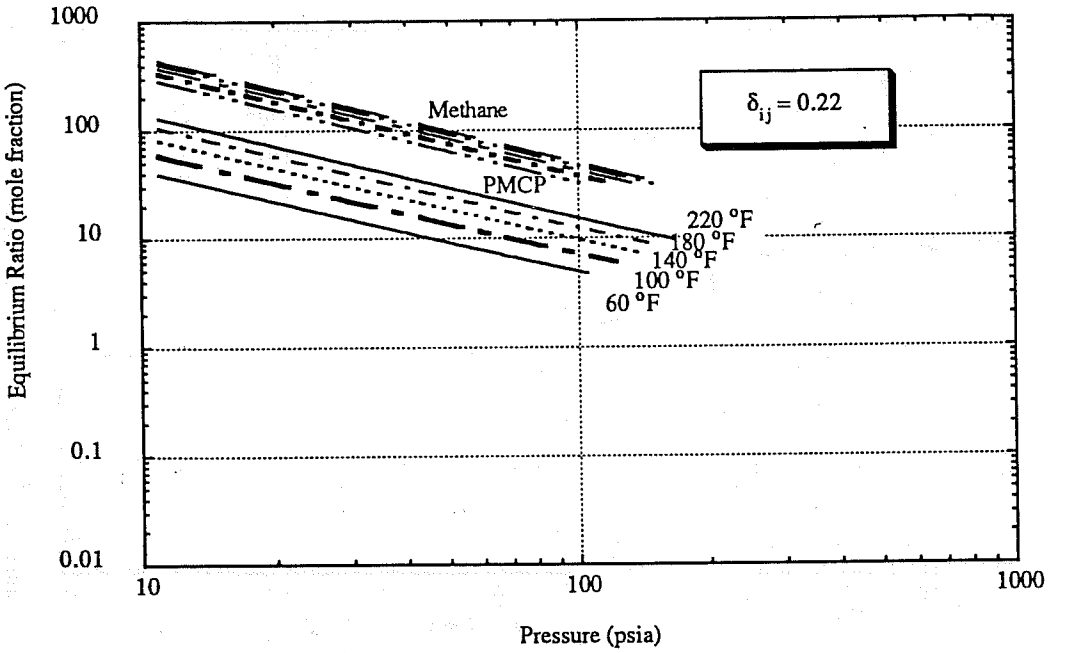

Fig. 52. Equilibrium ratio vs. pressure for PMCP from the Peng-Robinson equation of state using fluid descriptions from Well No. 73-11G

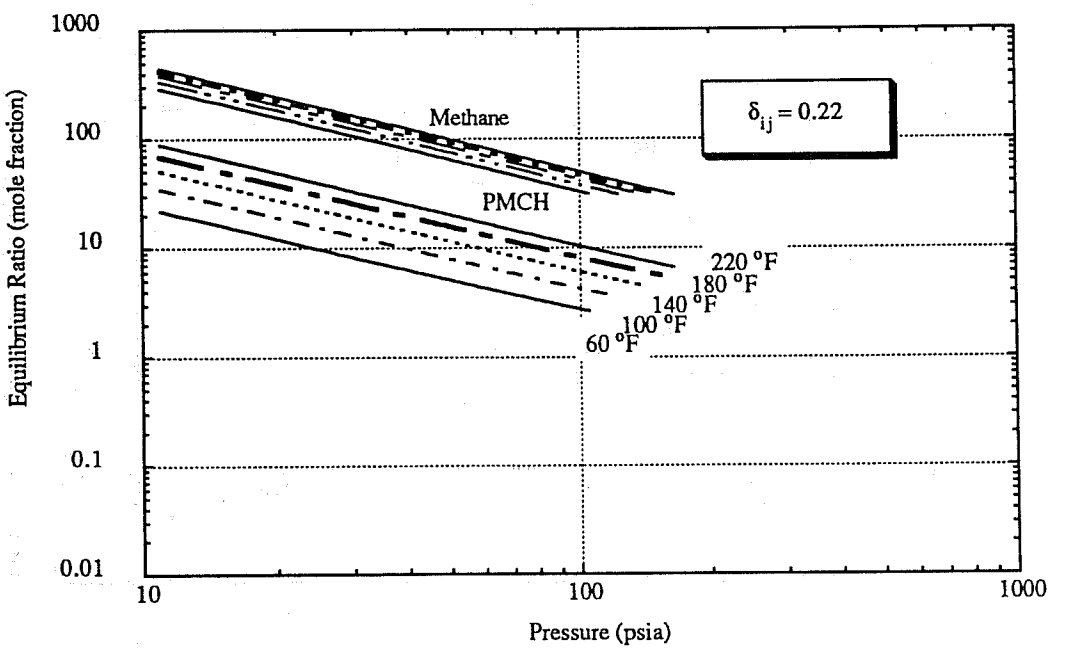

Fig. 53. Equilibrium ratio vs. pressure for PMCH from the Peng-Robinson equation of state using fluid descriptions from Well No. 73-11G

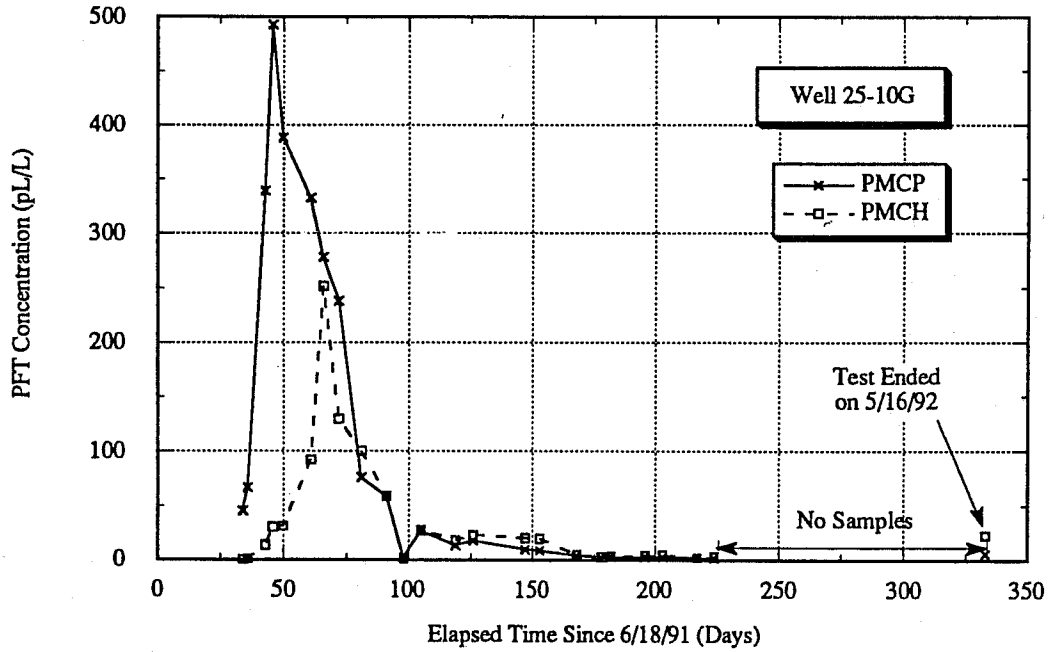

Fig. 54. Production data of PMCP and PMCH at Well 25-10G

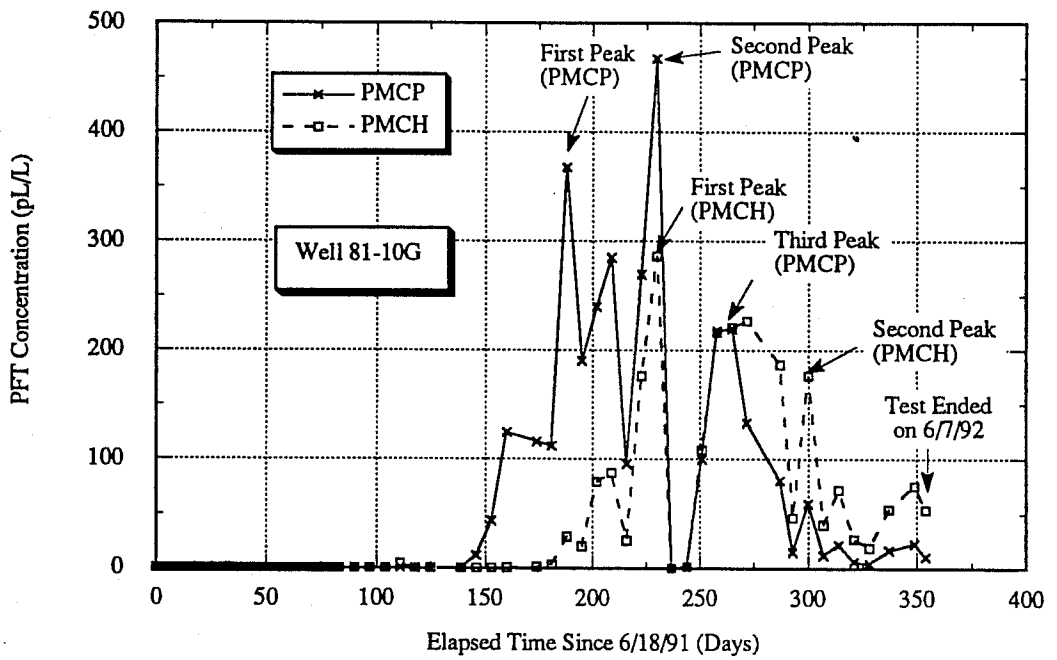

Fig. 55. Production data of PMCP and PMCH at Well 81-10G

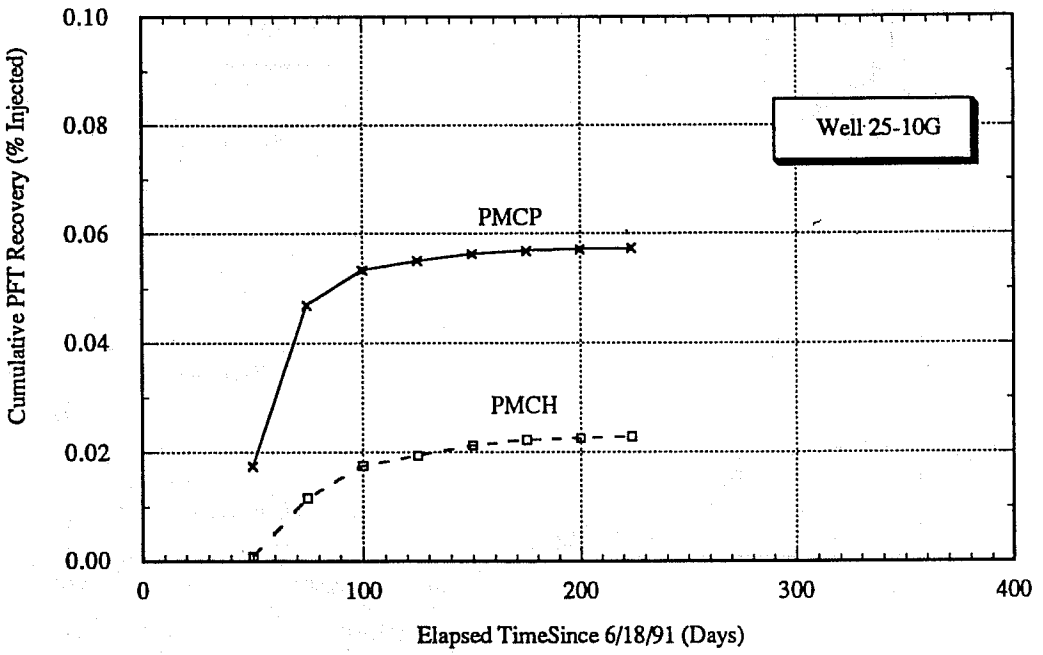

Fig. 56. Cumulative PMCP and PMCH recoveries at Well 25-10G

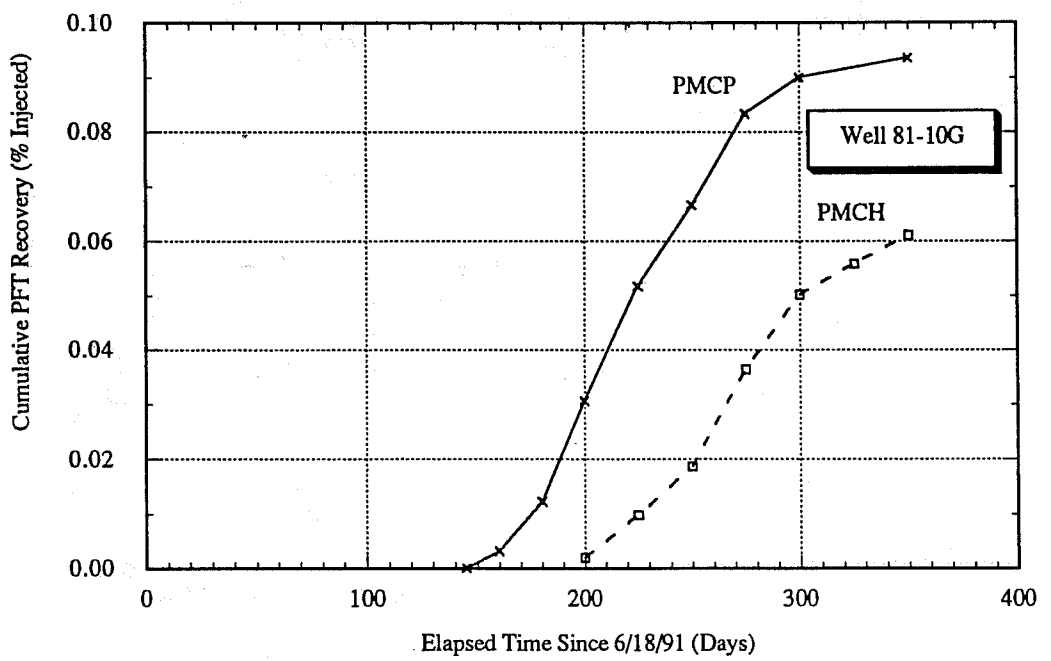

Fig. 57. Cumulative PMCP and PMCH recoveries at Well 81-10G

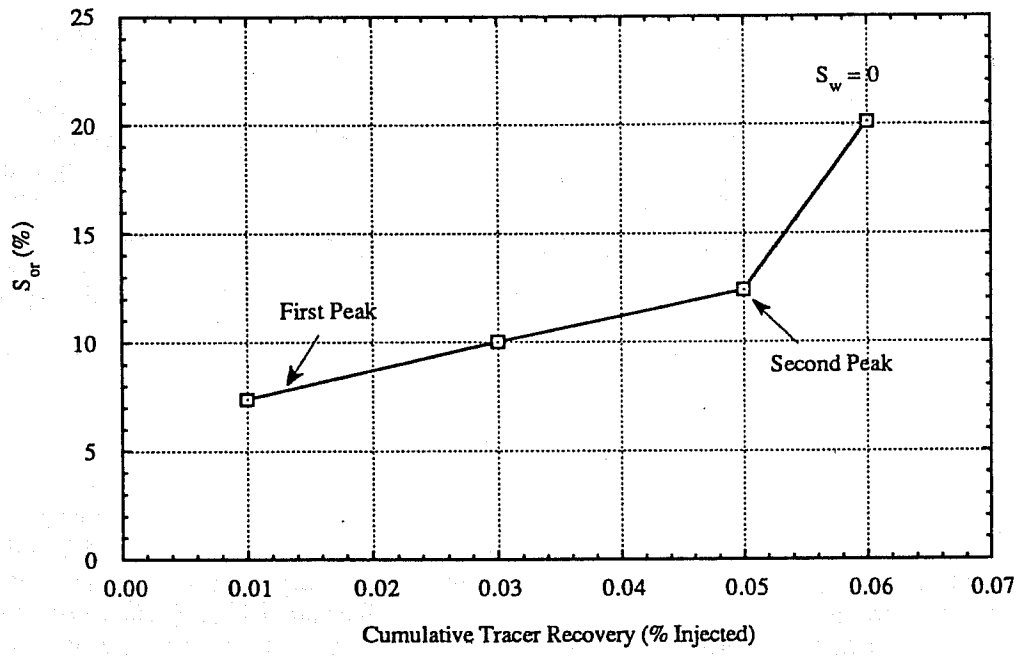

Fig. 58. S_{or} between Injector 34-10G and Well 81-10G

SECTION IV
AUTOMATIC HISTORY MATCHING

INTRODUCTION

In the second annual report of this project (Pope and Sepehrnoori, 1993) and in Ferreira *et al.* (1992), we reported results for the estimation of in-situ wettability of an oil reservoir from a novel single well tracer test. The measured signal from this test consists of multiple produced tracer concentrations when the well is backflowed plus optional water and oil cuts and bottom hole pressure. This presents the interpretation engineer with a formidable job of selecting the optimum reservoir parameters to characterize the reservoir consistent with these data. This is sometimes referred to as an inverse problem. Trial and error forward simulations using different sets of these parameters and manually comparing the simulated and measured responses to select the optimum set of parameters is one option, but this involves a great deal of time and effort and may not lead to the best estimates of the large, nonlinear set of parameters. Therefore, we developed an automated regression procedure to solve this problem as described below and in the dissertation of Ferreira (1992).

METHODS USED

Several methods for automatic history matching have been used in reservoir simulation as an attempt to obtain the optimal values of the reservoir properties (Dogru *et al.*, 1977; Jahns, 1966; Mattax and Dalton, 1990; Shah *et al.*, 1978). In well test analysis, the emphasis has been in automated type-curve analysis (Abbaszadeh-Denghani and Kamal, 1988; Barua *et al.*, 1988; Rosa and Horne, 1983; Rosa and Horne, 1991; Shah *et al.*, 1988) to obtain permeability, skin factor, wellbore storage, and storativity ratio and interporosity flow in double-porosity models. Most of the studies are related to single-phase flow only, and they have used the reservoir pressure as the main response to be matched.

The regression analysis for automatic history matching consists of performing a minimization of an objective function. When the objective function is formed by the sum of the squares of the differences between the data and the model results, it is considered a nonlinear least squares problem. The solution of the problem is obtained by minimizing the L_2-norm. This is the most frequent method in automatic history matching. Rosa and Horne (1991) recently proposed using the Least Absolute Value (LAV) as the criterion for the minimization, where the sum of the absolute values of the deviations of the data from the simulation results, or the L_1-norm, is minimized. They have shown that this approach gives better estimates when outliers are present in the data.

To verify which approach would give the better estimates for the SWWTT, we have used the least squares minimization (linear and nonlinear approximations) and the LAV minimization to solve the optimization problem.

Nonlinear Least Squares Approximation

The optimization problem can be posed as follows (IMSL, 1989):

$$\min f(\beta) = \frac{1}{2} R(\beta)^T R(\beta) = \frac{1}{2} \sum_{i=1}^{m} [r_i(\beta)]^2 \qquad (1)$$

$$\text{subject to } l_i \le \beta_i \le u_i,$$

where

$$r_i(\beta) = S(\beta, x_i) - d_i \,, \qquad (2)$$

S is the simulation result, **d** is the data observed (i = 1, ... , m observations), β is the vector of the reservoir parameters to be estimated (n parameters), and **l** and **u** are the vectors of the lower- and upper-bound values of β, respectively. This problem is solved in UTCHEM by using the IMSL (IMSL, 1989a) routine BCLSJ, which uses a modified Levenberg-Marquardt algorithm (Dennis and Schnabel, 1983; Fletcher, 1990; Gill *et al.*, 1988).

This routine requires the user to supply two subroutines, one to evaluate the function to be minimized and another to evaluate the Jacobian matrix. The modifications in the simulator were done to allow multiple simulations be performed in one run. The basic modification in the code is that the whole simulator becomes a subroutine, which is called by UTFCN, a subroutine to evaluate the objective function, and by UTJAC, a subroutine to evaluate the Jacobian. To obtain the Jacobian, we perform one simulation for each parameter β_j to be matched by making a small perturbation $\Delta\beta_j$ in just one parameter at each simulation. The derivatives are calculated numerically by

$$\frac{\partial S(\beta, x_i)}{\partial \beta_j} = \frac{S(\beta + \Delta\beta_j, x_i) - S(\beta, x_i)}{\Delta\beta_j} \quad . \tag{3}$$

Linear Approximation

Another approach to solve the optimization problem is first to linearize the model response, $S(\beta,\mathbf{x})$, by expanding it around an initial guess of the parameters, β^0, in a Taylor series up to first terms (Rosa and Horne, 1991):

$$S(\beta,\mathbf{x}) = S(\beta^0,\mathbf{x}) + (\beta_1 - \beta_1^0)\left[\frac{\partial S(\beta, x_i)}{\partial \beta_1}\right]_{\beta^0} + \ldots + (\beta_n - \beta_n^0)\left[\frac{\partial S(\beta, x_i)}{\partial \beta_n}\right]_{\beta^0} . \tag{4}$$

Then we form an overdetermined linear system of m equations in n unknowns:

$$\mathbf{y} = \mathbf{J}\,\mathbf{b}, \tag{5}$$

where

$$y_i = S(\beta^0, x_i) - d_i \ , \tag{6}$$

$$J_{i,j} = \left[\frac{\partial S(\beta, x_i)}{\partial \beta_j}\right]_{\beta^0} , \tag{7}$$

$$b_j = (\beta_j - \beta_j^0) \ . \tag{8}$$

In the equations above, **y** is the vector containing the differences between the simulation results, assuming an initial set of values for the parameters to be matched, and the data, **J** is the Jacobian matrix formed by the derivatives of the simulation result with respect to each of the parameters, and **b** is the solution vector. This system can be solved by minimizing the sum of the squares of the differences:

$$f(\beta) = \sum_{i=1}^{m}\left[y_i - \sum_{j=1}^{n} \beta_j . J_{i,j} \right]^2 . \qquad (9)$$

We have used the IMSL routine LSBRR (IMSL, 1989b) that solves a linear least squares problem with iterative refinement. The system can also be solved by minimizing the sum of the absolute values of the differences:

$$f(\beta) = \sum_{i=1}^{m}\left| y_i - \sum_{j=1}^{n} \beta_j . J_{i,j} \right| . \qquad (10)$$

We have used the IMSL routine RLAV (IMSL, 1989b) that solves a multiple linear regression model using the least absolute values criterion. It is based on the modification of a simplex algorithm for linear programming described by Barrodale and Roberts (Barrodale and Roberts, 1973 and 1974).

The problem is solved iteratively because S is an approximation, and the new values for the parameters are updated as

$$\beta_j = b_j + \beta_j^0 \qquad (11)$$

and are used as β_j^0 for the next iteration.

The modifications done in UTCHEM were again to allow multiple simulations to be performed in one run. In this case, the whole code is inside a loop to perform the simulations for the initial guess and to form the Jacobian matrix. Two subroutines were added: HMLSQ, that uses the least squares minimization, and HMLAV, that uses the least absolute values minimization.

Scaling

The objective of scaling the variables and responses before performing the optimization is to keep the variables and the responses within the same order of magnitude (Dennis and Schnabel, 1983; Gill *et al.*, 1988). Thus, undesirable weighting of some variable or response will be avoided. The scaling of the responses was done by dividing each value by the maximum value observed in the respective signal (L_∞-norm). The scaling of the parameters was done by using the transformation

$$\alpha_j = \frac{\beta_j - l_j}{u_j - l_j} \qquad (12)$$

to keep all variable values in the range [0 , 1].

Stopping or Convergence Criteria

The objective of our optimization problem is to obtain the minimum possible value for the objective function in an affordable number of iterations. The tolerances for stopping the history matching are input data to the simulator, so that the user can choose the desired degree of accuracy of the match. Besides the default criteria used by the IMSL routine BCLSJ (IMSL, 1989a), for the nonlinear approximation, we have included two other checks to stop the matching: the maximum relative error between the observed and calculated responses,

$$\max_{1\le i\le m} \left(\frac{\left| S(\beta, x_i) - d_i \right|}{d_i} \right), \qquad (13)$$

and the maximum error relative to the maximum value of the observed response,

$$\frac{\max\limits_{1\le i\le m}\left(\left|S(\beta,x_i)-d_i\right|\right)}{\max\limits_{1\le i\le m}\left(d_i\right)}\ . \tag{14}$$

For the linear approximation, we check the tolerance allowed for each parameter, the maximum relative error between the observed and calculated responses, and the relative change in the objective function value between iterations,

$$\frac{\left|f(\beta)-f(\beta)^{k-1}\right|}{f(\beta)^{k-1}}\ . \tag{15}$$

Statistical Analysis

The quality of the match can be obtained by estimating the confidence interval for each of the parameters. First we calculate an unbiased estimated variance of the match (Haan, 1991),

$$s_f^2=\frac{SSE}{m-n}\ , \tag{16}$$

where SSE is the sum of the squares of the residuals,

$$SSE=\sum_{i=1}^{m}\left[y_i-\sum_{j=1}^{n}\beta_j.J_{i,j}\right]^2. \tag{17}$$

Defining a matrix **A** as

$$A=\left(J^TJ\right)^{-1}, \tag{18}$$

the standard deviation σ_{β_j} of each individual parameter is obtained from (Haan, 1991)

$$\sigma_{\beta_j}^2=A_{jj}s_f^2. \tag{19}$$

The confidence interval for a given parameter can be obtained using

$$\beta_j-\sigma_{\beta_j}t_{1-\gamma/2:m-n}\le\beta_j\le\beta_j+\sigma_{\beta_j}t_{1-\gamma/2:m-n}\ , \tag{20}$$

where $t_{1-\gamma/2:m-n}$ is the value obtained from a Student t-distribution with level of significance γ and m-n degrees of freedom. For the nonlinear approximation, the correlation coefficient between any pair of parameters is computed from (Jahns, 1966)

$$C_{ij}=\frac{A_{ij}}{\sqrt{A_{ii}A_{jj}}}\ , \tag{21}$$

while for the linear approximation we first define (Haan, 1991)

$$z_{i,j} = \frac{\left(J_{i,j} - \overline{J_j}\right)}{\sigma_j}, \tag{22}$$

where $\overline{J_j}$ and σ_j are the mean and standard deviation of the j^{th} vector of the Jacobian matrix. The correlation matrix **C** is then calculated as

$$C = \frac{z^T z}{(n-1)}. \tag{23}$$

The limits on the correlation coefficient are $-1 \leq C_{ij} \leq 1$. When two parameters are linearly related, the value of C_{ij} is unity and they cannot be uniquely determined.

RESULTS

We will present results of the automatic history matching of simulated SWWTT's that we will refer to as synthetic field data. Since the most important properties that affect the test results are the rock relative permeabilities, we chose to history match these parameters to demonstrate the usefulness of this single-well tracer test. Initially, we will show the match of the parameters by using the different test responses, like bottomhole pressure, water cut, and tracer production data. We will present the results of the match of "smooth" data, that is, the direct result of a simulated SWWTT. Finally, we will show the history matching of "noisy" data, where we introduced some error into the simulated SWWTT results to represent possible measurement errors that can be seen in real field data. We have used the functions GASDEV and RAN1 (Press *et al.*, 1990) to obtain normally distributed random numbers between -1 and 1, which we multiply by the maximum allowed error relative to the simulated results and add to the respective test response:

$$S(\beta,x_i) = S(\beta,x_i)\ [\ 1 + (\text{random number})\ (\text{maximum allowable error})\ ]. \tag{24}$$

In one of the cases, we also introduced outliers to represent "bad" data points. We arbitrarily selected some data and changed their values. We will show, for some cases, results of the history matching of the same simulated SWWTT using different minimization methods.

Simulation Data

The simulations of the SWWTT's and their history matching were carried out considering 1D-radial geometry. The common data for all simulations are presented in Tables 1 through 3. Table 1 shows the reservoir properties and the test parameters used. Table 2 presents the tracers simulated, their properties, and the respective injected concentrations. Table 3 shows the data related to the grid used in the simulations. The relative permeability and capillary pressure data used to simulate the synthetic field data are given in Table 4. When a parameter is not being searched in the history matching, its value is kept constant during all iterations.

Using Different Signals in the History Matching

To investigate the errors in the estimates of the parameters using different signals in the automatic history matching, we considered the data of the simulated SWWTT from run number R1W34 as the synthetic field data. We performed the history matching using the bottomhole pressure as the only response in run number R1W47. In run number R1W46, we considered the water cut as the only response available. The tracers were considered the responses available in run number R1W45, and the simultaneous matching of all responses was considered in run number R1W35. The parameters being searched in these simulations were the water relative

permeability endpoint (k^o_{rw}) and exponent (e_w), the residual water saturation (S_{wr}), and the residual oil saturation (S_{or}). The tolerances for convergence and for stopping the search were the same for all simulations.

Figures 1 through 5 and Table 6 show the results of the history matching (simulation number R1W47) of the four parameters described above using the bottomhole pressure as the only response available. Figure 1 shows the ethanol concentration histories versus the ratio of the total production to the oil slug injected. The dots represent the synthetic field data considered from run number R1W34. The dashed line curve is the result obtained when the initial set of values for the parameters was used. The solid line curve is the tracer production history simulated using the values for the parameters of the last iteration of the match. As can be seen, the match of the tracer production is very poor. Figure 2 shows the water-cut histories. For this response the match seems to be very good. Figure 3 shows the bottomhole pressure drop histories. The dots represent the synthetic field data, the dashed line curve represents the simulation using the initial values considered for the parameters being searched, and the solid line curve is the result obtained using the values of the last iteration of the history matching. The agreement between the synthetic field data and the final match is not good yet, but the convergence to the desired tolerances was achieved. In Fig. 4, we show the relative permeability curves versus water saturation for the synthetic field data (that would be the true but unknown curves) represented by the connected dots, the initial set of values represented by the dashed lines, and the matched values for the parameters in solid lines. We can see that the matched values are not good yet. Table 5 and Fig. 5 summarize the results of the history matching of the simulated SWWTT of run R1W34 when the only response considered for the match was the bottomhole pressure. The errors in the estimated parameters are 7% and 6% on the endpoint and exponent of the water relative permeability, respectively, and about 15% on the residual phase saturation values. The bottomhole pressure is more sensitive to the endpoint and exponent of the relative permeability than to the residual phase saturations. In a field test, if tracers were not used, the match could be considered good because we would not know the true values of the parameters and the water-cut and pressure-drop responses would be close to the field data.

In simulation number R1W46, we considered only the water-cut response to match the water relative permeability endpoint and exponent and the residual phase saturations. Figures 6 through 10 and Table 6 show the results. The ethanol production histories for the synthetic field data, initial guess of the parameters, and the final match can be seen in Fig. 6. There is no agreement between the synthetic field data and the final matched values. Figure 7 shows the matching of the water-cut history. The result seems to be very good. The result of the match of the pressure drop is seen in Fig. 8 and is very similar to the match obtained in run number R1W47. The relative permeability curves corresponding to the synthetic field data, the initial set of values, and the matched values are presented in Fig. 9. The match is very poor. Table 6 and Fig. 10 show the errors of the matched values for the parameters. They are higher than in run number R1W47. The errors in estimating the parameters using only the water cut as the test response are 8% and 6% for the water relative permeability endpoint and exponent, respectively, 21% for the residual water saturation, and 18% for the residual oil saturation. Again in this case, if tracers were not used, the match could be considered good.

The same simulated SWWTT data of run R1W34 was history matched in run number R1W45 using only the tracer responses. We considered the methanol (aqueous, material balance tracer), the aqueous phase ethyl acetate (partitioning and reactant tracer), the ethanol (aqueous, product tracer), the octanol (oleic, material balance tracer), and the normal propanol (aqueous, product tracer) responses. The results of the match are presented in Figs. 11 through 15 and in Table 7. Figure 11 shows the match of the ethanol production history. Figure 12 shows the matched water-cut history, and as before the result is very good. The pressure drop results can be observed in Fig. 13, where we can see that they are closer to the synthetic field data than when the pressure signal itself was used to history match the parameters in run number R1W47. The relative permeability curves obtained from the matched parameters are now very close to the synthetic field data, as seen in Fig. 14. The errors between the matched values and the true data

are now very small, on the order of 3% for the water relative permeability endpoint and exponent, and less than 0.5% for the residual phase saturation values, as shown in Fig. 15 and Table 7. This shows how the tracers are much stronger signals than the pressure and water cut.

In simulation number R1W35, we used, simultaneously, all the responses considered in the cases discussed so far. Figures 16 through 20 and Table 8 show the results of the history matching. In Fig. 16 we show the ethanol histories, and we see that the match is very good. Figure 17 shows the match of the water-cut history, and as before the result is very good. In Fig. 18 we can see that the match of the pressure drop was improved and now is very good. The improvement in the matched values is also observed in Fig. 19, where we show the relative permeability curves. There is no separation between the true data and the matched curves. The match can be considered almost perfect. As Table 8 and Fig. 20 show, the errors between the true values and the matched ones are indeed very small, being less than 1% for the water relative permeability endpoint and exponent, and on the order of 0.1% for the residual phase saturation values. This shows that although the tracer responses are strong signals, the simultaneous match of all the responses that can be obtained during the test should be used because together they reduce the uncertainties and improve the values of the parameters being searched.

Comparisons between the simulation results described in this section are given in Tables 9 and 10 and in Fig. 21. In Table 9 we show the confidence intervals obtained from each history match. Table 10 shows the number of function evaluations, Jacobian evaluations, and the CPU time used in each of the simulations in order to achieve the desired tolerances. Figure 21 shows the summary of the calculated errors for each of the parameters when different signals were used in the match. For the same values of the tolerances, tracers are stronger signals than bottomhole pressure and water cut, although the time to obtain the results was the largest. The values of the matched parameters were all improved by using tracers. The biggest improvements were seen in the values for the residual phase saturations, where the errors are less than 0.5%. The improvements were even better when all the responses were considered simultaneously in the history match. One very important result of these simulations is that the Single-Well Wettability Tracer Test (SWWTT) allows the estimation of both residual phase saturations, although the reservoir is not required to be at that specific saturation like in other single-well tracer tests (Deans, 1971; Deans and Bragg, 1977; Mut and Deans, 1983).

Matching Smooth Data

In this section, we show results of the history matching of different synthetic field data. In some of the cases, we used different minimization methods to compare the results. Since the use of all the available responses gives the best estimation of the parameters, as shown in the last section, we used simultaneously all the information obtained from the simulated SWWTT's from run numbers R1W34, R1W30A , and R1W54, where we used relative permeability and capillary pressure curves characteristic of water-wet reservoirs, and run numbers R1O00 and R1O26, where we used curves characteristic of oil-wet reservoirs. For the first two tests, we will match the same parameters discussed before. For the last three tests, we also included the oil relative permeability exponent (e_o) as another parameter to be matched.

Run number R1W35, already discussed in the last section, was simulated using the Nonlinear Least Squares (NLSQ) method. In run number R1W35A, we considered the same simulated SWWTT of run number R1W34, but we used the Linear Least Squares method (LSQ) to perform the minimization for the history match. The results are presented in Figs. 22 through 26 and in Table 11. Figure 22 shows the ethanol histories. As before , the dots represent the synthetic field data, the dashed line curve represents the result obtained when the initial set of values for the parameters were used, and the solid line curve shows the result of the simulation when the matched values of the parameters were used. The match is very good. In Fig. 23, we can see the match of the water cut, and it is also very good. The match of the bottomhole pressure drop is shown in Fig. 24, and it is similar to the match for run number R1W35. The relative permeability curves are seen in Fig. 25, and we can observe that the synthetic field data and the matched curves agree very well. The calculated errors between the matched values and the true data are given in Table 11 and Fig. 26. The errors are very small, less than 1%, for the water relative permeability endpoint and

exponent, and less than 0.1% for the residual phase saturations, which can be considered a very good match.

The minimization method used in simulation number R1W35C was the Least Absolute Values (LAV). The results are shown in Fig. 27, where we show the ethanol-concentration histories, in Fig. 28, where the match of the water-cut history is shown, and in Fig. 29, where the bottomhole pressure drops are shown. The relative permeability curves are shown in Fig. 30. The agreement between the synthetic field data and the matched values is very good. Table 12 and Fig. 31 show that the errors calculated from the matched values of the parameters are on the order of 0.5% for the water relative permeability endpoint and exponent, and on the order of 0.05% for the residual phase saturations.

Comparing the results of the three methods, we can see that the overall match was better when the LAV method was used, as shown in Fig. 32 and Table 12, but the time necessary to obtain the matched values was greater than for the least squares methods. The NLSQ method used the least amount of CPU time to get the values of the searched parameters (Table 14).

In simulation number R1W30A, considered as synthetic field data, we used the capillary pressure curve characteristic of an intermediate-wet reservoir, in this case a moderately water-wet reservoir. The relative permeability curves were the same as used in simulation number R1W34. We performed history matching of the synthetic field data using all three minimization methods. The NLSQ method was used in run number R1W36D. Figure 33 shows the close agreement between the synthetic field data and the simulation result of the matched values for the ethanol production. A very good match was also obtained for the water-cut response (Fig. 34). Figure 35 shows that the match was also good for the pressure drop. The relative permeability curves are in very good agreement, as can be seen in Fig. 36. The errors between the matched values and the true data are very small, as shown in Table 15 and Fig. 37.

Simulation number R1W36E was performed considering the LSQ method for the history matching. The results (Figs. 38 through 42) are very similar to the ones obtained when using the NLSQ method. The errors between the matched values and the synthetic field data are very small (Table 16). They are less than 0.3% for the endpoint and exponent of the water relative permeability, and less than 0.03% for the residual phase saturations.

The LAV method was used in simulation number R1W36F. The results of the match of the ethanol-concentration history (Fig. 43), water-cut history (Fig. 44), bottomhole pressure drop (Fig. 45), and the relative permeability curves (Fig. 46) are similar to the match obtained in run numbers R1W36D and R1W36E . The errors are all smaller than 0.04% (Table 17 and Fig. 47).

Comparing the three methods, we can see that the match using LAV was the best. The history match using the LSQ method used the least amount of computer resources (Tables 18 and 19, and Fig. 48).

Simulation number R1W55 was performed to history match the simulated SWWTT data of run number R1W54, which has a different set of values for the relative permeability parameters and residual phase saturations. In this simulation, we also included the exponent of the oil relative permeability as another parameter to be matched. The NLSQ method for minimization was used. The match can be considered very good, as seen in Figs. 49 through 52, where we show the ethanol-concentration histories, the water-cut histories, the pressure-drop histories, and the relative permeability curves, respectively. The errors between the matched values of the parameters and the true data are very small, on the order of 1% for the water relative permeability endpoint and exponent, and on the order of 0.1% for the oil relative permeability exponent and residual phase saturations (Table 20 and Fig. 53). The history match simulations used 1466 seconds of CPU time.

History match simulation number R1O22C was performed to obtain the same parameters discussed above from a simulated SWWTT data of run number R1O00, which used parameter values that are characteristic of an oil-wet reservoir. Figure 54 shows the ethanol concentration histories. The dots represent the synthetic field data, the dashed curve represents the simulation using the initial set of values for the parameters being searched, and the solid curve again represents the final result using the matched values, and it shows a very close agreement with the true data. Figure 55 shows the good match obtained for the water-cut history. The match obtained

for the pressure drop is shown in Fig. 56 and is also a very good match. Since all the signals were matched very well, the relative permeability curves are in very good agreement, too (Fig. 57). The errors in estimating the parameters are all less than 1% (Table 21 and Fig. 58). The CPU time used for this history match was 762 seconds.

In simulation number R1O29A, we attempted to history match the simulated SWWTT data of run number R1O26, in which we used another set of relative permeability parameters and residual phase saturations, but still having characteristics of an oil-wet reservoir. Figure 59 shows the ethanol-concentration histories, and the match can be considered very good. Figure 60 shows the history match of the water-cut response, and the close agreement between the synthetic field data and the result of the simulation using the matched values for the parameters would also indicate a good match. The match of the bottomhole pressure drop, however, is very poor (Fig. 62). The comparison between the relative permeability curves (Fig. 62) would indicate that a very poor match was obtained. The errors between the matched values for the parameters and the true data are very large (Table 22 and Fig. 63). The reason for such a good match of the tracer and water-cut responses can be explained when we see the fractional flow curves of Fig. 64. They are very similar, although the relative permeability curves are very different. These results show again that the utilization of all information available from the test should be made. In this case, from the pressure match we could conclude that the water relative permeability endpoint is higher than it should be, because of the lower values of the pressure drop. The results also show that in some cases it is difficult to obtain a unique set of parameters, mainly when the displacement is near a piston-like one, as pointed out by Anterion *et al.* (1989). When this is the case, the match of the relative permeability is almost impossible, since the formation of a shock will "hide" part of the fractional flow curve.

Matching Noisy Data

In this section we give the results of the history matching of some noisy SWWTT data. In order to represent measurement errors, which are inevitable in any field test, we generated noisy synthetic field data from the same cases we described in the last section. For each response of the test, we added a randomly generated noise. The noise added was at most 10% of the value obtained from the simulations for the tracer and water-cut responses, and 0.5% at most for the bottomhole-pressure responses. We again used all the responses from the test in the history matching simulations. For some of the cases, we performed simulations using different minimization methods to compare the results. The parameters we searched in all simulations were the water relative permeability endpoint and exponent, the oil relative permeability exponent, the residual saturation to water, and the oil residual saturation.

In simulation number R1W53, we history matched the synthetic field data obtained from run number R1W34 with the addition of a random noise as described above. Besides this noise, we also selected some data points from each response to represent outliers, or bad data points. We arbitrarily increased or decreased the values of some responses. The minimization method used in this simulation was the Nonlinear Least Squares (NLSQ) method. The results of this history match are shown in Figs. 65 through 69 and in Table 23. As can be observed in Fig. 65, where we show the ethanol-concentration histories, the dots that represent the synthetic field data show some scattering as a result of the noise and the outliers added to the simulated SWWTT data of run number R1W34. The dashed curve again represents the result of a simulation in which the initial values considered for the parameters were used. The match of this tracer response can be considered good. Figure 66 shows the match of the water-cut history. The result of the simulation using the matched values for the parameters follows the trend of the water cut. Considering the scatter in the data, the match is good. The same matching quality can be observed in the pressure-drop response (Fig. 67). The relative permeability curves show a very good agreement between the values of the parameters matched and the true data considered (Fig. 68). The errors between the matched values of the parameters and the true data are given in Table 23 and Fig. 69, and they are all less than 5%, which indicates a very good match.

Simulation number R1W53A used the Linear Least Squares (LSQ) minimization method to perform the history matching of the same simulated SWWTT data that were used in the case

discussed above. The results of the simulation using the matched values for the parameters being searched are shown in Figs. 70 through 74 and Table 24, where we can see that they are very similar to the results obtained when using the NLSQ method. The same scattering is present in all the responses, but the simulation results followed the trend very much like before. The relative permeability curves obtained from the matched values of the parameters are shown in Fig. 73, and there is a good agreement with the synthetic field data. The errors are given in Table 24 and Fig. 74. They are lower than in run number R1W52D .

The Least Absolute Values (LAV) minimization method was used in the history matching simulation number R1W53C. We matched again the same simulated SWWTT data of run number R1W34, with the addition of the noise and some outliers in the responses. The matches of the ethanol-concentration history (Fig. 75), water-cut history (Fig. 76), and bottomhole-pressure-drop history (Fig. 77) are very much like the results when the other minimization methods were used. The relative permeability curves agree very well, as seen in Fig. 78, and the errors between the matched values of the parameters and the true data are less than 2% (Table 25 and Fig. 79).

Comparing the results obtained for the history matching of the simulated SWWTT data of run number R1W34, where we added a randomly distributed noise in all the signals to represent measurement errors and also arbitrarily introduced some outliers to represent some bad data points (Tables 26 and 27, and Fig 80), we can conclude that the two linear approximation methods give better results than the nonlinear approximation, and they used less CPU time to achieve the convergence. The LAV method for minimization used the least amount of time in this case.

History matching simulation number R1W52D was performed to match the simulated SWWTT data of run number R1W30A with the addition of a randomly distributed noise to represent measurement errors. We considered a maximum value of 10% for the errors in the tracer and water-cut responses, and a maximum error of 0.5% in the bottomhole-pressure response. In this case, we did not consider outliers. The minimization method used in this simulation was the NLSQ. The results of the history match are shown in Figs. 81 through 85 and in Table 28. Figures 81 and 82 show the match of the ethanol-concentration and water-cut histories , where we can see, despite the scatter in the data points, the close agreement between the synthetic field data and the simulation result when the matched values for parameters were used. The match of the bottomhole-pressure responses (Fig. 83) is not so good as for the tracer and water-cut responses. There is a good agreement between the true relative permeability curves and the curves calculated using the matched values of the parameters (Fig. 84). The water relative permeability endpoint and exponent values have the largest errors of the match, as shown in Table 28 and Fig. 85. The errors for the residual phase saturation values are less than 2%.

Simulation number R1W52H was performed to history match the same SWWTT data discussed above, but using the LSQ method for the minimization. The matches of the tracer (Fig. 86), water-cut (Fig. 87), and bottomhole-pressure (Fig. 88) responses are much better than the history matching described before. The relative permeability curves are now in very good agreement, as shown in Table 29 and Fig. 90, and in the relative permeability curves in Fig. 89. The errors are now less than 1% for all parameters matched.

The LAV minimization method was used in simulation number R1W52I to history match the same simulated SWWTT data of run number R1W30A with the addition of the randomly distributed noise. The quality of the match is very good, very similar to the match using LSQ, as seen in the agreement of the ethanol (Fig. 91), water-cut (Fig. 92), and bottomhole-pressure (Fig. 93) responses with the synthetic field data. As we see in Fig. 94, there is a very good agreement between the true and the history matched relative permeability curves. The errors are less than 1% for all matched parameters (Table 30 and Fig. 95).

A comparison between the results of the different minimization methods used for history matching the simulated SWWTT data of run number R1W30A with some noise added can be seen in Tables 31 and 32 and in Fig. 96. The errors were larger when the NLSQ method was used. The best results for the match were obtained when the LSQ method was used.

Simulation number R1W56 was performed for the history match of the simulated single-well wettability tracer test of run number R1W54, with the addition of randomly distributed noise to represent the measurement errors. No outliers were added to the responses. The values of the

maximum allowed errors were the same ones that we discussed before. Figure 97 shows the match of the ethanol-concentration history. Despite the scatter in the data, the agreement in the results between the synthetic field data and the simulation using the values of the matched parameters is very good. The agreement is not so good for the water-cut history, as seen in Fig. 98, but the shape of the response is very close to the synthetic field data. Similar matching quality is observed in the bottomhole-pressure-drop response (Fig. 99), where the overall trend and the same level of pressure drop was achieved when using the matched values of the parameters to simulate the tests. The match of the relative permeability parameters and residual phase saturations can be considered very good, as shown in Fig. 100. Table 33 and Fig. 101 show the errors between the matched values of the parameters and the true data. The errors are less than 2% for all parameters except for the residual water saturation, for which the error was about 4%.

In simulation number R1O33, we performed a history match of the simulated SWWTT data in the oil-wet reservoir of run number R1O00, but in this case we added a randomly distributed error in all the test responses. The maximum allowed variations were 10% on the tracers and water-cut signals, and 0.5% on the bottomhole-pressure response. No outliers were considered. Figure 102 shows the match of the ethanol-concentration history in a solid curve, which agrees very closely to the synthetic field data represented by the dots. Although showing more scatter, the match of the water cut (Fig. 103) and that of the pressure drop (Fig. 104) can be considered good. The true relative permeability curves and the ones calculated using the matched values for the parameters are very close to each other, as can be seen in Fig. 105, except for small variations in the water relative permeability endpoint and in the residual water saturation. The errors are acceptable, considering the level of the noise introduced into the simulation results of run number R1O00 (Table 34 and Fig. 106).

CONCLUSIONS

The reservoir simulator UTCHEM has been modified to perform automatic history matching of the SWWTT. The history matching is done by using optimization techniques to find the parameter values that minimize the difference between the observed and simulated responses. Three methods are available: (1) Nonlinear Least Squares, that uses the IMSL routine BCLSJ; (2) Linear Least Squares that uses the IMSL routine LSBRR that solves a linear least squares problem with iterative refinement; and (3) Least Absolute Values that uses the IMSL routine RLAV that solves a multiple linear regression model using the least absolute values criterion. Automatic history matching was successfully used to obtain the relative permeability parameters and the residual phase saturations from the test results. All three methods have estimated the values of the parameters within a reasonable error and at affordable computational times, even when randomly distributed errors and outliers were introduced in the simulated SWWTT responses to be matched. Overall, the least absolute values criterion for minimization gave the lowest errors.

The remarkable conclusion of these simulations is that the simultaneous matching of all the responses during this single-well tracer test can be done, and all the relative permeability parameters and both residual phase saturations can be estimated within a reasonable range of errors. We have shown that the parameters can be estimated even when measurement errors and outliers were included in the simulated test results.

Table 1. Reservoir and Test Parameters

Injection and Production Rate	200 bbl/day
Water Tracer Slug	20 bbl
Water Buffer	40 bbl
Oil Tracer Slug	20 bbl
Oil Buffer	40 bbl
Injection Time	0.6 days
Shut-In Time	5.4 days
Production Time	5.0 days
Oil Compressibility	15.0×10^{-6} psi^{-1}
Water Compressibility	3.0×10^{-6} psi^{-1}
Rock Compressibility	3.0×10^{-6} psi^{-1}
Porosity	25%
Permeability	233.3 md
Thickness	24 ft
Initial Water Cut	0.5
Longitudinal Dispersivity	0.1 ft
Oil Viscosity	1.0 cp
Water Viscosity	0.7 cp

Table 2. Tracer Data

Tracer Type	Partition Coefficient	Reaction Rate (days^{-1})	Injected Concentration (vol%)
Methanol - MeOH (Material Balance)	0.	0.	1.0
Ethyl Acetate - EtAc (Ester)	5.0	0.06	1.0
Ethanol - EtOH (Product)	0.	0.	0.
Octanol (Material Balance)	∞	0.	1.0
Propyl Acetate - PrAc (Ester)	10.0	0.07	1.0
Normal Propanol - NPA (Product)	0.	0.	0.

Table 3. Simulation Grid Data

Number of gridblocks	31
Well radius	0.25 ft
Outer radius	171.2 ft
Δr's for blocks No.	
1	0.25 ft
2	2.0 ft
3-11	1.0 ft
12-16	2.0 ft
17-21	3.0 ft
22-26	5.0 ft
27-29	10.0 ft
30	20.0 ft
31	40.0 ft

Table 4. Relative Permeability and Capillary Pressure Data

PARAMETER	SYNTHETIC FIELD DATA RUNS				
	R1W34	R1W30A	R1W54	R1O00	R1O26
Residual Water Saturation (S_{wr})	0.24	0.24	0.27	0.24	0.20
Residual Oil Saturation (S_{or})	0.34	0.34	0.34	0.34	0.25
Oil Relative Permeability Endpoint (k^o_{ro})	1.0	1.0	1.0	1.0	1.0
Oil Relative Permeability Exponent (e_o)	1.4	1.4	2.0	2.1	2.8
Water Relative Permeability Endpoint (k^o_{rw})	0.35	0.35	0.15	0.70	0.50
Water Relative Permeability Exponent (e_w)	2.3	2.3	2.0	2.1	1.8
Water-Wet Capillary Pressure Endpoint (c_{pcw})	15.	15.	15.	0.	0.
Water-Wet Capillary Pressure Exponent (n_{pcw})	4.	4.	4.	0.	0.
Oil-Wet Capillary Pressure Endpoint (c_{pco})	0.	-10.	0.	-15.	-15.
Oil-Wet Capillary Pressure Exponent (n_{pco})	0.	6.	0.	4.	4.
Water Saturation at Zero Capillary Pressure (S*)	0.66	0.576	0.576	0.24	0.20

Table 5. Summary of the History Matching Using Bottomhole Pressure Only (Run R1W47)

PARAMETER	TRUE DATA	INITIAL GUESS	FINAL MATCH	ERROR	ERROR (%)
k^o_{rw}	0.35	0.20	0.3251	-0.0249	-7.11
e_w	2.30	2.00	2.1623	-0.1377	-5.99
Swr	0.24	0.30	0.2755	0.0355	14.79
S_{or}	0.34	0.30	0.2912	-0.0488	-14.35

Table 6. Summary of the History Matching Using Water Cut Only (Run R1W46)

PARAMETER	TRUE DATA	INITIAL GUESS	FINAL MATCH	ERROR	ERROR (%)
k^o_{rw}	0.35	0.20	0.3227	-0.0273	-7.80
e_w	2.30	2.00	2.1519	-0.1481	-6.44
Swr	0.24	0.30	0.2907	0.0507	21.13
S_{or}	0.34	0.30	0.2775	-0.0625	-18.38

Table 7. Summary of the History Matching Using Tracers Only (Run R1W45)

PARAMETER	TRUE DATA	INITIAL GUESS	FINAL MATCH	ERROR	ERROR (%)
k^o_{rw}	0.35	0.20	0.3386	-0.0114	-3.26
e_w	2.30	2.00	2.2362	-0.0638	-2.77
Swr	0.24	0.30	0.2412	0.0012	0.50
S_{or}	0.34	0.30	0.3413	0.0013	0.38

Table 8. Summary of the History Matching Using Tracers, Water Cut, and Bottomhole Pressure (Run R1W35)

PARAMETER	TRUE DATA	INITIAL GUESS	FINAL MATCH	ERROR	ERROR (%)
k_{rw}^{o}	0.35	0.20	0.3465	-0.0035	-1.00
e_w	2.30	2.00	2.2815	-0.0185	-0.80
Swr	0.24	0.30	0.2402	0.0002	0.08
S_{or}	0.34	0.30	0.3404	0.0004	0.12

Table 9. Comparison of the Different Responses Used for the History Matching (Runs R1W47, R1W46, R1W45, and R1W35)

PARAMETER	95% CONFIDENCE INTERVALS (%)			
	(R1W47)	(R1W46)	(R1W45)	(R1W35)
k_{rw}^{o}	0.760	0.127	0.165	0.011
e_w	0.166	0.098	0.143	0.004
Swr	1.300	0.719	0.029	0.208
S_{or}	1.222	0.753	0.021	0.071

R1W47 - Using Bottomhole Pressure
R1W46 - Using Water Cut
R1W45 - Using Tracers
R1W35 - Using Tracers, Water Cut, and Bottomhole Pressure

Table 10. Number of Evaluations and CPU Time (Runs R1W47, R1W46, R1W45, and R1W35)

	(R1W47)	(R1W46)	(R1W45)	(R1W35)
FEV	3	6	8	6
JAC	2	5	8	5
CPU	177	390	576	362

FEV - Number of Function Evaluations
JAC - Number of Jacobian Evaluations
CPU - CPU time in seconds using a CRAY Y-MP

Table 11. Summary of the History Matching Using Linear Least Squares (Run R1W35A)

PARAMETER	TRUE DATA	INITIAL GUESS	FINAL MATCH	ERROR	ERROR (%)
k_{rw}^{o}	0.35	0.20	0.3471	-0.0029	-0.83
e_w	2.30	2.00	2.2845	-0.0155	-0.67
Swr	0.24	0.30	0.2402	0.0002	0.08
S_{or}	0.34	0.30	0.3403	0.0003	0.09

Table 12. Summary of the History Matching Using Least Absolute Values (Run R1W35C)

PARAMETER	TRUE DATA	INITIAL GUESS	FINAL MATCH	ERROR	ERROR (%)
k_{rw}^{o}	0.35	0.20	0.3517	0.0017	0.49
e_w	2.30	2.00	2.3090	0.0090	0.39
Swr	0.24	0.30	0.2399	-0.0001	-0.04
S_{or}	0.34	0.30	0.3398	-0.0002	-0.06

Table 13. Comparison of the Methods Used for the History Matching (Runs R1W35, R1W35A, and R1W35C)

PARAMETER	95% CONFIDENCE INTERVALS (%)		
	NLSQ (R1W35)	LSQ (R1W35A)	LAV (R1W35C)
k_{rw}^{o}	0.011	0.017	0.017
e_w	0.004	0.018	0.013
Swr	0.208	0.008	0.004
S_{or}	0.071	0.006	0.006
NLSQ - Nonlinear Least Squares LSQ - Linear Least Squares LAV - Least Absolute Values			

Table 14. Number of Evaluations and CPU Time (Runs R1W35, R1W35A, and R1W35C)

	NLSQ (R1W35)	LSQ (R1W35A)	LAV (R1W35C)
FEV	6	8	10
JAC	5	8	10
CPU	362	465	575
FEV - Number of Function Evaluations JAC - Number of Jacobian Evaluations CPU - CPU time in seconds using a CRAY Y-MP			

Table 15. Summary of the History Matching Using Nonlinear Least Squares (Run R1W36D)

PARAMETER	TRUE DATA	INITIAL GUESS	FINAL MATCH	ERROR	ERROR (%)
k_{rw}^{o}	0.35	0.20	0.3492	-0.0008	-0.23
e_w	2.30	2.00	2.2970	-0.003	-1.27
Swr	0.24	0.30	0.2399	-0.0001	-0.04
S_{or}	0.34	0.30	0.3401	0.0001	0.03

Table 16. Summary of the History Matching Using Linear Least Squares (Run R1W36E)

PARAMETER	TRUE DATA	INITIAL GUESS	FINAL MATCH	ERROR	ERROR (%)
k_{rw}^{o}	0.35	0.20	0.3510	0.001	0.29
e_w	2.30	2.00	2.3045	0.0045	0.20
Swr	0.24	0.30	0.2400	0.00002	0.01
S_{or}	0.34	0.30	0.3399	-0.0001	-0.03

Table 17. Summary of the History Matching Using Least Absolute Values (Run R1W36F)

PARAMETER	TRUE DATA	INITIAL GUESS	FINAL MATCH	ERROR	ERROR (%)
k_{rw}^{o}	0.35	0.20	0.35003	0.00003	0.01
e_w	2.30	2.00	2.3002	0.0002	0.01
Swr	0.24	0.30	0.23999	-0.00001	-0.04
S_{or}	0.34	0.30	0.33999	-0.00001	-0.03

Table 18. Comparison of the Methods Used for the History Matching (Runs R1W36D, R1W36E, and R1W36F)

PARAMETER	95% CONFIDENCE INTERVALS (%)		
	NLSQ (R1W36D)	LSQ (R1W36E)	LAV (R1W36F)
k_{rw}^{o}	0.046	0.003	0.003
e_w	0.009	0.004	0.004
Swr	0.071	0.004	0.004
S_{or}	0.297	0.003	0.001
NLSQ - Nonlinear Least Squares LSQ - Linear Least Squares LAV - Least Absolute Values			

Table 19. Number of Evaluations and CPU Time (Runs R1W36D, R1W36E, and R1W36F)

	NLSQ (R1W36D)	LSQ (R1W36E)	LAV (R1W36F)
FEV	5	4	5
JAC	4	4	5
CPU	302	247	297
FEV - Number of Function Evaluations JAC - Number of Jacobian Evaluations CPU - CPU time in seconds using a CRAY Y-MP			

Table 20. Summary of the History Matching (Run R1W55)

PARAMETER	TRUE DATA	INITIAL GUESS	FINAL MATCH	ERROR	ERROR (%)	95% CONFIDENCE INTERVAL(%)
k^o_{rw}	0.15	0.30	0.1519	0.0019	1.27	0.046
e_w	2.00	2.70	2.0247	0.0247	1.24	0.044
e_o	2.00	1.60	2.0032	0.0032	0.16	0.015
Swr	0.27	0.22	0.2701	0.0001	0.04	0.022
S_{or}	0.29	0.36	0.2897	-0.003	-0.10	0.024
Number of Function Evaluations = 19 Number of Jacobian Evaluations = 18 CPU time (CRAY Y-MP) = 1466 seconds						

Table 21. Summary of the History Matching (Run R1O22C)

PARAMETER	TRUE DATA	INITIAL GUESS	FINAL MATCH	ERROR	ERROR (%)	95% CONFIDENCE INTERVAL(%)
k^o_{rw}	0.70	0.55	0.6935	0.0065	-0.93	0.014
e_w	2.10	2.50	2.0850	-0.0150	-0.71	0.005
e_o	2.10	1.70	2.1022	0.0022	0.10	0.014
Swr	0.24	0.20	0.2408	0.0008	0.33	0.179
S_{or}	0.34	0.30	0.3404	0.0004	0.12	0.159
Number of Function Evaluations = 11 Number of Jacobian Evaluations = 8 CPU time (CRAY Y-MP) = 762 seconds						

Table 22. Summary of the History Matching (Run R1O29A)

PARAMETER	TRUE DATA	INITIAL GUESS	FINAL MATCH	ERROR	ERROR (%)	95% CONFIDENCE INTERVAL(%)
k^o_{rw}	0.50	0.80	0.8500	0.3500	70.00	0.005
e_w	1.80	2.50	1.8843	0.0843	4.68	0.000
e_o	2.80	2.00	2.5377	-0.2623	-9.37	0.004
Swr	0.20	0.15	0.2200	0.0200	10.00	1.295
S_{or}	0.25	0.30	0.2400	-0.0100	-4.00	1.492
Number of Function Evaluations = 32 Number of Jacobian Evaluations = 15 CPU time (CRAY Y-MP) = 1702 seconds						

Table 23. Summary of the History Matching Using Nonlinear Least Squares (Run R1W53)

PARAMETER	TRUE DATA	INITIAL GUESS	FINAL MATCH	ERROR	ERROR (%)
k^o_{rw}	0.35	0.20	0.3648	0.0148	4.23
e_w	2.30	2.00	2.3977	0.0977	4.25
e_o	1.40	1.80	1.4186	0.0186	1.33
Swr	0.24	0.30	0.2339	-0.0061	-2.54
S_{or}	0.34	0.30	0.3435	0.0035	1.03

Table 24. Summary of the History Matching Using Linear Least Squares (Run R1W53A)

PARAMETER	TRUE DATA	INITIAL GUESS	FINAL MATCH	ERROR	ERROR (%)
k^o_{rw}	0.35	0.20	0.3534	0.0034	0.97
e_w	2.30	2.00	2.3451	0.0451	1.96
e_o	1.40	1.80	1.4171	0.0171	1.22
Swr	0.24	0.30	0.2351	-0.0049	-2.04
S_{or}	0.34	0.30	0.3346	-0.0054	-1.59

Table 25. Summary of the History Matching Using Absolute Values (Run R1W53C)

PARAMETER	TRUE DATA	INITIAL GUESS	FINAL MATCH	ERROR	ERROR (%)
k^o_{rw}	0.35	0.20	0.3523	0.0023	0.66
e_w	2.30	2.00	2.3445	0.0445	1.93
e_o	1.40	1.80	1.3983	-0.0017	-0.12
Swr	0.24	0.30	0.2370	-0.0030	-1.25
S_{or}	0.34	0.30	0.3381	-0.0019	-0.56

Table 26. Comparison of the Methods Used for the History Matching (Runs R1W53, R1W53A, and R1W53C)

PARAMETER	95% CONFIDENCE INTERVALS (%)		
	NLSQ (R1W53)	LSQ (R1W53A)	LAV (R1W53C)
k_{rw}^{o}	13.78	5.68	10.59
e_w	10.06	4.21	8.04
e_o	8.13	8.13	7.99
Swr	3.60	3.32	3.35
S_{or}	3.10	2.85	2.83
NLSQ - Nonlinear Least Squares LSQ - Linear Least Squares LAV - Least Absolute Values			

Table 27. Number of Evaluations and CPU Time (Runs R1W53, R1W53A, and R1W53C)

	NLSQ (R1W53)	LSQ (R1W53A)	LAV (R1W53C)
FEV	11	5	4
JAC	9	5	4
CPU	774	365	291
FEV - Number of Function Evaluations JAC - Number of Jacobian Evaluations CPU - CPU time in seconds using a CRAY Y-MP			

Table 28. Summary of the History Matching Using Nonlinear Least Squares (Run R1W52D)

PARAMETER	TRUE DATA	INITIAL GUESS	FINAL MATCH	ERROR	ERROR (%)
k_{rw}^{o}	0.35	0.45	0.3109	-0.0391	-11.17
e_w	2.30	2.00	2.1326	-0.1674	-7.28
e_o	1.40	1.80	1.4568	0.0568	4.06
Swr	0.24	0.20	0.2438	0.0038	1.58
S_{or}	0.34	0.30	0.3412	0.0012	0.35

Table 29. Summary of the History Matching Using Linear Least Squares (Run R1W52H)

PARAMETER	TRUE DATA	INITIAL GUESS	FINAL MATCH	ERROR	ERROR (%)
k_{rw}^{o}	0.35	0.45	0.3486	-0.0014	-0.40
e_w	2.30	2.00	2.2849	-0.0151	-0.66
e_o	1.40	1.80	1.4037	0.0037	0.26
Swr	0.24	0.20	0.2418	0.0018	0.75
S_{or}	0.34	0.30	0.34003	0.00003	0.01

Table 30. Summary of the History Matching Using Least Absolute Values (Run R1W52I)

PARAMETER	TRUE DATA	INITIAL GUESS	FINAL MATCH	ERROR	ERROR (%)
k_{rw}^{o}	0.35	0.45	0.3473	-0.0027	-0.77
e_w	2.30	2.00	2.2855	-0.0145	-0.63
e_o	1.40	1.80	1.4142	0.0142	1.01
Swr	0.24	0.20	0.2423	0.0023	0.96
S_{or}	0.34	0.30	0.3396	-0.0004	-0.12

Table 31. Comparison of the Methods Used for the History Matching (Runs R1W52D, R1W52H, and R1W52I)

PARAMETER	95% CONFIDENCE INTERVALS (%)		
	NLSQ (R1W52D)	LSQ (R1W52H)	LAV (R1W52I)
k_{rw}^{o}	2.26	5.55	5.30
e_w	0.24	3.22	3.07
e_o	0.46	2.13	2.04
Swr	6.10	1.90	1.85
S_{or}	6.07	1.22	1.21
NLSQ - Nonlinear Least Squares LSQ - Linear Least Squares LAV - Least Absolute Values			

Table 32. Number of Evaluations and CPU Time (Runs R1W52D, R1W52H, and R1W52I)

	NLSQ (R1W52D)	LSQ (R1W52H)	LAV (R1W52I)
FEV	17	4	4
JAC	10	4	4
CPU	962	285	288
FEV - Number of Function Evaluations JAC - Number of Jacobian Evaluations CPU - CPU time in seconds using a CRAY Y-MP			

Table 33. Summary of the History Matching (Run R1W56)

PARAMETER	TRUE DATA	INITIAL GUESS	FINAL MATCH	ERROR	ERROR (%)	95% CONFIDENCE INTERVAL(%)
k_{rw}^{o}	0.15	0.30	0.1491	-0.0009	-0.60	2.09
e_w	2.00	2.70	1.9849	-0.0151	-0.76	0.22
e_o	2.00	1.60	2.0327	0.0327	1.64	0.21
Swr	0.27	0.22	0.2804	0.0104	3.85	9.64
S_{or}	0.29	0.36	0.2951	0.0051	1.76	9.61
Number of Function Evaluations = 27 Number of Jacobian Evaluations = 17 CPU time (CRAY Y-MP) = 1572 seconds						

Table 34. Summary of the History Matching (Run R1O33)

PARAMETER	TRUE DATA	INITIAL GUESS	FINAL MATCH	ERROR	ERROR (%)	95% CONFIDENCE INTERVAL(%)
k_{rw}^{o}	0.70	0.55	0.7889	0.0889	12.70	0.450
e_w	2.10	2.50	2.2789	0.1789	8.52	0.233
e_o	2.10	1.70	2.0790	-0.0210	-1.00	0.380
Swr	0.24	0.20	0.2313	-0.0087	-3.63	2.741
S_{or}	0.34	0.30	0.3344	-0.0056	-1.65	3.651
Number of Function Evaluations = 18 Number of Jacobian Evaluations = 9 CPU time (CRAY Y-MP) = 991 seconds						

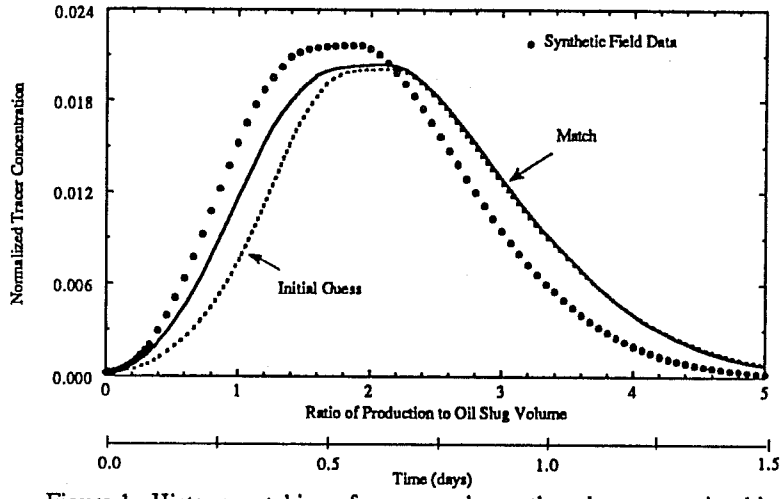

Figure 1. History matching of aqueous phase ethanol-concentration history, using bottomhole pressure only (Runs R1W34 and R1W47)

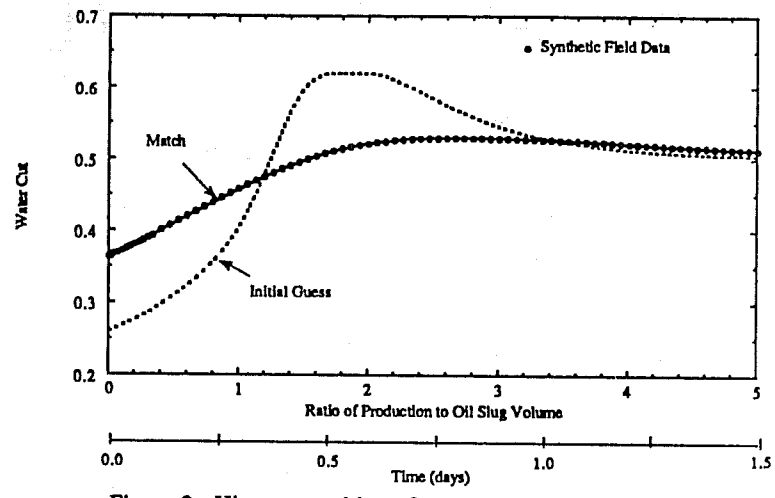

Figure 2. History matching of water-cut history, using bottomhole pressure only (Runs R1W34 and R1W47)

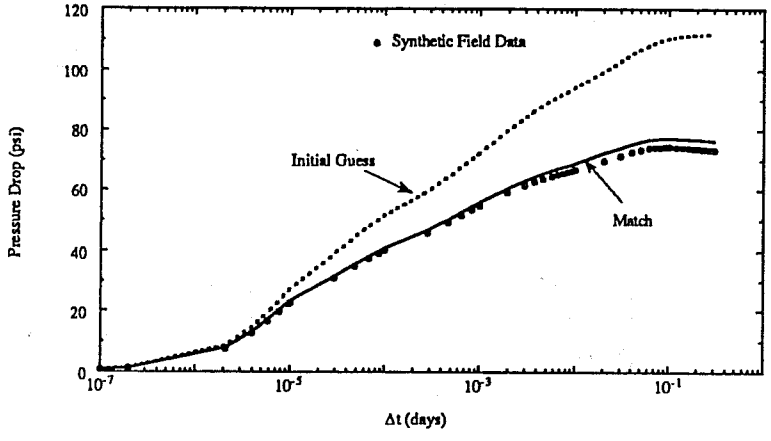

Figure 3. History matching of the bottomhole-pressure-drop history during wate injection, using bottomhole pressure only (Runs R1W34 and R1W47.

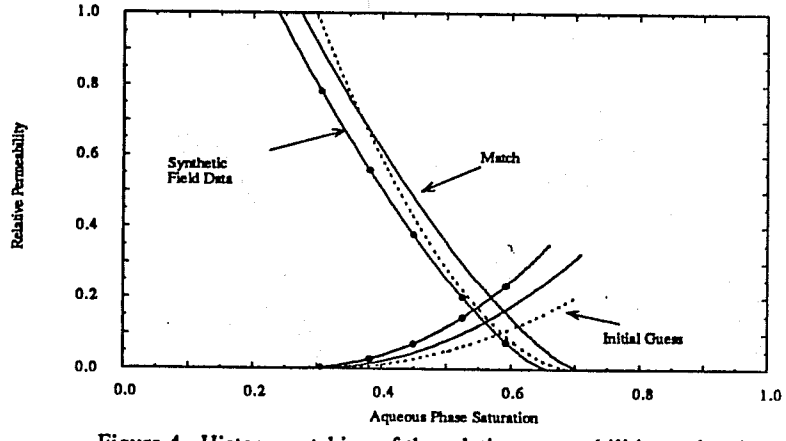

Figure 4. History matching of the relative permeabilities and residual phase saturations, using bottomhole pressure only (Runs R1W34 and R1W47)

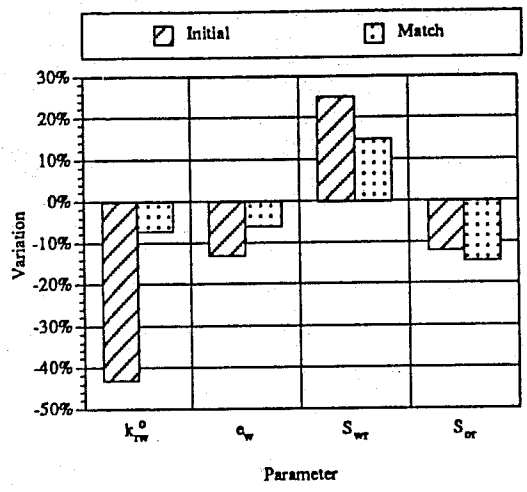

Figure 5. Initial variation and final match of the parameters using bottomhole pressure only (Run R1W47)

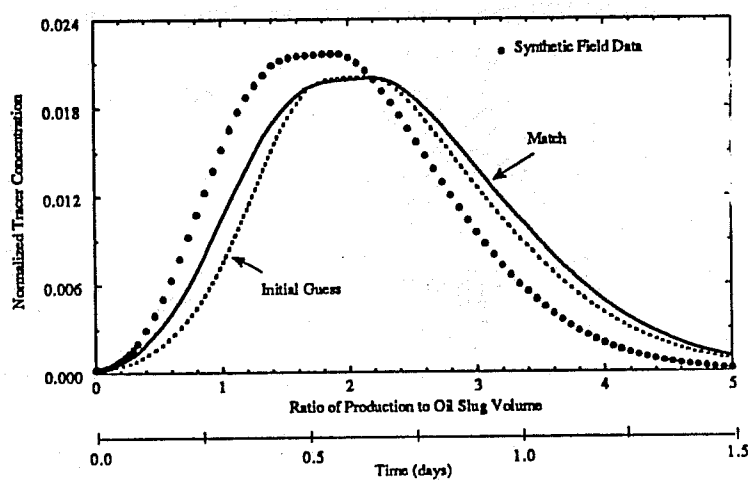

Figure 6. History matching of aqueous phase ethanol-concentration history, using water cut only (Runs R1W34 and R1W46)

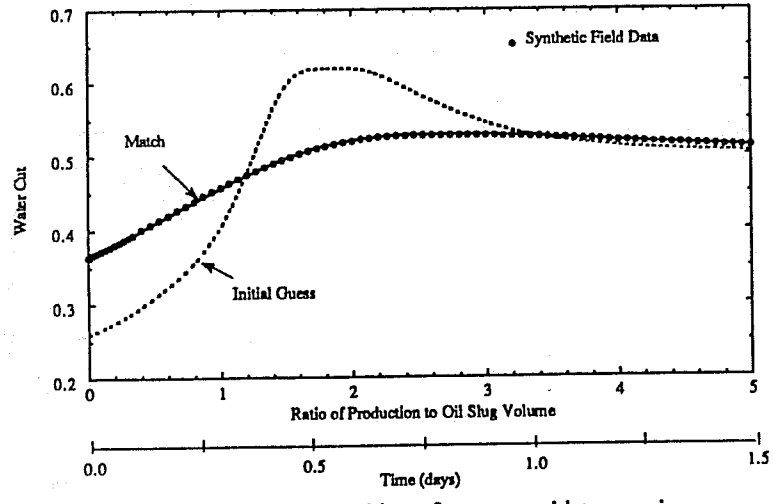

Figure 7. History matching of water-cut history, using water cut only (Runs R1W34 and R1W46)

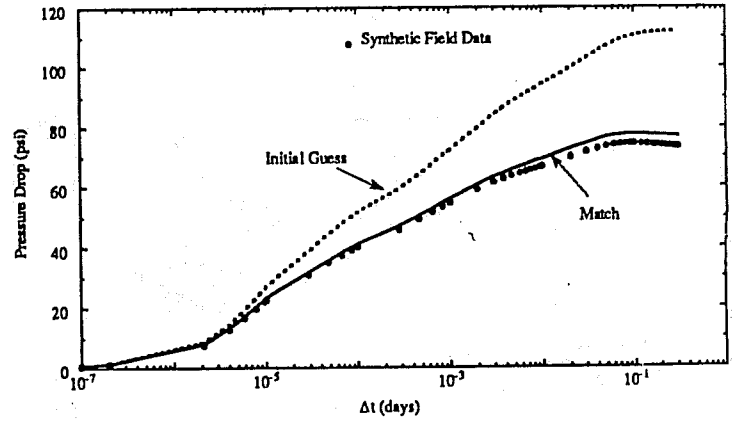

Figure 8. History matching of the bottomhole-pressure-drop history during water injection, using water cut only (Runs R1W34 and R1W46)

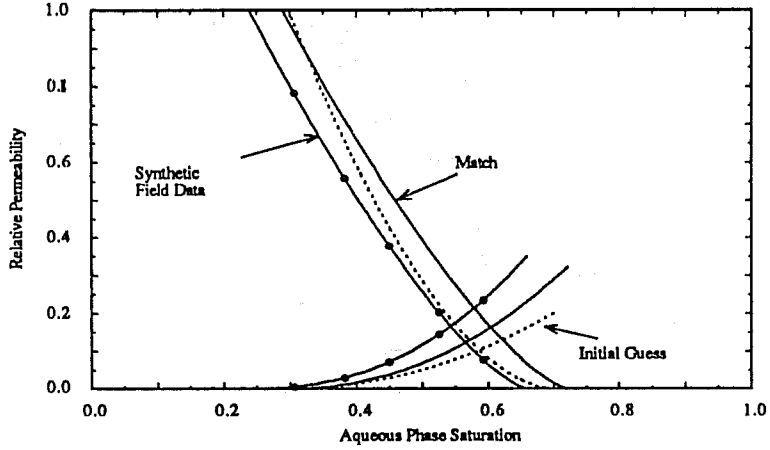

Figure 9. History matching of the relative permeabilities and residual phase saturations, using water cut only (Runs R1W34 and R1W46)

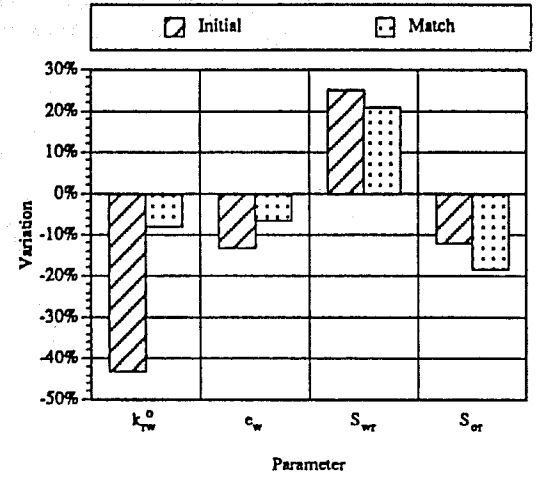

Figure 10. Initial variation and final match of the parameters using water cut only (Run R1W46)

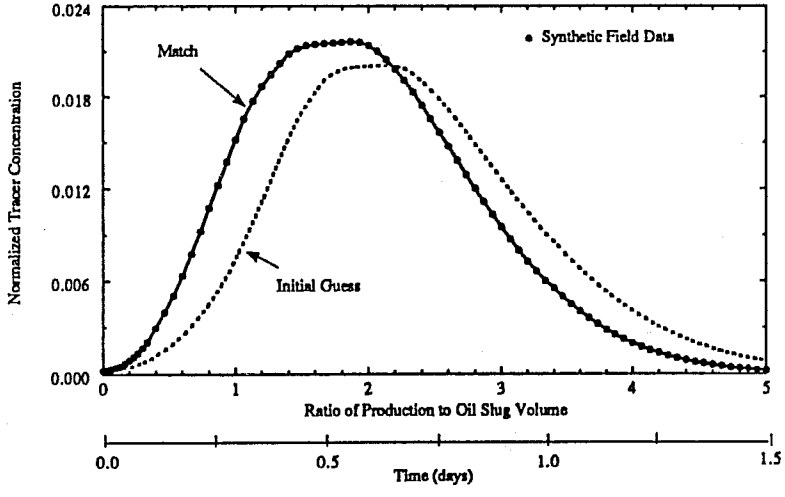

Figure 11. History matching of aqueous phase ethanol-concentration history using tracers only (Runs R1W34 and R1W45)

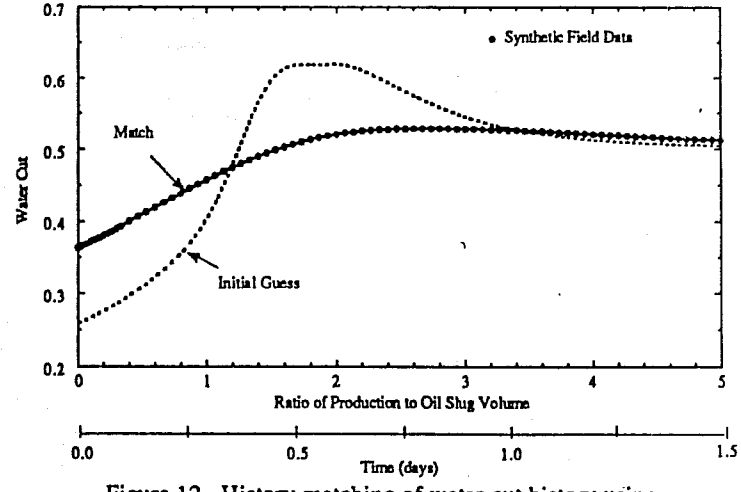

Figure 12. History matching of water-cut history using tracers only (Runs R1W34 and R1W45)

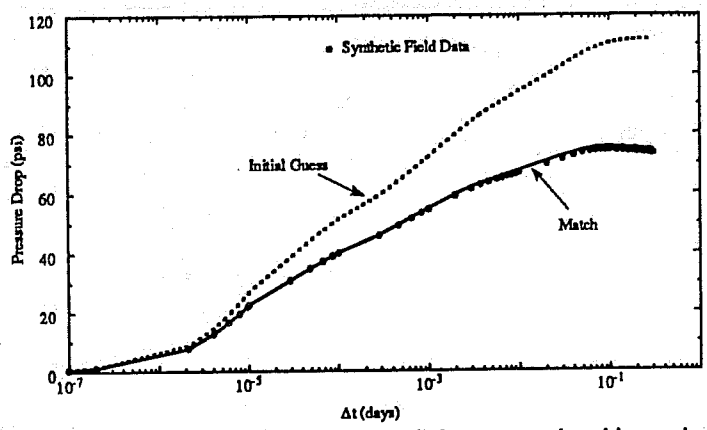

Figure 13. History matching of the bottomhole-pressure-drop history during water injection using tracers only (Runs R1W34 and R1W45)

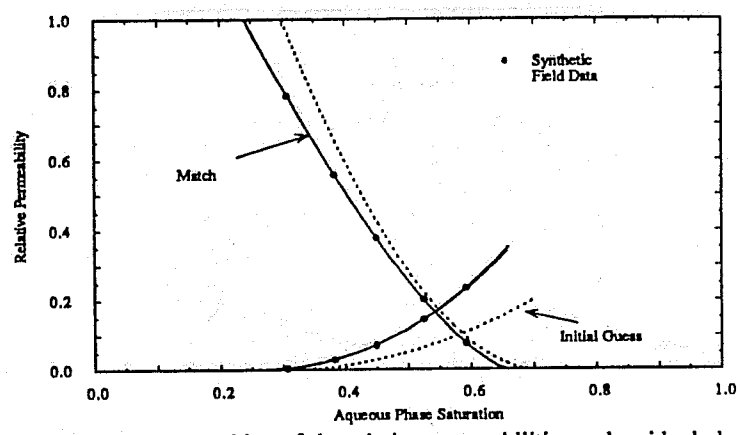

Figure 14. History matching of the relative permeabilities and residual phase saturations using tracers only (Runs R1W34 and R1W45)

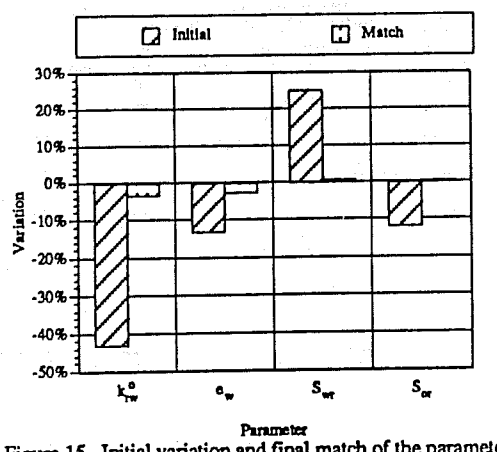

Figure 15. Initial variation and final match of the parameters using tracer only (Run R1W45)

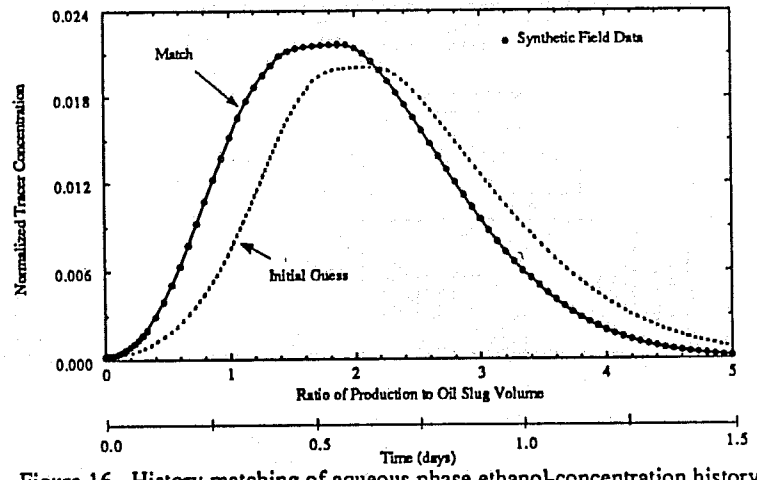

Figure 16. History matching of aqueous phase ethanol-concentration history using tracers, water cut, and bottomhole pressure (Runs R1W34 and R1W35)

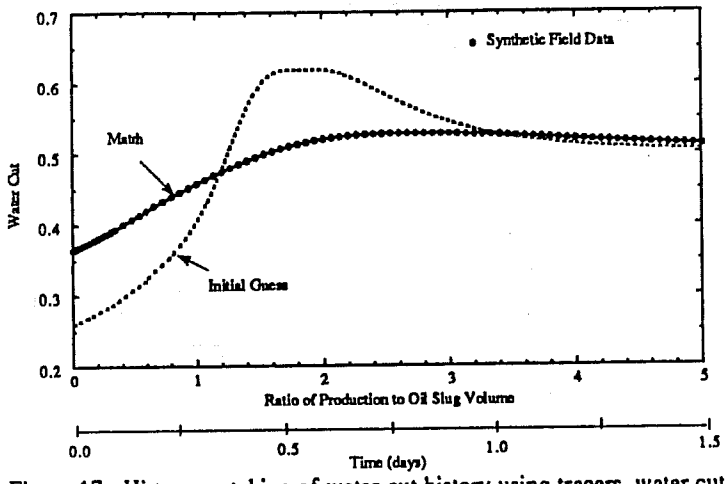

Figure 17. History matching of water-cut history using tracers, water cut, and bottomhole pressure (Runs R1W34 and R1W35)

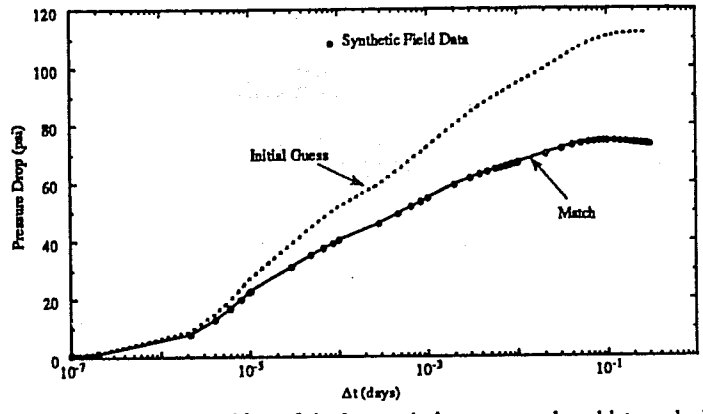

Figure 18. History matching of the bottomhole-pressure-drop history during water injection using tracers, water cut, and bottomhole pressure (Runs R1W34 and R1W35)

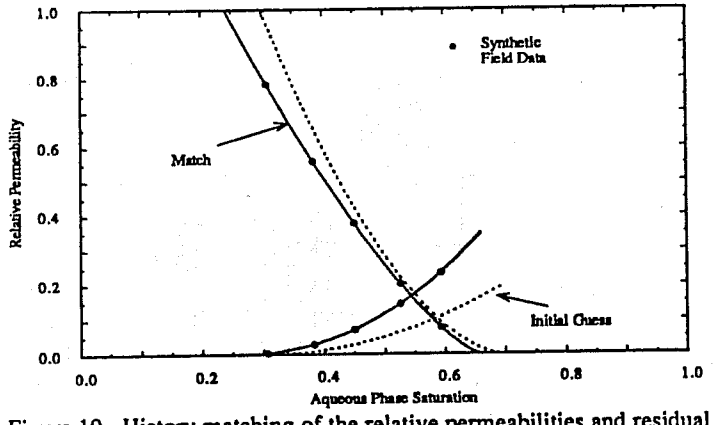

Figure 19. History matching of the relative permeabilities and residual phase saturations using tracer, water cut, and bottomhole pressure (Runs R1W34 and R1W35)

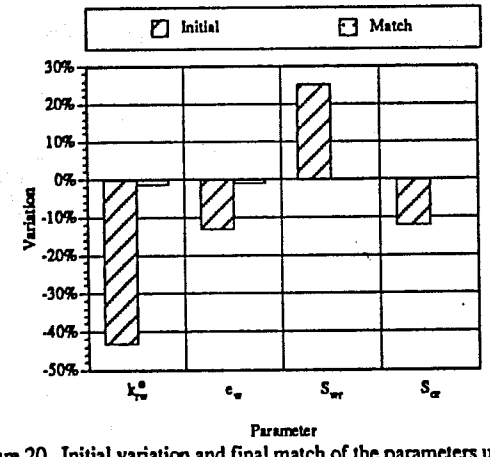

Figure 20. Initial variation and final match of the parameters using tracers, water cut, and bottomhole pressure (Run R1W35)

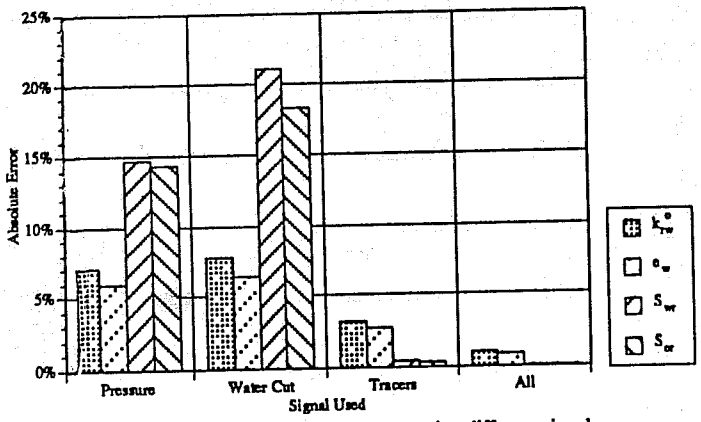

Figure 21. Error in estimating parameters using different signals (Runs R1W47, R1W46, R1W45, and R1W35)

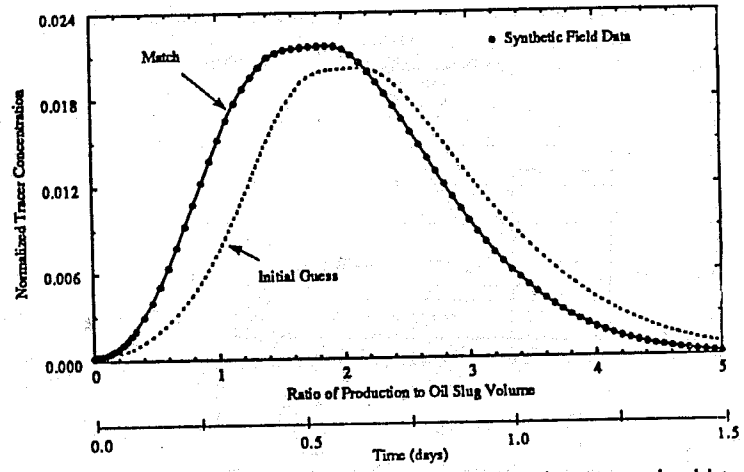

Figure 22. History matching of aqueous phase ethanol-concentration history using linear least squares (Runs R1W34 and R1W35A)

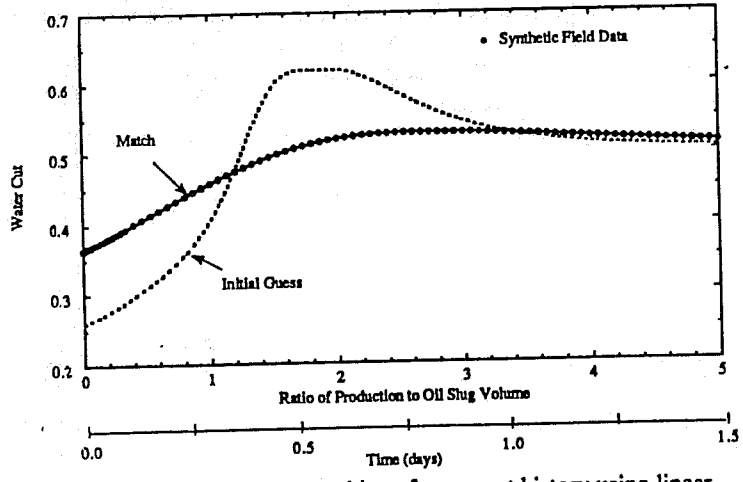

Figure 23. History matching of water-cut history using linear least squares (Runs R1W34 and R1W35A)

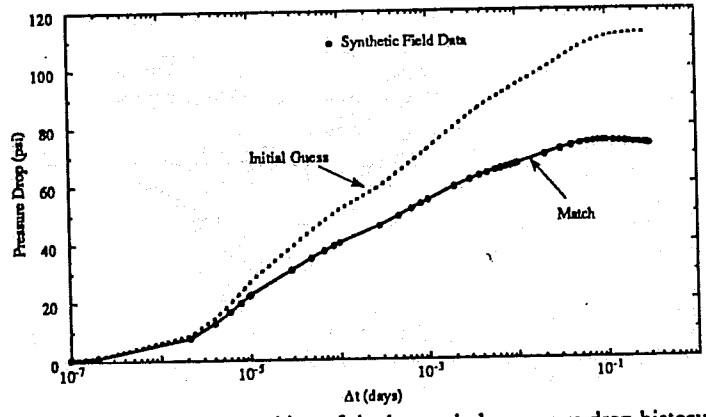

Figure 24. History matching of the bottomhole-pressure-drop history during water injection using linear least squares (Runs R1W34 and R1W35A)

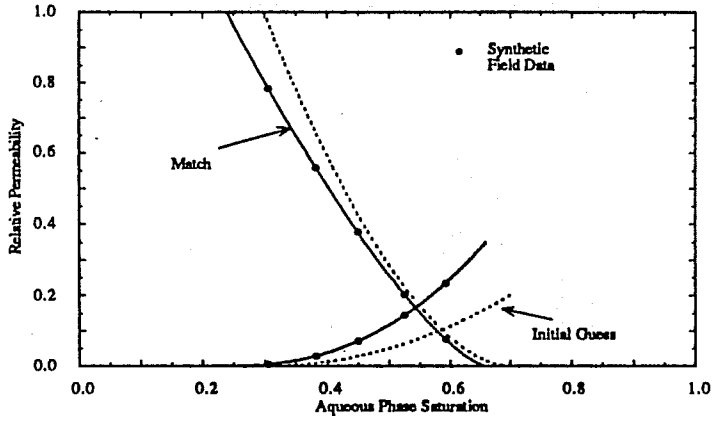

Figure 25. History matching of the relative permeabilities and residual phase saturations using linear least squares (Runs R1W34 and R1W35A)

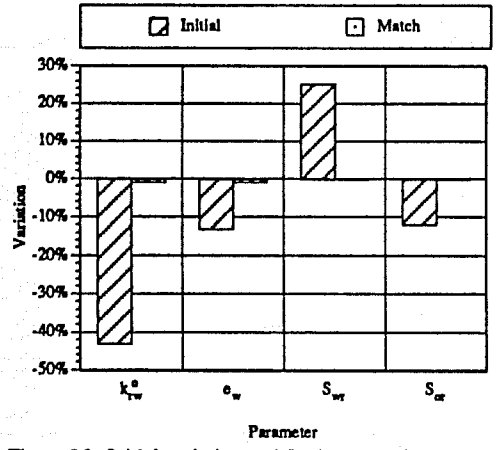

Figure 26. Initial variation and final match of the parameters using linear least squares (Run R1W35A)

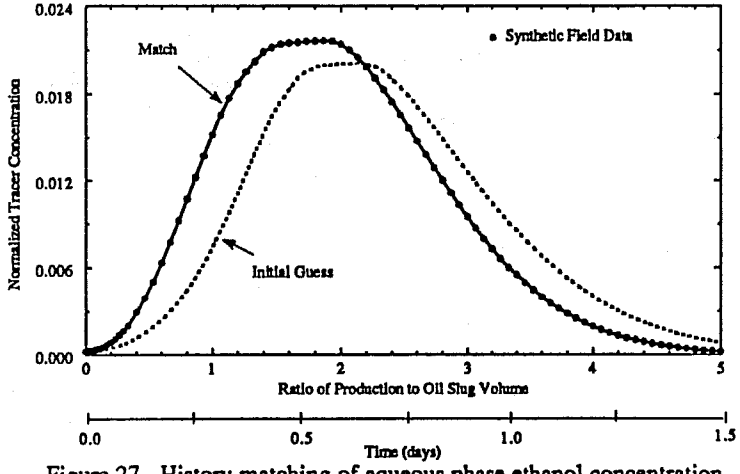

Figure 27. History matching of aqueous phase ethanol-concentration history using least absolute values minimization (Runs R1W34 and R1W35C)

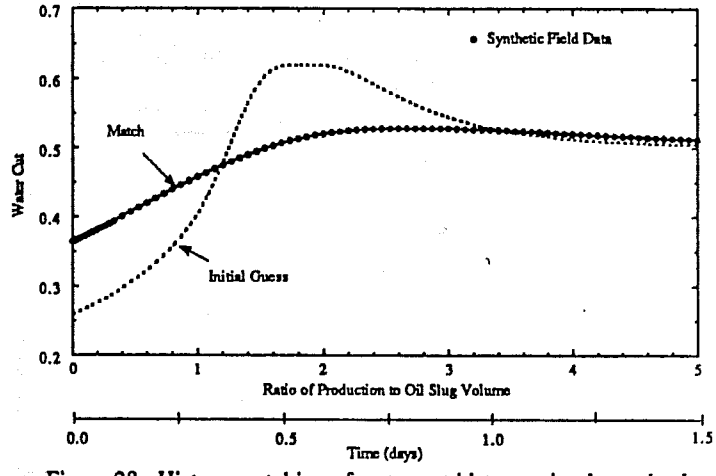

Figure 28. History matching of water-cut history using least absolute values minimization (Runs R1W34 and R1W35C)

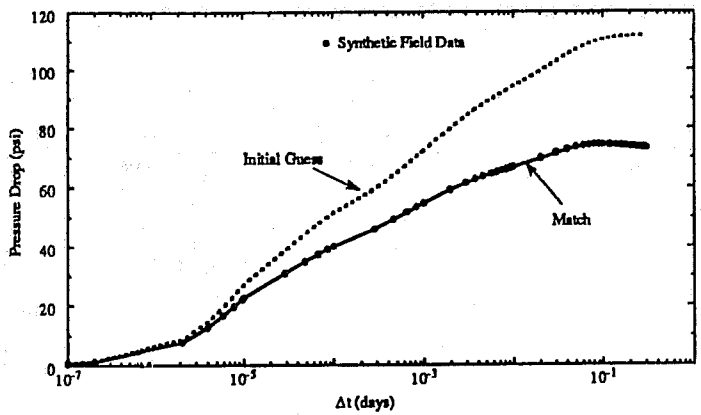

Figure 29. History matching of the bottomhole-pressure-drop history during water injection using least absolute values minimization (Runs R1W34 and R1W35C)

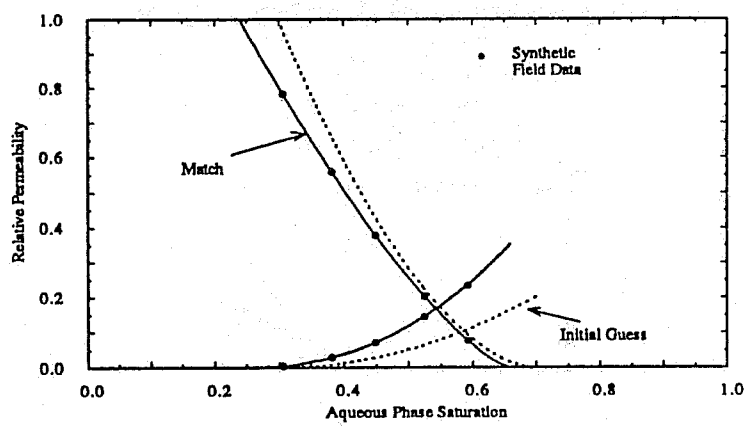

Figure 30. History matching of the relative permeabilities and residual phase saturations using least absolute values minimization (Runs R1W34 and R1W35C)

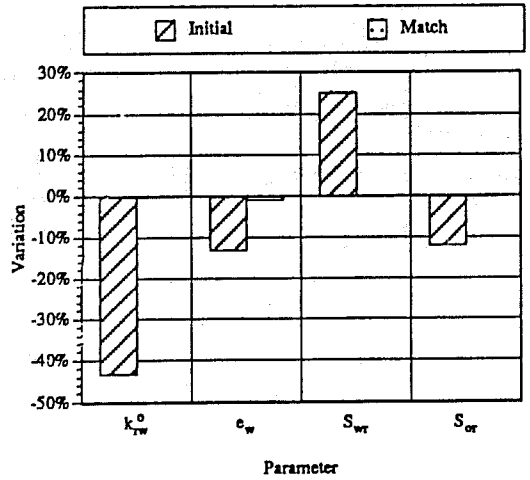

Figure 31. Initial variation and final match of the parameters using least absolute values (Run R1W35C)

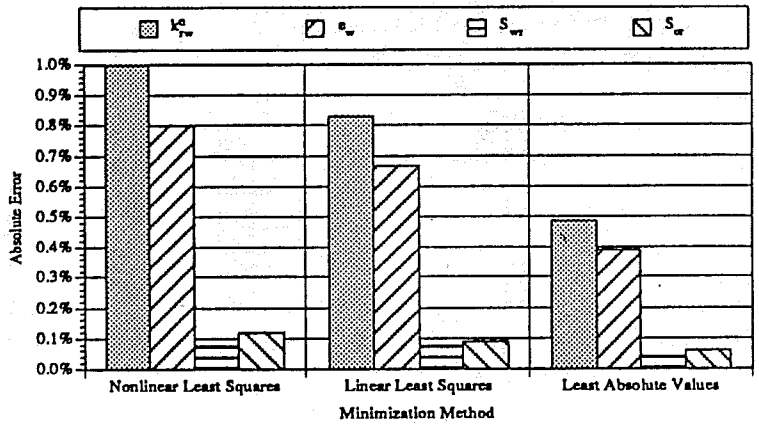

Figure 32. Error in estimating parameters using different minimization methods (Runs R1W35, R1W35A, and R1W35C)

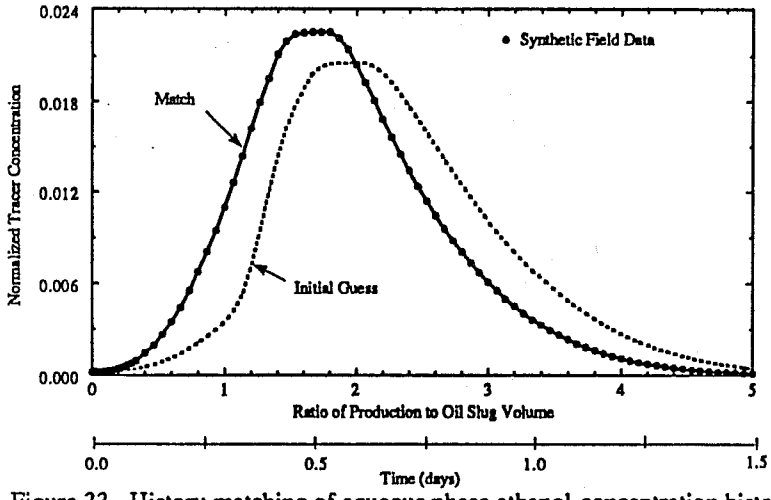

Figure 33. History matching of aqueous phase ethanol-concentration history, intermediate-wet reservoir (Runs R1W30A and R1W36D)

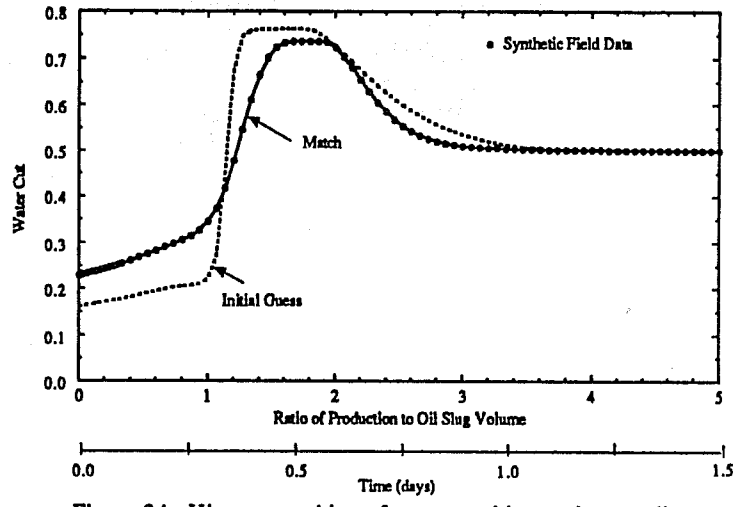

Figure 34. History matching of water-cut history, intermediate-wet reservoir (Runs R1W30A and R1W36D)

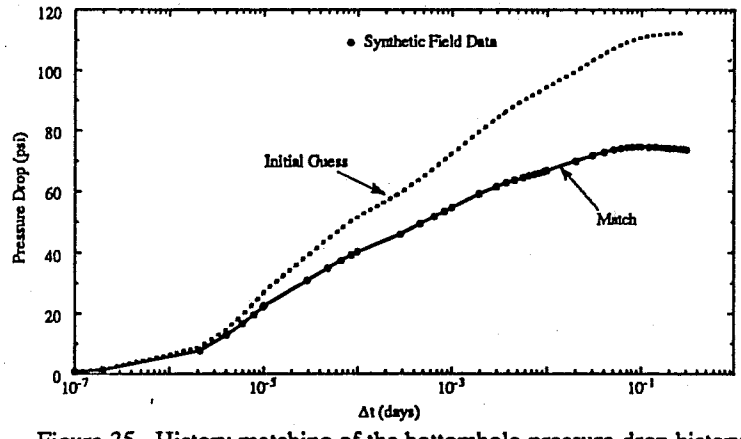

Figure 35. History matching of the bottomhole-pressure-drop history during water injection intermediate-wet reservoir (Runs R1W30A and R1W36D)

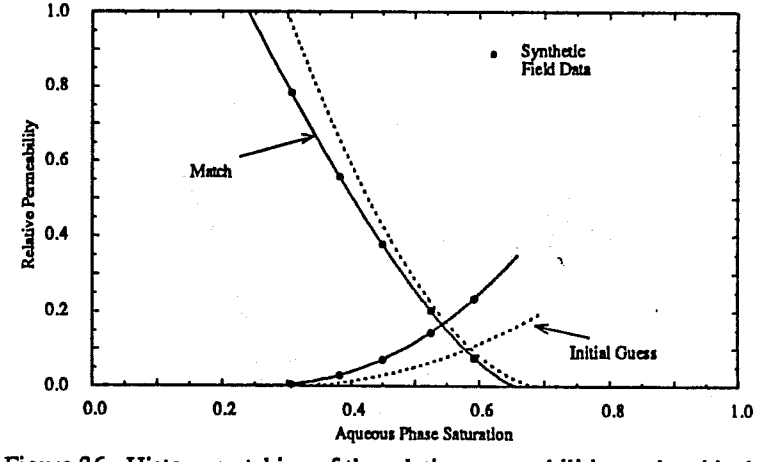

Figure 36. History matching of the relative permeabilities and residual phase saturations (Runs R1W30A and R1W36D)

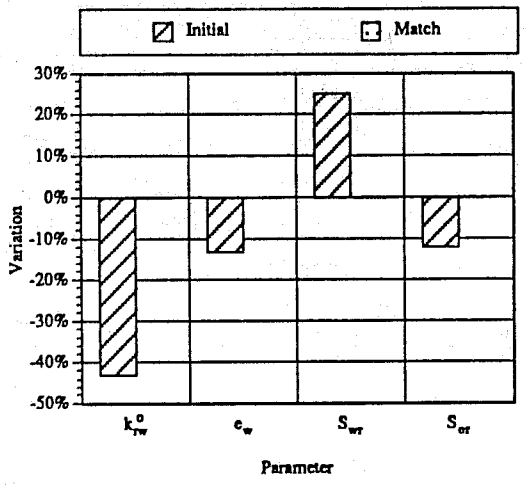

Figure 37. Initial variation and final match of the parameters using nonlinear least squares, intermediate-wet reservoir (Run R1W36D)

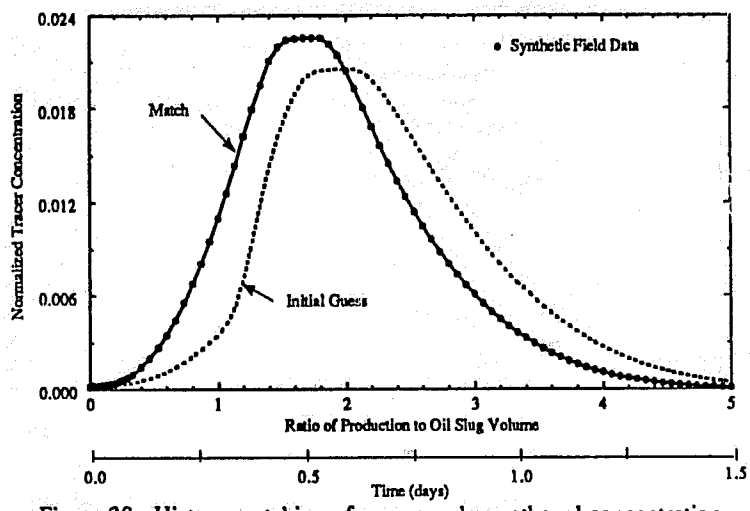

Figure 38. History matching of aqueous phase ethanol-concentration history, intermediate-wet reservoir, using linear least squares (Runs R1W30A and R1W36E)

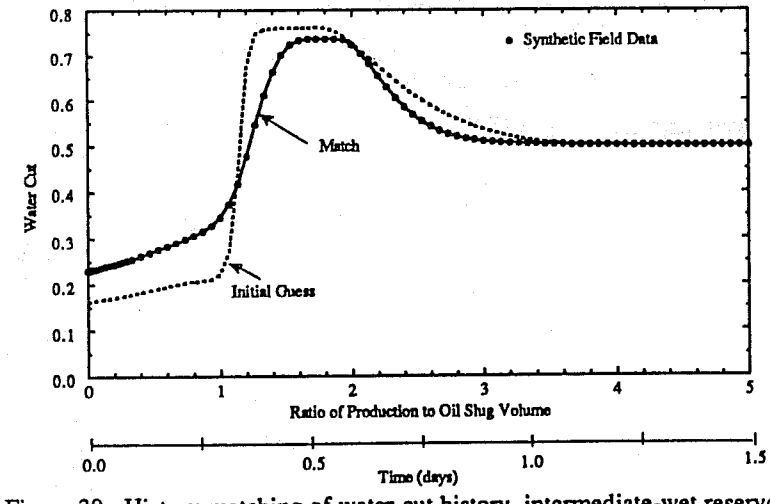

Figure 39. History matching of water-cut history, intermediate-wet reservoir, using linear least squares (Runs R1W30A and R1W36E)

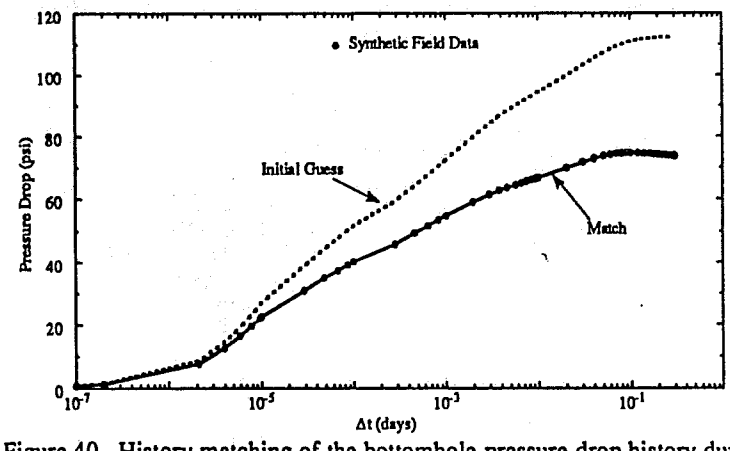

Figure 40. History matching of the bottomhole-pressure-drop history during water injection, intermediate-wet reservoir, using linear least squares (Runs R1W30A and R1W36E)

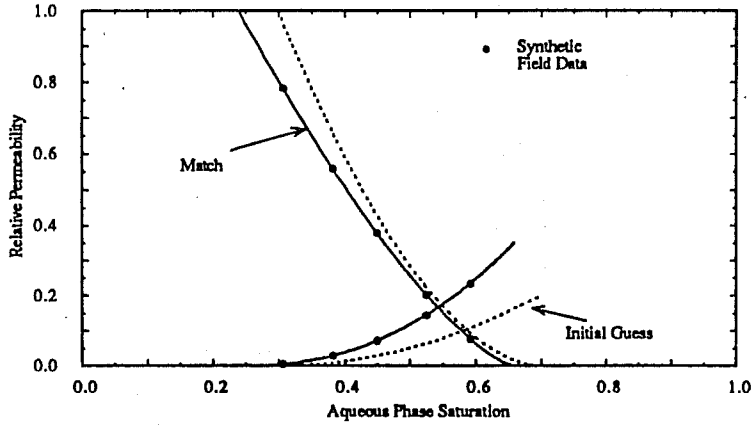

Figure 41. History matching of the relative permeabilities and residual phase saturations, using linear least squares (Runs R1W30A and R1W36E)

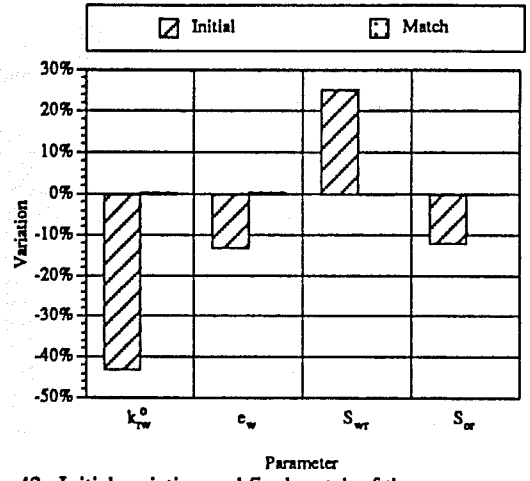

Figure 42. Initial variation and final match of the parameters using linear least square, intermediate wet reservoir (Run R1W36E)

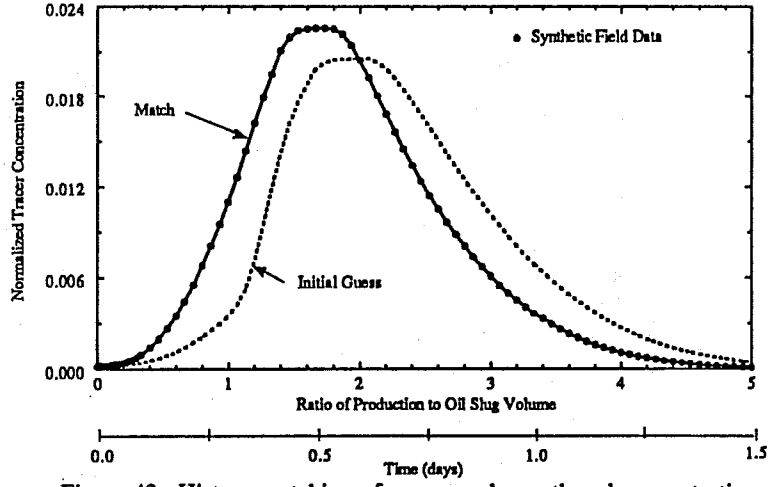

Figure 43. History matching of aqueous phase ethanol-concentration history, intermediate-wet reservoir, using least absolute values minimization (Runs R1W30A and R1W36F)

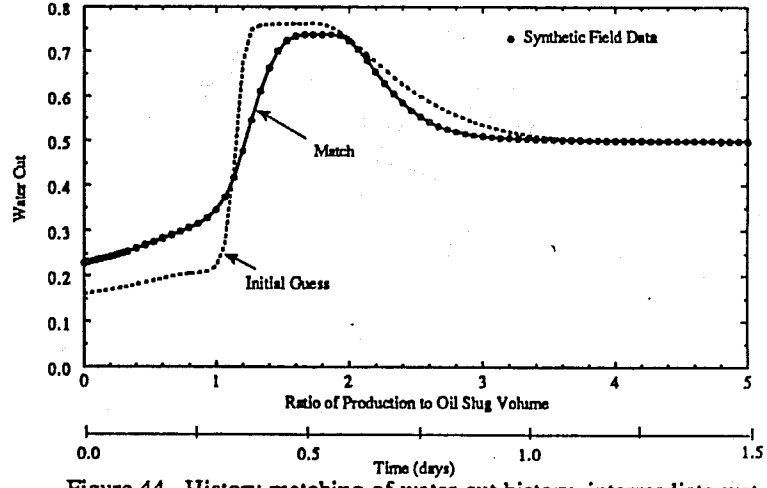

Figure 44. History matching of water-cut history, intermediate-wet reservoir, using least absolute values minimization (Runs R1W30A and R1W36F)

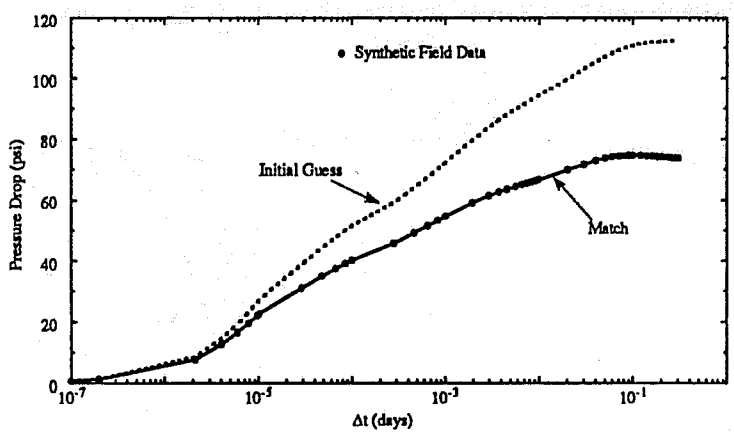

Figure 45. History matching of the bottomhole-pressure-drop history during water injection, intermediate-wet reservoir, using least absolute values minimization (Runs R1W30A and R1W36F)

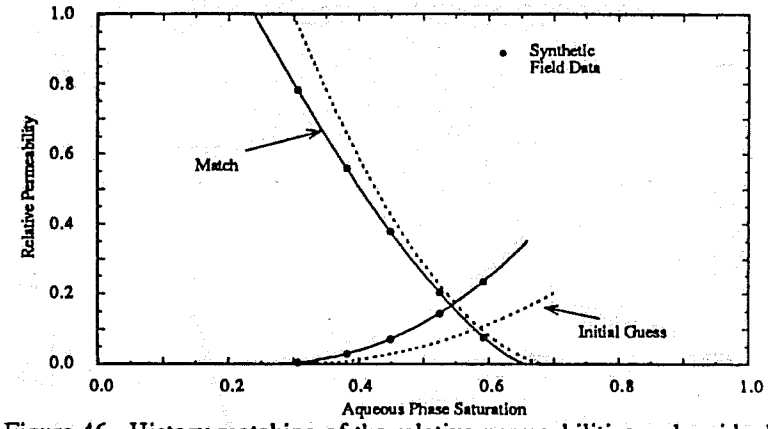

Figure 46. History matching of the relative permeabilities and residual phase saturations, using least absolute values minimization (Runs R1W30A and R1W36F)

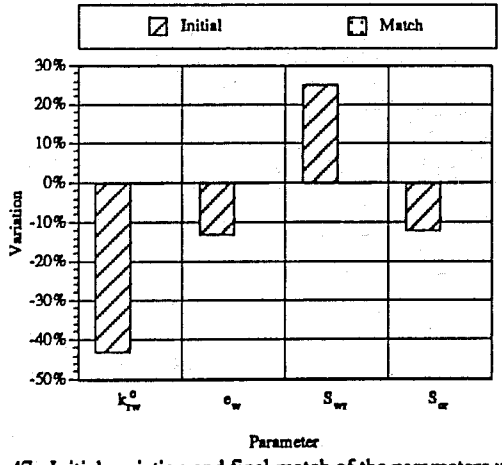

Figure 47. Initial variation and final match of the parameters using least absolute values, intermediate wet reservoir (Run R1W36F)

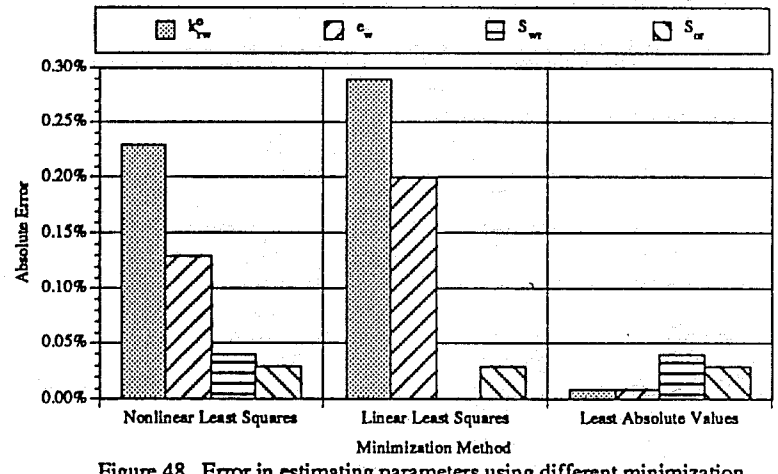

Figure 48. Error in estimating parameters using different minimization methods, intermediate-wet reservoir (Runs R1W36D, R1W36E, and R1W36F)

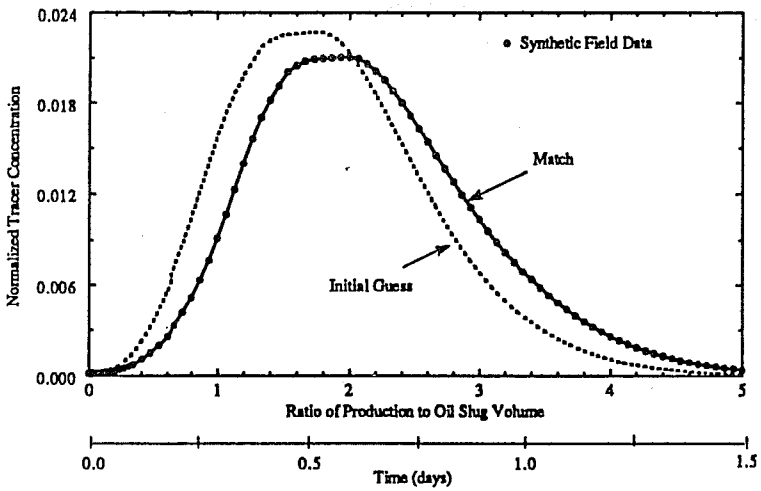

Figure 49. History matching of aqueous phase ethanol-concentration history (Runs R1W54 and R1W55)

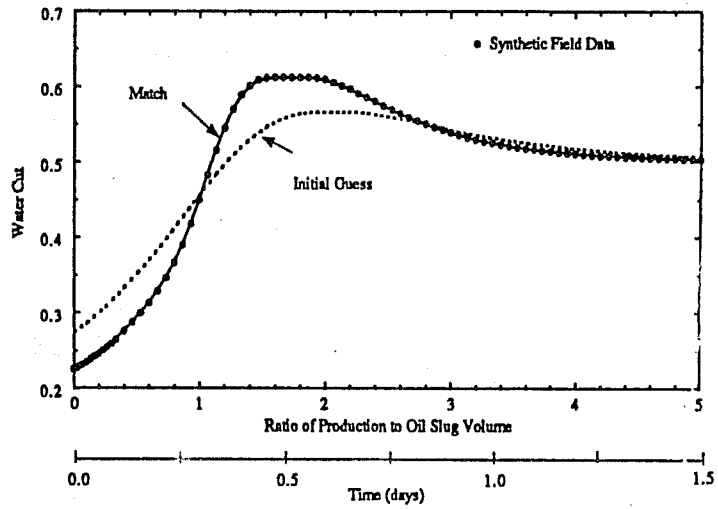

Figure 50. History matching of water-cut history (Runs R1W54 and R1W55)

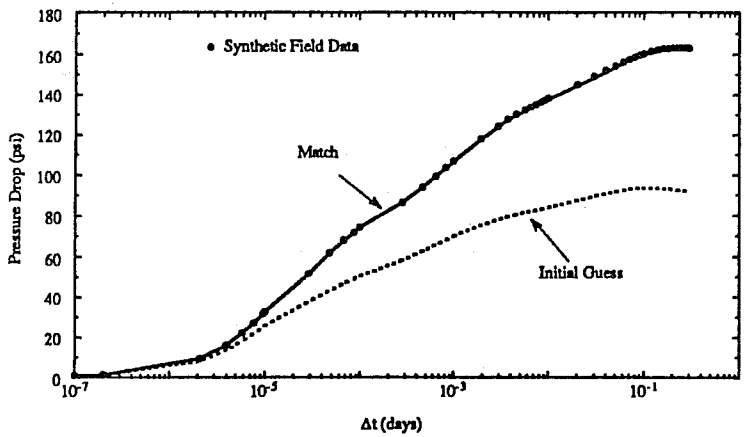

Figure 51. History matching of the bottomhole-pressure-drop history during water injection (Runs R1W54 and R1W55)

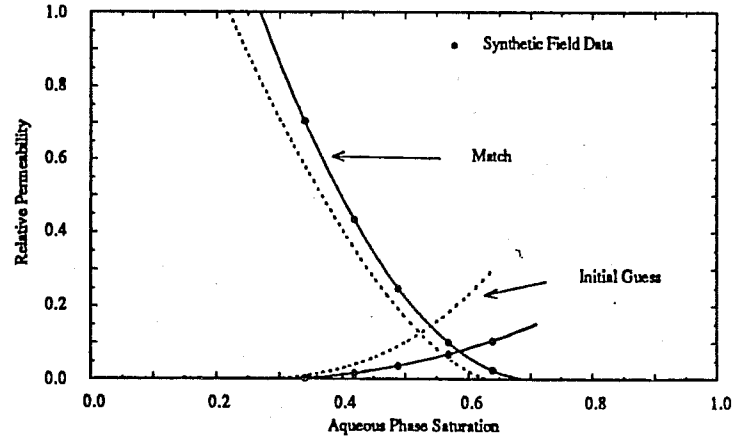

Figure 52. History matching of the relative permeabilities and residual phase saturations (Runs R1W54 and R1W55)

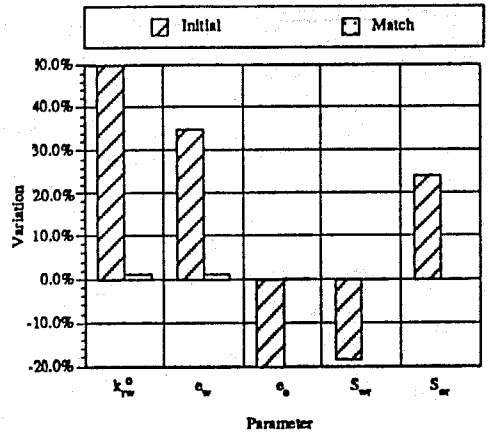

Figure 53. Initial variation and final match of the parameters (Run R1W55)

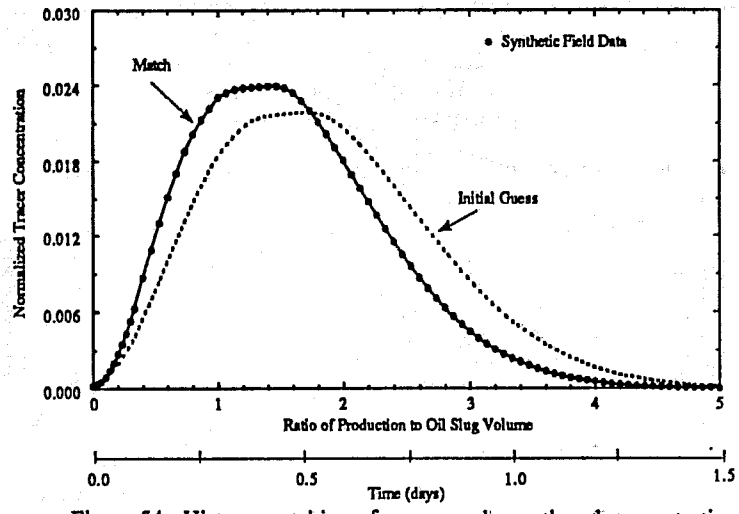

Figure 54. History matching of aqueous phase ethanol-concentration history (Runs R1O00 and R1O22C)

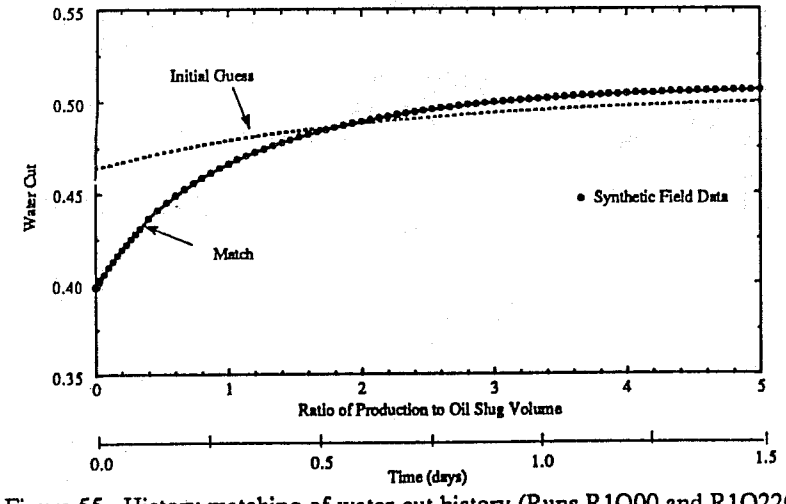

Figure 55. History matching of water-cut history (Runs R1O00 and R1O22C)

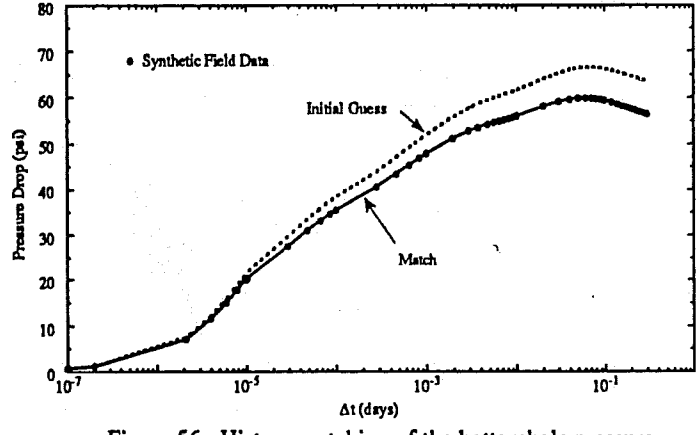

Figure 56. History matching of the bottomhole-pressure-drop history (Runs R1O00 and R1O22C)

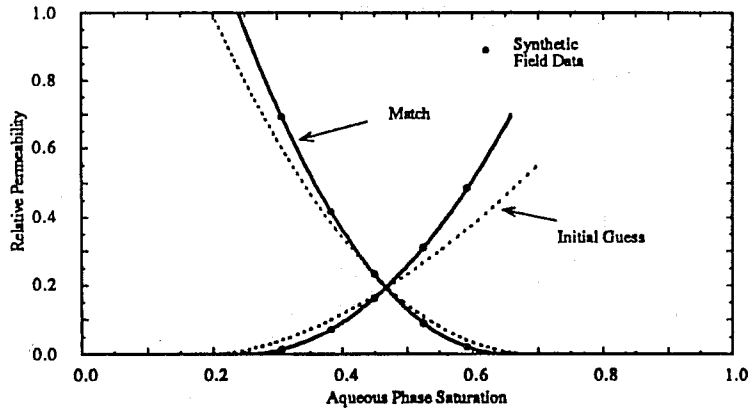

Figure 57. History matching of the relative permeabilities and residual phase saturations (Runs R1O00 and R1O22C)

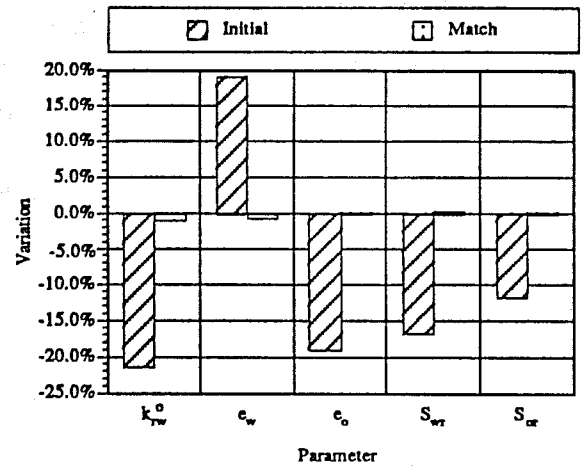

Figure 58. Initial variation and final match of the parameters (Run R1O22C)

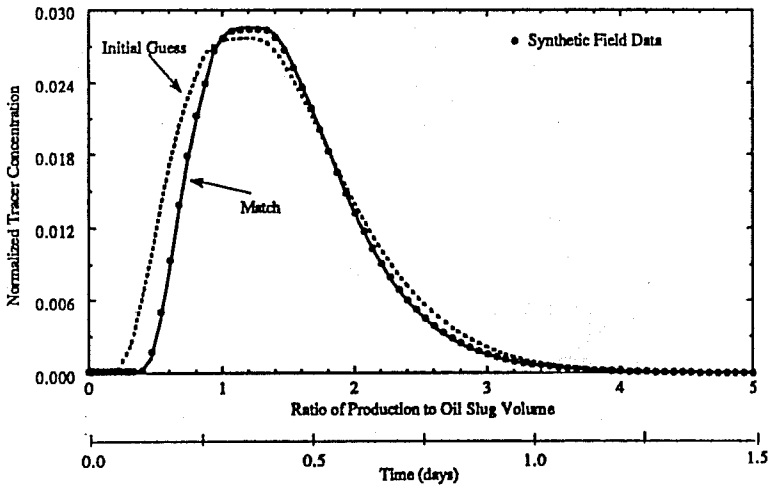

Figure 59. History matching of aqueous phase ethanol-concentration history (Runs R1O26 and R1O29A)

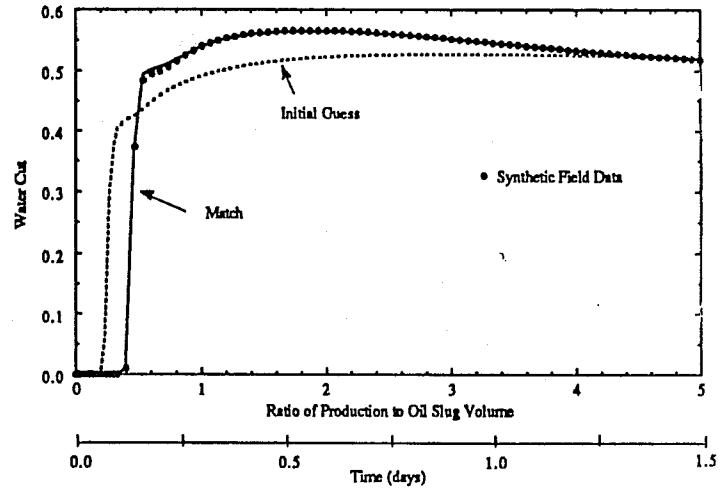

Figure 60. History matching of water-cut history (Runs R1O26 and R1O29A)

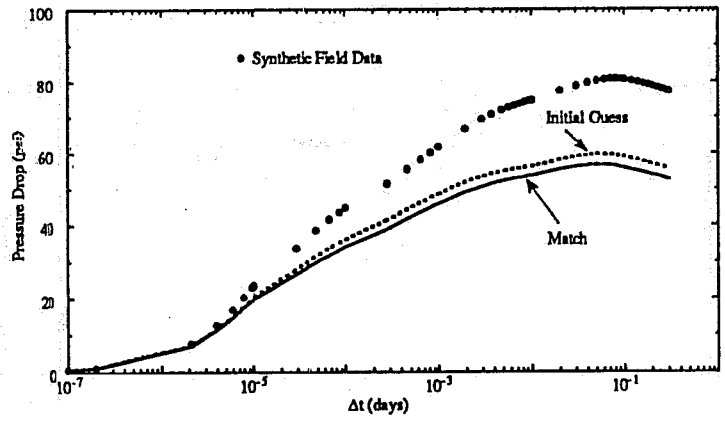

Figure 61. History matching of the bottomhole-pressure-drop history (Runs R1O26 and R1O29A)

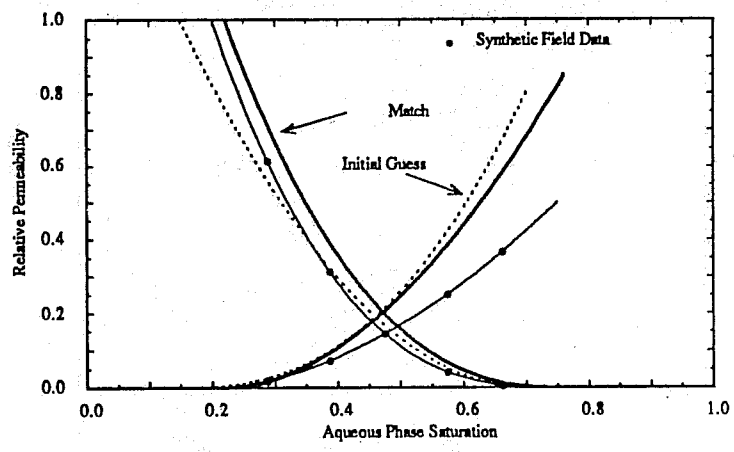

Figure 62. History matching of the relative permeabilities and residual phase saturations (Runs R1O26 and R1O29A)

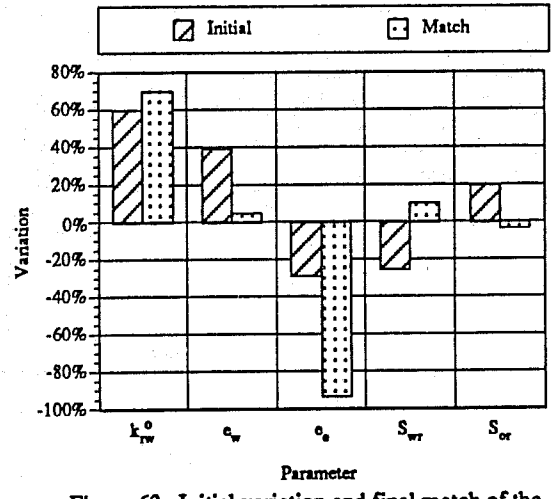

Figure 63. Initial variation and final match of the parameters (Run R1O29A)

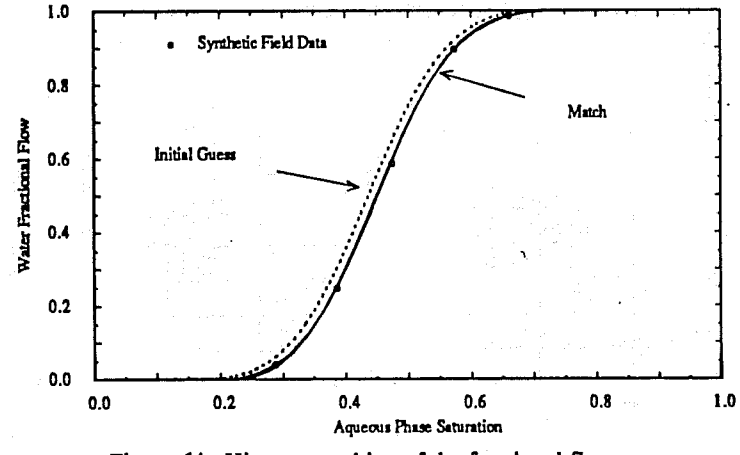

Figure 64. History matching of the fractional flow curve (Runs R1O26 and R1O29A)

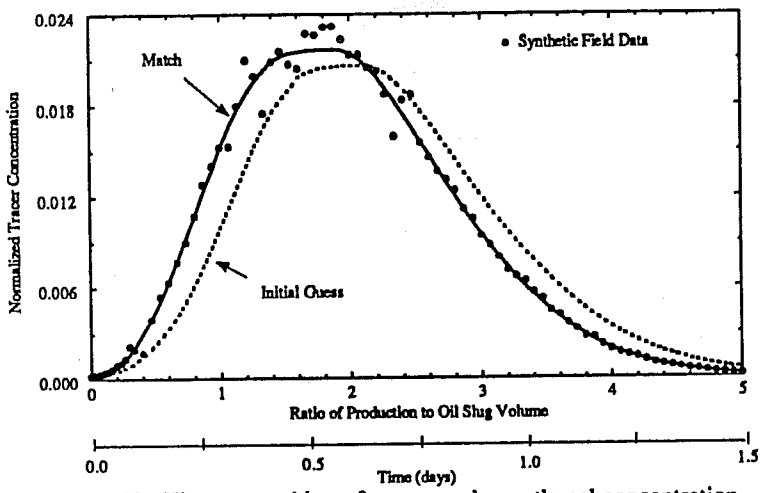

Figure 65. History matching of aqueous phase ethanol-concentration history, 10% randomly distributed error added (Runs R1W34 and R1W53)

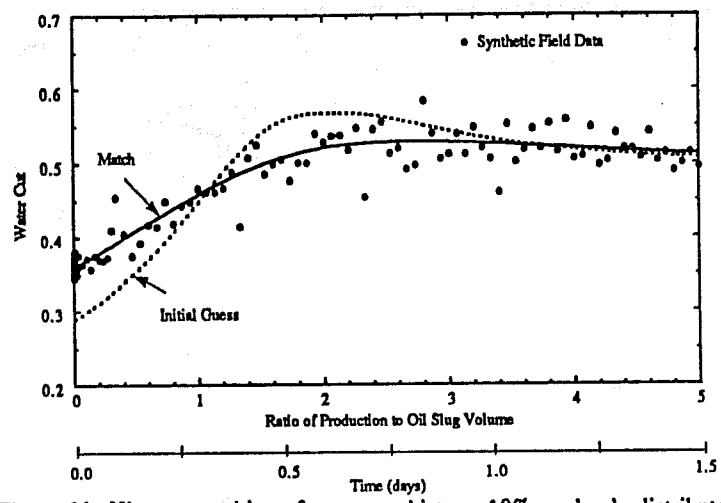

Figure 66. History matching of water-cut history, 10% randomly distributed error added (Runs R1W34 and R1W53)

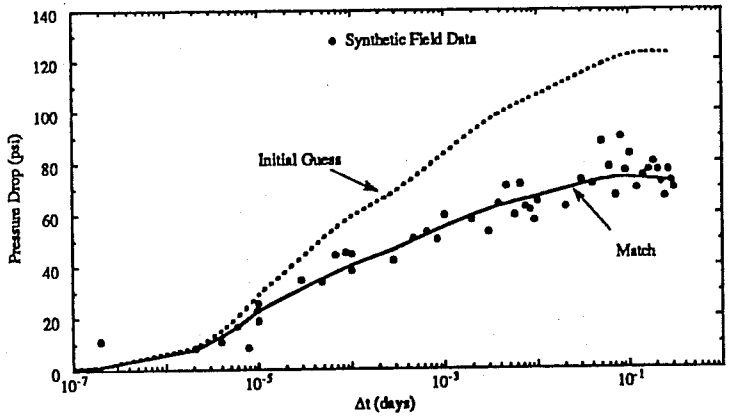

Figure 67. History matching of the bottomhole-pressure-drop history during water injection, 0.5% randomly distributed error added (Runs R1W34 and R1W53)

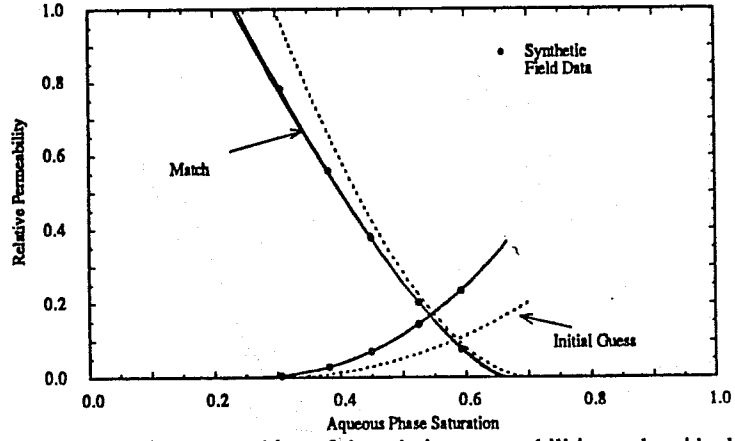

Figure 68. History matching of the relative permeabilities and residual phase saturations (Runs R1W34 and R1W53)

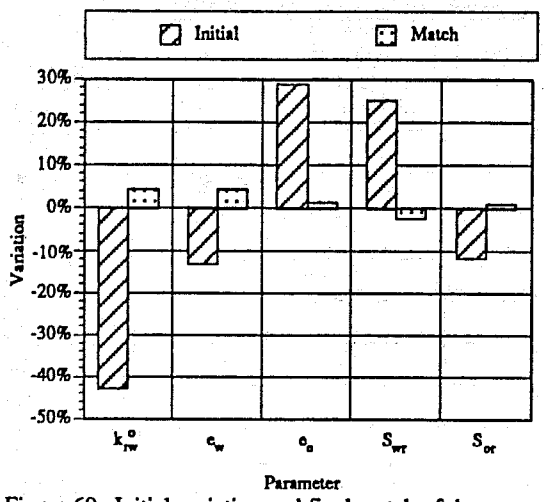

Figure 69. Initial variation and final match of the parameters using nonlinear least squares (Run R1W53)

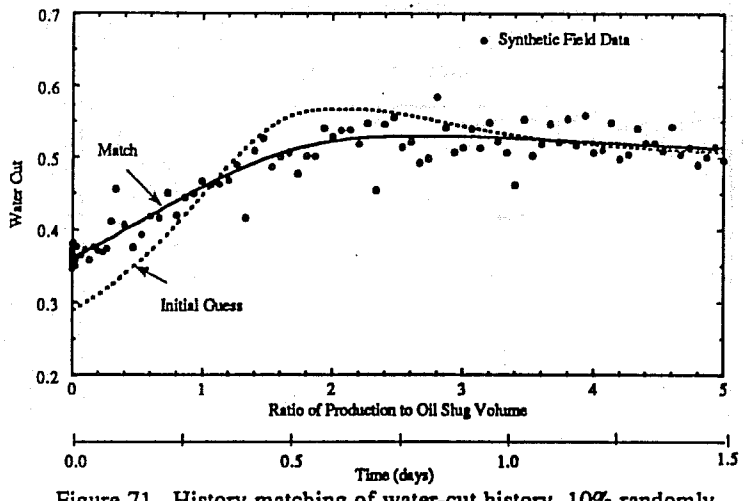

Figure 71. History matching of water-cut history, 10% randomly distributed error added, using linear least squares (Runs R1W34 and R1W53A)

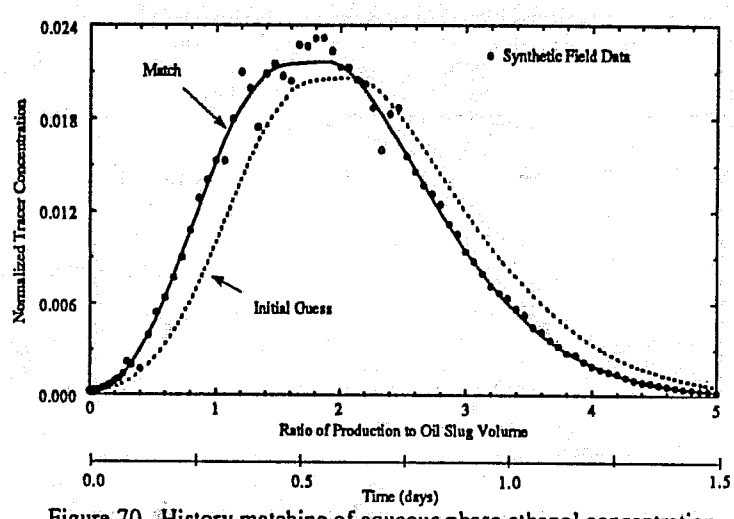

Figure 70. History matching of aqueous phase ethanol-concentration history, 10% randomly distributed error added, using linear least squares (Runs R1W34 and R1W53A)

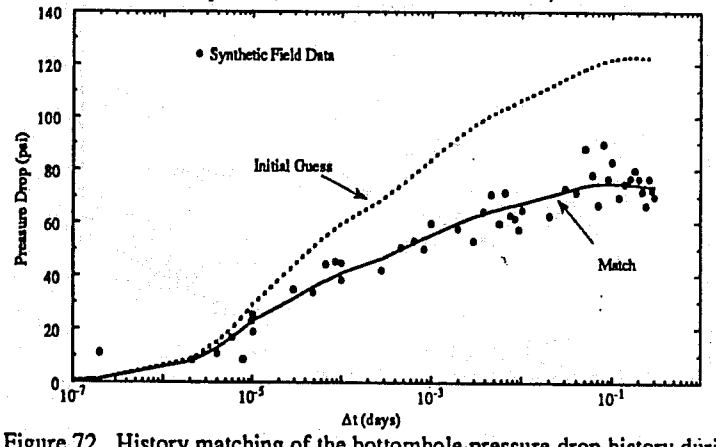

Figure 72. History matching of the bottomhole-pressure-drop history during water injection, 0.5% randomly distributed error added, using linear least squares (Runs R1W34 and R1W53A)

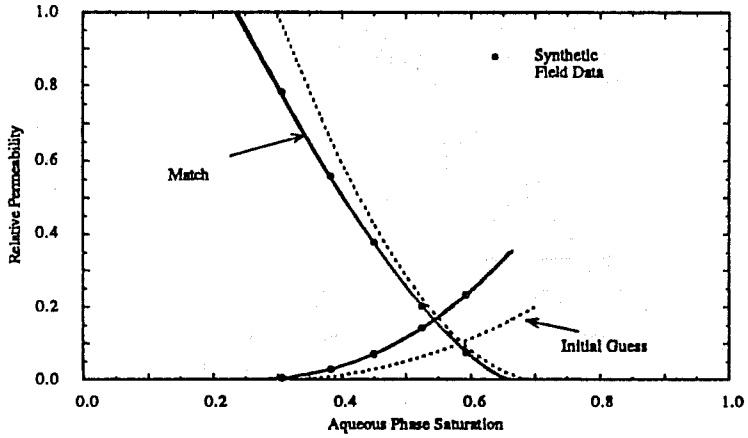

Figure 73. History matching of the relative permeabilities and residual phase saturations, using linear least squares (Runs R1W34 and R1W53A)

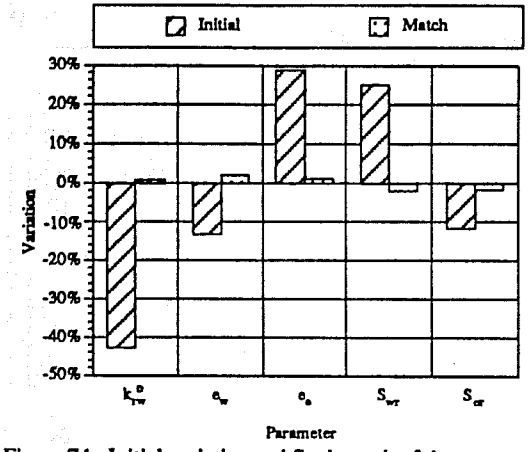

Figure 74. Initial variation and final match of the parameters using linear least squares (Run R1W53A)

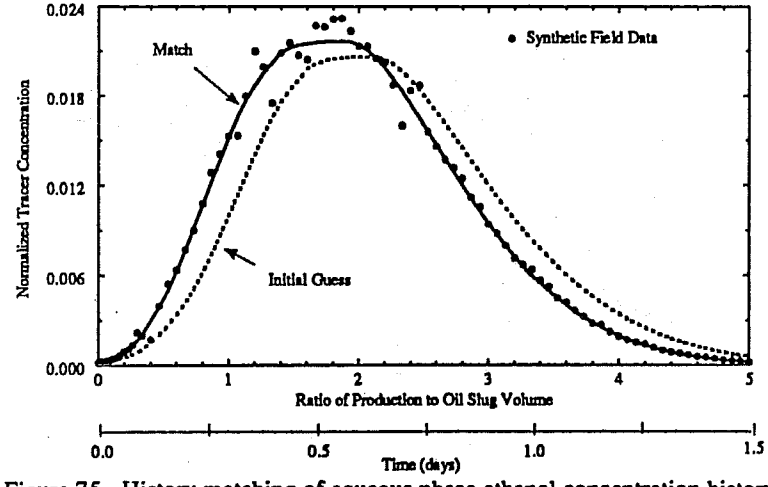

Figure 75. History matching of aqueous phase ethanol-concentration history, 10% randomly distributed error added, using least absolute values minimization (Runs R1W34 and R1W53C)

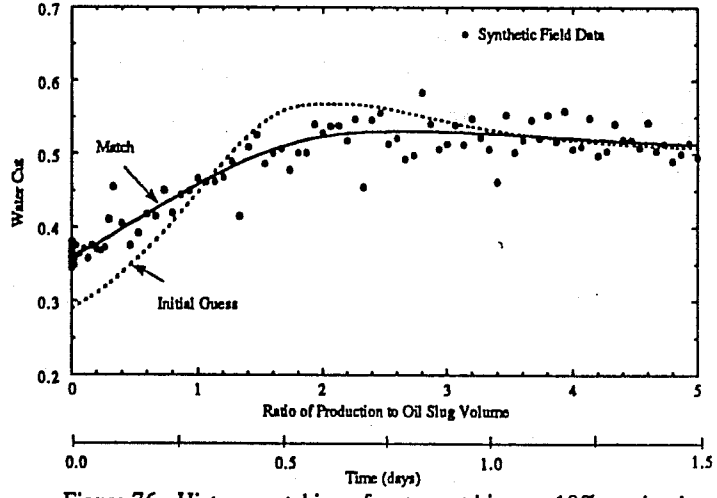

Figure 76. History matching of water-cut history, 10% randomly distributed error added, using least absolute values minimization (Runs R1W34 and R1W53C)

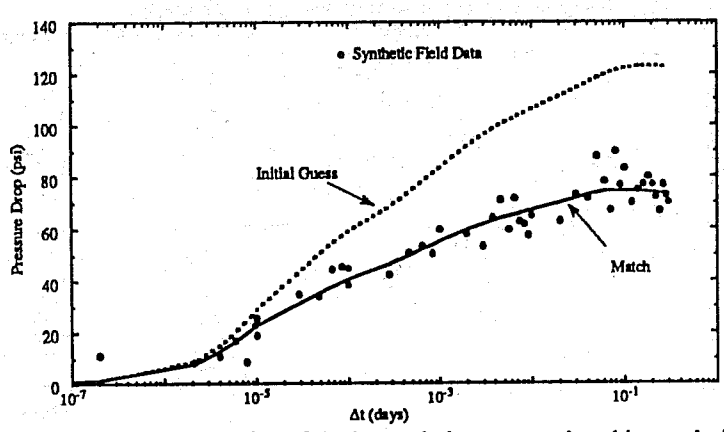

Figure 77. History matching of the bottomhole-pressure-drop history during water injection, 0.5% randomly distributed error added, using least absolute values (Runs R1W34 and R1W53C)

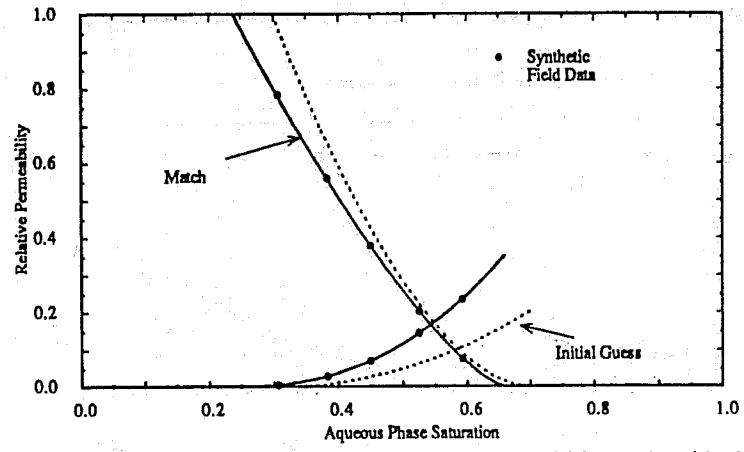

Figure 78. History matching of the relative permeabilities and residual phase saturations, using least absolute values minimization (Runs R1W34 and R1W53C)

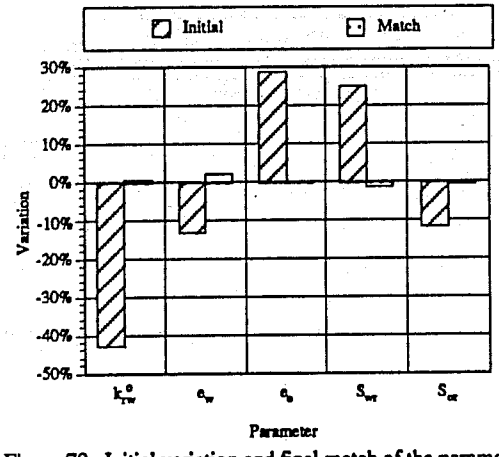

Figure 79. Initial variation and final match of the parameters using least absolute values (Run R1W53C)

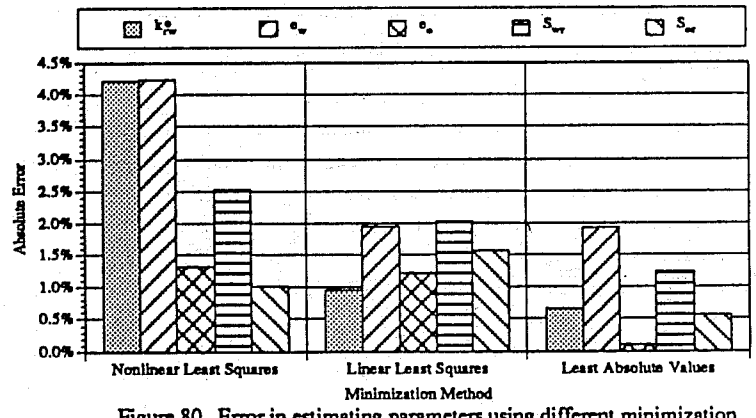

Figure 80. Error in estimating parameters using different minimization methods (Runs R1W53, R1W53A, and R1W53C)

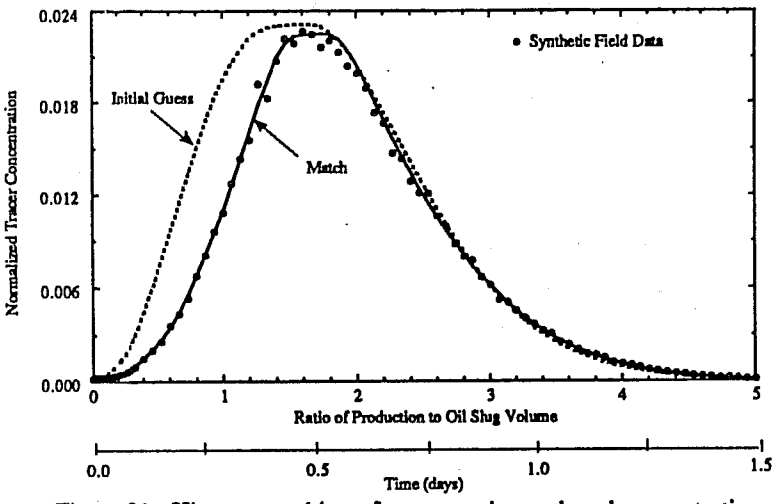

Figure 81. History matching of aqueous phase ethanol-concentration history, 10% randomly distributed error added (Runs R1W30A and R1W52D)

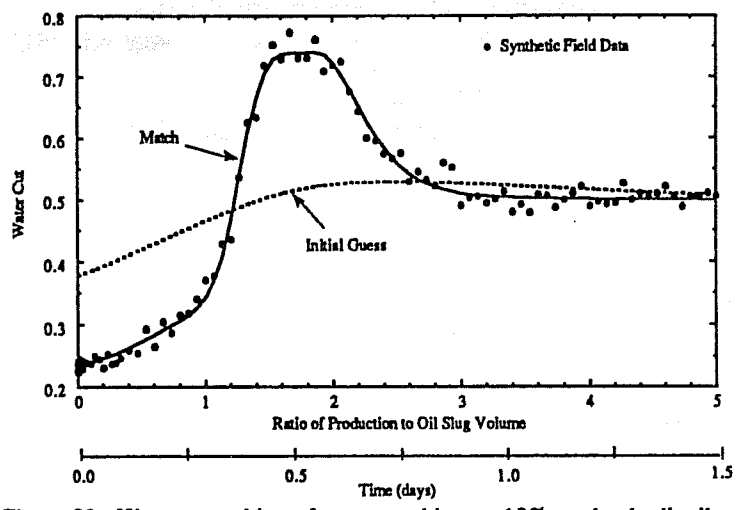

Figure 82. History matching of water-cut history, 10% randomly distributed error added (Runs R1W30A and R1W52D)

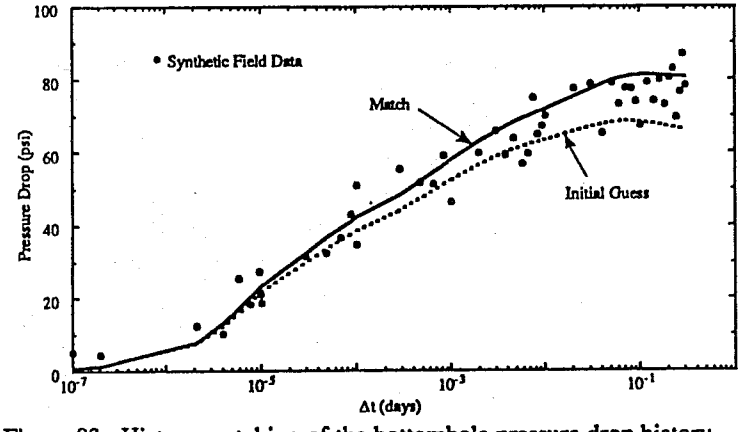

Figure 83. History matching of the bottomhole-pressure-drop history during water injection, 0.5% randomly distributed error added (Runs R1W30A and R1W52D)

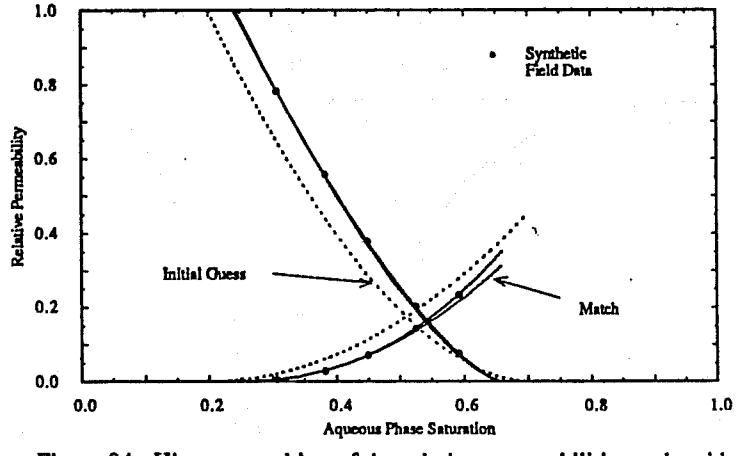

Figure 84. History matching of the relative permeabilities and residual phase saturations (Runs R1W30A and R1W52D)

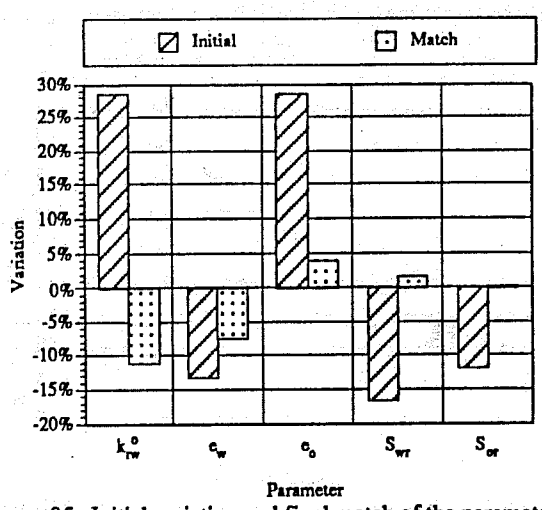

Figure 85. Initial variation and final match of the parameters using nonlinear least squares (Run R1W52D)

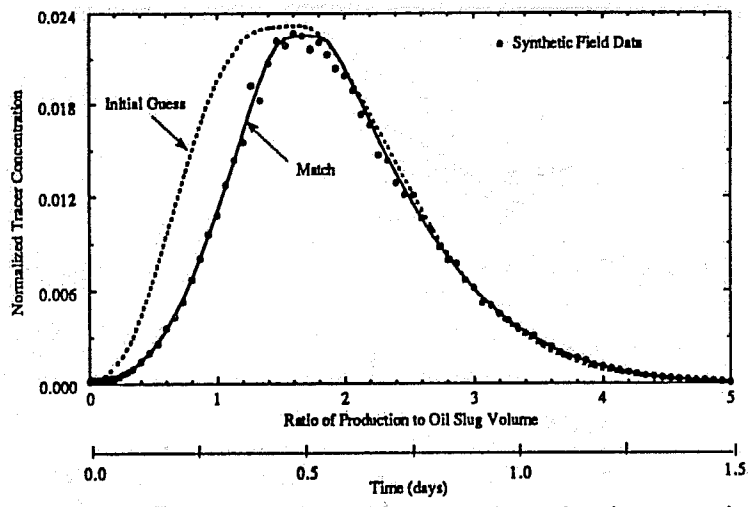

Figure 86. History matching of aqueous phase ethanol-concentration history, 10% randomly distributed error added, using linear least squares (Runs R1W30A and R1W52H)

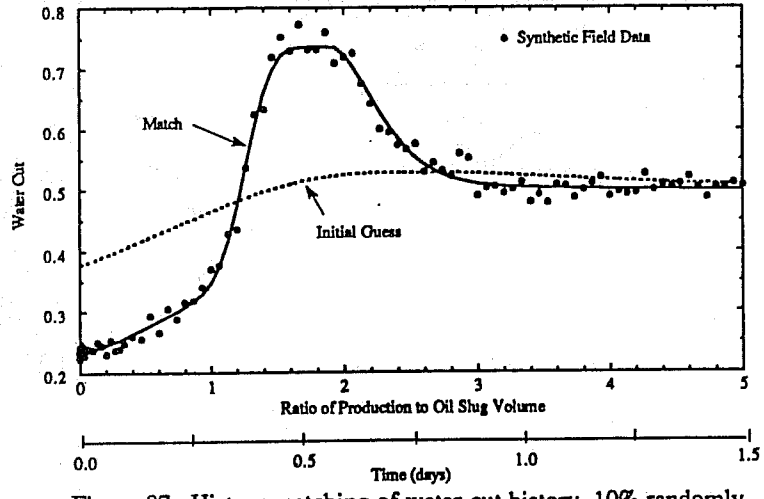

Figure 87. History matching of water-cut history, 10% randomly distributed error added, using linear least squares (Runs R1W30A and R1W52H)

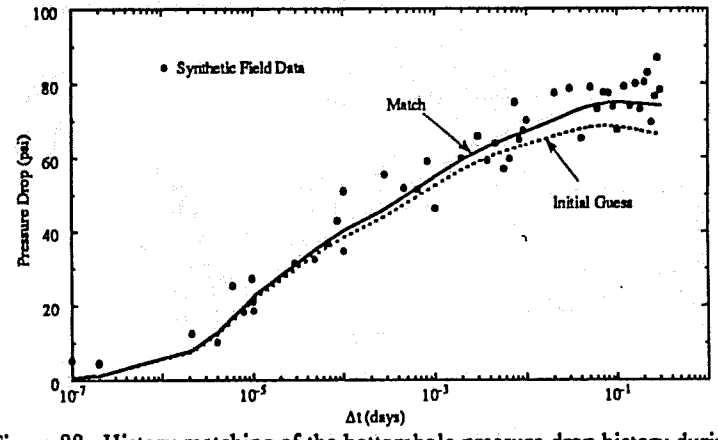

Figure 88. History matching of the bottomhole-pressure-drop history during water injection, 0.5% randomly distributed error added, using linear least squares (Runs R1W30A and R1W52H)

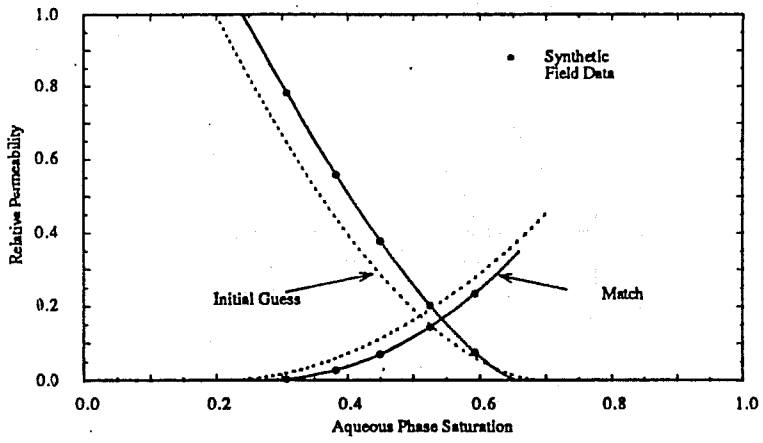

Figure 89. History matching of the relative permeabilities and residual phase saturations, using linear least squares (Runs R1W30A and R1W52H)

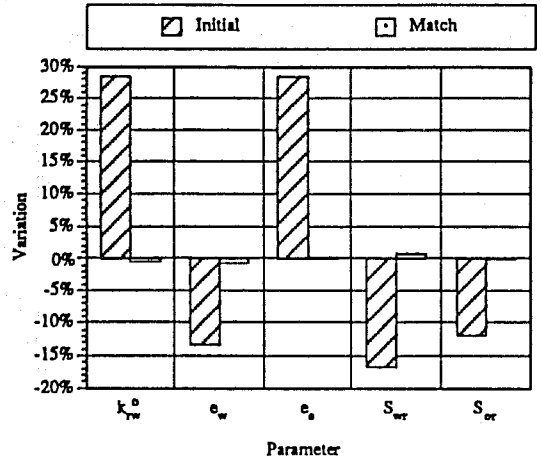

Figure 90. Initial variation and final match of the parameters using linear least squares (Run R1W52H)

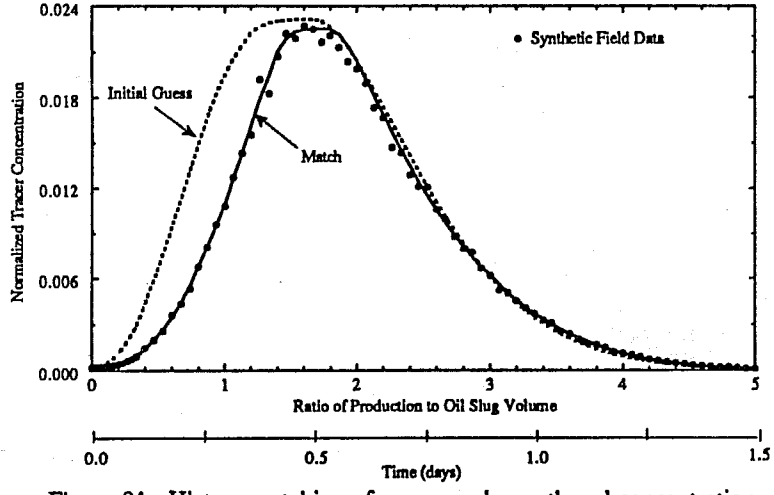

Figure 91. History matching of aqueous phase ethanol-concentration history, 10% randomly distributed error added, using least absolute values (Runs R1W30A and R1W52I)

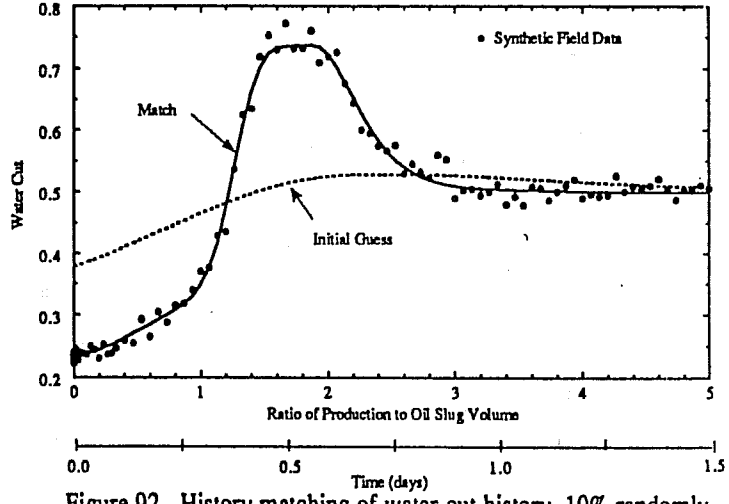

Figure 92. History matching of water-cut history, 10% randomly distributed error added, using least absolute values minimization (Runs R1W30A and R1W52I)

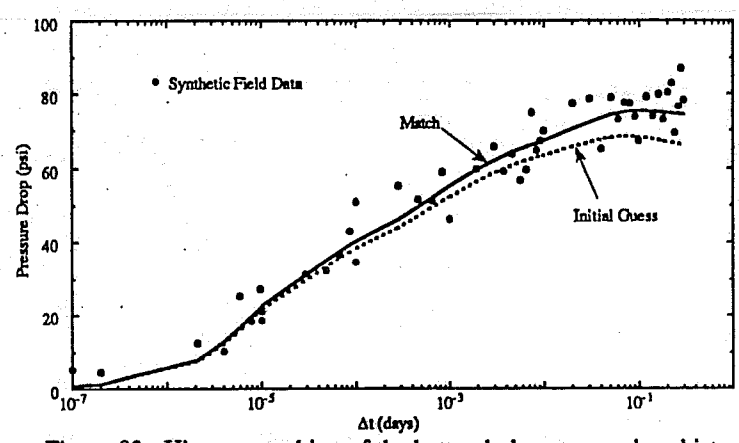

Figure 93. History matching of the bottomhole-pressure-drop history during water injection, 0.5% randomly distributed error added, using least absolute values minimization (Runs R1W30A and R1W52I)

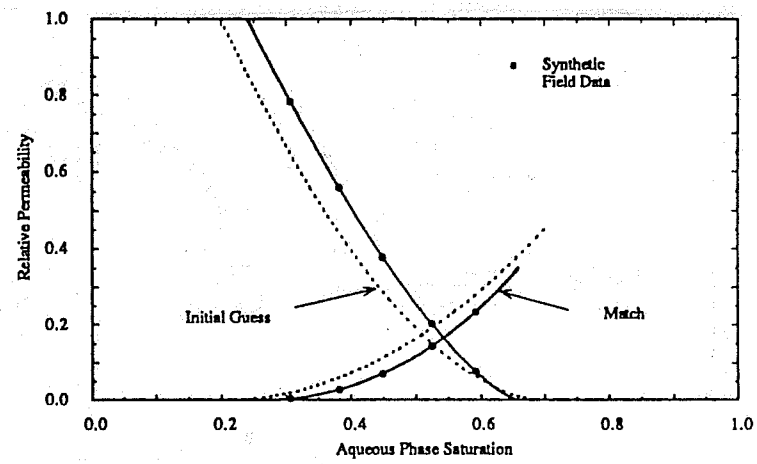

Figure 94. History matching of the relative permeabilities and residual phase saturations, using least absolute values minimization (Runs R1W30A and R1W52I)

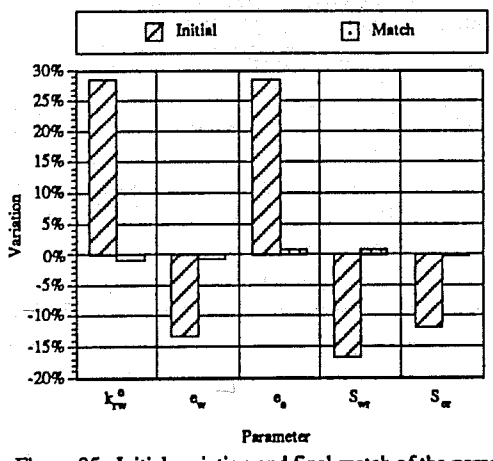

Figure 95. Initial variation and final match of the parameters using least absolute values (Run R1W52I)

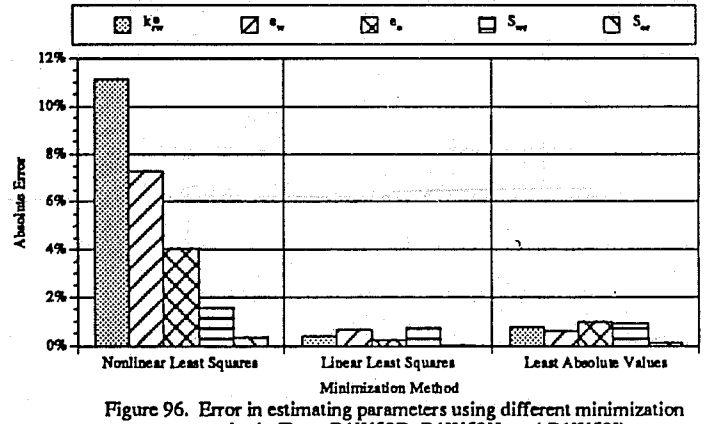

Figure 96. Error in estimating parameters using different minimization methods (Runs R1W52D, R1W52H, and R1W52I)

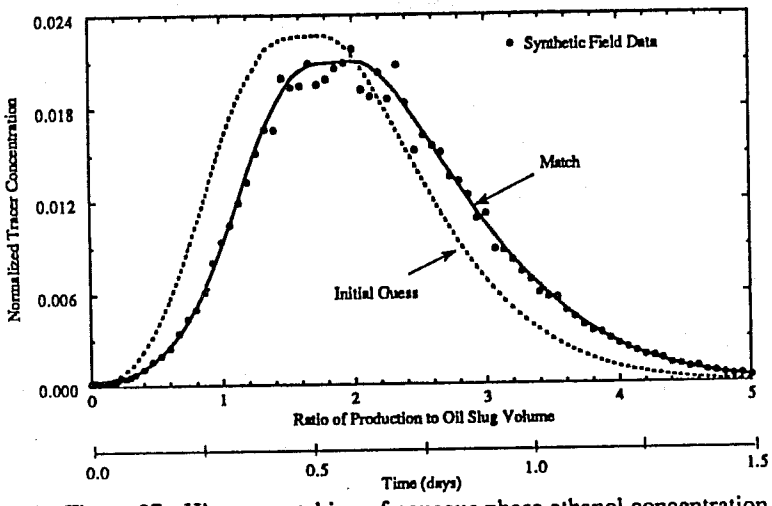

Figure 97. History matching of aqueous phase ethanol-concentration history (Runs R1W54 and R1W56)

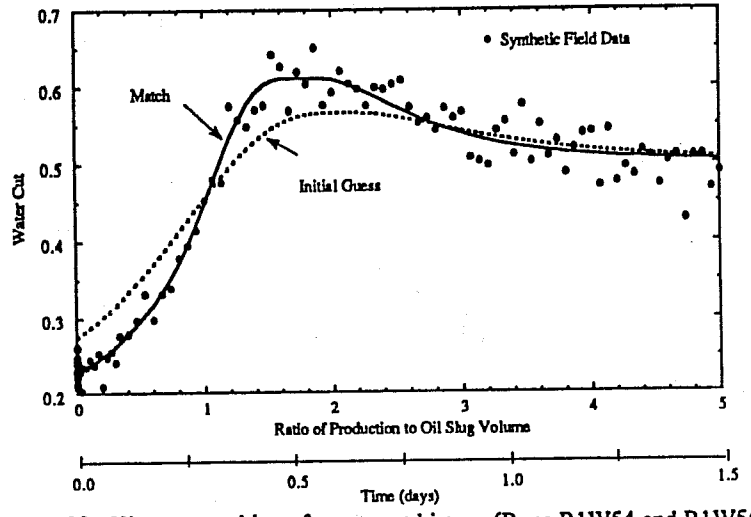

Figure 98. History matching of water-cut history (Runs R1W54 and R1W56)

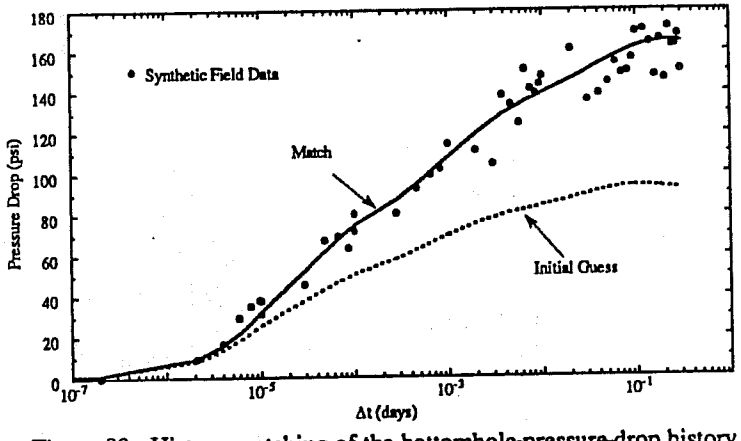

Figure 99. History matching of the bottomhole-pressure-drop history during water injection (Runs R1W54 and R1W56)

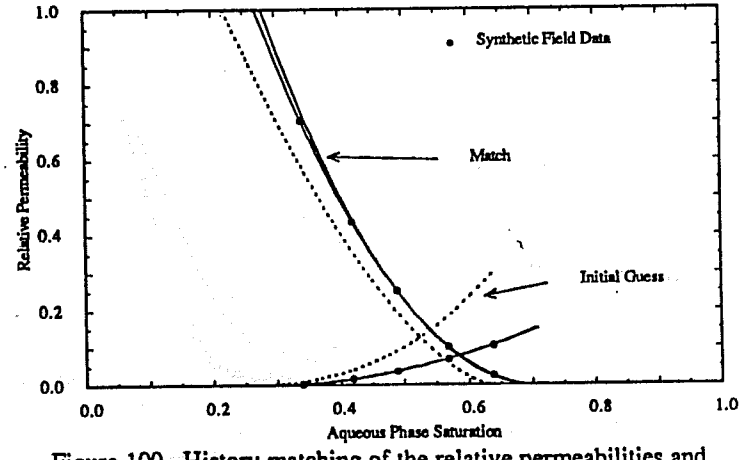

Figure 100. History matching of the relative permeabilities and residual phase saturations (Runs R1W54 and R1W56)

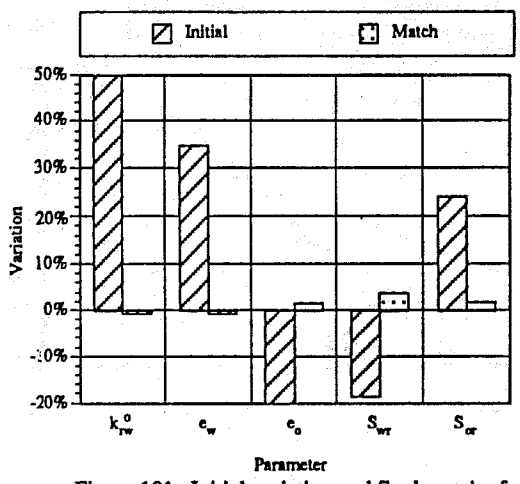

Figure 101. Initial variation and final match of the parameters (Run R1W56)

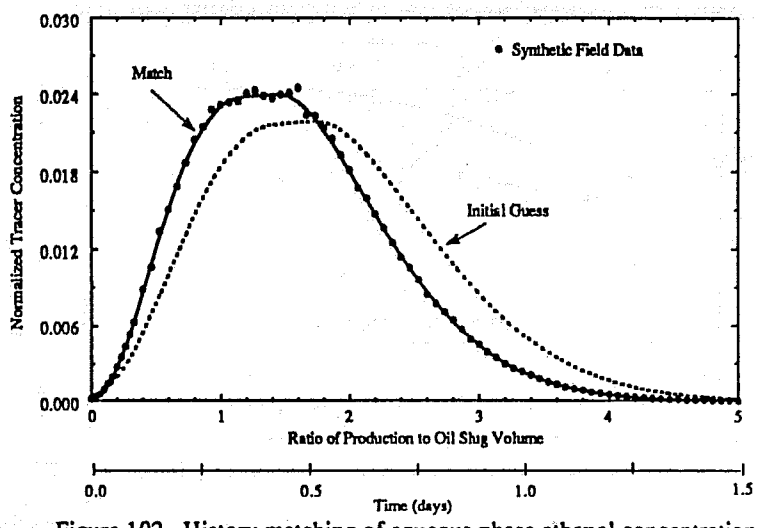

Figure 102. History matching of aqueous phase ethanol-concentration history, 10% error added (Runs R1O00 and R1O33)

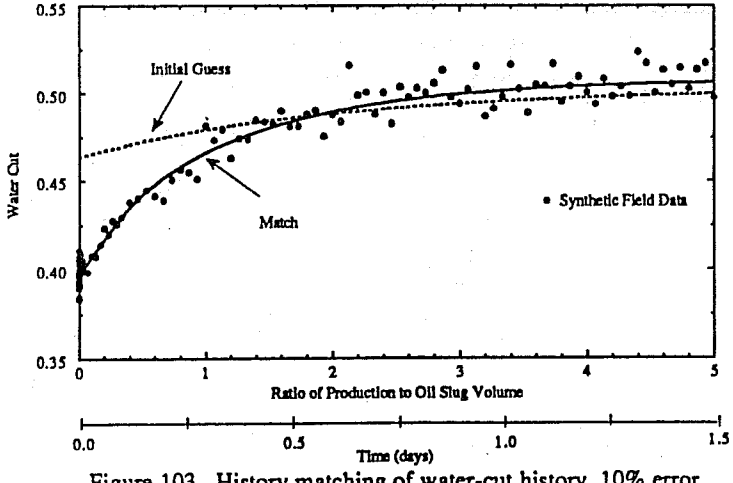

Figure 103. History matching of water-cut history, 10% error added (Runs R1O00 and R1O33)

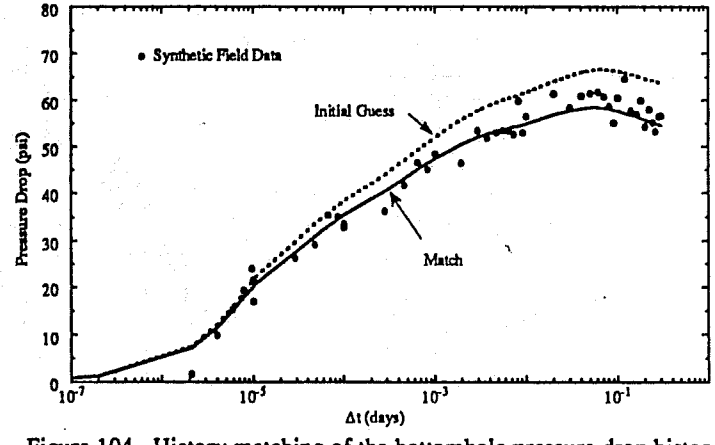

Figure 104. History matching of the bottomhole-pressure-drop history, 0.5% error added (Runs R1O00 and R1O33)

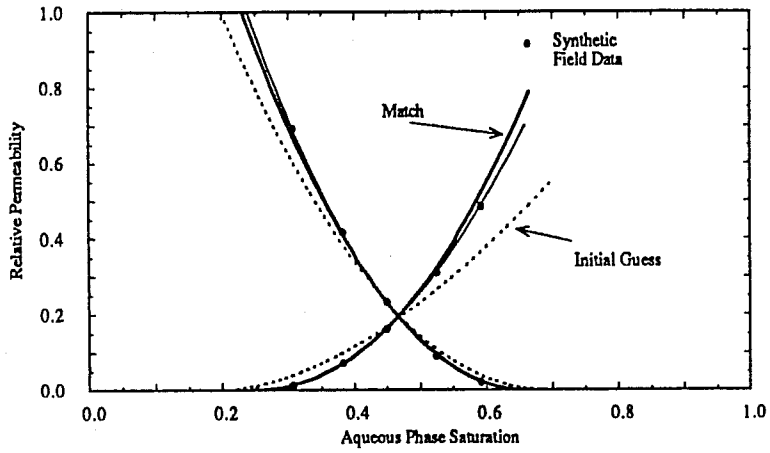

Figure 105. History matching of the relative permeabilities and residual phase saturations (Runs R1O00 and R1O33)

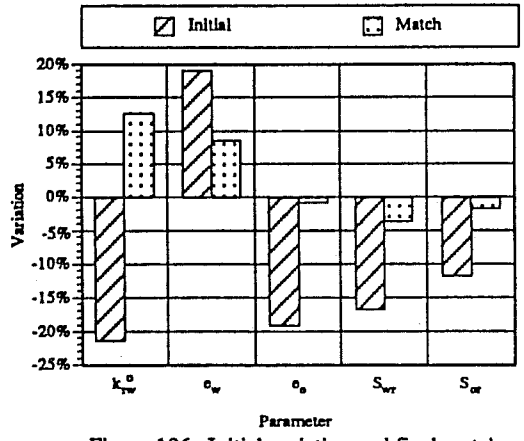

Figure 106. Initial variation and final match of the parameters (Run R1O33)

NOMENCLATURE

a	=	constant in the equation of state
a_{ik}	=	equation-of-state parameter
A	=	area (ft^2)
A	=	matrix (Section IV)
b	=	constant in the equation of state
$\mathbf{b}$	=	solution vector
B	=	equation-of-state parameter
B_g	=	gas formation-volume factor (reservoir volume/surface volume)
c	=	produced tracer concentration
c_D	=	dimensionless tracer concentration
c_{Dk}	=	dimensionless tracer concentration for layer k
c_{DT}	=	overall dimensionless tracer concentration from all layers
$c_{i,g}$	=	concentration of tracer i in the vapor phase (per volume basis)
$c_{i,o}$	=	concentration of tracer i in the oleic phase (per volume basis)
$c_{i,w}$	=	concentration of tracer i in the aqueous phase (per volume basis)
C	=	tracer concentration (volume fraction)
C	=	correlation coefficient matrix (Section IV)
C_o	=	injected tracer concentration (volume fraction)
$\mathbf{d}$	=	vector of the test responses
e_o	=	exponent of oil relative permeability curve
e_w	=	exponent of water relative permeability curve
f	=	function to be minimized
$\hat{f}_i^l$	=	fugacity of tracer i in the liquid phase in the mixture
$\hat{f}_i^v$	=	fugacity of tracer i in the vapor phase in the mixture
$\hat{f}_i^{oleic}$	=	fugacity of tracer i in the oleic phase in the mixture
$\hat{f}_i^{aq}$	=	fugacity of tracer i in the aqueous phase in the mixture
f_i^0	=	fugacity of tracer i at reference state
H	=	reservoir thickness (ft)
$\mathbf{J}$	=	Jacobian matrix
k	=	permeability (md)
k_{ro}^o	=	endpoint relative permeability curve for oil
k_{rw}^o	=	endpoint relative permeability curve for water
k_X	=	horizontal permeability (md)
k_Z	=	vertical permeability (md)
K_i	=	equilibrium ratio (mole fraction)
$K_{T,i}$	=	tracer partition coefficient per volume basis
$\mathbf{l}$	=	vector of the lower-bound values of the parameters
L	=	distance between injector and producer (ft)
m_i	=	mass of tracer injected (lb_m)
m_p	=	mass of tracer produced (lb_m)
N_{Pe}	=	Peclet number (dimensionless)
P_c	=	critical pressure (psia)
P_i^{vap}	=	vapor pressure of pure tracer i
Q	=	rate between injector and producer (ft^3)

Q_i = injection rate (ft^3)
Q_p = production rate (ft^3)
r = distance from injector (ft)
r_i = residue at x_i
R_L = effective length-thickness ratio
s = Laplace transform variable
s_f^2 = estimate of the variance of the match
S = simulation results
S_g = gas saturation (fraction)
S_{oi} = initial oil saturation (fraction)
S_{or} = residual water saturation (fraction)
S_w = water saturation (fraction)
S_{wr} = residual water saturation (fraction)
SSE = sum of the squares of the residuals
t = time (days)
$\bar{t}$ = first moment
t_D = dimensionless time
T_b = normal boiling point at 1 atm (° C)
T_c = critical temperature (° R)
T_{fp} = normal freezing point (° C)
u = flux (ft/day)
$\mathbf{u}$ = vector of the upper-bound values of the parameters
v = total velocity (ft/day)
v_x = X component of velocity (ft/day)
v_y = Y component of velocity (ft/day)
v_z = Z component of velocity (ft/day)
V = cumulative produced water volume since start of tracer injection (ft^3)
V_{DP} = Dykstra-Parsons coefficient
W_t = molecular weight (lb_m/lb mol)
x_D = dimensionless distance
x_i = mole fraction of tracer i in the liquid phase
x_i = position in time where a response is known (Section IV)
x_i^{aq} = mole fraction of tracer i in the aqueous phase
x_i^{oleic} = mole fraction of tracer i in oleic phase
y = vector containing the differences between the initial guess simulation and the data
y_i = mole fraction of tracer i in gaseous phase

Greek Symbols

α = scaled variable
β = vector of the parameters being searched
γ_i^{aq} = activity coefficient of tracer i in the aqueous phase
γ_i^{oleic} = activity coefficient of tracer i in the oleic phase
δ_{ij} = binary interaction parameter
δ_{ik} = binary interaction parameter
Δ = variation, gridblock dimension

ζ^{l} = liquid phase molar density (lb mole/ft3)
ζ^{oleic} = oleic phase molar density (lb mol/ft3)
ζ^{v} = vapor phase molar density (lb mol/ft3)
μ_o = oil viscosity (cp)
μ_w = water viscosity (cp)
ρ_L = liquid density (gm/cc)
$\sigma_{\ln k}$ = standard deviation of ln k
$\sigma^2_{\beta j}$ = variance of the parameter
ϕ = porosity (fraction)
ω = Pitzer's accentric factor

Subscripts

j = parameter number j (Section IV)
i = function number (Section IV)

Superscript

T = transpose of a matrix or vector (Section IV)

REFERENCES

Aarts, E. H. L. and J.H.M. Korst: *Simulated Annealing and Boltzmann Machines* John Wiley & Sons, Chichester, U.K. (1989).

Abbaszadeh-Denghani, M. and M. Kamal: "Automatic Type-Curve Matching for Well Test Analysis," *SPE Form. Eval.* (September 1988) **4**, 567-577.

Albright, J.C.: "Use of Well Logs to Characterize Fluid Flow in the Maljamar CO_2 Pilot," paper SPE 13142 presented at the SPE 59th Annual Technical Conference and Exhibition, Houston, TX, September 16-19, 1984.

Anterion, F., R. Eymard, and B. Karcher: "Use of Parameter Gradients for Reservoir History Matching," paper SPE 18433 presented at the 1989 SPE Symposium on Reservoir Simulation, Houston, TX, February 6-8.

Aris R.: "On the Dispersion of Linear Kinematic Waves," *Proc. Roy. Soc.* (London), **A245**, 268 (1958).

Barrodale, I. and F.D.K. Roberts: "An Improved Algorithm for Discrete L_1 Approximation," *SIAM Journal on Numerical Analysis* (October 1973) **10**, 839-848.

Barrodale, I. and F.D.K. Roberts: "Solution of an Overdetermined System of Equations in the L_1 Norm," *Communications of the ACM* (June 1974) **17**, 319-320.

Barua, J., R.N. Horne, J.L. Greenstadt, and L. Lopez: "Improved Estimation Algorithms for Automated Type-Curve Analysis of Well Tests," *SPE Form. Eval.* (March 1988) **3**, 186-196.

Beier, R.A. and C.Q. Sheely: "Tracer Surveys to Identify Channels for Remedial Work Prior to CO_2 Injection at MCA Unit, New Mexico," paper SPE/DOE 17371 presented at the SPE/DOE Enhanced Oil Recovery Symposium, Tulsa, OK, April 17-20, 1988.

Bernardo Gil, M.G.: "Mutual Binary Solubilities: Perfluoromethylcyclohexane-hydrocarbons," *Fluid Phase Equil.*, **41**, 205-214 (1988).

Cooke, C.E. Jr.: "Method of Determining Residual Oil Saturation in Reservoirs," U.S. Patent No. 3,590,923 (July 6, 1971).

Datta Gupta, A.: personal communication (1992).

Datta Gupta, A.: "Stochastic Heterogeneity, Dispersion and Field Tracer Response," Ph.D. dissertation, The U. of Texas, Austin (1992).

Datta Gupta, A., L.W. Lake, G.A. Pope, and M.J. King, "A Type-Curve Approach to Analyzing Two-Well Tracer Tests," paper SPE/DOE 24139 presented at the SPE/DOE Eighth Symposium on Enhanced Oil Recovery, Tulsa, OK, April 22-24, 1992.

Deans, H.A. and J.R. Bragg: "Method for Determining Fluid Saturations in Reservoirs," U.S. Patent 4,090,398 (January 1977).

Deans, H.A. and S. Majoros: "The Single-Well Chemical Tracer Method for Measuring Residual Oil Saturation," Final Report DOE/BC/20006-18, October 1980.

Deans, H.A.: "Method of Determining Fluid Saturations in Reservoirs," U.S. Patent 3,623,842 (November 30, 1971).

Dennis, J.E. and R.B. Schnabel: *Numerical Methods for Unconstrained Optimization and Nonlinear Equations*, Prentice Hall Inc., Englewood Cliffs, NJ (1983).

Dogru, A.H., T.N. Dixon, and T.F. Edgar: "Confidence Limits on the Parameters and Predictions of Slightly Compressible, Single-Phase Reservoirs," *Soc. Pet. Eng. J.* (February 1977) **17**, 42-56; *Trans.*, AIME, **263**

Dustad, ø., T. Bjørnstad, and I.A. Hundere: "Measurements and Application of Partition Coefficients of Compounds Suitable for Tracing Gas Injected into Oil Reservoirs," Revue De L'Institut Francais Du Petrole, **47**(2), 205-215 (1992).

Ferreira, L.E.A.: "Reservoir Characterization Using Single-Well Tracer Tests," Ph.D. dissertation, The U. of Texas, Austin (1992).

Ferreira, L.E.A., F.J. Descant, M. Delshad, G.A. Pope, and K. Sepehrnoori: "A Single-Well Tracer Test to Estimate Wettability," paper SPE/DOE 24136 presented at the SPE/DOE Eighth Symposium on Enhanced Oil Recovery, Tulsa, OK, April 22-24, 1992.

Fletcher, R.: *Practical Methods for Optimization,* John Wiley & Sons, New York, NY (1990).

Ganapathy, S., D.G. Wreath, M.T. Lim, B.A. Rouse, G.A. Pope, and K. Sepehrnoori: "Simulation of Heterogeneous Sandstone Experiments Characterized Using CT Scanning," *SPE Form. Eval.* (December 1993), 273-279.

Garey, M.R. and D.S. Johnson: *Computers and Intractability: A Guide to the Theory of NP-Completeness*, W.H. Freeman, San Francisco, CA (1979).

Gesink, J.C., E.A. Vanden Bergen, and A.R. de Monchy: "Use of Gamma Ray-Emitting Tracers and Subsequent Gamma Ray Logging in an Observation Well to Determine the Preferential Flow Zones in a Reservoir," paper SPE 12185 presented at the SPE 58th Annual Technical Conference and Exhibition, San Francisco, CA, October 5-8, 1983.

Gill, P.E., W. Murray, and M.H. Wright: *Practical Optimization,* Academic Press Inc., San Diego, CA (1988).

Goldberg, D.E.: *Genetic Algorithms in Search, Optimization and Machine Learning*, Addison Wesley Publishing Company, New York (1989).

Haan, C.T.: *Statistics Methods in Hydrology,* The Iowa State University Press, Ames, Iowa (1991).

Himmelblau, D.M. and K.B. Bischoff: *Process Analysis and Simulation: Deterministic Systems*, John Wiley & Sons, Inc., New York, 1968.

Hundere, I.: "Determination of Partitioning Coefficients of PFT-Tracers in Oil/Gas System," personal communication, December 20,1991.

Huyakorn, P.S., P.F. Anderson, F.J. Molz, O. Guven, and J.G. Melville: "Simulations of Two-Well Tracer Test in Stratified Aquifers at the Chalk River and the Mobile Sites," *Water Resources Research* (1986) **22**, No. 7, 1016-1030.

IMSL FORTRAN Subroutines for Mathematical Analysis, MATH/LIBRARY, User's Manual, Version 1.1 (December 1989).

IMSL FORTRAN Subroutines for Statistical Analysis, STAT/LIBRARY, User's Manual, Version 1.1 (January 1989).

Jahns, O.H: "A Rapid Method for Obtaining a Two-Dimensional Reservoir Description from Well Pressure Response Data," *Soc. Pet. Eng. J.* (December 1966) **6**, 315-327.

Johnson, D.S., C.R. Aragon, L.A. McGeoch, and C. Schevon: "Optimization by Simulated Annealing: An Experimental Evaluation, Part I, Graph Partitioning," *Oper. Res.* (1989) **37**, 865-892.

Johnson, D.S., C.R. Aragon, L.A. McGeoch, and C. Schevon: "Optimization by Simulated Annealing: An Experimental Evaluation, Part II, Graph Coloring and Number Partitioning," *Oper. Res.* (1991) **39**, 378-406.

Khan, S.A.: "An Expert System to Aid in Compositional Simulation of Miscible Gas Flooding," Ph.D. dissertation, The U. of Texas, Austin (1992).

Kirkpatrick, S., C.D. Gelatt, and M.P. Vecchi: "Optimization by Simulated Annealing," *Science* (May 13, 1983) **220**, 671-680.

Kurihara, M.: personal communication (1994).

Levenspeil, O. and W.K. Smith: "Diffusion-Type Model for the Longitudinal Mixing in Flow," *Chem. Eng. Sci.*, **6**, 227 (1957).

Marle, C.M.: *Multiphase Flow in Porous Media*, Editions Technip, Paris (1981).

Maroongroge, V.: "Modeling and Application of Tracers for Reservoir Characterization," Ph.D. dissertation, The U. of Texas, Austin (Aug. 1994).

Mattax, C.C. and R.L. Dalton: *Reservoir Simulation*, Monograph Series, Soc. Pet. Eng., Dallas, TX (1990) **13**.

"MER Performance Review, 26R Reservoir, N/A Reservoir," (1991).

Mut, A.D. and H.A. Deans: "Alcohol Extraction Technique for the In-Situ Determination of Resident Water Saturation and Resident Brine Salinity," paper SPE 12094 presented at the 1983 SPE Annual Tech. Conf. and Exhibition, San Francisco, CA, October 5-8.

Neuman, S.P.: "Universal Scaling of Hydraulic Conductivities and Dispersivities in Geologic Media," *Water Resour. Res.*, **26**(8), 2377-2391 (1990).

Pande, K.: personal communication (June 17, 1991).

Peng, D.Y. and D.B. Robinson: "A New Two-Constant Equation of State," *Ind. Eng. Chem. Fundam.* (1976) **15**, No. 1, 59-64.

Pickens, J.F. and G.E. Grisak: "Scale Dependent Dispersion in a Stratified Granular Aquifer," *Water Resources Research* (1981) **17**, No. 4, 1191-1211.

Pickens, J.F., J.A. Cherry, G.E. Grisak, W.F. Merritt, and B.A. Risto: "A Multilevel Device for Ground-Water Sampling and Piezometric Monitoring," *Ground Water* (1978) **16**, No. 5, 322-327.

Pope, G.A. and K. Sepehrnoori: "Innovative Techniques for the Description of Reservoir Heterogeneity Using Tracers," 2nd Technical Annual Progress Report for the period October 1991 – September 1992, work performed under contract No. DE-AC22-90BC14653 (Feb. 1993).

Pope, G.A. and K. Sepehrnoori: "Innovative Techniques for the Description of Reservoir Heterogeneity Using Tracers," Quarterly Report for the period October 1992 – December 1992, work performed under contract No. DE-AC22-90BC14653 (1993).

Pope, G.A. and K. Sepehrnoori: "Innovative Techniques for the Description of Reservoir Heterogeneity Using Tracers," Quarterly Report for the period January 1993 – March 1993, work performed under contract No. DE-AC22-90BC14653 (1993).

Pope, G.A. and K. Sepehrnoori: "Innovative Techniques for the Description of Reservoir Heterogeneity Using Tracers," Quarterly Report for the period April 1993 – June 1993, work performed under contract No. DE-AC22-90BC14653 (1993).

Press, W.H., B.P.M, Flannery, S.A. Teukolsky, and W.T. Vetterling: *Numerical Recipes The Art of Scientific Computing (FORTRAN Version),* Cambridge University Press, New York, NY (1990).

Reid, R.C., J.M. Prausnitz, and B.E. Poling: *The Properties of Gases & Liquids*, 4th ed., McGraw-Hill Book Company, Singapore (1988).

Reudelhuber, F.O.: "Reservoir Fluid Study For Unit Operation-N.P.R. No. 1, Standard Oil Company of California, Operator: Well No. 73-11G, Elk Hills Field, Kern County, Ca.," Core Laboratories, Inc. (July 18, 1952).

Rial, M.R.: "Naval Petroleum Reserve No. 1, Kern County, California, 26R Detailed Reservoir Study, Final Report," Scientific Software -Intercomp, Inc. (April 1990).

Robinson, B.A.: "Non-Reactive and Chemically Reactive Tracers: Theory and Applications," Ph.D. dissertation, MIT, Cambridge, MA (1985).

Rosa, A.J. and R.N. Horne: "Automated Type-Curve Matching in Well Test Analysis Using Laplace Space Determination of Parameter Gradient," paper SPE 12131 presented at the 1983 SPE Annual Tech. Conf. and Exhibition, San Francisco, CA, October 5-8.

Rosa, A.J. and R.N. Horne: "Automated Well Test Analysis Using Robust (LAV) Nonlinear Parameter Estimation," paper SPE 22679 presented at the 1991 SPE Annual Tech. Conf. and Exhibition, Dallas, TX, October 6-9.

Sandler, S.I.: *Chemical and Engineering Thermodynamics*, 2nd ed., John Wiley & Sons, New York (1989).

Sen, M., A. Datta Gupta; P.L. Stoffa, L.W. Lake, and G.A. Pope: "Stochastic Reservoir Modeling Using Simulated Annealing and Genetic Algorithm," paper SPE 24754 presented at the SPE 67th Annual Technical Conference and Exhibition, Washington, DC, October 4-7, 1992.

Senum, G.I., R.N. Dietz, T.W. D'Ottavio, R.W. Goodrich, E.A. Cote, and D.J. Spandau: "A Perfluorocarbon Tracer Transport and Dispersion Experiment in the North Sea Ekofisk Oil Field," prepared for the U.S. Dept. of Energy under Contract No. DE-AC02-76CH00016, Bartlesville, OK. (July 1990).

Senum, G.I., R. Fajer, W.E. DeRose, B.R. Harris, Jr., and W.L. Ottaviani: "Petroleum Reservoir Characterization by Perfluorocarbon Tracers," paper SPE/DOE 24137 presented at the SPE/DOE Eighth Symposium on Enhanced Oil Recovery, Tulsa, OK, April 22-24, 1992.

Shah, P.C., G.R. Gavalas, and J.H Seinfeld: "Error Analysis in History Matching: The Optimum Level of Parametrization," *Soc. Pet. Eng. J.* (June 1978) **18**, 219-228.

Shah, P.C., M. Karakas, F. Kuchuk, and L.C. Ayestarán: "Estimation of the Permeabilities and Skin Factors in Layered Reservoirs with Downhole Rate and Pressure Data," *SPE Form. Eval.* (September 1988) **3**, 555-566.

Stiles, L.H., R.M. Chiquito, C.J. George, and L.D. Long: "Design and Operation of a CO_2 Tertiary Pilot: Means San Andres Units," paper SPE 11987 presented at the SPE 58th Annual Technical Conference and Exhibition, San Francisco, CA, October 5-8, 1983.

Tang, J.S. and B.C. Harker: "Interwell Tracer Test to Determine Residual Oil Saturation in a Gas-Saturated Reservoir, Part II, Field Application," paper CIM/SPE 90-130 presented at the 41st Annual Technical Joint Meeting of the Petroleum Society of CIM/SPE, Calgary, Canada, June 11-13, 1990.

Tester, J.W., R.L. Bivins, and R.M. Potter: "Interwell Tracer Analyses of a Hydraulically Fractured Granitic Geothermal Reservoir," *Soc. Pet. Eng. J.*, **22**, 537-554 (1982).

Van der Laan, E.T.: "Notes on the Diffusion-Type Model for the Longitudinal Mixing in Flow (O. Levenspeil, and W.K. Smith)," *Chem. Eng. Sci.*, **7**, 187 (1958).

Van Larrhoven, A.P.J.M. and E.H.L. Aarts: *Simulated Annealing: Theory and Practice*, Kluwer Academic Publishers, Dordrecht, The Netherlands (1987).

Wang, M.: "A Study of Residual Oil Saturation by Polymerflooding on Heterogeneous Porous Media Through Laboratory Coreflooding Experiments," Ph.D. dissertation, The U. of Texas, Austin (1994).

Watson, J.P.: "26R Reservoir Perfluorocarbon Tracer Field Study Recommendation," Work Request W90-0031, Bechtel Petroleum Operations, Inc. (August 10, 1990).

Wreath, D.G.: "A Study of Polymerflooding and Residual Saturation," M.S. thesis, The U. of Texas, Austin (1989).

Yang, A.P.: "Stochastic Heterogeneity and Dispersion," Ph.D. dissertation, The U. of Texas, Austin (1990).

Yu, J.: personal communication (1993).

☆U.S. GOVERNMENT PRINTING OFFICE: 1994 - 660-029/00050